frontiers | Research Topics

Frontier research in equatorial aeronomy and space physics

Edited by
David Hysell, Jorge Luis Chau and Marco Milla

Published in
Frontiers in Astronomy and Space Sciences
Frontiers in Physics

ISSN 1664-8714
ISBN 978-2-8325-6270-3
DOI 10.3389/978-2-8325-6270-3

Generative AI statement
Any alternative text (Alt text) provided alongside figures in the articles in this ebook has been generated by Frontiers with the support of artificial intelligence and reasonable efforts have been made to ensure accuracy, including review by the authors wherever possible. If you identify any issues, please contact us.

About Frontiers

Frontiers is more than just an open access publisher of scholarly articles: it is a pioneering approach to the world of academia, radically improving the way scholarly research is managed. The grand vision of Frontiers is a world where all people have an equal opportunity to seek, share and generate knowledge. Frontiers provides immediate and permanent online open access to all its publications, but this alone is not enough to realize our grand goals.

Frontiers journal series

The Frontiers journal series is a multi-tier and interdisciplinary set of open-access, online journals, promising a paradigm shift from the current review, selection and dissemination processes in academic publishing. All Frontiers journals are driven by researchers for researchers; therefore, they constitute a service to the scholarly community. At the same time, the *Frontiers journal series* operates on a revolutionary invention, the tiered publishing system, initially addressing specific communities of scholars, and gradually climbing up to broader public understanding, thus serving the interests of the lay society, too.

Dedication to quality

Each Frontiers article is a landmark of the highest quality, thanks to genuinely collaborative interactions between authors and review editors, who include some of the world's best academicians. Research must be certified by peers before entering a stream of knowledge that may eventually reach the public - and shape society; therefore, Frontiers only applies the most rigorous and unbiased reviews. Frontiers revolutionizes research publishing by freely delivering the most outstanding research, evaluated with no bias from both the academic and social point of view. By applying the most advanced information technologies, Frontiers is catapulting scholarly publishing into a new generation.

What are Frontiers Research Topics?

Frontiers Research Topics are very popular trademarks of the *Frontiers journals series*: they are collections of at least ten articles, all centered on a particular subject. With their unique mix of varied contributions from Original Research to Review Articles, Frontiers Research Topics unify the most influential researchers, the latest key findings and historical advances in a hot research area.

Find out more on how to host your own Frontiers Research Topic or contribute to one as an author by contacting the Frontiers editorial office: frontiersin.org/about/contact

Frontier research in equatorial aeronomy and space physics

Topic editors

David Hysell — Cornell University, United States

Jorge Luis Chau — Leibniz Institute of Atmospheric Physics (LG), Germany

Marco Milla — Pontifical Catholic University of Peru, Peru

Citation

Hysell, D., Chau, J. L., Milla, M., eds. (2025). *Frontier research in equatorial aeronomy and space physics*. Lausanne: Frontiers Media SA.

doi: 10.3389/978-2-8325-6270-3

Table of contents

frontiers | Frontiers in Astronomy and Space Sciences

TYPE Editorial
PUBLISHED 08 April 2025
DOI 10.3389/fspas.2025.1595863

OPEN ACCESS

EDITED AND REVIEWED BY
Joseph E. Borovsky,
Space Science Institute (SSI), United States

*CORRESPONDENCE
D. L. Hysell,
david.hysell@cornell.edu

RECEIVED 18 March 2025
ACCEPTED 28 March 2025
PUBLISHED 08 April 2025

CITATION
Hysell DL, Chau JL and Milla MA (2025) Editorial: Frontier research in equatorial aeronomy and space physics.
Front. Astron. Space Sci. 12:1595863.
doi: 10.3389/fspas.2025.1595863

Editorial: Frontier research in equatorial aeronomy and space physics

D. L. Hysell[1]*, J. L. Chau[2] and M. A. Milla[3]

[1]Department of Earth and Atmospheric Sciences, Cornell University, Ithaca, NY, United States, [2]Leibniz Institute of Atmospheric Physics at the University of Rostock, Kuehlungsborn, Germany, [3]Instituto de Radioastronomia, Pontificia Universidad Católica del Perú, Lima, Peru

KEYWORDS

equatorial aeronomy, ionosphere, space weather, forecasting, Frontier research

Editorial on the Research Topic
Frontier research in equatorial aeronomy and space physics

Pioneering aeronomy and space physics research has long been underway near the geomagnetic equator where, for example, a magnetic observatory has been in operation in Huancayo, Peru, since 1919 when it was founded by the Carnegie Institution (Ishitsuka, 2015). In the 1930s, the Huancayo Observatory also hosted cosmic ray detectors and an ionosonde prototype which can be seen today as having been the first pulsed radars in operation anywhere. The ionosonde propelled ionospheric research and discovered so-called "equatorial spread *F*" (ESF), a disruptive form of space weather that obscures ionograms among its many effects (Booker and Wells, 1938). ESF continues to consume much of the attention of the aeronomy community. Due in part to the notoriety of the Huancayo Observatory, the Jicamarca Radio Observatory was established near Lima in the 1960s at about the same time as the Arecibo Radio Observatory in Puerto Rico. Well before it was even completed, Jicamarca was producing some of the earliest incoherent scatter radar observations of the ionosphere (Woodman et al., 2019). Early results from Jicamarca identified some discrepancies in the theory of incoherent scatter emerging at that time and paved the way to their resolution (Bowles et al., 1962; Farley, 1964; Dougherty, 1964). Jicamarca also detected intense coherent scatter from field-aligned plasma density irregularities (FAIs) in the *F* region that would be associated with ESF (Farley et al., 1970). Moreover, it observed FAIs in the *E* region coming from the electrojet, a strong, permanent current system that had been studied systematically much earlier at Huancayo (Bowles et al., 1960). Pioneering observational and theoretical studies established a variety of plasma instabilities as the causes of *E*- and *F*-region FAIs shortly thereafter (Farley, 1963; Balsley and Farley, 1971; Woodman and La Hoz, 1976). These discoveries ushered an age of computational simulations and explorations of the instabilities in question. Notably, the instabilities do not rely on solar or geomagnetic activity for their existence, distinguishing the equatorial zone from middle and high latitudes.

In subsequent years, additional plasma instabilities would be discovered to inhabit the equatorial ionosphere where the horizontal geomagnetic field lines support a range of instability mechanisms that cannot operate elsewhere. These include unstable, long-lived, non-specular meteor trail echoes (Chapin and Kudeki, 1994), the so-called "150-km echoes" found in the daytime valley region (Balsley, 1964),

seemingly unrelated irregularities that sometimes occur in the nighttime valley region (Chau and Hysell, 2004), and topside irregularities characterized by a lower-hybrid resonance observed in the inner magnetosphere during solar minimum (Derghazarian et al., 2021). That some of these phenomena have been discovered only recently hints at the possibility of still more instability mechanisms awaiting discovery.

The purpose of this Research Topic was to capture contemporary discovery research pertaining to observation, theory, and modeling of processes in the equatorial ionosphere. Unsurprisingly, most of the submissions deal with plasma instabilities and irregularities. More surprisingly, some of them prompt a reexamination of the theory used in aeronomy research, the experimental methods, and some of the assumptions underlying causality and variability, particularly as it pertains to space weather.

The equatorial plasma depletions or bubbles (EPBs) at the root of ESF were reconsidered by a number of authors in this Research Topic. Wu et al. demonstrated a novel method for geolocating plasma irregularities responsible for radio scintillations globally using satellite measurements. Kirchman et al. argued that practical forecasts of the phenomenon based mainly on background electric field measurements are possible and practical, but the underlying electric fields themselves are highly variable even during quiet times and remain difficult to predict. However, Yokoyama showed that the *E*-region conductivity also plays a crucial role in EPB occurrence. Additionally, Bossart et al. found an association between EPB occurrence and the positive/northward meridional wind phase of the quasi-two-day wave in the mesosphere. Finally, Huba reviewed the complicated role of meridional winds on EPB occurrence including destabilization associated with the midnight temperature maximum. Together, the papers constitute a study of overlooked influences on equatorial ionospheric stability that cannot be neglected.

Subjects of the Research Topic were not confined to EPBs, however. Yamazaki et al. examined the afternoon equatorial electrojet from the point of view of CSES satellite data, showing that the current is governed mainly by the DE3 and DE2 tidal modes while also scaling in intensity with the local electron density.

To the extent quiet-time ionospheric variability arises from variability in the mesospheric and lower thermospheric winds, methods of forecasting the latter takes on central importance in equatorial aeronomy and space weather. Mauricio et al. describe a hybrid model combining time-series analysis with machine learning, showing that it outperforms other models based on conventional, established forecast methods. Machine learning was also applied by Villalba et al., here to the emerging problem of ionogram forecasting.

However, storm-time effects cannot be neglected when considering variability in the equatorial ionosphere. Fejer et al. reviewed experimental and theoretical work relating storm-time drivers to climatological equatorial electrodynamic responses, highlighting the complex and spatially structured pathways involved and outlining the most important questions that remain. Valladares et al. examined large-scale traveling ionospheric and atmospheric disturbances (LSTIDs, LSTADs) from the points of view of space- and ground-based ionospheric measurements, following the flow of energy from polar to equatorial regions carried by these perturbations.

Finally, fundamental theoretical questions regarding how the ionosphere is modeled were examined in this Research Topic. Dimant derived a new set of five-moment fluid equations for electrons and ions starting from kinetic theory, taking into account conditions appropriate for the partially-magnetized *E* region. Their model equations form a basis for more accurate fluid simulations of the *E* region going forward. Koontaweepunya et al. furthermore considered how the strong electric fields in the electrojets can cause the ions to depart from Maxwellian distributions both theoretically and from the point of view of particle-in-cell simulations. They found that the non-Maxwellian distributions led to more isotropic heating than would otherwise be predicted.

The equatorial ionosphere continues to be a wellspring of discovery science with both fundamental and practical findings regularly coming to prominence as the field enters its second century. The future of the research discipline remains bright, with several new instrumentation deployments, experimental campaigns, and model developments in planning or underway. These include sweeping upgrades nearing completion at the Jicamarca Radio Observatory, the modern phased-array Incoherent Scatter Radar in Sanya with tristatic capabilities, the deployment of two LWA-class radio array telescopes (J-ARGUS) that will work together with and also independently of Jicamarca, the deployment of SIMONe-class multistatic meteor radar systems in South America, a NASA sounding rocket campaign (Cielo) tentatively planned for Punta Lobos, Peru in 2028, contributions to equatorial aeronomy by the DYNAMIC and GDC missions, and improvements to coupled GCMs to tackle the problems highlighted by this Research Topic. Research avenues where theory, model and simulation, and experimental work in concert are especially promising.

Author contributions

DH: Writing – original draft. JC: Writing – review and editing. MM: Writing – review and editing.

Funding

The author(s) declare that no financial support was received for the research and/or publication of this article.

Conflict of interest

The authors declare that the research was conducted in the absence of any commercial or financial relationships that could be construed as a potential conflict of interest.

The author(s) declared that they were an editorial board member of Frontiers, at the time of submission. This had no impact on the peer review process and the final decision.

Generative AI statement

The author(s) declare that no Generative AI was used in the creation of this manuscript.

Publisher's note

References

Balsley, B. B. (1964). Evidence of a stratified echoing region at 150 kilometers in the vicinity of the magnetic equator during daylight hours. *J. Geophys. Res.* 69 (1925), 1925–1930. doi:10.1029/jz069i009p01925

Balsley, B. B., and Farley, D. T. (1971). Radar studies of the equatorial electrojet at three frequencies. *J. Geophys. Res.* 76, 8341–8351. doi:10.1029/ja076i034p08341

Booker, H. G., and Wells, H. W. (1938). Scattering of radio waves by the *F* region. *Terres. Magn.* 43, 249–256. doi:10.1029/te043i003p00249

Bowles, K. L., Cohen, R., Ochs, G. R., and Balsley, B. B. (1960). Radar echoes from field aligned *E* region ionization above the magnetic equator and their resemblance to auroral echoes. *J. Geophys. Res.* 65, 1853–1855. doi:10.1029/jz065i006p01853

Bowles, K. L., Ochs, G. R., and Green, J. L. (1962). On the absolute intensity of incoherent scatter echoes from the ionosphere. *J. Res. NBS - D. Rad. Prop.* 66D, 395. doi:10.6028/jres.066d.041

Chapin, E., and Kudeki, E. (1994). Radar interferometric imaging studies of long-duration meteor echoes observed at Jicamarca. *J. Geophys. Res.* 99, 8937–8949. doi:10.1029/93ja03198

Chau, J. L., and Hysell, D. L. (2004). High altitude large-scale plasma waves in the equatorial electrojet at twilight. *Ann. Geophys.* 22, 4071–4076. doi:10.5194/angeo-22-4071-2004

Derghazarian, S., Hysell, D. L., Kuyeng, K., and Milla, M. A. (2021). High altitude echoes from the equatorial topside ionosphere during solar minimum. *J. Geophys. Res.* 126. doi:10.1029/2020JA028424

Dougherty, J. P. (1964). Model Fokker-Planck equation for a plasma and its solution. *Phys. Fluids* 1, 1788–1799. doi:10.1063/1.2746779

Farley, D. T. (1964). The effect of Coulomb collisions on incoherent scattering of radio waves by a plasma. *J. Geophys. Res.* 69, 197–200. doi:10.1029/jz069i001p00197

Farley, D. T. (1963). A plasma instability resulting in field-aligned irregularities in the ionosphere. *J. Geophys. Res.* 68, 6083–6097. doi:10.1029/jz068i022p06083

Farley, D. T., Balsley, B. B., Woodman, R. F., and McClure, J. P. (1970). Equatorial spread *F*: implications of VHF radar observations. *J. Geophys. Res.* 75, 7199–7216. doi:10.1029/ja075i034p07199

Ishitsuka, J. K. (2015). 93 years of geomagnetic data acquisition at the huancayo observatory. *Sun Geosph.* 10, 173–176.

Woodman, R. F., Farley, D. T., Balsley, B. B., and Milla, M. A. (2019). The early history of the Jicamarca Radio Observatory and the incoherent scatter technique. *Hist. Geo Space. Sci.* 10, 245–266. doi:10.5194/hgss–10–245–2019

Woodman, R. F., and La Hoz, C. (1976). Radar observations of *F* region equatorial irregularities. *J. Geophys. Res.* 81, 5447–5466. doi:10.1029/ja081i031p05447

frontiers | Frontiers in Astronomy and Space Sciences

TYPE Methods
PUBLISHED 30 May 2024
DOI 10.3389/fspas.2024.1407457

OPEN ACCESS

EDITED BY
Marco Milla,
Pontifical Catholic University of Peru, Peru

REVIEWED BY
Jeff Klenzing,
National Aeronautics and Space Administration, United States
Yuichi Otsuka,
Nagoya University, Japan

*CORRESPONDENCE
Qian Wu,
qwu@ucar.edu

RECEIVED 26 March 2024
ACCEPTED 09 May 2024
PUBLISHED 30 May 2024

CITATION
Wu Q, Braun J, Sokolovskiy S, Schreiner W, Pedatella N, Weiss J-P, Cherniak I and Zakharenkova I (2024), GOLD plasma bubble observations comparison with geolocation of plasma irregularities by back propagation of the high-rate FORMOSA7/COSMIC 2 scintillation data.
Front. Astron. Space Sci. 11:1407457.
doi: 10.3389/fspas.2024.1407457

GOLD plasma bubble observations comparison with geolocation of plasma irregularities by back propagation of the high-rate FORMOSA7/COSMIC 2 scintillation data

Qian Wu[1,2]*, John Braun[2], Sergey Sokolovskiy[2], William Schreiner[2], Nicholas Pedatella[1,2], Jan-Peter Weiss[2], Iurii Cherniak[2] and Irina Zakharenkova[2]

[1]High Altitude Observatory, National Center for Atmospheric Research, Boulder, CO, United States, [2]COSMIC Program, University Corporation for Atmospheric Research, Boulder, CO, United States

Using the high-rate phase and amplitude scintillation data from FORMOSA7/COSMIC two mission and back-propagation method, we geolocate plasma irregularities that cause scintillations. The results of geolocation are compared with the NASA GOLD UV image data of plasma bubbles. The root mean square of the zonal difference between estimated locations of plasma irregularities and plasma bubbles are about 1.5° and for single intersection cases 0.5° in the magnetic longitude. The geolocation data provide more accurate scintillation location around the globe compared to assigning to the tangent point and is valuable space weather product, which will be routinely available for public use.

KEYWORDS

scintillation, COSMIC, plasma bubble, geolocation, gold

Introduction

Using the FORMOSA7/COSMIC 2 (F7/C2) mission (Anthes and Schreiner, 2019; Yue et al., 2014) GNSS high-rate phase and amplitude data and back-propagation method (Sokolovskiy et al., 2002), we geolocate plasma irregularities that cause scintillations (below we call this geolocation of scintillation for brevity). In the equatorial region, the scintillations are often associated with the plasma bubbles. Plasma bubbles are caused by the Rayleigh-Tayler (R-T) instability on the bottom side of the ionosphere [e.g., Sultan, 1996; Wu, 2015; 2017]. As bubble occurs, the ionosphere develops elongated depletions along the magnetic field lines during the post-sunset hours. The pre-reversal enhancement of the vertical ion drift can lead to positive growth rate of the R-T instability [e.g., Sultan 1996; Wu, 2015]. Inside the bubbles, which have scales hundreds of kilometers, the smaller-scale irregularities develop. These irregularities with scales of order of 1 km or less are responsible for the

scintillation localizable by back propagation. Thus, the geolocation method detects the small-scale plasma irregularities in the bubble, not the bubble itself. This space weather application has a great value as the ionospheric scintillation which affects GNSS signals can greatly disrupt the GNSS and other radio communication systems potentially causing great economical losses.

The US-Taiwan joint mission F2/C2 has six equatorial orbiting satellites and was launched into space on 25 June 2019. All six satellites carry GNSS receivers called Tri-GNSS Radio Occulation System (TGRS) (Tien et al., 2012). The TGRS instruments have an on-board trigger mechanism to transmit high-rate (100 Hz for GLONASS and 50 Hz for GPS) phase and amplitude data (later stored in the scnPhs files) to the ground. The trigger is activated by the on-board GNSS signal S4 value greater than 0.1. By applying the back propagation method to the data from scnPhs files, the F7/C2 team has been producing geolocation of scintillations on a routine basis. In the past, when the S4 value from GNSS RO missions were analyzed, the scintillation was often assigned to the tangent point, which is not true most of the time. The back-propagation method derived geolocation of the scintillation are more accurate compared to using the tangent point. Moreover, the F7/C2 can provide geolocation around the globe.

Because of the strong connection between the scintillation and plasma bubbles, we can assume that bubbles and scintillations are co-located in most of the cases. Detecting and locating bubbles is not easy. Ground based all sky cameras can capture bubbles [e.g., Okoh et al., 2017] as depletions in the O 630 nm redline emission. But they have very limited coverage and are affected by weather conditions. Satellite UV imagers can also detect bubbles in the O 135.6 nm emission, which is proportional to the ion density squared. In the past, most of satellite UV imaging detectors were on high inclination orbits such as TIMED GUVI and DMSP SSUSI instrument (Comberiate and Paxton, 2010). The NASA mission GOLD UV imager (Eastes et al., 2017; Eastes et al., 2020) on board

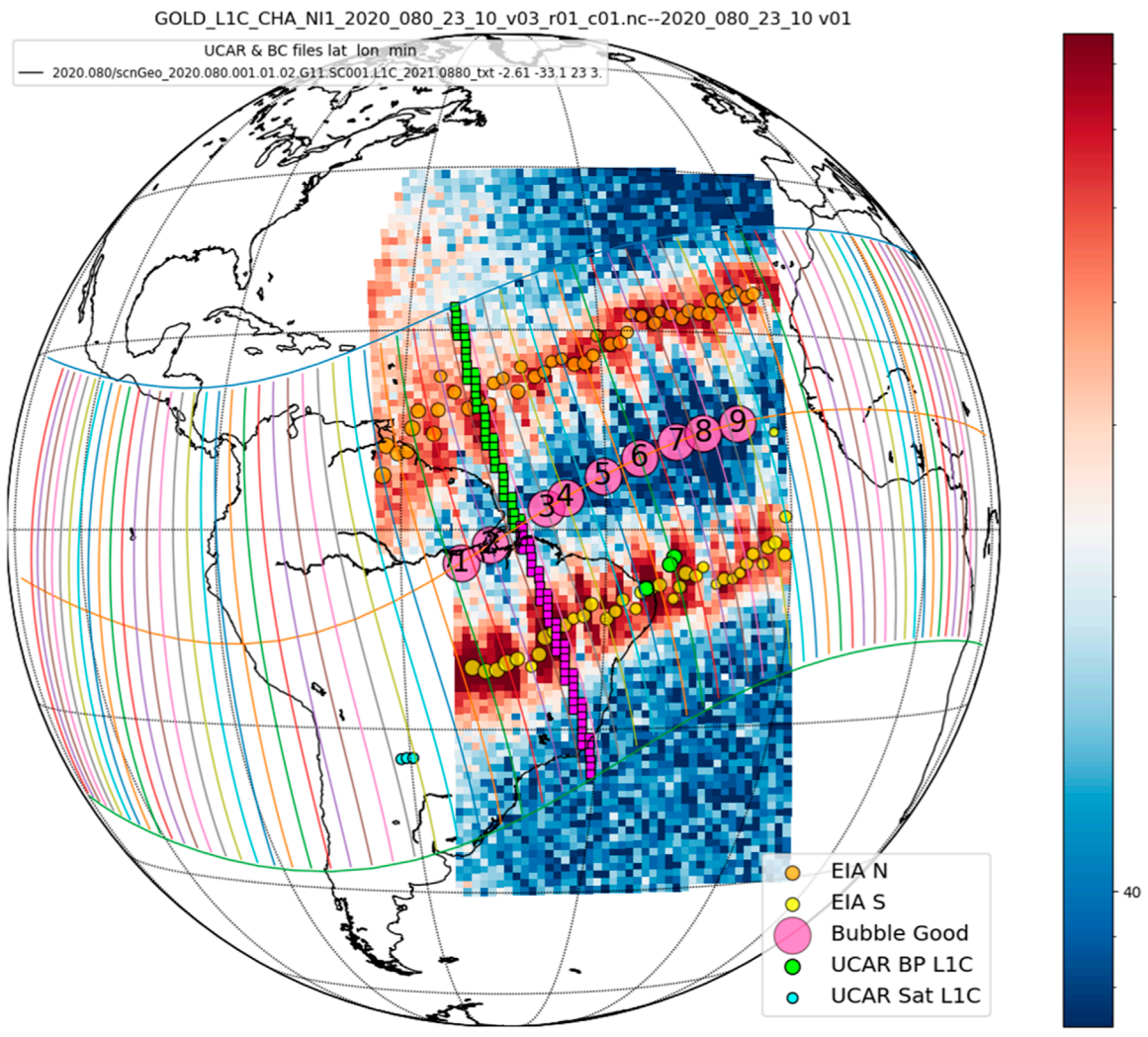

FIGURE 1
Example of GOLD Image of Bubbles with the F7/C2 Geolocations of the Scintillations. The equatorial ionosphere anomalies are also plotted (EIA N, S, orange and yellow circles). Bubbles are plotted at the magnetic equator (magenta cycles). F7/C2 locations (UCAR Sat L1C, cyan circles) and scintillation geolocation (UCAR BP L1C, green circles) are shown. The GOLD image binning pattern for the northern (lime squares) and southern (magenta squares) hemisphere within a 1-degree grid are displayed.

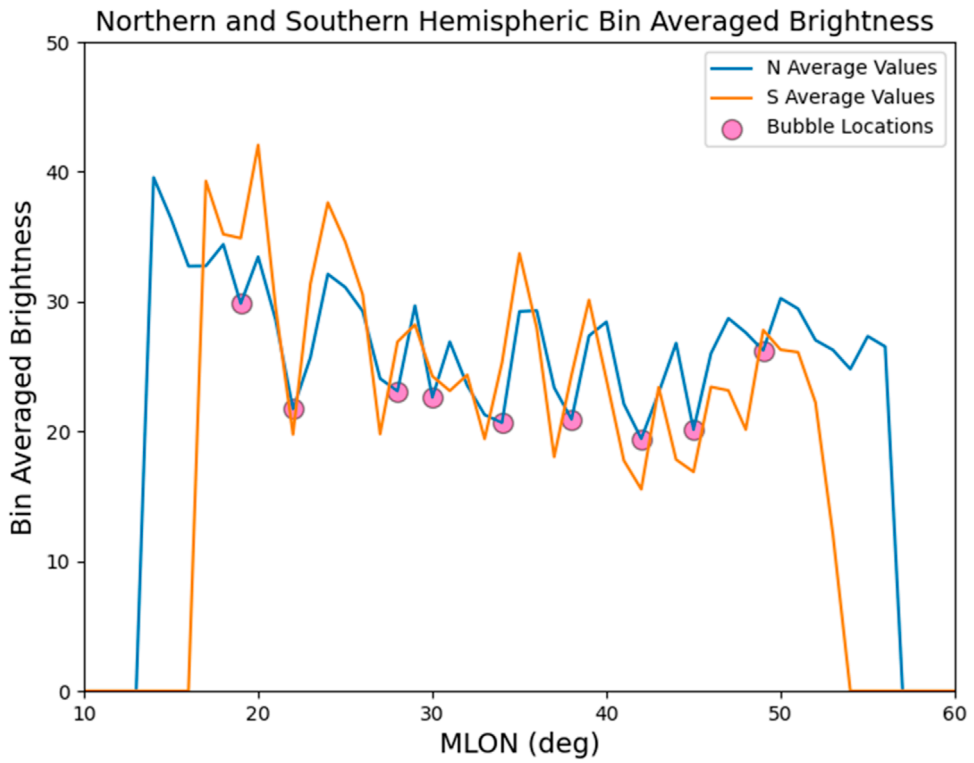

FIGURE 2
The GOLD UV brightness averaged within 1° magnetic longitude grid between 0 and 25 MLAT (north, blue color) and 0 to −25 MLAT (south, orange color). Selected bubble locations at northern UV brightness minima (with southern companions with in 2 degree of MLON). The nine bubbles are also plotted in Figure 1.

a geosynchronous orbit is the first to provide continuous coverage over the American sector and has frequently observed bubbles in the night time data.

Because the F7/C2 back propagation geolocation data will be used for operational purposes, a validation is needed. That can be accomplished by using bubble detection to locate the source of the scintillation and compare with the geolocation results. The GOLD UV bubble images become a logical choice to for this purpose in the American sector. The first step is to develop an algorithm to the determine the bubble locations based on the GOLD UV images.

In this paper, we describe a GOLD UV image bubble location algorithm and comparison with the geolocation. We will discuss the results of validation of the F7/C2 geolocation product and summarize our findings.

GOLD bubble analysis method

GOLD is a NASA mission of UV imager on a geo-synchronous satellite over the American sector (47.5W) [e.g., Eastes et al., 2017; 2020]. The GOLD images cover the American sector, we used the nighttime mode data, which is taken after dusk. We use intensity of the O 135.6 nm emission line in the GOLD UV spectra. Bubbles are often seen in the images.

The GOLD instrument has two identical channels A and B, when the solar terminator just across Africa, channel B is used to do both northern and southern hemisphere for the night mode observation. The northern and southern scan each lasts about 15 min. Hence the combined north and south scan lasts about 30 min. As the solar terminator reaches the American continent, both Channel A and B are used for the night mode observation. Channel A for the northern and B for the southern hemisphere. Because of using two channels, the combined north and south scan lasts only 15 min.

To determine the bubble locations in the magnetic longitude, we bin the GOLD image pixels in 1-degree magnetic longitudinal grids from 25° magnetic north to the magnetic equator. We bin the pixels from the magnetic equator to 25° south for the southern hemisphere with the same magnetic longitudinal grid. Figure 1 shows an example of the binning pattern for the northern (lime) and southern (magenta) hemispheres and GOLD image of plasma bubbles identified. In this way, we have a northern and southern track of binned magnetic longitudinal variation of the UV 135.6 nm emission. To locate bubbles, we search all minimum values in both the northern and southern tracks of the binned GOLD UV 135.6 nm emission (see Figure 2). We should expect the bubbles coincide with the minima in the UV emission. To reduce false positive bubble identifications, we compare the minimum locations in both the northern and southern tracks, if we cannot find minimum within 2 degrees of magnetic longitude in both tracks, we will not flag the minimum as a bubble location. Another reason for comparing the northern and southern track is to ensure the depletion remain roughly in the same magnetic longitude. Because GOLD image is a 2D projection of a 3D ionosphere with plasma bubbles, the depletion from the bubble in the GOLD image may deviate from the same

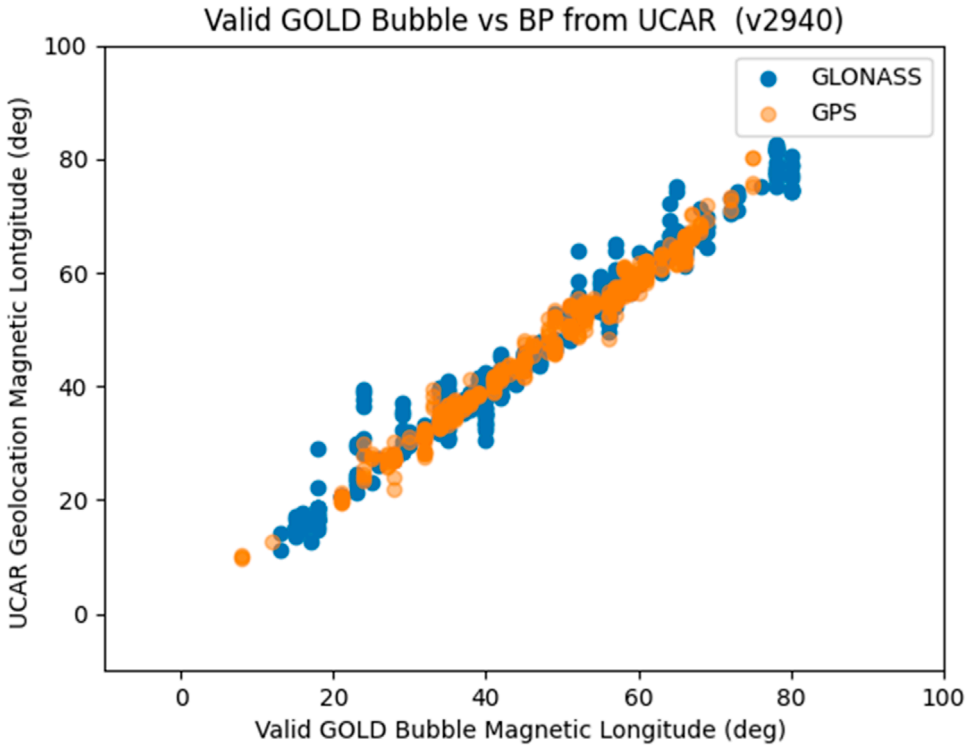

FIGURE 3
The GOLD bubble magnetic longitudes vs. that of the geolocations from GLONASS (blue) and GPS (orange) L1 signals.

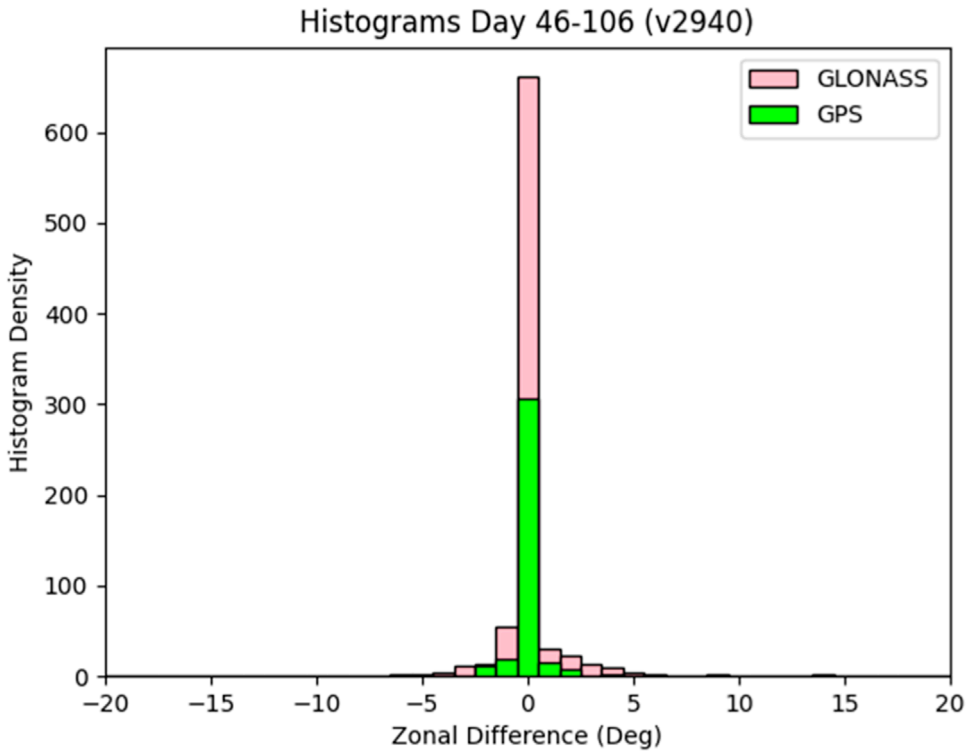

FIGURE 4
Zonal difference distribution between the GOLD bubble and F7/C2 geolocation scintillation. GLONASS and GPS are in different colors.

TABLE 1 GOLD bubble and F7/C2 geolocation zonal difference distribution.

Error (deg)	Samples	%
All	845	100
<5	830	98
<2	772	91
<1	711	84
0	581	69

magnetic longitude. If that is case, our selection criterion will not select the bubble for comparison with geolocation. If we find both northern and southern bubbles, then we pick the northern location for the bubble. Figure 2 shows the nine minima in northern and all nine have companion minima in the southern hemisphere and they are selected as shown in the figure. The locations are plotted on GOLD image in Figure 1.

We also estimate the depth and width of the bubbles. The key to estimate these depth and width is to calculate the baseline for a non-disturbed condition. We used a polynomial fit of the binned UV longitudinal variation of the northern and southern tracks. Because the existing bubbles, the fitted curves will be lower than an ideal baseline. To address this issue with a simple algorithm, we remove the binned UV data below the fitted curve, then use the remaining UV data points above the first fitting curve to do another polynomial fit along the magnetic longitude. The second fit will be much closer to the ideal baseline. We then use that as the baseline in our analysis. The same procedure is used for both northern and southern tracks. To estimate the width of the bubble, we pick the separation of the half way points between the bottom of bubble and the baseline. We will use the larger of the northern and southern bubble width for the bubble width. The deeper depth of the two will be used to represent bubble depth.

While this method can automatically determine bubble locations when the UV emission is strong and bubble depletion contrast is clear, we still have cases, where the bubbles are not apparent in the GOLD images. To ensure no falsely identified bubbles are used in analysis, we used visual inspection of the GOLD images to confirm the automatic search results. The visual inspection is performed by a group of people to reduce bias.

Back propagation method

Back propagation (BP) method has been used to geolocate the scintillation based on the GNSS high-rate phase and amplitude data (Sokolovskiy et al., 2002). The method is based on several assumptions. First, plasma irregularities must occupy limited volume so that wave propagation is considered in the phase screen approximation. In other words, radio waves undergo only phase fluctuations inside the volume. Amplitude fluctuations (observed along receiver trajectory which crosses the direction of wave propagation) develop after propagation through the volume and increase with the distance from the volume due to focusing/defocusing effects caused by the phase fluctuations induced by plasma irregularities. The phase and amplitude measured by the receiver in orbit can be used as the boundary condition for solving wave equation in a vacuum and reconstruction of the phase and amplitude fluctuations back from transmitter to receiver. Amplitude fluctuations decrease from receiver to the region with irregularities and then increase again due to imaginary focusing/defocusing. Thus, the region of minimum amplitude fluctuations traces the region with irregularities. Second, irregularities must be anisotropic (elongated) to reduce wave propagation problem from three to two dimensions. This is needed because the phase and amplitude are measured on 1-dimensional receiver trajectory which is insufficient for solving 3-dimensional wave propagation problem. Third, direction of irregularities must be known for orientation of the BP plane. In the equatorial F region plasma irregularities are aligned with the magnetic field lines which allows to use the magnetic field model (IGRF-13) for orientation of the BP plane. Compared to (Sokolovskiy et al., 2002), the BP method was fully automated and further enhancements improving geolocation accuracy were included (this will be discussed in a separate publication).

In this study, we applied BP in 10-s intervals. This is the trade-off between two conditions: (i) the scanned volume must be large enough to include multiple irregularities which cause scintillation (to reduce the boundary effects in BP) and (ii) must be small enough so that statistical structure of the irregularities must not be substantially different inside the volume. Both (i) and (ii) are required for a more reliable estimation of the distance to minimum of amplitude scintillation by BP.

Comparison of the bubble location and scintillation geolocation

We selected the time period from Day 044–106 in 2020 for the GOLD bubble and F7/C2 scnPhs file geolocation comparison. The selection of the time is associated with F7/C2 calibration/validation of other instruments and mostly coincides with the bubble active period in the American sector.

Figure 1 not only shows the GOLD UV image with bubbles, but also F7/C2 geolocated scintillations. In the figure we also located north and south equatorial ionosphere anomaly (EIA). Since the GOLD bubble has time cadence of 30 min or 15 min, the F2/C2 geolocation (based on 10-s data intervals) can have multiple overlaps with the same GOLD images. We will associate the geolocation with the GOLD bubble that is closest in magnetic longitude to the geolocation. If the geolocation is within the width of the GOLD bubble, then we label that as zero difference. If it is outside the GOLD bubble width, then the distance from edge of the bubble to the geolocation will be assigned as the longitudinal difference. In the case shown in Figure 1, we have three geolocations from one scnPhs file (green circles). The F7/C2 satellite locations are on the west (cyan circles). The scnPhs file data are from the forward POD antenna facing east. Two geolocations on the east, will be associated with bubble # 6, whereas the one on the west will be linked to bubble # 5. UCAR geolocation has the tendency to pick the scintillation near the EIAs as shown in this case. Because both northern and southern hemisphere GOLD data are used, if only one hemisphere data is

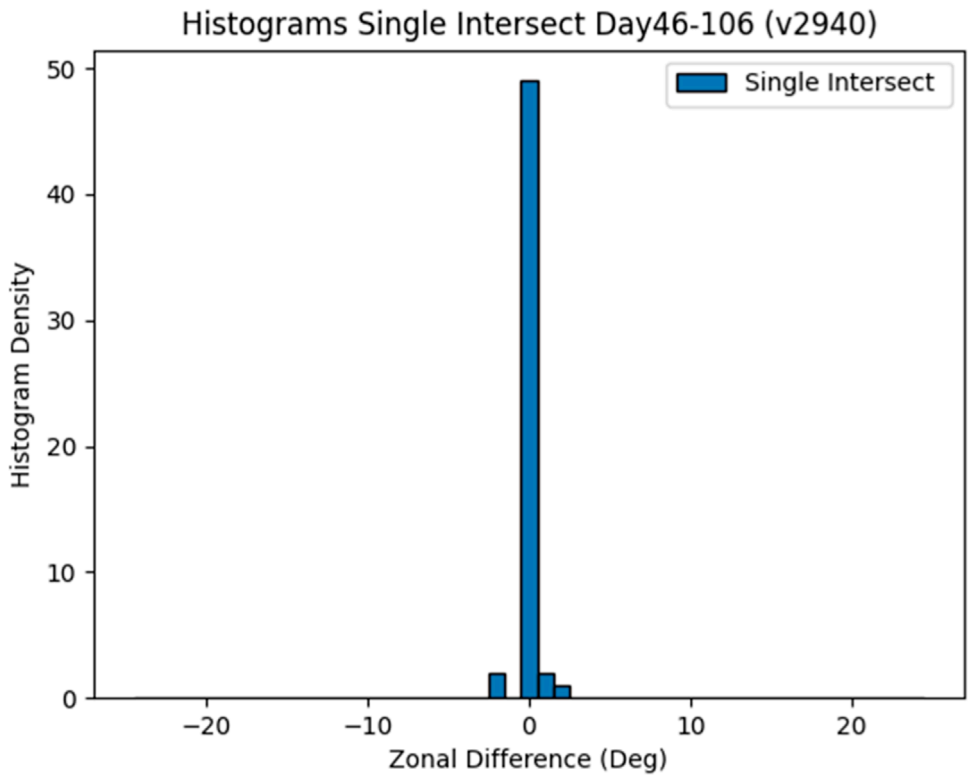

FIGURE 5
Zonal difference distribution between GOLD bubble and F7/C2 geolocation scintillation for single intersection cases.

TABLE 2 Zonal difference statistics between GOLD bubble and F7/C2 scintillation for single intersection cases.

Error (deg)	Samples	%
All	54	100
<5	54	100
<2	54	100
<1	50	92
0	45	83

available, no bubbles will be picked at that magnetic longitude. In Figure 1, there could be a bubble beyond bubble # nine on the east, which was not picked because of missing the southern hemisphere data as shown in Figure 2 the southern hemisphere brightness data end earlier compared to the northern track.

Before the comparison, we inspected all GOLD images with geolocations overplotted on top. The geolocations that are on the edge of GOLD UV image data or do not intersect with the bubbles were removed. A total of 8 GLONASS and 10 GPS scnPhs files were removed for these reasons. A total of 84 GLONASS and 63 GPS scnPhs files are used for our comparison. Out of these scnPhs files we have 479 GLONASS and 366 GPS geolocations based on 10-s intervals.

Figure 3 shows the GOLD bubble magnetic longitudes vs. the F7/C2 geolocation scintillation longitudes. There is a general good agreement between the bubble locations vs. geolocation of scintillations for both GLONASS and GPS. To be more quantitative of the zonal difference, the distribution is plotted in Figure 4. The numerical distributions of zonal difference are listed in Table 1. The RMS of the distribution is 1.57 deg and mean is 0.13 of the distribution.

There are 15 geolocations from seven scnPhs files with zonal differences larger than 5° in magnetic longitude. After a close examination of GOLD images, we determined that in those cases, the GOLD image either show weak structures which were not selected by visual inspection or the GOLD images have poor contrast. In other words, the GOLD data in those cases did not provide good references for comparison. The images may be selected because there are other selected GOLD bubbles. Compared to the total number of the geolocations, the number of outliers is small.

We have many multiple bubble cases as shown in Figure 1. We would like to see how the geolocation performs in single bubble intersection cases. A total of eight scnPhs files with 54 geolocations were selected for this zonal difference analysis. The distribution is shown in Figure 5 and the same statistical values are listed in Table 2. The RMS for the differences is 0.45 deg in magnetic longitude and mean value difference is 0.00. That shows in the case of single intersection the geolocation can be accurate up to half degree in longitude (~50 km). There are no outliers for the single intersection case.

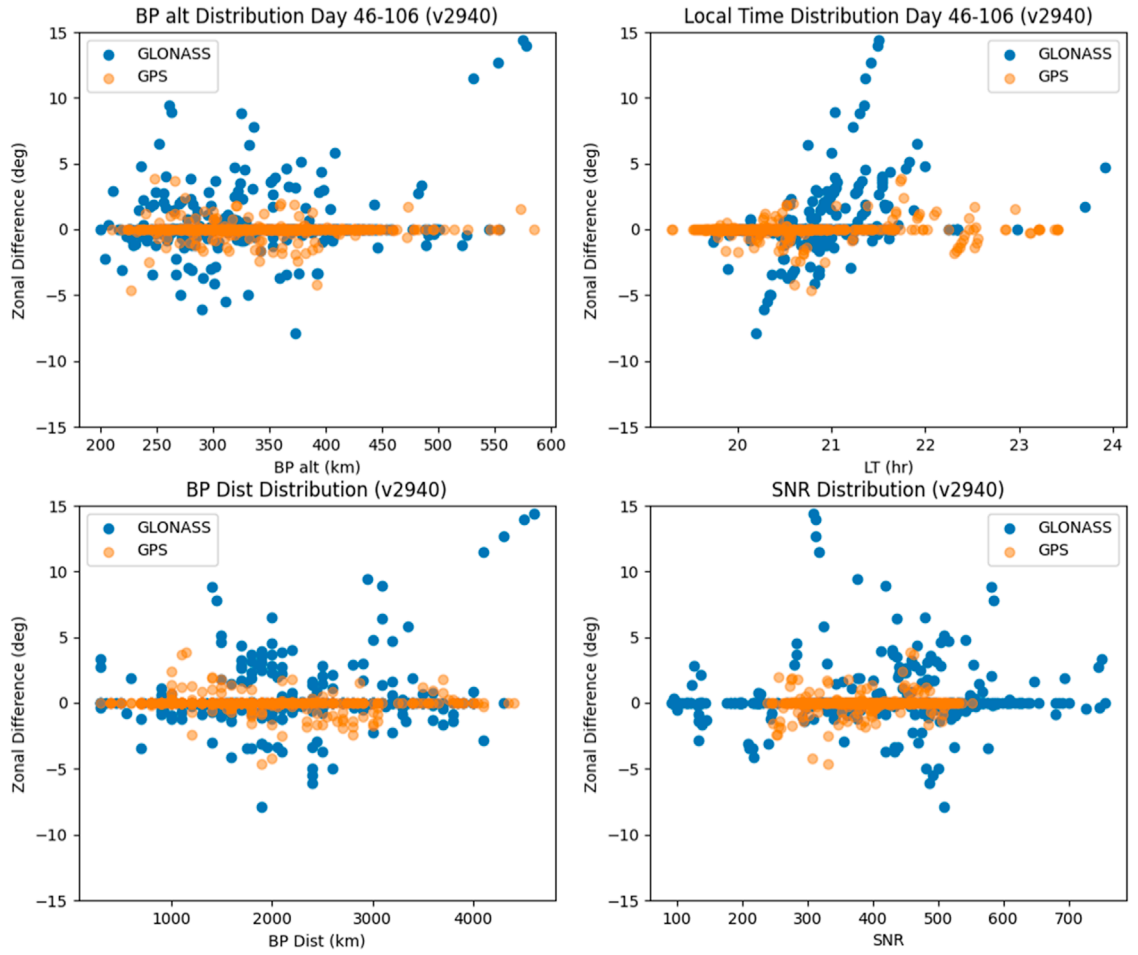

FIGURE 6
Zonal difference vs. altitude (upper left), local time (upper right), geolocation distance (lower left), and SNR (Signal to Noise Ratio) of the GNSS signals (lower right).

The zonal difference dependences on the scintillation altitude, local time, geolocation distance, and GNSS signal SNR are plotted in Figure 6. We do not see a clear trend of the zonal difference vs. these parameters. That implies that the geolocation method should work well over these parameter ranges. Finally, the scintillation altitude and local time distribution are plotted in Figure 7. As the ionospheric density gradually decreases moving into the night, we see fewer scintillations at high altitude. We have a cutoff at 600 km for geolocations. Also the GOLD observations do not extend deep into the night due to low UV emissions. Most of the bubbles occur near dusk after sunset, which is why we see more geolocations before 22 LT.

Discussion

The scnPhs files (including high rate phase and amplitude data and orbits) along with the scnGeo files including geolocation results (coordinates of the localized irregularities for those 10-s intervals with successful BP) are new products from F7/C2. In this analysis, we only used results obtained with GLONASS and GPS L1 signals. Taking advantage of the availability of the GOLD UV image data, we were able to show a good agreement between the F7/C geolocation and the GOLD bubble locations. This suggests that the scintillations selected in the local time interval in the GNSS signals are mostly caused by the plasma bubbles. In the cases with multiple bubbles, the overall statistics show the zonal difference RMS of about 1.5°, whereas the single intersection cases have about 0.5° RMS (~55 km) zonal difference. Since we used 10 s intervals (maximum ~70 km of the ray cross track) for the BP method, the 70 km may be considered the spatial resolution of geolocation. The RMS of the zonal difference is consistent with the spatial resolution of the BP method. Note that the minimum separation from GOLD image neighboring bubble is 2° in case we have multiple bubbles. That is not to say we have multi-bubbles all the time and the GOLD bubble location and COSMIC geolocation separation can be larger than 2° as shown in the statistical results.

The results also show the robustness of the geolocation method, as we did not see many outliers in our comparison. Geolocation will greatly improve our statistics of bubble

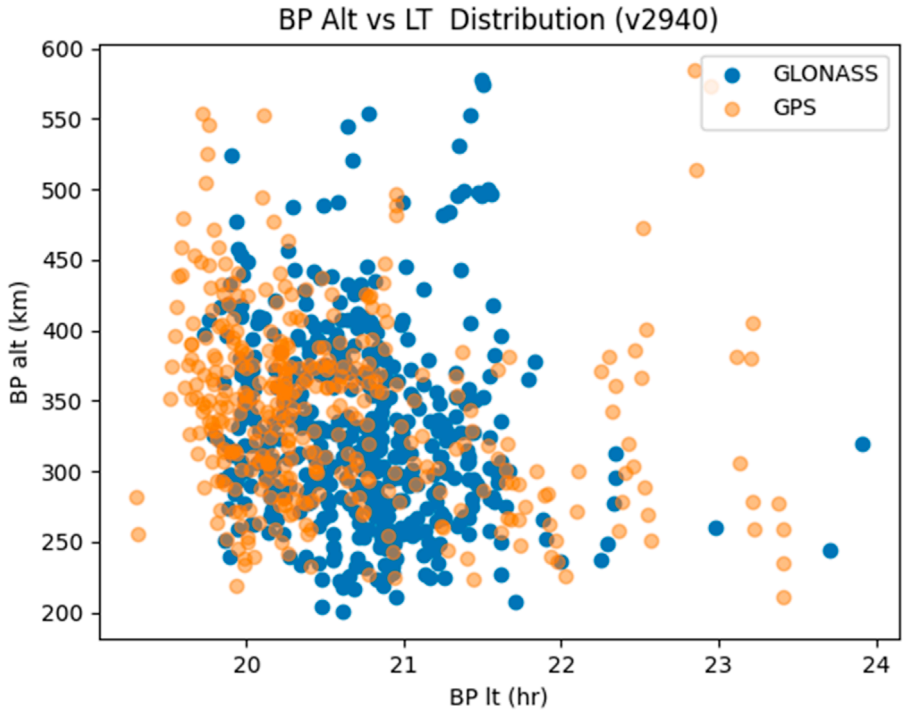

FIGURE 7
F7/C2 geolocation of the scintillation altitude and local time distribution.

occurrence compared to past COSMIC GNSS S4 based analysis [e.g., Wu et al., 2021]. That will help to track down possible trigger mechanism by pin-pointing the scintillation locations. Another useful information from the geolocation files is altitude of the scintillation. While we did not analyze the altitude in this study, the altitude information may help characterizing the bubble evolution.

The GOLD bubble location algorithm also works well. When the GOLD quality is good, the method can determine the bubbles in GOLD images very accurately. The north and south track comparison helps to reduce false positive for bubble location. Overall, the F7/C2 scnPhs file based geolocation will be an important space weather product. It will pin point the scintillations at regions, where the observational coverage has been lacking.

Summary

1. F7/C2 high rate scnPhs files enable the back-propagation method to geolocate the scintillations at all longitudes for accurate scintillation locations.
2. Comparison with GOLD bubble locations show a good agreement between the geolocation of scintillation and the bubble locations. The zonal difference is about 1.5 deg in magnetic longitude for all cases and 0.5 deg for single intersection cases.
3. The GOLD bubble location determine method provides accurate bubble information.

Data availability statement

The raw data supporting the conclusion of this article will be made available by the authors, without undue reservation.

Author contributions

QW: Writing–original draft, Writing–review and editing. JB: Investigation, Writing–review and editing. SS: Investigation, Methodology, Software, Writing–review and editing. WS: Investigation, Writing–review and editing. NP: Investigation, Writing–review and editing. J-PW: Investigation, Writing–review and editing. IC: Investigation, Writing–review and editing. IZ: Investigation, Writing–review and editing.

Funding

The author(s) declare that financial support was received for the research, authorship, and/or publication of this article. This research is supported by the following grants. This work was supported by Air Force Contract FA8803-19-C-0004. National Center for Atmospheric Research is supported by the National Science Foundation corporative agreement 1852977 and grants AGS-2054356 AGS-2120511 and NASA grants 80NSSC20K0199, NNX17AG69G, 20-GIGI20-007.

Acknowledgments

The GOLD nighttime data are available from https://gold.cs.ucf.edu/data/search/. The F7/C2 geolocation data used in this study are available upon request.

Conflict of interest

The authors declare that the research was conducted in the absence of any commercial or financial relationships that could be construed as a potential conflict of interest.

Publisher's note

All claims expressed in this article are solely those of the authors and do not necessarily represent those of their affiliated organizations, or those of the publisher, the editors and the reviewers. Any product that may be evaluated in this article, or claim that may be made by its manufacturer, is not guaranteed or endorsed by the publisher.

References

Anthes, R. A., and Schreiner, W. S. (2019). Six new satellites watch the atmosphere over Earth's equator. *Eos Wash(. DC)* 100. doi:10.1029/2019EO131779

Comberiate, J., and Paxton, L. J. (2010). Coordinated UV imaging of equatorial plasma bubbles using TIMED/GUVI and DMSP/SSUSI. *Space weather.* 8, S10002. doi:10.1029/2009SW000546

Eastes, R. W., McClintock, W. E., Burns, A. G., Anderson, D. N., Andersson, L., Aryal, S., et al. (2020). Initial observations by the GOLD mission. *J. Geophys. Res. Space Phys.* 125, e2020JA027823. doi:10.1029/2020JA027823

Eastes, R. W., McClintock, W. E., Burns, A. G., Anderson, D. N., Andersson, L., Codrescu, M., et al. (2017). The global-scale observations of the limb and disk (GOLD) mission. *Space Sci. Rev.* 212 (1-2), 383–408. doi:10.1007/s11214-017-0392-2

Okoh, D., Rabiu, B., Shiokawa, K., Otsuka, Y., Segun, B., Falayi, E., et al. (2017). First study on the occurrence frequency of equatorial plasma bubbles over West Africa using an all-sky airglow imager and GNSS receivers. *J. Geophys. Res. Space Phys.* 122 (12), 430. doi:10.1002/2017JA024602

Sokolovskiy, S., Schreiner, W., Rocken, C., and Hunt, D. (2002). Detection of high-altitude ionospheric irregularities with GPS/MET. *Geophys. Res. Lett.* 29 (3). doi:10.1029/2001GL013398

Sultan, P. J. (1996). Linear theory and modeling of the Rayleigh-Taylor instability leading to the occurrence of the equatorial spread F. *J. Geophys Res.* 101 (26), 875–926. doi:10.1029/96JA00682

Tien, J. Y., Okihiro, B. B., Esterhuizen, S. X., Franklin, G. W., Meehan, T. K., Munson, T. N., et al. (2012). "Next generation scalable space-borne GNSS science receiver," in Proc. 2012 int. tech. meet. inst. navig., Newport Beach, CA, September 17 - 21, 2012, 882–914.

Wu, Q. (2015). Longitudinal and seasonal variation of the equatorial flux tube integrated Rayleigh-Taylor instability growth rate. *J. Geophys. Res. Space Phys.* 120. doi:10.1002/2015JA021553-T

Wu, Q. (2017). Solar effect on the Rayleigh-Taylor instability growth rate as simulated by the NCAR TIEGCM. *J. Atmos. Solar-Terrestrial Phys.* 156, 97–102. doi:10.1016/j.jastp.2017.03.007

Wu, Q., Chou, M. Y., Schreiner, W., Braun, J., Pedatell, N., and Cherniak, I. (2021). COSMIC observation of stratospheric gravity wave and ionospheric scintillation correlation. *J. Atmos. Solar-terrestrial Phys.* 217, 105598. doi:10.1016/j.jastp.2021.105598

Yue, X., Schreiner, W. S., Pedatella, N., Anthes, R. A., Mannucci, A. J., Straus, P. R., et al. (2014). Space weather observations by GNSS radio occultation: from FORMOSAT-3/COSMIC to FORMOSAT-7/COSMIC-2. *Weather* 12 (11), 616–621. doi:10.1002/2014SW001133

frontiers | Frontiers in Astronomy and Space Sciences

TYPE Review
PUBLISHED 17 September 2024
DOI 10.3389/fspas.2024.1471140

OPEN ACCESS

EDITED BY
David Hysell,
Cornell University, United States

REVIEWED BY
Vladimir Truhlik,
Institute of Atmospheric Physics (ASCR), Czechia
Yong-Qiang Hao,
Sun Yat-sen University, China

*CORRESPONDENCE
Bela G. Fejer,
bela.fejer@usu.edu

RECEIVED 26 July 2024
ACCEPTED 27 August 2024
PUBLISHED 17 September 2024

CITATION
Fejer BG, Navarro LA and Chakrabarty D (2024) Recent results and outstanding questions on the response of the electrodynamics of the low latitude ionosphere to solar wind and magnetospheric disturbances.
Front. Astron. Space Sci. 11:1471140.
doi: 10.3389/fspas.2024.1471140

Recent results and outstanding questions on the response of the electrodynamics of the low latitude ionosphere to solar wind and magnetospheric disturbances

Bela G. Fejer[1]*, Luis A. Navarro[2] and Dibyendu Chakrabarty[3]

[1]Center for Atmospheric and Space Sciences, Utah State University, Logan, UT, United States, [2]Space Weather, Technology, and Education Center, University of Colorado, Boulder, CO, United States, [3]Space and Atmospheric Sciences Division, Physical Research Laboratory, Ahmedabad, India

Storm-time ionospheric electrodynamics effects have been the subject of extensive studies. The solar wind/magnetosphere/ionosphere and thermosphere disturbance wind dynamos have long been identified as the main drivers of low latitude storm-time electrodynamics. Extensive detailed studies showed that climatology of low latitude disturbance electric fields and currents is in good agreement with results from global theoretical and numerical models. Over the last decade, however, numerous studies have highlighted that the response of low latitude electrodynamics to enhanced geomagnetic activity is significantly more complex than previously considered. It is now clear that the electrodynamic disturbance processes are affected by a larger number of solar wind and magnetospheric parameters and that they also have more significant spatial dependence. This is especially pronounced during and after large geomagnetic storms when multiple simultaneous disturbance processes are also active. In this work, we briefly review the main past experimental and modeling studies of low latitude disturbance electric fields, highlight new results, discuss outstanding questions, and present suggestions for future studies.

KEYWORDS

geomagnetic storms and substorms, magnetospheric effects on low latitude ionosphere, electrodynamics response to solar wind disturbances, electrodynamics response to magnetospheric disturbances, low latitude ionosphere

1 Introduction

The response of electrodynamics of the low latitude ionosphere to enhanced geomagnetic activity has long been subject of numerous studies. Starting in the late 1970s, it was clearly established that the solar wind magnetosphere and the ionosphere disturbance wind dynamos are the main processes driving storm-time global ionospheric electric field and current perturbations. The solar wind magnetospheric dynamo drives short-lived (up to a few hours) so-called prompt penetration electric fields processes resulting from the leakage of high-latitude potential to lower latitudes when there is a temporary imbalance between region 1 and region 2 Birkeland currents (e.g., Wolf, 1970;

Kelley et al., 1979; Senior and Blanc, 1984; Spiro et al., 1988; Sazykin, 2000; Huang C.-S. et al., 2007; Wolf et al., 2007; Fejer et al., 2007; Fejer, 2011; Chakrabarty et al., 2015). Shorter-lived ionospheric prompt penetration electric fields and currents extending down to equatorial latitudes are also often driven by magnetospheric substorms (e.g., Kikuchi, 2000; Kikuchi et al., 2008; Chakrabarty et al., 2008; 2015; Wei et al., 2009; Wei et al., 2015; Huang C.-S., 2009; Fejer et al., 2021; 2024), solar wind dynamic pressure changes (e.g., Rout et al., 2019; Huang C.-S., 2020; Le et al., 2024), solar flares (e.g., Zhang R. et al., 2017) and ULF waves (e.g., Huang C.-S., 2020). The thermosphere disturbance dynamo, generated by storm-time enhanced energy and momentum deposition into the high-latitude ionosphere, drives longer lasting (up to a few days) global ionospheric electric field and current perturbations (e.g., Blanc and Richmond, 1980; Scherliess and Fejer, 1997; Fejer et al., 2017; Pandey et al., 2018; Navarro et al., 2019). Storm and post-storm prompt penetration and disturbance electric fields cause large perturbations on low latitude thermospheric winds, composition, and plasma density, and affect the occurrence of low latitude plasma irregularities (e.g., Fejer et al., 1999; Chakrabarty et al., 2006; Balan et al., 2008; Fuller-Rowell al., 2008; Fagundes et al., 2016; Xiong et al., 2015; Heelis and Maute, 2020; Navarro and Fejer, 2020).

The climatology of low latitude prompt penetration and disturbance electric fields has been known for over 2 decades, but there is still very little information on their temporal and longitudinal variations [e.g., Abdu, 2016; Abdu et al., 2007; Fejer and Maute, 2021]. Recent studies reported large spatial/temporal changes on disturbance electric fields due, for example, to IMF By changes, season, hemispheric dependent high latitude convection rotations and skewings, and to polar electrojet effects. Furthermore, as pointed out by Dick Wolf (private communication, 2022): "For the last 15 years or so, it has become very clear that plasma distributions are not approximately constant along the plasma sheet tailward boundary, as assumed by old style convection models. As a result, bubbles of depleted plasma sporadically occurring in the plasma sheet, probably because of reconnection, can sometimes make their way deep into the inner magnetosphere". Highly dynamic related processes, such as auroral streamers and substorms (e.g., Yadav et al., 2023), likely cause the electrodynamic response of the low latitude ionosphere to geomagnetic activity to be much richer and complex than previously thought. In the meantime, global ionospheric storm time models have recently undergone major improvements and now have increasingly been used in global simulations of complex storm events.

In the following sections, we first describe recent findings on the effects of solar wind, magnetospheric and high latitude drivers on low latitude ionospheric electric fields and currents. We also discuss recent studies of high latitude electrodynamics that are likely to affect the electrodynamics of the low latitude ionosphere. Next, we illustrate the complex longitude dependent response of equatorial ionospheric electrodynamic electric fields during extended periods of high geomagnetic activity emphasizing the challenges in effects of individual storm drivers. We then summarize recent results on low latitude storm-time modeling. Finally, we highlight outstanding questions and present suggestions for improving our understanding of this complex subject.

2 Drivers of low latitude storm-time electrodynamics

2.1 IMF Bz effects

The north-south (Bz) component of IMF is the most important driver of dayside reconnection and of solar wind, magnetosphere coupling (e.g., Wolf, 1970). Polarity changes in IMF Bz have long been known as the main drivers of low latitudes storm-time ionospheric disturbances. As extensively documented, southward (northward) IMF Bz excursions faster than shielding time constant (~30 min) drive undershielding (overshielding) electric fields. These electric fields cause upward/westward (downward/eastward) prompt penetration equatorial plasma drifts during the day and with opposite polarity at night with peak values near the terminators (e.g., Fejer et al., 1990; Fejer et al., 1997; Huang C.-S., 2015; Kikuchi and Hashimoto, 2016). Slower Bz turnings do not give rise to significant penetration of electric fields. Regression analysis of IMF Bz and conductivity-corrected equatorial electrojet data suggests higher prompt penetration efficiency during northward than southern turnings (Bhaskar and Vichare, 2013). The ratio of the equatorial zonal penetration and the motional solar wind (dawn-dusk) electric fields is ~0.1 during the day (e.g., Kelley et al., 2003; Huang C.-S. et al., 2010; Huang C.-S. et al., 2010; Manoj et al., 2012) and larger near sunrise and sunset (e.g., Fejer and Scherliess, 1997; Wei et al., 2008; Fejer, 2011). The amplitudes of the meridional/perpendicular prompt penetration electric fields are about twice larger (e.g., Sazykin, 2000; Fejer and Emmert, 2003; Huang C.-S. et al., 2010). These ratios vary with solar wind and magnetospheric parameters (e.g., Spiro et al., 1988; Garner et al., 2004) and under the effect of additional solar wind (e.g., dynamic pressure) and magnetospheric (e.g., substorms) processes.

The lifetimes of Prompt penetration electric fields associated with rapid southward IMF Bz turnings faster are generally ~1–2 h [e.g., Fejer and Scherliess, 1997; Manoj and Maus., 2012], although much longer values (up to ~10 h) have also been suggested (e.g., Huang C.-S., et al., 2010a; Huang C.-S., et al., 2010b). For slowly varying southward IMF Bz conditions, short-lived prompt penetrations equatorial electric fields can be driven by magnetospheric substorms, changes in IMF By, and solar wind dynamic pressure changes. This is illustrated in Figure 1 with F-region vertical plasma drift measurements over Jicamarca, Peru (11.9°S, 76.8°W; dip latitude ~0°). Over this site, eastward/downward electric fields of 1 mV/m correspond to upward/westward drifts of ~40 m/s. Equatorial storm time electric fields during extended periods of southward IMF Bz will be discussed in detail later.

Rout et al. (2022) presented evidence for quasiperiodic (1.5–2 h) fluctuations in low latitude ionospheric electric fields, solar wind zonal electric field and global geomagnetic fluctuations during High-Intensity Long-Duration Continuous AE Activity (HILDCAA) events. Recently, Milan et al. (2023) concluded that the AE/AL disturbances during HILDCAAs are caused by high-intensity quasi-periodic substorms driven by high but intermittent dayside reconnection rate due to fast solar wind and quasi-periodically varying IMF. Low latitude ionospheric electric fields during these events, however, should also be directly affected by IMF Bz sign fluctuations.

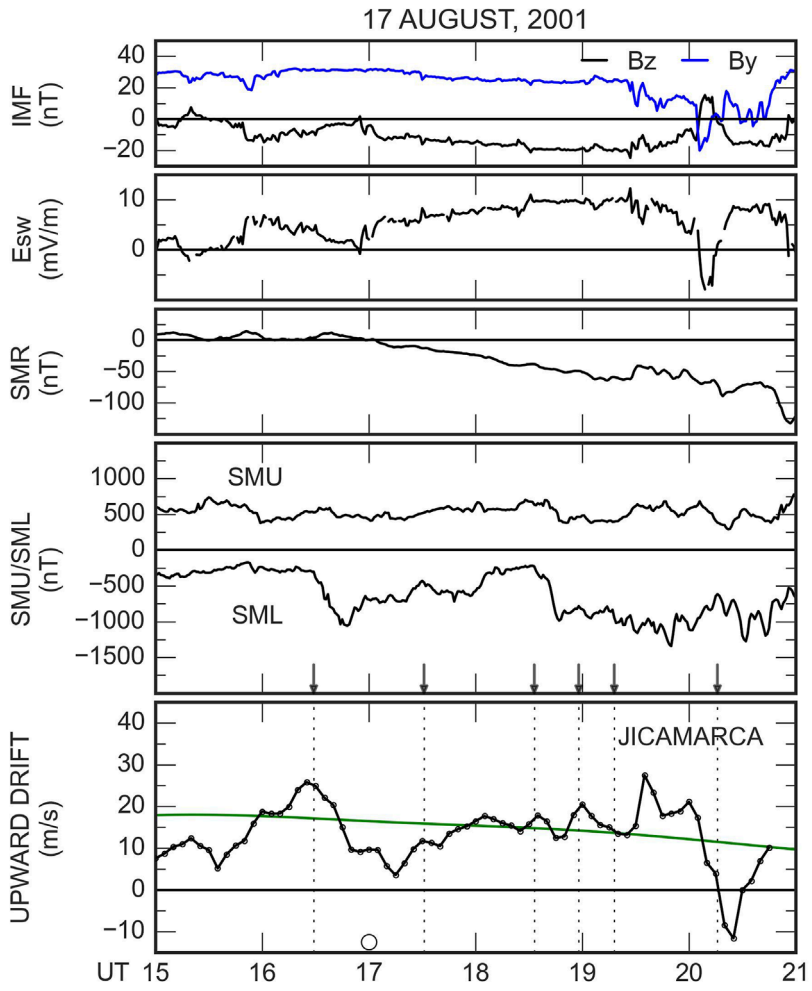

FIGURE 1
(From top to bottom) IMF Bz/By, solar wind motional east-west electric field, SuperMAG ring current (SMR) and auroral current (SMU/SML) indices with substorm onset times (small arrows in the bottom panel), Jicamarca vertical plasma drifts during the initial phase of the 17 August 2001slowly developing magnetic storm. The smooth curve denotes the quiet-time drift pattern.

Even though prompt penetration effects are most often associated with IMF Bz turnings and southward conditions, it has been known for some time that this is not always the case. Recent studies have reexamined earlier investigations (e.g., Kelley and Makela, 2002; Zhao B. et al., 2008) of equatorial prompt penetration electric fields and currents lasting longer than a few hours under northward IMF (NBz) and duskward (By > 0) conditions. Li et al. (2023) discussed one such event in connection with energy deposition at higher latitudes than under southward IMF Bz. They also showed that Thermosphere-Ionosphere-Electrodynamics General Circulation Model (TIE-GCM) simulations reproduced the observed changes in high latitude convection, Joule heating and thermospheric winds, as well as resulting low latitude westward prompt penetration electric fields. Wang and Luhr (2024) presented extensive CHAMP and Swarm measurements showing that, under long-duration NBz, the polar electrojet driven low-high latitude ionospheric electrodynamical coupling is strongly dependent on IMF By sign, local time, and season.

2.2 IMF By effects

The dawn-dusk (By) component of IMF modulates the dayside reconnection rate and affects the ionospheric convection patterns (e.g., Heelis, 1984; Cunnock et al., 1992). Tsurutani et al. (2008) pointed out that the polarity of equatorial prompt penetration electric field perturbations near dawn and dusk could be affected due to possible skewing and asymmetry between the DP2 convection vortices. Tenfjord et al. (2015) described the role of IMF By on asymmetric currents, convection patterns and substorm onset locations in the two hemispheres (e.g., Østgaard et al., 2004; 2011). Only recently have IMF By effects on the electrodynamics of the low latitude ionospheric have been studied in detail.

Chakrabarty et al. (2017) suggested that unusual equatorial prompt penetration electric fields with identical polarity near dawn and dusk over nearly antipodal stations in Indian and South American could be explained as resulting from IMF By driven asymmetric and skewed DP2 current lobes. This role of IMF By under southward Bz is also supported by consistently

observed (e.g., Kumar et al., 2023; Chakraborty and Chakrabarty, 2023) high latitude out-of-phase and low latitude in-phase variations of the geomagnetic X component over the antipodal stations corresponding to longitudes in the day and night sectors. We note that asymmetric and distorted high latitude currents should also have major spatial and temporal effects on equatorial disturbance dynamo electric fields.

It is now evident that, contrary to what has been generally assumed, the dependence of auroral currents on IMF By is not symmetric with respect with its sign (e.g., Friis-Christensen et al., 1972; 1985). This dependence is particularly strong in the AL index and during the solstices. During northern hemisphere winter (i.e., under negative tilt angle of the Earth's magnetic dipole relative to the Sun-Earth line), for example, the northern AL index can ~40% stronger for By > 0 than for By < 0. Holappa and Buzulukova (2022) suggested that this interhemispheric effect can be accounted for in the Newell et al. (2007) solar wind magnetosphere coupling function dF_{MP}/dt through $(1 - 0.04\,By \tan \psi)$, where ψ is the dipole tilt angle and By is nT. Reistad et al. (2022) reported more frequent substorm occurrence when IMF B_y and dipole tilt have opposite signs. This was attributed to a more efficient global dayside reconnection rate. We note in passing that Cowley (1981), Cowley et al. (1991) and Laundal and Ostgaard (2009) suggested stronger and more efficient solar wind dynamo in the southern hemisphere under large positive IMF Bx. The hemispheric asymmetries caused by IMF By and possibly IMF Bx should play a major role on the spatial and temporal variability of both equatorial prompt penetration and disturbance electric fields near sunrise and sunset, particularly during the solstices.

There are other aspects regarding IMF By effects on equatorial disturbance electric fields remain unclear such as what proportion of IMF Bz and IMF By is the most effective one and whether a stable and significantly high IMF By is more effective than the polarity reversal in IMF By or *vice versa*. In the absence of modelling and clinching evidence, one should not discard the role of any of the above factors *ab initio*.

2.3 Solar wind density and dynamic pressure effects

Increased solar wind dynamic pressure causes magnetospheric compression and drives enhanced the two-cell convection and DP-2 currents (e.g., Liou et al., 2017). In the daytime equatorial ionosphere, they give rise to short-lived (~30 min) upward and westward plasma drift perturbations (e.g., Fejer and Emmert, 2003; Huang C.-S., 2020; Nilam et al., 2020). Sharp dynamic pressure decreases cause prompt penetration electric fields with opposite polarity (e.g., Le et al., 2024). These polarities do not appear to depend on the directions of IMF Bz and By (Nilam et al., 2020). Earlier, Wei et al. (2012) illustrated the control of the equatorial prompt penetration electric field by the solar wind density during a saturation of cross the polar cap potential, and Rout et al. (2016) reported brief (~30 min) simultaneous increases in the high-latitude convection and electric equatorial electric fields under northward IMF Bz after an increase in the solar wind density. Similar effects in equatorial plasma drifts and thermospheric winds were reported by Navarro and Fejer (2020) following solar wind dynamic pressure increases.

2.4 Substorm effects

Induction electric fields resulting from magnetospheric substorm dipolarizations (e.g., Wolf et al., 1982) are increasingly been recognized as important drivers of short-lived (~0.5 h) equatorial prompt penetration electric fields and currents (Kikuchi et al., 2003; Wei et al., 2009; Huang C.-S, 2012; Chakrabarty et al., 2010; 2015; Hui et al., 2017; Tulasi Ram et al., 2016; Fejer et al., 2021; 2024; Kikuchi, 2021; Sori et al., 2022; Fejer and Navarro, 2022). Magnetospheric substorms always occur when IMF Bz is southward for over ~2 h after its southward turning (e.g., Caan et al., 1977). They are often associated with changes in the solar wind drivers including IMF polarity reversals), sharp changes in the solar wind ram pressure, and with internal magnetospheric triggers (Liou et al., 2018). MHD simulations (Tanaka et al., 2010; Ebihara et al., 2014) showed that during substorms, region-2 field aligned currents driven by anisotropic plasma pressure in the inner magnetosphere can cause overshielding-like effects (i.e., daytime westward electric fields). Liou et al. (2020) reported that, on average, there are ~1/3 more substorms for IMF By > 0 than for IMF By < 0, which was attributed to the asymmetry in enhanced convection.

Substorm onset and expansion phases have been associated with both eastward (e.g., Hui et al., 2017; Huang C.-S., 2020) and westward (Kikuchi et al., 2003; Hui et al., 2017) daytime equatorial prompt penetration electric fields. A statistical analysis of disturbed equatorial electrojet using AE index by Yamasaki and Kosch (2015) indicates that the average equatorial electrojet perturbation electric field associated with substorm onset is eastward and lasts for 30–60 min. Their derived short-and long-term climatological responses of the electrojet to substorms are consistent with Jicamarca prompt penetration and disturbance dynamo electric field patterns. Gao et al. (2023) also reported substorm driven prompt penetration and disturbance dynamo patterns consistent with previous results. As mentioned earlier, substorms often occur during periods of changing solar wind parameters and, therefore, it is usually difficult to isolate their contributions to penetration electric fields.

Jicamarca radar drift measurements during periods of nearly steady southward IMF Bz and By and small changes in the solar wind dynamic pressure strongly suggest that substorm onsets and expansion phases (recovery phases) are mostly associated with eastward/poleward (westward/equatorward) prompt penetration electric fields during daytime-evening and with opposite polarities at night. This is consistent with plasma sheet heating and resulting in reduction in shielding during substorm expansion phase (Baumjohann et al., 1996). The eastward and westward perturbation electric fields during onset-expansion and recovery phase often appear to have comparable lifetimes and amplitudes, as in the case of longer lasting (~3 h) equatorial electric fields during the so-called sawtooth events (Huang C.-S., 2012). Substorm driven equatorial vertical drifts are generally small (less than ~5–10 m/s) during the day.

Figure 2 presents in the top 5 panels the IMF Bz/By, solar motional electric field and dynamic pressure, and the SMR,

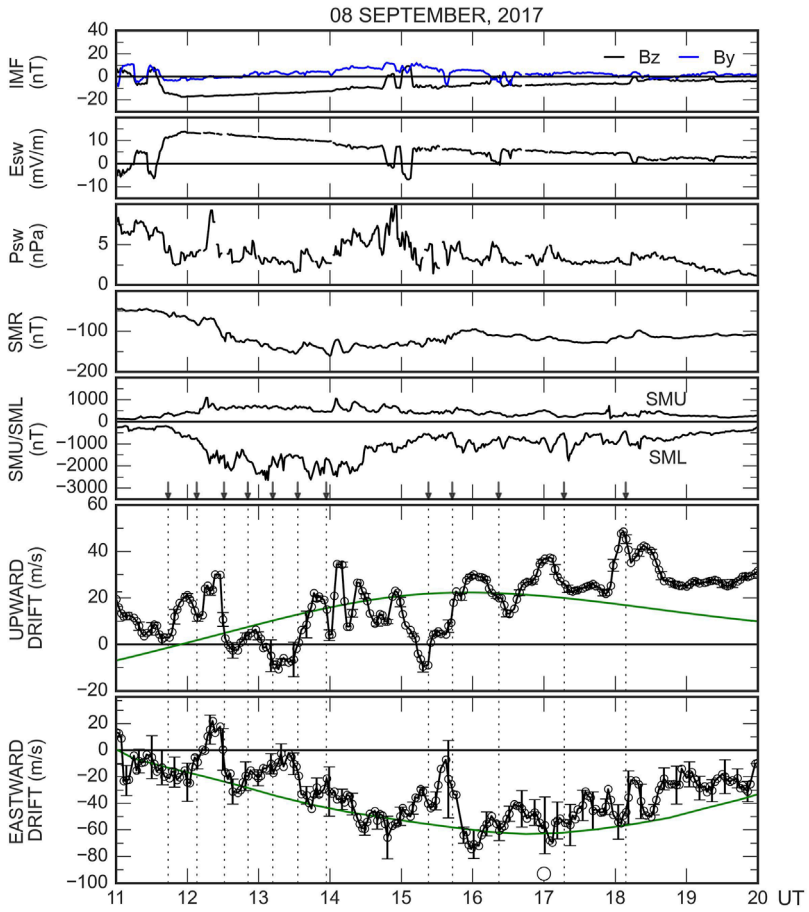

FIGURE 2
(Top five panels) solar wind IMF Bz/By, motional east-west electric field and dynamic pressure, and SuperMAG ring current (SMR) and auroral current (SMU/SML) indices with and substorm onset times (small arrows). (Bottom panels) Height averaged Jicamarca vertical and zonal plasma drifts. The circle at 17 UT indicates noon over Jicamarca and the green curves denote the quiet time vertical and zonal drift patterns (adapted from Fejer and Navarro, 2022).

SMU, and SML indices, and in the two bottom panels, the daytime vertical and zonal F-region vertical drifts measured over Jicamarca during the mostly steady southward IMF Bz period encompassing the second main and recovery phases of the September 2017 large geomagnetic storm. This Figure shows upward/westward perturbation drifts during periods of slowly varying southward IMF Bz and solar wind dynamic pressure, and two large overshielding events at ~12:30–13:30 UT and 15:00–16:00 UT. The first, which occurred after increase in the solar wind dynamic pressure, could be interpreted as resulting from the substorm associated process increased Region 2 Field-Aligned Currents (R2 FACs) caused by inner magnetospheric anisotropic plasma pressure (e.g., Ebihara et al., 2014). This process will be discussed further later. The second overshielding event, shown in Figure 2, occurred during substorm activity following rapid fluctuations in the solar wind dynamic pressure and IMF Bz sign. Yadav et al. (2023) associated dayside and nightside equatorial electrojet overshieldings with equatorward extending streamers resulting from plasma sheet burst flows. They suggested that these auroral streamers, which can be associated with sharp decreases in the SML index, cause overshieldings also by strenghtening Region 2 Field-Aligned Currents (R2 FACs) over R1 FACs.

The low latitude ionospheric typical electrodynamic response to long-lasting southward IMF Bz-driven geomagnetic storms is the nearly continuous occurrence of short-lived (time scales ~30–60 min) substorm-driven prompt penetration electric fields. This was the case, for example, of the equatorial electrojet response to the CME driven July 2012 large geomagnetic studied in detail by Bagiya et al. (2014), Liu et al. (2014), Kuai et al., 2017. In this event, over a period of about 30 h of slowly varying southward IMF Bz, SuperMAG identified 30 substorms, which gave rise to the observed daytime short-lived equatorial electrojet eastward current perturbations, including under strong disturbance dynamo conditions (Figure 5 in Liu et al., 2014). Substorm-driven prompt penetration electric fields under strong disturbance dynamo electric fields were also reported by Fejer et al. (2024). Low latitude electrodynamic signatures during long-lasting southward IMF Bz will be discussed further later.

Substorm associated equatorial prompt penetration electric fields often have very large amplitudes (over ~100 m/s) near

dusk (e.g., Fejer et al., 2021; 2024). Figure 3 shows solar wind, magnetospheric, and high latitude ionospheric parameters, and Jicamarca vertical drifts and coherent backscattered power from 3-m plasma irregularities close to dusk during 27–28 August 2015. This was a period of moderate recurrent geomagnetic activity when the solar wind electric fields (~3 mV/m) were typically too small for directly driving noticeable equatorial prompt penetration electric fields. These substorm associated prompt penetration electric fields caused one of the largest dusk side upward drift perturbations (~60 m/s) ever recorded over Jicamarca during June solstice (Fejer et al., 2021). The large and sudden backscattered power decrease at ~00:15 UT is indicative of strong westward prompt penetration electric fields associated with substorm recovery. Substorm associated prompt penetration electric fields near dusk are most easily identified during periods of small prereversal velocity enhancements, i.e., primarily near June solstice over Jicamarca. Fejer et al. (2008) reported that this is also the season with highest amplitude prompt penetration electric fields near the terminators.

2.5 Solar flare effects

Sudden increases in solar X-ray and Extreme Ultraviolet (EUV) radiation during solar flares lead to large and rapid ionospheric changes (e.g., Tsurutani et al., 2020). Low latitude solar flare effects were discussed in several papers (e.g., Qian et al., 2012; Fejer and Maute, 2021). Zhang K. et al. (2021) reported solar associated increases in daytime eastward equatorial electrojet current and simultaneous decreases in the eastward electric fields, as indicated by Jicamarca vertical drifts. They suggested that the eastward electric field decreases may be due to disturbed ionospheric dynamo caused by flare enhanced Cowling conductivity and perhaps also to overshielding effects. Pedatella et al. (2019) and Chen et al. (2021) presented numerical simulations of sudden daytime equatorial upward drifts (eastward electric field) decreases similar to Jicamarca observations after flare onsets. The simulations of Chen et al. (2021) also indicate that solar flares increase global daytime currents and reduce the eastward electric fields extending from the equator to middle latitudes. Both simulations suggest that the above electrodynamic effects resulted largely from flare-induced conductivity enhancements; prompt penetration electric field effects were not considered.

2.6 SAPS/SAID effects

The occurrence of large poleward-directed electric fields in the evening sub-auroral ionosphere was first pointed out by Galperin et al. (1974) who called them Polarization Jets (PJs). Similar intense narrow electric field structures were called Sub-Auroral Ion Drifts (SAIDs) (Spiro et al., 1979). These two structures and the longer lasting broader latitudinal region of intense sunward plasma drift (e.g., Yeh et al., 1991), are now commonly referred to as Sub-Auroral Polarization Streams (SAPS) (e.g., Foster and Burke, 2002; Foster and Vo, 2002). SAPS are characteristic features of the low conductivity subauroral region during the main and recovery phases of strong magnetic storms (e.g., Foster and Burke, 2002; Foster and Vo, 2002). These poleward electric fields are caused by the separation of the ion and electron plasma sheet edges in the magnetosphere. Huang C.-S et al. (2020b) presented Defense Meteorological Satellite Program (DMSP) satellite measurements showing SAPS peak westward velocities highly correlated with Dst index lasting up to 2 days during both the storm main phase with southward IMF and recovery phase with northward IMF. Huang C.-S et al. (2021) suggested that during very large storms SAPS plasma flows/electric fields near dusk penetrate to the equatorial region driving peak westward plasma drifts of up to 200–300 m/s. They these disturbance drifts related to Dst approximately (correlation 0.87) through $\Delta V = 0.52$ Dst, where 0.52 Dst is in nT. The DMSP equatorial vertical drift measurements during these periods were not discussed. Jicamarca radar measurements during the 22–23 April 2023 geomagnetic storm presented by Fejer et al. (2024) show ~100 m/s westward disturbance drifts near dusk under large, nearly steady, southward IMF Bz and SMR~120 nT, Dst~100 nT conditions. During this period, the vertical drifts had very large amplitude fluctuations typical of substorm driven prompt penetration electric fields.

Huang C.-S et al. (2021) reported CHAMP satellite measurements close to midnight showing large westward disturbance winds rapidly (within 2 h) extending down to equatorial latitudes, and DMSP measured eastward drifts extending down to ~20° magnetic latitudes at 0930 LT. Huang C.-S. (2020) suggested that SAPS associated equatorial zonal disturbance drifts do not result from southward IMF Bz driven prompt penetration electric fields. SAPS have recently also been associated with equatorial electrojet disturbance dynamo effects (Zhang K. et al., 2021).

2.7 Disturbance dynamo effects

The disturbance dynamo mechanism (Blanc and Richmond, 1980; Scherliess and Fejer, 1997) is the dominant driver of low latitude low latitude electric field and current perturbations in the recovery phase of geomagnetic storms. Fejer et al. (2017) reviewed their causes and recent results on their middle and low latitude electrodynamic effects. Navarro et al. (2019) showed that over Jicamarca the average disturbance dynamo vertical drifts are downward and generally small during daytime. Pandey et al. (2018) suggested that, in presence of a favorable semidiurnal tidal component (particularly during equinoctial months in high solar activity period), the disturbance dynamo related electric field perturbations during daytime can be as large as at nighttime. Near dusk, the disturbance dynamo vertical drifts are downward, have largest values during the autumnal equinox, smallest during May-June, and increase strongly with solar flux and enhanced geomagnetic activity (e.g., Fejer, 2002). At night, they are upward, do not change much with season, and increase with solar flux and geomagnetic activity (Navarro et al., 2019). The zonal disturbance dynamo drifts are eastward during the day and westward at night with generally largest values near midnight (e.g., Fejer et al., 2005; Navarro and Fejer, 2020).

Disturbance dynamo and prompt penetration electric fields have also been studied recently using the magnetic response of

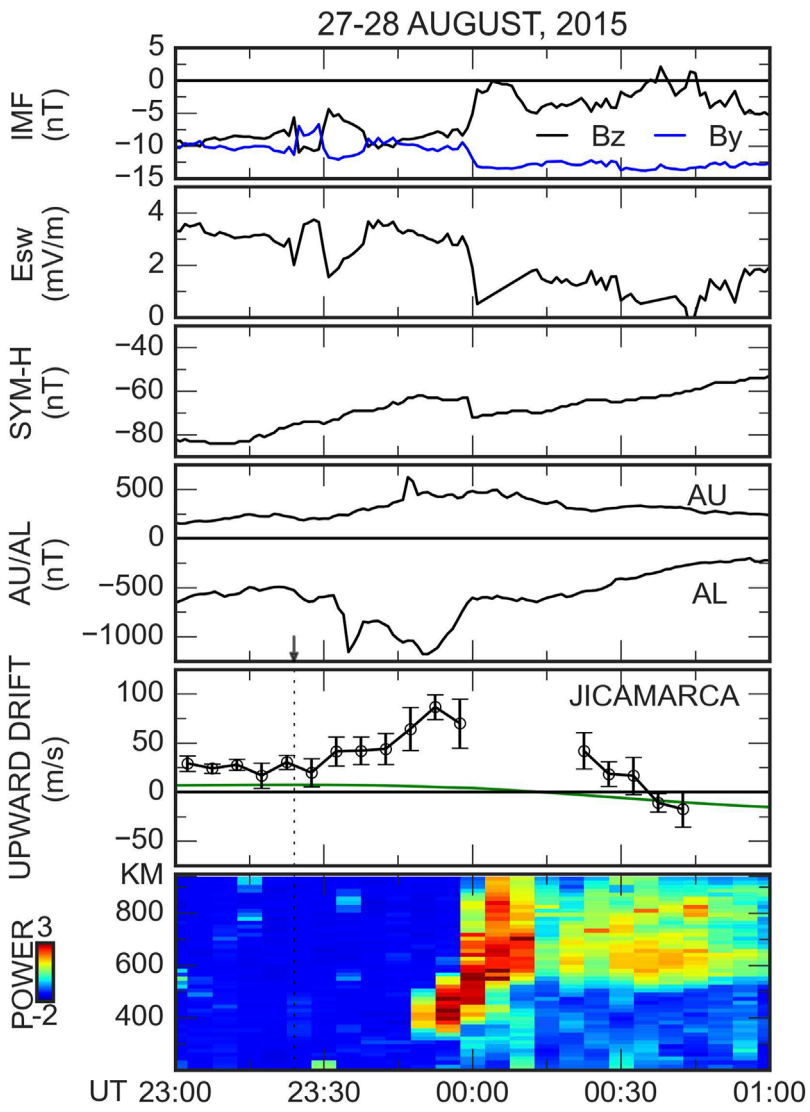

FIGURE 3
Solar wind and magnetospheric indices, average Jicamarca vertical drifts and coherent backscattered power during August 27–28, 2015. The green line corresponds to the quiet drift pattern. The errors bars denote the standard deviations of the drifts. Over Jicamarca UT = LT + 5 h. Adapted from Fejer et al., 2021.

their equivalent current systems (e.g., Rodriguez-Zuluaga et al., 2016; Bulusu et al., 2018; Younas et al., 2021). The disturbance dynamo magnetic signatures, the so-called Ddyn (e.g., Le Huy and Amory-Mazaudier, 2005; Amory-Mazaudier et al., 2017), appear as storm-time negative geomagnetic field excursions relative to their diurnal quiet time values, i.e., as anti-Sq circulations. Rodriguez-Zuluaga et al. (2016) reported good agreement between Equatorial Ionization Anomaly (EIA) and disturbance dynamo parameters during high-speed solar wind stream (HSSW), but not during coronal mass ejection (CME) events. Younas et al. (2021) showed that D_{dyn} is longest lasting during equinox, and that HSSW generated D_{dyn} occur globally and generally last longer than the more localized CME) generated D_{dyn}.

3 Equatorial ionospheric electrodynamics during the December 2006 large geomagnetic storm

The CME driven 14–15 December 2006 large geomagnetic storm started at ~1414 UT with a large shock as a result of the sudden increase in the solar wind speed from 650 to 980 km/s. After the shock, the solar wind speed underwent a gradual decrease but remained above 600 km/s for most of this long-lasting storm. The storm main phase started at ~2310 UT on14th following the IMF Bz rapid southward turning. Lei et al. (2008), Wang et al. (2008) used Coupled Magnetosphere Ionosphere Thermosphere (CMIT) model simulations to study the thermospheric and ionospheric response to the initial phase (~8 h) of this

storm. Veenadhari et al. (2019) examined substorm electrodynamic signatures during this storm and Ranjan et al. (2023) studied this storm-driven ionospheric variability over the Indian sector.

Figure 4 shows in the top 5 panels the ACE satellite measured IMF Bz/By and motional electric field (positive duskward), and the SMR, SMU, SML geomagnetic indices from 00 UT to 10 UT on 15 December. The next two panels present the equatorial electrojet data over Micronesia and India determined from the difference of the magnetic field horizontal components over Yap (9.6°N, 138.1°E) and Okinawa (26.3°N, 127.8°E) and Tirunelveli (8.7°N, 77.8°E) and Alibag (18.7°N, 72.9°E), respectively (Veenadhari et al., 2019). The bottom panels show the vertical drift velocity and backscattered power from 3-m plasma irregularities measured by the JULIA probe. Over the ~120–160 km height range, these drifts are the nighttime equivalents to the daytime so-called 150 km drifts. The power from the ~110 km region results from the backscatter of electrojet two-stream and gradient-drift plasma irregularities (e.g., Fejer and Kelley, 1980). Height changes in the electrojet backscattered power are indicative of zonal electric field reversals and occurrence of gradient drift plasmas irregularities.

Figure 4 indicates that following the main phase onset, the IMF Bz remained southward for several hours, except for brief northward excursions at ~0520 UT. The IMF By oscillated up to 00 UT on the 15th, increased to ~10 nT to ~06 UT, and then decreased to ~5 nT. The solar wind dynamic pressure (not shown) was very small after ~01 UT. The SMR went down to −163 nT at 0055 UT, and the SMU and SML had peak values ~1,000 and ~2,400 nT, respectively. Over this period, the SuperMAG website lists 20 substorm onsets based on the Newell and Gjerloev (2011) criteria.

The solar wind, auroral electrojet, ring current, storm-time equatorial electrojet data, and complementary geosynchronous particle flux measurements from LANL (Los Alamos National Laboratory) satellites (not shown) during this event were discussed in detail by Veenadhari et al. (2019). They pointed out that the sharp decrease in storm time electrojet at 0100 UT over the Japanese sector and at 0525 UT over the Indian sector, shown in Figure 4, were most likely due to change in solar wind dynamic pressure and sudden sharp IMF Bz northward turning, respectively. Figure 4 also shows particularly large decreases in the East Asian and Indian storm - time electrojet data between 0200 and 0400 UT when the solar wind dynamic pressure was low and steady, and the IMF Bz was southward and slowly changing. Veenadhari et al. (2019) pointed out that, over this period, LANL satellite dusk geosynchronous particle flux and Asymmetric-D and Asymmetric-H data indicated the occurrence of substorms. They suggested that these strong daytime overshieldings driving westward equatorial electrojet currents during the large southward IMF Bz can be interpreted as due to substorm driven increased Region 2 Field-Aligned Currents (R2 FACs) (e.g., Ebihara et al., 2014). Veenadhari et al., (2019) pointed out that this daytime overshielding does fit the standard disturbance dynamo signatures. On the other hand, we believe that disturbance dynamo effects cannot be fully ruled out.

The last two panels of Figure 4 show generally very strong upward drifts (often over 150 m/s) and electrojet backscattered power up to ~04 UT (23 LT) over Jicamarca. This is particularly the case during 02–04 UT when there was strong counter electrojet activity in the East Asian and Indian sectors. Over this period, h'F and hmF2 over Jicamarca reached over ~500 km (among the highest ever recorded), and the radar measurements showed very strong spread F activity, which will be discussed later. From ~04–08 UT, the Jicamarca data show large short-lived vertical drifts enhancements (overshieldings) with corresponding variations in the height and strength of the electrojet backscattered power. We associate these large vertical drift enhancements with the occurrence of strong substorms. After ~08 UT, there were there were no further upward drift enhancements, and the electrojet backscattered power became strong again, which is indicative of strong westward electric fields driven two-stream electrojet irregularities.

Figure 5 show highly structured early night equatorial 3-m plasma irregularities over Jicamarca rapidly expending to high latitudes as expected from the actions of the very strong and highly variable upward drifts shown in Figure 5, and consistent with elevated h'F and hmF2 values. The large structuring of the plasma irregularities is consistent with highly variable substorm associated vertical and zonal prompt penetration electric fields. The F-region irregularities and the electrojet backscattered power weakened significantly a about ~04 UT (23 LT) consistent with decrease of upward drifts. Later, the F-region irregularities systematically move downward in spite of occasional occurrence of upward drifts.

Huang C.-S. (2019) presented dusk-evening upward drifts of up to ~180 m/s measured by five DMSP satellites during 00–12 UT on 15 December 2006. These large upward drifts were interpreted as caused by continuous penetration of solar wind electric fields, in partial agreement with the radar data. The simultaneous occurrence of strong daytime overshielding, as indicated by the morning daytime electrojet data and evening and early night strong undershielding, as shown by the radar and DMSP data is not consistent with the expected prompt penetration electric field pattern (e.g., Fejer and Scherliess, 1997). We speculate that these apparently contradictory results might have been caused by strong rotations and/or skewing of the northern and southern high latitude convection patterns. The fundamental point highlighted by this Asian and South American data is that interpretations based on single site observations cannot be generalized to other longitudinal sectors. This clearly points to the need for multiple measurements at least during major magnetic storms.

4 Recent modeling studies

Magnetic-field aligned currents driven global convection changes (e.g., Wolf, 1970) often give rise to strong global electron electrodynamic perturbations (e.g., Nishida el al., 1966; Kelley et al., 1979; Fejer, 2011; Kikuchi, 2021). The basic characteristics of storm time driven low latitude short and longer lasting low latitude electrodynamic perturbations have been largely explained by numerous theoretical and numerical more than 2 decades ago (e.g., Blanc and Richmond, 1980; Senior and Blanc, 1984; Spiro et al., 1988; Sazykin, 2000; Richmond et al., 2003; Maruyama et al., 2011). However, these models did not accurately account for the coupling of the magnetosphere to the ionosphere and thermosphere, which made it particularly difficult to accurately simulate penetrating electric fields (e.g., Lu et al., 2012). Recently, Lu et al. (2020) showed that the TIEGCM driven by realistic storm-time magnetospheric forcing was able to reproduce many observed large-scale ionospheric features during 17 March 2015 storm determined from GNSS

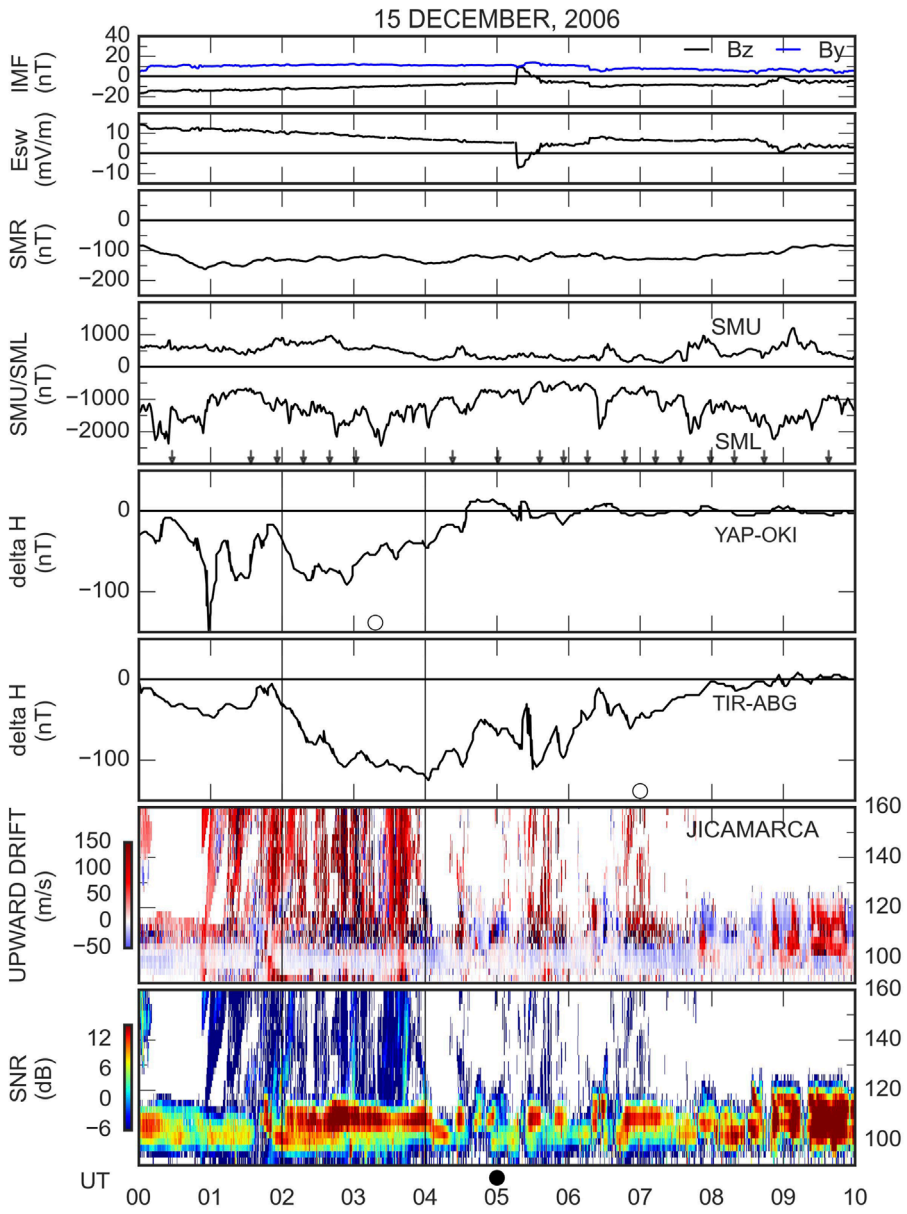

FIGURE 4
(Top four panels) Solar wind IMF Bz/By and motional east-west electric field, and SuperMAG ring current (SMR) and auroral current (SMU/SML) indices with and substorm onset times (small arrows). (Fifth and sixth panels) Equatorial electrojet magnetic fields data from the East Asian and Indian sectors (adapted from Veenadhari et al., 2019). (Bottom two panels) Jicamarca vertical plasma drifts and backscattered power from 3-m plasma irregularities. The open and full circles denote local noon and midnight, respectively.

TEC data. Although no comparisons were made with measured low latitude electric fields and currents, the modelled equatorial prompt penetration electric fields, in response to a rapid IMF southward excursion, were consistent with their expected patterns. Maute et al. (2021) presented TIEGCM simulations of hemispheric asymmetric electric potential using the Weimer electric potential, the Assimilative Mapping of Ionospheric Electrodynamics (AMIE) derived electric potential, and auroral parametrization from field-aligned currents based on AMPERE data. The simulated equatorial electric fields using the different potentials were generally consistent with each other and with expected patterns during daytime, but not near dawn and dusk. Recently, Wu et al. (2024) reported simulations of prompt penetration electric field during the initial phase of the 3–4 November 2021 using the recently developed Multiscale Atmosphere-Geospace Environment (MAGE) mode MAGE that are generally consistent with measurements from the Ionospheric Connection Explorer (ICON) satellite. MAGE, which combines a MHD (Magnetohydrodynamics), the Rice Convection Model (RCM) of the ring current, and the TIEGCM models (e.g., Lin et al., 2022; Wu et al., 2024), has a faster high latitude driver for the ionosphere thermosphere models allowing for more realistic simulations of SAPS and prompt

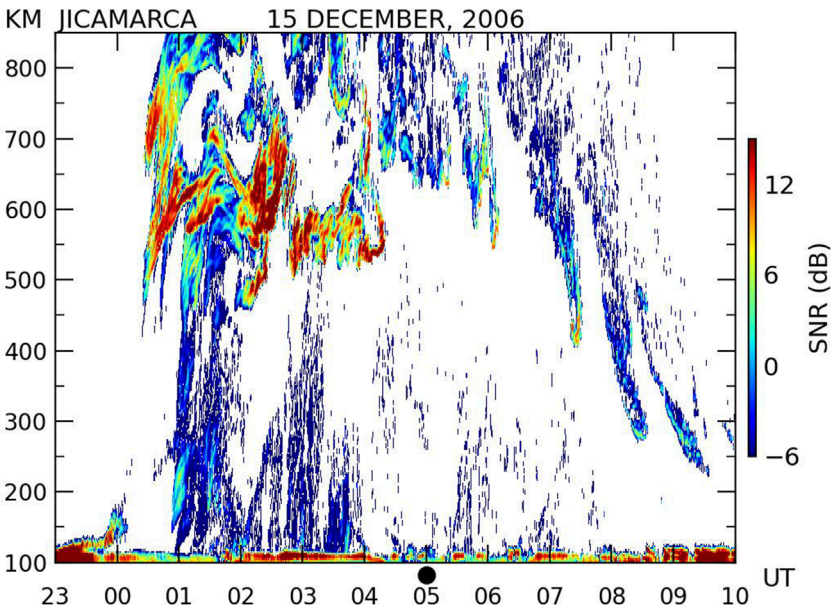

FIGURE 5
Backscattered power from 3-m plasma irregularities over Jicamarca during the 15 December 2006 geomagnetic storm. The full circle denotes local midnight.

penetration electric fields. Hopefully, storm-time simulations using these upgraded models will be extended down to low latitudes more often.

5 Summary and suggestions for future studies

We have seen that, over the last 2 decades, several studies examined the roles of solar wind, magnetosphere and high latitude ionospheric processes in driving geomagnetically active low latitude electrodynamics (e.g., Fejer, 2011; Tulasi Ram et al., 2012; Fejer et al., 2024; Wu et al., 2024; Chakrabarty et al., 2015; 2017; Huang C.-S. 2020a; b; Li et al., 2023; Wang and Luhr, 2024). They reported initial results on complex longitude dependent electrodynamic responses caused by simultaneous multiple disturbance drivers, IMF By convection rotations and skewing, long lasting substorm activity, and season dependent interhemispheric asymmetries. At present, the most pressing outstanding questions revolve around the roles of IMF By sign and season and hemispheric dependent convection pattern changes. These processes play particularly important roles on low latitude electrodynamic processes near dawn and dusk. Additional very important remaining questions include the conditions for the occurrence of very large amplitude substorms near dusk and possibly also near dawn, and of large amplitude overshielding driven by region 2 field-aligned current under slowly varying southward IMF Bz. Overall, however, the main challenge is how to account for the short- and -longer term effects of these very diverse solar wind, magnetosheric, and high latitude parameters.

Significantly more extensive comprehensive ground-based and *in-situ* satellite measurements are required for detailed studies of the above questions. In terms of ground-based data, additional routine measurements of ionospheric electrodynamics parameters over Africa and Asia are particularly desirable. The use of common parameters would greatly improve the study of low latitude electrodynamics during quiet and disturbed conditions. For instance, equatorial electrojet magnetic field measurements converted into vertical plasma drifts (i.e., zonal electric fields) using the dual magnetometer procedure developed by Anderson et al. (2002) would greatly facilitate comparisons with ground-based electrojet, radar and satellite electric field measurements. Since convection patterns changes appear increasingly important for low latitude studies, significantly more frequent use of northern and southern SuperDARN and other high and middle latitude measurements and low latitude data is clearly desirable.

The development of effective predictive models is the ultimate objective of space weather research. The development of increasingly comprehensive models like MAGE is a significant step forward towards this objective. MAGE simulations routinely extended to low latitudes would greatly improve low latitude electrodynamics studies. In the meantime, simulations studies with models like the TIEGCM and RCM, even with idealized input parameters, can help to improve the understanding of the effects of different physical processes and also can guide experimental studies in singling out the effects of different driving parameters. The recent experimental and modeling studies indicate the strong continued interest in the study of solar wind/magnetosphere low latitude coupling and their electrodynamic effects.

Author contributions

BF: Writing–original draft, Writing–review and editing. Luis A LN: Writing–review and editing. DC: Writing–review and editing.

Funding

The author(s) declare that financial support was received for the research, authorship, and/or publication of this article. LN was supported by NASA-ECIP award #80NSSC23K1066. The work of DC is supported by the Department of Space, Government of India. The Jicamarca Radio Observatory is a facility of the Instituto Geofisico del Perú operated with support from NSF award AGS-1732209 through Cornell University.

Acknowledgments

We thank the Jicamarca staff and for the radar observations. The Jicamarca Radio Observatory is a facility of the Instituto Geofisico del Perú operated with support from NSF award AGS-1732209 through Cornell University. We acknowledge the substorm timing list identified by the Newell and Gjerloev technique (Newell and Gjerloev, 2011), the SMU and SML indices (Newell and Gjerloev, 2011); and the SuperMAG collaboration (Newell and Gjerloev, 2011). LN was supported by NASA-ECIP award #80NSSC23K1066.

Conflict of interest

The authors declare that the research was conducted in the absence of any commercial or financial relationships that could be construed as a potential conflict of interest.

Publisher's note

References

Abdu, M. A. (2016). Electrodynamics of ionospheric weather over low latitudes. *Geos. Lett.* 3, 11–13. doi:10.1186/s40562-016-0043-6

Abdu, M. A., Maruyama, T., Batista, I. S., Saito, S., and Nakamura, M. (2007). Ionospheric responses to the October 2003 superstorm: longitude/local time effects over equatorial low and middle latitudes. *J. Geophys. Res.* 112, A10306. doi:10.1029/2006JA012228

Amory-Mazaudier, C., Bolaji, O. S., and Doumbia, V. (2017). On the historical origins of the CEJ, DP2, and Ddyn current systems and their roles in the predictions of ionospheric responses to geomagnetic storms at equatorial latitudes. *J. Geophys. Res. Space Phys.* 122, 7827–7833. doi:10.1002/2017JA024132

Anderson, D., Anghel, A., Yumoto, K., Ishitsuka, M., and Kudeki, E. (2002). Estimating daytime vertical ExB drift velocities in the equatorial F-region using ground-based magnetometer observations. *Geophys. Res. Lett.* 29 (12), 37–41. doi:10.1029/2001gl014562

Bagiya, M. S., Hazarika, R., Laskar, F. I., Sunda, S., Gurubaran, S., Chakrabarty, D., et al. (2014). Effects of prolonged southward interplanetary magnetic field on low-latitude ionospheric electron density. *J. Geophys. Res. Space Phys.* 119, 5764–5776. doi:10.1002/2014JA020156

Balan, N., Thampi, S. V., Lynn, K., Otsuka, Y., Alleyne, H., Watanabe, S., et al. (2008). F3 layer during penetration electric field. *J. Geophys. Res.* 113, A00A07. doi:10.1029/2008JA013206

Baumjohann, W., Kamide, Y., and Nakamura, R. (1996). Substorms, storms, and the near-Earth tail. *J. Geomagn. Geoelectr.* 48, 177–185. doi:10.5636/jgg.48.177

Bhaskar, A., and Vichare, G. (2013). Characteristics of penetration electric fields to the equatorial ionosphere during southward and northward IMF turnings. *J. Geophys. Res. Space Phys.* 118, 4696–4709. doi:10.1002/jgra.50436

Blanc, M., and Richmond, A. D. (1980). The ionospheric disturbance dynamo. *J. Geophys. Res.* 85 (A4), 1669–1686. doi:10.1029/JA085iA04p01669

Bulusu, J., Chandrasekhar, N. P., and Nagarajan, N. (2018). Effect of disturbance electric fields on equatorial electrojet over Indian longitudes. *J. Geophys. Res. Space Phys.* 123, 5894–5916. doi:10.1029/2018JA025247

Caan, N. N., McPheron, R. L., and Russel, C. T. (1977). Characteristics of the association between interplanetary magnetic field and substorms. *J. Geophys. Res.* 82 (29), 4837–4842. doi:10.1029/JA082i029p04837

Chakrabarty, D., Hui, D., Rout, D., Sekar, R., Bhattacharyya, A., Reeves, G. D., et al. (2017). Role of IMF b_y in the prompt electric field disturbances over equatorial ionosphere during a space weather event. *J. Geophys. Res. Space Phys.* 122, 2574–2588. doi:10.1002/2016JA022781

Chakrabarty, D., Rout, D., Sekar, R., Narayanan, R., Reeves, G. D., Pant, T. K., et al. (2015). Three different types of electric field disturbances affecting equatorial ionosphere during a long-duration prompt penetration event. *J. Geophys. Res. Space Phys.* 120, 4993–5008. doi:10.1002/2014JA020759

Chakrabarty, D., Sekar, R., Narayanan, R., Patra, A. K., and Devasia, C. V. (2006). Effects of interplanetary electric field on the development of an equatorial spread f event. *J. Geophys. Res.* 111, A12316. doi:10.1029/2006JA011884

Chakrabarty, D., Sekar, R., Sastri, J. H., Pathan, B. M., Reeves, G. D., Yumoto, K., et al. (2010). Evidence for oi 630.0 nm dayglow variations over low latitudes during onset of a substorm. *J. Geophys. Res.* 115, A10316. doi:10.1029/2010JA015643

Chakrabarty, D., Sekar, R., Sastri, J. H., and Ravindran, S. (2008). Distinctive effects of interplanetary electric field and substorm on nighttime equatorial f layer: a case study. *Geophys. Res. Lett.* 35, L19108. doi:10.1029/2008GL035415

Chakraborty, S., and Chakrabarty, D. (2023). Global asymmetry in ΔX variations during the 06 April 2000 geomagnetic storm: relative roles of IMF B_z and b_y. *J. Geophys. Res. Space Phys.* 128. doi:10.1029/2022JA031047

Chen, J., Lei, J., Wang, W., Liu, J., Maute, A., Qian, L., et al. (2021). Electrodynamical coupling of the Geospace system during solar flares. *J. Geophys. Res. Space Phys.* 126. doi:10.1029/2020JA028569

Cowley, S. W. H. (1981). Magnetospheric asymmetries associated with the y-component of the IMF. *Planet. Space Sci.* 29, 79–96. doi:10.1016/0032-0633(81)90141-0

Cowley, S. W. H., Morelli, J. P., and Lockwood, M. (1991). Dependence of convective flows and particle precipitation in the high-latitude dayside ionosphere on the X and Y components of the interplanetary magnetic field. *J. Geophys. Res.* 96, 5557–5564.

Cumnock, J. A., Heelis, R. A., and Hairston, M. R. (1992). Response of the ionospheric convection pattern to a rotation of the interplanetary magnetic field on January 14, 1988. *J. Geophys. Res. Space Phys.* 97 (A12), 19449–19460. doi:10.1029/92ja01731

Ebihara, Y., Tanaka, T., and Kikuchi, T. (2014). Counter equatorial electrojet and overshielding after substorm onset: global MHD simulation study. *J. Geophys. Res.* 119 (9), 7281–7296. doi:10.1002/2014JA020065

Fagundes, P. R., Cardoso, F. A., Fejer, B. G., Venkatesh, K., Ribeiro, B. A. G., and Pillat, V. G. (2016). Positive and negative GPS-TEC ionospheric storm effects during the extreme space weather event of March 2015 over the Brazilian sector. *J. Geophys. Res. Space Phys.* 121 (6), 5613–5625. doi:10.1002/2015JA022214

Fejer, B. G. (1997). The electrodynamics of the low latitude ionosphere: recent results and future challenges. *J. Atmos. Sol. Terr. Phys.* 59, 1465–1482. doi:10.1016/s1364-6826(96)00149-6

Fejer, B. G. (2002). Low latitude storm time ionospheric electrodynamics. *J. Atmos. Sol. Terr. Phyics.* 64, 1401–1408. doi:10.1016/s1364-6826(02)00103-7

Fejer, B. G. (2011). Low latitude ionospheric electrodynamics. *Space Sci. Rev.* 158 (1), 145–166. doi:10.1007/s11214-010-9690-7

Fejer, B. G., Blanc, M., and Richmond, A. D. (2017). Post-storm middle and low-latitude ionospheric electric fields effects. *Space Sci. Rev.* 206, 407–429. doi:10.1007/s11214-016-0320-x

Fejer, B. G., and Emmert, J. T. (2003). Low-latitude ionospheric disturbance electric field effects during the recovery phase of the 19 – 21 October 1998 magnetic storm. *J. Geophys. Res.* 108 (A12), 1454. doi:10.1029/2003JA010190

Fejer, B. G., Jensen, J. W., Kikuchi, T., Abdu, M. A., and Chau, J. L. (2007). Equatorial ionospheric electric fields during the November 2004 magnetic storm. *J. Geophys. Res.* 112 (A10). doi:10.1029/2007JA012376

Fejer, B. G., Jensen, J. W., and Su, S. (2008). Seasonal and longitudinal dependence of equatorial disturbance vertical plasma drifts. *Geophys. Res. Lett.* 35, L20106. doi:10.1029/2008gl035584

Fejer, B. G., and Kelley, M. C. (1980). Ionospheric irregularities. *Rev. Geophys.* 18 (2), 401–454. doi:10.1029/rg018i002p00401

Fejer, B. G., Laranja, S. R., and Condor, P. (2024). Multi-process driven unusually large equatorial perturbation electric fields during the April 2023 geomagnetic storm. *Front. Astron. Space Sci.* 11, 1351735. doi:10.3389/fspas.2024.1351735

Fejer, B. G., and Maute, A. (2021). Equatorial ionospheric electrodynamics. *Ionos. Dyn. Appl.*, 159–183. doi:10.1002/9781119815617.ch9

Fejer, B. G., and Navarro, L. A. (2022). First observations of equatorial ionospheric electric fields driven by storm-time rapidly recurrent magnetospheric substorms. *J. Geophys. Res. Space Phys.* 127 (12), e2022JA030940. doi:10.1029/2022ja030940

Fejer, B. G., Navarro, L. A., Sazykin, S., Newheart, A., Milla, M., and Condor, P. (2021). Prompt penetration and substorm effects over Jicamarca during the september 2017 geomagnetic storm. *J. Geophys. Res. Space Phys.* 126 (8), 1–11. doi:10.1029/2021JA029651

Fejer, B. G., and Scherliess, L. (1997). Empirical models of storm time equatorial zonal electric fields. *J. Geophys. Res.* 102 (A11), 24047–24056. doi:10.1029/97JA02164

Fejer, B. G., Scherliess, L., and de Paula, E. R. (1999). Effects of the vertical plasma drift velocity on the generation and evolution of equatorial spread F. *J. Geophys. Res. Space Phys.* 104 (A9), 19859–19869. doi:10.1029/1999JA900271

Fejer, B. G., Souza, J. R., Santos, A. S., and Costa Pereira, A. E. (2005). Climatology of F region zonal plasma drifts over Jicamarca. *J. Geophys. Res. Space Phys.* 110, A12310. doi:10.1029/2005JA011324

Fejer, B. G., Spiro, R. W., Wolf, R. A., and Foster, J. C. (1990). Latitudinal variation of perturbation electric fields during magnetically disturbed periods: 1986 SUNDIAL observations and model results. *Ann. Geophys.* 8 (6), 441–454.

Foster, J. C., and Burke, W. J. (2002). SAPS: a new categorization for sub-auroral electric fields. *EOS Trans. Am. Geophys Union* 83, 393–394. doi:10.1029/2002EO000289

Foster, J. C., and Vo, H. B. (2002). Average characteristics and activity dependence of the subauroral polarization stream. *J. Geophys. Res.* 107 (A12), 1475. doi:10.1029/2002JA009409

Friis-Christensen, E., Kamide, Y., Richmond, A. D., and Matsushita, S. (1985). Interplanetary magnetic field control of high-latitude electric fields and currents determined from Greenland magnetometer data. *J. Geophys. Res. Space Phys.* 90 (A2), 1325–1338. doi:10.1029/ja090ia02p01325

Friis-Christensen, E., Lassen, K., Wilhjelm, J., Wilcox, J. M., Gonzalez, W., and Colburn, D. S. (1972). Critical component of the interplanetary magnetic field responsible for large geomagnetic effects in the polar cap. *J. Geophys. Res.* 77 (19), 3371–3376. doi:10.1029/ja077i019p03371

Fuller-Rowell, T. J., Richmond, A. D., and Maruyama, N. (2008). "Global modeling of storm-time thermospheric dynamics and electrodynamics," in *Midlatitude ionospheric dynamics and disturbances*. Editors P. M. Kintner, A. J. Coster, T. Fuller-Rowell, A. J. Mannucci, M. Mendillo, and R. Heelis, 187–200. (Am. Geophys. Union Geophysical Monograph 181, 2008.

Galperin, Y., Ponomarev, V. N., and Zosimova, A. G. (1974). Plasma convection in the polar ionosphere. *Ann. Geophys.* 30, 1.

Gao, S., Cai, H., Zhan, W., Wan, X., Xiong, C., Zhang, H., et al. (2023). Characterization of local time dependence of equatorial spread F responses to substorms in the American sector. *Space Weather Space Clim.* 13, 2. doi:10.1051/swsc/2022039

Garner, T. W., Wolf, R. A., Spiro, R. W., Burke, W. J., Fejer, B. G., Sazykin, S., et al. (2004). Magnetospheric electric fields and plasma sheet injection to low L-shells during the 4–5 June 1991 magnetic storm: Comparison between the Rice Convection Model and observations. *J. Geophys. Res.* 109 (A02). doi:10.1029/2003JA010208

Heelis, R. A. (1984). The effects of interplanetary magnetic field orientation on dayside high latitude ionospheric convection. *J. Geophys. Res. Space Phys.* 89 (A5), 2873–2880. doi:10.1029/ja089ia05p02873

Heelis, R. A., and Maute, A. (2020). Challenges to understanding the Earth's ionosphere and thermosphere. *J. Geophys. Res. Space Phys.* 125, e2019JA027497. doi:10.1029/2019JA027497

Holappa, L., and Buzulukova, N. Y. (2022). Explicit IMF b_y-dependence of Energetic Protons and the ring current. *Geophys. Res. Lett.* 49, e2022GL098031. doi:10.1029/2022gl098031

Huang, C.-S. (2009). Eastward electric field enhancement and geomagnetic positive bay in the dayside low-latitude ionosphere caused by magnetospheric substorms during sawtooth events. *Geophys. Res. Lett.* 36, L18102. doi:10.1029/2009GL040287

Huang, C.-S. (2012). Statistical analysis of dayside equatorial ionospheric electric fields and electrojet currents produced by magnetospheric substorms during sawtooth events. *J. Geophys. Res.* 117, A02316. doi:10.1029/2011JA017398

Huang, C.-S. (2015). Storm-to-storm main phase repeatability of the local time variation of disturbed low-latitude vertical ion drifts. *Geophys. Res. Lett.* 42, 5694–5701. doi:10.1002/2015GL064674

Huang, C.-S. (2019). Long-lasting penetration electric fields during geomagnetic storms: observations and mechanisms. *J. Geophys. Res. Space Phys.* 124, 9640–9664. doi:10.1029/2019JA026793

Huang, C.-S. (2020a). Systematical analyses of global ionospheric disturbance current systems caused by multiple processes: penetration electric fields, solar wind pressure impulses, magnetospheric substorms, and ULF waves. *J. Geophys. Res. Space Phys.* 125 (9), e2020JA027942. doi:10.1029/2020JA027942

Huang, C.-S. (2020b). Westward plasma drifts in the nighttime equatorial ionosphere during severe magnetic storms: a new type of penetration electric fields caused by subauroral polarization stream. *J. Geophys. Res. Space Phys.* 125, e2020JA028300. doi:10.1029/2020JA028300

Huang, C.-S., Rich, F. J., and Burke, W. J. (2010b). Storm time electric fields in the equatorial ionosphere observed near the dusk meridian. *J. Geophys. Res.* 115, A08313. doi:10.1029/2009JA015150

Huang, C.-S., Sazykin, S., Chau, J. L., Maruyama, N., and Kelley, M. C. (2007). Penetration electric fields: efficiency and characteristic time scale. *J. Atmos. Sol. Terr. Phys.* 69 (10-11), 1135–1146. doi:10.1016/j.jastp.2006.08.016

Huang, C.-S., Sazykin, S., Chau, J. L., Maruyama, N., and Kelley, M. C. (2010a). Penetration of electric fields: efficiency and characteristic time scale. *J. Atmos. Sol. Terr. Phys.* 69. doi:10.1016/j/jastp.2006.08.06

Huang, C.-S., Zhang, Y., Wang, W., Lin, D., and Wu, Q. (2021). Low-latitude zonal ion drifts and their relationship with subauroral polarization streams and auroral return flows during intense magnetic storms. *J. Geophys. Res. Space Phys.* 126, e2021JA030001. doi:10.1029/2021JA030001

Hui, D., Chakrabarty, D., Sekar, R., Reeves, G. D., Yoshikawa, A., and Shiokawa, K. (2017). Contribution of storm time substorms to the prompt electric field disturbances in the equatorial ionosphere. *J. Geophys. Res. Space Phys.* 122 (5), 5568–5578. doi:10.1002/2016JA023754

Kelley, M. C., Fejer, B. G., and Gonzales, C. A. (1979). An explanation for anomalous equatorial ionospheric electric fields associated with a northward turning of the interplanetary magnetic field. *Geophys. Res. Lett.* 6 (4), 301–304. doi:10.1029/GL006i004p00301

Kelley, M. C., and Makela, J. J. (2002). B_y dependent prompt penetrating electric fields at the magnetic equator. *Geophys. Res. Lett.* 29 (7), 571–573. doi:10.1029/2001GL014468

Kelley, M. C., Makela, J. J., Chau, J. L., and Nicolls, M. J. (2003). Penetration of the solar wind electric field into the magnetosphere/ionosphere system. *Geophys. Res. Lett.* 30 (4), 1158. doi:10.1029/2002GL016321

Kikuchi, T. (2021). Penetration of the magnetospheric electric fields to the low latitude ionosphere. *Ionos. Dyn. Appl.*, 313–338. doi:10.1002/9781119815617.ch14

Kikuchi, T., Hashimoto, K., and Nozaki, K. (2008). Penetration of magnetospheric electric fields to the equator during a geomagnetic storm. *J. Geophys. Res.* 113, A062. doi:10.1029/2007JA012628

Kikuchi, T., and Hashimoto, K. K. (2016). Transmission of the electric fields to the low latitude ionosphere in the magnetosphere-ionosphere current circuit. *Geosci. Lett.* 3, 4. doi:10.1186/s40562-016-0035-6

Kikuchi, T., Hashimoto, K. K., Kitamura, T.-I., Tachihara, H., and Fejer, B. (2003). Equatorial counterelectrojets during substorms. *J. Geophys. Res. Space Phys.* 108 (A11), 1406. doi:10.1029/2003JA009915

Kuai, J., Liu, L., Lei, J., Liu, J., Zhao, B., Chen, Y., et al. (2017). Regional differences of the ionospheric response to the July 2012 geomagnetic storm. *J. Geophys. Res. Space Phys.* 122 (4), 4654–4668. doi:10.1002/2016ja023844

Kumar, A., Chakrabarty, D., Fejer, B. G., Reeves, G. D., Rout, D., Sripathi, S., et al. (2023). A case of anomalous electric field perturbations in the equatorial ionosphere during postsunset hours: Insights. *J. Geophys. Res. Space Phys.* 128, e2022JA030826. doi:10.1029/2022JA030826

Laundal, K. M., and Østgaard, N. (2009). Asymmetric auroral intensities in the Earth's Northern and Southern hemispheres. *Nature* 460 (7254), 491–493. doi:10.1038/nature08154

Le, G., Liu, G., Yizengaw, E., Wu, C. C., Zheng, Y., Vines, S., et al. (2024). Responses of field-aligned currents and equatorial electrojet to sudden decrease of solar wind dynamic pressure during the March 2023 geomagnetic storm. *Geophys. Res. Lett.* 51 (10), e2024GL109427. doi:10.1029/2024gl109427

Le Huy, M., and Amory-Mazaudier, C. (2005). Magnetic signature of the ionospheric disturbance dynamo at equatorial latitudes: "D_{dyn}". *J. Geophys. Res.* 110, A10301. doi:10.1029/2004JA010578

Lei, J., Wang, W., Burns, A. G., Solomon, S. C., Richmond, A. D., Wiltberger, M., et al. (2008). Observations and simulations of the ionospheric and thermospheric response to the December 2006 geomagnetic storm: initial phase. *J. Geophys. Res.* 113, A01314. doi:10.1029/2007JA012807

Li, Q., Li, S., Chen, J., Liu, J., Zhang, R., Liu, L., et al. (2023). Polar and equatorial ionospheric electrodynamical coupling under a prolonged northward B_z interval. *J. Geophys. Res. Space Phys.* 128, e2023JA032079. doi:10.1029/2023JA032079

Lin, D., Wang, W., Merkin, V. G., Huang, C., Oppenheim, M., Sorathia, K., et al. (2022). Origin of dawnside subauroral polarization streams during major geomagnetic storms. *AGU Adv.* 3, e2022AV000708. doi:10.1029/2022AV000708

Liou, K., Sotirelis, T., and Gjerloev, J. (2017). Statistical study of polar negative magnetic bays driven by interplanetary fast-mode shocks. *J. Geophys. Res. Space Phys.* 122, 7463–7472. doi:10.1002/2017JA024465

Liou, K., Sotirelis, T., and Mitchell, E. (2020). Control of the east-west component of the interplanetary magnetic field on the occurrence of magnetic substorms. *Geophys. Res. Lett.* 47, e2020GL087406. doi:10.1029/2020GL087406

Liou, K., Sotirelis, T., and Richardson, I. (2018). Substorm occurrence and intensity associated with three types of solar wind structure. *J. Geophys. Res. Space Phys.* 123, 485–496. doi:10.1002/2017JA024451

Liu, J., Liu, L., Nakamura, T., Zhao, B., Ning, B., and Yoshiwaka, A. (2014). A case study of ionospheric storm effects during long-lasting southward IMF *z*-driven geomagnetic storm. *J. Geophys. Res.* 119, 7716–7731. doi:10.1002/2014JA020273

Lu, G., Goncharenko, L., Nicolls, M. J., Maute, A., Coster, A., and Paxton, L. J. (2012). Ionospheric and thermospheric variations associated with prompt penetration electric fields. *J. Geophys. Res.* 117, A08312. doi:10.1029/2012JA017769

Lu, G., Zakharenkova, I., Cherniak, I., and Dang, T. (2020). Large-scale ionospheric disturbances during the 17 March 2015 storm: a model-data comparative study. *J. Geophys. Res. Space Phys.* 125, e2019JA027726. doi:10.1029/2019JA027726

Manoj, C., and Maus, S. (2012). A real-time forecast service for the ionospheric equatorial zonal electric field. *Space weather.* 10, S09002. doi:10.1029/2012sw000825

Maruyama, N., Fuller-Rowell, T., Codrescu, M. V., Anderson, D., Richmond, A. D., Maute, A., et al. (2011) "Modeling the storm time electrodynamics," in *Aeronomy of the Earth's Atmosphere and ionosphere*. Editors M. A. Abdu, D. Pancheva, and A. Bhattacharyya (Dordrecht: Springer), 455–464.

Maute, A., Richmond, A. D., Lu, G., Knipp, D. J., Shi, Y., and Anderson, B. (2021). Magnetosphere-ionosphere coupling via prescribed field-aligned current simulated by the TIEGCM. *J. Geophys. Res. Space Phys.* 126, e2020JA028665. doi:10.1029/2020JA028665

Milan, S. E., Mooney, M. K., Bower, G., Fleetham, A. L., Vines, S. K., and Gjerloev, J. (2023). Solar wind-magnetosphere coupling during high-intensity long-duration continuous AE activity (HILDCAA). *J. Geophys. Res. Space Phys.* 128, e2023JA032027. doi:10.1029/2023JA032027

Navarro, L. A., and Fejer, B. G. (2020). Storm-time coupling of equatorial nighttime F region neutral winds and plasma drifts. *J. Geophys. Res. Space Phys.* 125 (9), e2020JA028253. doi:10.1029/2020ja028253

Navarro, L. A., Fejer, B. G., and Scherliess, L. (2019). Equatorial disturbance dynamo vertical plasma drifts over Jicamarca: Bimonthly and solar cycle dependence. *J. Geophys. Res. Space Phys.* 124 (6), 4833–4841. doi:10.1029/2019ja026729

Newell, P. T., and Gjerloev, J. W. (2011). Evaluation of SuperMAG auroral electrojet indices as indicators of substorms and auroral power. *J. Geophys. Res. Space Phys.* 116 (A12), A12211. doi:10.1029/2011JA016779

Newell, P. T., Sotirelis, T., Liou, K., Meng, C.-I., and Rich, F. J. (2007). A nearly universal solar wind-magnetosphere coupling function inferred from 10 magnetospheric state variables. *J. Geophys. Res.* 112, A01206. doi:10.1029/2006JA012015

Nilam, B., Ram, S. T., Shiokawa, K., Balan, N., and Zhang, Q. (2020). The solar wind density control on the prompt penetration electric field and equatorial electrojet. *J. Geophys. Res. Space Phys.* 125, e2020JA027869. doi:10.1029/2020JA027869

Nishida, A., and Jacobs, J. A. (1962). Equatorial enhancement of world-wide changes. *J. Geophys. Res.* 67, 4937–4940. doi:10.1029/jz067i012p04937

Østgaard, N., Laundal, K. M., Juusola, L., Åsnes, A., Håland, S. E., Weygand, J. M., et al. (2011). Inter hemispherical asymmetry of substorm onset locations and the interplanetary magnetic field. *Geophys. Res. Lett.* 38, L08104. doi:10.1029/2011GL046767

Østgaard, N., Mende, S. B., Frey, H. U., Immel, T. J., Frank, L. A., Sigwarth, J. B., et al. (2004). Interplanetary magnetic field control of the location of substorm onset and auroral features in the conjugate hemispheres. *J. Geophys. Res.* 109, A07204. doi:10.1029/2003JA010370

Pandey, K., Chakrabarty, D., and Sekar, R. (2018). Critical evaluation of the impact of disturbance dynamo on equatorial ionosphere during daytime. *J. Geophys. Res. Space Phys.* 123 (11), 9762–9774. doi:10.1029/2018ja025686

Pedatella, N. M., Chau, J. L., Vierinen, J., Qian, L., Reyes, P., Kudeki, E., et al. (2019). Solar flare effects on 150-km echoes observed over Jicamarca: WACCM-X simulations. *Geophys. Res. Lett.* 46, 10951–10958.

Qian, L., Burns, A. G., Solomon, S. C., and Chamberlin, P. C. (2012). Solar flare impacts on ionospheric electrodyamics. *Geophys. Res. Lett.* 39, L06101. doi:10.1029/2012GL051102

Ranjan, A. K., Sunil Krishna, M. V., Amory-Mazaudier, C., Fleury, R., Sripathi, S., Vichare, G., et al. (2023). Variability of ionosphere over Indian longitudes to a variety of space weather events during December 2006. *Space weather.* 21, e2023SW003595. doi:10.1029/2023SW003595

Reistad, J. P., Holappa, L., Ohma, A., Gabrielse, C., Sur, D., Asikainen, T., et al. (2022). Dependence of the global dayside reconnection rate on interplanetary magnetic field by and the earth's dipole tilt. *Front. Astronomy Space Sci.* 9, 973276. doi:10.3389/fspas.2022.973276

Richmond, A. D., Peymirat, C., and Roble, R. G. (2003). Long-lasting disturbances in the equatorial ionospheric electric field simulated with a coupled magnetosphere-ionosphere-thermosphere model. *J. Geophys. Res.* 118 (A3), 1118. doi:10.1029/2002JA009758

Rodríguez-Zuluaga, J., Radicella, S. M., Nava, B., Amory-Mazaudier, C., and Alazo-Cuartas, K. (2016). Distinct responses of the low-latitude ionosphere to CME and HSSWS: the role of the IMF B_z oscillation frequency. *J. Geophys. Res. Space Phys.* 121 (11), 528–548. doi:10.1002/2016JA022539

Rout, D., Chakrabarty, D., Sekar, R., Reeves, G. D., Ruohoniemi, J. M., Pant, T. K., et al. (2016). An evidence for prompt electric field disturbance driven by changes in the solar wind density under northward IMF *z* condition. *J. Geophys. Res. Space Phys.* 121, 4800–4810. doi:10.1002/2016JA022475

Rout, D., Pandey, K., Chakrabarty, D., Sekar, R., and Lu, X. (2019). Significant electric field perturbations in low latitude ionosphere due to the passage of two consecutive ICMEs during 6–8 September 2017. *J. Geophys. Res. Space Phys.* 124, 9494–9510. doi:10.1029/2019JA027133

Rout, D., Singh, R., Pandey, K., Pant, T., Stolle, C., Chakrabarty, D., et al. (2022). Evidence for presence of a global quasi-resonant mode of oscillations during high-intensity long-duration continuous AE activity (HILDCAA) events. *Earth Plan. Space* 74 (1), 91–11. doi:10.1186/s40623-022-01642-1

Sazykin, S. (2000). *Theoretical studies of penetration of magnetospheric electric fields to the ionosphere. ProQuest Dissertations and Theses Global*. Logan, UT: Utah State University.

Scherliess, L., and Fejer, B. G. (1997). Storm-time dependence of equatorial disturbance dynamo zonal electric fields. *J. Geophys. Res.* 102, 24037–24046. doi:10.1029/97JA02165

Senior, C., and Blanc, M. (1984). On the control of magnetospheric convection by the spatial distribution of ionospheric conductivities. *J. Geophys. Res.* 89 (A1), 261–284. doi:10.1029/JA089iA01p00261

Sori, T., Shinbori, A., Otsuka, Y., Tsugawa, T., Nishioka, M., and Yoshikawa, A. (2022). Generation mechanisms of plasma density irregularity in the equatorial ionosphere during a geomagnetic storm on 21–22 December 2014. *J. Geophys. Space Phys.* 127 (5), e2021JA030240. doi:10.1029/2021JA030240

Spiro, R. W., Heelis, R. A., and Hanson, W. B. (1979). Rapid subauroral ion drifts observed by Atmosphere Explorer C. *Geophys. Res. Lett.* 6, 657–660. doi:10.1029/gl006i008p00657

Spiro, R. W., Wolf, R. A., and Fejer, B. G. (1988). Penetration of high-latitude electric field effects to low latitude during SUNDIAL 1984. *Ann. Geophys.* 6, 39–50.

Tanaka, T., Nakamizo, A., Yoshikawa, A., Fujita, S., Shinagawa, H., Shimazu, H., et al. (2010). Substorm convection and current system deduced from the global simulation. *J. Geophys. Space Phys.* 115 (A5). doi:10.1029/2009JA014676

Tenfjord, P., Østgaard, N., Snekvik, K., Laundal, K. M., Reistad, J. P., Haaland, S., et al. (2015). How the IMF by induces a by component in the closed magnetosphere and how it leads to asymmetric currents and convection patterns in the two hemispheres. *J. Geophys. Res. Space Phys.* 120, 9368–9384. doi:10.1002/2015JA021579

Tsurutani, B. T., Lakhina, G. S., and Hajra, R. (2020). The physics of space weather/solar-terrestrial physics (STP): what we know now and what the current and future challenges are. *Nonlinear Process. Geophys.* 27, 75–119. doi:10.5194/npg-27-75-2020

Tsurutani, B. T., Verkhoglyadova, O. P., Mannucci, A. J., Saito, A., Araki, T., Yumoto, K., et al. (2008). Prompt penetration electric fields (PPEFs) and their ionospheric effects during the great magnetic storm of 30–31 October 2003. *J. Geophys. Res.* 113, A05311. doi:10.1029/2007JA012879

Tulasi Ram, S., Balan, N., Veenadhari, B., Gurubaran, S., Ravindran, S., Tsugawa, T., et al. (2012). First observational evidence for opposite zonal electric fields in equatorial E and F region altitudes during a geomagnetic storm period. *J. Geophys. Res.* 117, A09318. doi:10.1029/2012JA018045

Tulasi Ram, S., Yokoyama, T., Otsuka, Y., Shiokawa, K., Sripathi, S., Veenadhari, B., et al. (2016). Duskside enhancement of equatorial zonal electric field response to convection electric fields during the St. Patrick's Day storm on 17 March 2015. *J. Geophys. Res. Space Phys.* 121, 538–548. doi:10.1002/2015JA021932

Veenadhari, B., Kikuchi, T., Kumar, S., Ram, S. T., Chakrabarty, D., Ebihara, Y., et al. (2019). Signatures of substorm related overshielding electric field at equatorial latitudes under steady southward IMF Bz during main phase of magnetic storm. *Adv. Space Sci.* 64 (10), 1975–1988. doi:10.1016/j.asr.2019.04.001

Wang, H., and Lühr, H. (2024). IMF b_y effects on the strength and latitude of polar electrojets: CHAMP and Swarm Joint observations. *J. Geophys. Res. Space Phys.* 129, e2023JA032049. doi:10.1029/2023JA032049

Wang, W., Lei, J., Burns, A. G., Wiltberger, M., Richmond, A. D., Solomon, S. C., et al. (2008). Ionospheric electric field variations during a geomagnetic storm simulated by a coupled magnetosphere ionosphere thermosphere (CMIT) model. *Geophys. Res. Lett.* 35, L18105. doi:10.1029/2008GL035155

Wei, Y., Hong, M., Wan, W., Du, A., Lei, J., Zhao, B., et al. (2008). Unusually long lasting multiple penetration of interplanetary electric field to equatorial ionosphere under oscillating IMF B_z. *Geophs. Res. Lett.* 35, L02102. doi:10.1029/2007GL032305

Wei, Y., Pu, Z., Hong, M., Zong, Q., Ren, Z., Fu, S., et al. (2009). Westward ionospheric electric field perturbations on the dayside associated with substorm processes. *J. Geophys. Res.* 114, A12209. doi:10.1029/2009JA014445

Wei, Y., Wan, W., Zhao, B., Hong, M., Ridley, A., Ren, Z., et al. (2012). Solar wind density controlling penetration electric field at the equatorial ionosphere during a saturation of cross polar cap potential. *J. Geophys. Res.* 117, A09308. doi:10.1029/2012JA017597

Wei, Y., Zhao, B., Guozhu, L., and Wan, W. (2015). Electric field penetration into Earth's ionosphere: a brief review. *Sci. Bull.* 60 (8), 748–761. doi:10.1007/s11434-015-0749-4

Wolf, R. A. (1970). Effects of ionospheric conductivity on convective flow of plasma in the magnetosphere. *J. Geophys. Res.* 75 (25), 4677–4698. doi:10.1029/JA075i025p04677

Wolf, R. A., Harel, M., Spiro, R. W., Voigt, G.-H., and Chen, C.-K. (1982). Computer simulation of inner magnetospheric dynamics for the magnetic storm of July 29, 1977. *J. Geophys. Res.* 87 (A8), 5949–5962. doi:10.1029/JA087iA08p05949

Wolf, R. A., Spiro, R. W., Sazykin, S., and Toffoletto, F. R. (2007). How the Earth's inner magnetosphere works: an evolving picture. *J. Atmos. Sol. Terr. Phys.* 69 (3), 288–302. doi:10.1016/j.jastp.2006.07.026

Wu, Q., Wang, W., Lin, D., Huang, C., and Zhang, Y. (2024). Penetrating electric field during the Nov 3–4, 2021 geomagnetic storm. *J. Atmos. Sol. Terr. Phys.* 257, 106219. doi:10.1016/j.jastp.2024.106219

Xiong, C., Luhr, H., and Fejer, B. G. (2015). Global features of the disturbance winds during storm time deduced from CHAMP observations. *J. Geophys. Res. Space Phys.* 120, 5137–5150. doi:10.1002/2015JA021302

Yadav, S., Lyons, L. R., Nishimura, Y., Weygand, J. M., Liu, J., Zhang, S. R., et al. (2023). Association of equatorward extended auroral streamers with overshielding conditions at equatorial latitudes: first observations. *J. Geophys. Res. Space Phys.* 128 (11), e2023JA031726. doi:10.1029/2023ja031726

Yamazaki, Y., and Kosch, M. J. (2015). The equatorial electrojet during geomagnetic storms and substorms. *J. Geophys. Res. Space Phys.* 120, 2276–2287. doi:10.1002/2014ja020773

Yeh, H.-C., Foster, J. C., Rich, F. J., and W. Swider, W. (1991). Storm time electric field penetration observed at mid-latitude. *J. Geophys. Res.* 96, 5707–5721.

Younas, W., Amory-Mazaudier, C., Khan, M., and Le Huy, M. (2021). Magnetic signatures of ionospheric disturbance dynamo for CME and HSSWs generated storms. *Space weather.* 19, e2021SW002825. doi:10.1029/2021SW002825

Zhang, K., Wang, H., Yamazaki, Y., and Xiong, C. (2021). Effects of subauroral polarization streams on the equatorial electrojet during the geomagnetic storm on June 1, 2013. *J. Geophys. Res. Space Phys.* 126, e2021JA029681. doi:10.1029/2021JA029681

Zhang, R., Liu, L., Le, H., and Chen, Y. (2021). Equatorial ionospheric electrodynamics during solar flares. *Geophys. Res. Lett.* 44, 4558–4565. doi:10.1002/2017gl073238

Zhao, B., Wan, W., Liu, L., Igarashi, K., Nakamura, M., Paxton, L. J., et al. (2008). Anomalous enhancement of ionospheric electron content in the Asian-Australian region during a geomagnetically quiet day. *J. Geophys. Res.* 113, A11302. doi:10.1029/2007JA012987

frontiers | Frontiers in Astronomy and Space Sciences

TYPE Methods
PUBLISHED 24 September 2024
DOI 10.3389/fspas.2024.1442315

OPEN ACCESS

EDITED BY
Daniel Okoh,
The National Space Research and Development Agency (NASRDA), Nigeria

REVIEWED BY
Xiukuan Zhao,
Chinese Academy of Sciences (CAS), China
Taiwo Ojo,
University of Toronto, Canada

*CORRESPONDENCE
Christian Mauricio,
20220334@lamolina.edu.pe

RECEIVED 01 June 2024
ACCEPTED 09 August 2024
PUBLISHED 24 September 2024

CITATION
Mauricio C, Suclupe J, Milla M, López de Castilla C, Kuyeng K, Scipion D and Rodriguez R (2024) Short-term prediction of horizontal winds in the mesosphere and lower thermosphere over coastal Peru using a hybrid model.
Front. Astron. Space Sci. 11:1442315.
doi: 10.3389/fspas.2024.1442315

Short-term prediction of horizontal winds in the mesosphere and lower thermosphere over coastal Peru using a hybrid model

Christian Mauricio[1]*, Jose Suclupe[2], Marco Milla[3], Carlos López de Castilla[1], Karim Kuyeng[4], Danny Scipion[4] and Rodolfo Rodriguez[5]

[1]Departamento de Estadística e Informática, Universidad Nacional Agraria La Molina, Lima, Perú, [2]Leibniz Institute of Atmospheric Physics, Rostock University, Kühlungsborn, Germany, [3]Instituto de Radioastronomía, Pontificia Universidad Católica del Perú, Lima, Perú, [4]Radio Observatorio de Jicamarca, Instituto Geofísico del Perú, Lima, Perú, [5]Estación Científica Ramón Mugica, Universidad de Piura, Piura, Perú

The mesosphere and lower thermosphere (MLT) are transitional regions between the lower and upper atmosphere. The MLT dynamics can be investigated using wind measurements conducted with meteor radars. Predicting MLT winds could help forecast ionospheric parameters, which has many implications for global communications and geo-location applications. Several literature sources have developed and compared predictive models for wind speed estimation. However, in recent years, hybrid models have been developed that significantly improve the accuracy of the estimates. These integrate time series decomposition and machine learning techniques to achieve more accurate short-term predictions. This research evaluates a hybrid model that is capable of making a short-term prediction of the horizontal winds between 80 and 95 km altitudes on the coast of Peru at two locations: Lima (12°S, 77°W) and Piura (5°S, 80°W). The model takes a window of 56 data points as input (corresponding to 7 days) and predicts 16 data points as output (corresponding to 2 days). First, the missing data problem was analyzed using the Expectation Maximization algorithm (EM). Then, variational mode decomposition (VMD) separates the components that dominate the winds. Each resulting component is processed separately in a Long short-term memory (LSTM) neural network whose hyperparameters were optimized using the Optuna tool. Then, the final prediction is the sum of the predicted components. The efficiency of the hybrid model is evaluated at different altitudes using the root mean square error (RMSE) and Spearman's correlation (r). The hybrid model performed better compared to two other models: the persistence model and the dominant harmonics model. The RMSE ranged from 10.79 to 27.04 $m s^{-1}$, and the correlation ranged from 0.55 to 0.94. In addition, it is observed that the prediction quality decreases as the prediction time increases. The RMSE at the first step reached 6.04 $m s^{-1}$ with a correlation of 0.99, while at the sixteenth step, the RMSE increased up to 30.84 $m s^{-1}$ with a correlation of 0.5.

KEYWORDS

MLT, EM, VMD, LSTM, OPTUNA

1 Introduction

The mesosphere and lower thermosphere (MLT) is the region of coupling between the lower and upper atmosphere. It is a region of complex chemical processes and dynamics (Liu et al., 2021). Understanding of this region is still in progress and it is of interest in atmospheric science and space traffic management.

The MLT dynamics is characterized by waves of different scales generated by other sources. For instance, on planetary scales, it is characterized by solar tides and planetary waves. The solar tides present periods of subharmonics of solar days and are generated mainly by the solar radiation absorption of tropospheric water vapor and stratospheric ozone (Forbes, 1995). On the other hand, the planetary waves have periods of days, e.g., the quasi-two-day waves with periods of 2 days generated *in situ* by baroclinic instabilities (McCormack et al., 2014). Moreover, the mesoscale gravity waves have periods of minutes to hours and can be generated by orographic sources and deep convection (Piani et al., 2000).

The MLT dynamics has usually been investigated using global circulation models (e.g., Liu et al., 2018), rockets (e.g., Staszak et al., 2021), satellites (e.g., Gasperini et al., 2023), lidars (e.g., Emmert et al., 2021), and radars (e.g., Chau et al., 2021). On the central and northern coast of Peru, two multi-static meteor radar networks, SIMONe Jicamarca (12°S, 77°W) in Lima and SIMONe Piura (5°S, 80°W) in Piura, allow us to measure winds between 75 and 105 km altitude since 2019 and 2021, respectively (Chau et al., 2021). Recently, diverse investigations have been conducted in the low-latitude Peruvian sector. For example, Suclupe et al. (2023) studied the climatology of large-scale dynamics, and Conte et al. (2024) studied the mesoscale dynamics.

The MLT region at low latitudes is significant for studying the effect of the lower atmospheric forces on the ionosphere (Immel et al., 2006; Vincent, 2015), a region with important implications for global communications and geo-location applications.

From another point of view, Yang et al. (2023) mention that near space (between 20 and 100 km altitude) is frequented by various aerospace vehicles. Like other research, they describe that there are complex dynamic processes, but emphasize that neutral atmospheric wind is a critical atmospheric parameter that influences the design and construction of aerospace vehicles. They argue that accurate wind prediction at these altitudes is essential for aerospace research. Similarly, Dhadly et al. (2023) mention that the upper atmosphere (between 85 and 500 km altitude) has complex dynamics and that the behavior of the climate in this region directly impacts communication and navigation technologies that are important to humanity. They add that, due to our increasing dependence on these space technologies, predicting the dynamics in the upper atmosphere will become increasingly important.

In wind predictive models, several investigations have been carried out mainly at the tropospheric level (e.g., Hussin et al., 2021; Hanifi et al., 2022). These investigations usually use two types of models: statistical and machine learning models. Hussin et al. (2021) mention that there are statistical models such as autoregressive (AR), moving average (MA), autoregressive moving average (ARMA), autoregressive Integrated Moving Average (ARIMA), generalized autoregressive conditional heteroskedasticity (GARCH), and ARIMA-GARCH. However, statistical models require the assumption of constant variance, and the original wind speed data do not meet this assumption. Hanifi et al. (2022) highlight that machine learning models are more appropriate methods for this data and that their success depends on an adequate selection of hyperparameters. They argue that the integrated use of Long Short-Term Memory (LSTM) neural networks and the hyperparameter optimizer Optuna accelerates the optimal choice of hyperparameters and gives more accurate estimates.

Recently, a time series decomposition technique called variational mode decomposition (VMD) has been introduced. This technique is applied before statistical modeling or modeling with machine learning and helps to deal with the problem of high variability. Ali et al. (2018) evaluate the application of this technique with two models for 1-step, 5-step, and 10-step forecasting horizons. In the first method, they use VMD with the ARIMA model. The second method uses VMD with artificial neural networks (ANN). These prediction methods are compared with other hybrid models such as empirical mode decomposition (EMD) with ARIMA, EMD with ANN, ensemble empirical mode decomposition (EEMD) with ARIMA, EEMD with ANN, complete ensemble empirical mode decomposition with Adaptive Noise (CEEMDAN) with ARIMA, and CEEMDAN with ANN. They conclude that the integration of VMD with ARIMA and VMD with ANN significantly outperforms existing hybrid models, for all prediction horizons.

In the prediction of wind speeds in the MLT region, Yang et al. (2023) also propose to use VMD before inputting the data into the prediction model. They used the hybrid VMD- PSO-LSTM model, which can decompose the wind time series for more accurate predictions. To do this, they used the VMD technique, which decomposes the original time series into principal components that dominate the signal. Then, each component is fed into the LSTM neural network, which finds the best hyperparameter values with the help of the particle swarm optimization (PSO) algorithm. This methodology is compared with the seasonal auto-regressive integrated moving average (SARIMA) statistical model and the hybrid models EMD-PSO-LSTM, EEMD-PSO-LSTM, CEEMDAN-PSO-LSTM and VMD-PSO-LSTM. Time horizons of 1 step, 3 steps, and 5 steps are predicted. They conclude that the proposed method has better efficiency and stability in wind speed prediction in all their comparisons.

This research studies the predictability of the mesospheric and lower thermospheric winds. In Peru, this prediction analysis has already been developed by Mauricio et al. (2023), whose model is based on the methodology used by Yang et al. (2023). The techniques used are missing data imputation, time series decomposition, and deep learning. These can identify the main components of the winds and then perform better predictions. Mauricio et al. (2023) modified the methodology of Yang et al. (2023). They added a missing data imputation analysis and used the Optuna hyperparameter optimizer in the modeling because it offers a better way to analyze the model quality.

The present research is a continuation of the work carried out by Mauricio et al. (2023). A new decomposition of the time series and a new hyperparameter search with Optuna have been performed. The main objective is to compare the efficiency of the hybrid model with a model of dominant harmonics based on the MLT climatology over Peru. The intention is to demonstrate that the

TABLE 1 Original data set.

	Lima	Piura
Description	Wind speeds in two components: zonal and meridional	
Heights	80.5, 85.5, 90.5 and 95.5 km	
Development of the model	September 2020 -November 2021 number of rows in the dataset: 21,888	October 2021 -December 2022 number of rows in the dataset: 21,888
Analysis 2023	Data of 2023 number of rows in the dataset: 17,519	

hybrid model gives more accurate predictions. This will be evaluated with the root mean square error (RMSE) and nonparametric Spearman correlation (r).

2 Materials and methods

2.1 Original data set

The zonal and meridional winds were estimated using the homogeneous method (e.g., Chau et al., 2021) recorded by SIMONe (Spread-spectrum Interferometric Multistatic meteor radar Observing Network) radars in Lima (12°S, 77°W) and Piura (5°S, 80°W). These systems have a horizontal coverage of approximately 400 km in diameter (Chau et al., 2021). The horizontal winds have a resolution of 1-h, and 2-km and were estimated every 30-min and 1-km (sampling) at heights of 80.5 km, 85.5 km, 90.5 km, and 95.5 km.

The available data for the Lima and Piura stations is described on Table 1. The period is different because the stations started operating in different years. The data sets are divided into two parts. The first part is used for model development, covering the training, validation and testing stages. In the case of Lima, the period runs from September 2020 to November 2021. In the case of Piura, the period runs from October 2021 to December 2022. In both cases, those periods were chosen since they have the same amount of records so that the modeling would be similar, although they differ on the amount of missing data (Figure 1).

In the second part, the performance of the proposed model is evaluated in both stations using data from the year 2023. In this section, the number of records and the period coincide, but they differ on the amount of missing data (Figure 2).

2.2 Missing data imputation

Missing data imputation was performed using the Expectation–maximization (EM) algorithm, which applies to data following a Gaussian distribution. This algorithm is used to estimate the parameters of a probability distribution from incomplete data by iteratively maximizing the likelihood of the available data. In the context of multivariate Gaussian data, the probability distribution can be characterized by the vector of means and the variance-covariance matrix (Schneider, 2001).

The EM algorithm has two stages: the E-step, which assumes the population mean and variance are known, and the M-step, which uses these values to estimate the population mean and covariance matrix. This iteration process continues until the parameter estimates of interest no longer change significantly. Maximum likelihood methods for incomplete multivariate data, particularly in the case of normally distributed data, focus on estimating the observed data parameters, such as the vector of means and the variance-covariance matrix. If the data follow a multivariate normal distribution, one can apply known properties to estimate those unknown parameters (Pigott, 2001).

The imputation analysis consisted of two parts. First, the imputation procedure described by Mauricio et al. (2023) was replicated. Additionally, the descriptive statistical indicators were presented to comprehend the process better. The second part involved exclusively imputing data from the year 2023, because these were obtained at a later point in time. Figure 2 shows the percentages of missing data for the year 2023, for the Lima and Piura stations. The absence of data was mainly due to two reasons. First, during the first months of the year, the equipment was affected by the presence of heavy rains in the region, caused by cyclone Yaku and the El Niño Costero phenomenon. Secondly, during the year, there were some radar hardware failures. These unexpected situations forced the radars to be inoperative at certain intervals.

In case of high percentages of missing data, the time series is partitioned in such a way as to omit the time intervals with accumulated absences. The maximum percentage limit allowed in each subseries is 6%, which is an approximate value of that detected in the article of Mauricio et al. (2023). Then, for each subseries, the percentage is reanalyzed. If the percentage is less than 6%, we proceed with the estimation of the missing data. Otherwise, the time subseries are further separated until their percentages are lower than 6%.

2.3 Data preprocessing

Once the missing data are imputed, they are averaged every 3 h. Data not belonging to the year 2023 are divided chronologically into train (70%), validation (10%) and test (20%). Training and validation data are used for the building and optimization of the model, while the test data is used specifically for the metric evaluation. The intention is that the test data is not involved in the modeling and optimization, to avoid overfitting (Mauricio et al.,

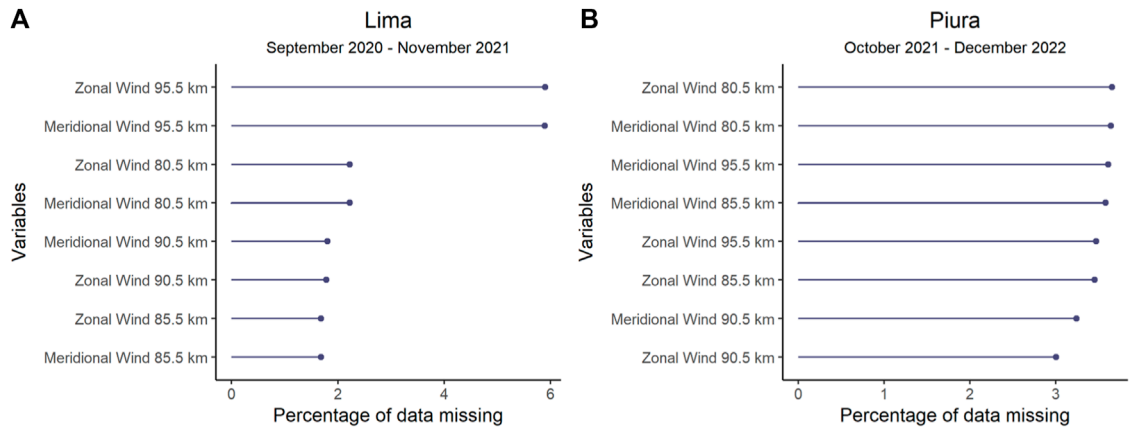

FIGURE 1
Missing data at the model development stage. **(A)** shows the percentage of missing data in Lima. **(B)** shows the percentage of missing data in Piura.

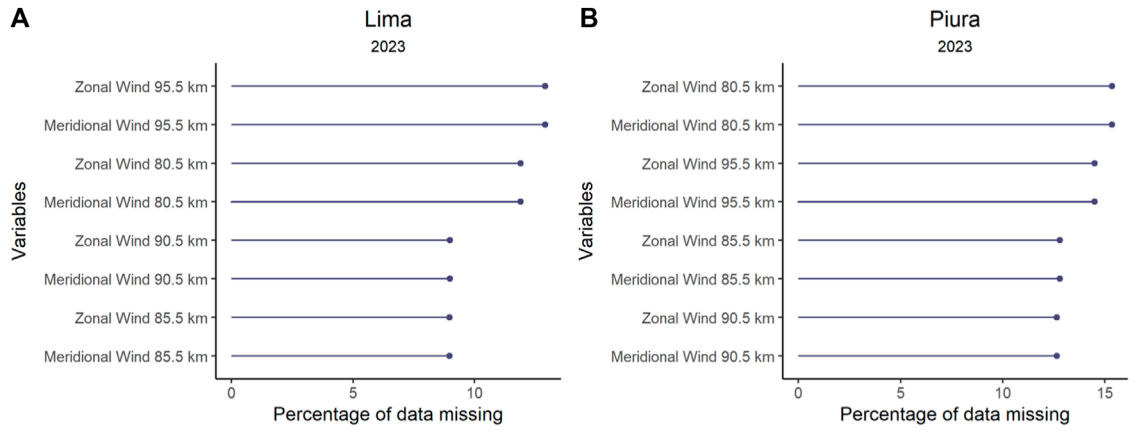

FIGURE 2
Missing data in the year 2023. **(A)** presents the percentage of missing data in Lima. **(B)** shows the percentage of missing data in Piura.

2023). Finally, each data block is normalized based on the training data, before moving on to the time series decomposition stage.

2.4 Time serie decomposition

Variational mode decomposition (VMD) is a method used in signal processing. This method was proposed in 2014 to overcome the limitations of techniques such as wavelet analysis and Empirical Mode Decomposition (EMD). The VMD technique decomposes a sequence, such as wind time series, into multiple subsequences known as intrinsic modal function (IMF) components. The importance of VMD is its ability to optimally adapt the center frequency and bandwidth of each IMF according to the signal characteristics, which makes it effective in dealing with non-smoothness in data series, such as wind speed data (Yang et al., 2023). The VMD algorithm has as input a signal or time series x(t), which is decomposed into subseries called modes or harmonic signals $u_k(t)$, where k is the number of total modes.

$$\mathbf{x(t)} = \sum_{\mathbf{k=1}}^{\mathbf{K}} \mathbf{u_k(t)}$$

$$\mathbf{u_k} = \mathbf{A_k(t)\cos\left(\phi_k(t)\right)}$$

Each mode has an instantaneous amplitude $A_k(t)$, an instantaneous phase $\phi_k(t)$, a limited spectral bandwidth $B(u_k(t))$ and an instantaneous center frequency ω_k (Ali, Khan, and Rehman, 2018), where it is assumed that each mode varies slower than the phase and is non-negative (Gan et al., 2021). The complete mathematical process that follows this decomposition and bandwidth estimation can be found in the article of Dragomiretskiy and Zosso (2014).

The VMD algorithm package in Python was obtained from the code developed by Carvalho et al. (2020). The choice of components is determined under two complementary rules. The first rule follows the methodology of Yang et al. (2023) which involves observing center frequencies. It starts by decomposing the original time series

TABLE 2 Evaluation of the optimal number of components, with center frequencies.

K	IMF 1	IMF 2	IMF 3	IMF 4	IMF 5	IMF 6	IMF 7	IMF 8	IMF 9	IMF 10	IMF 11	IMF 12
1	0.0027											
2	0.0031	0.1944										
3	0.0030	0.1271	0.2665									
4	0.0030	0.1247	0.2430	0.3674								
5	0.0030	0.1231	0.1721	0.2520	0.3707							
6	0.0026	0.0596	0.1261	0.2079	0.2747	0.3748						
7	0.0025	0.0585	0.1250	0.1758	0.2491	0.3620	0.4436					
8	0.0025	0.0582	0.1247	0.1727	0.2455	0.3058	0.3718	0.4506				
9	0.0025	0.0570	0.1236	0.1501	0.1943	0.2496	0.3101	0.3732	0.4526			
10	0.0025	0.0560	0.1230	0.1419	0.1853	0.2467	0.3023	0.3636	0.4061	0.4621		
11	0.0016	0.0261	0.0690	0.1244	0.1533	0.1970	0.2499	0.3069	0.3669	0.4093	0.4634	
12	0.0016	0.0242	0.0659	0.1238	0.1440	0.1780	0.2185	0.2588	0.3123	0.3685	0.4108	0.4641

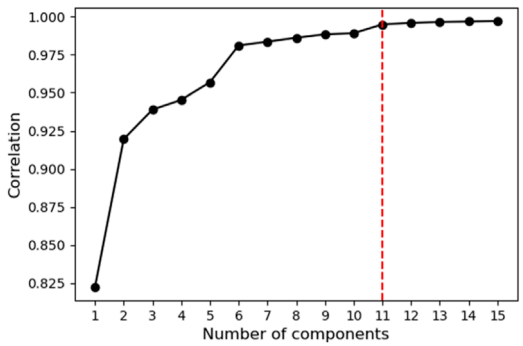

FIGURE 3
Correlations were calculated between the actual data and the sum of the components of zonal wind at Lima at 80.5 km height. When k = 11, the correlation appears to be constant.

with different values of k, where each component has an associated central frequency. The optimal number of components is then obtained when the central frequency values are approximate.

Table 2 shows the decomposition of the normalized time series of the zonal wind at Lima at 80.5 km height, and the central frequencies are obtained for different values of k. It is observed that when the series are decomposed in k = 10, k = 11 and k = 12, the last central frequencies are approximately 0.4621, 0.4634, and 0.4641, respectively. Then, it can be deduced that the time series can be optimally decomposed into 12 components.

A second complementary way of determining the optimal number of components is proposed by evaluating the correlation between the initial series data and the sum of the IMF components. Being an additive decomposition, the sum of the components results in the estimate of the initial data. Figure 3 shows the correlation between the normalized data of the zonal wind at Lima at 80.5 km height and the sum of its IMF components, for different values of k. It is observed that when the series is decomposed from 11 components to more, the correlation values are approximate and almost constant. In this instance, both rules give similar results. Then it is determined that the number of components for this series is 12. Figure 4 shows the 12 components.

2.5 Long short-term memory neural network

Long short-term memory neural network (LSTM) is an enhancement of the recurrent neural network (RNN), which has limitations such as gradient bursting and fading, lack of retention of historical information over time; and not distinguish between information that should be further processed and information that should be deleted. The LSTM network uses control gates that help solve the above problems. Within the LSTM block, there is a ring buffer and three gates named: input, forget, and output. Like RNNs, the LSTM network also has a hidden layer that processes the flow of information (Son and Jung, 2020).

Figure 5 shows the basic structure of the LSTM network. Its main features are the hidden layer h_t, the memory cell c_t and the control gates (represented by the letters inside the circles). The first gate is the forgetting gate (letter f), which evaluates the elements to be purged from the cell state c_{t-1} and outputs a resultant vector f_t. Then the cell state $\tilde{c}$ is partially updated, processing the input x_t and the previous hidden state h_{t-1}. The second gate is the input gate (letter i) which has a resultant vector i_t. This gate has the task of evaluating which information from the partial cell state $\tilde{c}_t$ serves to fully update the

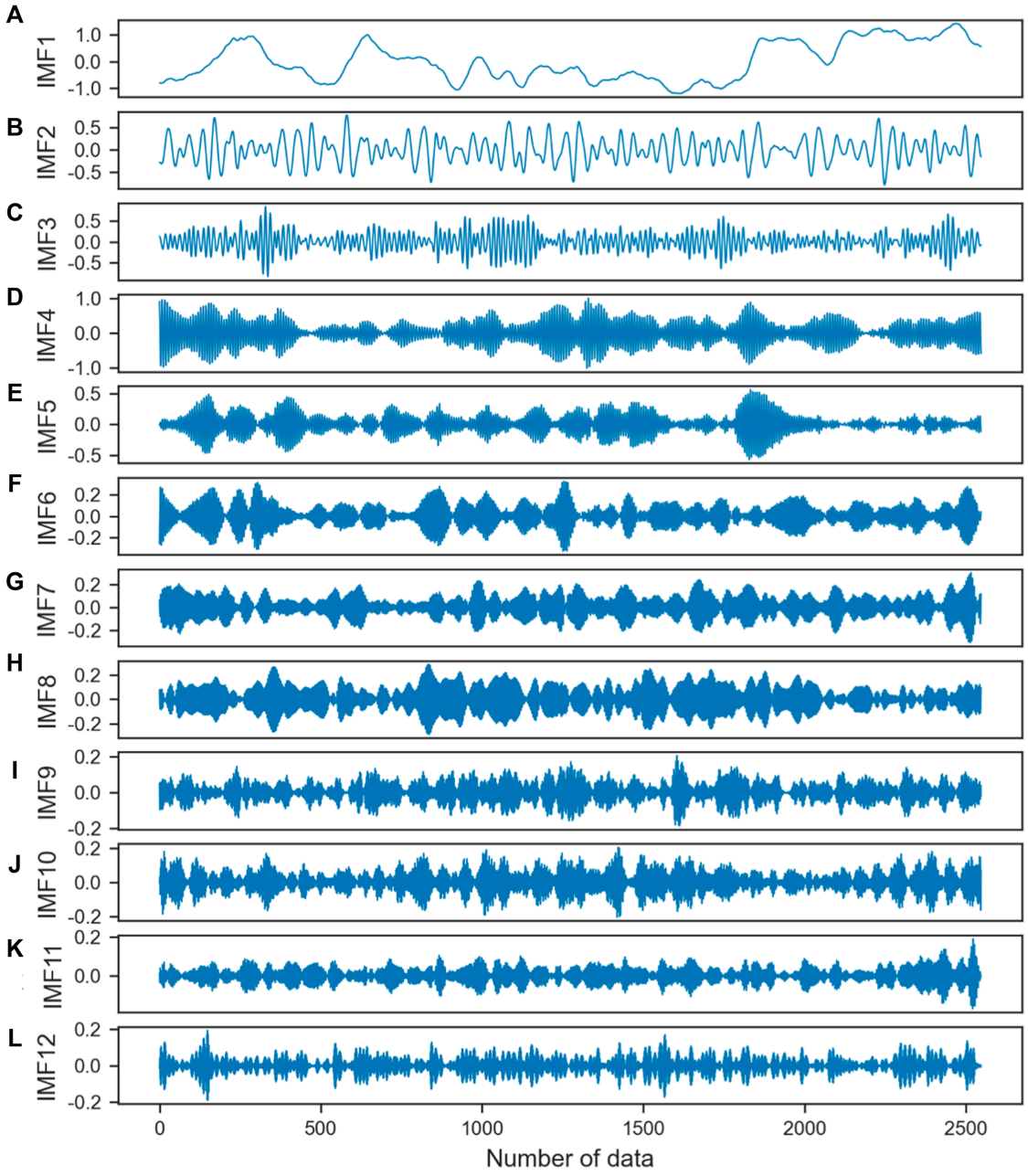

FIGURE 4
Components of the zonal wind at Lima at 80.5 km altitude. **(A–L)** show the 12 time series into which the original time series was decomposed.

current time cell state c_t. Finally, there is the output gate (letter o) that controls the sending of the information from the current cell state c_t to the new hidden state h_t (Kratzert et al., 2018).

LSTM neural networks can be implemented using the function of the same name from the TensorFlow library in Python. Like the methodology proposed by Yang et al. (2023) a model with LSTM was performed for each IMF of each time series. For example, if a time series is determined to have 12 modal components, then 12 models with LSTM should be performed.

Before inputting the data to the neural network, the dimensions of the input and output data must be specified. In this case, we have experimented with a window of 56 consecutive data, corresponding to a period of 1 week. While the output data are 16 steps in the future, corresponding to 2-day records. Subsequently, hyperparameters such as dropout, number of layers and neurons, Adam optimizer, learning rate, and batch size were added (Mauricio et al., 2023).

Additionally, the Ridge regularization was introduced, which is a penalty applied to the loss function of the proposed model. This regularization was also used in the paper by Rosa et al. (2020), who performed a similar analysis with VMD and LSTM for the Piura River flow time series in Peru.

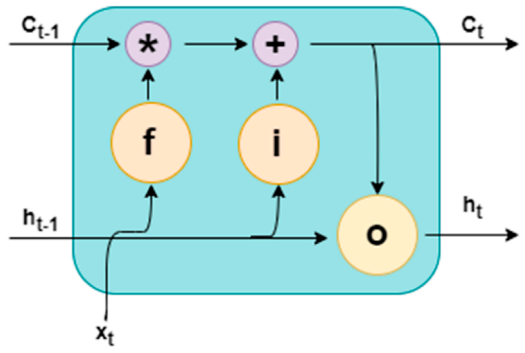

FIGURE 5
Neural network operation.

TABLE 3 Hyperparameter options.

Hyperparameters	
Layers	1
Neurons in layer	Values between 1 and 100
Dropout	Values between 0.0 and 0.5
Learning rate	Values between 0.00001 and 0.1
Epoch	100,120,140,160,180 years 200
Batch size	16, 24, 32, 40, 48, 56, 64
Lambda (regularizer L2)	Values between 0.001 and 0.01

2.6 Optuna

Akiba et al. (2019) presented Optuna, a framework designed for hyperparameter optimization in the context of machine learning and deep learning. Optuna is based on a sequential optimization approach that uses the adaptive search tree-based optimization (TPE) algorithm to efficiently explore the hyperparameter space. Optuna is characterized by its ability to dynamically adapt to the hyperparameter space, allowing it to converge more quickly to optimal solutions. This is achieved by systematically exploring hyperparameter combinations, where decisions are based on previous observations to steer the search towards promising regions of the search space. The framework offers a simple user interface and seamless integration with machine learning and deep learning libraries, facilitating its use in a variety of applications. In addition, Optuna provides advanced tools such as experiment management and result visualization to facilitate the organization and analysis of optimization results. Optuna's scalability stands out, as it is designed to handle large datasets and complex search spaces efficiently. This makes it suitable for both small-scale applications and large-scale research projects requiring complex model optimization. In summary, Optuna represents a significant breakthrough in automated hyperparameter optimization, offering a powerful and efficient solution for improving model performance. Its ability to dynamically adapt to the hyperparameter space and its seamless integration with popular libraries make it a valuable tool for researchers and practitioners in the field of machine learning.

Table 3 shows the set of hyperparameters used in this study. During optimization, Optuna provides tools that help to plot the loss curve that allows to evaluation of the learning performance of the models. Figure 6 shows the loss curves for the 12 components of the Piura zonal wind at 80.5 km altitude. Optuna has by default that the X-axis represents the number of epochs and the Y-axis represents the mean square error (MSE). However, since the data are normalized, the MSE values have no units of measurement.

2.7 Hybrid model

In summary of what has been explained in the previous paragraphs, the hybrid model applied in combines the VMD, LSTM and Optuna techniques (Figure 7). First, time series of normalized and complete data are obtained, which are then decomposed into their optimal components using the VMD algorithm. These components are reorganized into windows of 56 data, equivalent to 7 days. Each of these blocks is fed into an individual LSTM neural network, where the hyperparameters are optimized with Optuna. The output of each LSTM provides windows of 16 steps, corresponding to 2 days. Finally, the final prediction is the denormalization of the sum of the estimates calculated for each component.

2.8 Persistence model

Mauricio et al. (2023) used a persistence model that consists of the wind speed values of two previous days being repeated in the following 2 days. Through this model, a time series is reconstructed and compared with the hybrid model estimates. The intention is to demonstrate that the hybrid model is superior to the simplicity of the persistence model.

2.9 Model of dominant harmonics

The model of dominant harmonics was built from a sum of sinusoidal series with specified periods. In this model, the mean winds (an average of meridional wind and an average of zonal wind), as well as the amplitudes and phases of specific waves, were fitted using the least squares method, with a 7-day window. The selected periods correspond to the dominant wave periods obtained by the MLT climatology over the Peruvian sector (see Suclupe et al., 2023 for more details), which are 48, 24, 12, 8, and 6 h. Finally, the model was interpolated in a window of 2 days to compare it with the proposed hybrid model.

2.10 Evaluation of the hybrid model

Mauricio et al. (2023) reconstructed the time series by making predictions with a 16-step horizon. This approach involved the generation of sequential predictions of consecutive blocks of

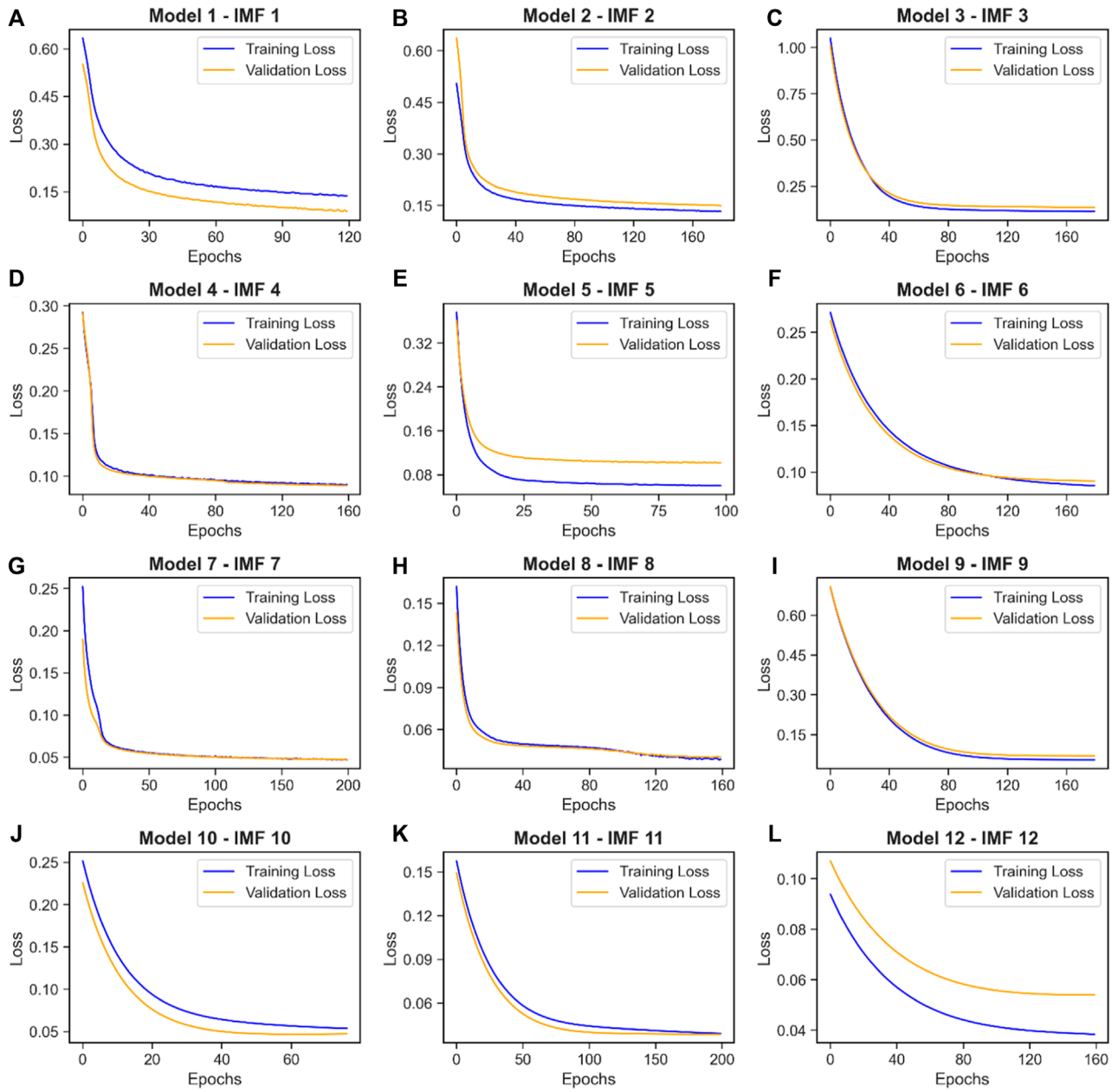

FIGURE 6
Training and validation loss curves for each component of the Piura zonal wind at 80.5 km altitude. **(A–L)** show that the training loss and validation loss curves decrease similarly in all cases.

16 steps within the time series. Specifically, predictions were initially applied to steps 1 through 16. Then, the process was repeated for steps 17 through 32, and so on, ensuring progressive coverage of the entire time series in 16-step intervals. This method allowed the evaluation of the predictive capability of the proposed model versus a 2-day persistence model, for multiple segments (training, validation, testing and February 2023 data), ensuring a complete evaluation of its performance over time. The metric used was RMSE and the proposed model was shown to be better.

In this paper, the RMSE was again used and the nonparametric Spearman correlation metric (r) was added. This coefficient is used to measure the strength and direction of the association between two variables, regardless of the distribution of the data. Assuming that the results show a mostly positive correlation, a correlation is considered to be very weak if its value is between 0.00 and 0.20, weak between 0.21 and 0.40, moderate between 0.41 and 0.60, strong between 0.61 and 0.80, and very strong between 0.81 and 1.00.

It was decided to evaluate the hybrid model in three stages. The first stage is related to evaluating that the estimates of the

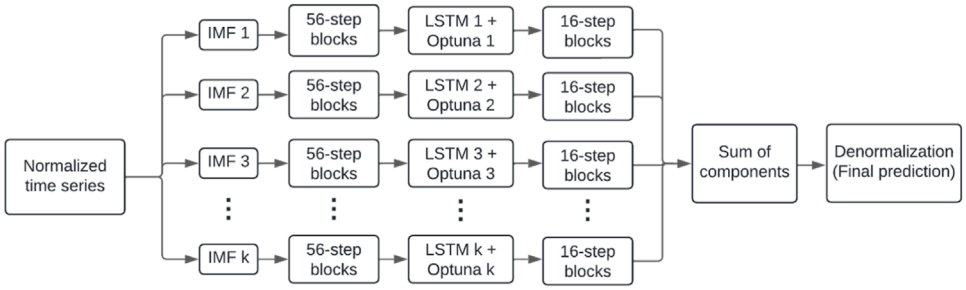

FIGURE 7
Diagram of the hybrid model.

proposed model do not present overfitting and that it is superior to a simple model such as the persistence model. Similar to the analysis performed by Mauricio et al. (2023), the entire time series is estimated using 16-step predictions. That is, the 16-step blocks are joined and form a complete time series. It is confirmed that there is no overfitting when the calculated metrics of the hybrid model are similar in the training, validation and test data sets. On the other hand, it is confirmed that the hybrid model is better than the persistence model when the metrics of the hybrid model are better than those of the persistence model, using the same data sets.

The second stage was the step-by-step analysis. This method involves generating multiple predictions using continuous input windows. Predictions are made using the first 56 input steps, then the input window is shifted one position and new predictions are made using the next 56 steps, and so on. This process is repeated until the entire time series is covered. This approach facilitates obtaining vectors of estimates of all 1-steps, all 2-steps and so on up to the vector of 16-steps. This analysis was only performed on the test data, evaluating the predictive model performance at each time step.

In the third stage, the original data for the year 2023 (January to December) are available. The objective is to evaluate whether the hybrid model is better than the model of dominant harmonic for the year 2023. As in the first stage, a time series is reconstructed through the estimated consecutive blocks of 16 steps. It is evaluated which model is better, observing which one has better metrics.

3 Results

3.1 Data imputation

Table 4 shows the comparison of the descriptive statistics values before and after imputation for data previous to 2023. This was mentioned by Mauricio et al. (2023), but the values were not shown there.

In the second stage, the 2023 data were analyzed and a summary of the information on the amount of missing data was obtained. The result shows that the percentages were in the range between 8% and 15% (Table 5). As these percentages of missing data are higher than 6%, the time series was subdivided into blocks with lower percentages and the imputation process was replicated.

3.2 VMD decomposition

The VMD decomposition analysis to determine the number of components of each time series is shown in Table 6. The values show convergence between 11 and 12 components. Above these values, the method is not optimal.

3.3 Evaluation of the hybrid model

3.3.1 Comparison with persistence model

The metrics in Tables 7, 8 are analyzed with the training, validation and test data sets for the Lima and Piura locations, respectively. The metrics show that the hybrid model is better than the persistence model in both locations.

In the case of Lima, the hybrid model has RMSE values that vary between 12.38 $m\,s^{-1}$ and 22.5 $m\,s^{-1}$, while the correlation values vary between 0.81 and 0.94. In comparison, the persistence model has higher RMSE with values that vary between 26.36 $m\,s^{-1}$ and 47.52 $m\,s^{-1}$, while the correlation values are lower and vary between 0.24 and 0.64.

In the case of Piura, the RMSE values vary between 10.79 $m\,s^{-1}$ and 27.04 $m\,s^{-1}$, while the correlation values vary between 0.67 and 0.93. In comparison, the persistence model has higher RMSE with values that vary between 29.01 $m\,s^{-1}$ and 43.78 $m\,s^{-1}$, while the correlation values are lower than 0.48.

In addition, the values of the hybrid model metrics in the three data sets (training, validation and test), do not have large differences. This is an indicator that the model does not have overfitting.

3.3.2 Step analysis

As noted in the methodology, this analysis was only performed on the test data set. The metrics calculated for each time step show an increase in RMSE (Figure 8) and a decrease in correlation (Figure 9). This indicates that within the windows of 16 prediction steps, the first steps fit better than the last steps.

In the case of Lima, the RMSE values increase from 6.46 $m\,s^{-1}$ to 30.84 $m\,s^{-1}$, while the correlation values decrease from 0.99 to 0.66. For example, the meridional wind at 85.5 km of altitude, has the best 1-step with an RMSE of 6.46 $m\,s^{-1}$ and a

10.3389/fspas.2024.1442315

TABLE 4 Comparison of descriptive statistics before and after imputation.

		Before data imputation				After data imputation			
Height		80.5 km	85.5 km	90.5 km	95.5 km	80.5 km	85.5 km	90.5 km	95.5 km
Zonal wind over Lima	Mean	1.44	−0.48	−5.10	−7.47	1.45	−0.48	−5.00	−8.30
	Standard deviation	31.09	33.36	37.98	40.62	31.11	33.35	38.00	40.85
	Min	−109.97	−146.21	−134.82	−149.52	−109.97	−146.21	−134.82	−149.52
	Q1	−21.00	−23.85	−31.07	−34.92	−20.97	−23.85	−31.00	−36.02
	Median	2.33	−0.10	−4.16	−7.37	2.28	−0.12	−4.11	−8.06
	Q3	25.12	23.03	21.44	19.79	25.09	22.99	21.56	19.15
	Max	87.58	107.67	145.81	145.40	102.64	123.87	145.81	145.40
	Skewness	−0.16	−0.07	−0.09	0.01	−0.15	−0.07	−0.09	0.01
	Kurtosis	−0.48	−0.20	−0.26	−0.01	−0.47	−0.20	−0.26	−0.01
Meridional wind over Lima	Mean	−2.97	−4.22	−4.46	−1.73	−2.99	−4.22	−4.43	−1.31
	Standard deviation	31.65	39.33	45.22	49.21	31.67	39.37	45.27	49.16
	Min	−105.98	−124.41	−129.33	−139.68	−113.33	−166.54	−150.39	−174.41
	Q1	−25.72	−33.56	−37.46	−38.43	−25.72	−33.56	−37.41	−37.62
	Median	−3.27	−5.43	−4.03	−1.13	−3.29	−5.40	−3.90	−0.58
	Q3	19.45	24.00	28.17	33.67	19.40	23.99	28.18	33.93
	Max	112.53	120.89	139.03	149.94	112.53	120.89	139.03	195.99
	Skewness	0.05	0.16	0.00	0.06	0.05	0.15	0.00	0.06
	Kurtosis	−0.36	−0.39	−0.50	−0.52	−0.35	−0.37	−0.49	−0.48
Zonal wind over Piura	Mean	−2.99	−6.22	−9.32	−11.83	−2.97	−6.20	−9.25	−11.73
	Standard deviation	27.84	30.44	34.19	38.77	27.96	30.52	34.20	38.79
	Min	−130.96	−132.43	−145.58	−146.29	−130.96	−145.27	−145.58	−146.29
	Q1	−21.04	−26.76	−32.01	−38.80	−21.08	−26.76	−31.97	−38.66
	Median	−2.33	−5.47	−8.31	−10.60	−2.30	−5.46	−8.27	−10.58
	Q3	15.41	14.20	13.85	15.75	15.48	14.28	13.91	15.82
	Max	147.98	143.47	138.13	137.72	147.98	143.47	138.13	137.72
	Skewness	−0.04	−0.07	−0.11	−0.10	−0.05	−0.07	−0.11	−0.09
	Kurtosis	0.38	−0.06	−0.10	−0.19	0.38	−0.03	−0.10	−0.19

(Continued on the following page)

TABLE 4 (*Continued*) Comparison of descriptive statistics before and after imputation.

Height		Before data imputation				After data imputation			
		80.5 km	85.5 km	90.5 km	95.5 km	80.5 km	85.5 km	90.5 km	95.5 km
Meridional wind over Piura	Mean	−2.69	−2.77	−4.53	−5.25	−2.60	−2.71	−4.59	−5.31
	Standard deviation	31.36	34.00	36.41	41.20	31.41	34.02	36.47	41.28
	Min	−149.54	−142.49	−144.62	−148.40	−149.54	−142.49	−149.39	−148.40
	Q1	−23.94	−26.94	−30.37	−34.36	−23.90	−26.83	−30.41	−34.45
	Median	−3.45	−4.05	−5.08	−5.44	−3.30	−3.93	−5.21	−5.56
	Q3	17.76	20.32	20.21	22.58	17.89	20.41	20.20	22.55
	Max	149.34	123.16	135.49	148.12	149.34	123.16	135.49	148.12
	Skewness	0.14	0.14	0.13	0.08	0.13	0.13	0.12	0.08
	Kurtosis	0.12	−0.16	−0.16	−0.20	0.12	−0.15	−0.14	−0.19

TABLE 5 Missing data in 2023.

Height(km)	Lima				Piura			
	Zonal Wind		Meridional Wind		Zonal Wind		Meridional Wind	
	Amount	Percentage	Amount	Percentage	Amount	Percentage	Amount	Percentage
80.5	2084	11.90	2084	11.90	2,689	15.30	2,689	15.30
85.5	1,572	8.97	1,572	8.97	2,241	12.80	2,241	12.80
90.5	1,574	8.98	1,574	8.98	2,216	12.60	2,216	12.60
95.5	2,262	12.90	2,262	12.90	2,539	14.50	2,539	14.50

TABLE 6 Number of IMF for each time series.

Height(km)	Lima		Piura	
	Zonal Wind	Meridional Wind	Zonal Wind	Meridional Wind
80.5	12	12	12	11
85.5	11	12	12	12
90.5	12	11	12	12
95.5	12	12	12	12

correlation of 0.99, while the 16-step has an RMSE of 23.05 and a correlation of 0.8.

In the case of Piura, the RMSE values increase from 6.04 $m\,s^{-1}$ to 30.41 $m\,s^{-1}$, while the correlation values decrease from 0.99 to 0.5. For example, the zonal wind at 85.5 km of altitude, has the best 1-step with an RMSE of 6.04 $m\,s^{-1}$ and a correlation of 0.98, while the 16-step has an RMSE of 17.42 $m\,s^{-1}$ and a correlation of 0.79.

3.3.3 Comparison with the model of dominant harmonics

The comparison of metrics between the hybrid model and the model of dominant harmonics with data from 2023 is shown in Table 9 for Lima and Table 10 for Piura.

In the case of Lima, the hybrid model has RMSE values ranging from 14.92 $m\,s^{-1}$ to 26.95 $m\,s^{-1}$, while the correlation values

TABLE 7 Evaluation of the hybrid model for Lima data.

		Zonal Wind				Meridional Wind			
		Real vs Hybrid model		Real vs Persistence		Real vs Hybrid model		Real vs Persistence	
Height	Data set	RMSE ($m\,s^{-1}$)	r	RMSE ($m\,s^{-1}$)	r	RMSE ($m\,s^{-1}$)	r	RMSE ($m\,s^{-1}$)	r
80.5 km	Train	12.38	0.91	26.36	0.61	13.30	0.90	29.90	0.49
	Validation	13.42	0.82	28.39	0.25	14.39	0.84	30.32	0.38
	Test	16.84	0.83	35.69	0.30	14.37	0.88	30.51	0.51
85.5 km	Train	20.92	0.92	32.16	0.44	13.60	0.94	34.52	0.54
	Validation	22.06	0.92	37.13	0.33	18.58	0.88	38.81	0.46
	Test	21.64	0.92	40.99	0.24	15.92	0.91	33.41	0.64
90.5 km	Train	14.22	0.91	36.95	0.40	19.07	0.91	38.76	0.58
	Validation	15.40	0.91	43.38	0.27	21.87	0.88	43.75	0.52
	Test	14.73	0.93	42.99	0.39	21.63	0.85	39.76	0.54
95.5 km	Train	19.31	0.84	41.09	0.34	19.33	0.91	42.06	0.56
	Validation	20.84	0.81	44.30	0.24	22.37	0.87	45.09	0.49
	Test	22.50	0.84	47.52	0.34	19.07	0.91	43.68	0.53

TABLE 8 Evaluation of the hybrid model for Piura data.

		Zonal Wind				Meridional Wind			
		Real vs Hybrid model		Real vs Persistence		Real vs Hybrid model		Real vs Persistence	
Height	Data set	RMSE ($m\,s^{-1}$)	r	RMSE ($m\,s^{-1}$)	r	RMSE ($m\,s^{-1}$)	r	RMSE ($m\,s^{-1}$)	r
80.5 km	Train	11.93	0.89	29.01	0.38	14.59	0.85	30.18	0.41
	Validation	11.92	0.86	33.71	−0.03	20.09	0.77	36.55	0.34
	Test	11.98	0.88	30.40	0.30	18.48	0.78	33.63	0.40
85.5 km	Train	10.79	0.93	32.49	0.36	15.13	0.87	32.30	0.44
	Validation	12.87	0.92	38.92	0.08	16.88	0.87	35.66	0.43
	Test	12.01	0.90	35.63	0.21	18.11	0.83	35.16	0.41
90.5 km	Train	13.90	0.90	36.38	0.34	18.07	0.84	35.27	0.44
	Validation	15.63	0.91	39.95	0.39	27.04	0.67	38.45	0.37
	Test	15.50	0.87	39.18	0.22	21.33	0.77	38.82	0.30
95.5 km	Train	17.91	0.87	40.58	0.34	16.97	0.90	40.31	0.43
	Validation	22.80	0.84	43.09	0.48	17.95	0.88	42.32	0.38
	Test	17.03	0.89	42.57	0.26	20.29	0.80	43.78	0.22

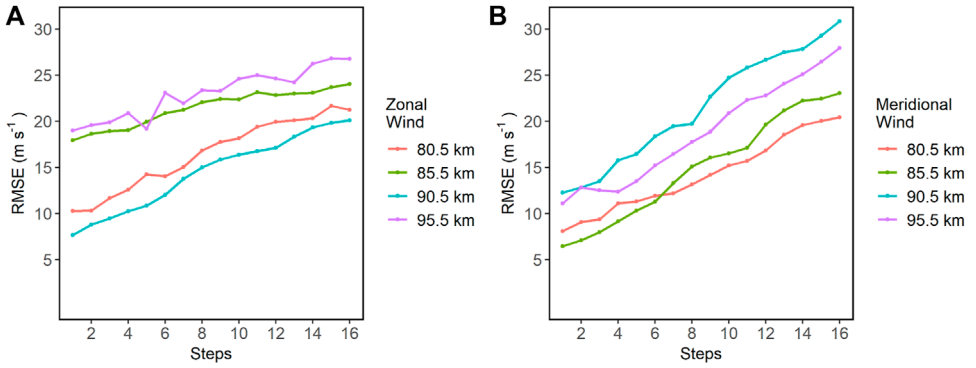

FIGURE 8
RMSE values for each time step in Lima. **(A)** shows the RMSE values for the zonal wind. **(B)** shows the RMSE values for the meridional wind.

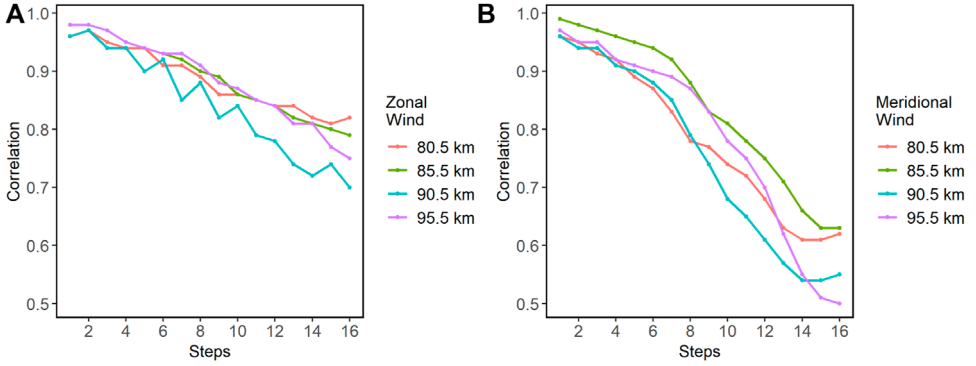

FIGURE 9
Correlation values for each time step in Piura. **(A)** shows the correlation values for the zonal wind. **(B)** shows the correlation values for the meridional wind.

TABLE 9 Comparison metrics between the hybrid model and interpolation in 2023 (Lima).

	Zonal Wind				Meridional Wind			
	Real vs Hybrid model		Real vs Dominant harmonics model		Real vs Hybrid model		Real vs Dominant harmonics model	
Height	RMSE (m s^{-1})	r	RMSE (m s^{-1})	r	RMSE (m s^{-1})	r	RMSE (m s^{-1})	r
80.5	15.53	0.83	23.68	0.63	14.92	0.80	26.23	0.44
85.5	21.85	0.69	27.01	0.51	15.28	0.86	31.24	0.51
90.5	23.40	0.71	31.55	0.41	23.21	0.81	37.76	0.51
95.5	26.95	0.70	36.03	0.43	23.99	0.84	41.21	0.58

range from 0.69 to 0.86. The model of dominant harmonics has RMSE values ranging between 23.68 m s^{-1} and 41.21 m s^{-1}, while correlation values vary between 0.41 and 0.63. Figure 10 shows the time series predictions of the zonal wind in Lima at 80.5 km altitude, made by both models, with their respective scatter diagrams. The hybrid model has an RMSE of 15.53 m s^{-1} and a correlation of 0.83, while the model of dominant harmonics has an RMSE of 23.68 m s^{-1} and a correlation of 0.63. It is observed that the hybrid model has a lower RMSE value and a higher correlation value. Additionally, in the scatter plot, the predictions of the hybrid model are better fitted to the data in Lima.

In the case of Piura, the hybrid model has RMSE values ranging from 15.47 m s^{-1} to 26.80 m s^{-1}, while the correlation values range from 0.55 to 0.80. The model of dominant

TABLE 10 Comparison metrics between the hybrid model and interpolation in 2023 (Piura).

	Zonal Wind				Meridional Wind			
	Real vs Hybrid model		Real vs Dominant harmonics model		Real vs Hybrid model		Real vs Dominant harmonics model	
Height	RMSE ($m\,s^{-1}$)	r	RMSE ($m\,s^{-1}$)	r	RMSE ($m\,s^{-1}$)	r	RMSE ($m\,s^{-1}$)	r
80.5	15.47	0.75	21.87	0.50	16.31	0.68	25.39	0.34
85.5	15.80	0.75	24.99	0.43	16.78	0.73	29.97	0.26
90.5	26.80	0.55	28.90	0.34	21.40	0.74	37.50	0.28
95.5	25.20	0.62	32.89	0.35	19.34	0.80	41.57	0.40

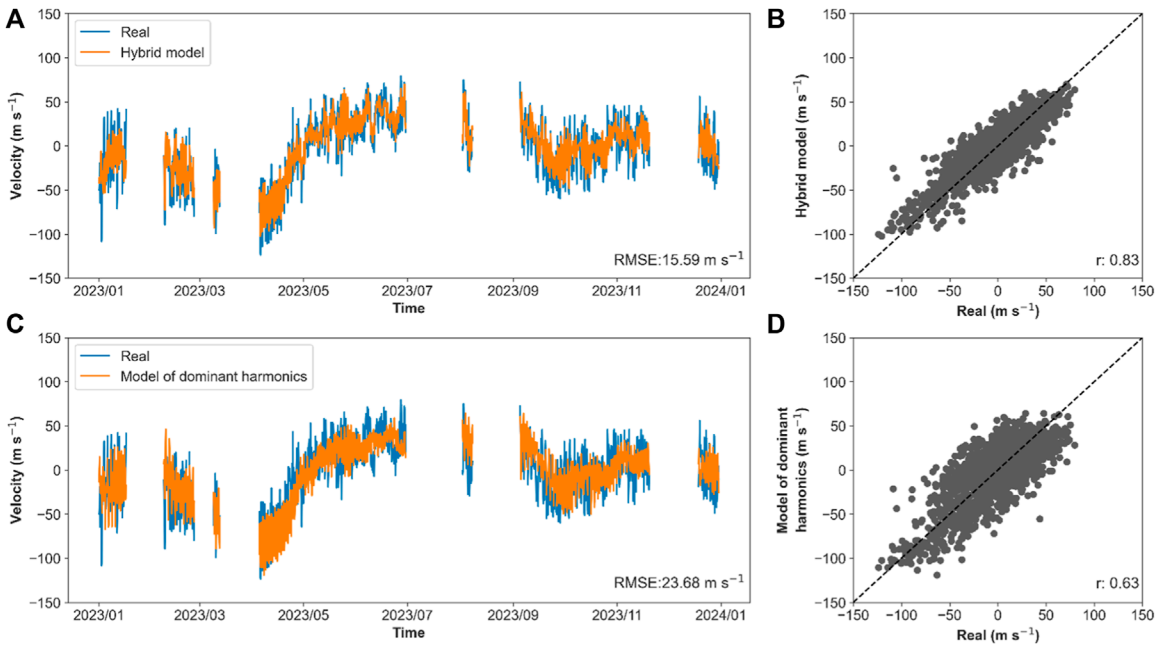

FIGURE 10
Comparison between the hybrid and dominant harmonics model estimates for the zonal wind at 80.5 km height in Lima in the year 2023. **(A)** shows the 2023 time series versus the hybrid model estimates. **(B)** shows the scatter plot of the 2023 data versus the hybrid model estimates. **(C)** shows the 2023 time series versus the model of dominant harmonic estimates. **(D)** shows the scatter plot of the 2023 data versus the model of dominant harmonic estimates.

harmonics has RMSE values ranging between 21.87 $m\,s^{-1}$ and 41.57 $m\,s^{-1}$, while correlation values vary between 0.26 and 0.5. Figure 11 shows the time series predictions of the meridional wind in Piura at 95.5 km altitude, made by both models, with their respective scatter diagrams. The hybrid model has an RMSE of 19.34 $m\,s^{-1}$ and a correlation of 0.80, while the model of dominant harmonics has an RMSE of 41.57 $m\,s^{-1}$ and a correlation of 0.40. Similar to the results for Lima, the hybrid model is found to have a lower RMSE, a higher correlation, and less dispersion with respect to the model of dominant harmonics. Also, their scatter plot indicates that the predictions of the hybrid model better fit the 2023 data collected in Piura.

4 Discussion and conclusions

The imputation of missing data for 2023 was performed under the assumption that the percentage limit of missing data is 6%. However, it is necessary to have sufficient data to allow this analysis to be carried out. If there are only a few data points available, the distribution may not be symmetrical because of certain values that dominate that period. In addition, it is essential to have at least 72 continuous data to be able to make predictions and calculate metrics (56 input data points and 16 output data points).

In determining the number of components of the time series, convergence is observed between the values of 11 and 12 components. Exceeding these values can lead to poor estimates

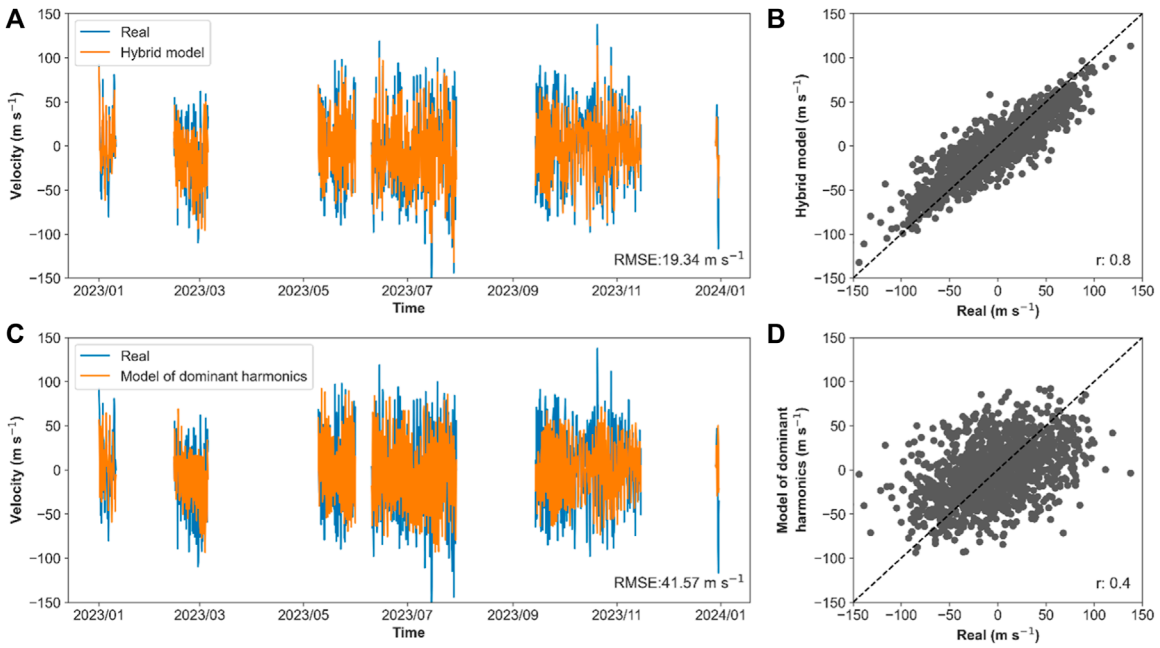

FIGURE 11
Comparison between the estimates made by the hybrid model and the model of dominant harmonics, for the meridional wind at 95.5 km height in Piura in the year 2023. **(A)** shows the 2023 time series versus the hybrid model estimates. **(B)** shows the scatter plot of the 2023 data versus the hybrid model estimates. **(C)** shows the 2023 time series versus the model of dominant harmonic estimates. **(D)** shows the scatter plot of the 2023 data versus the model of dominant harmonic estimates.

of the original series. Having these limits defined helps to avoid making unnecessary models of the components, avoiding execution times and the use of computational resources. Additionally, for future research, associations between these components and other meteorological time measurements could be evaluated.

During the modeling phase, the inclusion of the regularizer (L2) resulted in a marked improvement in the visualization of the loss curves for both the training and validation sets, which helped to avoid overfitting the models. As for Optuna, only 30 search iterations per component were performed. Although a more exhaustive search could provide even more accurate estimates, the complexity of the model, with 11 or 12 components, implies lengthy processing and higher consumption of computational resources. Similarly, increasing the number of epochs and the number of layers could improve the search, but the processing would be much longer.

On the other hand, the amount of data used in the modeling corresponds to a period of approximately 1 year. Since the SIMONe radars are still active, this amount of data could increase. This would allow a better recognition of temporal patterns to make better estimates.

As for the input and output data, there is also a possibility for improvement. Two paths can be followed. First, keep the same input data window to predict fewer output steps. For example, one can predict 8 steps corresponding to 1 day of records. Second, one can increase the size of the input window to 112, corresponding to 2 weeks of records, while keeping the 16 output steps.

Detailed analysis of the predictions reveals a significant deterioration in the metrics towards the final steps. This observation justifies the exploration of predictions with a shorter time horizon than the 16 steps, keeping the same input window. When reconstructing the time series using blocks of 16 estimates, it was observed that certain parts of these series did not correctly match the actual data. This mismatch was mainly attributed to the low precision of the estimates for the last steps. Despite the challenges, the proposed hybrid model has shown better performance than the model of dominant harmonics when comparing the predictions to the actual 2023 data using RMSE and correlation metrics. In other words, the hybrid model more accurately matched the actual data. Possibly, the hybrid model can capture other significant waves of planetary scale and mesoscale. This speculation will be evaluated in future works.

Data availability statement

The raw data supporting the conclusions of this article will be made available by the authors, without undue reservation.

Author contributions

CM: Writing–original draft, Writing–review and editing. JS: Writing–original draft, Writing–review and editing. MM: Writing–review and editing. CL: Writing–review and editing. KK: Writing–review and editing. DS: Writing–review and editing. RR: Writing–review and editing.

Funding

The author(s) declare financial support was received for the research, authorship, and/or publication of this article. This work was supported and financed by PROCIENCIA (Peru), under contract No 075-2021-FONDECYT.

Acknowledgments

We also wish to thank the Leibniz Institute of Atmospheric Physics for providing MLT winds from SIMONe radar networks. We also thank Jorge Chau for his suggestions that contributed to the development of this work. Additionally, we acknowledge the collaboration of the Estación Ramón Mujica of the Universidad of Piura and the Radio Observatorio de Jicamarca of the Instituto Geofísico del Perú for providing support in the operation of the SIMONe radar system. Finally, we extend our gratitude to the Pontificia Universidad Católica del Perú y la Universidad Nacional Agraria La Molina for guiding the methodology of data processing.

Conflict of interest

The authors declare that the research was conducted in the absence of any commercial or financial relationships that could be construed as a potential conflict of interest.

Publisher's note

References

Akiba, T., Sano, S., Yanase, T., Ohta, T., and Koyama, M. (2019). "Optuna: a next-generation hyperparameter optimization framework," in In Proceedings of the ACM SIGKDD International Conference on Knowledge Discovery and Data Mining (Association for Computing Machinery), 2623–2631.

Ali, M., Khan, A., and Rehman, N. (2018). Hybrid multiscale wind speed forecasting based on variational mode decomposition. *Int. Trans. Electr. Energy Syst.* 28 (1), e2466. doi:10.1002/etep.2466

Carvalho, V. R., Moraes, M. F. D., Braga, A. P., and Mendes, E. M. A. M. (2020). Evaluating five different adaptive decomposition methods for EEG signal seizure detection and classification. *Biomed. Signal Process. Control* 62, 102073. doi:10.1016/j.bspc.2020.102073

Chau, J. L., Urco, J. M., Vierinen, J., Harding, B. J., Clahsen, M., Pfeffer, N., et al. (2021). Multistatic specular meteor radar network in Peru: system description and initial results. *Earth Space Sci.* 8 (1), 1–22. doi:10.1029/2020EA001293

Conte, J. F., Chau, J. L., Yiğit, E., Suclupe, J., and Rodríguez, R. (2024). Investigation of mesosphere and lower thermosphere dynamics over central and northern Peru using SIMONe systems. *J. Atmos. Sci.* 81 (1), 93–104. doi:10.1175/JAS-D-23-0030.1

Dhadly, M., Sassi, F., Emmert, J., Drob, D., Conde, M., Wu, Q., et al. (2023). Neutral winds from mesosphere to thermosphere—past, present, and future outlook. *Front. Astronomy Space Sci.* 9. doi:10.3389/fspas.2022.1050586

Dragomiretskiy, K., and Zosso, D. (2014). Variational mode decomposition. *IEEE Trans. Signal Process.* 62 (3), 531–544. doi:10.1109/TSP.2013.2288675

Emmert, J. T., Drob, D. P., Picone, J. M., Siskind, D. E., Jones, M., Mlynczak, M. G., et al. (2021). NRLMSIS 2.0: a whole-atmosphere empirical model of temperature and neutral species densities. *Earth Space Sci.* 8 (3). doi:10.1029/2020EA001321

Forbes, J. M. (1995). Tidal and planetary waves'. In. *Geophysical monograph series*, edited by R. M. Johnson, and T. L. Killeen, 67–87. Washington, D. C.: American Geophysical Union. doi:10.1029/GM087p0067

Gan, M., Pan, H., Chen, Y., and Pan, S. (2021). Application of the variational mode decomposition (VMD) method to river tides. *Estuar. Coast. Shelf Sci.* 261, 107570. doi:10.1016/j.ecss.2021.107570

Gasperini, F., Jones, M. A., Harding, B. J., and Immel, T. J. (2023). Direct observational evidence of altered mesosphere lower thermosphere mean circulation from a major sudden stratospheric warming. *Geophys. Res. Lett.* 50 (7). doi:10.1029/2022GL102579

Hanifi, S., Lotfian, S., Zare-Behtash, H., and Cammarano, A. (2022). Offshore wind power forecasting—a new hyperparameter optimisation algorithm for deep learning models. *Energies* 15 (19), 6919. doi:10.3390/en15196919

Hussin, N. H., Yusof, F., Jamaludin, A. R., and Norrulashikin, S. M. (2021). Forecasting wind speed in peninsular Malaysia: an application of arima and arima-garch models. *Pertanika J. Sci. Technol.* 29 (1), 31–58. doi:10.47836/pjst.29.1.02

Immel, T. J., Sagawa, E., England, S. L., Henderson, S. B., Hagan, M. E., Mende, S. B., et al. (2006). Control of equatorial ionospheric morphology by atmospheric tides. *Geophys. Res. Lett.* 33 (15). doi:10.1029/2006GL026161

Kratzert, F., Klotz, D., Brenner, C., Schulz, K., and Herrnegger, M. (2018). Rainfall-runoff modelling using Long short-term memory (LSTM) networks. *Hydrology Earth Syst. Sci.* 22 (11), 6005–6022. doi:10.5194/hess-22-6005-2018

Liu, H., Yamazaki, Y., and Lei, J. (2021). Day-to-Day variability of the thermosphere and ionosphere. *Geophys. Monogr. Ser.*, 275–300. doi:10.1002/9781119815631.ch15

Liu, H.Li, Bardeen, C. G., Foster, B. T., Lauritzen, P., Liu, J., Lu, G., et al. (2018). Development and validation of the whole atmosphere community climate model with thermosphere and ionosphere extension (WACCM-X 2.0). *J. Adv. Model. Earth Syst.* 10 (2), 381–402. doi:10.1002/2017MS001232

Mauricio, C., Suclupe, J., Milla, M., López de Castilla, C., Karim, K., Rodriguez, R., et al. (2023). "Short-term prediction of wind speed in the mesosphere and lower thermosphere over Peru's coastal north and central," in 2023 IEEE CHILEAN Conference on Electrical, Electronics Engineering, Information and Communication Technologies (CHILECON), Valdivia, Chile, 05-07 December 2023 (IEEE), 1–6.

McCormack, J. P., Coy, L., and Singer, W. (2014). Intraseasonal and interannual variability of the quasi 2 Day wave in the northern hemisphere summer mesosphere. *J. Geophys. Res. Atmos.* 119 (6), 2928–2946. doi:10.1002/2013JD020199

Piani, C., Durran, D., Alexander, M. J., and Holton, J. R. (2000). A numerical study of three-dimensional gravity waves triggered by deep tropical convection and their role in the dynamics of the QBO. *J. Atmos. Sci.* 57 (22), 3689–3702. doi:10.1175/1520-0469(2000)057<3689:ANSOTD>2.0.CO;2

Pigott, T. D. (2001). A review of methods for missing data. *Educ. Res. Eval.* 7 (4), 353–383. doi:10.1076/edre.7.4.353.8937

Rosa, L., La, G., and Sanchez, I. (2020). "Hybrid models based on mode decomposition and recurrent neural networks for streamflow forecasting in the chira river in Peru," in Proceedings of the 2020 IEEE Engineering International Research Conference, EIRCON 2020, Lima, Peru, 21-23 October 2020 (Institute of Electrical and Electronics Engineers Inc).

Schneider, T. (2001). Analysis of incomplete climate data: estimation of mean values and covariance matrices and imputation of missing values. *J. Clim.* 14 (5), 853–871. doi:10.1175/1520-0442(2001)014<0853:AOICDE>2.0.CO;2

Son, N., and Jung, M. (2020). Analysis of meteorological factor multivariate models for medium- and long-term photovoltaic solar power forecasting using Long short-term memory. *Appl. Sci.* 11 (1), 316. doi:10.3390/app11010316

Staszak, T., Strelnikov, B., Latteck, R., Renkwitz, T., Friedrich, M., Baumgarten, G., et al. (2021). Turbulence generated small-scale structures as PMWE formation mechanism: results from a rocket campaign. *J. Atmos. Solar-Terrestrial Phys.* 217, 105559. doi:10.1016/j.jastp.2021.105559

Suclupe, J., Chau, J. L., Federico Conte, J., Milla, M., Pedatella, N. M., and Kuyeng, K. (2023). Climatology of mesosphere and lower thermosphere diurnal tides over Jicamarca (12^°S, 77 ^°W): observations and simulations. *Earth, Planets Space. Springer Sci. Bus. Media Deutschl. GmbH* 75, 186. doi:10.1186/s40623-023-01935-z

Vincent, R. A. (2015). The dynamics of the mesosphere and lower thermosphere: a brief review. *Prog. Earth Planet. Sci.* 2 (1), 4. doi:10.1186/s40645-015-0035-8

Yang, S., Yang, H., Li, N., and Ding, Z. (2023). Short-term prediction of 80–88 Km wind speed in near space based on VMD–PSO–LSTM. *Atmosphere* 14 (2), 315. doi:10.3390/atmos14020315

frontiers | Frontiers in Astronomy and Space Sciences

TYPE Mini Review
PUBLISHED 11 October 2024
DOI 10.3389/fspas.2024.1472642

OPEN ACCESS

EDITED BY
Marco Milla,
Pontifical Catholic University of Peru, Peru

REVIEWED BY
Yun Gong,
Wuhan University, China
Tatsuhiro Yokoyama,
Kyoto University, Japan
Esfhan Alam Kherani,
National Institute of Space Research (INPE), Brazil

*CORRESPONDENCE
J. D. Huba,
jdhuba@gmail.com

RECEIVED 29 July 2024
ACCEPTED 23 September 2024
PUBLISHED 11 October 2024

CITATION
Huba JD (2024) Impact of meridional winds on the development of equatorial plasma bubbles: a review.
Front. Astron. Space Sci. 11:1472642.
doi: 10.3389/fspas.2024.1472642

Impact of meridional winds on the development of equatorial plasma bubbles: a review

J. D. Huba*

Syntek Technologies, Fairfax, VA, United States

The impact of meridional winds on the onset and evolution of equatorial plasma bubbles (EPBs) is reviewed. The conventional wisdom had been that transequatorial meridional winds have a stabilizing effect on the development of EPBs during equatorial spread *F* (ESF). However, this result is based on a uniform transequatorial meridional wind. Subsequently, it was demonstrated that a non-uniform meridional wind could have a stabilizing or destabilizing effect on EPB formation depending on the direction of wind gradient. The destabilization of EPBs associated with equatorward flowing meridional winds has recently been investigated during a midnight temperature maximum event and a geomagnetic storm. Although the neutral wind is a direct destabilizing influence in these cases, the large decrease in the Pedersen conductance caused by meridional equatorward winds is the primary reason for the large increase in the growth rate of the generalized Rayleigh-Taylor instability. We review the theoretical and modeling studies of this topic as well as observational studies that have been made to assess the relationship between meridional winds and ESF.

KEYWORDS

equatorial plasma bubbles, meridional wind, equatorial irregularities, equatorial spread F, generalized Rayleigh-Taylor instability

1 Introduction

The subject of the impact of meridional winds on the development of equatorial plasma bubbles (EPBs) has received considerable attention over the last 35 years (Huba and Krall, 2013; Huba et al., 2023; Huba and Lu, 2024). The generalized Rayleigh-Taylor instability (GRTI) (Sultan, 1996; Huba, 2022) is believed responsible for the generation of EPBs (Booker and Wells, 1938; Haerendel, 1974; Hysell, 2000) and a number of theoretical studies have focused on the impact of meridional winds on the GRTI to assess their role in EPB development.

The first study was performed by Maruyama (1988). He demonstrated that a uniform transequatorial meridional wind enhances the field-line integrated Pedersen conductivity and that this can reduce the growth rate of the generalized Rayleigh-Taylor instability. Zalesak and Huba (1991) extended the analysis of Maruyama (1988) to consider the direct effect of the wind on the development of the instability. They found that, in fact, the instability can be completely stabilized for a sufficiently strong meridional wind. These results were borne out in a 3D simulation study by Krall et al. (2009).

The work of Maruyama (1988) spurred interest in observational studies to assess the relationship between meridional winds and equatorial spread *F* (ESF). The study by

Mendillo et al. (1992) was limited to only two nights but the observations suggested the meridional wind suppressed (ESF) on one of the nights. A subsequent study (Mendillo et al., 2001) did not find convincing evidence for the "wind suppression" mechanism for ESF. In contrast, the observational study by Abdu et al. (2006) concluded that magnetic meridional winds negatively influence ESF development by reducing the pre-reversal enhancement electric field and direct suppression of the instability. Yet in other studies, Devasia et al. (2002) and Jyoti et al. (2004) found that under certain circumstances equatorward neutral winds appeared to be needed for ESF to develop. Thus, the observational studies of the impact of meridional winds on EPB development is mixed: in some cases the wind appears to suppress ESF, and in other cases the wind appears necessary to generate ESF.

A possible resolution to these "conflicting" observations was suggested by Huba and Krall (2013). They revisited this problem and demonstrated that a non-uniform meridional wind could have a stabilizing or *destabilizing* effect on EPB formation depending on the direction of wind gradient. Thus, the exact nature of the meridional wind is a key factor in how it affects the development of EPBs.

Recently, Huba et al. (2023) and Huba and Lu (2024) focused on equatorward flowing neutral winds and showed that they can be very destabilizing and generate EPBs. The primary reason for the large increase in the growth rate of the GRTI is a large decrease in the Pedersen conductivity. This is in contrast to the work of Maruyama (1988) who found that a uniform transequatorial meridional wind increased the Pedersen conductivity which led to a decrease in the growth rate of the GRTI.

We review the aforementioned theoretical and modeling studies, as well as the observational studies relating measurements of the meridional wind to the onset and evolution of ESF.

2 Theory

The theory of the stabilizing effects of meridional winds on the Rayleigh-Taylor instability was first developed by Maruyama (1988) and expanded upon by Zalesak and Huba (1991). Krall et al. (2009) elaborated on the theory and confirmed the stabilizing influence of meridional winds on the GRTI through numerical simulation studies using SAMI3/ESF (Huba et al., 2008). Recently, a more thorough analysis of the GRTI was presented by Huba (2022).

$$\gamma = \gamma_g + \gamma_{wc}, \tag{1}$$

where

$$\gamma_g = -\frac{\int \sigma_{Hc}\left(g_p/L_n\right) ds}{\int \sigma_P \, ds} \tag{2}$$

and

$$\gamma_{wc} = -\frac{\int \sigma_P \left(V_{wc}/L_n\right) ds}{\int \sigma_P \, ds}, \tag{3}$$

with $L_n^{-1} = \partial \ln n_0/\partial p$ and

$$\sigma_P \simeq \sum_i \frac{nec}{B}\frac{\nu_{in}}{\Omega_i} \qquad \sigma_{Hc} \simeq \sum_i \frac{nec}{B}\frac{1}{\Omega_i}.$$

Gravity being directed downwards, $g_p < 0$ and γ_g is always positive (destabilizing) in the bottomside F-layer. $V_{wc} = V_{mp} - V_p$ provides both positive and negative contributions depending on the sign of $\mathbf{V}_{wc} \cdot \nabla n$; here, V_{mp} is the meridional wind and V_p is the E × B drift in the meridional plane.

In Figure 1 we show a schematic indicating the important factors that affect the growth rate of the Rayleigh-Taylor instability associated with a meridional wind. In this figure we show a meridional wind (dark blue vector) in the northward direction and an upward density gradient (dark green vector) in the bottomside F layer. The components of the meridional wind relative to the geomagnetic field are also shown: V_{ms} is the component along the geomagnetic field and V_{mp} is the component transverse to the geomagnetic field.

First, the component of the neutral wind along the geomagnetic field (V_{ms}) alters the local conductivity because of collisional drag on the ions. When the wind moves the plasma to higher altitudes (V_{msl}) the conductivity is decreased and when the wind moves the plasma to lower altitudes (V_{msr}) is increased. For a uniform meridional wind this leads to an increase in the field-line integrated Pedersen conductivity (for the ionosphere-thermosphere models used in Maruyama (1988); Krall et al. (2009)). This reduces the growth rate of the instability because $\int \sigma_P \, ds$ is in the denominator in Equation 1 and is the stabilizing effect first recognized by Maruyama (1988). However, if the meridional wind has a gradient such the $V_{msl} \gg V_{msr}$ this stabilizing effect is mitigated or possibly reversed. Alternatively, if $V_{msl} \ll V_{msr}$ then the stabilizing effect is amplified (Huba and Krall, 2013).

Second, the component of the neutral wind transverse to the geomagnetic field (V_{mp}) is a stabilizing influence when $\mathbf{V}_{mp} \cdot \nabla n > 0$ which is the case for V_{mpr}; it is a destabilizing influence when $\mathbf{V}_{mp} \cdot \nabla n < 0$ which is the case for V_{mpl}. The affect on the growth rate is complicated because it involves the field-line integration of neutral wind weighted by the Pedersen conductivity as shown in Equation 3. For the case of a uniform neutral wind, the stabilizing influence dominates and can completely stabilize the instability for a sufficiently strong meridional wind. This is the stabilizing effect described by Zalesak and Huba (1991). However, non-uniform meridional winds can have a destabilizing affect on the instability when $\partial V_m/\partial\theta < 0$, i.e., $V_{msl} > V_{msr}$ in Figure 1. This effect is especially pronounced for the case of equatorward winds when the meridional wind both reduces the field-line integrated conductivity and is directed opposite to the density gradient (Huba and Krall, 2013).

3 Modeling

Krall et al. (2009) performed an extensive simulation study of the impact of the meridional wind on the development of equatorial plasma bubbles (EPBs). They used a constant transhemispheric meridional wind and their results confirmed the results of Maruyama (1988) and Zalesak and Huba (1991). As an example we show Figure 2 which plots the maximum vertical E × B velocity ($u_{p,max}$) as a function of time for different values of the meridional wind. The slope of each curve is a proxy for the growth rate. As the meridional neutral wind speed increases the slope of each curve up to 50 m/s decreases indicating a stabilizing effect. For the case

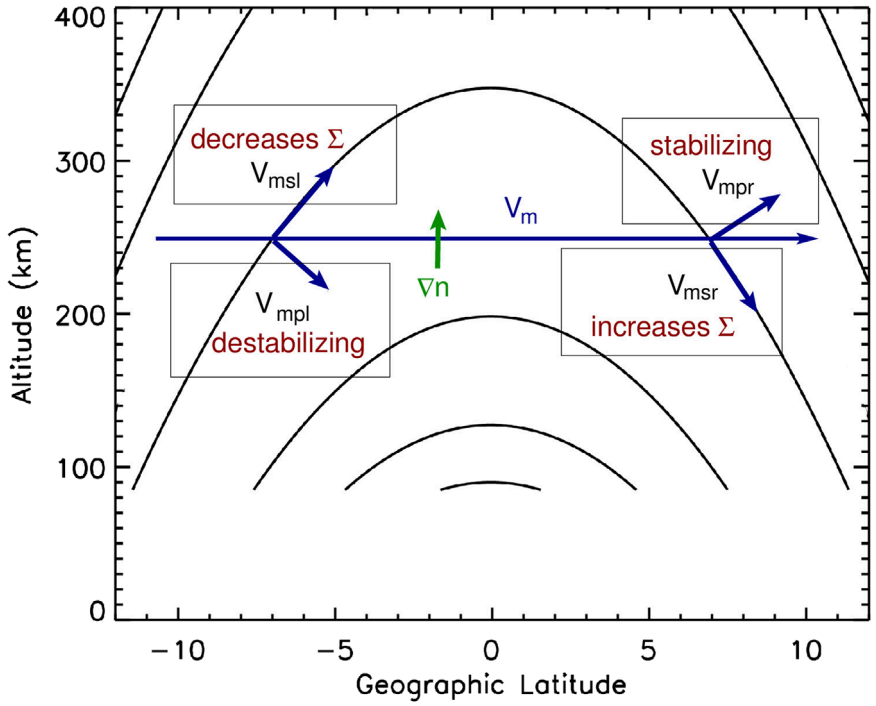

FIGURE 1
Schematic of the impact of meridional wind components on the growth rate and conductivity.

where the wind speed is 60 m/s the slope is negative indicating the instability is completely suppressed as suggested by Zalesak and Huba (1991).

Huba and Krall (2013) expanded the previous work of Krall et al. (2009) to include an inhomogeneous meridional wind; they demonstrated that, depending on the direction of the latitudinal gradient of the wind, the meridional wind could be stabilizing or *destabilizing*. Specifically, a wind profile with a positive gradient as a function of latitude ($\partial V_m/\partial\theta \geq 0$) is a stabilizing influence on the generalized Rayleigh-Taylor instability; however, a wind profile with a negative gradient ($\partial V_m/\partial\theta < 0$) can have a destabilizing influence. Here, V_m is the meridional wind and θ is the geographic latitude and is positive towards the north pole.

As "extreme" cases, they considered equatorward flowing winds ($\partial V_m/\partial\theta < 0$) and poleward flowing winds ($\partial V_m/\partial\theta > 0$). The wind profile used was

$$V_m = \pm V_{m0} \tanh(\theta/\Delta\theta) \quad (4)$$

where $V_{m0} = 40$ m/s and $\Delta\theta = 5°$.

The results are shown in Figure 3 where the labels *eq* and *po* refer to equatorward winds and poleward winds, respectively. Figure 3A shows the meridional wind profiles as a function of latitude based on Equation 4. Figure 3B shows the maximum upward $E \times B$ drift as a function of time for the equatorward case and poleward case meridional wind profiles. The case for no meridional wind is labeled "0" (dashed curve). The growth times of the instability in each case is as follows: 80eq (13 min), 0 (22 min), and 80po (41 min). Thus, the equatorward meridional wind profile is destabilizing while the poleward meridional wind profile is stabilizing relative to the case of no meridional wind.

The contrast in the development of the generalized Rayleigh-Taylor instability for the equatorward and poleward meridional wind cases is exemplified in Figure 4. Electron density contours are shown at time $t =$ 20:44 LT as a function of longitude and altitude for cases 80eq (top) and 80po (bottom). The equatorward flow case has a well-developed plasma bubble that extends to almost 800 km while the poleward flow case has only developed a minor density undulation on the bottomside *F* layer.

The modeling results described above were based on the SAMI3/ESF code (Huba et al., 2008) which models a narrow range of longitude at night; nominally about 4° in longitude as shown in Figure 4. Recently, progress has been made in modeling the development of EPBs on a global scale (Huba and Liu, 2020) using the coupled SAMI3/WACCM-X code. Specifically the SAMI3 model (Huba and Joyce, 2010) has been one-way coupled to the global whole earth model WACCM-X (Liu et al., 2018). Here, the thermospheric variables (i.e., neutral densities, temperature, and winds) calculated by WACCM-X are used as inputs to SAMI3. There is no feedback from SAMI3 to WACCM-X though. The global models are run at high resolution in both latitude and longitude (~ 0.5°–0.625°) which corresponds to grid scales ~ 50–70 km.

Huba et al. (2023) investigated the development of an EPB during a period of low geomagnetic activity at solar minimum near the summer solstice using the coupled SAMI3/WACCM-X code. The parameters used were for August 22 with F10.7 = 71.6, F10.7A = 72.4, Ap = 6 and Kp = 1. The role of the meridional wind on the EPB growth is highlighted in Figure 5 which shows contour plots of the electron density (a, b), E × B velocity (c, d), zonal neutral wind (e, f), meridional neutral wind (g, i), latitude derivative of the meridional neutral wind (h, j), and neutral temperature (k, l)

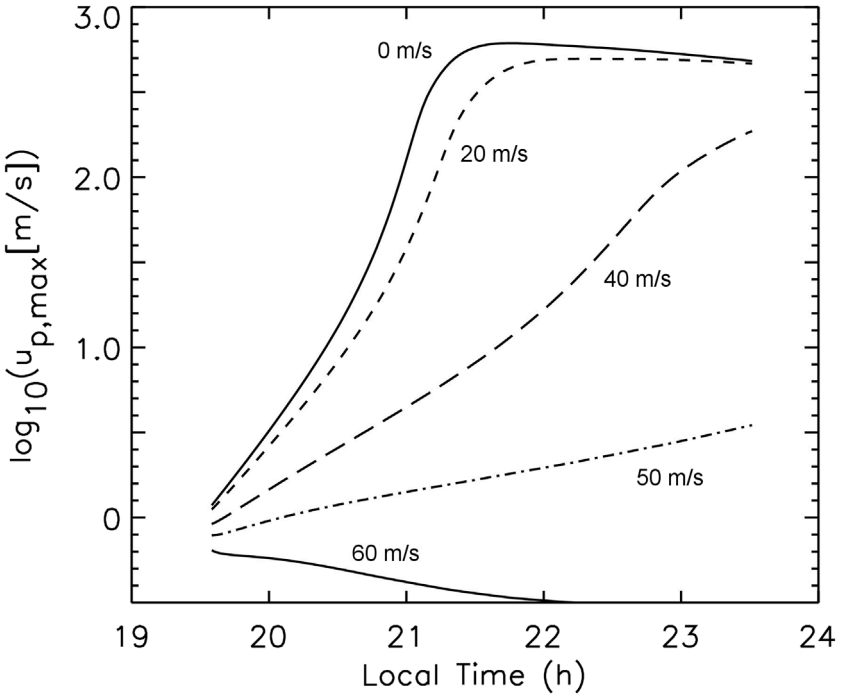

FIGURE 2
Line plots showing $\log_{10}(u_{p,max})$ versus local time for no wind (solid), 20 m/s (dashes), 40 m/s (long dashes), and 50 m/s (dash-dot), and 60 m/s (lower solid line). [from Krall et al. (2008)].

at times 11:59 UT (left panels) and 12:29 UT (right panels) as a function of latitude and altitude at longitude 168°. As stated in Huba et al. (2023) we note the following. The early uplift of the EPB is apparent in Figure 5A at latitude $\theta \sim 6°$ with the development of ionization crests at $\theta \sim -5°$ and 15° as well as the enhanced E × B drift in the flux tubes with apex heights ~ 400–500 km. At this time, there is also a reduction in both the zonal neutral wind (Figure 5E) and meridional neutral wind (Figure 5G). The meridional neutral wind is "equatorward" at latitude $\theta \sim 6°$, i.e., it is directed northward for $\theta < 6°$ and is directed southward $\theta > 6°$. This leads to a strong (negative) meridional gradient as well as an increase in the neutral temperature (Figure 5K) (i.e., midnight temperature maximum). Thirty minutes later, at 12:29 UT, the EPB has now fully developed and risen to ~ 600 km (Figure 5B). The E × B drift inside the EPB has increased substantially to ≳ 180 m/s (Figure 5D). The zonal neutral wind remains relatively weak (few 10 s m/s) at 168° (Figure 5F) but the meridional neutral wind is northward with a velocity ~ 200 m/s (Figure 5H) at $\theta \sim 6°$. The derivative of the meridional neutral wind has significantly decreased (Figure 5I) at this latitude and the peak has shifted northward. Lastly, there is a relatively broad midnight temperature maximum in latitude (Figure 5L) (Herrero et al., 1993). Additionally, Meriwether et al. (2008) show both positive and negative gradients in the wind at ~ 19:30 LT over Arequipa, Peru. They found converging (i.e., equatorward) neutral wind flows 1–2 hrs prior to the MTM. We note that there were several other bottom side irregularities in longitude away from 168° that did not develop EPBs. The important difference is that there were strong "equatorward" flows at 168° and not at the other longitudes with irregularities.

The reason for the development of the EPB in Figure 5 is described in Figure 6 from Huba et al. (2023). This figure shows line plots of the (a) electron density (n_e), E × B velocity ($V_{E\times B}$), derivative of the meridional neutral wind ($dV/d\theta$), and (b) the Pedersen conductance as a function of time at longitude 168° and altitude 400 km, as well as (c) the maximum GRTI growth rates (γ, γ_g, and γ_{wc}) in the altitude range 250–800 km and the Pedersen conductance. In Figure 6A the electron density reaches a minimum of ~ 2×10^3 cm^{-3} at 12:15 UT and the E × B velocity reaches a maximum of 120 m/s at 12:30 UT. Significantly, the derivative of the meridional neutral wind reaches a minimum of ~ −70 m/s/deg at 12:00 UT. In Figure 6B we see a large increase in the GRTI growth rate γ starting at ~ 11:45 UT and peaking at ~ 12:15 UT. During this period there is over an order-of-magnitude decrease in the Pedersen conductance Σ_P. Decomposing the growth rate into the gravitational (γ_g) and wind/drift (γ_{wc}) components we find that the dominant driving term is gravity; the wind/drift term leads to a positive growth rate but is much smaller than that associated with gravity. The reason for this is the large decrease in the Pedersen conductance that affects γ_g much more than γ_{wc} as evident in Equations 2, 3.

The aforementioned simulation study was for quiet geomagnetic conditions and generated a single EPB that rose to ~ 600 km. However, a recent simulation study of the September 2018 (Huba and Lu, 2024) found that a series of large-scale EPBs formed in the western Pacific sector during the recovery phase of the storm on 8 September 2017. They attributed this behavior to large, equatorward flowing neutral winds caused by high latitude heating of the thermosphere during the storm.

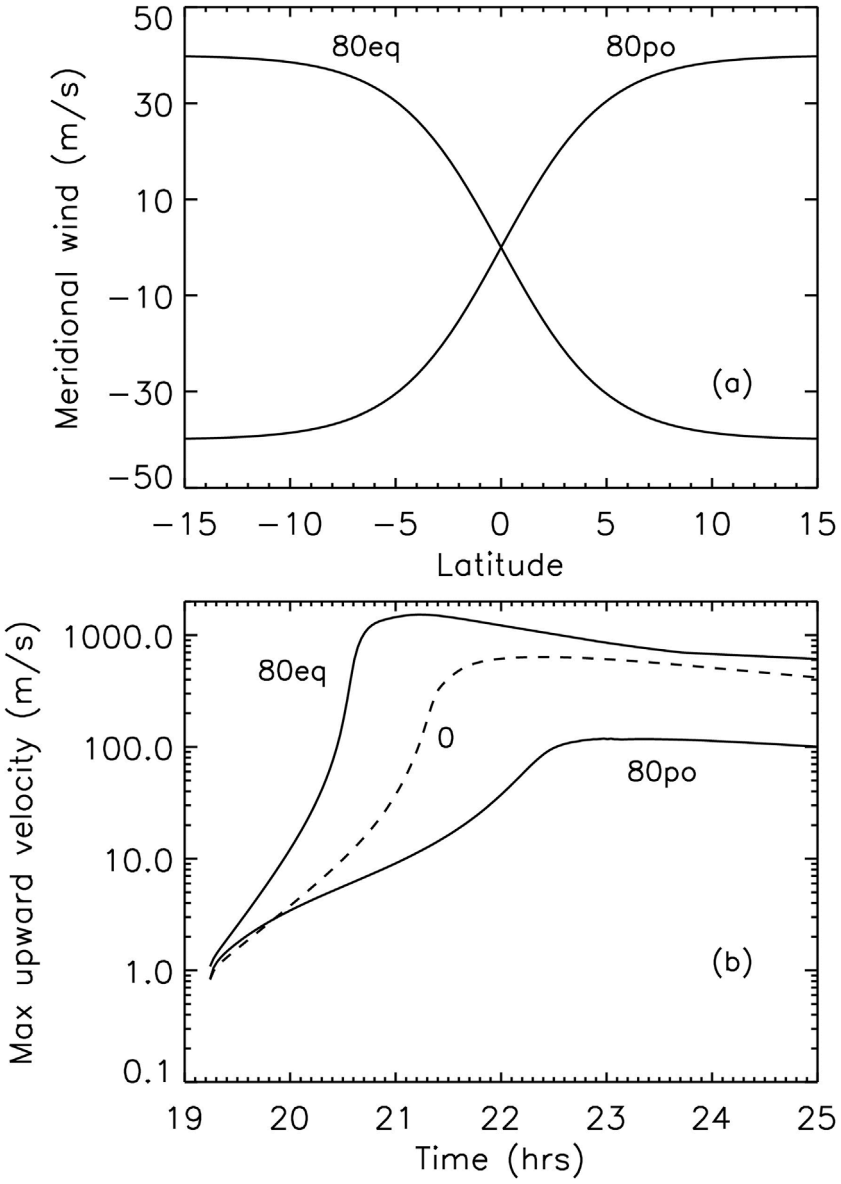

FIGURE 3
Plots of **(A)** the meridional neutral wind profiles as a function of latitude for $V_{m0} = \pm 40$ m/s, and **(B)** maximum upward $E \times B$ drift velocity as a function of time. [from Huba and Krall (2013)].

The simulation used the coupled SAMI3/WACCM-X code to model the days 6–8 September 2017. The geophysical parameters considered are F10.7 = 134.9, 130.4, 118.5, F10.7A = 84.3, 84.3, 84.3, and Ap = 8, 36, 106 for each day, respectively. In Figure 7 contour plots of the electron density (a, e), meridional wind (b, f), E × B drift (d, h) (all at 494 km), and the Pedersen conductance (c, g) on September 8 are shown. The left panels (a, b, c, d) are at 14:14 UT and the right panels (e, f, g, h) are at 15:29 UT. There are "weak" EPBs evident in the longitude range 180° W to 90° W evident in Figure 7A; these are fossil EPBs that had formed earlier at 13:59 UT Of note, there are strong equatorward flowing meridional winds in the northern hemisphere between 90° E and 90° W and in the southern hemisphere between 135° E and 135° W in Figure 7B. There is a decrease in the Pedersen conductance in both the low- and mid-latitude regions associated with the equatorward winds as indicated in Figure 7C. Lastly, there is an increase in the E × B drift perpendicular to the magnetic field in the meridional plane (i.e., at the magnetic equator the drift is vertical while at mid-latitudes it has vertical and latitudinal components) in Figure 7D.

Figures 7E–H correspond to Figures 7A–D but 75 min later at 15:29 UT. The equatorward meridional winds in Figure 7F have become more intense closer to the equator as well as a reduction in the Pedersen conductance at low- to mid-latitudes. However, the most striking features that have developed are shown in Figures 7E, H. In Figure 7E a span of EPBs developed in the longitude range ~ 90° E to 180° E; several extend in latitude from ~ −15° to 30°. Subsequently, several EPBs rise to over 2,000 km.

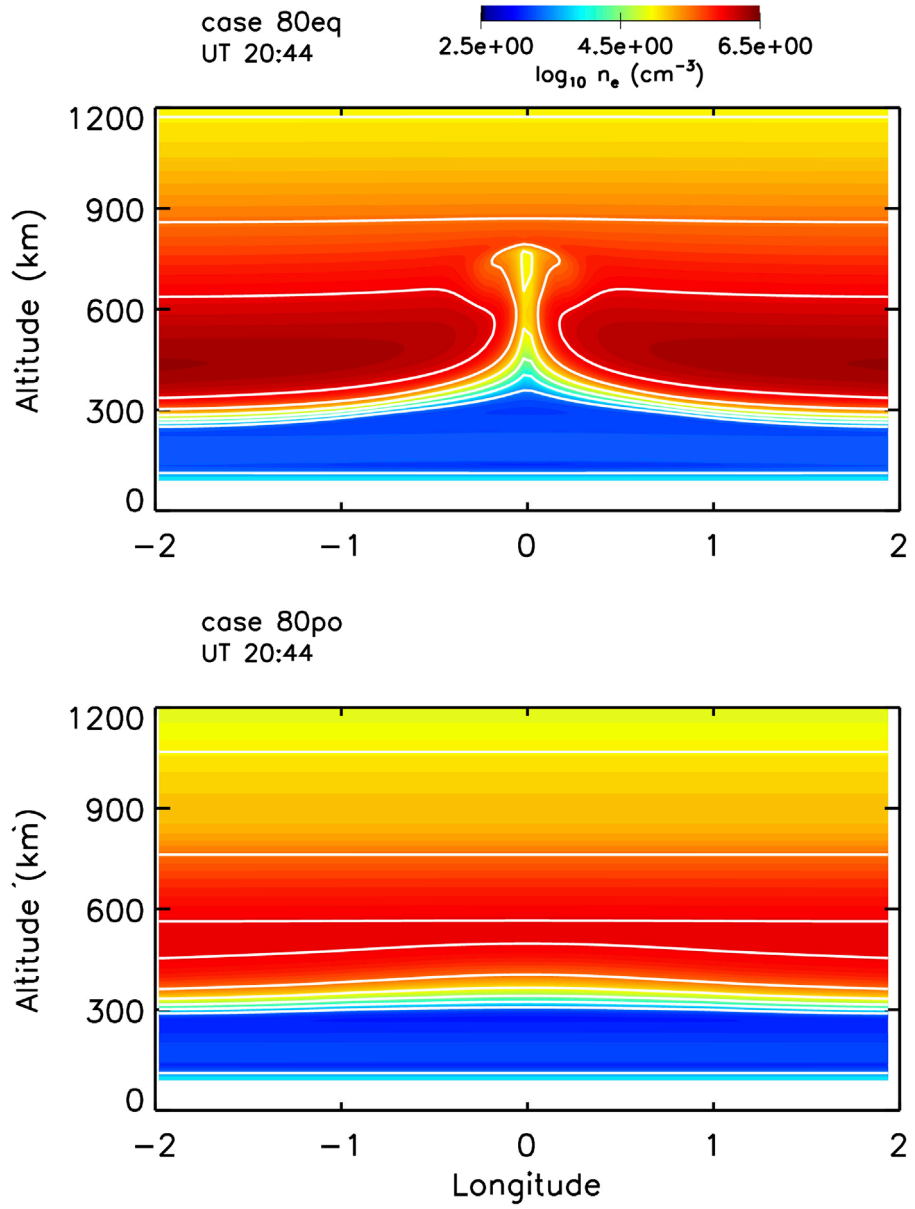

FIGURE 4
Contour plots of the electron density at time $t =$ 20:44 LT for the cases 80eq (top) and 80po (bottom). [from Huba and Krall (2013)].

Attendant with these EPBs are large E × B velocities that exceed 200 m/s as shown in Figure 7H.

4 Observations

The initial observational studies of the relationship between transhemispheric meridional winds and ESF focused on the suppression of ESF because of the work by Maruyama (1988). Mendillo et al. (1992) performed a two-day case study using the ALTAIR radar and optical imaging data. They found that ESF was suppressed on the first night (14 August 1988) but not the next night (15 August 1988). They attribute the suppression of ESF on the first night to a north-to-south meridional wind based on a reduction of the northern meridional gradient in 6,300 Å airglow. A subsequent study by Mendillo et al. (2001) during the Multi-Instrumented Studies of Equatorial Thermospheric Aeronomy (MISETA) campaign found "no convincing evidence for the wind suppression mechanism."

Thampi et al. (2006) developed a prediction parameter *C* based on observations that combined electrodynamic processes and meridional winds. The former is related to the E × B uplift of the ionosphere due to the pre-reversal enhancement of the eastward electric field and the latter to the asymmetry in the equatorial ionization crests (EIA) caused by the transhemispheric wind. They reported that an "EIA asymmetry alone does not suffice to make a deterministic forecast for the generation of ESF on a given day" because ESF was not observed on some days with a strong

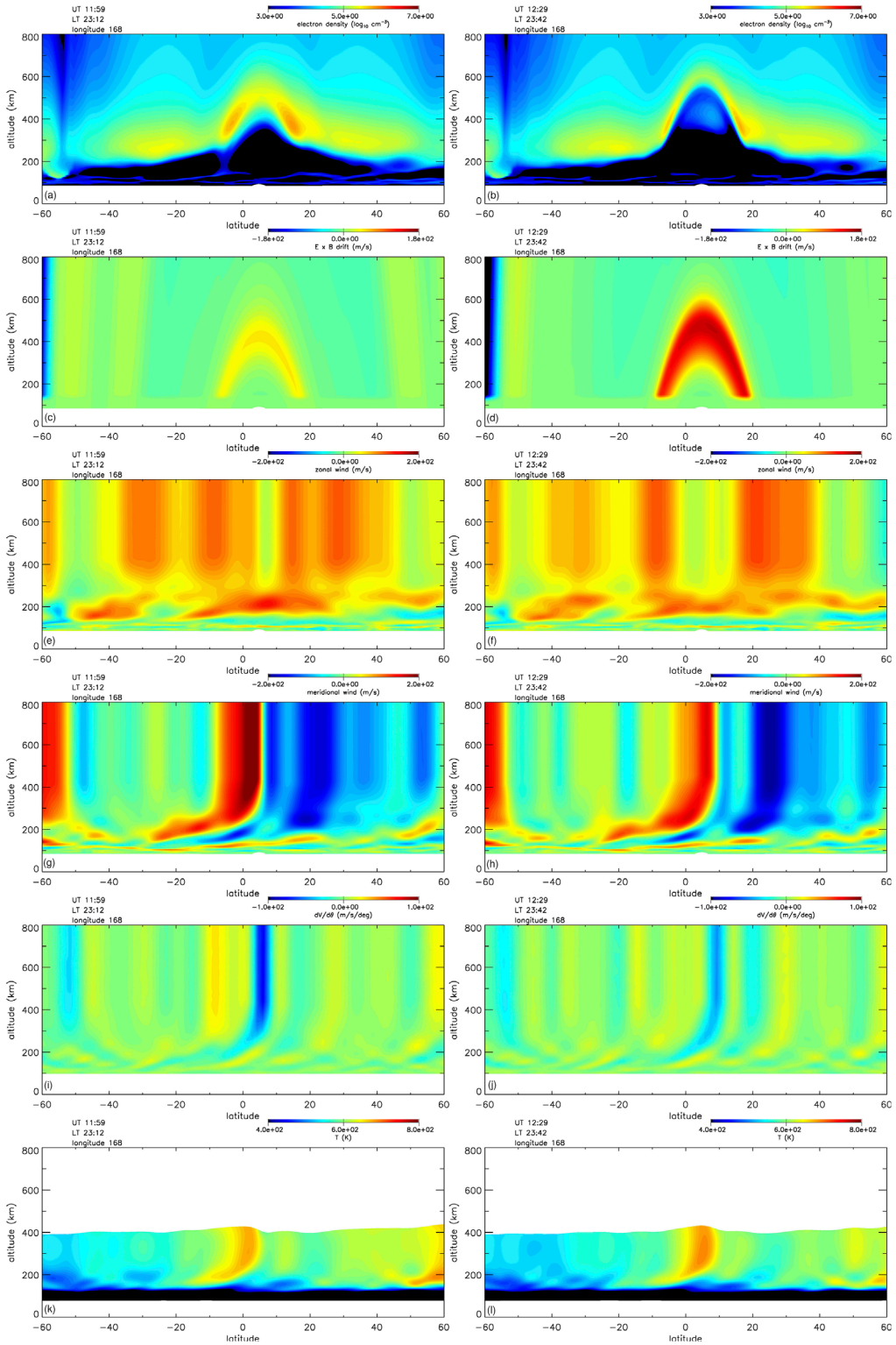

FIGURE 5
Contour plots of the electron density **(A, B)**, E × B velocity **(C, D)**, zonal neutral wind **(E, F)**, meridional neutral wind **(G, I)**, latitude derivative of the meridional neutral wind **(H, J)**, and neutral temperature **(K, L)** at times 11:59 UT **(A, C, E, G, I)** and 12:29 UT **(B, D, F, H, K)** as a function of latitude and altitude at longitude 168°.

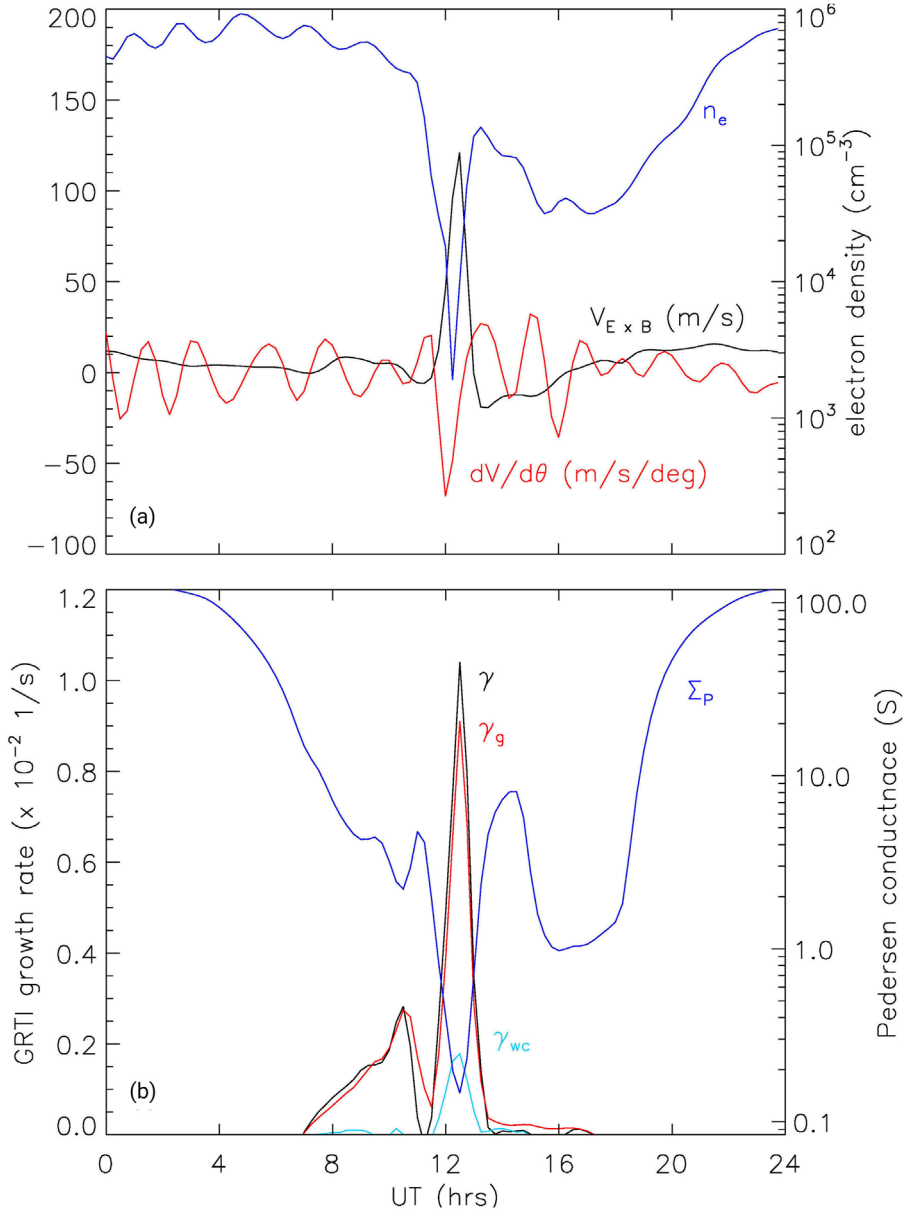

FIGURE 6
Line plots of **(A)** the electron density (n_e), E × B velocity (V_{ExB}), derivative of the meridional wind ($dV/d\theta$), **(B)** the maximum GRTI growth rates (γ, γ_g, and γ_{wc}) in the altitude range 250–800 km. Here, local midnight is at 11:12 UT and the midnight temperature maximum (labeled MTM) occurs at ~ 01:18 LT.

EIA asymmetry while observed on other days with a strong EIA asymmetry. This supports the suggestion that the actual behavior of the meridional wind can enhance or suppress ESF.

Maruyama et al. (2007) developed an ionosonde network in the Southeast Asian sector consisting of a meridional chain and a pair near the equator designed to estimate the meridional wind based on nighttime ionospheric height variations. Maruyama et al. (2009) used this network to infer the meridional winds for the spring and fall equinoxes in 2004 and 2005, and correlated the results with the occurrence of equatorial irregularities. They found that the transequatorial meridional winds were larger in September than March, and suggested that this was why equatorial irregularities occurred less frequently in September than in March. Numerical simulations were performed using the SAMI3/ESF model to support this contention. A Brazilian study during 1999 and 2001 by Abdu et al. (2006) also concluded that magnetic meridional winds negatively influence ESF development by reducing the pre-reversal enhancement electric field and direct suppression of the instability.

On the other hand, Devasia et al. (2002) and Jyoti et al. (2004) found that under certain circumstances equatorward neutral winds appeared to be needed for ESF to develop. Specifically, Devasia et al. (2002) argued that when the h'F base height of the *F*-layer is below 300 km, equatorward winds appear necessary to trigger ESF. However, they suggest that under these conditions

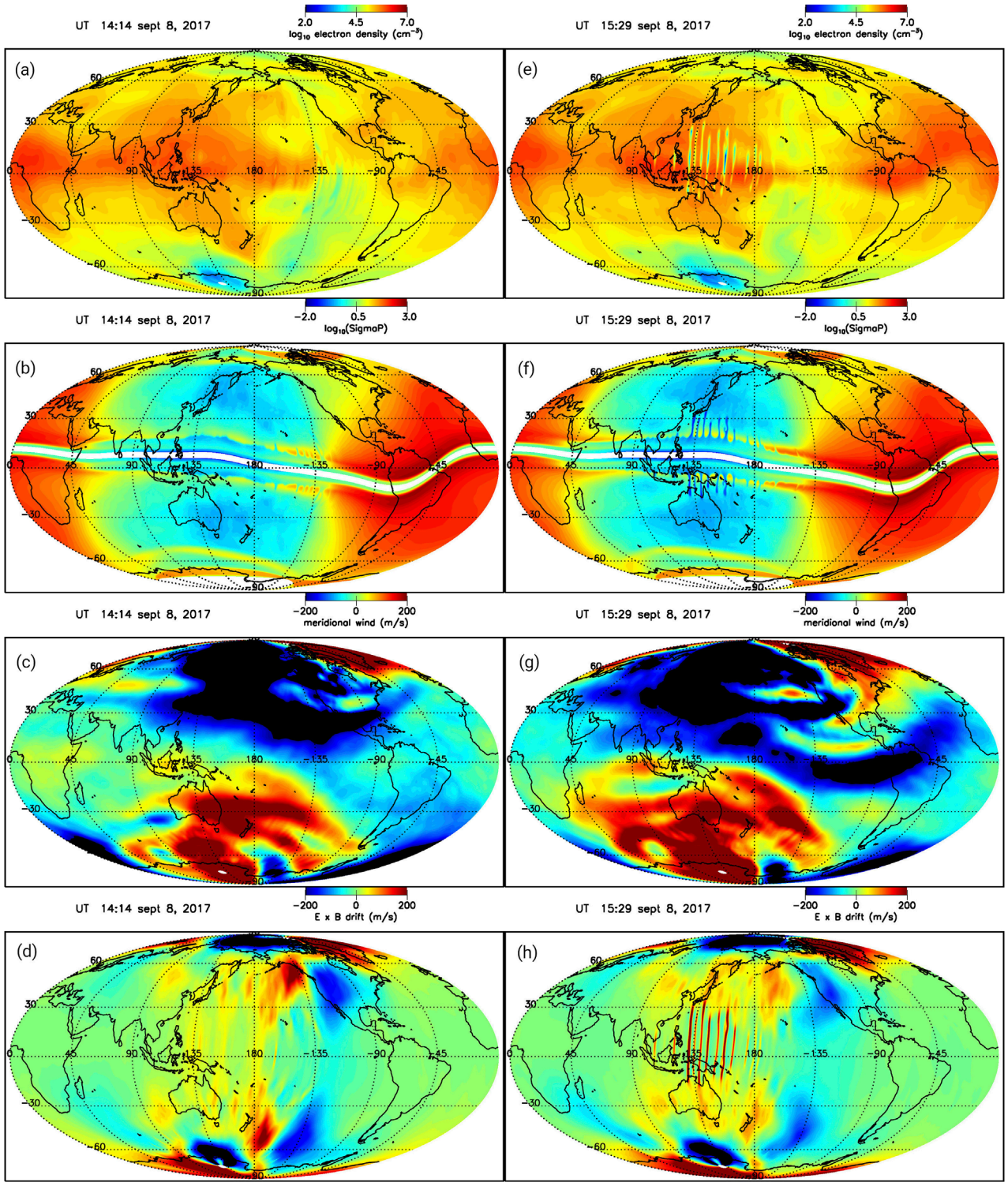

FIGURE 7
Contour plots of the electron density **(A, E)**, meridional wind **(B, F)**, E × B drift **(D, H)** (all at 394 km), and the Pedersen conductance **(C, G)**. The left panels **(A–D)** are at 14:14 UT and the right panels **(E–H)** are at 15:29 UT.

there is a downward neutral wind that amplifies the instability; they did not consider changes in the conductance that could impact the instability. Jyoti et al. (2004) found a similar result and suggested that the effect of an equatorward neutral wind impacted the equatorial ionization anomaly (EIA), the equatorial temperature and wind anomaly (ETWA), and neutral dynamics to effectively enable instability at lower h'F heights (<300 km) via a downward wind (Sekar and Raghavarao, 1987).

Sreekumar and Sripathi (2016), Sreekumar and Sripathi (2017) studied nighttime thermospheric meridional winds in the Indian

sector during the period March–December 2013. They derived the wind structure based on the h'F and hpF2 methods using ionosonde data. Comparing the results of the two methods to the HWM07 empirical wind model, it was found that the h'F was in better agreement. They related their h'F wind measurements to GPS scintillation data (i.e., an indicator of equatorial spread *F*) and found that longer duration scintillation events were associated with equatorward winds while non-scintillation days the winds were poleward.

Gao et al. (2023) studied the relationship between geomagnetic substorms and the occurrence of equatorial spread *F*. They used Jicamarca incoherent and coherent (JULIA) radar measurements to identify periods of equatorial spread *F*, and an AL-based identification algorithm (Newell and Gjerloev, 2011) to identify substorm activity. They find a distinct correlation between ESF and substorms. Specifically, in the post-sunset sector (1,800–2,400 LT) the ESF occurrence rate was a maximum ~ 0.5 h after sunset, while in the post-midnight sector (0000–0006 LT) it was ~ 3.0–3.5 h after midnight. They attributed the former to a prompt penetration field enhancing the pre-reversal upward E × B drift, and the latter to the disturbance dynamo electric field generating an upward E × B drift. This last result is consistent with the stormtime simulation study by Huba and Lu (2024). In particular, an upward E × B drift developed prior to the development of post-midnight EPBs on the storm day (shown in their Figure 5C). On the previous (non-storm) day the post-midnight drift was negative.

Zhan and Rodrigues (2018) investigated the dynamics of equatorial spread *F* in the American sector during the June solstice. Using incoherent scatter radar measurements and the ionosphere model SAMI2 (Huba et al., 2000) in conjunction with GRTI theory they also found that equatorward meridional winds are destabilizing. However, in their analysis they found that the equatorward winds *increased* the conductance and that the increase in the GRTI growth rate was attributed to a modification of the electron density profile.

5 Discussion

Although not surprising, the results of this paper highlight the potential importance of meridional neutral winds in the development of EPBs during equatorial spread *F*. Nominally, EPBs form in the post-sunset sector and are usually associated with enhanced upward E × B drifts (e.g., > 30 m/s) driven by the pre-reversal eastward electric field (e.g., Hysell et al., 2015). For this situation it is not clear meridional winds play a significant role in the development of ESF. However, during periods of low solar activity (e.g., F10.7 $\lesssim$ 80) the post-sunset E × B is typically small (Scherliess and Fejer, 1999) and ESF is unlikely to occur. On the other hand, for example, there are observations of ESF occurring in the post-midnight sector during solar minimum conditions (during the June solstice) in the absence of post-sunset EPBs (Heelis et al., 2010; Li et al., 2011; Zhan et al., 2018). During these periods it appears that the meridional wind can play a pivotal role in the generation of EPBs at the onset of ESF (Huba et al., 2023).

It also appears meridional winds can play a dramatic role in the development of large-scale EPBs during magnetic storms (Gao et al., 2023; Huba and Lu, 2024). During geomagnetic storms, heating of the thermosphere at high-latitude generates strong modifications to both the zonal and meridional winds that propagates equatorward over a period of several hours. This can lead to an upward E × B drift in the midnight sector because of modification of the zonal wind, and to an enhancement in the growth rate of the GRTI associated with the reduction in conductance caused by equatorward neutral winds.

The dominant theme of this review is that meridional winds can affect the onset and evolution of EPBs during ESF, primarily by modification of the conductance which directly impacts the growth rate of the GRTI. This doesn't necessarily obviate the possibility of other factors playing a roll such as seeding mechanisms (e.g., gravity waves), modification of the lower *F* layer gradient, or downward vertical winds. Moreover, the state of the ionosphere-thermosphere system is also a factor. For the theoretical and modeling studies described in this review, equatorward winds decrease the conductance while poleward winds increase the conductance as shown in Figure 1. It is possible that this is not always the case (e.g., Zhan and Rodrigues, 2018) and the blanket statement that "equatorward winds promote the development of ESF and poleward winds suppress the development of ESF" may not be universally true.

We also note that Kherani et al. (2005) presented a theoretical and modeling study of the collisional interchange instability. In this work a linear, local analysis was performed that considered a 3D potential equation (in contrast to the current analysis which assumes equipotential field lines). They found that a meridional wind can generate a density gradient along the magnetic field line that has a stabilizing influence on the instability when considering parallel oscillations (e.g., $k_{\parallel}$).

In conclusion, additional measurements of the neutral wind, in conjunction with observations of EPBs and ESF, are needed to provide a clearer understanding of ESF onset and evolution, and in particular the day-to-day variability of ESF. To this end the Ionospheric Connections Explorer (ICON) satellite mission data provides an invaluable resource for neutral wind and plasma data to address this problem (Immel et al., 2018).

Author contributions

JH: Writing–original draft, Writing–review and editing.

Funding

The author(s) declare that financial support was received for the research, authorship, and/or publication of this article. This research was supported by NASA grants 80NSSC21K1305, ICON Explorers Program through contracts NNG12FA45C and NNG12FA42I, and DRIVE Science Center for Geospace Storms (CGS) under award (80NSSC22M0163), and AFOSR (FA9550-22-C-0001).

Conflict of interest

Author JH is employed by Syntek Technologies.

The author(s) declared that they were an editorial board member of Frontiers, at the time of submission. This had no impact on the peer review process and the final decision.

Publisher's note

References

Abdu, M. A., Iyer, K. N., de Medeiros, R. T., Batista, I. S., and Sobral, J. H. A. (2006). Thermospheric meridional wind control of equatorial spread *F* and evening prereversal electric field. *Geophys. Res. Lett.* 33, L07106. doi:10.1029/2005GL024835

Booker, H. G., and Wells, H. G. (1938). Scattering of radio waves by the *F*-region of the ionosphere. *Terr. Mag. Atmos. Elec.* 43, 249–256. doi:10.1029/te043i003p00249

Devasia, C. V., Jyoti, N., Viswanathan, K. S., Tiwari, D., and Sridharan, R. (2002). On the plausible linkage of thermospheric meridional winds with equatorial spread *F*. *J. Atmos. Sol. Terr. Phys.* 64 (1), 1–12. doi:10.1016/s1364-6826(01)00089-x

Gao, S., Cail, H., Zhan, W., Wan, X., Xiong, C., Zhang, H., et al. (2023). Characterization of local time dependence of equatorial spread *F* responses to substorms in the American sector. *J. Space Weather Space Clim.* 13 (2), 2. doi:10.1051/swsc/2022039

Haerendel, G. (1974). *Theory of equatorial spread F*, Munich, Germany: Max Planck Institute for Extraterrestrial Physics.

Heelis, R. A., Stoneback, R., Earle, G. D., Haaser, R. A., and Abdu, M. A. (2010). Medium-scale equatorial plasma irregularities observed by coupled ion-neutral dynamics investigation sensors aboard the communication navigation outage forecast system in a prolonged solar minimum. *Ionosphere and Upper Atmosphere* 115, A10321. doi:10.1029/2010JA015596

Herrero, F. A., Spencer, N. W., and Mayr, H. G. (1993). Thermosphere and *F*-region plasma dynamics in the equatorial region. *Adv. Space Res.* 13, 201–220. doi:10.1016/0273-1177(93)90019-8

Huba, J. D., Joyce, G., and Fedder, J. A. (2000). SAMI2 (Sami2 is another model of the Ionosphere): a new low-latitude Ionosphere model. *J. Geophys. Res.* 105, 23035

Huba, J. D., Joyce, G., and Krall, J. (2008). Three-dimensional equatorial spread *F* modeling. *Geophys. Res. Lett.* 35, L10102. doi:10.1029/2008GL033509

Huba, J. D., and Joyce, G. (2010). Global modeling of equatorial plasma bubbles. *Geophys. Res. Lett.* 37, L17104. doi:10.1029/2010GL044281

Huba, J. D., and Krall, J. (2013). Impact of meridional winds on equatorial spread *F*: revisited. *Geophys. Res. Lett.* 40, 1268–1272. doi:10.1002/grl.50292

Huba, J. D., and Liu, H.-L. (2020). Global modeling of equatorial spread *F* with SAMI3/WACCM-X. *Geoophy. Res. Lett.* 47, e2020GL088258. doi:10.1029/2020GL088258

Huba, J. D. (2022). Generalized Rayleigh-Taylor instability: ion inertia, acceleration forces, and *E* region drivers. *J. Geophys. Res. Space Phys.* 127, e2022JA030474. doi:10.1029/2022JA030474

Huba, J. D., Liu, H.-L., and McInerney, J. (2023). Modeling the development of an equatorial plasma bubble during a midnight temperature maximum with SAMI3/WACCM-X. *Geoophy. Res. Lett.* 50, e2023GL104388. doi:10.1029/2023GL104388

Huba, J. D., and Lu, G. (2024). Modeling equatorial plasma bubbles with Sami3/WACCM-X september 2017 storm. *Geophys. Res. Lett.* 5, e2024GL109071. doi:10.1029/2024GL109071

Hysell, D. L. (2000). An overview and synthesis of plasma irregularities in equatorial spread *F*. *J. Atmos. Sol. Terr. Phys.* 62, 1037–1056. doi:10.1016/s1364-6826(00)00095-x

Hysell, D. L., Milla, M. A., Condori, L., and Vierinen, J. (2015). Data-driven numerical simulations of equatorial spread F in the Peruvian sector 3: solstice. *J. Geophys. Res. Space Phys.* 120 (10)–809. doi:10.1002/2015JA021877

Immel, T. J., England, S. L., Mende, S. B., Heelis, R. A., Englert, C. R., Edelstein, J., et al. (2018). The ionospheric connection explorer mission: mission goals and design. *Space Sci. Rev.* 214, 13. doi:10.1007/s11214-017-0449-2

Jyoti, N., Devasia, C. V., Sridharan, R., and Tiwari, D. (2004). Threshold height (h'F)c for the meridional wind to play a deterministic role in the bottom side equatorial spread *F* and its dependence on solar activity. *Geophys. Res. Lett.* 31, L12809. doi:10.1029/2004GL019455

Kherani, A. E., Mascarenhas, M., de Paula, E. R., Sobral, J. H. A., and Bertoni, F. (2005). A three-dimensional simulation of collisional-interchange-instability in the equatorial-low-latitude ionosphere. *Space Sci. Rev.* 121, 253–269. doi:10.1007/s11214-006-6158-x

Krall, J., Huba, J. D., Joyce, G., and Zalesak, S. T. (2009). Three-dimensional simulation of equatorial spread *F* with meridional wind effects. *Ann. Geophys.* 27, 1821–1830. doi:10.5194/angeo-27-1821-2009

Li, G., Ning, B., Abdu, M. A., Yue, X., Liu, L., Wan, W., et al. (2011). On the occurrence of postmidnight equatorial F region irregularities during the June solstice. *J. Geophys. Res.* 116, A04318. doi:10.1029/2010JA016056

Liu, H. L., Bardeen, C. G., Foster, B. T., Lauritzen, P., Liu, J., and Lu, G. (2018). Development and validation of the whole atmosphere community climate model with thermosphere and ionosphere extension (WACCM-X 2.0). *J. Adv. Model. Earth Sys.* 10, 381. doi:10.1002/2017MS001233

Maruyama, T. (1988). A diagnostic model for equatorial spread *F*, 1, Model description and application to electric field and neutral wind effects. *J. Geophys. Res.* 93 (14), 14611–14622. doi:10.1029/ja093ia12p14611

Maruyama, T., Kawamura, M., Saito, S., Nozaki, K., Kato, H., Hemmakorn, N., et al. (2007). Low latitude ionosphere-thermosphere dynamics studies with inosonde chain in Southeast Asia. *Ann. Geophys.* 25, 1569–1577. doi:10.5194/angeo-25-1569-2007

Maruyama, T., Saito, S., Kawamura, M., Nozaki, K., Krall, J., and Huba, J. D. (2009). Equinoctial asymmetry of a low-latitude ionosphere-thermosphere system and equatorial irregularities: evidence for meridional wind control. *Ann. Geophys.* 27, 2027–2034. doi:10.5194/angeo-27-2027-2009

Mendillo, M., Baumgardner, J., Pi, X., Sultan, P., and Tsunoda, R. (1992). Onset conditions for equatorial spread *F*. *J. Geophys. Res.* 97 (13), 13865–13876. doi:10.1029/92ja00647

Mendillo, M., Meriwether, J., and Biondi, M. (2001). Testing the thermospheric neutral wind suppression mechanism for day-to-day variability of equatorial spread *F*. *J. Geophys. Res.* 106, 3655–3663. doi:10.1029/2000ja000148

Meriwether, J., Faivre, M., Fesen, C., Sherwood, P., and Veliz, O. (2008). New results on equatorial thermospheric winds and the midnight temperature maximum. *Ann. Geophys.* 26, 447–466. doi:10.5194/angeo-26-447-2008

Newell, P. T., and Gjerloev, J. W. (2011). Evaluation of SuperMAG auroral electrojet indices as indicators of substorms and auroral power. *J. Geophys Res. Space Phys.* 116. doi:10.1029/2011JA016779

Scherliess, L., and Fejer, B. (1999). Radar and satellite global equatorial *F* region vertical drift model. *J. Geophys. Res.* 104, 6829–6842. doi:10.1029/1999ja900025

Sekar, R., and Raghavarao, R. (1987). Role of vertical winds on the Rayleigh-Taylor mode instabilities of the night-time equatorial ionosphere. *J. Atmos. Terr. Phys.* 49, 981–985. doi:10.1016/0021-9169(87)90104-8

Sreekumar, S., and Sripathi, S. (2016). Nighttime thermospheric meridional winds as inferred from ionosonde parameters over Indian region and their plausible effects on plasma irregularities. *Adv. Space Res.* 58 (92), 92–107. doi:10.1016/j.asr.2016.04.009

Sreekumar, S., and Sripathi, S. (2017). A seasonal study on the role of h'F/meridional winds in influencing the development of ESF irregularities over Indian sector. *Adv. Space Res.* 60, 652–666. doi:10.1016/j.asr.2017.04.009

Sultan, P. J. (1996). Linear theory and modeling of the Rayleigh-Taylor instability leading to the occurrence of equatorial spread *F*. *J. Geophys. Res.* 101 (26), 26875–26891. doi:10.1029/96ja00682

Thampi, S. V., Ravindran, S., Pant, T. K., Devasia, C. V., Sreelatha, P., and Sridharan, R. (2006). Deterministic prediction of post-sunset ESF based on the strength and asymmetry of EIA from ground based TEC measurements: preliminary results. *Geophys. Res. Lett.* 33, L13103. doi:10.1029/2006GL026376

Zalesak, S. T., and Huba, J. D. (1991). Effect of meridional winds on the development of equatorial spread *F*. *Eos Trans. AGU 72, Spring Meet. Suppl.* 211.

Zhan, W., Rodrigues, F., and Milla, M. (2018). On the genesis of postmidnight equatorial spread *F*: results for the American/Peruvian sector. *Geophys. Res. Lett.* 45, 7354–7361. doi:10.1029/2018GL078822

Zhan, W., and Rodrigues, F. S. (2018). June solstice equatorial spread *F* in the American sector: a numerical assessment of linear stability aided by incoherent scatter radar mearsurements. *J. Geophys. Res. Space Phys.* 123, 755. doi:10.1002/2017JA024969

frontiers | Frontiers in Astronomy and Space Sciences

TYPE Original Research
PUBLISHED 01 November 2024
DOI 10.3389/fspas.2024.1465230

OPEN ACCESS

EDITED BY
David Hysell,
Cornell University, United States

REVIEWED BY
Yun Gong,
Wuhan University, China
Yen-Jung Wu,
University of California, Berkeley,
United States

*CORRESPONDENCE
Katrina Bossert,
katrina.bossert@asu.edu

RECEIVED 15 July 2024
ACCEPTED 02 September 2024
PUBLISHED 01 November 2024

CITATION
Bossert K, Kumari K, Inchin P, Norrell J, Eckermann S, Pautet P-D, Martinis C, Kjellstrand CB, Phillips S, Snively J, Zhao Y and Zettergren M (2024) Influences of the quasi-two-day wave on plasma bubble behavior over south America.
Front. Astron. Space Sci. 11:1465230.
doi: 10.3389/fspas.2024.1465230

Influences of the quasi-two-day wave on plasma bubble behavior over south America

Katrina Bossert[1,2]*, Komal Kumari[3], Pavel Inchin[4], Jessica Norrell[1], Stephen Eckermann[5], Pierre-Dominique Pautet[6], Carlos Martinis[7], Carl Bjorn Kjellstrand[1], Sophie Phillips[1], Jonathan Snively[8], Yucheng Zhao[6] and Matthew Zettergren[8]

[1]School of Earth and Space Exploration, Arizona State University, Tempe, AZ, United States, [2]School of Mathematical and Statistical Sciences, Arizona State University, Tempe, AZ, United States, [3]High Altitude Observatory, National Center for Atmospheric Research, Boulder, CO, United States, [4]Computational Physics, Inc., Springfield, VA, United States, [5]U.S. Naval Research Laboratory, Washington, DC, United States, [6]Center for Atmospheric and Space Sciences, Utah State University, Logan, UT, United States, [7]Center for Space Physics, Astronomy Department, Boston University, Boston, MA, United States, [8]Physical Sciences Department, Embry-Riddle Aeronautical University, Daytona Beach, FL, United States

Equatorial Plasma Bubbles (EPBs) are a region of depleted ionospheric densities. EPBs are known to fluctuate both seasonally and day to day, and have been linked to changes in solar activity, geomagnetic activity, and seeding resulting from dynamics occurring at lower altitudes. Here, EPB activity is investigated over a 15-day period with overlapping coincident ground-based 630 nm oxygen airglow measurements, near-infrared hydroxyl mesospheric temperature mapper (MTM) measurements, and Rate Of change of Total Electron Content Index (ROTI) values. The data are compared with the Navy Global Environmental Model (NAVGEM) reanalysis over the same time period. It is found that several days with strong EPB activity coincided with the positive/northward meridional wind phase of the quasi-two-day wave (QTDW) in the mesosphere. These initial observations indicate correlations of the QTDW phase and the occurrence rates of EPBs, and suggest a need for further investigations to assess potential causal relationships that may affect the variability and prevalence of EPBs.

KEYWORDS

equatorial plasma bubbles, quasi-two-day-wave, roti, gravity waves (GWs), airglow

1 Introduction

Equatorial plasma bubbles (EPBs) can have significant implications for the state of the ionosphere as well as ionospheric radio remote sensing and communications (Hysell, 2000; Sousasantos et al., 2023). While there have been advances over the years in understanding EPBs, there are still outstanding issues towards understanding both their smaller-scale mechanisms, global scale modeling, and forecasting (Huba, 2022). EPBs have been known to vary from day to day (Aa, et al., 2023a), seasonally (Chou et al., 2020; Stolle, et al., 2006), and with differing geomagnetic activity (Martinis et al., 2005; Abdu, 2012; Carmo et al., 2023; Amadi et al., 2023). EPB formation occurs most prominently during the hours after sunset, when a steep gradient in electron density forms contributing to the growth rate of

the Rayleigh-Taylor (R-T) instability (Sultan, 1996; Huang and Hairston, 2015; Hudson and Kennel, 1975), ultimately leading to equatorial spread F (ESF). While the generation of ESF is linked to this post-sunset time period, the R-T instability is further triggered by meridional wind gradients in the F-region, which can change due to a number of factors (Huba and Krall, 2013). These driving factors that cause EPB seeding include geomagnetic and solar activity (Adhya and Valladares, 2023; Sori et al., 2021; Kepkar et al., 2020) and gravity wave (GW) propagation into the thermosphere and ionosphere (Yokoyama et al., 2019; Chou et al., 2023; Saha et al., 2022; Takahashi et al., 2009; Fritts et al., 2008; Singh et al., 1997).

Observations of EPBs and ESF have been made over many decades via multiple measurement techniques (e.g., Bhattacharyya, 2022, and references therein). Recently, ICON and GOLD satellite missions have provided insight into EPB variability and generation (Huba et al., 2021; Karan et al., 2020; Karan et al., 2023; Aa et al., 2023b; Park et al., 2022). However, EPBs have also been studied with numerous ground-based instruments (Aa et al., 2019; Haase et al., 2010; Hysell and Burcham, 1998). The research presented here uses Rate Of change of Total electron content Index (ROTI) and 630.0 nm oxygen airglow from an all-sky imager to classify the presence and extent of EPBs. Airglow imaging provides spatial observations allowing for the 2D study of EPB formation and evolution (Pautet et al., 2009; Martinis et al., 2009). ROTI has been used in numerous studies of ESF and EPBs, due to its correlation with larger-scale plasma irregularities that are associated with ESF and airglow depletions (Carmo et al., 2023; Lay, 2018; de Jesus et al., 2020; Rajesh et al., 2022).

The Quasi-Two-Day Wave (QTDW) is a large-scale wave that is often observed to be westward propagating with a zonal wavenumber of 3 (Ern et al., 2013; Burks and Leovy, 1986; Lieberman et al., 2017). The QTDW is caused by the instability of the summer hemisphere easterly jet, which results in an amplitude that is most notable in meridional winds in the mesosphere and lower thermosphere (MLT) region (Singh et al., 2024). It is typically observed in the summertime hemisphere, and has been well studied through multiple observations (He et al., 2021; Craig et al., 1980; Pancheva et al., 2018; Iimura et al., 2021; Walterscheid et al., 2015; Hecht et al., 2010). The QTDW has been shown to modulate the ionospheric dynamo and electron density (Yue et al., 2012; Pancheva et al., 2006; Forbes et al., 2021). Studies also have demonstrated the implications and interactions of the QTDW with GW dissipation, generation, and filtering (Ern et al., 2013; Yasui et al., 2021; Jacobi and Pogoreltsev, 2006). These findings underscore the multiple possible pathways through which the QTDW may influence the lower thermosphere and ionosphere. In the observations presented in this case study, relationships between EPB appearance and extent are compared with QTDW phase within the MLT region using ROTI, hydroxyl mesospheric temperature mapper (MTM) measurements, and 630 nm airglow images, in conjunction with the Navy Global Environmental Model (NAVGEM) output. Additionally, these observations are compared with GW activity in the stratosphere and mesosphere as measured by the MTM, the Atmospheric InfraRed Sounder (AIRS) and NAVGEM. These are reported and discussed in the subsequent Sections 2, 3.

2 Materials and methods

Observations from multiple instruments were used from the period over 10–24 January 2015. These measurements demonstrate fluctuations in ROTI and airglow associated with plasma bubbles. The ionosphere-thermosphere measurements are combined with hydroxyl MTM measurements in conjunction with NAVGEM reanalysis data for comparison of coincident dynamics in the MLT region.

2.1 ROTI observations over south America

The ionospheric irregularities are based on the ROTI (Pi et al., 1997), which represents a standard derivation of the rate of change of TEC (ROT):

$$ROTI = \sqrt{\langle ROT^2 \rangle - \langle ROT \rangle^2} \tag{1}$$

where

$$ROT = \frac{TEC_t - TEC_{t-\delta t}}{\delta t} \tag{2}$$

Here, TEC is calculated based on 30 s phase observations at GPS L1 and L2 frequencies for each satellite-station pair (Inchin et al., 2023). For this case study, 88 stations extending throughout Chile are used. The time window of 5 min is chosen to calculate a variance in Equation 1, using the ROT calculated in Equation 2. The ROTI values are calculated using GPS receiver sites in South America using a 40-degree elevation cut off. Figure 1A shows all data points included south of geographic latitude 15S. Figure 1B shows data points of ROTI for geographic latitudes south of 30S. This plot highlights ionosphere fluctuations occurring at more southern latitudes and furthermore demonstrates a periodic nature to these southern increased ROTI values. To highlight regions of increased ROTI, Figure 1C shows the average ROTI value of datapoints binned in a 1-h period. Most peaks in ROTI occur between 1-3UT, which corresponds to post-sunset local times as is expected for the onset of EPB (Sultan, 1996; Huang, 2018; Panda et al., 2019). However, there are exceptions to post-sunset formation, and spikes in ROTI are observed after midnight LT in some instances. During the observation period, this was the case on 23 January. These post-midnight EPBs may be generated by a different mechanism, but are still frequently observed (Martinis et al., 2005; Otsuka, 2018; Yizengaw et al., 2013). In the observations presented, the largest post-sunset ROTI values were observed on 16, 18, 20, and 24 January, with mean values at these times ranging from 0.1 to 0.18 TECu/min. The lowest ROTI values were on 13 and 15 January, with mean values of measured ROTI post-sunset around or less than 0.03 TECu/min.

2.2 Optical ground-based observations

Airglow emissions in the thermosphere at 630 nm have previously been used to study depletions associated with EPBs near 250 km in altitude (Martinis et al., 2018; Hickey and Martinis, 2018). Data from an imager at the El Leoncito observatory (31.8S, 69.4W) that belongs to the Boston University network of all-sky

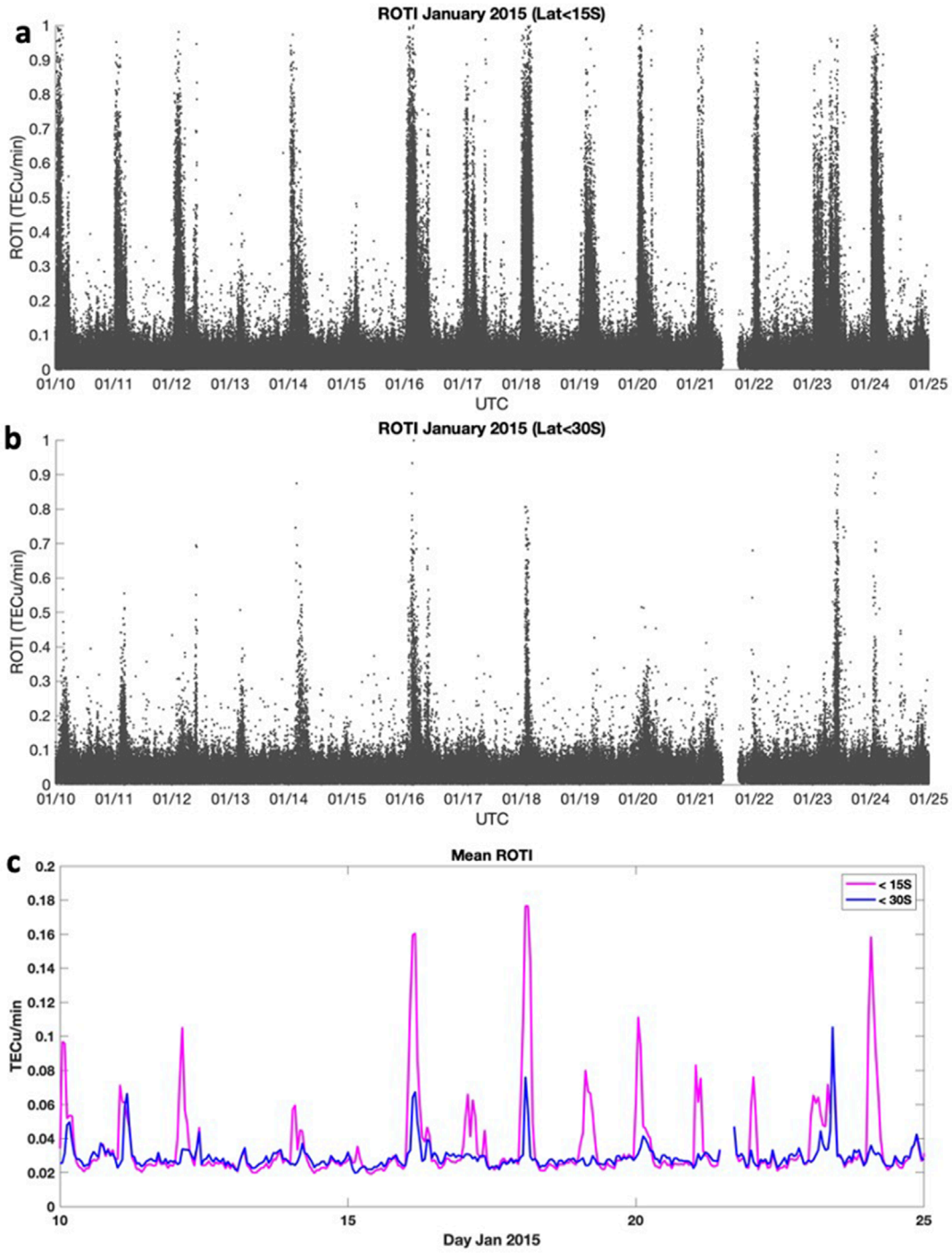

FIGURE 1
Plot **(A)** shows the ROTI values at all geographic locations south geographic latitude 15S. Plot **(B)** is the same as plot **(A)** but for locations south of 30S. Plot **(C)** shows the average of ROTI values binned into 1 h time intervals for locations south of 15S (pink) and 30S (blue).

imagers (Martinis et al., 2018) were used to classify the presence of ESF associated depletions in 630 nm airglow from 10–24 January. Each hour was classified with an activity level as either (1) a depletion extending to magnetic latitude 20S or further, (0.5) north of magnetic latitude 20S, (−1) clear with no visible depletions, or (0) no data available. Figure 2A summarizes these observations. From January 16–24, depletions were observed on all nights. The nights of January 16, 18, and 24 demonstrate depletions extending farthest southward beyond −20 MLAT. Examples of significant depletions are shown in Figures 2D, E for January 16 and 18 respectively. To determine conditions that may contribute to differing EPB on each day, geomagnetic and solar conditions were compared to the observations. The SuperMAG Auroral Electrojet (SME) index (Gjerloev, 2012; Newell and Gjerloev, 2011a; 2011b) is indicative of

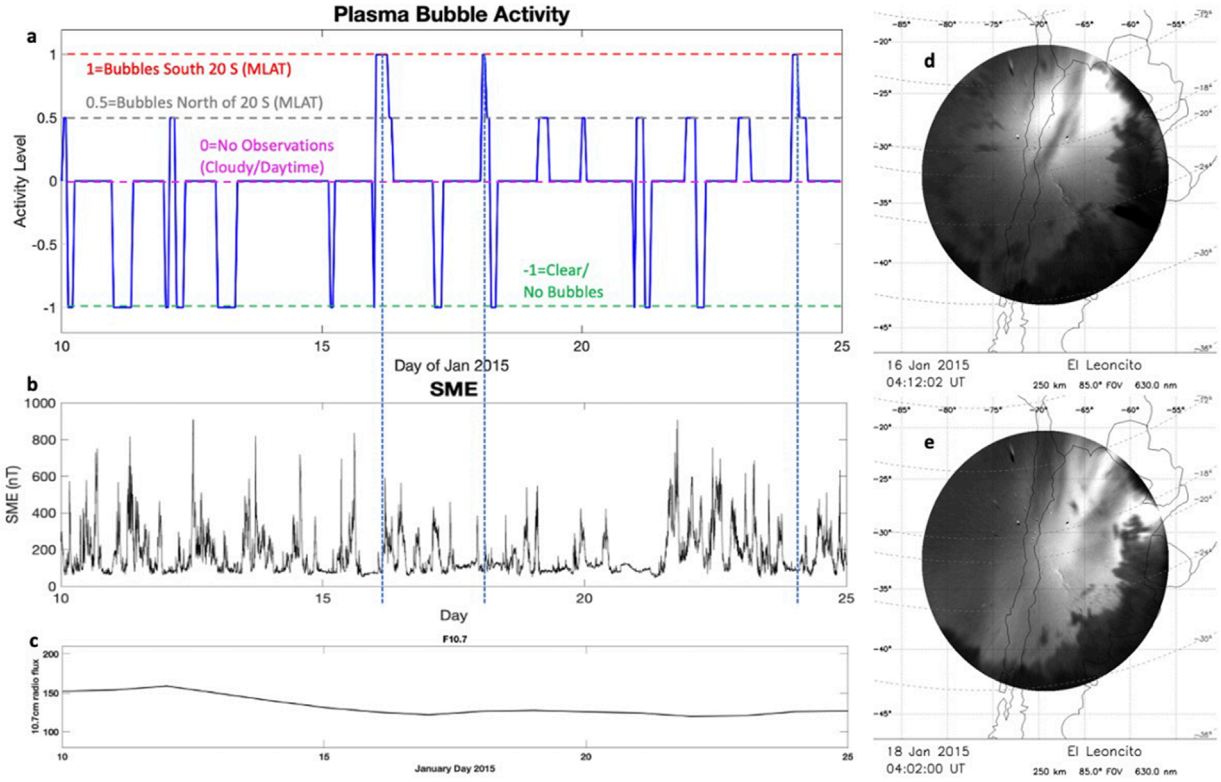

FIGURE 2
Plot **(A)** shows depletions observed in the 630 nm airglow with a value of one corresponding to depletions extending further south than −20 MLAT, a value of 0.5 corresponding to depletions north of −20 MLAT, a value of −1 indicating data but no observed depletions, and a value of 0 indicating no data. Plot **(B)** shows the SME index indicating the level of auroral activity. Plot **(C)** shows the F10.7 value indicating solar activity. Plots **(D)** and **(E)** show significant depletions in the 630 nm airglow on 16 and 18 January 2015.

global auroral power and indicates times of increased geomagnetic activity. This dataset is plotted in Figure 2B, and while fluctuations exist, there are no notable differences between days of significant depletions versus no depletions. Additionally, solar activity is denoted with the F10.7 index and plotted in Figure 2C. These values show little variation over the period of observations, indicating that the fluctuations in EPB activity were not necessarily related to solar activity in this case.

The MTM located at the nearby Andes Lidar Observatory (ALO) (30.3S, 70.7W) measures temperatures from hydroxyl (OH) airglow near 87 km in altitude (PugmireJonathan Rich, 2018). These measurements provide information regarding middle atmospheric dynamics with regards to both larger-scale temperature averages, and GW activity down to horizontal wavelengths of 10 km. Figure 3A shows nightly temperature averages from the MTM using 5 × 5 zenith pixel averages from each image over the period of observations, where an apparent 2-day fluctuation in temperatures from warm to cooler values is observed. A previous comparison of the MTM OH rotational temperatures (OH T) with other well-calibrated instruments (an FTIR spectrometer and sodium lidar) has shown that nightly mean temperatures, referenced to the 87 km lidar mean temperatures, are accurate to about +/−5K (Pendleton et al., 2000; Zhao et al., 2005). Further details of the MTM data reduction and analysis are given in Taylor et al. (1999; 2001). In the study presented here, the nightly averages show differences of 20–30K between consecutive nights from 15–24 January 2015. Warmer values are observed on and before January 15, and on January 17, 19, 21, and 23. Cooler values are observed on January 16, 18, 20, 22, and 24. These fluctuations in temperature indicate the presence of a QTDW. The three largest histogram ROTI values are indicated on nights with red dots. The pink dot indicates the fourth largest histogram ROTI value, which corresponds to an EPB that was not observed south of −20 MLAT. These four nights coincide with the coldest average nightly temperatures measured by the MTM, and suggest a potential correlation in EPB activity with the colder MLT temperatures.

The nightly standard deviation (stdev) for each night of OH T measurements from the MTM is plotted in Figure 3B. This metric provides insight into GW activity present on a given night. A higher stdev indicates more wave activity. Figure 3C shows a zonal keogram (one line of data taken from the center of the MTM field of view along the zonal direction plotted for each mapper image over time) on a lower stdev night, and Figure 3D shows a zonal keogram on a more active night, with waves present that have periods ranging from several minutes to hours. The largest temperature perturbation on this day appears to be associated with dynamical changes occurring on the time scale of several hours, indicating a gravity wave that is likely much larger (100 s km to >1,000 km) than the field of view of the MTM. On 22 January, a minimum in temperature was observed. However, EPBs did not extend beyond −20MLAT and ROTI values

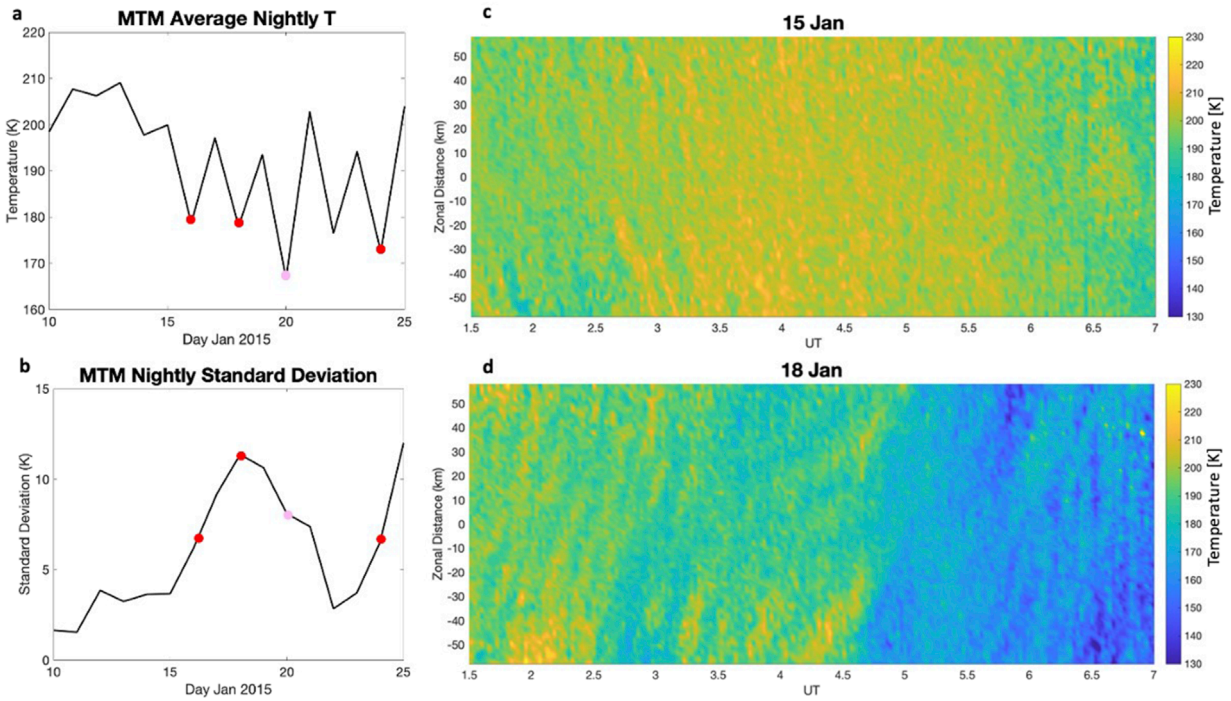

FIGURE 3
Plot **(A)** data show the nightly average OH temperatures plotted from the MTM. A 2-day fluctuation is apparent in the data from 15–24 January, with the three nights of largest ROTI values and 630 nm depletions extending below 20S MLAT denoted with red dots, and the fourth largest night of ROTI values is denoted in pink. These significant nights of EPB activity fall on the nights of coldest average temperatures. Plot **(B)** shows the nightly stdev of temperatures, a metric that denotes GW activity. Plots **(C)** and **(D)** show zonal keograms of MTM data for lower stdev (15 January) and higher stdev (18 January) nights, allowing for both long period and short period temperature fluctuations associated with GWs to be observed, especially on the more active night in **(D)**.

were similar to warm phase nights. On this particular night, a lower OH T stdev was measured, indicating lower GW activity over the field of view of the MTM.

3 Results

3.1 QTDW influences

Concurrent dynamics in the mesosphere were further investigated using NAVGEM reanalysis (Eckermann et al., 2018) that is extended above 100 km via hydrostatic blending with HWM winds and MSIS temperature and composition (Inchin et al., 2023). We note here that the NAVGEM reanalysis only contains observations up to 100 km and hydrostatically relaxes to MSIS and HWM climatology above this altitude. Thus, large scale influences associated with the QTDW are not reflected above 100 km. Figures 4A, B show global meridional (V), and zonal (U), winds plotted at 85 km in altitude for 18 January 2015, a day with significant ROTI values and 630 nm airglow depletions. The QTDW is primarily manifested in meridional winds, has zonal wavenumber of 3, and maximizes near 85 km in altitude, which is illustrated in Figure 4A. The QTDW is not readily apparent in zonal winds shown in Figure 4B, though may still have associated zonal wind amplitude. The phase over South America at the beginning of 18 January is mainly aligned with positive/northward meridional wind. The QTDW is present from the equatorial region to near 60S. Figures 4C, D show NAVGEM meridional and zonal winds averaged from 70-45W and 10-30S. Figure 4E shows the fit to zonal wavenumber three in meridional winds, demonstrating a strong presence of the QTDW, which increases in amplitude in the second half of the study period from ~50 m/s to ~80 m/s. Figure 4F shows the frequency-wavenumber spectrum verifying the presence of the QTDW. Figure 5 shows the ROTI data from Figure 1C overplotted with meridional winds from Figure 4C to demonstrate overlap of EPBs with the QTDW. The ROTI values show the strongest peaks aligning with the diurnal tidal winds near 200 km, expected for post sunset EPBs. Most notably, the strongest peaks occurred when the meridional winds associated with the QTDW are at a positive/northward peak near 85 km. This MLT trend is not observed in zonal winds, which do not have a strong QTDW signature (Figure 4D).

While post-sunset spikes in the ROTI and depletions in the 630 nm airglow are present on most days, the largest occurrences (highest ROTI, furthest southward depletions) coincide with the positive meridional winds associated with the QTDW in the mesosphere. Additionally, these stronger instances did not show a correlation with the solar or geomagnetic activity over the 2-week case study period. This suggests there may be a lower atmospheric influence associated with stronger EPBs linked to the meridional wind in the mesosphere. The MTM demonstrated that these increased times of EBPs corresponded both to colder

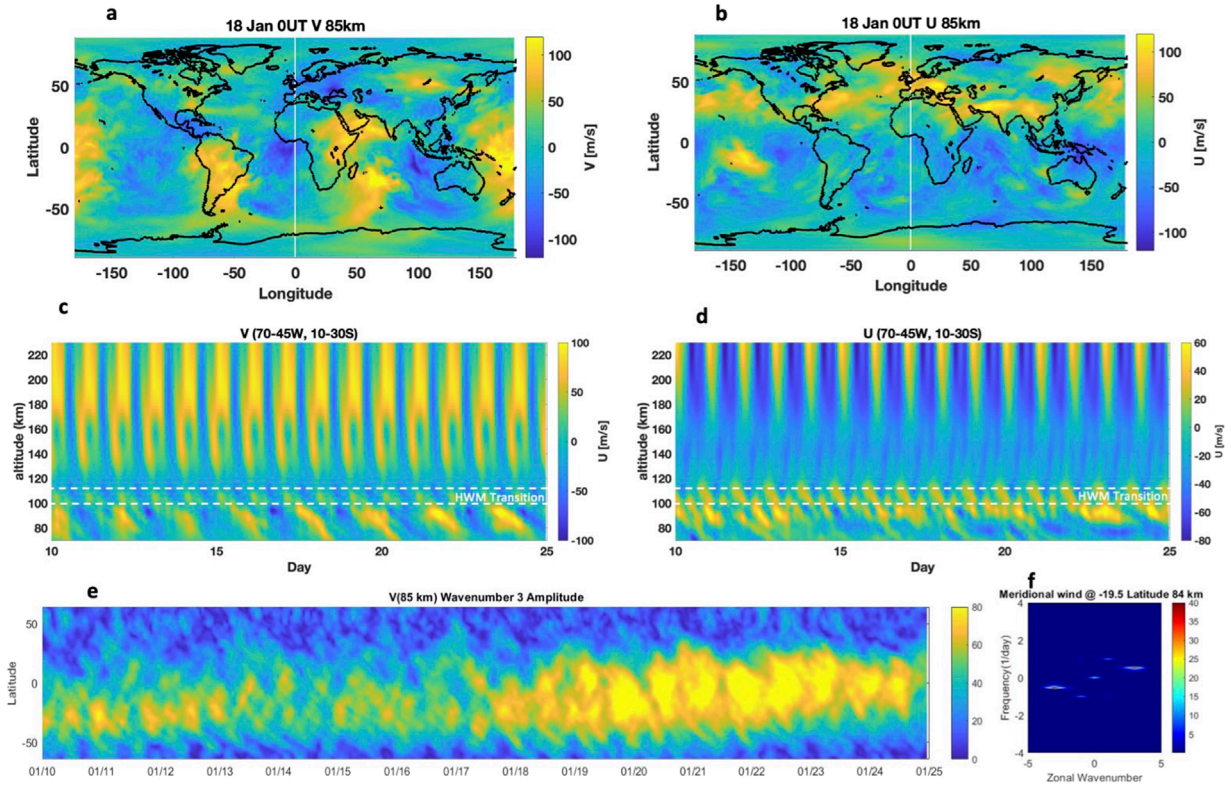

FIGURE 4
Plots **(A)** and **(B)** show NAVGEM meridional and zonal winds on 18 January 2015 at 0UT. The meridional wind clearly shows the QTDW signature (zonal wavenumber 3) in the southern hemisphere. Plots **(C)** and **(D)** show the NAVGEM meridional and zonal winds averaged from 45 to 70W and 10 to 30S, and plotted over altitude and time, which demonstrate a 2-day wave period in the meridional winds. Plot **(E)** shows the zonal wavenumber three fit of meridional winds over the 15 day period. Plot **(F)** shows a frequency-wavenumber plot demonstrating the presence of a QTDW.

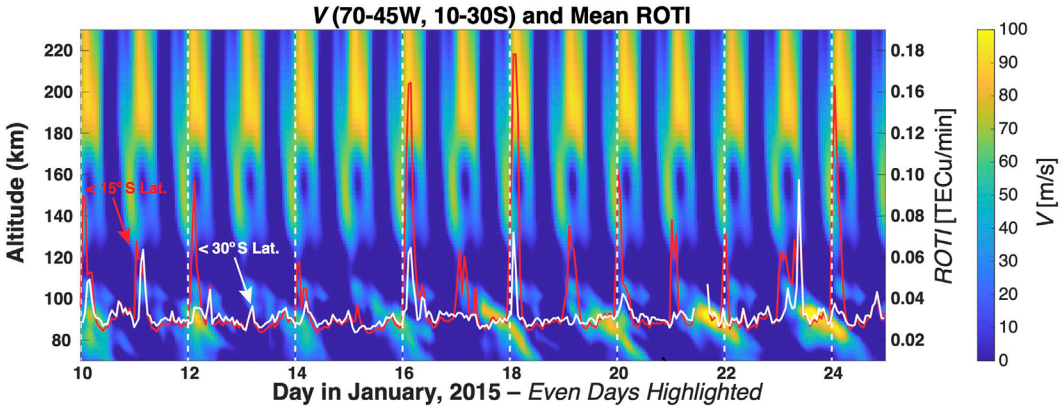

FIGURE 5
NAVGEM meridional winds averaged from 45 to 70W and 10 to 30S, and plotted over altitude and time overlapped with ROTI histograms from Figure 1C. The strongest ROTI values overlap with times where winds near 85–90 km are most strongly positive.

temperatures in the mesosphere and increased GW activity associated with higher stdev in the temperature measurements. These stronger events occurred starting January 16 and were not observed between January 10–15. Additionally, two nights where no peaks in ROTI were present, and no depletions were observed in the 630 nm airglow (13 and 15 January) corresponded to lower MTM OH T standard deviation (lower GW activity), higher MTM OH T, and southward meridional wind near 85 km associated with the QTDW during times of lower QTDW global amplitudes.

The coincidence of increased EPB activity during times of increased GW activity in the mesosphere and northward winds in the mesosphere implies that some aspects of lower atmosphere dynamics may influence the presence of EPBs. This has been well established, for instance, with studies of GW seeding of EPBs (Yokoyama et al., 2019; Taori et al., 2011; Fritts et al., 2008). Additionally, the influence of the QTDW on the ionosphere has been previously demonstrated (e.g., Yue et al., 2012). The observations presented here suggest that the QTDW itself may play a role in EPB generation, and/or provides a mechanism or environment for increased GW activity in a manner that may contribute to EPB seeding.

3.2 GW and interhemispheric influences

The MTM provides OH T data, from which stdev can be calculated. The OH T stdev indicates wave activity in a manner that can be compared over the 2-week period of study. The strongest wave activity observed in the MTM occurred also on days that overlapped with the coldest temperatures, and also coincided with the strongest EPB events and ROTI values observed over the study period. However, the MTM instrument itself is south of the magnetic equator, and it is expected that EPB seeding occurs closer to the equator. To gain more insight into links between variability in the lower atmosphere and ROTI/depletions in the ionosphere/thermosphere, the AIRS instrument onboard the NASA Aqua Satellite was used to determine brightness temperature perturbation variances in the stratosphere near 40 km in altitude, and is sensitive to GWs with vertical wavelengths of >10 km (Hoffmann and Alexander, 2009). The variances are associated with GW activity and were taken over regions in the northern hemisphere near the polar vortex and over the southern hemisphere region near ALO and coincident convection, both of which are potential sources of GWs that can influence the thermosphere. Additionally, AIRS brightness temperature perturbation variances near the equator were also included. Figure 6A shows the MTM standard deviation values to highlight days with higher GW activity in the MLT for comparison to AIRS data, and Figure 6B shows the resulting AIRS brightness temperature variances over the period from 10–24 January 2015. AIRS temperature perturbation variances in the northern hemisphere overlapping the polar vortex (40–60N) demonstrate an increase in GW activity that agrees with the MTM data from near 87 km and 30 S, and both measurements demonstrate a peak in activity near 18 January. There were no notable changes in AIRS brightness temperature variances near the equator. Some variability was observed in the southern hemisphere region (20-40 S) during this time period.

The standard deviation of temperatures was used from NAVGEM over several regions during the same time period to compare to the MTM and AIRS measurements. To obtain the temperature standard deviations, a sliding 24-h period of data over 30–50 km in altitude and a longitude range from 45W-70W was divided into five latitude regions. The resulting standard deviations are shown in Figure 6C. The stratospheric temperature standard deviations in the northern hemisphere sectors peak near 12 January and 18 January, and show a minimum in activity near 14 January. These variations are not observed near the equatorial region or south of the equator in the stratosphere. Note that the AIRS satellite observations were not sensitive to the peak in activity on 12 January shown by NAVGEM, which may be due in part to AIRS variance calculations being sensitive to longer vertical wavelength GWs and horizontal GW scales <500 km. In Figure 6D, the same analysis is performed again from 75-95 km and shows clear decreases in temperature standard deviation near 14 January for northern, equatorial, and southern latitudes in this longitudinal sector, implying a link between northern and southern hemispheric dynamics at altitudes in the MLT region. Note that the polar region is not included at these altitudes due to semidiurnal tidal dominance. From 16 January onward, all latitudinal study regions show some daily variability in temperature standard deviation, but no significant decreases in temperature standard deviation over the time period.

These findings imply that mesospheric temperature and meridional winds associated with the QTDW as well as GW activity on a larger scale may be linked to EPB activity. The times of lowest EPB activity in the first half of the observation period overlap with both decreased GW variances in the stratosphere in the northern hemisphere, and decreased temperature standard deviation in the MLT over the equatorial region and southern hemisphere. Additionally, the two nights of no EPB activity on 13 and 15 January correspond to southward meridional winds in the mesosphere associated with a specific phase of the QTDW. During the second half of the observation period from 16–24 January, post sunset EPBs (increased ROTI and observed 630 nm airglow depletions) were observed on every night, with the four strongest nights overlapping northward meridional winds and coldest temperatures in the MLT region.

Strong northward meridional winds associated with the QTDW, which allow for southward GW propagation to higher altitudes in the thermosphere during this time period would have implications for GW-induced perturbations in the thermosphere. Additionally, NAVGEM demonstrated a lower standard deviation of temperature during periods of lower EPB activity, and higher standard deviation of temperature during times of increased activity overlapping the region of the polar vortex (20–60N). Disruptions to the polar vortex in the northern hemisphere have been shown to influence the QTDW amplitude both at lower latitudes (Ma et al., 2017) and in the southern hemisphere (McCormack et al., 2009; Ern et al., 2013). It is also noted in this longitudinal sector (45–70W), the magnetic equator is located southward of the geographic equator, ~10S, placing it well within the region of the QTDW. Thus, this southward position would allow for GW propagation through the QTDW wind field before reaching the thermosphere, potentially providing seed perturbations for EPBs near the geomagnetic equator via GWs generated at lower latitudes in the northern hemisphere. Furthermore, the presence of the QTDW itself, and its structure in the upper-mesospheric and lower thermospheric temperature and winds, may have implications for EPB seeding as well.

4 Discussion

An oscillation was observed in EBPs (ROTI and 630 nm airglow) over the Western region of South America during 10–24 January

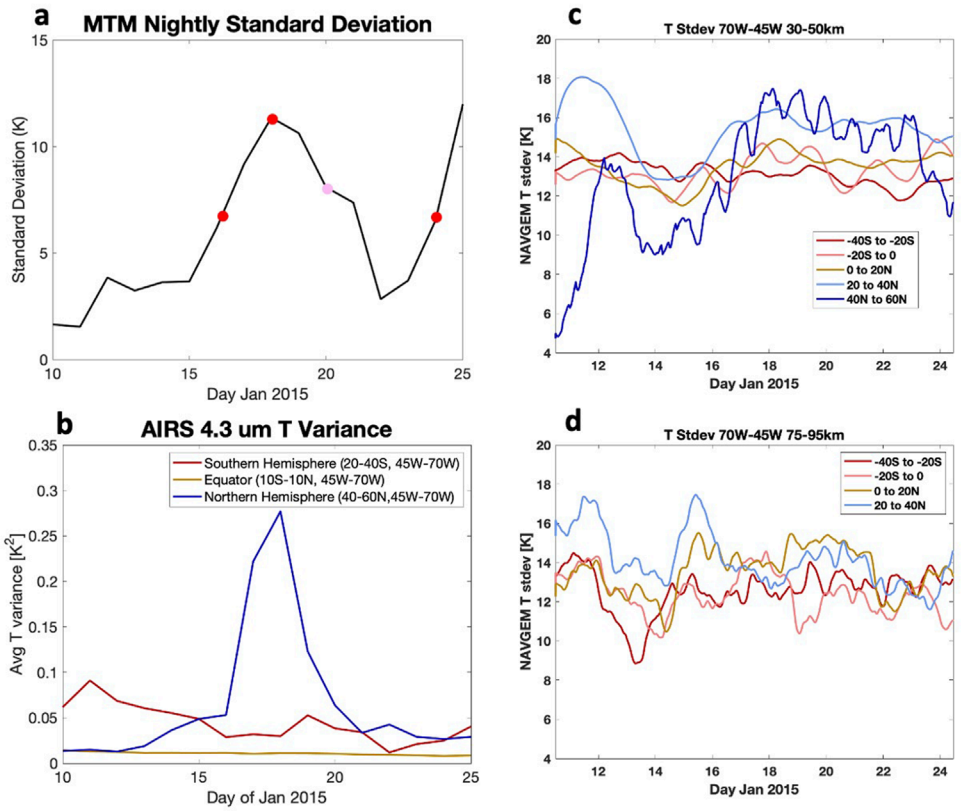

FIGURE 6
Plot **(A)** shows the MTM standard deviation of temperatures. The three nights of largest ROTI values and 630 nm depletions extending below 20S MLAT denoted with red dots, and the fourth largest night of ROTI values is denoted in pink. Plot **(B)** shows AIRS 4.3 μm brightness temperature perturbation variances plotted in the latitude sector from 45W-75W. The data are calculated for regions overlapping the polar vortex in the northern hemisphere (blue line), regions overlapping the equator (gold line), and regions overlapping the ground-based observations in the southern hemisphere (red line). Plot **(C)** shows NAVGEM temperature standard deviation for five latitudinal ranges moving over a 24-h window that includes values from 30 to 50 km in altitude, and 45W–70W in longitude. The stratospheric data indicate a significant dip in wave activity in the northern hemisphere but not in the southern hemisphere near 14 January. Plot **(D)** shows the same as Plot **(C)** but for altitudes from 75 to 95 km, and indicates a dip in wave activity near 14 January in the northern and southern hemispheres.

2015. The strongest peaks in the oscillation coincided with the northward meridional wind phase of the QTDW in the mesosphere region near 85 km in altitude. MTM data demonstrated that the strongest peaks in EPB activity inferred from the ROTI values and 630 nm airglow depletions coincided with days where the coldest temperatures were measured near 87 km by the MTM OH T. These peaks also coincided with higher standard deviations of MTM OH T and higher AIRS temperature perturbation variances in the northern hemisphere (40–60N). Additionally, 2 days with no observed EPBs corresponded to lower GW activity in the stratosphere observed by AIRS in the northern hemisphere, lower MTM and NAVGEM simulated temperature standard deviations in the MLT region, and southward winds and higher temperatures associated with the QTDW in the mesosphere. These observations were made over a time period of relatively quiet solar and geomagnetic activity.

While the period of study is 2 weeks, it indicates the possible role that the QTDW and interhemispheric coupling, both in the neutral atmosphere and the ionosphere, may play in the occurrence and intensity of EPBs. It is important to note that multiple factors play a role in the prevalence of EPBs and their generation and seeding mechanisms. The data presented here demonstrate one aspect of neutral atmospheric dynamical correlations with EPBs, which can arise from multiple sources. Further studies are needed to understand longer term trends associated with the QTDW and EPBs.

Data availability statement

Publicly available datasets were analyzed in this study. This data can be found here: Quick-look images and movies of 630 nm airglow observations from El Leoncito Observatory are available from the Boston University. All-Sky Imager network Archives: www.buimaging.com GPS observations are freely available through Centro Sismologico Nacional archive (https://gps.csn.uchile.cl/) Mesospheric Temperature Mapper Data are available on USU Box (password upon request): http://digitalcommons.usu.edu/ail/ NAVGEM output for this time period are cleared for public release and available upon request from stephen.eckermann.civ@us.navy.mil.

Author contributions

KB: Formal Analysis, Investigation, Methodology, Project administration, Supervision, Writing–original draft, Writing–review and editing. KK: Formal Analysis, Investigation, Methodology, Software, Writing–review and editing. PI: Data curation, Formal Analysis, Investigation, Methodology, Software, Writing–review and editing. JN: Formal Analysis, Investigation, Software, Writing–review and editing. SE: Data curation, Software, Writing–review and editing. P-DP: Data curation, Formal Analysis, Writing–review and editing. CM: Data curation, Writing–review and editing. CK: Formal Analysis, Writing–review and editing. SP: Formal Analysis, Writing–review and editing. JS: Funding acquisition, Investigation, Project administration, Writing–review and editing. YZ: Data curation, Writing–review and editing. MZ: Writing–review and editing.

Funding

The author(s) declare that financial support was received for the research, authorship, and/or publication of this article. This research was supported under DARPA Cooperative Agreement HR00112120003 via a subcontract with Embry-Riddle Aeronautical University. This work is approved for public release; distribution is unlimited. The content of the information does not necessarily reflect the position or the policy of the Government, and no official endorsement should be inferred. (KB, JN, CBK, PI, JS, MZ, KK). NRL's research was supported by the DARPA AtmoSense program, and NRL's NAVGEM reanalysis runs were made possible by the DoD High-Performance Computer Modernization Program via grants of computer time at the Navy DoD Supercomputing Resource Center. Additional research by KB, KK, SP, and JN was funded under NSF AGS 1944027 and NASA 80NSSC21K0002. Support for the operations of the USU MTM and associated OH data analyses were proved by NSF AGS 1911970. CM acknowledges the support of NSF Aeronomy grant #2152365. CM thanks the Director and personnel of CASLEO (Complejo Astronomico El Leoncito) for their continuing support of the BU all-sky imager.

Conflict of interest

Author PI was employed by Computational Physics, Inc.

The remaining authors declare that the research was conducted in the absence of any commercial or financial relationships that could be construed as a potential conflict of interest.

Publisher's note

References

Aa, E., Zhang, S.-R., Coster, A. J., Erickson, P. J., and Rideout, W. (2023a). Multi-instrumental analysis of the day-to-day variability of equatorial plasma bubbles. *Front. Astron. Space Sci.* 10, 1167245. doi:10.3389/fspas.2023.1167245

Aa, E., Zhang, S.-R., Liu, G., Eastes, R. W., Wang, W., Karan, D. K., et al. (2023b). Statistical analysis of equatorial plasma bubbles climatology and multi-day periodicity using GOLD observations. *Geophys. Res. Lett.* 50, e2023GL103510. doi:10.1029/2023gl103510

Aa, E., Zou, S., Ridley, A. J., Zhang, S.-R., Coster, A. J., Erickson, P. J., et al. (2019). Merging of storm time midlatitude traveling ionospheric disturbances and equatorial plasma bubbles. *Space weather.* 17, 285–298. doi:10.1029/2018SW002101

Abdu, M. A. (2012). Equatorial spread F/plasma bubble irregularities under storm time disturbance electric fields. *J. Atmos. Sol. Terr. Phys.* 75, 44–56. doi:10.1016/j.jastp.2011.04.024

Adhya, P., and Valladares, C. E. (2023). Magnetic storm effects on the occurrence and characteristics of plasma bubbles. *J. Geophys. Res. Space Phys.* 128, e2023JA031292. doi:10.1029/2023JA031292

Amadi, B. C., Qian, L., de Paula, E. R., MclNerney, J. M., Kherani, E. A., Santos, A. M., et al. (2023). Intensification and weakening of equatorial plasma bubble development observed by GOLD during different phases of a geomagnetic storm. *J. Geophys. Res. Space Phys.* 128, e2022JA031262. doi:10.1029/2022JA031262

Bhattacharyya, A. (2022). Equatorial plasma bubbles: a review. *Atmosphere* 13 (10), 1637. doi:10.3390/atmos13101637

Burks, D., and Leovy, C. (1986). Planetary waves near the mesospheric easterly jet. *Geophys. Res. Lett.* 13 (3), 193–196. doi:10.1029/gl013i003p00193

Carmo, C. S., Dai, L., Denardini, C. M., Figueiredo, CAOB, Wrasse, C. M., Resende, L. C. A., et al. (2023). Equatorial plasma bubbles features over the Brazilian sector according to the solar cycle and geomagnetic activity level. *Front. Astron. Space Sci.* 10, 1252511. doi:10.3389/fspas.2023.1252511

Chou, M.-Y., Wu, Q., Pedatella, N. M., Cherniak, I., Schreiner, W. S., and Braun, J. (2020). Climatology of the equatorialplasma bubbles captured byFORMOSAT-3/COSMIC. *J. Geophys. Res. Space Phys.* 124. doi:10.1029/2019JA027680

Chou, M.-Y., Yue, J., Sassi, F., McDonald, S., Tate, J., Pedatella, N., et al. (2023). Modeling the day-to-day variability of midnight equatorial plasma bubbles with Sami3/SD-WACCM-X. *J. Geophys. Res. Space Phys.* 128, e2023JA031585. doi:10.1029/2023JA031585

Craig, R., Vincent, R., Fraser, G., and Smith, M. J. (1980). The quasi 2-day wave in the Southern Hemisphere mesosphere. *Nature* 287, 319–320. doi:10.1038/287319a0

de Jesus, R., Batista, I. S., Takahashi, H., de Paula, E. R., Barros, D., Figueiredo, C. A. O. B., et al. (2020). Morphological features of ionospheric scintillations during high solar activity using GPS observations over the South American sector. *J. Geophys. Research:Space Phys.* 124. doi:10.1029/2019JA027441

Eckermann, S. D., Ma, J., Hoppel, K. W., Kuhl, D. D., Allen, D. R., Doyle, J. A., et al. (2018). High-altitude (0-100 km) global atmospheric reanalysis system: description and application to the 2014 austral winter of the Deep Propagating Gravity-Wave Experiment (DEEPWAVE). *Mon. Wea. Rev.* 146, 2639–2666. doi:10.1175/MWR-D-17-0386.1

Ern, M., Preusse, P., Kalisch, S., Kaufmann, M., and Riese, M. (2013). Role of gravity waves in the forcing of quasi two-day waves in the mesosphere: an observational study. *J. Geophys. Res. Atmos.* 118, 3467–3485. doi:10.1029/2012JD018208

Forbes, J. M., Heelis, R., Zhang, X., Englert, C. R., Harding, B. J., He, M., et al. (2021). Q2DW-tide and -ionosphere interactions as observed from ICON and ground-based radars. *J. Geophys. Res. Space Phys.* 126, e2021JA029961. doi:10.1029/2021JA029961

Fritts, D. C., Vadas, S. L., Riggin, D. M., Abdu, M. A., Batista, I. S., Takahashi, H., et al. (2008). Gravity wave and tidal influences on equatorial spread F based on observations during the Spread F Experiment (SpreadFEx). *Ann. Geophys.* 26, 3235–3252. doi:10.5194/angeo-26-3235-2008

Gjerloev, J. W. (2012). The SuperMAG data processing technique. *J. Geophys. Res.* 117 (A9), A09213. doi:10.1029/2012JA017683

Haase, J. S., Dautermann, T., Taylor, M. J., Chapagain, N., Calais, E., and Pautet, D. (2010). Propagation of plasma bubbles observed in Brazil from GPS and airglow data. *Adv. Space Res.* 47, 1758–1776. doi:10.1016/j.asr.2010.09.025

He, M., Chau, J. L., Forbes, J. M., Zhang, X., Englert, C. R., Harding, B. J., et al. (2021). Quasi-2-day wave in low-latitude atmospheric winds as viewed from the

ground and space during January–March, 2020. *Geophys. Res. Lett.* 48, e2021GL093466. doi:10.1029/2021GL093466

Hecht, J. H., Walterscheid, R. L., Gelinas, L. J., Vincent, R. A., Reid, I. M., and Woithe, J. M. (2010). Observations of the phase-locked 2 day wave over the Australian sector using medium-frequency radar and airglow data. *J. Geophys. Res.* 115, D16115. doi:10.1029/2009JD013772

Hickey, D. A., and Martinis, C. (2018). All-sky imaging observations of the interaction between the brightness wave and ESF airglow depletions. *JGR Space Phys.* 125. doi:10.1029/2019JA027232

Hoffmann, L., and Alexander, M. J. (2009). Retrieval of stratospheric temperatures from Atmospheric Infrared Sounder radiance measurements for gravity wave studies. *J. Geophys. Res.* 114, D07105. doi:10.1029/2008JD011241

Huang, C. S. (2018). Effects of the postsunset vertical plasma drift on the generation of equatorial spread F. *Prog. Earth Planet Sci.* 5, 3. doi:10.1186/s40645-017-0155-4

Huang, C. -S., and Hairston, M. R. (2015). The postsunset vertical plasma drift and its effects on the generation of equatorial plasma bubbles observed by the C/NOFS satellite. *J. Geophys. Res. Space Physics* 120, 2263–2275. doi:10.1002/2014JA020735

Huba, J. D. (2022). Generalized Rayleigh-Taylor instability: ion inertia, acceleration forces, and *E* region drivers. *JGR. Space Phys.* 127, e2022JA030474. doi:10.1029/2022JA030474

Huba, J. D., Hellis, R., and Maute, A. (2021). Large-scale O+ depletions observed by ICON in the post-midnight topside ionosphere: data/model comparison. *Geophys. Res. Lett.* 48, e2020GL0920061. doi:10.1029/2020gl092061

Huba, J. D., and Krall, J. (2013). Impact of meridional winds on equatorial spread F: revisited. *Geophys. Res. Lett.* 40 (7), 1268–1272. doi:10.1002/grl.50292

Hudson, M. K., and Kennel, C. F. (1975). Linear theory of equatorial spread F. *J. Geophys. Res.* 80, 4581–4590. doi:10.1029/ja080i034p04581

Hysell, D. L. (2000). An overview and synthesis of plasma irregularities in equatorial spread-F. *J. Atmos. Solar-Terr. Phys.* 62, 1037–1056. doi:10.1016/S1364-6826(00)00095-X

Hysell, D. L., and Burcham, J. D. (1998). JULIA radar studies of equatorial spread F. *J. Geophys. Res.* 103, 29155–29167. doi:10.1029/98ja02655

Iimura, H., Fritts, D. C., Lieberman, R. S., Janches, D., Mitchell, N. J., Franke, S. J., et al. (2021). Climatology of quasi-2-day wave structure and variability at middle latitudes in the northern and southern hemispheres. *J. Atmos. Solar-Terrestrial Phys.* 221, 105690. doi:10.1016/j.jastp.2021.105690

Inchin, P. A., Bhatt, A., Cummer, S. A., Eckermann, S. D., Harding, B. J., Kuhl, D. D., et al. (2023). Multi-Layer evolution of acoustic-gravity waves and ionospheric disturbances over the United States after the 2022 hunga Tonga volcano eruption. *AGU Adv.* 4. doi:10.1029/2023AV000870

Jacobi, C. K. F., and Pogoreltsev, A. (2006). Quasi two-day-wave modulation of gravity wave flux and consequences for the planetary wave propagation in a simple circulation model. *J. Atmos. Solar-Terrestrial Phys.* 68, 283–292. doi:10.1016/j.jastp.2005.01.017

Karan, D. K., Daniell, R. E., England, S. L., Martinis, C. R., Eastes, R. W., Burns, A. G., et al. (2020). First zonal drift velocity measurement of equatorial plasma bubbles (EPBs) from a geostationary orbit using GOLD data. *J. Geophys. Res. Space Phys.* 125, e2020JA028173. doi:10.1029/2020JA028173

Karan, D. K., Eastes, R. W., Daniell, R. E., Martinis, C. R., and McClintock, W. E. (2023). GOLD mission's observation about the geomagnetic storm effects on the nighttime equatorial ionization anomaly (EIA) and equatorial plasma bubbles (EPB) during a solar minimum equinox. *Space weather.* 21, e2022SW003321. doi:10.1029/2022SW003321

Kepkar, A., Arras, C., Wickert, J., Schuh, H., Alizadeh, M., and Tsai, L.-C. (2020). Occurrence climatology of equatorial plasma bubbles derived using FormoSat-3/COSMIC GPS radio occultation data. *Ann. Geophys.* 38, 611–623. doi:10.5194/angeo-38-611-2020

Lay, E. H. (2018). Ionospheric irregularities and acoustic/gravity wave activity above low-latitude thunderstorms. *Geophys. Res. Lett.* 45, 90–97. doi:10.1002/2017GL076058

Lieberman, R. S., Riggin, D. M., Nguyen, V., Palo, S. E., Siskind, D. E., Mitchell, N. J., et al. (2017). Global observations of 2 day wave coupling to the diurnal tide in a high-altitude forecast-assimilation system. *J. Geophys. Res. Atmos.* 122, 4135–4149. doi:10.1002/2016JD025144

Ma, Z., Gong, Y., Zhang, S., Zhao, Q., Huang, C., Huang, K., et al. (2017). Responses of quasi 2 Day waves in the MLT region to the 2013 SSW revealed by a meteor radar chain. *Geophys. Res. Lett.* 44, 9142–9150. doi:10.1002/2017GL074597

Martinis, C., Baumgardner, J., Mendillo, M., Su, S.-Y., and Aponte, N. (2009). Brightening of 630.0 nm equatorial spread-Fairglow depletions. *J. Geophys. Res.* 114, A06318. doi:10.1029/2008JA013931

Martinis, C., Baumgardner, J., Wroten, J., and Mendillo, M. (2018). All-sky-imaging capabilities for ionospheric space weather research using geomagnetic conjugate point observing sites. *Adv. Space Res.* 61, 1636–1651. doi:10.1016/j.asr.2017.07.021

Martinis, C., Mendillo, M. J., and Aarons, J. (2005). Toward a synthesis of equatorial spread F onset and suppression during geomagnetic storms. *J. Geophys. Res. Space. Phys.* 110. doi:10.1029/2003JA010362

McCormack, J. P., Coy, L., and Hoppel, K. W. (2009). Evolution of the quasi 2-day wave during January 2006. *J. Geophys. Res.* 114, D20115. doi:10.1029/2009JD012239

Newell, P. T., and Gjerloev, J. W. (2011a). Evaluation of SuperMAG auroral electrojet indices as indicators of substorms and auroral power. *J. Geophys. Res.* 116 (A12), A12211. doi:10.1029/2011JA016779

Newell, P. T., and Gjerloev, J. W. (2011b). Substorm and magnetosphere characteristic scales inferred from the SuperMAG auroral electrojet indices. *J. Geophys. Res.* 116 (A12), 12232. doi:10.1029/2011JA016936

Otsuka, Y. (2018). Review of the generation mechanisms of post-midnight irregularities in the equatorial and low-latitude ionosphere. *Prog. Earth Planet Sci.* 5, 57. doi:10.1186/s40645-018-0212-7

Pancheva, D., Mukhtarov, P., and Siskind, D. E. (2018). Climatology of the quasi-2-day waves observed in the MLS/Aura measurements (2005–2014). *J. Atmos. Solar-Terrestrial Phys.* 171, 210–224. doi:10.1016/j.jastp.2017.05.002

Pancheva, D. V., Mukhtarov, P. J., Shepherd, M. G., Mitchell, N. J., Fritts, D. C., Riggin, D. M., et al. (2006). Two-day wave coupling of the low-latitude atmosphere-ionosphere system. *J. Geophys. Res.* 111, A07313. doi:10.1029/2005JA011562

Panda, D., Senapati, B., Tyagi, B., and Kundu, B. (2019). Effects of Rayleigh-Taylor instability and ionospheric plasma bubbles on the global navigation satellite System signal. *J. Asian Earth Sci.* 170, 225–233. doi:10.1016/j.jseaes.2018.11.006

Park, J., Mende, S. B., Eastes, R. W., and Frey, H. U. (2022). Climatology of equatorial plasma bubbles in ionospheric connection explorer/far-UltraViolet (ICON/FUV) limb images. *J. Astron. Space Sci.* 39 (3), 87–98. doi:10.5140/JASS.2022.39.3.87

Pautet, P.-D., Taylor, M. J., Chapagain, N. P., Takahashi, H., Medeiros, A. F., Sao Sabbas, F. T., et al. (2009). Simultaneous observations of equatorial F-region plasma depletions over Brazil during the Spread-F Experiment (SpreadFEx). *Ann. Geophys.* 27, 2371–2381. doi:10.5194/angeo-27-2371-2009

Pendleton, W. R., Jr., Taylor, M. J., and Gardner, L. C. (2000). Terdiurnal oscillations in OH Meinel rotational temperatures for fall conditions at northern mid-latitude sites. *Geophys. Res. Lett.* 27 (12), 1799–1802. doi:10.1029/2000gl003744

Pi, X., Mannucci, A. J., Lundqwister, U. J., and Ho, C. M. (1997). Monitoring of global ionospheric irregularities using the worldwide GPS Network. *Geophys. Res. Lett.* 24, 2283–2286. doi:10.1029/97GL02273

PugmireJonathan Rich (2018). Mesospheric gravity wave climatology and variances over the Andes mountains. *All Graduate Theses Diss. Spring 1920 Summer*, 7387. doi:10.26076/4a0e-3308

Rajesh, P. K., Lin, C. C. H., Lin, J. T., Lin, C. Y., Liu, J. Y., Matsuo, T., et al. (2022). Extreme poleward expanding super plasma bubbles over Asia-Pacific region triggered by Tonga volcano eruption during the recovery-phase of geomagnetic storm. *Geophys. Res. Lett.* 49, e2022GL099798. doi:10.1029/2022GL099798

Saha, S., Pallamraju, D., and Ghodpage, R. N. (2022). Investigations of equatorial plasma bubbles as observed in the OI 630 nm nightglow emissions over off-equatorial and low-latitudinal locations over Indian longitudes. *Adv. Space Res* 70, 3686–3698. doi:10.1016/j.asr.2022.08.023

Singh, D., Mitra, G., Guharay, A., Pallamraju, D., and Gurubaran, S. (2024). Quasi-two-day wave amplification through interhemispheric coupling during the 2010 austral summer. *Adv. Space Res.* 73 (7), 3452–3463. doi:10.1016/j.asr.2023.06.044

Singh, S., Johnson, F. S., and Power, R. A. (1997). Gravity wave seeding of equatorial plasma bubbles. *J. Geophys. Res.* 102 (A4), 7399–7410. doi:10.1029/96ja03998

Sori, T., Shinbori, A., Otsuka, Y., Tsugawa, T., and Nishioka, M. (2021). The occurrence feature of plasma bubbles in the equatorial to midlatitude ionosphere during geomagnetic storms using long-term GNSS-TEC data. *J. Geophys. Res. Space Phys.* 126, e2020JA029010. doi:10.1029/2020ja029010

Sousasantos, J., Gomez Socola, J., Rodrigues, F. S., Eastes, R. W., Brum, C. G. M., and Terra, P. (2023). Severe L-band scintillation over low-to-mid latitudes caused by an extreme equatorial plasma bubble: joint observations from ground-based monitors and GOLD. *Earth, Planets Space* 75, 41–1. doi:10.1186/s40623-023-01797-5

Stolle, C., Luhr, H., Rother, M., and Balasis, G. (2006). Magnetic signatures of equatorial spread F as observed by the CHAMP satellite. *J. Geophys. Res.* 111, A02304. doi:10.1029/2005JA011184

Sultan, P. J. (1996). Linear theory and modeling of the Rayleigh-Taylor instability leading to the occurrence of equatorial spread F. *J. Geophys. Res. Space Phys.* 101, 26875–26891. doi:10.1029/96JA00682

Takahashi, H., Taylor, M. J., Pautet, P.-D., Medeiros, A. F., Gobbi, D., Wrasse, C. M., et al. (2009). Simultaneous observation of ionospheric plasma bubbles and mesospheric gravity waves during the SpreadFEx Campaign. *Ann. Geophy.* 27 (4), 1477–1487. doi:10.5194/angeo-27-1477-2009

Taori, A., Patra, A. K., and Joshi, L. M. (2011). Gravity wave seeding of equatorial plasma bubbles: an investigation with simultaneous F region, E region, and middle atmospheric measurements. *J. Geophys. Res.* 116, A05310. doi:10.1029/2010JA016229

Taylor, M. J., Gardner, L. C., and Pendleton, W. R., Jr. (2001). Long period wave signatures in mesospheric OH Meinel (6,2) band intensity and rotational temperature at midlatitudes. *Adv. Space Res.* 27 (6 – 7), 1171–1179. doi:10.1016/s0273-1177(01)00153-3

Taylor, M. J., Pendleton, W. R., Jr., Gardner, C. S., and States, R. J. (1999). Comparison of terdiurnal tidal oscillations in mesospheric OH rotational temperature and Na lidar temperature measurements at midlatitudes for fall/spring conditions. *Earth Planets Space* 51, 877–885. doi:10.1186/bf03353246

Walterscheid, R. L., Hecht, J. H., Gelinas, L. J., MacKinnon, A., Vincent, R. A., Reid, I. M., et al. (2015). Simultaneous observations of the phase-locked 2 day wave at adelaide, cerro pachon, and Darwin. *J. Geophys. Res. Atmos.* 120, 1808–1825. doi:10.1002/2014JD022016

Yasui, R., Soto, K., and Miyoshi, Y. (2021). Roles of rossby waves, rossby-gravity waves, and gravity waves generated in the middle atmosphere for interhemispheric coupling. *J. Atmos. Sci.* 78, 3867–3888. doi:10.1175/JAS-D-21-0045.1

Yizengaw, E., Retterer, P. E. E., Roddy, P., Groves, K., Caton, R., Baki, P., et al. (2013). Post-midnight bubbles and scintillations in the quiet-time June solstice. *Geophys Res. Lett.* 40, 5592–5597. doi:10.1002/2013GL058307

Yokoyama, T., Jin, H., Shinagawa, H., and Liu, H. (2019). Seeding of equatorial plasma bubbles by vertical neutral wind. *Geophys. Res. Lett.* 46, 7088–7095. doi:10.1029/2019GL083629

Yue, J., Wang, W., Richmond, A. D., and Liu, H.-L. (2012). Quasi-two-day wave coupling of the mesosphere and lower thermosphere-ionosphere in the TIME-GCM: two-day oscillations in the ionosphere. *J. Geophys. Res.* 117, A07305. doi:10.1029/2012JA017815

Zhao, Y., Taylor, M. J., and Chu, X. (2005). Comparison of simultaneous Na lidar and mesospheric nightglow temperature measurements and the effects of tides on the emission layer heights. *J. Geophys. Res.* 110, D09S07. doi:10.1029/2004JD005115

frontiers | Frontiers in Astronomy and Space Sciences

TYPE Original Research
PUBLISHED 22 November 2024
DOI 10.3389/fspas.2024.1460312

OPEN ACCESS

EDITED BY
David Hysell,
Cornell University, United States

REVIEWED BY
Ciarán D Beggan,
Natural Environment Research Council (NERC), United Kingdom
Enrique Rojas Villalba,
Massachusetts Institute of Technology, United States

*CORRESPONDENCE
Yosuke Yamazaki,
yamazaki@iap-kborn.de

RECEIVED 05 July 2024
ACCEPTED 04 November 2024
PUBLISHED 22 November 2024

CITATION
Yamazaki Y, Stolle C, Xiong C, Alken P, Yang Y, Zhima Z, Harding B and Yan R (2024) Day-to-day and longitudinal variability of the equatorial electrojet as viewed from the Sun-synchronous CSES satellite. *Front. Astron. Space Sci.* 11:1460312. doi: 10.3389/fspas.2024.1460312

Day-to-day and longitudinal variability of the equatorial electrojet as viewed from the Sun-synchronous CSES satellite

Yosuke Yamazaki[1]*, Claudia Stolle[1], Chao Xiong[2], Patrick Alken[3], Yanyan Yang[4,5], Zeren Zhima[4,5], Brian Harding[6] and Rui Yan[4,7]

[1]Leibniz Institute of Atmospheric Physics at the University of Rostock, Kühlungsborn, Germany, [2]Department of Space Physics, College of Electronic Information, Wuhan University, Wuhan, China, [3]Cooperative Institute for Research in Environmental Sciences, University of Colorado Boulder, Boulder, CO, United States, [4]National Institute of Natural Hazards, Ministry of Emergency Management of China, Beijing, China, [5]Center for Satellite Application in Earthquake Science, China Earthquake Administration, Beijing, China, [6]Space Sciences Laboratory, University of California, Berkeley, Berkeley, CA, United States, [7]School of Information Engineering, Institute of Disaster Prevention, Langfang, China

The intensity of the equatorial electrojet (EEJ) derived from the magnetic field measurements by the China Seismo-Electromagnetic Satellite (CSES) is analyzed for the low solar activity period of July 2018–April 2022. The CSES spacecraft flies in a Sun-synchronous orbit, providing the first continuous satellite observations of the afternoon EEJ at a fixed local time at 2 p.m. The EEJ intensities from CSES and concurrent observations from the Swarm satellite mission show a good correlation, supporting the reliability of the CSES EEJ data. Spectral analysis of the CSES data reveals the presence of three distinct oscillatory components in the day-to-day variation of the afternoon EEJ: (1) an eastward-propagating 2–3-day oscillation with zonal wavenumber 1, (2) a westward-propagating 5–6-day oscillation with zonal wavenumber 1, and (3) a zonally-symmetric 14–15-day oscillation. These oscillations result from upward-propagating waves in the atmosphere. That is, the first two can be attributed to the ultra-fast Kelvin wave and quasi-6-day wave, respectively, while the latter is likely due to the atmospheric lunar tide. The CSES EEJ data are also compared with lower thermospheric wind measurements by the Michelson Interferometer for Global High-Resolution Thermospheric Imaging (MIGHTI) onboard the Ionospheric Connection Explorer (ICON). The results suggest that the EEJ intensity correlates negatively with the equatorial eastward wind at 100–115 km, consistent with earlier studies. Contributions of different tidal wind components to longitudinal structures of the EEJ are evaluated. A four-peak structure during July–September can be largely explained by the eastward-propagating diurnal tide with zonal wavenumber 3 (DE3), while a two- or three-peak structure during December–January is mainly due to the combined effect of DE3 and the eastward-propagating diurnal tide with zonal wavenumber 2 (DE2). Furthermore, the CSES EEJ data are compared with the electron density measurements from the Langmuir probe onboard CSES. There is a positive correlation between the EEJ intensity and *in-situ* electron densities at ~510 km from the same orbit, reflecting the plasma fountain effect. The correlation tends to be higher in

the summer hemisphere, which may be due to the meridional wind in the thermosphere.

KEYWORDS

China seismo-electromagnetic satellite (CSES), equatorial electrojet (EEJ), ionospheric currents, ionospheric dynamo, neutral winds, atmosphere-ionosphere coupling, vertical coupling, atmospheric tides and planetary waves

1 Introduction

When geomagnetic storms are absent, daily variations of the geomagnetic field on the ground at middle and low latitudes are primarily due to electric currents in the E-region ionosphere (e.g., Campbell, 2003; Yamazaki and Maute, 2017). These ionospheric currents are generated through the process called ionospheric wind dynamo (e.g., Richmond, 1995; Maute, 2021), where the kinetic energy possessed by the neutral atmosphere is partially converted into electromagnetic energy through collisional interactions between neutral and plasma particles. The E-region dynamo currents are mostly confined to the dayside ionosphere, as the electrical conductivity of the E-region ionosphere is much lower on the night side due to low plasma density (e.g., Richmond, 2011). On the dayside, there are usually two large-scale vortices of the dynamo current: one counter-clockwise vortex in the Northern Hemisphere and one clockwise vortex in the Southern Hemisphere, which can be deduced from magnetic field measurements at the ground (e.g., Matsushita and Maeda, 1965; Campbell et al., 1993; Takeda, 2002a; Owolabi et al., 2022; Chen et al., 2024) and in space (e.g., Pedatella et al., 2011; Chulliat et al., 2016; Alken et al., 2017; Yamazaki, 2022). The intensity of the zonal current is enhanced along the magnetic equator, where the geomagnetic field is perfectly horizontal (e.g., Hirono, 1950; Chapman, 1951). The unique configuration of the geomagnetic field at the magnetic equator allows the establishment of a vertical electric field, which drives a Hall current in the zonal direction (e.g., Sugiura and Poros, 1969; Richmond, 1973; Raghavarao and Anandarao, 1987; Du and Stening, 1999). This additional Hall current is commonly referred to as the equatorial electrojet (EEJ) (e.g., Forbes, 1981; Rastogi, 1989; Lühr et al., 2021a). The EEJ is confined near the magnetic equator, within approximately ±3° latitude from the magnetic equator, where the vertical electric field can be maintained (e.g., Doumouya et al., 1998; Rigoti et al., 1999; Rabiu et al., 2013). The EEJ is usually directed eastward but occasionally turns westward, which is sometimes referred to as counter electrojet (e.g., Mayaud, 1977; Zhou et al., 2018; Soares et al., 2019; Zhang et al., 2024).

The intensity of the EEJ is determined by various factors. For instance, the EEJ intensity varies with local time, season, longitude and solar activity (e.g., Doumouya et al., 2003; Alken and Maus, 2007; Abdul Hamid et al., 2015). The local time and solar activity dependence can be ascribed to the effect of solar extreme ultraviolet radiation on the electrical conductivity of the E-region ionosphere (e.g., Takeda, 2002b). The seasonal dependence of the EEJ is primarily controlled by neutral wind forcing (Yamazaki et al., 2014b). The change in the solar zenith angle (and hence solar radiation ionization) plays only a secondary role for the seasonal variation of the EEJ (Chapman and Rao, 1965). The longitude dependence of the EEJ is partly due to the background geomagnetic field (e.g., Rastogi, 1962; Doumbia and Grodji, 2016; Pandey et al., 2021), which affects the E-region conductivity (Takeda and Araki, 1985), and partly due to neutral wind forcing by atmospheric tides (e.g., England et al., 2006; Lühr et al., 2008; Soares et al., 2018). Moreover, the EEJ intensity depends on the phase of the Moon (e.g., Rastogi and Trivedi, 1970; Lühr et al., 2012; Yamazaki et al., 2017), which can be understood as the effect of neutral wind forcing associated with the atmospheric lunar tide (e.g., Vial and Forbes, 1994; Pedatella et al., 2012b; Zhang and Forbes, 2013). The EEJ intensity is also subject to the influence of geomagnetic activity (e.g., Rastogi, 1977; Yamazaki and Kosch, 2015; Xiong et al., 2016a). This is generally attributed to the prompt penetration of the polar electric field into equatorial latitudes (e.g., Nishida, 1968; Kikuchi et al., 2008; Manoj et al., 2008; Yizengaw et al., 2016) and to the dynamo electric field generated by storm-time winds (e.g., Blanc and Richmond, 1980; Le Huy and Amory-Mazaudier, 2005; Pandey et al., 2018). Even in the apparent absence of variability in solar and geomagnetic activity, the EEJ intensity can exhibit large day-to-day variability (e.g., Marriott et al., 1979; Reddy, 1989), as neutral winds are constantly changing.

The E-region vertical electric field that drives the EEJ is closely associated with the vertical current and zonal electric field (e.g., Hysell et al., 2002; Alken and Maus, 2010). The zonal electric field at low latitudes is mapped along equipotential magnetic field lines to the equatorial F-region (> 150 km), where both ions and electrons tend to move with the E × B drift (e.g., Heelis, 2004). Observations have found a good correlation between the EEJ intensity with the equatorial E × B vertical plasma drift velocity (e.g., Anderson et al., 2002; Alken et al., 2013a; Kumar et al., 2016). Since the E × B drift is a primary transport mechanism for F-region plasmas and thus is an important factor determining the F-region plasma density, there is also a correlation between the EEJ intensity and F-region plasma density (e.g., Rush and Richmond, 1973; Rastogi and Klobuchar, 1990; Chen et al., 2008; Stolle et al., 2008; Venkatesh et al., 2015). Therefore, understanding the behavior of the EEJ is important not only for the E-region electrodynamics but also for the F-region dynamics and its broader impact on space weather phenomena (e.g., Stening, 2003).

The equatorial zonal wind at altitudes of the E-region ionosphere (90–150 km) plays an important role for determining the EEJ intensity (e.g., Yamazaki et al., 2014a; 2021; Harding et al., 2022). Neutral winds at these altitudes are predominantly due to atmospheric solar tides (e.g., McLandress et al., 1996; Wu et al., 2008a; b; Yamazaki et al., 2023). They consist of two parts: locally-generated tides and upward-propagating tides from below. The two parts exert a comparable influence on the EEJ (Yamazaki et al., 2014b). Locally-generated tides are produced through *in situ* absorption of solar radiation by thermospheric constituents such as O, O_2 and N_2. They are primarily vertically trapped mode

of the diurnal tide (e.g., Forbes, 1982; Hagan et al., 2001). On the other hand, upward-propagating tides are generated mainly in the troposphere and stratosphere (e.g., Hagan and Forbes, 2002; 2003). They propagate vertically upward and reach the lower thermosphere before being dissipated (e.g., Oberheide et al., 2011; Truskowski et al., 2014). Upward-propagating tides at E-region altitudes are highly variable, as their production and vertical propagation are dependent on the meteorological state of the lower and middle atmosphere (e.g., Miyoshi and Fujiwara, 2003; Liu, 2014; Dhadly et al., 2018; Zhou X. et al., 2022; Oberheide et al., 2024). Thus, upward-propagating tides, along with other upward-propagating waves, can be an important source of the day-to-day and longitudinal variability of the EEJ (e.g., Kawano-Sasaki and Miyahara, 2008; Yamazaki et al., 2014a).

A mathematical expression for a tidal wave in an atmospheric variable such as temperature, density and wind velocities is given as follows:

$$A_{ns}\cos\left[2\pi\left(n\frac{t}{24}-s\frac{\lambda}{360}\right)-P_{ns}\right], \quad (1)$$

where A_{ns} and P_{ns} are the amplitude and phase of the tide, t is the universal time in hours, and λ is the longitude in degrees. n is a positive integer, with n = 1, 2, 3, 4 corresponding to the 24-h (diurnal), 12-h (semidiurnal), 8-h (terdiurnal) and 6-h tides, respectively. $|s|$ is the zonal wavenumber (i.e., the number of wave cycles that can fit along the latitude circle at a given latitude). $s > 0$ and $s < 0$ correspond to eastward and westward propagating waves, respectively, and $s = 0$ represents the oscillation that is independent of longitude, which is often referred to as zonally-symmetric oscillation (e.g., Pancheva et al., 2007; Forbes et al., 2018). We use the conventional tidal nomenclature such as DE3, SW2 and T0 (e.g., Forbes et al., 2003; Jones Jr et al., 2013), where the first letter indicates the period (i.e., "D" for diurnal, "S" for semidiurnal, and "T" for terdiurnal), the second letter represents the propagation direction (i.e., "E" for eastward and "W" for westward), and the last number is the zonal wavenumber (i.e., $|s|$). Different components of tides can be evaluated by fitting Equation 1 to atmospheric measurements obtained at any given height and latitude (e.g., Forbes et al., 2008). Lühr and Manoj (2013) applied this method to EEJ data and examined the tidal composition of the EEJ based on 10 years of satellite magnetic field measurements. Soares et al. (2022), combining EEJ data from multiple satellites and ground stations, determined the tidal composition of the EEJ for individual years. Both studies found that migrating tides ($n+s$ = 0) such as DW1 and SW2 are dominant tidal components of the EEJ. Some non-migrating tides ($n+s \neq 0$) such as DE3 and DE2 are also found to be significant tidal components of the EEJ. The tidal composition of the EEJ is, however, not necessarily the same as the tidal composition of neutral winds that drive the EEJ. This is because the tidal composition of the EEJ is determined not only by tidal winds but also by the E-region conductivity, which is strongly local-time dependent. Thus, tidal wind components contributing to the EEJ have yet to be identified.

Apart from atmospheric tides, the EEJ is also influenced by some global-scale atmospheric waves with a period longer than a day. For instance, the westward-propagating quasi-6-day wave (Q6DW) with zonal wavenumber 1 is often observed in the lower thermosphere (e.g., Lieberman et al., 2003; Gan et al., 2018; Qin et al., 2021), and studies have reported the occurrence of ~6-day oscillation in the EEJ intensity during Q6DW events (e.g., Yamazaki et al., 2018; 2020a). Similarly, the eastward-propagating ultra-fast Kelvin wave (UFKW) with a period of 2–3 days and zonal wavenumber 1 is frequently detected in the equatorial lower thermosphere (e.g., Forbes et al., 2009; Davis et al., 2012; Gu et al., 2014), and corresponding 2–3-day oscillations have been observed in the EEJ (e.g., Yamazaki et al., 2020b; Lühr et al., 2021b; Sun et al., 2024). Other planetary waves, such as the westward-propagating quasi-2-day wave (Q2DW) with zonal wavenumber 3 (e.g., Yue et al., 2012; Gu et al., 2013; He et al., 2021) and quasi-16-day wave (16DW) with zonal wavenumber 1 (e.g., Forbes et al., 1995; Day and Mitchell, 2010; Fan et al., 2022), also seem to have some influence on the ionospheric electrodynamics (e.g., Yamada, 2009; Elhawary and Forbes, 2016; Jadhav et al., 2023; 2024), but their capability of modulating the EEJ intensity is still to be established.

Characterization of the EEJ variability due to tides and other global-scale waves mentioned above can greatly benefit from global observations by low-Earth-orbit (LEO) satellites. When a LEO satellite flies over the magnetic equator, the magnetic effect of the EEJ is observed as a latitudinally localized depression in the field strength (e.g., Cain and Sweeney, 1972; Jadhav et al., 2002; Lühr et al., 2004; Alken et al., 2015; Stolle et al., 2021). The intensity of the EEJ can be estimated from the magnitude of the magnetic field depression. Since LEO satellites have orbital periods of 90–120 min, they complete 12–16 orbits per day. In other words, 12–16 measurements of the dayside EEJ intensity can be made in each day at different longitudes.

The EEJ data from the CHAMP (Reigber et al., 2002) and Swarm (Friis-Christensen et al., 2006; 2008) missions have been extensively analyzed in previous studies (e.g., Lühr et al., 2004; Alken et al., 2015). In both missions, the spacecraft have been deployed in a near-circular near-polar orbit that slowly precesses in local time at a rate of about 5 minutes per day. Thus, for instance, the local time of the EEJ measurement changes by more than 2 hours in a month. This change in the local time sometimes made it difficult to accurately interpret the day-to-day variation of the EEJ observed by CHAMP and Swarm, because the EEJ variation associated with the local time change and other changes (e.g., changes in geomagnetic activity or neutral wind forcing) cannot be distinguished. The day-to-day variation of the EEJ may be more easily captured by ground-based magnetometer measurements. However, it is difficult to obtain good longitudinal coverage with ground-based observations. A solution to this problem is to use EEJ data from a Sun-synchronous orbit, where the local time is always the same. The SAC-C satellite mission (Colomb et al., 2004) operated in a Sun-synchronous orbit at an altitude of ~700 km and provided the EEJ data at a fixed local time of 10:25 a.m. during the solar maximum period of 2001–2003 (Alken and Maus, 2007). In this study, we employ the EEJ data from the China Seismo-Electromagnetic Satellite (CSES) (Shen et al., 2018), which flies in a Sun-synchronous orbit at approximately 2 a.m.–2 p.m. The CSES data provide the first continuous satellite observations of the afternoon EEJ at 2 p.m. local time.

Zhou Y. et al. (2022) presented a preliminary analysis of the CSES magnetic field measurements for detecting the EEJ. This study extends the analysis of the EEJ magnetic signatures derived from CSES, and advances the characterization of its spatial and temporal variability on day-to-day and seasonal time scales. In Section 3.1, we

will conduct a statistical comparison between CSES and Swarm EEJ to validate the reliability of the CSES EEJ data. In Section 3.2, we will perform a spectral analysis of the CSES EEJ to provide insight into the source of the day-to-day EEJ variability. In Section 3.3, we will compare the CSES EEJ data with neutral wind measurements by the Ionospheric Connection Explorer (ICON) satellite mission (Immel et al., 2018) to evaluate the effect of neutral winds on the EEJ. In Section 3.4, we will show how the seasonal and longitudinal variations of the EEJ are related to those in neutral winds. We will also examine the tidal components that are important for the longitudinal structure of the EEJ. In Section 3.5, we will compare the CSES EEJ data (evaluated at 110 km altitude) with CSES *in-situ* measurements of the electron density (~510 km altitude), providing insight into electrodynamic coupling between the ionospheric E and F regions.

2 Data

The intensity of the EEJ was derived using the 1 Hz scalar magnetic field measurements by CSES (Yang et al., 2021). The data are available from the mission website (https://www.leos.ac.cn/). The method for retrieving the EEJ intensity is the same as that developed for the Swarm Level 2 (L2) Product of the EEJ (Alken et al., 2013b; 2015). Briefly, the method involves the following three steps. In the first step, the core field, lithospheric field, and magnetospheric field are evaluated and removed from the observed magnetic field. In the second step, the residual field is further separated into the "Sq field," which is large-scale, and the "EEJ field," which is localized near the magnetic equator. In the final step, the EEJ intensity is estimated according to the Biot-Savart law using an inversion model of the EEJ that assumes line currents at an altitude of 110 km following zonally along the magnetic equator. More detailed description of each step can be found in the article by Alken (2020).

As mentioned, the CSES spacecraft flies in a Sun-synchronous orbit, and the local time of the equatorial crossing is 2 a.m. and 2 p.m. We use the measurements made at 2 p.m. during the period July 2018–April 2022. Figure 1A shows the number of observations in each month. In addition to the total number of observations, the numbers of eastward and westward EEJ events are also indicated. The occurrence rate of the westward EEJ is approximately 20%, which is consistent with previous studies based on ground-based observations and other satellites (e.g., Soares et al., 2019). The absence of data during January–May 2020 and during June 2021–January 2022 is not due to a lack of magnetic field measurements; instead, it is because the EEJ data were still to be processed at the time of writing this paper.

Figure 1B shows monthly values of the daily mean EEJ intensity. Green shading indicates the magnitude of the day-to-day variability. On each day, the CSES spacecraft completes ~15 orbits. The longitude of the equatorial crossing changes by 23.7° from one orbit to the next. Thus, the CSES satellite effectively covers all longitudes in 1 day ($15 \times 23.7\ ^\circ = 355.5^\circ$). For this reason, the daily mean is a good representation of the longitudinally averaged EEJ at 2 p.m. local time. In Figure 1B, the mean EEJ intensity during the last 3 month (February–April 2022) is appreciably higher than that over the preceding period. This is due to an increase in solar activity. Figure 1C shows monthly mean values of the $F_{10.7}$ index (Tapping, 2013), representing solar radiation activity, which controls E-region ionization and hence the E-region conductivity. The EEJ intensity is known to increase with increasing $F_{10.7}$ (e.g., Yamazaki et al., 2010; Matzka et al., 2017). Solar activity affects not only the mean EEJ intensity but also the occurrence rate of the westward EEJ. It is known that an increase in solar activity results in a decrease in the occurrence of the westward EEJ in the afternoon (e.g., Marriott et al., 1979; Soares et al., 2018), which can be confirmed in Figure 1A.

We perform a validation of the CSES EEJ data through comparisons with EEJ intensities derived from the magnetic field measurements by Swarm. The Swarm constellation, operational since November 2013, consists of three identical satellites, namely, Swarm A, Swarm B and Swarm C. Swarm A and C fly side by side at an altitude of approximately 460 km, while Swarm B flies separately at a higher altitude of ~510 km. As one of the L2 products of Swarm, EEJ data from each satellite are available at the ESA Swarm website (https://swarm-diss.eo.esa.int/). For the present study, we use the EEJ intensities from Swarm A and B.

We use neutral wind observations by the ICON mission. Measurement of the horizontal wind velocity is made by the Michelson Interferometer for Global High-Resolution Thermospheric Imaging (MIGHTI) instrument onboard ICON (e.g., Englert et al., 2017; Harding et al., 2017). Version 5 of the MIGHTI wind product based on the oxygen green-line emission at 557.7 nm wavelength is used for the evaluation of the local wind effect on the EEJ. We use only the measurements with the "wind quality factor" being one, corresponding to the best quality data. Detailed description and validation of version 5 ICON/MIGHTI data can be found in the article by Englert et al. (2023). The Level 2.2 MIGHTI Cardinal Winds can be downloaded from the ICON mission website (https://icon.ssl.berkeley.edu/Data/Data-Product-Matrix) as well as from DOI in Harding et al. (2023).

We also use the empirical wind model of Yamazaki et al. (2023), which is based on the ICON/MIGHTI green-line wind measurements during April 2020–March 2022. It uses a formula similar to Equation 1 in the introduction section with n being from 0 to 4 and s being from −4 to 4, where the $[n = 0, s = 0]$ term corresponds to the zonal-mean wind (ZMW), the $[n = 0, s > 0]$ terms correspond to stationary planetary waves (SPWs), and the rest of the (n, s) terms are tides. Besides, the model takes into account the dependence of each (n, s) component on month of year. The model outputs are zonal and meridional wind velocities for the latitude range of 12°S to 40°N and for the altitude range of 91–112 km.

The Langmuir probe (LAP) onboard CSES (Yan et al., 2018) provides electron density (N_e) data at the satellite location (~510 km altitude). We make a comparison between the CSES EEJ intensity and N_e from the same orbital path to assess the relationship of the two quantities. The CSES LAP data can be obtained from the same website as the CSES magnetic field data (https://www.leos.ac.cn/). The validation of CSES N_e data is presented by Yan et al. (2020) through comparisons with other satellite and ground-based observations. Yan et al. (2022) described artificial signals found in the CSES N_e data. We have eliminated those artificial signals before the comparison with the EEJ data is performed.

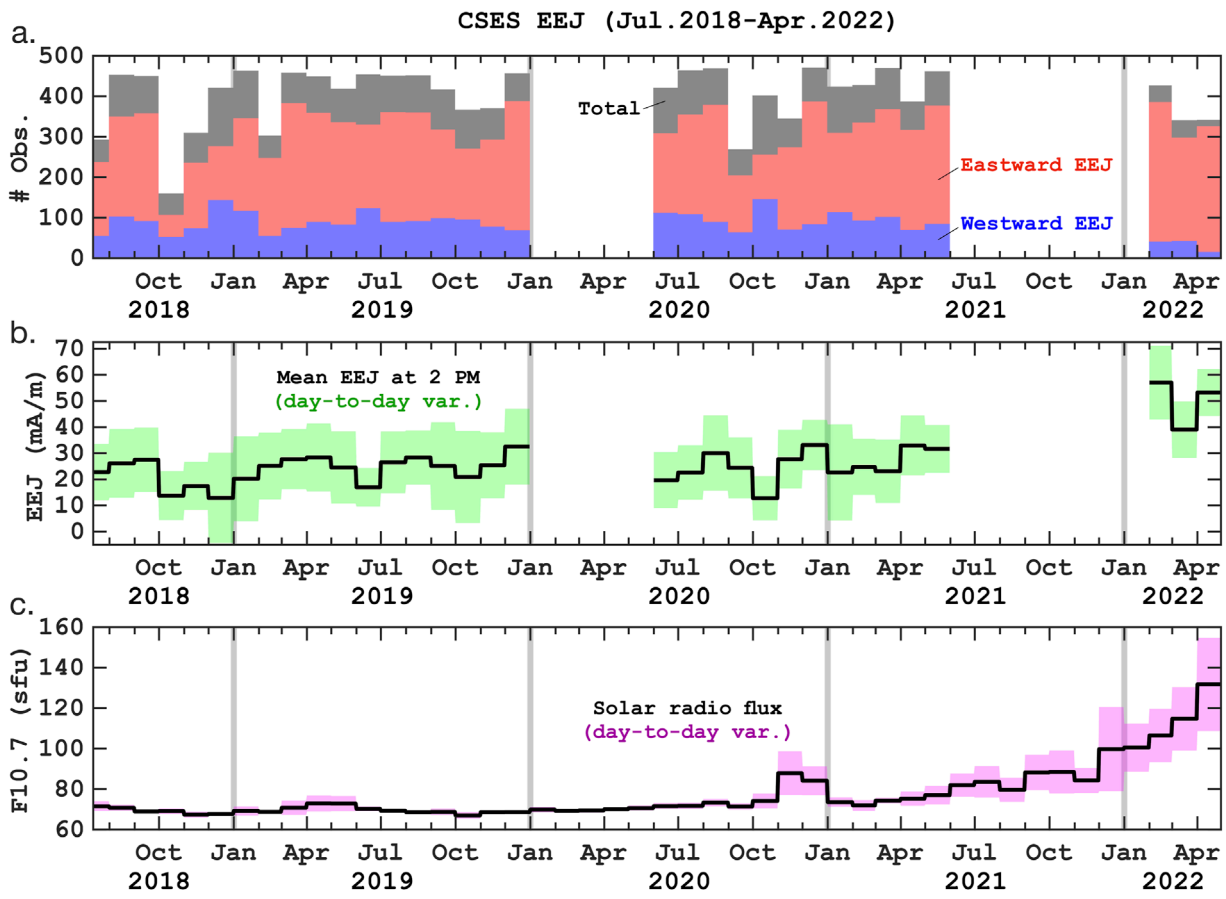

FIGURE 1
(A) Number of CSES equatorial electrojet (EEJ) measurements at 2 p.m. local time in each month during July 2018–April 2022. Besides the total number of measurements, the numbers of eastward and westward EEJ events are also indicated. **(B)** Monthly mean values of the daily mean EEJ intensity. Shading indicates the magnitude of the day-to-day variability (±1σ) of the daily mean EEJ intensity. **(C)** Monthly mean values of the daily solar radio flux index $F_{10.7}$. Shading indicates the magnitude of the day-to-day variability (±1σ) of the $F_{10.7}$ index.

3 Results and discussion

3.1 Comparison with swarm EEJ

Figure 2 presents comparisons of the EEJ intensities derived from CSES and Swarm magnetic field measurements. Only the data during concurrent measurements by CSES and Swarm are used. Our criteria for a CSES-Swarm conjunction are as follows: (1) the time difference between the two measurements is less than 15 min, and (2) the longitudinal separation of the two measurements is less than 15°. 497 concurrent measurements are found for the CSES-Swarm A pair (Figure 2A), while 265 concurrent measurements are found for the CSES-Swarm B pair (Figure 2B). In both cases, there is a good correlation between the EEJ intensities from CSES and Swarm, with the correlation coefficient of R ~0.9. The results support the reliability of the CSES EEJ data. However, the slope of the regression line is less than 1.0 in both cases: 0.85 [0.82–0.89] for the CSES-Swarm A pair and 0.86 [0.79–0.91] for the CSES-Swarm B pair, where the range in the square brackets indicates the 95% confidence interval estimated by the bootstrap method. The results seem to imply a systematic underestimation of the CSES EEJ compared to the Swarm EEJ. The cause of this discrepancy is unclear. We do not attempt to calibrate the CSES EEJ with Swarm EEJ; however, possible underestimation of the CSES EEJ intensity by ~15% should be kept in mind while interpreting the results presented in this paper. The intersect of the regression line is small in both cases (1–2 mA/m), and thus the direction of the CSES EEJ (i.e., eastward or westward) is considered to be accurate.

3.2 Spectral analysis of day-to-day variability

Characteristics of the day-to-day variability of the afternoon EEJ are examined. Figure 3A displays the CSES EEJ intensity during the selected period of 2 April–30 May 2021, as a function of time (day of year; DoY) and longitude, highlighting the day-to-day variability of the EEJ at 2 p.m. local time. A close inspection of the data reveals a wave-like pattern that appears to propagate westward, as indicated by the white dashed lines. Figure 3B depicts the amplitude spectrum obtained by the Fourier-wavelet analysis described by Yamazaki (2023). The horizontal axis shows the zonal wavenumber

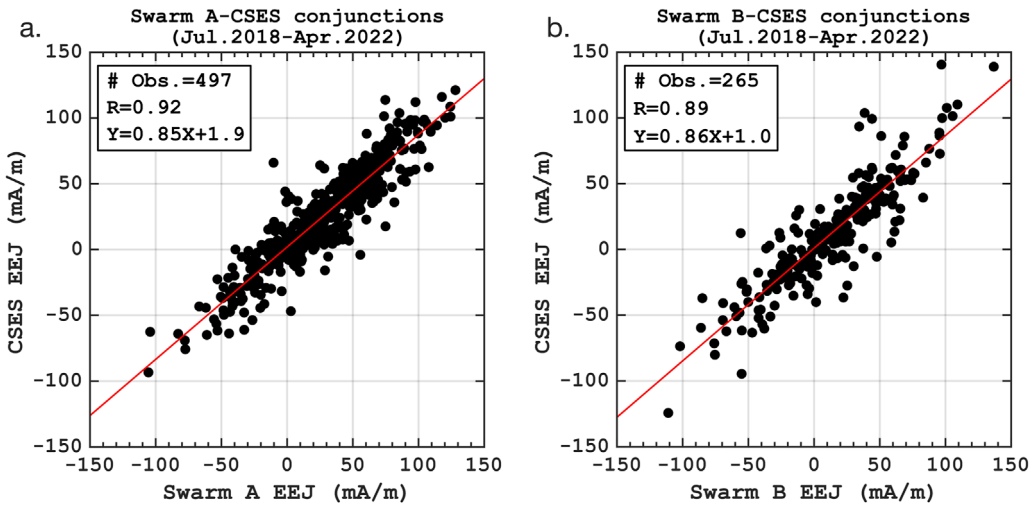

FIGURE 2
Comparison of the equatorial electrojet (EEJ) intensity derived from the magnetic field measurements by CSES with those from concurrent magnetic field measurements by **(A)** Swarm A and **(B)** Swarm B.

and the vertical axis shows the period of oscillation. The Fourier-wavelet technique involves the Fourier transform in longitude and the wavelet transform in time, and is applicable to 2-D longitude-time data for evaluating global-scale waves (e.g., tides and planetary waves) with different zonal wavenumbers. The spectrum shows an amplitude peak at a period of ~6 days and zonal wavenumber −1, indicating the involvement of a westward-propagating Q6DW. Previously, Yamazaki et al. (2018) reported several events where EEJ intensities from CHAMP and Swarm satellites show Q6DW signatures.

Figure 3C depicts the CSES EEJ intensity during another selected period of 2 January 2019–18 February 2019. A temporal oscillation is seen in the EEJ intensity, as indicated by the white dashed line. Unlike the previous example presented in Figure 3A, the phase of the oscillation is constant with respect to longitude. The Fourier-wavelet spectrum shown in Figure 3D reveals an amplitude peak at a period of 14–15 days and zonal wavenumber 0. This semimonthly oscillation can be attributed to the effect of the atmospheric lunar tide, which appears as a 14.8 days oscillation in the EEJ at a fixed local time (e.g., Rastogi and Trivedi, 1970; Yamazaki et al., 2012). The dominant mode of the atmospheric lunar tide is the semidiurnal M_2 oscillation with a period of 12.42 h (e.g., Lindzen and Chapman, 1969). The 14.8-day oscillation is basically an alias caused by the sampling of the M_2 oscillation at a rate of 24.0 h. During January–February 2019, the new Moon occurred on 6 January (DoY = 6) and 4 February (DoY = 35), and the full Moon occurred on 21 January (DoY = 21) and 19 February (DoY = 50). The CSES EEJ at 2 p.m. local time is seen to be relatively weak on the days of the new Moon and full Moon, which is consistent with previously reported lunar tidal effect on the EEJ (e.g., Yamazaki et al., 2012). Moreover, previous studies reported that the amplitude of the semimonthly EEJ oscillation can be amplified during sudden stratospheric warming events (e.g., Park et al., 2012; Yamazaki, 2013; Siddiqui et al., 2015; 2018). In January 2019, there was an Arctic sudden stratospheric warming event (e.g., Siddiqui et al., 2021), which might have contributed to the semimonthly oscillation in the EEJ during this month.

As demonstrated in Figure 3, the Fourier-wavelet spectrum of the CSES EEJ can be obtained for any given period of time. The average spectrum for the entire period of July 2018–May 2021 is derived to provide a climatological picture of the CSES EEJ spectrum under solar minimum conditions (see Figure 1C for solar activity). Figure 4A shows the result, revealing three distinct components: (1) an eastward-propagating oscillation with a period of 2–3 days and zonal wavenumber 1, (2) a westward-propagating oscillation with a period of 5–6 days and zonal wavenumber 1, and (3) a zonally-symmetric oscillation with a period of 14–15 days. They correspond to different modes of atmospheric waves, namely, the UFKW, Q6DW and atmospheric lunar tide, respectively. It is noted that previous studies based on CHAMP and Swarm magnetic field measurements were not able to provide the climatological spectrum of the EEJ at a fixed local time similar to Figure 4A because the local time of the EEJ measurement by these satellites changes over time.

The day-to-day variation of the EEJ could contain signatures of varying solar and geomagnetic activity. The wavelet spectra presented in Figure 4B reveal the presence of 27-, 13.5- and 9-day oscillations in the daily geomagnetic activity index *Ap* (Matzka et al., 2021) and a 27-day oscillation in the solar activity index $F_{10.7}$ during July 2018–May 2021. The 27-day oscillation represents the effect of solar rotation, and 13.5- and 9-day oscillations are its harmonics. These oscillations do not seem to have a significant impact on the EEJ in our dataset. One may suspect the influence of the *Ap* oscillation at 13.5 days on the EEJ oscillation at 14–15 days. However, if the 13.5-day oscillation in *Ap* is effective in modulating the EEJ, the 27- and 9-day oscillations should also be visible in the EEJ spectrum (Figure 4A), which is not the case. Besides, there is no correlation between the occurrence of the 14–15-day EEJ oscillation and the 13.5-day *Ap* oscillation. For example, during 2 January–18 February 2019, when the EEJ exhibited a large semimonthly oscillation (Figures 3C,D), the 13.5-day oscillation was absent in *Ap* (not shown

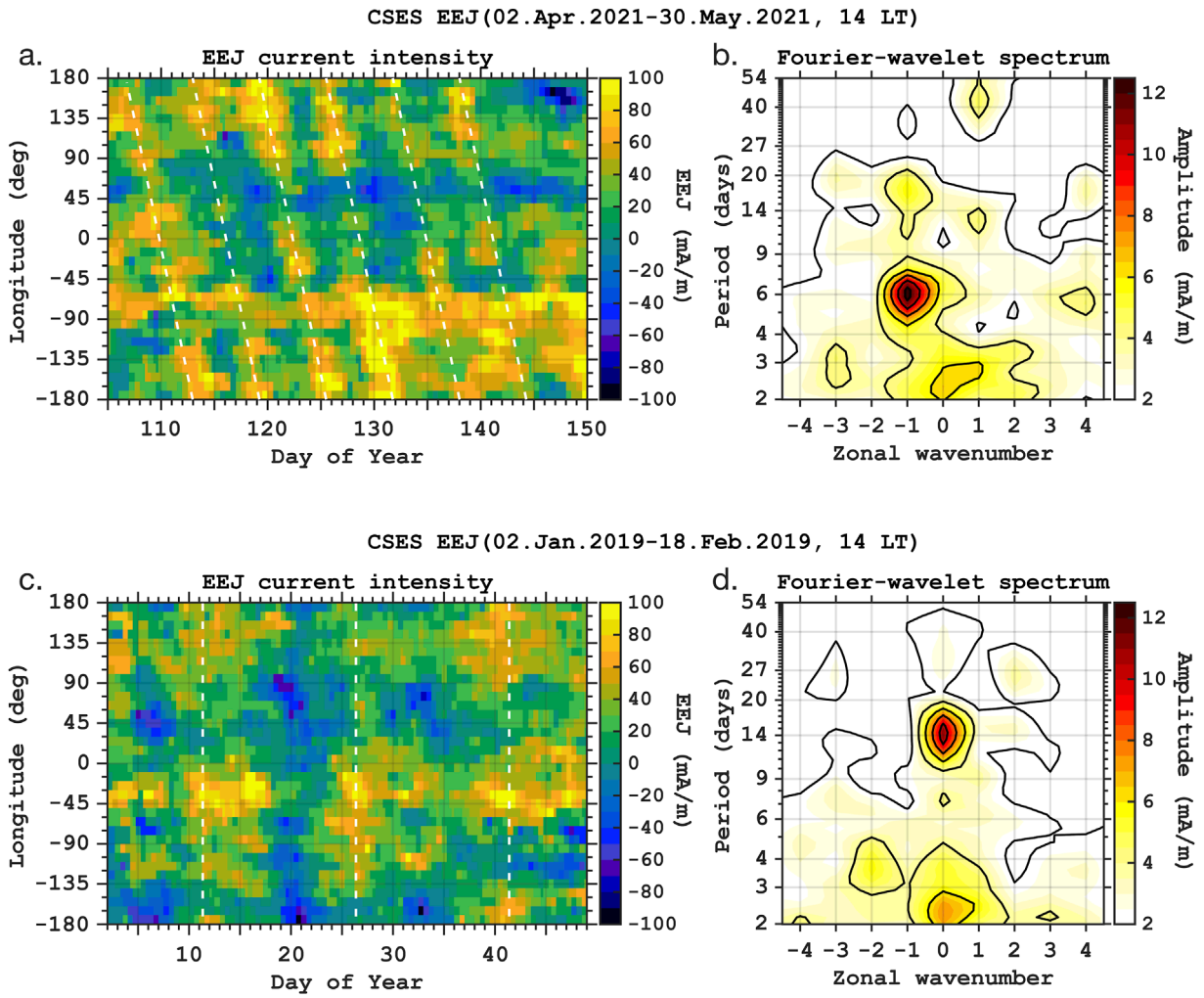

FIGURE 3
(A) An example of the CSES equatorial electrojet (EEJ) data at 2 p.m. local time, plotted as a function of time (day of year) and longitude for the time period 2 April 2021–30 May 2021, and **(B)** the corresponding zonal wavenumber-period spectrum as derived using the Fourier-wavelet technique (Yamazaki, 2023). Positive and negative zonal wavenumbers correspond to eastward- and westward-propagating waves, respectively. **(C, D)** Same as **(A, B)** but for the time period 2 January–18 February 2019.

here). Figures 4C,D are the same as Figure 4A but for different periods of time (i.e., January–December 2019 for Figure 4B and July 2020–May 2021 for Figure 4C). The results obtained for these two separate 1-year periods are remarkably similar, indicating that the influences of the UFKW, Q6DW and atmospheric lunar tide on the EEJ are robust.

It is important to note that UFKW and Q6DW signatures in the EEJ spectrum (Figure 4) do not necessarily mean the direct effects of these waves on the EEJ. It is known that when measurements from a Sun-synchronous satellite are analyzed, a spectral peak corresponding to a planetary wave cannot be distinguished from those associated with the secondary waves arising from the nonlinear interaction between the same planetary wave and any migrating (i.e., Sun-synchronous) tide (e.g., Forbes and Zhang, 2015). In the present context, secondary waves from the nonlinear interaction between the UFKW and a migrating tide can alias into the UFKW signature. Similarly, secondary waves from the nonlinear interaction between the Q6DW and a migrating tide can alias into the Q6DW signature. Miyoshi and Yamazaki (2020) examined the strong Q6DW signature in the noon-time EEJ during September 2019 using a numerical model, and demonstrated that the spectral peak corresponding to the Q6DW in the noon-time EEJ was largely due to neutral wind forcing by the secondary waves resulting from the nonlinear interaction between the Q6DW and migrating semidiurnal tide, rather than forcing by the Q6DW itself. At this time, it is not clear whether the EEJ spectral peaks corresponding to UFKW and Q6DW in Figure 4 are directly caused by these waves, or by the secondary waves from their nonlinear interactions with migrating tides which produce identical spectral peaks. For the lunar tide, on the other hand, its direct effect on the E-region dynamo currents is well established through previous research (e.g., Tarpley, 1970; Eccles et al., 2011).

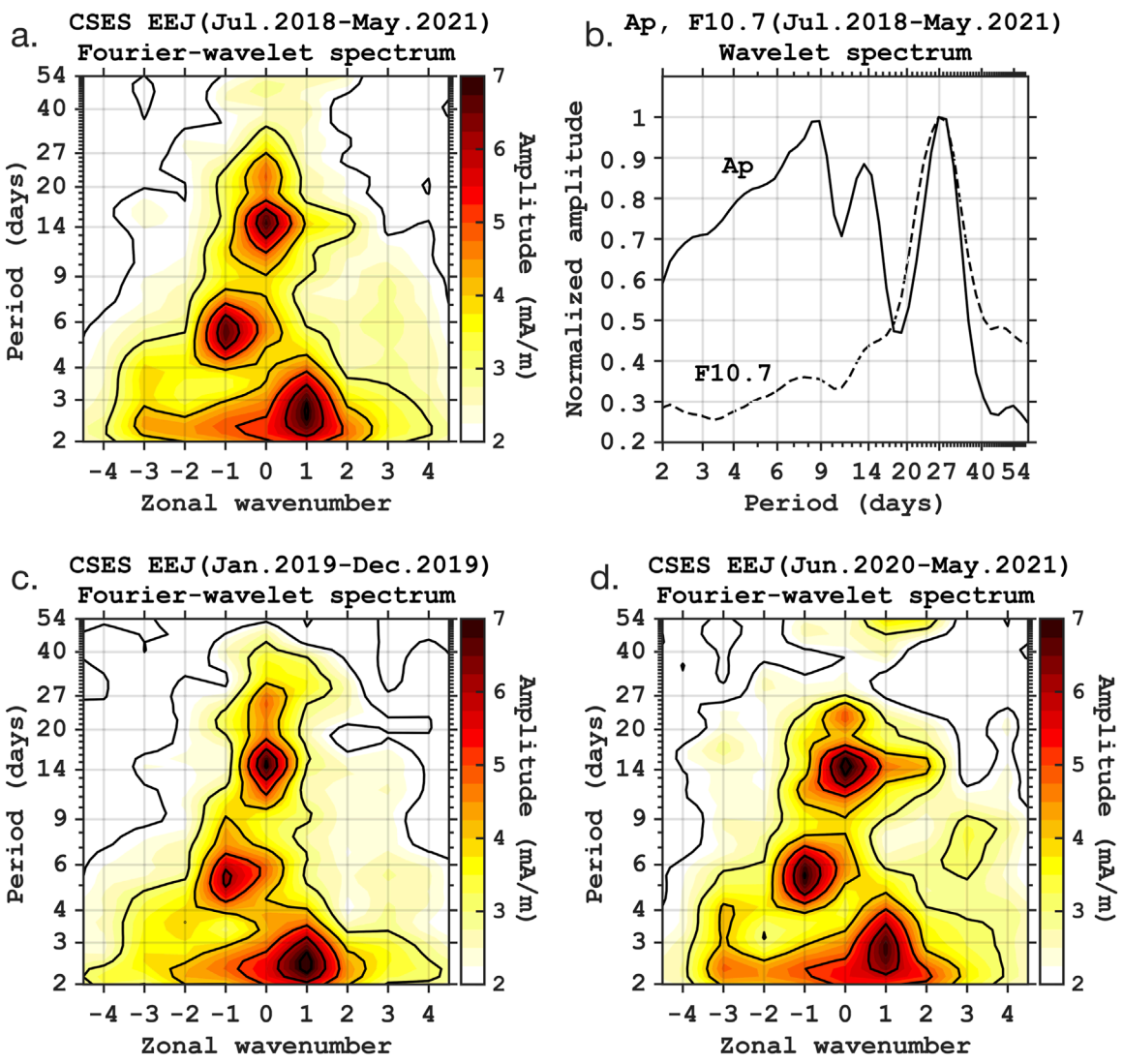

FIGURE 4
(A) Zonal wavenumber-period spectrum of the CSES equatorial electrojet (EEJ) intensity at 2 p.m. local time, averaged over the time period July 2018–May 2021. Positive and negative zonal wavenumbers correspond to eastward- and westward-propagating waves, respectively. **(B)** Wavelet amplitude spectra of the geomagnetic activity index *Ap* and solar activity index $F_{10.7}$ during July 2018–May 2021. The amplitudes are normalized by the corresponding maximum values. **(C)** Same as **(A)** but over the 1-year period January–December 2019. **(D)** Same as **(A)** but over the 1-year period July 2020–May 2021.

3.3 Comparison with ICON/MIGHTI winds

The influence of the neutral wind on the EEJ is examined using concurrent measurements of the EEJ by CSES and wind profiles by ICON/MIGHTI. The criteria for a ICON/MIGHTI-CSES conjunction are as follows: 1) the wind measurement is obtained within ±15 min from the time of the EEJ observation at the magnetic equator; 2) the wind measurement is obtained within ±5° from the magnetic equator; 3) the wind measurement is obtained within ±10° from the longitude of the EEJ measurement. These criteria are the same as those used by Yamazaki et al. (2021) for a comparison of ICON/MIGHTI winds and Swarm EEJ. Also following Yamazaki et al. (2021), only the data obtained under the quiet geomagnetic activity condition Hp30 < 3 are used, where Hp30 (Yamazaki et al., 2022) is a geomagnetic activity index similar to the three-hourly Kp index (Matzka et al., 2021) but with a higher temporal resolution of 30 min. When there are more than one wind profiles that satisfy all the criteria for the same EEJ measurement, we use only one wind profile that has the smallest time difference from the EEJ measurement.

The results obtained from the analysis of the concurrent measurements of the CSES EEJ and ICON/MIGHTI winds are presented in Figure 5. Figure 5A compares the average magnetic eastward wind profiles during times of the eastward and westward EEJ. During times of the eastward EEJ, the average wind tends to be westward at all heights with relatively small height variation, while during times of the westward EEJ, the average wind is eastward at 100–120 km and westward above. Such a systematic difference

is not seen in the average magnetic northward wind profiles for the eastward and westward EEJ, as depicted in Figure 5B. Earlier, Yamazaki et al. (2021) also reported the difference in the magnetic eastward wind profiles during times of the eastward and westward EEJ based on the Swarm EEJ and ICON/MIGHTI winds, but they were not able to completely separate the wind effect on the EEJ from the local time variation of the EEJ, as the local time of the Swarm EEJ measurement constantly changes. The results presented in Figures 5A,B are in alignment with those by Yamazaki et al. (2021) but at a fixed local time of 2 p.m., eliminating the ambiguity due to the local time change.

Figures 5C,D provide examples showing the relationship between the magnetic eastward wind and EEJ. At 106 km, there is a negative correlation ($R = -0.56$) between the two parameters, while at 135 km, the correlation is positive ($R = 0.54$). The results are consistent with previous observations based on the Swarm EEJ and ICON/MIGHTI winds (Yamazaki et al., 2021). The results are also consistent with those in the simulation study by Yamazaki et al. (2014a), which predicted that the EEJ intensity correlates negatively and positively with the equatorial eastward wind in the Hall region (100–120 km) and Pedersen region (120–180 km), respectively. We further extend the correlation analysis including other latitudes. Figure 5E presents the distribution of the correlation coefficient between the ICON/MIGHTI magnetic eastward wind and CSES EEJ as a function of magnetic latitude and altitude. The magnetic latitude is based on quasi-dipole (QD) coordinates (e.g., Laundal and Richmond, 2017). Significant correlation ($p < 0.05$) is found mostly between 100 and 115 km and between 120 and 160 km in altitude. The region of relatively high negative correlation ($R < -0.5$) is limited near the magnetic equator between 105 and 110 km, while the region of relatively high positive correlation ($R > 0.5$) is limited between 130 and 140 km. They do not extend deep into middle latitudes, being mostly confined below 15° magnetic latitude. Figure 5F is similar to Figure 5E but shows the correlation coefficient between the magnetic northward wind and EEJ. In this case, significant correlation is found around 10–30° magnetic latitude and between 110 and 140 km in altitude. However, the correlation is weak everywhere ($|R| < 0.5$), indicating that the meridional wind is not as effective as the equatorial zonal wind in modulating the EEJ. The spatial patterns of the correlation coefficient depicted in Figures 5E,F are in qualitative agreement with those predicted by Yamazaki et al. (2014a). It is noted that Figures 5E,F mainly focuses on the Northern Hemisphere, because ICON/MIGHTI measurements are limited between ~10°S and ~40°N latitude.

3.4 Seasonal and longitudinal variability

Figure 6 depicts the seasonal and longitudinal variations of the EEJ (Figures 6A,C,D) and eastward wind (Figure 6B), which are all evaluated at a fixed local time of 2 p.m. Figure 6A is derived from the CSES EEJ data during 2019 under the geomagnetically quiet condition of Hp30 < 3. Figures 6C,D are based on the principal component analysis of the EEJ data (Kp≤3) from Swarm A and B satellites and several ground-based magnetometers during 2018 and 2017 as described by Soares et al. (2022). The seasonal and longitudinal variations of the CSES EEJ for 2019 (Figure 6A) are in fair agreement with those derived from independent data for 2018 and 2017 (Figures 6C,D) with correlation coefficients $R = 0.70$ for the 2018 case and $R = 0.72$ for the 2017 case. Differences are expected from the year-to-year variation of the EEJ. Figure 6B shows the eastward wind at 2.5°N latitude and at 109 km altitude as derived from the empirical model of Yamazaki et al. (2023), which is based on the ICON/MIGHTI wind measurements (Hp30 < 3) during April 2020–March 2022. The selected latitude (2.5°N) corresponds to the model grid closest to the zonal mean of the geographic latitude of the magnetic equator. As expected from the results in the previous section, there are some similarities between the seasonal-longitudinal patterns in the eastward wind and the EEJ. The correlation coefficients between the patterns in the eastward wind and the EEJ are $R = -0.33$, $R = -0.37$ and $R = -0.39$ for the 2019, 2018 and 2017 cases, respectively. It is noted that these comparisons are not based on simultaneous measurements of the EEJ and wind like those presented in the previous section. Also, the empirical model of Yamazaki et al. (2023) outputs the geographic eastward wind, not the magnetic eastward wind that was used in the previous section. Nevertheless, the correlations are reasonably good and close to those presented in the previous section (Figures 5C,E).

It is known that the longitudinal variation of the EEJ is dominated by a four-peak pattern during July–September (e.g., Lühr et al., 2008; Lühr and Manoj, 2013), which can also be seen in Figures 6A,C,D. A similar four-peak pattern exists in the eastward wind during these months (Figure 6B). Figure 7A compares the four-peak structures in the EEJ and eastward wind. It shows that the EEJ tends to be weak where the eastward wind at 109 km is strong, and *vice versa*. Since the wind velocities in the Yamazaki et al. (2023) model are described as a superposition of contributions by the zonal-mean wind, tides and stationary planetary waves, which are assigned with different combinations of n and s, it is possible to assess the relative importance of different (n, s) components for the four-peak structure in the zonal wind presented in Figure 7A. The table in Figure 7B lists the five largest (n, s) components of the eastward wind at longitudes of local maxima and minima. The components that have the magnitude larger than 5 m/s are highlighted in red, in consideration that the estimated 1-σ uncertainty of individual components is typically in the range of 1.0–4.5 m/s (Yamazaki et al., 2023). The results suggest that DE3 is largely responsible for the four-peak structure in the eastward wind during July–September. Previous theoretical studies also concluded that DE3 is the major contributor to the four-peak structure of the equatorial zonal electric field and current (e.g., Ren et al., 2010; Jin et al., 2008; Wan et al., 2012; Pedatella et al., 2012a). The production mechanism and seasonal variation of DE3 are discussed in detail by Zhang et al. (2010). Apart from DE3, migrating tides (DW1 and SW2) and other non-migrating tides (DE2 and DE1) are relatively large, but their individual contributions are less than half of that by DE3. It is noted that although migrating tides do not have any longitudinal structure at a fixed local time, they can contribute to individual longitudinal peaks of the EEJ.

It is also known that during December–January, the four-peak pattern is largely absent from the longitudinal variation of the EEJ, and a two- or three-peak pattern is more evident (e.g., Lühr et al., 2008; Lühr and Manoj, 2013). Figure 8 is similar to Figure 7 but for December–January. In Figure 8A, the EEJ has two prominent local maxima around 45°W and 125°E longitudes. They coincide with the local minima of the eastward wind, underscoring the importance

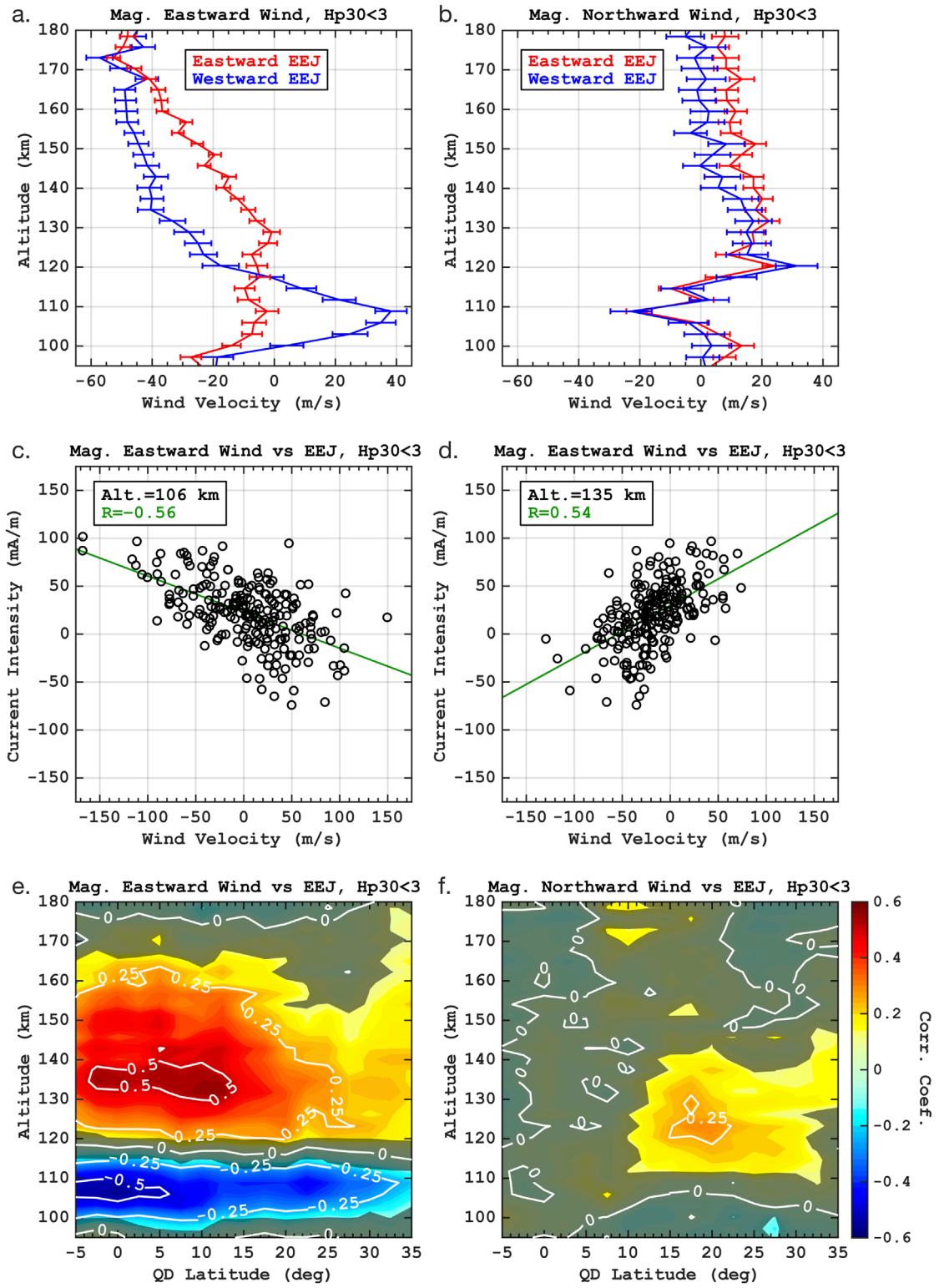

FIGURE 5
(A) Average vertical profiles of the ICON/MIGHTI magnetic eastward wind during concurrent measurements with the CSES equatorial electrojet (EEJ) at 2 p.m. local time for times of the eastward and westward EEJ. **(B)** Same as **(A)** but for the magnetic meridional wind. **(C)** Scatter plot for the ICON/MIGHTI magnetic eastward wind velocity at 106 km and the CSES EEJ intensity at 2 p.m. local time from their concurrent measurements. Note that the EEJ intensity is evaluated at an altitude of 110 km. The green line shows the linear regression. **(D)** Same as **(C)** but for the ICON/MIGHTI magnetic eastward wind velocity at 135 km. **(E)** Correlation coefficient between the CSES EEJ intensity at 2 p.m. local time at 110 km altitude at the magnetic equator and the ICON/MIGHTI magnetic eastward wind observed at the same time, plotted as a function of quasi-dipole (QD) latitude and altitude. The shading indicates the lack of statistical significance at the 95% confidence level. **(F)** Same as **(E)** but for the ICON/MIGHTI magnetic northward wind.

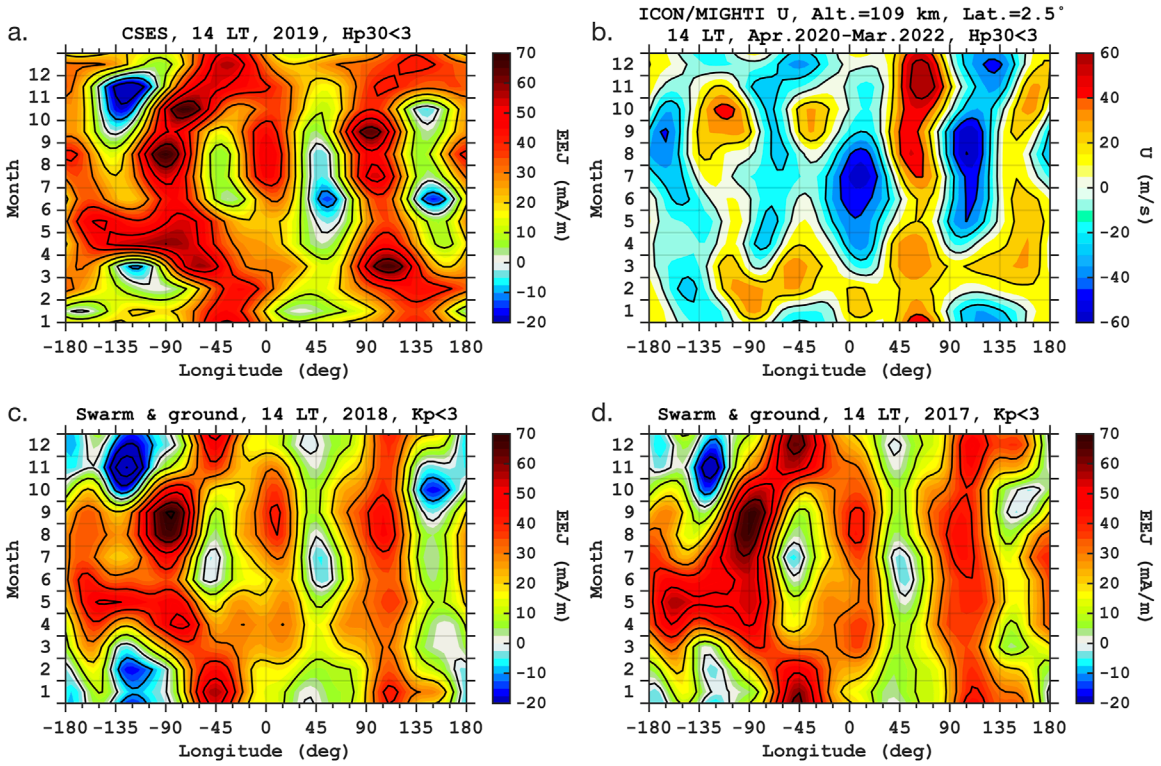

FIGURE 6
(A) CSES equatorial electrojet (EEJ) intensity at 2 p.m. local time at 110 km altitude for the year 2019, plotted as a function of longitude and month. **(B)** Eastward wind velocity at 2 p.m. local time at a latitude of 2.5°N and an altitude of 109 km, as derived from the empirical wind model of Yamazaki et al. (2023). **(C)** EEJ intensity at 2 p.m. local time at 110 km altitude for the year 2018, as derived from the analysis of Soares et al. (2022). **(D)** Same to **(C)** but for the year 2017.

of the local wind effect on the EEJ. The table in Figure 8B suggests that there is no single dominant component that determines the longitudinal structure of the zonal wind during December–January, unlike the July–September case where DE3 is much larger than other components (see the table in Figure 7B). Nevertheless, eastward-propagating diurnal tides DE2 and DE3 are the most significant components. Westward-propagating semidiurnal tides SW2, SW3 and SW4 are also relatively large. It is interesting to note that DE3 is still important during December–January, while the amplitude of DE3 reaches its seasonal minimum around the December solstice (e.g., Forbes et al., 2003; Oberheide et al., 2006).

3.5 Comparison with *in-situ* electron density measurements

The *in-situ* measurements of N_e from the LAP instrument onboard CSES (~510 km altitude) are analyzed along with the CSES EEJ data. The N_e data are used only when the EEJ data are available from the same orbit; see Figure 1A for the EEJ data availability. Also, only the measurements made under the geomagnetically quiet condition of Hp30 < 3 are used. Figure 9A depicts the QD-latitude dependence of CSES/LAP N_e at 2 p.m. local time during August 2018–May 2021. The meridional structure of N_e for a given month exhibits a single peak near the magnetic equator within approximately ±10° QD latitude. This is somewhat unexpected, as previous studies based on *in-situ* measurements of N_e at 2~p.m. local time by other LEO satellites have shown a double-peak meridional structure known as the equatorial ionization anomaly (EIA), characterized by a density trough at the magnetic equator and density crests at approximately ±15° QD latitudes (e.g., Xiong et al., 2013; 2016b). The discrepancy may be attributable to two factors. The first is the altitude of the CSES satellite, which is higher than those of the satellites used in Xiong et al. (2013, 2016b). The double-peak EIA structure of N_e is most evident at the altitude of the peak plasma density (300–400 km) (e.g., Lin et al., 2007; Tulasi Ram et al., 2009), and thus may not be visible at the altitude of the CSES satellite (~510 km). The second is solar activity, which was very low during the period of interest (August 2018–May 2021; see Figure 1C for $F_{10.7}$). The altitude of the daytime peak plasma density over low latitudes tends to be lower during low solar activity periods (e.g., Yue et al., 2015; Zhao et al., 2017), which would make it difficult for the CSES satellite at ~510 km to observe the double-peak EIA structure of N_e. It is noted that the meridional profile of CSES/LAP N_e from an individual orbit sometimes shows the double-peak structure, although it is not visible in the average meridional profiles depicted in Figure 9A.

Figure 9A also presents the seasonal variation in CSES/LAP N_e at 2 p.m. local time. N_e shows a semiannual variation with equinoctial maxima around the magnetic equator between

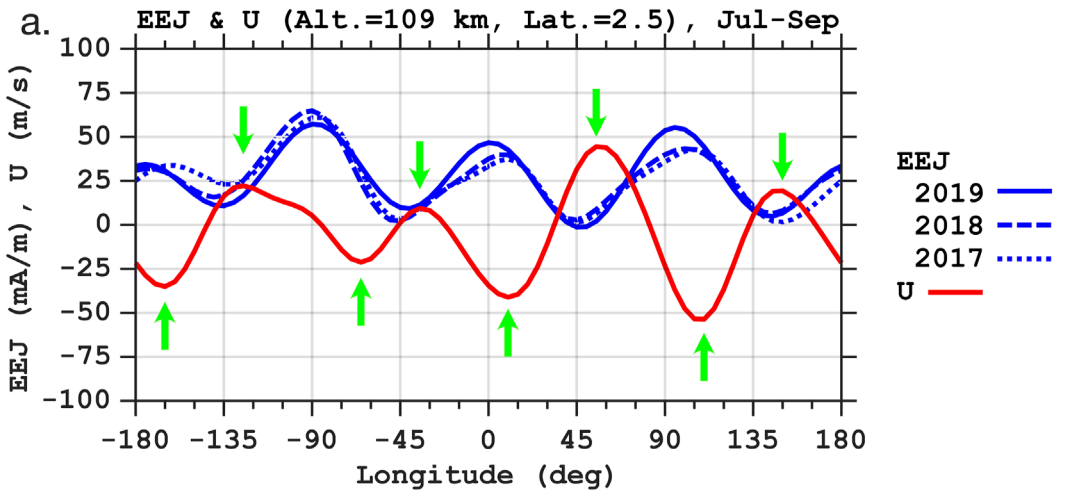

b.

	-165°	-125°	-65°	-35°	10°	55°	110°	150°
1	DE3 (-28.8)	DE3 (28.7)	DE3 (-19.1)	DE3 (28.7)	DE3 (-28.7)	DE3 (28.7)	DE3 (-25.5)	DE3 (28.8)
2	SW2 (-7.3)	DE1 (5.3)	SW2 (-7.3)	SPW1 (4.6)	SW2 (-7.3)	DE2 (10.2)	DE2 (-11.1)	DE2 (7.4)
3	DW1 (-6.5)	Q0 (3.7)	DW1 (-6.4)	Q0 (3.7)	DW1 (-6.4)	DE1 (5.3)	SW2 (-7.3)	Q0 (3.8)
4	DE1 (-4.1)	ZMW (3.6)	QW4 (-2.8)	ZMW (3.6)	DE1 (-5.1)	Q0 (3.7)	DW1 (-6.4)	ZMW (3.5)
5	Q0 (-3.8)	SW3 (3.4)	Q0 (-2.7)	TW3 (2.5)	DE2 (-3.7)	ZMW (3.7)	SPW1 (-3.5)	TW3 (2.5)

FIGURE 7
(A) Eastward wind velocity at 2 p.m. local time at a latitude of 2.5°N and an altitude of 109 km during July–September, as derived from the empirical wind model of Yamazaki et al. (2023), along with the equatorial electrojet (EEJ) intensity at 2 p.m. local time at 110 km altitude at the magnetic equator for the years 2017, 2018 and 2019. The EEJ data for 2019 are obtained from the CSES magnetic field measurements, while those for 2017 and 2018 are based on the analysis presented by Soares et al. (2022). **(B)** Tidal composition of the eastward wind at longitudes of local maxima and minima. The components with the magnitude larger than 5 m/s are highlighted in red.

approximately ±10° QD latitude. An annual variation with a local-summer maximum becomes more prominent with increasing latitude. The results are in agreement with the earlier study by Zhu et al. (2023), which examined the annual and semiannual variations in CSES/LAP N_e. The seasonal dependence of N_e involves various mechanisms. One important factor is the seasonal variation in the solar zenith angle. The main constituent of the F-region plasma is atomic oxygen ion O^+, which is produced through the photoionization of atomic oxygen O. The ionization by solar radiation depends on the solar zenith angle (Chapman, 1931), which varies semiannually at low latitudes and annually at higher latitudes due to Earth's geometry relative to the Sun. Another important factor is the seasonal variation in neutral composition. The O^+ density is controlled not only by the production of O^+ through the photoionization of O, but also by the loss of O^+ by recombination through ion-exchange reactions that involve N_2. Thus, the O^+ density (and hence N_e) varies with the density ratio $[O]/(N_2)$ (e.g., Rishbeth, 1998). The neutral composition of the thermosphere, $[O]/(N_2)$, varies with the season due to the large-scale circulation of the thermosphere (Fuller-Rowell, 1998) as well as wave forcing from the middle atmosphere (Jones Jr et al., 2017; 2018).

Figure 9B displays the correlation coefficient between the CSES EEJ and N_e as a function of magnetic latitude and month of year. The correlation was calculated between the EEJ at the magnetic equator and N_e binned at every 0.5° QD latitude from the same orbit. At low latitudes below ±20° QD latitude, the correlation is positive and significant ($p < 0.01$) throughout the year but R varies considerably, in the range of 0.10–0.73, depending on the latitude and month. The positive correlation at low latitudes is anticipated as the effect of the equatorial plasma fountain (e.g., Balan et al., 2018). That is, in the presence of the eastward electric field, which is associated with the EEJ, low-latitude plasmas move upward to F-region altitudes by the $E \times B$ drift. Stolle et al. (2008) reported a positive correlation between the EEJ intensity and F-region plasma density. However, they did their analysis exclusively at the South American sector, and did not reveal seasonal dependence. In this respect, our analysis is an extension of previous work. Stolle et al. (2008) found that the maximum response of the F-region plasma density to a change in

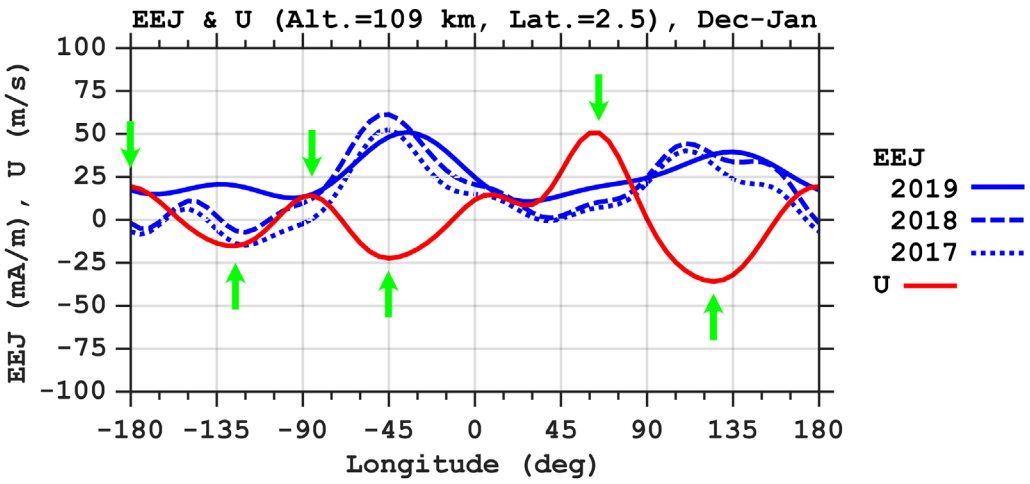

	-180°	-125°	-85°	-45°	65°	125°
1	DE2 (12.3)	DE2 (-12.9)	DE3 (9.0)	DE3 (-9.4)	DE2 (10.8)	DE2 (-10.8)
2	DE3 (9.4)	DE3 (-7.4)	DE2 (7.2)	SW4 (-8.6)	SW4 (9.8)	DE3 (-6.9)
3	QW4 (4.6)	SW2 (-6.5)	SW3 (7.1)	SW2 (-6.5)	SPW1 (5.2)	SW3 (-6.9)
4	TW3 (4.5)	SPW1 (-4.8)	QW4 (4.6)	DW3 (-4.2)	SPW4 (4.9)	SW2 (-6.5)
5	SPW2 (3.4)	DW2 (-4.7)	TW3 (4.5)	ZMW (-3.6)	DW2 (4.8)	SW4 (-6.4)

FIGURE 8
Same as Figure 7 but for December–January.

the EEJ intensity occurs a few hours after the EEJ variation. In the present study, we are not able to assess the delay in the N_e response to the EEJ because CSES N_e and EEJ measurements are made at the same local time.

At higher latitudes (above ±20°), the correlation is significant only in the summer hemisphere. The hemispheric difference in the N_e response to the EEJ might be due to the effect of the meridional wind. The neutral wind at F-region altitudes blows from the summer hemisphere to the winter hemisphere (e.g., Dickinson et al., 1977; Drob et al., 2015). The meridional wind pushes the plasmas upward along the magnetic field line in the summer hemisphere and downward in the winter hemisphere. Thus, the meridional wind acts to help and hinder the vertical transport of the plasmas to higher altitudes in the summer and winter hemispheres, respectively, which might affect the detectability of the N_e response to the EEJ at the CSES altitude (~510 km).

Figure 10 compares the latitudinal structures of N_e during times of the eastward and westward EEJ. N_e is greater during times of the eastward EEJ regardless of the month. The difference in N_e is more prominent in the Southern Hemisphere during October–March and in the Northern Hemisphere during April–September, which could be due to the meridional wind effect discussed above. Whether the EEJ is eastward or westward, the double-peak EIA structure is hardly visible in the average meridional profiles of CSES/LAP N_e at ~510 km under these low solar activity conditions.

4 Summary and conclusion

The magnetic field measurements by the CSES mission provide the first continuous satellite observations of the afternoon equatorial electrojet (EEJ) at a fixed local time of 2 p.m. during the low solar activity period of July 2018–April 2022. The method used for the retrieval of the EEJ is the same as that developed for the Swarm EEJ product (Alken et al., 2013b; 2015). The comparison between the CSES and Swarm EEJ intensities during satellite conjunctions reveals a good correlation between the two (Figure 2), supporting the reliability of the CSES data in capturing the EEJ variability. The CSES data, however, seem to underestimate the EEJ intensity by ~15%, the reason for which is still to be investigated.

Using the CSES data, it is possible to derive the zonal wavenumber-period spectrum of day-to-day EEJ variation for any given time period (e.g., Figure 3). The climatological mean spectrum of the EEJ at 2 p.m. local time is presented for the first time (Figure 4), which reveals three distinct oscillatory

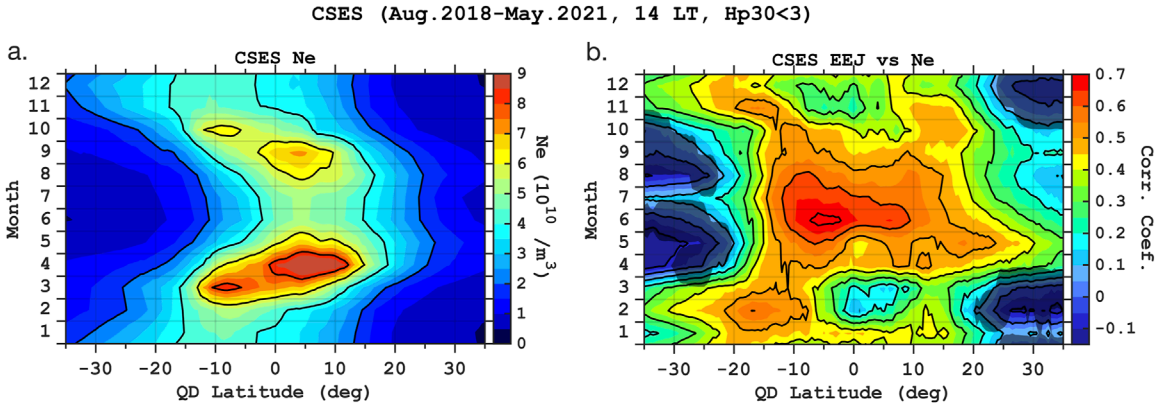

FIGURE 9
(A) Electron density (N_e) at 2 p.m. local time at an altitude of ~510 km observed by the Langmuir probe onboard CSES, plotted as a function of quasi-dipole (QD) latitude and month. **(B)** Correlation coefficient between the CSES equatorial electrojet (EEJ) intensity at 2 p.m. local time at 110 km altitude and CSES N_e from the same orbit. The shading indicates the lack of statistical significance at the 95% confidence level.

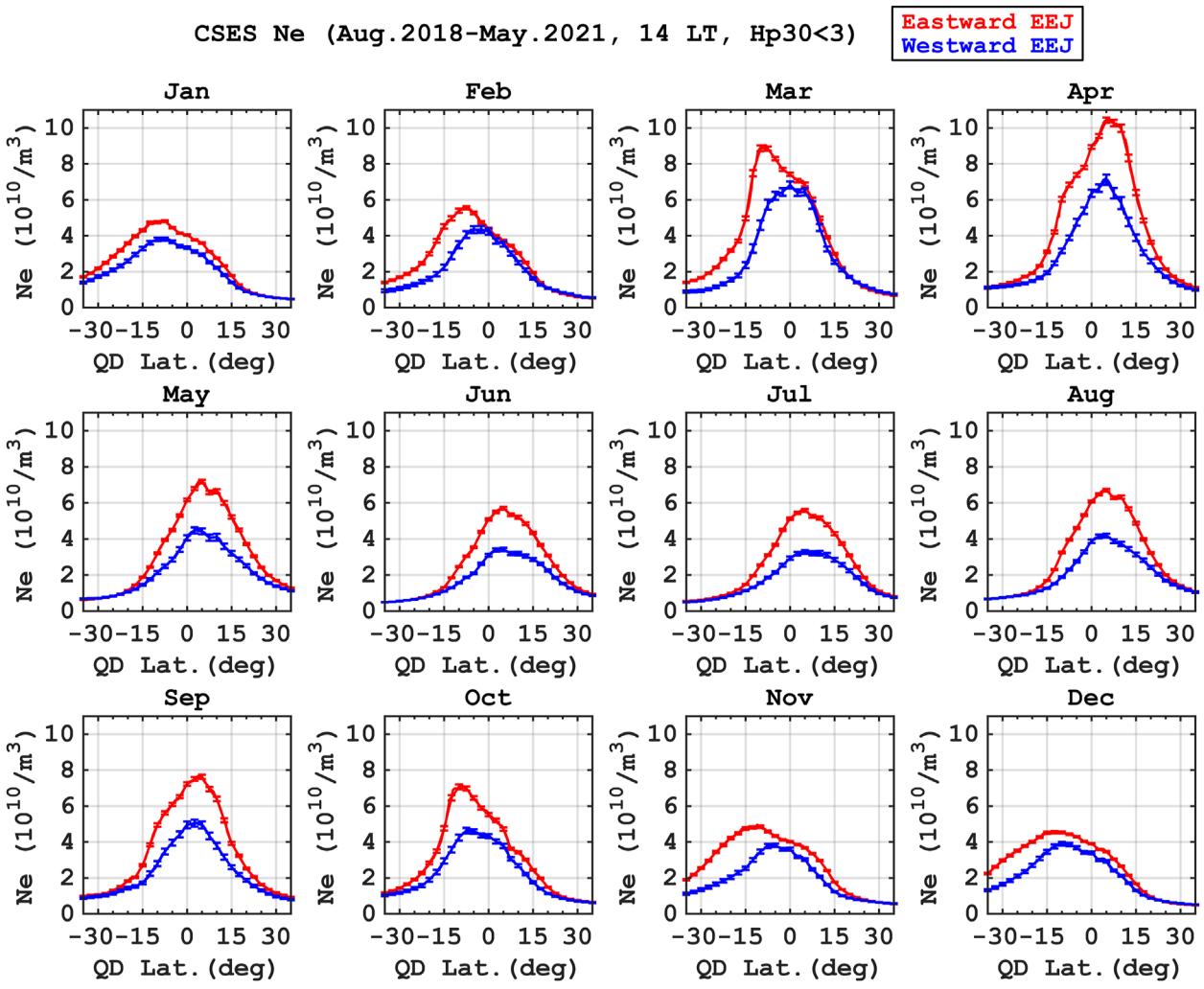

FIGURE 10
Electron density (N_e) at 2 p.m. local time at an altitude of ~510 km observed by the Langmuir probe onboard CSES during times of the eastward and westward equatorial electrojet (EEJ) at 110 km altitude.

components with comparable amplitudes: (1) an eastward-propagating 2–3-day oscillation with zonal wavenumber 1, (2) a westward-propagating 5–6-day oscillation with zonal wavenumber 1, and (3) a zonally-symmetric 14–15-day oscillation. They all can be associated with atmospheric waves that propagate from the lower atmosphere. That is, (1), (2) and (3) can be attributed to the ultra-fast Kelvin wave, quasi-6-day wave, and atmospheric lunar tide, respectively. However, uncertainty remains as to whether (1) and (2) are caused by the direct effect of those waves or by the secondary waves resulting from their nonlinear interactions with migrating tides.

The comparison of the CSES EEJ with the concurrent measurements of neutral winds by ICON/MIGHTI shows that the EEJ intensity at 2 p.m. local time at 110 km altitude is positively and negatively correlated with the magnetic eastward wind in the Hall region (100–115 km) and Pedersen region (120–160 km) over the magnetic equator, respectively (Figure 5). This is consistent with Swarm-ICON/MIGHTI observations including different local times (Yamazaki et al., 2021). The present results exclude the possibility that the correlation between the EEJ and magnetic eastward wind is due to similarity in their local time variations. Also, the dependence of the correlation on QD latitude (Figures 5E,F) is addressed. The results are in agreement with the previous model predictions at the local noon (Yamazaki et al., 2014a).

The longitudinal and seasonal variations of the EEJ are compared with those in the equatorial zonal wind at 109 km as derived from the empirical model of Yamazaki et al. (2023) (Figure 6), which expresses wind velocities as a superposition of contributions by the zonal-mean wind, tides and stationary planetary waves. The longitudinal variation of the EEJ at 2 p.m. local time is dominated by a four-peak pattern during July–September, which can be largely explained by the non-migrating diurnal tide DE3 (Figure 7). During December–January, a two- or three-peak pattern is more evident, which is mainly due to the combined effect of the non-migrating diurnal tides DE3 and DE2 (Figure 8).

The CSES EEJ data are also compared with the *in-situ* electron density (N_e) measurements by the LAP instrument onboard CSES from the same orbit. There is a positive correlation between the EEJ intensity and N_e at low latitudes (below ±20° magnetic latitude) regardless of the season (Figures 9, 10), which can be explained as the effect of the equatorial plasma fountain. The magnitude of the correlation is seasonally dependent. For example, the correlation coefficient R is larger for April–September (0.4–0.7) than for October–March (0.1–0.4) near the magnetic equator. The positive correlation extends to higher latitudes but only in the summer hemisphere. The reduced correlation in the winter hemisphere might be due to the meridional wind, which pushes the plasmas down along the magnetic field line, possibly preventing the plasmas to reach the altitude of the CSES spacecraft (~510 km).

Data availability statement

Publicly available datasets were analyzed in this study. This data can be found here: CSES scalar magnetic field measurements and electron density measurements are available on the website at https://www.leos.ac.cn. Swarm EEJ data are available on the website at https://swarm-diss.eo.esa.int. ICON/MIGHTI neutral wind data are available on the website at https://icon.ssl.berkeley.edu/Data/Data-Product-Matrix. The EEJ data for 2017 and 2018 presented in Figures 6–8 are available on the website https://doi.org/10.5880/GFZ.2.3.2022.003.

Author contributions

YoY: Writing–original draft, Writing–review and editing. CS: Writing–review and editing. CX: Funding acquisition, Writing–review and editing. PA: Data curation, Funding acquisition, Methodology, Writing–review and editing. YaY: Data curation, Writing–review and editing. ZZ: Data curation, Funding acquisition, Writing–review and editing. BH: Data curation, Funding acquisition, Validation, Writing–review and editing. RY: Data curation, Methodology, Validation, Writing–review and editing.

Funding

The author(s) declare that financial support was received for the research, authorship, and/or publication of this article. This work is supported by the Dragon six cooperation 2024–2028 (Project No. 95437), the National Key Research and Development Program of China 2023YFE0117300, and the National Natural Science Foundation of China Grant No. 42274214. This work is also supported by Swarm DISC activities funded by ESA under contract No. 4000109587/13/I-NB.

Acknowledgments

The authors thank the engineering and science teams of the CSES, Swarm and ICON missions. CSES is supported by China National Space Administration (CNSA) and China Earthquake Administration (CEA). The Swarm mission is supported by the European Space Agency (ESA). The ICON mission is supported by National Aeronautics and Space Administration (NASA) Explorers Program (NNG12FA45C and NNG12FA42I).

Conflict of interest

The authors declare that the research was conducted in the absence of any commercial or financial relationships that could be construed as a potential conflict of interest.

The handling editor declared a past collaboration with the author CS at the time of review.

Publisher's note

References

Abdul Hamid, N. S., Liu, H., Uozumi, T., and Yoshikawa, A. (2015). Empirical model of equatorial electrojet based on ground-based magnetometer data during solar minimum in fall. *Earth, planets space* 67, 205–208. doi:10.1186/s40623-015-0373-1

Alken, P. (2020). "Estimating currents and electric fields at low latitudes from satellite magnetic measurements," in *Ionospheric multi-spacecraft analysis tools* (Springer), 233–254.

Alken, P., Chulliat, A., and Maus, S. (2013a). Longitudinal and seasonal structure of the ionospheric equatorial electric field. *J. Geophys. Res. Space Phys.* 118, 1298–1305. doi:10.1029/2012JA018314

Alken, P., and Maus, S. (2007). Spatio-temporal characterization of the equatorial electrojet from CHAMP, Ørsted, and SAC-C satellite magnetic measurements. *J. Geophys. Res. Space Phys.* 112. doi:10.1029/2007JA012524

Alken, P., and Maus, S. (2010). Relationship between the ionospheric eastward electric field and the equatorial electrojet. *Geophys. Res. Lett.* 37. doi:10.1029/2009GL041989

Alken, P., Maus, S., Chulliat, A., Vigneron, P., Sirol, O., and Hulot, G. (2015). Swarm equatorial electric field chain: first results. *Geophys. Res. Lett.* 42, 673–680. doi:10.1002/2014GL062658

Alken, P., Maus, S., Vigneron, P., Sirol, O., and Hulot, G. (2013b). Swarm SCARF equatorial electric field inversion chain. *Earth, Planets Space* 65, 1309–1317. doi:10.5047/eps.2013.09.008

Alken, P., Maute, A., Richmond, A., Vanhamäki, H., and Egbert, G. (2017). An application of principal component analysis to the interpretation of ionospheric current systems. *J. Geophys. Res. Space Phys.* 122, 5687–5708. doi:10.1002/2017JA024051

Anderson, D., Anghel, A., Yumoto, K., Ishitsuka, M., and Kudeki, E. (2002). Estimating daytime vertical ExB drift velocities in the equatorial F-region using ground-based magnetometer observations. *Geophys. Res. Lett.* 29, 37-1–37-4. doi:10.1029/2001GL014562

Balan, N., Liu, L., and Le, H. (2018). A brief review of equatorial ionization anomaly and ionospheric irregularities. *Earth Planet. Phys.* 2, 1–19. doi:10.26464/epp2018025

Blanc, M., and Richmond, A. (1980). The ionospheric disturbance dynamo. *J. Geophys. Res. Space Phys.* 85, 1669–1686. doi:10.1029/JA085iA04p01669

Cain, J., and Sweeney, R. (1972). *POGO observations of the equatorial electrojet. Tech. Rep. X-645-72-299*. Greenbelt, Maryland: Goddard Space Flight Center.

Campbell, W. H. (2003). *Introduction to geomagnetic fields*. Cambridge: Cambridge University Press.

Campbell, W. H., Arora, B. R., and Schiffmacher, E. R. (1993). External Sq currents in the India-Siberia region. *J. Geophys. Res. Space Phys.* 98, 3741–3752. doi:10.1029/92JA02552

Chapman, S. (1931). The absorption and dissociative or ionizing effect of monochromatic radiation in an atmosphere on a rotating earth. *Proc. Phys. Soc.* 43, 26–45. doi:10.1088/0959-5309/43/1/305

Chapman, S. (1951). The equatorial electrojet as detected from the abnormal electric current distribution above huancayo, Peru, and elsewhere. *Arch. Fuer Meteorol. Geophys. Bioklimatol. Ser. A* 4, 368–390. doi:10.1007/bf02246814

Chapman, S., and Rao, K. R. (1965). The H and Z variations along and near the equatorial electrojet in India, Africa and the Pacific. *J. Atmos. Terr. Phys.* 27, 559–581. doi:10.1016/0021-9169(65)90020-6

Chen, C.-H., Liu, J.-Y., Yumoto, K., Lin, C.-H., and Fang, T.-W. (2008). Equatorial ionization anomaly of the total electron content and equatorial electrojet of ground-based geomagnetic field strength. *J. Atmos. Solar-Terrestrial Phys.* 70, 2172–2183. doi:10.1016/j.jastp.2008.09.021

Chen, S. S., Yamazaki, Y., Denardini, C. M., Resende, L. C. A., Chagas, R. A. J., and Stolle, C. (2024). Tidal composition analysis of global Sq current system. *J. Geophys. Res. Space Phys.* 129, e2023JA032382. doi:10.1029/2023JA032382

Chulliat, A., Vigneron, P., and Hulot, G. (2016). First results from the Swarm dedicated ionospheric field inversion chain. *Earth, Planets Space* 68, 104–118. doi:10.1186/s40623-016-0481-6

Colomb, F., Alonso, C., Hofmann, C., and Nollmann, I. (2004). SAC-C mission, an example of international cooperation. *Adv. Space Res.* 34, 2194–2199. doi:10.1016/j.asr.2003.10.039

Davis, R. N., Chen, Y.-W., Miyahara, S., and Mitchell, N. J. (2012). The climatology, propagation and excitation of ultra-fast Kelvin waves as observed by meteor radar, Aura MLS, TRMM and in the Kyushu-GCM. *Atmos. Chem. Phys.* 12, 1865–1879. doi:10.5194/acp-12-1865-2012

Day, K., and Mitchell, N. (2010). The 16-day wave in the Arctic and Antarctic mesosphere and lower thermosphere. *Atmos. Chem. Phys.* 10, 1461–1472. doi:10.5194/acp-10-1461-2010

Dhadly, M. S., Emmert, J. T., Drob, D. P., McCormack, J. P., and Niciejewski, R. J. (2018). Short-term and interannual variations of migrating diurnal and semidiurnal tides in the mesosphere and lower thermosphere. *J. Geophys. Res. Space Phys.* 123, 7106–7123. doi:10.1029/2018JA025748

Dickinson, R. E., Ridley, E., and Roble, R. (1977). Meridional circulation in the thermosphere II. Solstice conditions. *J. Atmos. Sci.* 34, 178–192. doi:10.1175/1520-0469(1977)034<0178:mcitti>2.0.co;2

Doumbia, V., and Grodji, O. D. F. (2016). "On the longitudinal dependence of the equatorial electrojet," in *Ionospheric space weather: longitude and hemispheric dependences and lower atmosphere forcing* (Wiley Online Library), 115–125. doi:10.1002/9781118929216.ch10

Doumouya, V., Cohen, Y., Arora, B., and Yumoto, K. (2003). Local time and longitude dependence of the equatorial electrojet magnetic effects. *J. Atmos. solar-terrestrial Phys.* 65, 1265–1282. doi:10.1016/j.jastp.2003.08.014

Doumouya, V., Vassal, J., Cohen, Y., Fambitakoye, O., and Menvielle, M. (1998). Equatorial electrojet at African longitudes: first results from magnetic measurements. *Ann. Geophys.* 16, 658–666. doi:10.1007/s00585-998-0658-9

Drob, D. P., Emmert, J. T., Meriwether, J. W., Makela, J. J., Doornbos, E., Conde, M., et al. (2015). An update to the Horizontal Wind Model (HWM): the quiet time thermosphere. *Earth Space Sci.* 2, 301–319. doi:10.1002/2014EA000089

Du, J., and Stening, R. J. (1999). Simulating the ionospheric dynamo–II. Equatorial electric fields. *J. Atmos. Solar-Terrestrial Phys.* 61, 925–940. doi:10.1016/S1364-6826(99)00042-5

Eccles, V., Rice, D. D., Sojka, J. J., Valladares, C. E., Bullett, T., and Chau, J. L. (2011). Lunar atmospheric tidal effects in the plasma drifts observed by the Low-Latitude Ionospheric Sensor Network. *J. Geophys. Res. Space Phys.* 116. doi:10.1029/2010JA016282

Elhawary, R., and Forbes, J. (2016). Planetary wave variability of Sq currents. *J. Geophys. Res. Space Phys.* 121, 11–316. doi:10.1002/2016JA023242

England, S., Maus, S., Immel, T., and Mende, S. (2006). Longitudinal variation of the E-region electric fields caused by atmospheric tides. *Geophys. Res. Lett.* 33. doi:10.1029/2006GL027465

Englert, C. R., Harlander, J. M., Brown, C. M., Marr, K. D., Miller, I. J., Stump, J. E., et al. (2017). Michelson interferometer for global high-resolution thermospheric imaging (MIGHTI): instrument design and calibration. *Space Sci. Rev.* 212, 553–584. doi:10.1007/s11214-017-0358-4

Englert, C. R., Harlander, J. M., Marr, K. D., Harding, B. J., Makela, J. J., Fae, T., et al. (2023). Michelson interferometer for global high-resolution thermospheric imaging (MIGHTI) on-orbit wind observations: data analysis and instrument performance. *Space Sci. Rev.* 219, 27. doi:10.1007/s11214-023-00971-1

Fan, Y., Huang, C. M., Zhang, S. D., Huang, K. M., and Gong, Y. (2022). Long-term study of quasi-16-day waves based on ERA5 reanalysis data and EOS MLS observations from 2005 to 2020. *J. Geophys. Res. Space Phys.* 127, e2021JA030030. doi:10.1029/2021JA030030

Forbes, J., Hagan, M., Miyahara, S., Vial, F., Manson, A., Meek, C., et al. (1995). Quasi 16-day oscillation in the mesosphere and lower thermosphere. *J. Geophys. Res. Atmos.* 100, 9149–9163. doi:10.1029/94JD02157

Forbes, J., Zhang, X., Palo, S., Russell, J., Mertens, C., and Mlynczak, M. (2008). Tidal variability in the ionospheric dynamo region. *J. Geophys. Res. Space Phys.* 113. doi:10.1029/2007JA012737

Forbes, J. M. (1981). The equatorial electrojet. *Rev. Geophys.* 19, 469–504. doi:10.1029/RG019i003p00469

Forbes, J. M. (1982). Atmospheric tides: 1. Model description and results for the solar diurnal component. *J. Geophys. Res. Space Phys.* 87, 5222–5240. doi:10.1029/JA087iA07p05222

Forbes, J. M., and Zhang, X. (2015). Quasi-10-day wave in the atmosphere. *J. Geophys. Res. Atmos.* 120, 11–079. doi:10.1002/2015JD023327

Forbes, J. M., Zhang, X., Maute, A., and Hagan, M. E. (2018). Zonally symmetric oscillations of the thermosphere at planetary wave periods. *J. Geophys. Res. Space Phys.* 123, 4110–4128. doi:10.1002/2018JA025258

Forbes, J. M., Zhang, X., Palo, S. E., Russell, J., Mertens, C. J., and Mlynczak, M. (2009). Kelvin waves in stratosphere, mesosphere and lower thermosphere temperatures as observed by TIMED/SABER during 2002–2006. *Earth, planets space* 61, 447–453. doi:10.1186/BF03353161

Forbes, J. M., Zhang, X., Talaat, E. R., and Ward, W. (2003). Nonmigrating diurnal tides in the thermosphere. *J. Geophys. Res. Space Phys.* 108. doi:10.1029/2002JA009262

Friis-Christensen, E., Lühr, H., and Hulot, G. (2006). Swarm: a constellation to study the Earth's magnetic field. *Earth, planets space* 58, 351–358. doi:10.1186/BF03351933

Friis-Christensen, E., Lühr, H., Knudsen, D., and Haagmans, R. (2008). Swarm–an Earth observation mission investigating geospace. *Adv. Space Res.* 41, 210–216. doi:10.1016/j.asr.2006.10.008

Fuller-Rowell, T. (1998). The "thermospheric spoon": a mechanism for the semiannual density variation. *J. Geophys. Res. Space Phys.* 103, 3951–3956. doi:10.1029/97JA03335

Gan, Q., Oberheide, J., and Pedatella, N. M. (2018). Sources, sinks, and propagation characteristics of the quasi 6-day wave and its impact on the residual mean circulation. *J. Geophys. Res. Atmos.* 123, 9152–9170. doi:10.1029/2018JD028553

Gu, S.-Y., Dou, X., Lei, J., Li, T., Luan, X., Wan, W., et al. (2014). Ionospheric response to the ultrafast Kelvin wave in the MLT region. *J. Geophys. Res. Space Phys.* 119, 1369–1380. doi:10.1002/2013JA019086

Gu, S.-Y., Li, T., Dou, X., Wu, Q., Mlynczak, M., and Russell Iii, J. (2013). Observations of quasi-two-day wave by TIMED/SABER and TIMED/TIDI. *J. Geophys. Res. Atmos.* 118, 1624–1639. doi:10.1002/jgrd.50191

Hagan, M., and Forbes, J. (2002). Migrating and nonmigrating diurnal tides in the middle and upper atmosphere excited by tropospheric latent heat release. *J. Geophys. Res. Atmos.* 107, ACL–6. doi:10.1029/2001JD001236

Hagan, M., and Forbes, J. M. (2003). Migrating and nonmigrating semidiurnal tides in the upper atmosphere excited by tropospheric latent heat release. *J. Geophys. Res. Space Phys.* 108. doi:10.1029/2002JA009466

Hagan, M., Roble, R., and Hackney, J. (2001). Migrating thermospheric tides. *J. Geophys. Res. Space Phys.* 106, 12739–12752. doi:10.1029/2000JA000344

Harding, B. J., Makela, J. J., Englert, C. R., Marr, K. D., Harlander, J. M., England, S. L., et al. (2017). The MIGHTI wind retrieval algorithm: description and verification. *Space Sci. Rev.* 212, 585–600. doi:10.1007/s11214-017-0359-3

Harding, B. J., Wu, Y.-J. J., Alken, P., Yamazaki, Y., Triplett, C. C., Immel, T. J., et al. (2022). Impacts of the January 2022 Tonga volcanic eruption on the ionospheric dynamo: ICON-MIGHTI and Swarm observations of extreme neutral winds and currents. *Geophys. Res. Lett.* 49, e2022GL098577. doi:10.1029/2022GL098577

[Dataset] Harding, B. J., Englert, C. R., Harlander, J. M., Marr, K. D., Makela, J. M., Brown, C. M., et al. (2023). ICON Michelson interferometer for global high-resolution thermospheric imaging wind vectors green (version 05). *NASA Space Phys. Data Facil.* doi:10.48322/vtce-7y29

He, M., Chau, J. L., Forbes, J. M., Zhang, X., Englert, C. R., Harding, B. J., et al. (2021). Quasi-2-day wave in low-latitude atmospheric winds as viewed from the ground and space during January–March, 2020. *Geophys. Res. Lett.* 48, e2021GL093466. doi:10.1029/2021GL093466

Heelis, R. (2004). Electrodynamics in the low and middle latitude ionosphere: a tutorial. *J. Atmos. Solar-Terrestrial Phys.* 66, 825–838. doi:10.1016/j.jastp.2004.01.034

Hirono, M. (1950). On the influence of the hall current to the electrical conductivity of the ionosphere. i. *J. geomagnetism Geoelectr.* 2, 1–8. doi:10.5636/jgg.2.1

Hysell, D., Chau, J., and Fesen, C. (2002). Effects of large horizontal winds on the equatorial electrojet. *J. Geophys. Res. Space Phys.* 107, SIA–27. doi:10.1029/2001JA000217

Immel, T. J., England, S., Mende, S., Heelis, R., Englert, C., Edelstein, J., et al. (2018). The ionospheric connection explorer mission: mission goals and design. *Space Sci. Rev.* 214, 13–36. doi:10.1007/s11214-017-0449-2

Jadhav, A., Gurubaran, S., Ghodpage, R., Patil, P., and Batista, P. P. (2023). Imprint of mesospheric quasi 2-day wave in the ground geomagnetic field variations at low latitudes. *J. Geophys. Res. Space Phys.* 128, e2022JA031098. doi:10.1029/2022JA031098

Jadhav, A., Yamazaki, Y., Gurubaran, S., Stolle, C., Conte, F., Batista, P. P., et al. (2024). Quasi 16-day wave signatures in the interhemispheric field aligned currents: a new perspective toward atmosphere-ionosphere coupling. *J. Geophys. Res. Space Phys.* 129. doi:10.1029/2023JA032383

Jadhav, G., Rajaram, M., and Rajaram, R. (2002). A detailed study of equatorial electrojet phenomenon using Ørsted satellite observations. *J. Geophys. Res. Space Phys.* 107, SIA–12. doi:10.1029/2001JA000183

Jin, H., Miyoshi, Y., Fujiwara, H., and Shinagawa, H. (2008). Electrodynamics of the formation of ionospheric wave number 4 longitudinal structure. *J. Geophys. Res. Space Phys.* 113. doi:10.1029/2008JA013301

Jones, Jr. M., Emmert, J., Drob, D., Picone, J., and Meier, R. (2018). Origins of the thermosphere-ionosphere semiannual oscillation: reformulating the "thermospheric spoon" mechanism. *J. Geophys. Res. Space Phys.* 123, 931–954. doi:10.1002/2017JA024861

Jones, M., Emmert, J., Drob, D., and Siskind, D. (2017). Middle atmosphere dynamical sources of the semiannual oscillation in the thermosphere and ionosphere. *Geophys. Res. Lett.* 44, 12–21. doi:10.1002/2016GL071741

Jones, M., Forbes, J., Hagan, M., and Maute, A. (2013). Non-migrating tides in the ionosphere-thermosphere: *in situ* versus tropospheric sources. *J. Geophys. Res. Space Phys.* 118, 2438–2451. doi:10.1002/jgra.50257

Kawano-Sasaki, K., and Miyahara, S. (2008). A study on three-dimensional structures of the ionospheric dynamo currents induced by the neutral winds simulated by the Kyushu-GCM. *J. Atmos. Solar-Terrestrial Phys.* 70, 1549–1562. doi:10.1016/j.jastp.2008.05.004

Kikuchi, T., Hashimoto, K. K., and Nozaki, K. (2008). Penetration of magnetospheric electric fields to the equator during a geomagnetic storm. *J. Geophys. Res. Space Phys.* 113. doi:10.1029/2007JA012628

Kumar, S., Veenadhari, B., Ram, S. T., Su, S.-Y., and Kikuchi, T. (2016). Possible relationship between the equatorial electrojet (EEJ) and daytime vertical EB drift velocities in F region from ROCSAT observations. *Adv. Space Res.* 58, 1168–1176. doi:10.1016/j.asr.2016.06.009

Laundal, K. M., and Richmond, A. D. (2017). Magnetic coordinate systems. *Space Sci. Rev.* 206, 27–59. doi:10.1007/s11214-016-0275-y

Le Huy, M., and Amory-Mazaudier, C. (2005). Magnetic signature of the ionospheric disturbance dynamo at equatorial latitudes. *J. Geophys. Res. Space Phys.* 110. doi:10.1029/2007JA012686

Lieberman, R., Riggin, D., Franke, S., Manson, A., Meek, C., Nakamura, T., et al. (2003). The 6.5-day wave in the mesosphere and lower thermosphere: evidence for baroclinic/barotropic instability. *J. Geophys. Res. Atmos.* 108. doi:10.1029/2002JD003349

Lin, C., Liu, J., Fang, T.-W., Chang, P., Tsai, H., Chen, C., et al. (2007). Motions of the equatorial ionization anomaly crests imaged by FORMOSAT-3/COSMIC. *Geophys. Res. Lett.* 34. doi:10.1029/2007GL030741

Lindzen, R. S., and Chapman, S. (1969). Atmospheric tides. *Space Sci. Rev.* 10, 3–188. doi:10.1007/BF00171584

Liu, H.-L. (2014). "WACCM-X simulation of tidal and planetary wave variability in the upper atmosphere," in *Modeling the ionosphere–thermosphere system* (Wiley Online Library), 181–199. doi:10.1002/9781118704417.ch16

Lühr, H., Alken, P., and Zhou, Y.-L. (2021a) "The equatorial electrojet," in *Ionosphere dynamics and applications*, 281–299doi. doi:10.1002/9781119815617.ch12

Lühr, H., and Manoj, C. (2013). The complete spectrum of the equatorial electrojet related to solar tides: CHAMP observations. *Ann. Geophys.* 31, 1315–1331. doi:10.5194/angeo-31-1315-2013

Lühr, H., Maus, S., and Rother, M. (2004). Noon-time equatorial electrojet: its spatial features as determined by the CHAMP satellite. *J. Geophys. Res. Space Phys.* 109. doi:10.1029/2002JA009656

Lühr, H., Rother, M., Häusler, K., Alken, P., and Maus, S. (2008). The influence of nonmigrating tides on the longitudinal variation of the equatorial electrojet. *J. Geophys. Res. Space Phys.* 113. doi:10.1029/2008JA013064

Lühr, H., Siddiqui, T. A., and Maus, S. (2012). Global characteristics of the lunar tidal modulation of the equatorial electrojet derived from CHAMP observations. *Ann. Geophys. Copernic. Publ. Göttingen, Ger.* 30, 527–536. doi:10.5194/angeo-30-527-2012

Lühr, H., Zhou, Y.-L., and Alken, P. (2021b). Short-term variability of equatorial electrojet modulation by solar tidal and planetary waves, as derived from the swarm constellation. *J. Geophys. Res. Space Phys.* 126, e2020JA028884. doi:10.1029/2020JA028884

Manoj, C., Maus, S., Lühr, H., and Alken, P. (2008). Penetration characteristics of the interplanetary electric field to the daytime equatorial ionosphere. *J. Geophys. Res. Space Phys.* 113. doi:10.1029/2008JA013381

Marriott, R., Richmond, A., and Venkateswaran, S. (1979). The quiet-time equatorial electrojet and counter-electrojet. *J. geomagnetism Geoelectr.* 31, 311–340. doi:10.5636/jgg.31.311

Matsushita, S., and Maeda, H. (1965). On the geomagnetic solar quiet daily variation field during the IGY. *J. Geophys. Res.* 70, 2535–2558. doi:10.1029/JZ070i011p02535

Matzka, J., Siddiqui, T. A., Lilienkamp, H., Stolle, C., and Veliz, O. (2017). Quantifying solar flux and geomagnetic main field influence on the equatorial ionospheric current system at the geomagnetic observatory Huancayo. *J. Atmos. Solar-Terrestrial Phys.* 163, 120–125. doi:10.1016/j.jastp.2017.04.014

Matzka, J., Stolle, C., Yamazaki, Y., Bronkalla, O., and Morschhauser, A. (2021). The geomagnetic Kp index and derived indices of geomagnetic activity. *Space weather.* 19, e2020SW002641. doi:10.1029/2020SW002641

Maute, A. (2021). "The middle-and low-latitude neutral wind dynamo," in *Upper atmosphere dynamics and energetics*. Editors W. Wang, Y. Zhang, and L. J. Paxton (Wiley Online Library), 79–104. doi:10.1002/9781119815631.ch5

Mayaud, P. (1977). The equatorial counter-electrojet–a review of its geomagnetic aspects. *J. Atmos. Terr. Phys.* 39, 1055–1070. doi:10.1016/0021-9169(77)90014-9

McLandress, C., Shepherd, G. G., and Solheim, B. H. (1996). Satellite observations of thermospheric tides: results from the wind imaging interferometer on UARS. *J. Geophys. Res. Atmos.* 101, 4093–4114. doi:10.1029/95JD03359

Miyoshi, Y., and Fujiwara, H. (2003). Day-to-day variations of migrating diurnal tide simulated by a GCM from the ground surface to the exobase. *Geophys. Res. Lett.* 30. doi:10.1029/2003GL017695

Miyoshi, Y., and Yamazaki, Y. (2020). Excitation mechanism of ionospheric 6-day oscillation during the 2019 September sudden stratospheric warming event. *J. Geophys. Res. Space Phys.* 125, e2020JA028283. doi:10.1029/2020JA028283

Nishida, A. (1968). Coherence of geomagnetic DP 2 fluctuations with interplanetary magnetic variations. *J. Geophys. Res.* 73, 5549–5559. doi:10.1029/JA073i017p05549

Oberheide, J., Forbes, J., Zhang, X., and Bruinsma, S. (2011). Climatology of upward propagating diurnal and semidiurnal tides in the thermosphere. *J. Geophys. Res. Space Phys.* 116. doi:10.1029/2011JA016784

Oberheide, J., Lu, X., and Aggarwal, D. (2024). A statistical study of the day-to-day variability of diurnal and semidiurnal tides in the ionospheric dynamo region

from MIGHTI/ICON observations. *J. Geophys. Res. Space Phys.* 129, e2024JA032619. doi:10.1029/2024JA032619

Oberheide, J., Wu, Q., Killeen, T., Hagan, M., and Roble, R. (2006). Diurnal nonmigrating tides from TIMED Doppler Interferometer wind data: monthly climatologies and seasonal variations. *J. Geophys. Res. Space Phys.* 111. doi:10.1029/2005JA011491

Owolabi, C., Ruan, H., Yamazaki, Y., Kaka, R., Akinola, O., and Yoshikawa, A. (2022). Ionospheric current variations by empirical orthogonal function analysis: solar activity dependence and longitudinal differences. *J. Geophys. Res. Space Phys.* 127, e2021JA029903. doi:10.1029/2021JA029903

Pancheva, D. V., Mukhtarov, P. J., and Andonov, B. A. (2007). Zonally symmetric oscillations in the Northern Hemisphere stratosphere during the winter of 2003–2004. *Geophys. Res. Lett.* 34. doi:10.1029/2006GL028666

Pandey, K., Chakrabarty, D., and Sekar, R. (2018). Critical evaluation of the impact of disturbance dynamo on equatorial ionosphere during daytime. *J. Geophys. Res. Space Phys.* 123, 9762–9774. doi:10.1029/2018JA025686

Pandey, K., Sekar, R., Chakrabarty, D., and Anandarao, B. (2021). Investigation on longitudinal and decadal variations of the equatorial electrojet using a physical model. *Adv. Space Res.* 68, 182–200. doi:10.1016/j.asr.2021.02.040

Park, J., Lühr, H., Kunze, M., Fejer, B. G., and Min, K. W. (2012). Effect of sudden stratospheric warming on lunar tidal modulation of the equatorial electrojet. *J. Geophys. Res. Space Phys.* 117. doi:10.1029/2011JA017351

Pedatella, N., Forbes, J., and Richmond, A. (2011). Seasonal and longitudinal variations of the solar quiet (Sq) current system during solar minimum determined by CHAMP satellite magnetic field observations. *J. Geophys. Res. Space Phys.* 116. doi:10.1029/2010JA016289

Pedatella, N., Hagan, M., and Maute, A. (2012a). The comparative importance of DE3, SE2, and SPW4 on the generation of wavenumber-4 longitude structures in the low-latitude ionosphere during September equinox. *Geophys. Res. Lett.* 39. doi:10.1029/2012GL053643

Pedatella, N., Liu, H.-L., and Richmond, A. (2012b). Atmospheric semidiurnal lunar tide climatology simulated by the whole atmosphere community climate model. *J. Geophys. Res. Space Phys.* 117. doi:10.1029/2012JA017792

Qin, Y., Gu, S.-Y., Teng, C.-K.-M., Dou, X.-K., Yu, Y., and Li, N. (2021). Comprehensive study of the climatology of the quasi-6-day wave in the MLT region based on Aura/MLS observations and SD-WACCM-X simulations. *J. Geophys. Res. Space Phys.* 126, e2020JA028454. doi:10.1029/2020JA028454

Rabiu, A., Onwumechili, C., Nagarajan, N., and Yumoto, K. (2013). Characteristics of equatorial electrojet over India determined from a thick current shell model. *J. Atmos. solar-terrestrial Phys.* 92, 105–115. doi:10.1016/j.jastp.2012.10.014

Raghavarao, R., and Anandarao, B. (1987). Equatorial electrojet and the counter-electrojet. *Indian J. Radio Space Phys.* 16, 54–75.

Rastogi, R. (1962). Longitudinal variation in the equatorial electrojet. *J. Atmos. Terr. Phys.* 24, 1031–1040. doi:10.1016/0021-9169(62)90158-7

Rastogi, R. (1977). Geomagnetic storms and electric fields in the equatorial ionosphere. *Nature* 268, 422–424. doi:10.1038/268422a0

Rastogi, R. (1989). "The equatorial electrojet: magnetic and ionospheric effects," in *Geomagnetism*. Editor J. A. Jacobs (Academic Press), 3, 461–525.

Rastogi, R., and Klobuchar, J. (1990). Ionospheric electron content within the equatorial F_2 layer anomaly belt. *J. Geophys. Res. Space Phys.* 95, 19045–19052. doi:10.1029/JA095iA11p19045

Rastogi, R., and Trivedi, N. B. (1970). Luni-solar tides in H at stations within the equatorial electrojet. *Planet. Space Sci.* 18, 367–377. doi:10.1016/0032-0633(70)90174-1

Reddy, C. A. (1989). "The equatorial electrojet," in *Quiet daily geomagnetic fields* (Basel: Birkhäuser Verlag), 485–508. doi:10.1007/978-3-0348-9280-3_11

Reigber, C., Lühr, H., and Schwintzer, P. (2002). CHAMP mission status. *Adv. space Res.* 30, 129–134. doi:10.1016/S0273-1177(02)00276-4

Ren, Z., Wan, W., Xiong, J., and Liu, L. (2010). Simulated wave number 4 structure in equatorial F-region vertical plasma drifts. *J. Geophys. Res. Space Phys.* 115. doi:10.1029/2009JA014746

Richmond, A. (1973). Equatorial electrojet–I. Development of a model including winds and instabilities. *J. Atmos. Terr. Phys.* 35, 1083–1103. doi:10.1016/0021-9169(73)90007-X

Richmond, A. D. (1995). "Ionospheric electrodynamics," in *Handbook of atmospheric electrodynamics* (Boca Raton, FL: CRC Press), 249–290.

Richmond, A. D. (2011). "Electrodynamics of ionosphere-thermosphere coupling," in *Aeronomy of the earth's atmosphere and ionosphere* (Springer), 191–201. doi:10.1007/978-94-007-0326-1

Rigoti, A., Fh, C., Nb, T., and AL, P. (1999). Characteristics of the equatorial electrojet determined from an array of magnetometers in N-NE Brazil. *Earth, planets space* 51, 115–128. doi:10.1186/BF03352216

Rishbeth, H. (1998). How the thermospheric circulation affects the ionospheric F2-layer. *J. Atmos. Solar-Terrestrial Phys.* 60, 1385–1402. doi:10.1016/S1364-6826(98)00062-5

Rush, C., and Richmond, A. (1973). The relationship between the structure of the equatorial anomaly and the strength of the equatorial electrojet. *J. Atmos. Terr. Phys.* 35, 1171–1180. doi:10.1016/0021-9169(73)90013-5

Shen, X., Zhang, X., Yuan, S., Wang, L., Cao, J., Huang, J., et al. (2018). The state-of-the-art of the China Seismo-Electromagnetic Satellite mission. *Sci. China Technol. Sci.* 61, 634–642. doi:10.1007/s11431-018-9242-0

Siddiqui, T., Yamazaki, Y., Stolle, C., Maute, A., Laštovička, J., Edemskiy, I., et al. (2021). Understanding the total electron content variability over Europe during 2009 and 2019 SSWs. *J. Geophys. Res. Space Phys.* 126, e2020JA028751. doi:10.1029/2020JA028751

Siddiqui, T. A., Stolle, C., Lühr, H., and Matzka, J. (2015). On the relationship between weakening of the northern polar vortex and the lunar tidal amplification in the equatorial electrojet. *J. Geophys. Res. Space Phys.* 120, 10006–10019. doi:10.1002/2015JA021683

Siddiqui, T. A., Yamazaki, Y., Stolle, C., Lühr, H., Matzka, J., Maute, A., et al. (2018). Dependence of lunar tide of the equatorial electrojet on the wintertime polar vortex, solar flux, and QBO. *Geophys. Res. Lett.* 45, 3801–3810. doi:10.1029/2018GL077510

Soares, G., Yamazaki, Y., Matzka, J., Pinheiro, K., Morschhauser, A., Stolle, C., et al. (2018). Equatorial counter electrojet longitudinal and seasonal variability in the American sector. *J. Geophys. Res. Space Phys.* 123, 9906–9920. doi:10.1029/2018JA025968

Soares, G., Yamazaki, Y., Matzka, J., Pinheiro, K., Stolle, C., Alken, P., et al. (2019). Longitudinal variability of the equatorial counter electrojet during the solar cycle 24. *Studia Geophys. Geod.* 63, 304–319. doi:10.1007/s11200-018-0286-0

Soares, G., Yamazaki, Y., Morschhauser, A., Matzka, J., Pinheiro, K. J., Stolle, C., et al. (2022). Using principal component analysis of satellite and ground magnetic data to model the equatorial electrojet and derive its tidal composition. *J. Geophys. Res. Space Phys.* 127, e2022JA030691. doi:10.1029/2022JA030691

Stening, R. (2003). Space weather in the equatorial ionosphere. *Space Sci. Rev.* 107, 263–271. doi:10.1023/A:1025544310773

Stolle, C., Manoj, C., Lühr, H., Maus, S., and Alken, P. (2008). Estimating the daytime equatorial ionization anomaly strength from electric field proxies. *J. Geophys. Res. Space Phys.* 113. doi:10.1029/2007JA012781

Stolle, C., Michaelis, I., Xiong, C., Rother, M., Usbeck, T., Yamazaki, Y., et al. (2021). Observing Earth's magnetic environment with the GRACE-FO mission. *Earth, Planets Space* 73, 51–21. doi:10.1186/s40623-021-01364-w

Sugiura, M., and Poros, D. (1969). An improved model equatorial electrojet with a meridional current system. *J. Geophys. Res.* 74, 4025–4034. doi:10.1029/JA074i016p04025

Sun, R., Gu, S.-Y., Dou, X., Qin, Y., and Wei, Y. (2024). Different response of the ionospheric TEC and EEJ to ultra-fast Kelvin waves in the mesosphere and lower thermosphere. *Space weather.* 22, e2023SW003699. doi:10.1029/2023SW003699

Takeda, M. (2002a). Features of global geomagnetic Sq field from 1980 to 1990. *J. Geophys. Res. Space Phys.* 107, SIA–4. doi:10.1029/2001JA009210

Takeda, M. (2002b). The correlation between the variation in ionospheric conductivity and that of the geomagnetic Sq field. *J. Atmos. Solar-Terrestrial Phys.* 64, 1617–1621. doi:10.1016/S1364-6826(02)00140-2

Takeda, M., and Araki, T. (1985). Electric conductivity of the ionosphere and nocturnal currents. *J. Atmos. Terr. Phys.* 47, 601–609. doi:10.1016/0021-9169(85)90043-1

Tapping, K. (2013). The 10.7 cm solar radio flux ($F_{10.7}$). *Space weather.* 11, 394–406. doi:10.1002/swe.20064

Tarpley, J. (1970). The ionospheric wind dynamo–I: lunar tide. *Planet. Space Sci.* 18, 1075–1090. doi:10.1016/0032-0633(70)90109-1

Truskowski, A. O., Forbes, J. M., Zhang, X., and Palo, S. E. (2014). New perspectives on thermosphere tides: 1. Lower thermosphere spectra and seasonal-latitudinal structures. *Earth, Planets Space* 66, 1–17. doi:10.1186/s40623-014-0136-4

Tulasi Ram, S., Su, S.-Y., and Liu, C. (2009). FORMOSAT-3/COSMIC observations of seasonal and longitudinal variations of equatorial ionization anomaly and its interhemispheric asymmetry during the solar minimum period. *J. Geophys. Res. Space Phys.* 114. doi:10.1029/2008JA013880

Venkatesh, K., Fagundes, P. R., Prasad, D. V., Denardini, C. M., De Abreu, A., De Jesus, R., et al. (2015). Day-to-day variability of equatorial electrojet and its role on the day-to-day characteristics of the equatorial ionization anomaly over the Indian and Brazilian sectors. *J. Geophys. Res. Space Phys.* 120, 9117–9131. doi:10.1002/2015JA021307

Vial, F., and Forbes, J. (1994). Monthly simulations of the lunar semi-diurnal tide. *J. Atmos. Terr. Phys.* 56, 1591–1607. doi:10.1016/0021-9169(94)90089-2

Wan, W., Ren, Z., Ding, F., Xiong, J., Liu, L., Ning, B., et al. (2012). A simulation study for the couplings between DE3 tide and longitudinal WN4 structure in the thermosphere and ionosphere. *J. Atmos. solar-terrestrial Phys.* 90, 52–60. doi:10.1016/j.jastp.2012.04.011

Wu, Q., Ortland, D., Killeen, T., Roble, R., Hagan, M., Liu, H.-L., et al. (2008a). Global distribution and interannual variations of mesospheric and lower thermospheric neutral wind diurnal tide: 1. Migrating tide. *J. Geophys. Res. Space Phys.* 113. doi:10.1029/2007JA012542

Wu, Q., Ortland, D., Killeen, T., Roble, R., Hagan, M., Liu, H.-L., et al. (2008b). Global distribution and interannual variations of mesospheric and lower thermospheric neutral wind diurnal tide: 2. Nonmigrating tide. *J. Geophys. Res. Space Phys.* 113. doi:10.1029/2007JA012543

Xiong, C., Lühr, H., and Fejer, B. G. (2016a). The response of equatorial electrojet, vertical plasma drift, and thermospheric zonal wind to enhanced solar wind input. *J. Geophys. Res. Space Phys.* 121, 5653–5663. doi:10.1002/2015JA022133

Xiong, C., Lühr, H., and Ma, S. (2013). The magnitude and inter-hemispheric asymmetry of equatorial ionization anomaly-based on CHAMP and GRACE observations. *J. Atmos. Solar-Terrestrial Phys.* 105, 160–169. doi:10.1016/j.jastp.2013.09.010

Xiong, C., Zhou, Y.-L., Lühr, H., and Ma, S.-Y. (2016b). Diurnal evolution of the F region electron density local time gradient at low and middle latitudes resolved by the Swarm constellation. *J. Geophys. Res. Space Phys.* 121, 9075–9089. doi:10.1002/2016JA023034

Yamada, Y. (2009). Horizontal structure of the geomagnetic 2 day variation. *J. Geophys. Res. Space Phys.* 114. doi:10.1029/2009JA014307

Yamazaki, Y. (2013). Large lunar tidal effects in the equatorial electrojet during northern winter and its relation to stratospheric sudden warming events. *J. Geophys. Res. Space Phys.* 118, 7268–7271. doi:10.1002/2013JA019215

Yamazaki, Y. (2022). Solar and lunar daily geomagnetic variations and their equivalent current systems observed by Swarm. *Earth, Planets Space* 74, 99. doi:10.1186/s40623-022-01656-9

Yamazaki, Y. (2023). A method to derive Fourier–wavelet spectra for the characterization of global-scale waves in the mesosphere and lower thermosphere and its MATLAB and Python software (fourierwavelet v1. 1). *Geosci. Model Dev.* 16, 4749–4766. doi:10.5194/gmd-16-4749-2023

Yamazaki, Y., Harding, B., Stolle, C., and Matzka, J. (2021). Neutral wind profiles during periods of eastward and westward equatorial electrojet. *Geophys. Res. Lett.* 48, e2021GL093567. doi:10.1029/2021GL093567

Yamazaki, Y., Harding, B. J., Qiu, L., Stolle, C., Siddiqui, T. A., Miyoshi, Y., et al. (2023). Monthly climatologies of zonal-mean and tidal winds in the thermosphere as observed by ICON/MIGHTI during April 2020–March 2022. *Earth Space Sci.* 10, e2023EA002962. doi:10.1029/2023EA002962

Yamazaki, Y., and Kosch, M. J. (2015). The equatorial electrojet during geomagnetic storms and substorms. *J. Geophys. Res. Space Phys.* 120, 2276–2287. doi:10.1002/2014JA020773

Yamazaki, Y., Matthias, V., Miyoshi, Y., Stolle, C., Siddiqui, T., Kervalishvili, G., et al. (2020a)). September 2019 antarctic sudden stratospheric warming: quasi-6-day wave burst and ionospheric effects. *Geophys. Res. Lett.* 47, e2019GL086577. doi:10.1029/2019GL086577

Yamazaki, Y., Matzka, J., Stolle, C., Kervalishvili, G., Rauberg, J., Bronkalla, O., et al. (2022). Geomagnetic activity index Hpo. *Geophys. Res. Lett.* 49, e2022GL098860. doi:10.1029/2022GL098860

Yamazaki, Y., and Maute, A. (2017). Sq and EEJ–A review on the daily variation of the geomagnetic field caused by ionospheric dynamo currents. *Space Sci. Rev.* 206, 299–405. doi:10.1007/s11214-016-0282-z

Yamazaki, Y., Miyoshi, Y., Xiong, C., Stolle, C., Soares, G., and Yoshikawa, A. (2020b). Whole atmosphere model simulations of ultrafast Kelvin wave effects in the ionosphere and thermosphere. *J. Geophys. Res. Space Phys.* 125, e2020JA027939. doi:10.1029/2020JA027939

Yamazaki, Y., Richmond, A., Maute, A., Liu, H.-L., Pedatella, N., and Sassi, F. (2014a). On the day-to-day variation of the equatorial electrojet during quiet periods. *J. Geophys. Res. Space Phys.* 119, 6966–6980. doi:10.1002/2014JA020243

Yamazaki, Y., Richmond, A., and Yumoto, K. (2012). Stratospheric warmings and the geomagnetic lunar tide: 1958–2007. *J. Geophys. Res. Space Phys.* 117. doi:10.1029/2012JA017514

Yamazaki, Y., Richmond, A. D., Maute, A., Wu, Q., Ortland, D. A., Yoshikawa, A., et al. (2014b). Ground magnetic effects of the equatorial electrojet simulated by the TIE-GCM driven by TIMED satellite data. *J. Geophys. Res. Space Phys.* 119, 3150–3161. doi:10.1002/2013JA019487

Yamazaki, Y., Stolle, C., Matzka, J., and Alken, P. (2018). Quasi-6-day wave modulation of the equatorial electrojet. *J. Geophys. Res. Space Phys.* 123, 4094–4109. doi:10.1029/2018JA025365

Yamazaki, Y., Stolle, C., Matzka, J., Siddiqui, T. A., Lühr, H., and Alken, P. (2017). Longitudinal variation of the lunar tide in the equatorial electrojet. *J. Geophys. Res. Space Phys.* 122, 12–445. doi:10.1002/2017JA024601

Yamazaki, Y., Yumoto, K., Uozumi, T., Abe, S., Cardinal, M., McNamara, D., et al. (2010). Reexamination of the S_q-EEJ relationship based on extended magnetometer networks in the east Asian region. *J. Geophys. Res. Space Phys.* 115. doi:10.1029/2010JA015339

Yan, R., Guan, Y., Miao, Y., Zhima, Z., Xiong, C., Zhu, X., et al. (2022). The regular features recorded by the Langmuir probe onboard the low earth polar orbit satellite CSES. *J. Geophys. Res. Space Phys.* 127, e2021JA029289. doi:10.1029/2021JA029289

Yan, R., Guan, Y., Shen, X., Huang, J., Zhang, X., Liu, C., et al. (2018). The Langmuir Probe onboard CSES: data inversion analysis method and first results. *Earth Planet. Phys.* 2, 1–10. doi:10.26464/epp2018046

Yan, R., Zhima, Z., Xiong, C., Shen, X., Huang, J., Guan, Y., et al. (2020). Comparison of electron density and temperature from the CSES satellite with other space-borne and ground-based observations. *J. Geophys. Res. Space Phys.* 125, e2019JA027747. doi:10.1029/2019JA027747

Yang, Y., Zhou, B., Hulot, G., Olsen, N., Wu, Y., Xiong, C., et al. (2021). CSES high precision magnetometer data products and example study of an intense geomagnetic storm. *J. Geophys. Res. Space Phys.* 126, e2020JA028026. doi:10.1029/2020JA028026

Yizengaw, E., Moldwin, M. B., Zesta, E., Magoun, M., Pradipta, R., Biouele, C., et al. (2016). Response of the equatorial ionosphere to the geomagnetic DP 2 current system. *Geophys. Res. Lett.* 43, 7364–7372. doi:10.1002/2016GL070090

Yue, J., Wang, W., Richmond, A. D., and Liu, H.-L. (2012). Quasi-two-day wave coupling of the mesosphere and lower thermosphere-ionosphere in the TIME-GCM: two-day oscillations in the ionosphere. *J. Geophys. Res. Space Phys.* 117. doi:10.1029/2012JA017815

Yue, X., Schreiner, W. S., Kuo, Y.-H., and Lei, J. (2015). Ionosphere equatorial ionization anomaly observed by GPS radio occultations during 2006–2014. *J. Atmos. Solar-Terrestrial Phys.* 129, 30–40. doi:10.1016/j.jastp.2015.04.004

Zhang, J. T., and Forbes, J. M. (2013). Lunar tidal winds between 80 and 110 km from UARS/HRDI wind measurements. *J. Geophys. Res. Space Phys.* 118, 5296–5304. doi:10.1002/jgra.50420

Zhang, K., Wang, H., Song, H., Zhong, Y., Xia, H., Sun, Y., et al. (2024). The seasonal dependence of the unexpected afternoon westward equatorial electrojet during quiet time. *J. Geophys. Res. Space Phys.* 129, e2023JA032372. doi:10.1029/2023JA032372

Zhang, X., Forbes, J. M., and Hagan, M. E. (2010). Longitudinal variation of tides in the MLT region: 2. Relative effects of solar radiative and latent heating. *J. Geophys. Res. Space Phys.* 115. doi:10.1029/2009JA014898

Zhao, X., Ning, B., Zhang, M.-L., and Hu, L. (2017). Comparison of the ionospheric F2 peak height between ionosonde measurements and IRI2016 predictions over China. *Adv. Space Res.* 60, 1524–1531. doi:10.1016/j.asr.2017.06.056

Zhou, X., Yue, X., Yu, Y., and Hu, L. (2022a). Day-to-day variability of the MLT DE3 using joint analysis on observations from TIDI-TIMED and a meteor radar meridian chain. *J. Geophys. Res. Atmos.* 127, e2021JD035794. doi:10.1029/2021JD035794

Zhou, Y., Yang, Y., Zhu, J., Xiong, C., Wang, F., Zhima, Z., et al. (2022b). Characteristics of equatorial electrojet revealed by CSES observation. *Chin. J. Geophys.* 65, 4141–4151. doi:10.6038/cjg2022Q0288

Zhou, Y.-L., Lühr, H., Xu, H.-w., and Alken, P. (2018). Comprehensive analysis of the counter equatorial electrojet: average properties as deduced from CHAMP observations. *J. Geophys. Res. Space Phys.* 123, 5159–5181. doi:10.1029/2018JA025526

Zhu, K., Yan, R., Xiong, C., Zheng, L., Zhima, Z., Shen, X., et al. (2023). Annual and semi-annual variations of electron density in the topside ionosphere observed by CSES. *Front. Earth Sci.* 11, 1098483. doi:10.3389/feart.2023.1098483

frontiers | Frontiers in Astronomy and Space Sciences

TYPE Original Research
PUBLISHED 26 November 2024
DOI 10.3389/fspas.2024.1466909

OPEN ACCESS

EDITED BY
Jorge Luis Chau,
Leibniz Institute of Atmospheric Physics (LG), Germany

REVIEWED BY
Enrique Rojas Villalba,
Massachusetts Institute of Technology, United States
Jean-Pierre St-Maurice,
University of Saskatchewan, Canada

*CORRESPONDENCE
Y. S. Dimant,
dimant@bu.edu

RECEIVED 18 July 2024
ACCEPTED 22 October 2024
PUBLISHED 26 November 2024

CITATION
Dimant YS (2024) Deriving improved plasma fluid equations from collisional kinetic theory. *Front. Astron. Space Sci.* 11:1466909. doi: 10.3389/fspas.2024.1466909

Deriving improved plasma fluid equations from collisional kinetic theory

Y. S. Dimant*

Center for Space Physics, Boston University, Boston, MA, United States

Introduction: Developing a quantitative understanding of wave plasma processes in the lower ionosphere requires a reasonably accurate theoretical description of the underlying physical processes. For such a highly collisional plasma environment as the E-region ionosphere, kinetic theory represents the most accurate theoretical description of wave processes. For the analytical treatment, however, collisional kinetic theory is extremely complicated and succeeds only in a limited number of physical problems. To date, most research has applied oversimplified fluid models that lack a number of critical kinetic aspects, so the coefficients in the corresponding fluid equations are often accurate only to an order of magnitude.

Methods: This paper presents a derivation for the highly collisional, partially magnetized case relevant to E-region conditions, using methods of the collisional kinetic theory with a new set of analytic approximations.

Results: This derivation provides a more accurate reduction of the ion and, especially, electron kinetic equations to the corresponding 5-moment fluid equations. It results in a more accurate fluid model set of equations appropriate for most E-region problems.

Discussion: The results of this paper could be used for a routine practical analysis when working with actual data. The improved equations can also serve as a basis for more accurate plasma fluid computer simulations.

KEYWORDS

E-region ionosphere, magnetized plasma, plasma-neutral collisions, kinetic theory, fluid equations, 5-moment description

1 Introduction

At altitudes of the equatorial and high-latitude E-region ionospheres, the ionosphere is highly collisional in such a way that ions are almost demagnetized by their frequent collisions with the surrounding neutral molecules while electrons remain strongly magnetized. Strong DC electric fields perpendicular to the geomagnetic field cause electrojets and give rise to plasma instabilities whose nonlinear development produces plasma density irregularities that can be observed by radars and rockets.

Developing a quantitative understanding of wave plasma processes in the lower ionosphere requires an accurate theoretical description of the underlying physical processes. For such a dissipative environment, collisional plasma kinetic theory represents the most accurate theoretical description of wave processes. Particle-in-cell (PIC) simulations apply the kinetic approach as a comprehensive numeric experiment, but such massive computer simulations (Oppenheim and Dimant, 2004; Oppenheim et al., 2008;

Oppenheim and Dimant, 2013; Oppenheim et al., 2020) are usually quite costly. In many cases, simple estimates and parameter dependencies provided by an analytic approach will suffice. For the analytical treatment, however, the collisional kinetic theory is extremely complicated and succeeds only in a limited number of physical problems. To date, most research has applied an oversimplified fluid model that lacks many critical kinetic aspects. These models mostly apply to weakly collisional conditions. The coefficients in the simple fluid equations are often accurate only to an order of magnitude because they were not obtained using the full kinetic theory of electron-neutral collisions. This paper presents the derivation of improved fluid equations for the highly collisional, partially magnetized case relevant to E-region conditions, starting from a more consistent kinetic approach. It provides more accurate values for the fluid model coefficients.

There are different approaches to analytically describing low-frequency plasma processes in the E-region ionosphere, including both the kinetic theory and fluid models. Traditionally, the kinetic theory of the Farley–Buneman (FB) instability applied an oversimplified Bhatnagar–Gross–Krook (BGK) collision operator (Bhatnagar et al., 1954). This operator does not follow from an accurate Boltzmann collision operator [except assuming special conditions (St-Maurice and Schunk, 1977)] but represents an artificial construct. It dramatically simplifies the analytical treatment and satisfies the particle number conservation and the momentum and energy balances (albeit under certain conditions; see below). This simplified approach is reasonably applicable to the description of the heavy ions, but it is totally unacceptable to the description of the light electrons (Dimant and Sudan, 1995a).

More accurate approaches to the kinetic description of electrons under conditions of the E-region wave processes, such as the FB instability, have been developed by a few research groups. Stubbe (1990) modified the BGK terms to allow for different rates of electron energy and momentum losses. This simple modification, however, does not follow from the Boltzmann operator, and its applicability for given physical conditions should be verified. Later, two independent research groups developed more sophisticated and accurate approaches. Kissack and collaborators (Kissack et al., 1995; 1997; 2008a; b) applied Grad's method (Grad, 1949; Rodbard et al., 1995), while Dimant and Sudan (1995a) used an expansion in Legendre polynomials with respect to the angles in the velocity space (Gurevich, 1978; Allis, 1982). The latter kinetic approach has allowed the authors to predict a new electron thermal-driven instability in the lower-E/upper-D regions (Dimant and Sudan, 1995b; c), which has been later explained in terms of a much simpler fluid model (Dimant and Sudan, 1997). This effect has been verified by others (Robinson, 1998; St. -Maurice and Kissack, 2000). Later, a similar thermal-instability process has been suggested for ions (Kagan and Kelley, 2000; Dimant and Oppenheim, 2004; Dimant et al., 2023).

This paper presents a consistent reduction of the ion and electron kinetic equations to the 5-moment fluid equations by using a new set of analytic approximations. This derivation results in a more accurate fluid model appropriate for most E-region plasma problems. The main contribution of this work comes from relaxing the assumption of constant electron-neutral collision frequency and allowing significant deviations of the electron velocity distribution from the Maxwellian distribution (although the pitch-angle anisotropy of the electron distribution function always remains weak, as described in the text).

The results of this work could be used for a routine practical analysis when working with actual data. The improved equations can also serve as a basis for more accurate plasma fluid computer simulations. Concerning the latter, we note the following. These improved fluid equations include no Landau damping, so they cannot properly model the FB instability in the short-wavelength range of turbulence (of the order of the ion-neutral collisional mean free path and shorter), where this kinetic effect plays an important role. However, these improved fluid equations can successfully model plasma waves generated by the larger-scale gradient drift and thermal instabilities; see Dimant et al. (2023) and references therein. Even more so, as PIC simulations demonstrate (Oppenheim and Dimant, 2013), after the brief evolution of the FB instability to its dynamic nonlinear saturation, the energetically dominant part of the developed turbulence spectrum usually moves to longer wavelengths. In this later stage, the kinetic effects of Landau damping become less important, so the improved set of fluid equations could also be successfully employed for reasonably accurate modeling of the FB instability. A recent work has demonstrated the satisfactory applicability of fluid modeling to FB instability, both in the E-region ionosphere (Rojas et al., 2023) and in the solar chromosphere (Evans et al., 2023). Furthermore, the improved fluid equations can also model the dynamics of such plasma objects as quickly ionized chemically released gas clouds, sporadic E-layers, long-lived meteor plasma, etc.

The paper is organized as follows. Section 2 introduces the collisional kinetic equation and reviews the generic procedure for obtaining the moment equations. The collisional parts are not specified and remain in the general integral form. Section 3 describes the ion momentum equation obtained using the BGK collision model. The most important part is Section 4. It derives low-frequency electron fluid equations using a kinetic theory based on the efficient isotropization of the electron distribution function in the velocity space (Gurevich, 1978; Dimant and Sudan, 1995a). This requires a more detailed and sophisticated treatment. Section 4.1 derives the moment equations where the heat conductivity and frictional heating are given in terms of a still unspecified small directional part of the velocity distribution function. To illustrate major ideas of closing the derivation, Section 4.2 describes the simplest case of the constant (i.e., velocity-independent) kinetic collision parameters. Section 4.3 presents the general results obtained in detail in the Supplementary Appendix. Compared to the simplest electron fluid equations from Section 4.2, the general momentum and thermal-balance equations include more coefficients, as well as additional heat conductivity terms. The latter may appear collisionless, but they have arisen exclusively due to the velocity dependence of the kinetic electron-neutral collision frequency.

2 General kinetic framework

This section discusses a general approach to deriving the fluid model from the kinetic theory for any plasma particles. To avoid confusion, we will use the following nomenclature throughout this

article. We denote various kinds of particles (charged or neutral) by Latin subscripts: p, q, etc., that stand for electrons (e), ions of various kinds (i), and neutrals (n), while denoting vector components by Greek subscripts: α, β, etc.

The non-relativistic kinetics of charged particles of the kind p with the velocity $\vec{v}_p$ at a given location $\vec{r}$ and time t are described by the Boltzmann kinetic equation,

$$\partial_t f_p + \nabla\cdot\left(\vec{v}_p f_p\right) + \partial_{\vec{v}_p}\cdot\left[\frac{q_p}{m_p}\left(\vec{E}+\vec{v}_p\times\vec{B}\right)f_p\right] = \left(\frac{df_p}{dt}\right)_{col}, \quad (1)$$

where $f_p(\vec{v}_p,\vec{r},t)$ is the single-particle velocity distribution function. The left-hand side (LHS) of Equation (1) describes the collisionless (Vlasov) dynamics of the p-species charged particles in smoothed-over-many-particles electric ($\vec{E}$) and magnetic ($\vec{B}$) fields (for simplicity, we ignore here a gravity force). q_p and m_p are the p-particle charge and mass, respectively. The LHS of Equation (1) is intentionally written in a conservative (divergence) form that is more convenient for deriving the moment equations.

The right-hand side (RHS) of Equation (1), term $(df_p/dt)_{col} = \sum_q S_{pq}$, is the collisional operator describing binary collisions of the p-particles with all available kinds of charged and neutral particles denoted by q (including the p-particles themselves). In the general case, the partial components S_{pq} represent integral operators that involve products of $f_p(\vec{v}_p,\vec{r},t)$ by $f_q(\vec{v}_q,\vec{r},t)$. The partial operator S_{qq} is quadratically nonlinear, while S_{pq} with $p\neq q$ are linear with respect to f_p. The linear integral operators describe electron-neutral (e-n) and ion-neutral (i-n) collisions, while the quadratically nonlinear operators describe electron–electron (e-e) and ion–ion (i-i) collisions. The latter redistribute the energy and momentum within the same-species population. In the E-region ionosphere, where the Coulomb collisions are usually relatively weak, the e-e and i-i collisions can often be neglected. In a sufficiently dense day-time ionosphere, the e-e collisions can sometimes play a role, resulting mostly in the evolution of $f_e(\vec{v}_q,\vec{r},t)$ to a "more Maxwellian" distribution. This only helps improve the applicability of the fluid model compared to the more complicated kinetic theory (Dimant and Sudan, 1995a).

The binary collisions can be either elastic or inelastic. Elastic collisions conserve the total kinetic energy, momentum, and angular momentum of the colliding pair. The corresponding partial collisional operator, S_{pq}, can be described by the well-known Boltzmann collision integral (Shkarofsky et al., 1966; Gurevich, 1978; Lifshitz and Pitaevskii, 1981; Schunk and Nagy, 2009; Khazanov, 2011). During an inelastic collision of a charged particle with a neutral particle, a fraction of the total kinetic energy goes to the excitation (de-excitation) of the neutral particle (or ion) or to the release of electrons via ionization. Inelastic processes in the lower ionosphere often involve molecular dissociation, recombination with ions, and electron attachment, accompanied by photon radiation or absorption. The complete kinetic description of all these processes is complicated. In many cases, however, inelastic collisions are close to elastic, and one can continue using Boltzmann's integral with minor modifications (Gurevich, 1978; Shkarofsky et al., 1966). Kinetic Equation (1) with Boltzmann's collision integral *per se* represents a significant simplification over the full multi-particle kinetics, but it still remains quite difficult for a mathematical treatment and requires further simplifications.

Being interested in the fluid-model equations that follow from kinetic Equation (1), we review the conventional approach to deriving equations for the lowest-order moments of the distribution function below. The material in this section will serve as a guide for more specific derivations of the following sections.

The three lowest-order velocity moments include the p-species particle density,

$$n_p(\vec{r},t) \equiv \int f_p d^3v_p, \quad (2)$$

the mean fluid velocity,

$$\vec{V}_p(\vec{r},t) \equiv \left\langle \vec{v}_p \right\rangle = \frac{1}{n_p}\int \vec{v}_p f_p d^3v_p, \quad (3)$$

and the effective temperature,

$$T_p(\vec{r},t) = \frac{m_p}{3}\left\langle \left(\vec{v}_p - \vec{V}_p\right)^2 \right\rangle = \frac{m_p}{3n_p}\int \left(\vec{v}_p - \vec{V}_p\right)^2 f_p d^3v_p. \quad (4)$$

Note that in all equations, here and below, the temperatures are given in the energy units; that is, we imply that the temperatures in Kelvin (K) units are multiplied by the Boltzmann constant, although the K units will also be used in the text. The derivations below will also involve other velocity-averaged quantities defined by

$$\langle\cdots\rangle \equiv \frac{1}{n_p}\int (\cdots) f_p d^3v_p. \quad (5)$$

Integrations in Equations 2–5 are performed over the entire 3-D velocity space.

First, we consider the particle number balance. Integrating Equation 1 over the particle velocities with $f_p \to 0$ as $v_p \equiv |\vec{v}_p| \to \infty$, we easily obtain the continuity equation for the p-particle fluid,

$$\partial_t n_p + \nabla\cdot\left(n_p\vec{V}_p\right) = \int\left(\frac{df_p}{dt}\right)_{col} d^3v_p. \quad (6)$$

The RHS of Equation 6 includes various particle sources and losses, like ionization, recombination, and electron attachment. The collisions between the charged particles of the same species usually conserve the average particle number and, hence, do not contribute to the RHS of Equation 6.

Second, we obtain the momentum balance equation that involves the mean fluid drift velocity, $\vec{V}_p$. Integrating Equation 1 with the weighting function $m_p\vec{v}_p$, for a given vector-component α of the momentum density, we obtain

$$m_p\partial_t\left(n_p V_{p_\alpha}\right) + \sum_{\beta=1}^{3}\partial_{x_\beta}\mathbf{P}_{p_{\alpha\beta}} + m_p\sum_{\beta=1}^{3}\partial_{x_\beta}\left(n_p V_{p_\alpha}V_{p_\beta}\right)$$
$$= q_p\left[E_\alpha + \frac{1}{c}\left(\vec{V}_p\times\vec{B}\right)_\alpha\right]n_p + m_p\int v_{p_\alpha}\left(\frac{df_p}{dt}\right)_{col} d^3v_p, \quad (7)$$

where $\mathbf{P}_p$ is the total pressure tensor with vector components defined as

$$\mathbf{P}_{p_{\alpha\beta}} \equiv m_p\int\left(v_{p_\alpha} - V_{p_\alpha}\right)\left(v_{p_\beta} - V_{p_\beta}\right)f_p d^3v_p. \quad (8)$$

It combines the isotropic pressure, $P_p\delta_{mn}$ ($\delta_{mn}=1$ if $m=n$; otherwise$\delta_{mn}=0$), $P_p = n_pT_p$, with the viscosity tensor, $\mathbf{\Pi}_{p_{\alpha\beta}} \equiv \mathbf{P}_{p_{\alpha\beta}} -$

$P_p\delta_{\alpha\beta}$. Equation 7 includes momentum changes due to various average forces and those caused by particle density variations. To exclude the latter and separate the net effect of the total force, we multiply Equation 6 by $m_p\vec{V}_p$ and subtract the resultant equation from Equation 7. This yields the conventional momentum balance equation,

$$m_p n_p \frac{D_p\vec{V}_p}{Dt} = q_p n_p\left[\vec{E}+\frac{1}{c}\left(\vec{V}_p\times\vec{B}\right)\right]-\nabla\cdot\mathbf{P}_p+\vec{R}_p, \tag{9}$$

where $D_p/Dt\equiv\partial_t+\vec{V}_p\cdot\nabla$ is the convective (also called substantial or material) derivative for the average p-particle flow and

$$\vec{R}_p\equiv m_p\int\left(\vec{v}_p-\vec{V}_p\right)\left(\frac{df_p}{dt}\right)_{col}d^3v_p. \tag{10}$$

Here and below, the "dot"-products of a vector, $\vec{a}$, with a two-component tensor, $\mathbf{A}$, depending on the multiplier order, denote vectors with the components $(\vec{a}\cdot\mathbf{A})_\alpha\equiv\sum_{\beta=1}^{3}a_\beta\mathbf{A}_{\beta\alpha}$ or $(\mathbf{A}\cdot\vec{a})_\alpha\equiv\sum_{\beta=1}^{3}\mathbf{A}_{\alpha\beta}a_\beta$. The tensor divergence, $\nabla\cdot\mathbf{P}_p=\nabla P_p+\nabla\cdot\mathbf{\Pi}_p$, represents a vector which uses the obvious symmetry $\mathbf{P}_{p_{\alpha\beta}}=\mathbf{P}_{p_{\beta\alpha}}$ following from Equation 8. The RHS of Equation 9 includes all smooth forces acting on the average particle flow of the charged particles, such as the total Lorentz force, pressure gradient, and total friction, $\vec{R}_p$. The latter is associated with collisions of the given p-particles with all other charged or neutral particles. It includes no momentum exchange between the same-species particles because their mutual collisions automatically conserve the total momentum, $\int\vec{v}_pS_{pp}d^3v_p=0$.

Third, to obtain the total energy balance equation, we integrate Equation 1 with the weighting function $m_pv_p^2/2$ and obtain

$$\partial_t\mathcal{E}_p+\nabla\cdot\int\frac{m_pv_p^2}{2}\vec{v}_pf_pd^3v_p=\vec{j}_p\cdot\vec{E}+\frac{m_p}{2}\int v_p^2\left(\frac{df_p}{dt}\right)_{col}d^3v_p, \tag{11}$$

where $\mathcal{E}_p$ is the p-species average kinetic energy density and $\vec{j}_p$ is their electric current density,

$$\mathcal{E}_p\equiv\int\frac{m_pv_p^2}{2}f_pd^3v_p,\qquad\vec{j}_p\equiv q_pn_p\vec{V}_p. \tag{12}$$

Note that the particle gyromotion does not contribute to the kinetic energy balance. Before proceeding, we separate the mean drift velocity $\vec{V}_p$ from the kinetic particle velocity $\vec{v}_p$ so that (11) becomes

$$\begin{aligned}&\partial_t\left[n_p\left(\frac{m_pV_p^2}{2}+\frac{3T_p}{2}\right)\right]\\&\quad+\nabla\cdot\left[n_p\left(\frac{m_pV_p^2}{2}+\frac{5T_p}{2}\right)\vec{V}_p+\mathbf{\Pi}_p\cdot\vec{V}_p+\frac{n_pm_p}{2}\left\langle\left(\vec{v}_p-\vec{V}_p\right)^3\right\rangle\right]\\&=\vec{j}_p\cdot\vec{E}+\vec{V}_p\cdot\vec{R}_p+\frac{m_p}{2}\int\left(\vec{v}_p-\vec{V}_p\right)^2\left(\frac{df_p}{dt}\right)_{col}d^3v_p\\&\quad+\frac{m_pV_p^2}{2}\int\left(\frac{df_p}{dt}\right)_{col}d^3v_p,\end{aligned} \tag{13}$$

where $\left(\vec{v}_p-\vec{V}_p\right)^3=\left|\vec{v}_p-\vec{V}_p\right|^2\left(\vec{v}_p-\vec{V}_p\right)$. Equation 13 describes dynamic variations of the total energy density. It includes a part associated with the average fluid motion, $n_pm_pV_p^2/2$, and the internal thermal energy, n_pT_p. To extract the equation exclusively for the particle temperature, T_p, we multiply Equation 6 by $\left(m_pV_p^2/2+3T_p/2\right)$, take the scalar product of Equation 9 with $\vec{V}_p$, and subtract the resultant two equations from Equation 13. This yields

$$\begin{aligned}&\frac{3n_p}{2}\frac{D_pT_p}{Dt}+n_pT_p\nabla\cdot\vec{V}_p+\mathbf{\Pi}_p\cdot\nabla\cdot\vec{V}_p+\nabla\cdot\left[\frac{n_pm_p}{2}\left\langle\left(\vec{v}_p-\vec{V}_p\right)^3\right\rangle\right]\\&=\frac{m_p}{2}\int\left(\vec{v}_p-\vec{V}_p\right)^2\left(\frac{df_p}{dt}\right)_{col}d^3v_p+\left(\frac{m_pV_p^2}{2}-\frac{3T_p}{2}\right)\int\left(\frac{df_p}{dt}\right)_{col}d^3v_p,\end{aligned} \tag{14}$$

where $\mathbf{\Pi}_p\cdot\nabla\cdot\vec{V}_p\equiv\sum_{\alpha,\beta=1}^{3}\mathbf{\Pi}_{p_{\alpha\beta}}\nabla_\alpha\vec{V}_{p_\beta}$. Note that after this step, the electric field has been eliminated from the energy-balance equation. This is a crucial step in deriving the proper form of the frictional heating, as described below.

Typically, equations like Equation 14 represent the final form of the thermal-balance equation. These equations are most convenient for calculations. In order to clarify the physical meaning of some terms, however, it is helpful to recast Equation 14 in a slightly different form. Rewriting the continuity Equation 6 as

$$\frac{D_pn_p}{Dt}+n_p\nabla\cdot\vec{V}_p=\int\left(\frac{df_p}{dt}\right)_{col}d^3v_p,$$

we recast the two first terms in the LHS of Equation 14 as

$$\begin{aligned}\frac{3n_p}{2}\frac{D_pT_p}{Dt}+n_pT_p\nabla\cdot\vec{V}_p&=\frac{3n_p}{2}\frac{D_pT_p}{Dt}-T_p\frac{D_pn_p}{Dt}\\&\quad+T_p\int\left(\frac{df_p}{dt}\right)_{col}d^3v_p\\&=n_pT_p\frac{D_ps_p}{Dt}+T_p\int\left(\frac{df_p}{dt}\right)_{col}d^3v_p,\end{aligned} \tag{15}$$

where $s_p\equiv\ln\left(T_p^{3/2}/n_p\right)=\ln\left(P_p^{3/2}/n_p^{5/2}\right)$ represents the specific entropy of the p-species fluid (Braginskii, 1965) (for a single-atomic gas, this is the adiabatic coefficient $\gamma=5/3$). This recast allows interpreting $n_pT_p\nabla\cdot\vec{V}_p$ as the adiabatic heating (cooling) term. The two remaining terms in the LHS of Equation 14 describe the work performed by viscous forces and the fluid heat conductance. All these processes are collisionless.

All collisional processes in the thermal balance Equation 14 are described by its RHS. After rearranging the last term in Equation 15 to the RHS of Equation 14, the last term there becomes $\left(m_pV_p^2/2-5T_p/2\right)\int\left(df_p/dt\right)_{col}d^3v_p$. All integral terms involving $\left(df_p/dt\right)_{col}$ describe the frictional heating and thermal inflows (outflows) associated with possible emergence (disappearance) of p-particles as a result of ionization, recombination, etc. For the general form of $\left(df_p/dt\right)_{col}$, calculating the frictional heating is not an easy task. Below, we use two different kinds of further approximation: one is more appropriate for heavy single-charged ions (Section 3), while the other is suitable for light electrons (Section 4).

Before proceeding further, we emphasize that, in general, no truncated chain of moment equations is closed because, starting from the momentum equation, every further moment equation involves higher-order moments. To allow the moment equation chain to be rigorously truncated, the most appropriate is the near-equilibrium case when the particle distribution function, along with its small perturbations, remains reasonably close to Maxwellian (Dimant and Sudan, 1995a; Kissack et al., 1995). This case allows

describing the particle kinetics using a restricted number of spatially and temporarily varying parameters, such as the particle density, temperature, and average drift velocity (5-moment equations). In real situations, however, this is not always the case. That is why inconsistencies in the fluid description often happen (e.g., García-Colín et al., 2004; Velasco et al., 2002). Higher-order sets of equations allow more serious deviations from Maxwellian but still have a restricted number of additional fluid parameters. Fluid models that include restricted numbers of equations using approximate closures, such as the 5-, 8-, or 13-moment models (Schunk and Nagy, 2009), can be successfully employed in situations when there are no sharp gradients, extreme fields, abundant superthermal particles, or extremely large temperature differences between different species of the colliding particles. These conditions are usually met at the equatorial electrojet. If they cannot be met, then the adequate description of plasma dynamics may require a direct solution of the corresponding collisional kinetic equation.

3 BGK collision kinetics and the fluid model for ions

For ionospheric ions, an accurate fluid theory has been developed by several authors who derived the fluid-model equations using a rigorous collisional kinetic approach; see, for example, Schunk and Walker (1971), Schunk and Walker (1972), and St-Maurice and Schunk (1977); for references, see Shkarofsky et al. (1966), Gurevich (1978), and Schunk and Nagy (2009). This theory results, for example, in a comprehensive set of 13-moment fluid equations that contain many transport terms (Schunk and Nagy, 2009). For typical plasma processes in the E-region ionosphere, however, such comprehensive equations are often excessive, and a much simpler set of 5-moment ion equations would usually suffice.

The goal of this section is to demonstrate that the derivation of the 5-moment ion fluid equations that have been successfully used, for example, for the treatment of the E-region instabilities (Dimant and Oppenheim, 2004; Kovalev et al., 2008; Makarevich, 2020), does not require a full and rigorous kinetic theory. This set of equations can be derived from the ion kinetic equation, where the complicated Boltzmann collision integral is replaced by a much simpler and more practical model discussed below. Under certain conditions, usually fulfilled automatically in the E-region ionosphere, the resultant 5-moment ion equations provide quantitatively accurate frictional heating and cooling terms.

In the lower-E/upper-D regions of the ionosphere (or similar media), one can usually neglect Coulomb collisions between the charged particles, compared to their much more frequent collisions with the dominant neutrals. For the ion-neutral collision integral, one can use the simple BGK model (Bhatnagar et al., 1954). Disregarding ionization-recombination processes and assuming in the general case a neutral wind with the local velocity $\vec{V}_n$, for the laboratory frame of reference, we write the simplest BGK collision operator as

$$\left(\frac{df_i}{dt}\right)_{col}^{\mathrm{BGK}} = \nu_i\left(f_{\mathrm{eff}} - f_i\right), \tag{16}$$

where f_i is the real ion distribution function (IDF), while f_{eff} is a fictitious Maxwellian function, normalized to the locally varying ion density, $n_i(\vec{r},t)$, with the constant neutral temperature T_n:

$$f_{\mathrm{eff}}\left(\vec{v}_i,\vec{r},t\right) \equiv n_i\left(\vec{r},t\right)\left(\frac{m_i}{2\pi T_n}\right)^{3/2} \exp\left(-\frac{m_i\left(\vec{v}_i-\vec{V}_n\right)^2}{2T_n}\right). \tag{17}$$

This simple linear algebraic form of the model collision operator has also been called the "relaxation collision model" (St-Maurice and Schunk, 1973; St-Maurice and Schunk, 1974; St-Maurice and Schunk, 1977), the "Krook collision model" (Schunk and Nagy, 2009), the "model integral of elastic collisions" (Aleksandrov et al., 1984), and by some other terms. Note that the BGK collision model noticeably exaggerates the IDF distortion effect (Schunk and Nagy, 2009; Koontaweepunya et al., 2024). This happens for several reasons (Schunk and Nagy, 2009); in particular, because the BGK operator does not include any collisional angular scattering and hence does not include particle redistribution in the velocity space between the preferred direction of the imposed electric field and the two perpendicular directions.

For the BGK model, it is essential that the ion-neutral collision frequency, ν_i, is assumed constant. The standard justification for this is that at sufficiently low energies, the ion-neutral collisions are dominated by the long-range polarization interaction (Dalgarno et al., 1958; Schunk and Walker, 1971; Schunk and Walker, 1972), which results in the approximate constancy of ν_i ("Maxwell molecule collisions") (Schunk and Nagy, 2009). The model collision term in the form of Equation 16 conserves the local number of particles. Applied to both ions and neutrals, the BGK model also conserves the total momentum of the two colliding particles and, after some adjustment to the temperature in f_{eff} for unequal masses of the colliding species, conserves the total energy of the colliding particles as well (Aleksandrov et al., 1984).

Generally, the BGK model does not follow from Boltzmann's collision integral under any rigorous approximations, although this becomes possible under certain conditions (St-Maurice and Schunk, 1977). This model is a reasonable and simple fit for single-charged ions that collide, predominantly elastically, with the surrounding neutrals of the same (or close) mass. Recent 2-D hybrid computer simulations of the Farley–Buneman instability that used this kinetic equation for ions (Kovalev et al., 2008) have demonstrated a good agreement with similar results of the more accurate fully kinetic PIC or hybrid simulations (Janhunen, 1995; Oppenheim et al., 2008; Oppenheim et al., 1996; Oppenheim et al., 1995; Oppenheim and Dimant, 2004; Koontaweepunya et al., 2024). There are two major reasons why this oversimplified model works well for the ion-neutral collisions typical for the lower ionosphere. First, within a 1000 K temperature range, the ion-neutral collision frequency is almost velocity-independent (Schunk and Nagy, 2009). Second, collisions of ions with neutral particles of the same or close mass have roughly equal rates of the average momentum and energy transfer, described by the single parameter ν_i. Both these factors distinguish dramatically the ion-neutral collisions from the electron-neutral ones, as we discuss in the following section.

For the distribution function of single-charged positive ions, $f_i(\vec{v}_i,\vec{r},t)$, the BGK kinetic equation in the conservative (divergence) form is given by

$$\partial_t f_i + \nabla\cdot\left(\vec{v}_i f_i\right) + \partial_{\vec{v}_i}\cdot\left[\left(\frac{e\vec{E}}{m_i} + \Omega_i\vec{v}_i\times\hat{b}\right)f_i\right] = \nu_i\left(f_{\mathrm{eff}} - f_i\right). \tag{18}$$

In this section, we derive the 5-moment ion fluid model equations for $n_i = \int f_i d^3v_i$, $\vec{V}_i = \langle \vec{v}_i \rangle = \int \vec{v}_i f_i d^3v_i$, and $T_i = m_i \langle \delta\vec{v}_i^2 \rangle /3 = (m_i/3n_i) \int \delta\vec{v}_i^2 f_i d^3v_i$, where $\delta\vec{v}_i \equiv \vec{v}_i - \vec{V}_i$.

Following the steps described in the preceding section and assuming the laboratory frame of reference, we obtain from Equation 18 the ion continuity, momentum, and energy-balance equation,

$$\partial_t n_i + \nabla \cdot \left(n_i \vec{V}_i \right) = \frac{D_i n_i}{Dt} + n_i \nabla \cdot \vec{V}_i = 0, \tag{19}$$

$$m_i n_i \frac{D_i \vec{V}_i}{Dt} = m_i n_i \left(\frac{e\vec{E}}{m_i} + \Omega_i \vec{V}_i \times \hat{b} \right) - \nabla \cdot \mathbf{P}_i - \nu_i n_i m_i \left(\vec{V}_i - \vec{V}_n \right), \tag{20}$$

$$\frac{3n_i}{2} \frac{D_i T_i}{Dt} - T_i \frac{D_i n_i}{Dt} + \nabla \cdot \int m_i \delta\vec{v}_i \frac{\delta v_i^2}{2} f_i d^3v_i + \mathbf{\Pi}_{i_{\alpha\beta}} \nabla_\alpha V_{i\beta} = \frac{\nu_i m_i n_i \left(V_i - \vec{V}_n \right)^2}{2} + \frac{3}{2} \nu_i n_i \left(T_n - T_i \right). \tag{21}$$

The two last terms in the LHS of Equation 21 describe heat conduction. Generally, the thermal flux is given by the integral term, and $\mathbf{\Pi}_{i_{\alpha\beta}}$ should be determined from higher-order moment equations. In the strongly collisional lower ionosphere, assuming sufficiently long-wavelength processes (so that the fluid theory is applicable), these two terms can usually be neglected. This makes Equations 19–21 a closed set of the 5-moment equations for the ion density, n_i, temperature, T_i, and the three components of the ion drift velocity, $\vec{V}_i$. We should bear in mind, however, that the IDF may deviate from an isotropic Maxwellian function so that T_i is an effective temperature determined in the general case by Equation 4 (substituting $p = i$). For example, if the ion velocity distribution is approximated by a bi-Maxwellian function $\propto \exp[-(m_i/2)(V_\perp^2/T_\perp + V_\parallel^2/T_\parallel)]$, then $T_i = (2T_\perp + T_\parallel)/3$.

The first term in the RHS of Equation 21 describes the total rate of ion frictional heating. This term equals the rate that follows from a more detailed kinetic theory (Schunk and Nagy, 2009), $\nu_i m_i m_n n_i (V_i - V_n)^2/(m_i + m_n)$, provided $m_i = m_n$. Coincidentally, in the E region, the masses of the major ions (NO^+ and O_2^+) and neutrals (N_2 and O_2) are indeed close to each other, $m_i \simeq m_n \simeq$ 30 amu. Thus, in the E-region ionosphere, the BGK model of ion-neutral collisions should correctly describe the ion frictional heating so that one can successfully use it for ions Equations 19–21. The applicability of the fluid equations is better under moderate conditions when the IDF is reasonably close to Maxwellian so that their closing is better justified. Such moderate conditions mostly occur at the equatorial E region rather than at the high-latitude ionosphere, especially during the events of the strongly disturbed magnetosphere–ionosphere–thermosphere system.

To conclude this section, note that closed Equations 19–21 are mostly applicable to moderately disturbed conditions when the IDF is reasonably close to Maxwellian; otherwise, more equations for the higher-order moments are required. For strongly perturbed conditions, however, even higher-order closed sets of fluid equations are not fully applicable because, unlike the original kinetic Equation 18, any closed fluid equations do not include the important kinetic effect of Landau damping and hence they have limited applicability, for example, to describe the Farley–Buneman instability in the short-wavelength range of the turbulence spectrum where the wavelengths become comparable to, or shorter than, the ion mean free path.

4 Collisional kinetics and the fluid model for electrons

This section is the central piece of this paper. It derives the electron-fluid equations from an approximate but rigorous kinetic theory based on characteristics of the actual physical conditions and wave processes in the E-region ionosphere. For electrons, the oversimplified BGK collision model (employed above for ions) can apply only to plasma processes whose characteristic wave frequencies substantially exceed the electron collision frequencies. However, for low-frequency processes in the highly collisional E/D-region ionosphere, where the opposite condition usually holds (see Dimant and Sudan, 1995a, and references therein), the electron BGK collision model is totally unsuitable. The main reason is that the rate of electron-neutral collisional exchange of momentum, ν_e, is a few orders of magnitude larger than the corresponding rate of the energy exchange, $\delta_{en}\nu_e$ (Gurevich, 1978). This means that during collisions with heavy neutrals, the light electrons scatter over angles in the velocity space much more frequently than they change their kinetic energy. In low-frequency processes of the lower ionosphere, this leads to an efficient isotropization of the electron distribution function (EDF). The BGK model, however, completely ignores this feature. In addition, the BGK model does not cover the clearly pronounced velocity dependence of the kinetic electron-neutral collision frequency $\nu_e(v_e)$ (Gurevich, 1978; Schunk and Nagy, 2009). This velocity dependence plays an important role in some E-region instabilities (see, e.g., Dimant and Sudan, 1997, and references therein), and it modifies the instability and wave characteristics.

4.1 General kinetic approach and momentum equations

In a weakly ionized plasma of the lower ionosphere, collisions of an electron with other charged particles, including other electrons, ν_{ee}, ν_{ei}, are usually negligible compared to electron-neutral collisions, $\nu_e \approx \nu_e$. At altitudes above 75 km, strongly magnetized electrons, involved in low-frequency processes with $\omega \ll \nu_e \ll \Omega_e$, have an almost isotropic velocity distribution whose speed dependence can deviate significantly from Maxwellian. For such processes, an adequate kinetic description is by expanding the velocity distribution function $f_e(\vec{r}, t, \vec{v}_e)$ in Legendre polynomials with respect to angles in the velocity space (Shkarofsky et al., 1966; Gurevich, 1978; Khazanov, 2011). To the first-order accuracy with respect to a small anisotropy of $f_e(\vec{r}, t, \vec{v}_e)$, one can represent the total EDF as a combination of the major isotropic part, $F_0(\vec{r}, t, v_e)$, where $v_e \equiv |\vec{v}_e|$, and a relatively small directional part determined by a single vector-function $\vec{f}_1(\vec{r}, t, v_e)$ (Gurevich, 1978; Dimant and Sudan, 1995a),

$$f_e(\vec{r}, t, \vec{v}_e) \approx F_0(\vec{r}, t, v_e) + \frac{\vec{f}_1(\vec{r}, t, v_e) \cdot \vec{v}_e}{v_e} = F_0 + |\vec{f}_1| \cos\vartheta, \tag{22}$$

where ϑ is the angle between $\vec{f}_1$ and $\vec{v}_e$. Here, we assume that $|\vec{f}_1| \ll F_0$, along with similar inequalities for the speed derivatives

(see below). The major isotropic part, F_0, determines scalar velocity-averaged characteristics of the electron fluid, such as the electron density and temperature, while the small directional part, $|\vec{f}_1|\cos\vartheta$, determines vector characteristics, such as the average drift velocity and various fluxes. The other (neglected) terms of the expansion in Legendre polynomials are smaller than the two highest order terms by positive powers of the small parameter δ_{en}, which is discussed in the following paragraph. In this approximation, any higher-order anisotropies of the EDF are neglected. For electrons in the highly collisional E-region ionosphere, the higher-order anisotropies usually play no role (see below).

The assumption of $|\vec{f}_1| \ll F_0$ is well justified for electrons within the kinetic energy range $\mathcal{E}_e < 2$ eV ($v_e < 1000$ km/s). This range usually includes both the thermal bulk of electrons ($\mathcal{E}_e \lesssim 0.03$ eV for the cold E-region ionosphere) and a significant fraction of superthermal electrons. In this energy rate, the ratio of the mean, mostly inelastic, collisional energy loss to that of the predominantly elastic momentum loss, $\delta_{en}(v_e)v_e(v_e)/v_e(v_e) = \delta_{en}(v_e)$, is usually quite small: $\delta_{en}(v_e) \sim (2--4)\times 10^{-3}$ (Gurevich, 1978) (although it is two orders of magnitude larger than the corresponding purely elastic rate, $\delta_{en}^{\rm elas} \approx 2m_e/m_n$). The ratio of $|\vec{f}_1|$ to F_0 is typically $\sim\sqrt{\delta_{en}}$ so that the directional part of the EDF in Equation 22 turns out to be automatically small compared to the major isotropic part, $|\vec{f}_1| \ll F_0$. However, this raises the following question. If there were an imposed DC electric field, $\vec{E}\perp\vec{B}$, so strong that the corresponding $\vec{E}\times\vec{B}$-drift velocity, $\vec{V}_{\rm dr} = \vec{E}\times\vec{B}/B^2$, would be comparable to the mean electron thermal speed, $v_{Th}^e = (T_e/m_e)^{1/2}$, then the condition of $|\vec{f}_1| \ll F_0$ would become invalid. As a matter of fact, however, such a strong field would heat electrons so much that the heated thermal velocity v_{Th}^e would automatically exceed $\vec{V}_{\rm dr}$. If the new electron temperature is $\lesssim 23,000$ K (corresponding to 2 eV), then the approximation given by Equation 22 still holds. This is a significant difference of electrons from heavy ions with $\delta_{in} \simeq 1$.

If there was an imposed electric field, $\vec{E}$, and no magnetic field, then the electron distribution function $f(\vec{v}_e)$ would depend only on the electron speed v_e and the angle between the electron velocity $\vec{v}_e$ and the only preferred direction, that is, the direction $\vec{E}$. If one expands the EDF in the orthogonal polynomials with respect to $\cos\vartheta$ [see, for example, Equation (2.63) in Gurevich (1978)] and applies this expansion to the electron kinetic equation with the Boltzmann collision operator, then this will form an infinite chain of coupled equations for the corresponding terms of expansion, f_n.

Based on the smallness of the parameter $\delta_{en}(v_e)$, one can restrict the entire expansion to the first two Legendre polynomials, 1 and $\cos\vartheta$, that is, to the approximation given by Equation 22. The kinetic equation with the general electron-neutral collision operator, $(df_e/dt)_{\rm coll}$, leads to the two coupled equations for $F_0(v_e,\vec{r},t)$ and $\vec{f}_1(v_e,\vec{r},t)$ (Gurevich, 1978; Dimant and Sudan, 1995a).

$$\partial_t F_0 + \frac{v_e}{3}\,\nabla\cdot\vec{f}_1 - \frac{e}{3m_e v_e^2}\,\frac{\partial}{\partial v_e}\left(v_e^2\vec{E}\cdot\vec{f}_1\right) = S_0, \tag{23a}$$

$$\partial_t\vec{f}_1 - \Omega_e\hat{b}\times\vec{f}_1 + v_e\nabla F_0 - \frac{e\vec{E}}{m_e}\,\frac{\partial F_0}{\partial v_e} = \vec{S}_1, \tag{23b}$$

where

$$S_0 \equiv \frac{1}{2}\int_{-1}^{1}\left(\frac{df_e}{dt}\right)_{col} d(\cos\vartheta), \vec{S}_1 \equiv \frac{3}{2}\int_{-1}^{1}\left(\frac{df_e}{dt}\right)_{col}\frac{\vec{f}_1}{|\vec{f}_1|}\cos\vartheta\, d(\cos\vartheta) \tag{24}$$

(note that the expressions for $S_{0,1}$ in Dimant and Sudan (1995a) missed the correct normalization factors). Bearing in mind moderately fast wave processes, $\tau_{\rm rec}^{-1} \ll \omega \ll \nu_e$, where $\tau_{\rm rec}$ is an effective recombination lifetime at a given altitude, we will ignore ionization-recombination processes, as we did above for the ions. The kinetic description of electrons based on Equation 23a differs dramatically from any kinetic description based on the BGK collision model.

The theoretical approach leading to Equation 23a, b is explained in Gurevich (1978), Sect. 2.2.1. Here, we only outline it, starting from the simplest case of a totally unmagnetized plasma, $\vec{B} = 0$, where, in addition to that, all spatial gradients are directed parallel to $\vec{E}$. In this case, the only preferred direction is parallel to $\vec{E}$ so that the EDF f_e at a given location, $\vec{r}$, at a given time, t depends only on the electron speed v_e and the polar angle ϑ between $\vec{v}_e$ and the preferred direction. Expanding the angular part of $f_e(v_e,\vartheta,\vec{r},t)$ in the Legendre polynomials $P_k(x)$ as $f_e(v_e,\vartheta,\vec{r},t) = \sum_{k=0}^{\infty}P_k(\cos\vartheta)f_k(v_e,\vec{r},t)$ [see Equation (2.63) in Gurevich (1978)], substituting this expansion into the electron kinetic equation with the Boltzmann collision operator where only the electron-neutral collision component matters, and using the orthogonality of the Legendre polynomials $P_k(x)$, one obtains an infinite chain of coupled equations for $f_k(v_e)$. Using the conditions discussed above [and analyzed in more detail in Gurevich (1978)], one can cut the expansion in $P_k(\cos\vartheta)$ and the resultant infinite chain of equations to only the two first terms, $f_{0,1}$, corresponding to F_0 and $|\vec{f}_1|\cos\vartheta$ in our Equation 22.

When the magnetic field $\vec{B}$ is present and spatial gradients are arbitrarily directed, the situation is more complicated because there is no single preferred direction. However, because electrons are highly gyrotropic due to the fast Larmor rotation (in the perpendicular to $\vec{B}$ plane) and are prone to fast collisional scattering (in all directions), their velocity distribution remains mostly isotropic with only a small directional part. It is natural to assume that there is always a direction, $\vec{f}_1/|\vec{f}_1|$, around which the small angular-dependent part of the distribution function is almost axially symmetric and is proportional to $\vec{f}_1\cdot\vec{v}_e$. Unlike the unmagnetized case discussed above, this direction is not necessarily fixed but may be v_e-dependent and vary with $\vec{r}$, t. Restriction of the entire EDF to the ansatz given by Equation 22 reduces the electron kinetic equation with the Boltzmann collision operator to Equation (2.74) in Gurevich (1978), that is, to our Equations 23a, b. The unknown vector $\vec{f}_1$ is determined by solving the vectorial differential equation given by Equation 23b. Needless to say, the directional part of the electron velocity distribution $\propto\vec{f}_1$, that is, the second term in the RHS of Equation 22, always remains scalar.

Fluid equations based on Equations 23a, b, usually implying a nearly Maxwellian velocity distribution, have been successfully explored by a number of researchers [see, e.g., Gurevich (1978), Dimant and Sudan (1995a), and references therein]. However, the form of major fluid equations presented in Gurevich (1978), Chapter 5, does not clearly show the basic structure of generic Equations 9 and 14 or similar ions Equations 20 and 21. By this, we mean that Gurevich's equations show neither explicit adiabatic heating and cooling nor frictional heating $\propto V_{e,i}^2$. Adiabatic terms proportional to $(\gamma_{e,i}-1)$ in Gurevich (1978) Equations (5.3) and (5.4) and the corresponding terms in the following equations appear to have been

introduced "by hand" and are actually extraneous. One can verify that these adiabatic terms have already been implicitly distributed among other terms of the temperature balance equations within the corresponding fluxes given by Equations (5.8)–(5.11) in Gurevich (1978) so that they are accounted for in Gurevich (1978) Equations (5.3)–(5.4) twice.

The explicit adiabatic terms show up naturally in the kinetic approaches based on small perturbations of the distribution function shifted by the average particle drift velocity. These approaches differ from those based on perturbations of the non-shifted velocity distribution, as in Equation 22, resulting in Equations 23a, b. For relatively small drift velocities, however, the two different approaches should yield the same results. Below, we demonstrate that the kinetic approach based on Equation 22 and Equations 23a, b reproduces the electron-fluid equations in a rigorous and natural way with the correct adiabatic heating and cooling, frictional heating, etc. We will also calculate kinetic corrections associated with the general velocity dependence of the electron-neutral collision frequency and non-Maxwellian velocity distribution. The Supplementary Appendix contains details of these calculations.

In accord with the low-frequency condition of $\omega \ll \nu_e \ll \Omega_e$, we neglect in Equation (23b) the electron inertia term $\partial_t \vec{f}_1$ and use a standard approximation $\vec{S}_1 \approx -\nu_e(v_e)\vec{f}_1$ (Gurevich, 1978; Dimant and Sudan, 1995a). The latter follows from the Legendre polynomial expansion of the Boltzmann operator if we completely neglect the electron collisional energy losses and take into account only the angular scattering. This procedure is explained, for example, in Gurevich (1978), Section 2.2.2. This approximation allows us to close this set of equations in a simple way. As a result, we obtain

$$-\frac{e\vec{E}}{m_e}\frac{\partial F_0}{\partial v_e} - \Omega_e \hat{b}\times\vec{f}_1 + \nu_e \nabla F_0 = -\nu_e(v_e)\vec{f}_1. \tag{25}$$

Resolving this vector equation with respect to $\vec{f}_1$, we obtain

$$\vec{f}_1(v_e) = -\,\mathbf{N}(v_e)\cdot\vec{K}F_0, \tag{26}$$

where the kinetic electron mobility tensor $\mathbf{N}(v)$ and the differential vector operator $\vec{K}$ are given by

$$\mathbf{N}(v_e) \approx \begin{bmatrix} \dfrac{\nu_e(v_e)}{\Omega_e^2} & \dfrac{1}{\Omega_e} & 0 \\ -\dfrac{1}{\Omega_e} & \dfrac{\nu_e(v_e)}{\Omega_e^2} & 0 \\ 0 & 0 & \dfrac{1}{\nu_e(v_e)} \end{bmatrix}, \tag{27}$$

$$\vec{K} \equiv \nu_e \nabla - \frac{e\vec{E}}{m_e}\frac{\partial}{\partial v_e}. \tag{28}$$

Here and elsewhere, we neglect second-order small terms $\sim \nu_e^2$ compared to Ω_e^2 and represent all tensors in the matrix form for the Cartesian system $\hat{x},\hat{y},\hat{z}$ with the $\hat{z}$-axis along $\vec{B}$. We can write Equations 26 and 27 explicitly in terms of the parallel ($\|$) and perpendicular ($\perp$) to $\vec{B}$ components as

$$f_{1\|} = -\frac{1}{\nu_e(v_e)}K_\| F_0, \qquad \vec{f}_{1\perp} = -\left(\frac{\nu_e(v)\vec{K}_\perp}{\Omega_e^2} + \frac{\hat{b}}{\Omega_e}\times\vec{K}_\perp\right)F_0, \tag{29}$$

where $\hat{b} = \hat{z}$ is the unit vector along $\vec{B}$. The spatial derivatives in Equation 26 or 29 express the drift-diffusion approximation in the collisional kinetic theory, while the velocity derivatives describe electron energy variations caused by the electric field $\vec{E}$.

Now, we turn to the term S_0 in the RHS of Equation 23a. When using the approximate form for the term $\vec{S}_1$, we implied above that the collisional losses of the electron energy had been totally neglected. Calculation of the k-th degree term of the collision operator S_k involves an integration over the angle ϑ with the integrand proportional to $[1 - P_k(\vartheta)]$ (Shkarofsky et al., 1966; Gurevich, 1978). This integration works nicely for all $k \geq 1$, but for S_0 ($P_0(\vartheta) = 1$), it yields 0. This means that in order to calculate the term S_0, one needs better accuracy by taking into account the small collisional energy losses. Using proper Taylor expansions, such calculation yields a Fokker–Planck-like expression (Shkarofsky et al., 1966; Gurevich, 1978)

$$S_0 = \frac{1}{2v_e^2}\frac{\partial}{\partial v_e}\left[v_e^2\delta_{en}\nu_e\left(v_e F_0 + \frac{T_n}{m_e}\frac{\partial F_0}{\partial v_e}\right)\right], \tag{30}$$

where the parameter $\delta_{en}(v)$ describes the average fraction of energy lost by an electron with speed v during one electron-neutral collision. As a result, we obtain (Dimant and Sudan, 1995a)

$$\partial_t F_0 + \frac{1}{3v_e^2}\vec{K}\cdot\left(v_e^2\vec{f}_1\right) = \frac{1}{2v_e^2}\frac{\partial}{\partial v_e}\left[v_e^2\delta_{en}\nu_e\left(v_e F_0 + \frac{T_n}{m_e}\frac{\partial F_0}{\partial v_e}\right)\right]. \tag{31}$$

Expressing here $\vec{f}_1$ in terms of F_0 via Equation (26) or (29), we obtain a closed kinetic equation for the major isotropic distribution function, $F_0(\vec{r},t,v)$. Its solution, with the use of Equation (26) or (29), provides both parts of the distribution function so that its scalar and vector moments can be calculated by a straightforward speed integration. Using the standard expressions for lowest-order moments of the distribution function, such as the particle density, mean drift velocity, and temperature (see Equations 2–4) for the approximate electron velocity distribution given in the neutral frame of reference by Equation 22, after the integrations over the phase space angles, $d^3v_e = 2\pi v_e^2 dv_e d(\cos\vartheta)$, we obtain

$$n_e \approx 4\pi\int_0^\infty F_0 v_e^2 dv_e, \qquad \vec{V}_e \approx \frac{4\pi}{3n_e}\int_0^\infty \vec{f}_1 v_e^3 dv_e, \qquad T_e \approx \frac{4\pi m_e}{3n_e}\int_0^\infty F_0 v_e^4 dv_e. \tag{32}$$

A direct solution of the kinetic Equation 31 would be the most accurate and general way of describing the electron behavior (Dimant and Sudan, 1995a). However, the goal of this paper is to obtain a set of the lowest-order fluid equations in order to properly describe E-region plasma processes, even if this set of equations is not fully closed due to possible deviations of the EDF from Maxwellian.

As mentioned above, we start from particle conservation. Using the definitions of Equation 32 and integrating Equation 31 over v_e with the weighting function $4\pi v_e^2$, we obtain the standard electron continuity equation,

$$\partial_t n_e + \nabla\cdot\left(n_e\vec{V}_e\right) = 0. \tag{33}$$

The conventional way of obtaining the momentum equation is by integrating the kinetic equation with the weighting function $m_p\vec{v}_p$, as in obtaining Equation 7. For the light electrons, however, we have already reduced the original kinetic equation to the two coupled equations, where the second one, Equation 25, has a

vectorial form. Integrating it with the weighting function $4\pi v_e^3/(3n_e)$ and applying the integration by parts, we obtain

$$\frac{e\vec{E}}{m_e} - \Omega_e \hat{b}\times\vec{V}_e + \frac{\nabla(n_eT_e)}{m_en_e} + \frac{4\pi}{3n_e}\int_0^\infty \vec{f}_1 \nu_e v_e^3 dv_e = 0, \quad (34)$$

This equation describes the momentum balance of the inertialess electron fluid. Equation 34 includes the Lorentz force, pressure gradient, and collisional friction. As we show in the Supplementary Appendix, in the general case of a velocity-dependent collision frequency, $\nu_e(v)$, the last term in the LHS of Equation 34, in addition to the collisional friction, may also include an anisotropic addition to the total pressure gradient.

Taking a scalar product of Equation 34 with $m_en_e\vec{V}_e$, we obtain the expression

$$\vec{V}_e\cdot\left[n_e e\vec{E} + \nabla(n_eT_e)\right] + \frac{4\pi m_e}{3}\,\vec{V}_e\cdot\int_0^\infty \vec{f}_1 \nu_e v_e^3 dv_e = 0. \quad (35)$$

This expression represents the total work done by the electric field and other forces on the average electron flow. We will use this expression below.

Now, we derive an equation describing the total energy balance. Integrating Equation 31 with the weighting function $2\pi m_e v_e^4$, we obtain

$$\partial_t\left(\frac{3n_eT_e}{2}\right) + \frac{2\pi m_e}{3}\,\nabla\cdot\int_0^\infty \vec{f}_1 v_e^5 dv_e + n_e e\vec{E}\cdot\vec{V}_e = -2\pi m_e\int_0^\infty\left(\nu_e F_0 + \frac{T_n}{m_e}\frac{dF_0}{dv_e}\right)\delta_{en}\nu_e v_e^3 dv_e. \quad (36)$$

Using Equation 35, we eliminate from Equation 36 the work done by the electric field on the average flow, $n_e e\vec{E}\cdot\vec{V}_e$, and obtain

$$\partial_t\left(\frac{3n_eT_e}{2}\right) - \vec{V}_e\cdot\nabla(n_eT_e) + \frac{2\pi m_e}{3}\,\nabla\cdot\int_0^\infty \vec{f}_1 v_e^5 dv_e = \frac{4\pi m_e}{3}\,\vec{V}_e\cdot\int_0^\infty \vec{f}_1 \nu_e v_e^3 dv_e - 2\pi m_e\int_0^\infty\left(\nu_e F_0 + \frac{T_n}{m_e}\frac{dF_0}{dv_e}\right)\delta_{en}\nu_e v_e^3 dv_e. \quad (37)$$

Here, we have rearranged the terms between the two sides of the equation in such a way that all terms proportional to the collision frequency remain in the RHS while all other terms are put in the LHS. After so doing, it may be tempting to interpret the first term in the RHS of Equation 37 as the electron frictional heating. In the general case of velocity-dependent $\nu_e(v)$, however, this interpretation would not be perfectly accurate, as we show in the Supplementary Appendix and Section 4.3 below.

Equation 37 is not yet the final form of the thermal-balance equation. It needs to be further transformed into a form similar to Equation (14) or (21). In Supplementary Appendix, we develop this recast for the general case of velocity-dependent $\nu_e(v)$. However, we proceed with the simplest model of constant ν_e and δ_{en} below. This model is inaccurate for electron-neutral collisions of the lower ionosphere (Gurevich, 1978; Schunk and Nagy, 2009), but it will allow us to clarify basic ideas of closing Equation 37.

4.2 Constant collisional parameters

For constant ν_e and δ_{en}, using the definitions of Equation 32 and integrating the last term of Equation 37 by parts, we obtain

$$\partial_t\left(\frac{3n_eT_e}{2}\right) - \vec{V}_e\cdot\nabla(n_eT_e) + \frac{2\pi m_e}{3}\,\nabla\cdot\int_0^\infty \vec{f}_1 v_e^5 dv_e = m_e\nu_e n_e V_e^2 + \frac{3}{2}\,\delta_{en}\nu_e n_e(T_n - T_e), \quad (38)$$

Using Equation 26, we rewrite the third term in the LHS as

$$\frac{2\pi m_e}{3}\,\nabla\cdot\int_0^\infty \vec{f}_1 v_e^5 dv_e = -\frac{5}{2m_e}\,\nabla\cdot\mathbf{N}\cdot\left[\nabla(\lambda n_eT_e^2) + n_eT_e e\vec{E}\right]. \quad (39)$$

Here, the double-dot product involving a tensor means $\nabla\cdot\mathbf{N}\cdot\nabla\ldots = \sum_{\alpha,\beta=1}^3 \partial_{x_\alpha}(\mathbf{N}_{\alpha\beta}\partial_{x_\beta}\ldots)$ (and similarly for $\nabla\cdot\mathbf{N}\cdot\vec{E}$), and we have also introduced a dimensionless parameter of order unity, λ,

$$\lambda \equiv \frac{4\pi m_e^2}{15n_eT_e^2}\int_0^\infty v_e^6 F_0 dv_e = \frac{m_e\int_0^\infty v_e^6 F_0 dv_e}{5T_e\int_0^\infty v_e^4 F_0 dv_e} = \frac{3\left(\int_0^\infty F_0 v_e^2 dv_e\right)\int_0^\infty F_0 v_e^6 dv_e}{5\left(\int_0^\infty F_0 v_e^4 dv_e\right)^2}. \quad (40)$$

Note that for the Maxwellian isotropic part of the EDF,

$$F_0 = n_e\left(\frac{m_e}{2\pi T_e}\right)^{3/2}\exp\left(-\frac{m_e v_e^2}{2T_e}\right), \quad (41)$$

we have $\lambda = 1$.

Using Equations 32 and 28, we obtain

$$\vec{V}_e = -\frac{4\pi}{3n_e}\,\mathbf{N}\cdot\int_0^\infty v_e^3\vec{K}F_0 dv_e = -\mathbf{N}\cdot\left[\frac{e\vec{E}}{m_e} + \frac{\nabla(n_eT_e)}{m_en_e}\right]. \quad (42)$$

Multiplying Equation 42 by $m_en_eT_e$, we can rewrite it as

$$-\mathbf{N}\cdot\left(n_eT_e e\vec{E}\right) = m_en_eT_e\vec{V}_e + \mathbf{N}\cdot T_e\nabla(n_eT_e).$$

This relation allows us to eliminate the electric field from Equation 39 so that the latter becomes

$$\frac{2\pi m_e}{3}\,\nabla\cdot\int_0^\infty \vec{f}_1 v_e^5 dv_e = \frac{5}{2m_e}\,\nabla\cdot\left\{\mathbf{N}\cdot\left[(1-\lambda)T_e^2\nabla n_e - (2\lambda-1)n_eT_e\nabla T_e\right] + m_en_eT_e\vec{V}_e\right\}. \quad (43)$$

Using Equations 33 and 43, after a simple algebra,

$$\partial_t\left(\frac{3n_eT_e}{2}\right) - \vec{V}_e\cdot\nabla(n_eT_e) + \frac{5}{2}\,\nabla\cdot\left(n_eT_e\vec{V}_e\right) = \partial_t\left(\frac{3n_eT_e}{2}\right) - \vec{V}_e\cdot\nabla(n_eT_e) + \frac{5}{2}\,\nabla\cdot\left(n_eT_e\vec{V}_e\right) - \frac{5T_e}{2}\left[\partial_t n_e + \nabla\cdot\left(n_e\vec{V}_e\right)\right] = \frac{3n_e}{2}\,\frac{D_eT_e}{Dt} - T_e\,\frac{D_en_e}{Dt}, \quad (44)$$

we obtain the sought-for temperature balance equation in a more standard form,

$$\frac{3n_e}{2}\,\frac{D_eT_e}{Dt} - T_e\,\frac{D_en_e}{Dt} - \nabla\cdot\vec{q}_e = m_e\nu_e n_e V_e^2 + \frac{3}{2}\,\delta_{en}\nu_e n_e(T_n - T_e). \quad (45)$$

Here, the electron thermal flux density, $\vec{q}_e$, is given by

$$\vec{q}_e = \frac{5T_e}{2m_e}\,\mathbf{N}\cdot\left[(2\lambda-1)n_e\nabla T_e + (\lambda-1)T_e\nabla n_e\right] = \vec{q}_{e\parallel} + \vec{q}_{e\mathrm{P}} + \vec{q}_{e\mathrm{H}}, \quad (46)$$

where its explicit parallel, Pedersen, and Hall components are given by

$$\vec{q}_{e\parallel} = \frac{5T_e\left[(2\lambda-1)n_e\nabla_\parallel T_e + (\lambda-1)T_e\nabla_\parallel n_e\right]}{2m_e\nu_e},$$

$$\vec{q}_{e\mathrm{P}} = \frac{5T_e\nu_e\left[(2\lambda-1)n_e\nabla_\perp T_e + (\lambda-1)T_e\nabla_\perp n_e\right]}{2m_e\Omega_e^2},$$

$$\vec{q}_{e\mathrm{H}} = \frac{\Omega_e}{\nu_e}\left(\hat{b}\times\vec{q}_{e\mathrm{P}}\right) = \frac{5T_e\hat{b}\times\left[(2\lambda-1)n_e\nabla_\perp T_e + (\lambda-1)T_e\nabla_\perp n_e\right]}{2m_e\Omega_e}. \quad (47)$$

The two first terms in the LHS of Equation 45, as well as the similar ones in Equation 14 or (21), describe adiabatic heating or cooling of the electron fluid, while $\nabla\cdot\vec{q}_e$ describes the heat conductivity. Note that the Hall component of $\vec{q}_e$ can contribute to electron heat conductance only as a quadratically nonlinear effect because $\nabla\cdot\vec{q}_{eH}\propto(\nabla_\perp n_e\times\nabla_\perp T_e)$ only if the gradients of n_e and T_e are not parallel.

As mentioned above, for Maxwellian $F_0(v_e)$, we have $\lambda=1$ so that the term in $\vec{q}_e$ proportional to ∇n_e disappears. This fact can be understood as follows. If the major part of the EDF remains Maxwellian, then it is determined only by two space-dependent parameters: the density, n_e, and the temperature, T_e. If there is a density gradient but no temperature gradient, then electrons of all energies will diffuse from denser regions to less dense ones with no redistribution of the temperature and, hence, with no heat conductivity.

If the electron velocity distribution deviates from Maxwellian [this happens, for example, when a low-ionized plasma heated by strong electric fields is embedded in an abundant cold neutral atmosphere with a significantly different temperature (Milikh and Dimant, 2003)], then the situation is more complicated.

The effective electron temperature T_e, which is proportional to the mean electron chaotic energy, can be uniformly distributed, but the details of the electron energy distribution may differ significantly in different regions of space. The energy transport is stronger for electrons with higher energies than it is for lower-energy electrons. Hence, if there are spatial gradients of high-energy distribution tails, then more energetic particles provide stronger energy redistribution. This may make, for example, some less dense regions to be, on average, more energetic than the denser regions, even if they initially had equal effective temperatures. Moreover, it is even possible to imagine a situation when electron heat is transferred from cooler regions to hotter ones, leading to a further electron temperature elevation in the latter. This counter-intuitive but theoretically possible effect should not surprise because a strongly non-Maxwellian, that is, a strongly non-equilibrium plasma, cannot be adequately described by conventional equilibrium thermodynamics.

4.3 Velocity-dependent parameters

In the actual lower ionosphere, the electron-neutral kinetic collision frequency, ν_e, and the energy loss fraction, δ_{en}, have clearly pronounced velocity dependencies (Gurevich, 1978; Schunk and Nagy, 2009). This does not allow $\nu_e(v_e)$ and $\delta_{en}(v_e)$ to be factored out from the integrals in Equations 34–37, making the derivation of the general momentum and temperature balance equations more complicated than that described in Section 4.2. Such a derivation is developed in detail in the Supplementary Appendix, while we only present the results here. One of the major important outcomes of these calculations will be simple integral relations for the electron transport coefficients (see Equations 56–61), assuming not only the general velocity dependencies of ν_e but also general non-Maxwellian isotropic velocity distributions $F_0(v_e)$.

We note that the velocity dependence of the collisional frequency, $\nu_e(v_e)$, may automatically lead to the non-Maxwellian shape of the EDF. Indeed, if there is a sufficiently strong electric field parallel to $\vec{B}$, then the EDF becomes a Druyvesteyn kind (Shkarofsky et al., 1966; Gurevich, 1978). This parallel field should not necessarily be a DC field, but it can also be, for example, a turbulent AC field. In particular, such instability-driven turbulent fields lead to the well-known effect of anomalous electron heating (AEH) [see, for example, St-Maurice and Goodwin (2021), Zhang and Varney (2024), and references therein]. When strong AEH occurs, the EDF inevitably becomes non-Maxwellian, as can be seen from Figure 1 in Milikh and Dimant (2003). This fact could also be deduced from comparing the kinetic terms responsible for the electron differential collisional heating and cooling [see Equations 18 and 19 in Dimant and Sudan (1995a)]. Electric fields perpendicular to $\vec{B}$ are typically much stronger, but they often lead to smaller heating and are expected to cause lesser non-Maxwellian distortions of the EDF. The latter is because the kinetic heating and cooling terms are both linearly proportional to v_e in the perpendicular direction. If δ_{en} has a weak velocity dependence, then this proportionality partially neutralizes the effect of $\nu_e(v_e)$.

When the dominant heating occurs mostly in the direction parallel to $\vec{B}$, it spreads over all angles in the velocity space due to electron-neutral collisions with strong momentum changes. These momentum changes are determined by the rate ν_e, while the speed changes are determined by the much smaller rate $\delta_{en}\nu_e$. As a result, the EDF becomes close to isotropic, but its Druyvesteyn-like ν_e-dependence may deviate significantly from Maxwellian. Other factors may also cause significant deviations from a Maxwellian EDF in the E region. These factors include, for example, some chemical/ionization reactions, photoelectrons, and electron precipitation. Regarding the latter, we note that even superthermal particles at a high-energy tail of the EDF can affect the mean transport coefficients of the entire electron population (Dimant et al., 2021). Note also that the non-Maxwellian shape of the EDF has serious implications for the accurate interpretation of radar measurements, as discussed in Section 2.2 of Milikh and Dimant (2003).

Now, we proceed with presenting the results. In the general case of velocity-dependent ν_e and δ_{en}, electron continuity Equation (33) stays the same. The other two moment equations have the same basic structure as Equations (42) and (45), but they contain additional terms and include many dimensionless factors of order unity listed in Equations 56–61 below.

The general inertialess expression for the average electron drift velocity $\vec{V}_e$ is given by

$$\vec{V}_e=-\frac{1}{m_e}\,\mathbf{M}\cdot\left[e\vec{E}+\frac{\nabla_\perp(n_eT_e)}{n_e}+\frac{\beta_\parallel}{\alpha_\parallel}\,\frac{\nabla_\parallel(n_eT_e)}{n_e}\right],\qquad(48)$$

where

$$\mathbf{M}\equiv\frac{4\pi}{3n_e}\int_0^\infty\frac{d\left(v^3\mathbf{N}(v)\right)}{dv}\,F_0dv=\begin{bmatrix}\dfrac{\alpha_P\langle\nu_e\rangle}{\Omega_e^2} & \dfrac{1}{\Omega_e} & 0\\ -\dfrac{1}{\Omega_e} & \dfrac{\alpha_P\langle\nu_e\rangle}{\Omega_e^2} & 0\\ 0 & 0 & \alpha_\parallel\left\langle\dfrac{1}{\nu_e}\right\rangle\end{bmatrix},\qquad(49)$$

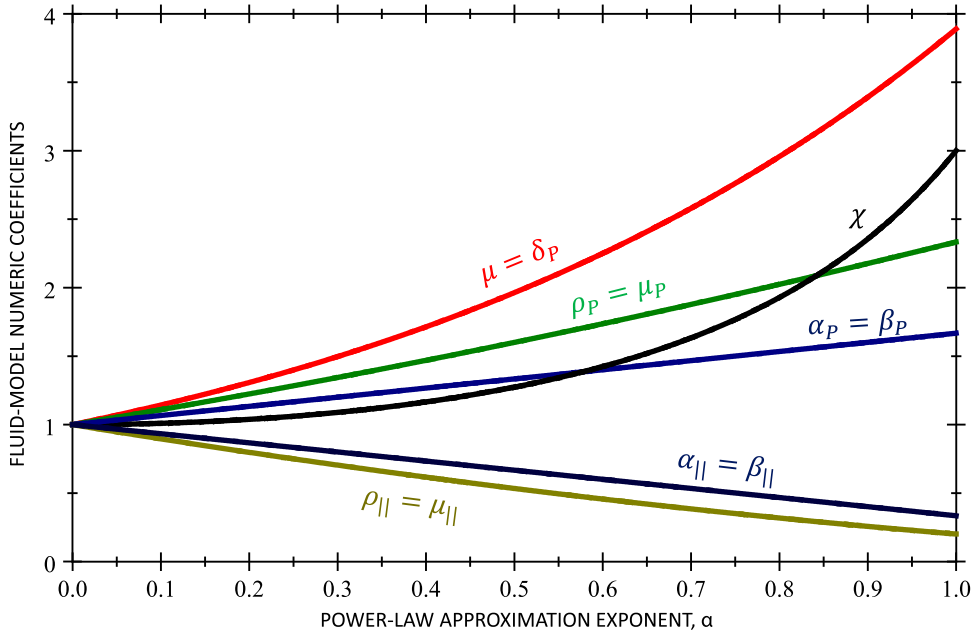

FIGURE 1
Fluid model coefficients for the power-law dependent *e-n* collision frequency, $\nu_e(v_e) \propto v_e^{2\alpha}$.

The tensor $\mathbf{N}$ is given by Equation 27, and $\langle\cdots\rangle_e$ denotes the velocity average over the major (isotropic) part of the EDF,

$$\langle\cdots\rangle_e = \frac{4\pi\int_0^\infty(\cdots)F_0(v_e)v_e^2dv_e}{n_e} = \frac{\int_0^\infty(\cdots)F_0(v_e)v_e^2dv_e}{\int_0^\infty F_0(v_e)v_e^2dv_e}. \quad (50)$$

The electron current density is given by $\vec{j}_e = en_e\vec{V}_e$ so that the electric conductivity tensor is given by $\boldsymbol{\sigma}_e = (n_e e^2/m_e)\mathbf{M}$. The corresponding diagonal terms represent the Pedersen ($\propto \alpha_P$) and parallel ($\propto \alpha_\parallel$), while the antisymmetric off-diagonal terms ($\propto 1/\Omega_e$) represent the Hall conductivity.

The general thermal-balance equation is given by

$$\frac{3n_e}{2}\frac{D_eT_e}{Dt} - T_e\frac{D_en_e}{Dt} + \frac{5}{2}\left(\frac{\rho_\parallel - \beta_\parallel}{\alpha_\parallel}\right)n_eT_e\nabla_\parallel\cdot\vec{V}_{e\parallel} + \left(\frac{5\rho_\parallel - 3\alpha_\parallel - 2\beta_\parallel}{2\alpha_\parallel}\right)\vec{V}_{e\parallel}\cdot\nabla_\parallel(n_eT_e) - \nabla\cdot\vec{q}_e = \alpha_P\langle\nu_e\rangle_e m_e n_e\left(V_{e\perp}^2 + \frac{V_\parallel^2}{\alpha_\parallel\xi}\right) - 2\pi m_e\int_0^\infty v_e^3\delta_{en}\nu_e\left(v_eF_0 + \frac{T_n}{m_e}\frac{dF_0}{dv_e}\right)dv_e, \quad (51)$$

where

$$\vec{q}_e \equiv \vec{q}_{eP} + \vec{q}_{eH} + \vec{q}_{e\parallel} = \mathbf{X}\cdot\frac{\nabla T_e}{T_e} + (\mathbf{X} - \mathbf{\Lambda})\cdot\frac{\nabla n_e}{n_e}, \quad (52)$$

is the thermal-flux density with

$$\mathbf{X} = \frac{5n_eT_e}{2m_e}\begin{bmatrix} \frac{\chi_P\langle\nu_e\rangle}{\Omega_e^2} & \frac{\chi_H}{\Omega_e} & 0 \\ -\frac{\chi_H}{\Omega_e} & \frac{\chi_P\langle\nu_e\rangle}{\Omega_e^2} & 0 \\ 0 & 0 & \frac{\chi_\parallel}{\langle\nu_e\rangle} \end{bmatrix}, \quad (53a)$$

$$\mathbf{\Lambda} = \frac{5n_eT_e}{2m_e}\begin{bmatrix} \frac{\mu_P\langle\nu_e\rangle}{\Omega_e^2} & \frac{\lambda}{\Omega_e} & 0 \\ -\frac{\lambda}{\Omega_e} & \frac{\mu_P\langle\nu_e\rangle}{\Omega_e^2} & 0 \\ 0 & 0 & \frac{\mu_\parallel}{\langle\nu_e\rangle} \end{bmatrix}. \quad (53b)$$

The explicit Pedersen, Hall, and parallel components of $\vec{q}_e$ are given by

$$\vec{q}_{eP} \equiv \frac{5T_e\langle\nu_e\rangle[\chi_Pn_e\nabla_\perp T_e + (\chi_P - \mu_P)T_e\nabla_\perp n_e]}{m_e\Omega_e^2},$$
$$\vec{q}_{eH} \equiv \frac{5T_e\hat{b}\times[\chi_Hn_e\nabla_\perp T_e + (\chi_H - \lambda)T_e\nabla_\perp n_e]}{m_e\Omega_e},$$
$$\vec{q}_{e\parallel} \equiv \frac{5T_e[\chi_\parallel n_e\nabla_\parallel T_e + (\chi_\parallel - \mu_\parallel)T_e\nabla_\parallel n_e]}{m_e\langle\nu_e\rangle_e}, \quad (54)$$

$$\chi_P \equiv 2\mu_P + \alpha_P - \beta_P - \rho_P, \qquad \chi_H \equiv 2\lambda - 1, \qquad \chi_\parallel \equiv 2\mu_\parallel - \beta_\parallel, \quad (55)$$

In addition to λ defined by (40), Equations 48–55 include

$$\alpha_P \equiv \frac{\int_0^\infty\frac{d(v^3\nu_e(v_e))}{dv_e}F_0dv_e}{3\int_0^\infty\nu_e(v_e)F_0v_e^2dv_e}, \qquad \alpha_\parallel \equiv \frac{\int_0^\infty\frac{d(v_e^3/\nu_e(v_e))}{dv}F_0dv_e}{3\int_0^\infty\frac{1}{\nu_e(v_e)}F_0v^2dv_e}, \quad (56)$$

$$\rho_\parallel \equiv \frac{\left(\int_0^\infty\frac{d}{dv_e}\left(\frac{v_e^5}{\nu_e(v_e)}\right)F_0dv_e\right)\left(\int_0^\infty v_e^2F_0dv_e\right)}{5\left(\int_0^\infty v_e^4F_0dv_e\right)\left(\int_0^\infty\frac{v_e^2}{\nu_e(v_e)}F_0dv_e\right)}, \quad (57a)$$

$$\rho_P \equiv \frac{\left(\int_0^\infty\frac{d}{dv_e}(\nu_e(v_e)v_e^5)F_0dv\right)\left(\int_0^\infty v_e^2F_0dv_e\right)}{5\left(\int_0^\infty v_e^4F_0dv_e\right)\left(\int_0^\infty\nu_e(v_e)v_e^2F_0dv_e\right)}, \quad (57b)$$

$$\beta_P \equiv \frac{\left(\int_0^\infty \nu_e(v_e) F_0 v_e^4 dv_e\right)\int_0^\infty F_0 v_e^2 dv_e}{\left(\int_0^\infty \nu_e(v_e) F_0 v_e^2 dv_e\right)\int_0^\infty F_0 v_e^4 dv_e}, \tag{58a}$$

$$\beta_\parallel \equiv \frac{\left(\int_0^\infty \frac{F_0 v_e^4}{\nu_e(v_e)}\, dv_e\right)\int_0^\infty F_0 v_e^2 dv_e}{\left(\int_0^\infty \frac{F_0 v^2}{\nu_e(v_e)}\, dv_e\right)\int_0^\infty F_0 v_e^4 dv_e}, \tag{58b}$$

$$\delta_P \equiv \frac{\left(\int_0^\infty v_e^2 F_0 v_e^4 dv_e\right)\left(\int_0^\infty F_0 v_e^2 dv_e\right)^2}{\left(\int_0^\infty \nu_e F_0 v_e^2 dv_e\right)^2\left(\int_0^\infty F_0 v_e^4 dv_e\right)}, \tag{59}$$

$$\mu_P \equiv \frac{3\left(\int_0^\infty \nu_e(v_e) F_0 v_e^6 dv_e\right)\left(\int_0^\infty F_0 v_e^2 dv_e\right)^2}{5\left(\int_0^\infty \nu_e(v_e) F_0 v_e^2 dv_e\right)\left(\int_0^\infty F_0 v_e^4 dv_e\right)^2}, \tag{60a}$$

$$\mu_\parallel \equiv \frac{3\left(\int_0^\infty \frac{F_0 v^6}{\nu_e(v_e)}\, dv_e\right)\left(\int_0^\infty F_0 v_e^2 dv_e\right)^2}{5\left(\int_0^\infty \frac{F_0 v^2}{\nu_e(v_e)}\, dv_e\right)\left(\int_0^\infty F_0 v_e^4 dv_e\right)^2}, \tag{60b}$$

$$\xi \equiv \left\langle \frac{1}{\nu_e} \right\rangle_e \langle \nu_e \rangle_e = \frac{\left(\int_0^\infty \nu_e(v_e) F_0(v_e) v_e^2 dv_e\right)\left(\int_0^\infty \nu_e^{-1}(v_e) F_0(v_e) v_e^2 dv_e\right)}{\left(\int_0^\infty F_0(v_e) v_e^2 dv_e\right)^2}. \tag{61}$$

For constant ν_e and arbitrary $F_0(v)$, we have $\alpha_{P,\parallel} = \rho_{P,\parallel} = \beta_{P,\parallel} = \mu = \delta_P = \xi = 1$, $\mu_{P,\parallel} = \lambda$, $\chi_{P,H,\parallel} = 2\lambda - 1$, and $\mathbf{M} = \mathbf{N}$ so that Equations 51–54 reduce to Equations 45–47. If, additionally, $F_0(v)$ is Maxwellian, then we have even simpler parameters: $\mu_{P,\parallel} = \chi_{P,H,\parallel} = \lambda = 1$.

In a broad range of electron energies, $\mathcal{E}_e \lesssim 0.3$ eV, which usually includes the entire electron thermal bulk, the velocity dependence of ν_e in the lower ionosphere can be approximated by a simple power-law dependence, $\nu_e \propto v_e^{2\alpha}$, with $\alpha \approx 5/6$ [(Gurevich, 1978), Sect. 2.3.1, see Fig. 7 there] or, practically to the same or even better accuracy, with $\alpha = 1$ (Dimant and Sudan, 1995a). For the general power-law dependent $\nu_e \propto v_e^{2\alpha}$ with α in the range between 0 and 1 and Maxwellian $F_0(v_e)$, Equations 56–61 simplify dramatically,

$$\alpha_P = \beta_P = 1 + \frac{2\alpha}{3}, \qquad \alpha_\parallel = \beta_\parallel = 1 - \frac{2\alpha}{3},$$

$$\rho_\parallel = \mu_\parallel = \frac{(3-2\alpha)(5-2\alpha)}{15}, \qquad \rho_P = \mu_P = \frac{(3+2\alpha)(5+2\alpha)}{15}, \tag{62}$$

$$\mu = \delta_P = \frac{\sqrt{\pi}\Gamma(5/2+2\alpha)}{3\Gamma^2(3/2+\alpha)}, \qquad \xi = \frac{1-4\alpha^2}{\sin\frac{\pi(2\alpha+1)}{2}} = \frac{4\alpha^2-1}{\sin\frac{\pi(2\alpha-1)}{2}}.$$

The case of $\alpha = 1/2$ corresponds to hard-sphere collisions. In this case, the indeterminate expression for ξ yields $4/\pi \approx 1.273$. For $\alpha = 5/6$ (Gurevich, 1978), we have $\alpha_P = \beta_P \approx 1.556$, $\alpha_\parallel = \beta_\parallel \approx 0.444$, $\rho_\parallel = \mu_\parallel \approx 0.296$, $\rho_P = \mu_P \approx 2.074$, $\mu = \delta_P \approx 3.095$, and $\xi \approx 2.053$. For $\alpha = 1$ (Dimant and Sudan, 1995a), all these factors deviate from unity even further; for example, $\alpha_\parallel = \beta_\parallel \approx 0.333$, $\mu = \delta_P \approx 3.889$, and $\xi = 3$. Thus, the quantitative effect of the velocity dependence of $\nu_e(v)$ is significant and should not be ignored. Figure 1 shows the coefficients given by Equation 62 for general values of the power-law exponent α within the physically realistic range $0 \le \alpha \le 1$.

Comparison of the general energy balance Equation 51 with Equation 45 shows that the velocity dependence of the collision parameters results not only in the more complicated heat conductivity, frictional heating, and cooling but also in additional terms associated with the plasma motion and gradients in the parallel to $\vec{B}$ direction (see the two terms in the LHS of Equation 51 that precede $-\nabla\cdot\vec{q}_e$). It is important that these seemingly collisionless terms originate entirely from electron-neutral collisions due to the velocity distribution of $\nu_e(v)$. Formally, these terms appear because the collision frequencies $\nu_e(v)$ mutually cancel each other in some fractions while their velocity dependencies still play a role. Similar effects in the Hall and Pedersen directions are absent because there is no such canceling. However, the Hall and Pedersen components hidden within the heat conductivity flux $\vec{q}_e$ may play an important role, provided there are sharp gradients in those directions.

Now, we discuss the last (cooling) term in the RHS of Equation 51. For general velocity-dependent $\delta_{en}(v)$, but a Maxwellian distribution function $F_0 \propto \exp[-m_e v^2/(2T_e)]$, we use Equation (32) to reduce this term to

$$-2\pi m_e \int_0^\infty v_e^3 \delta_{en} \nu_e \left(\nu_e F_0 + \frac{T_n}{m_e}\frac{dF_0}{dv_e}\right) dv_e = \frac{3}{2}\,\frac{\langle \delta_{en} v_e^2 \nu_e\rangle_e n_e}{\langle v_e^2\rangle_e}(T_n - T_e). \tag{63}$$

For general F_0, but constant δ_{en}, we can rewrite the cooling term in Equation 51 as

$$-2\pi m_e \int_0^\infty v_e^3 \delta_{en} \nu_e \left(\nu_e F_0 + \frac{T_n}{m_e}\frac{dF_0}{dv_e}\right) dv_e = \frac{3}{2}\,\delta_{en}\langle \nu_e\rangle_e n_e(\alpha_P T_n - \beta_P T_e), \tag{64}$$

where we integrated by parts and used Equations 56 and 58a. Equation 64 shows that for general non-Maxwellian F_0, the cooling term is not necessarily proportional to the temperature difference $(T_n - T_e)$. However, for the power-law dependent $\nu_e \propto v_e^{2\alpha}$ and Maxwellian F_0, according to Equation 62, we have $\beta_P = \alpha_P = 1 + 2\alpha/3$. In this case, the structure of the cooling term proportional to $\alpha_P \langle \nu_e\rangle n_e$ matches that of the frictional heating term for a purely perpendicular field, $\alpha_P \langle \nu_e\rangle m_e n_e V_{e\perp}^2$, as seen from the first term in the RHS of Equation 51.

5 Discussion

When applying a fluid model for analytic calculations or simulations, it is important to have the corresponding equations with accurate parameters applicable to the relevant physical conditions. These equations and parameters are usually derived from the kinetic theory, so their accuracy is determined by the accuracy of the underlying kinetic approach.

Based on two different kinetic approaches, this article derives the fluid model equations that describe low-frequency plasma processes in the highly dissipative E-region ionosphere. The treatment is restricted to collisions of the plasma particles, ions, or electrons with the neutral molecules only; no Coulomb collisions are considered. The neglect of Coulomb collisions at the E-region ionosphere is usually well justified, although sometimes electron–electron collisions may play a role, resulting in a more efficient "Maxwellization" of the electron distribution function (Dimant and Sudan, 1995a). Such Maxwellization makes the fluid model (as opposed to the pure kinetic theory) more applicable. For the plasma particle collisions with neutrals (elastic or inelastic), here,

we assume the known cross sections relevant for various elastic and inelastic collisional processes as functions of the colliding particle velocities. Assuming these known cross sections, we can always calculate velocity dependencies of the kinetic collision frequencies, $\nu_p(\vec{v}_p)$ $(p = i, e, n)$. These velocity dependencies of the collisional cross-sections can be taken from the literature [e.g., for the dominant electron-nitrogen collisions, see Itikawa (2006), Song et al. (2023), and references therein]. The resultant fluid model parameters are expressed in general integral forms through these known velocity dependencies. For the most important plasma processes, such as the small-to medium-scale cross-field plasma instabilities (the thermal Farley–Buneman and gradient drift instabilities), closed 5-moment multi-fluid models are usually sufficient for the accurate fluid description. Given the plasma species p, the 5-moment set of unknowns includes the particle densities (n_p), temperatures (T_p), and the three components of the mean drift velocity, $\vec{V}_p$.

For the ionospheric ions $(p = i)$, we have employed the well-known and fairly simple BGK collisional model. For the heavy ions, the applicability of the BGK collision operator can be justified by the fact that within the thermal bulk and around, the kinetic ion-neutral collision frequency ν_{in} is approximately constant, that is, velocity-independent; this approximation corresponds to Maxwell molecule collisions (Schunk and Nagy, 2009). Additionally, the ion masses in the E-region ionosphere are fairly close to the neutral-molecule masses, $m_i \simeq m_n$. As we demonstrate in Section 3, in the case of $m_i = m_n$, the oversimplified BGK model results even in quantitatively accurate frictional heating and cooling terms; see the RHS of Equation 21. We should bear in mind, however, that for sufficiently strong electric field, $E \gtrsim m_i \nu_i v_{Ti}/e$, that is, when the mean ion drift speed, $eE/(m_i\nu_i)$, becomes on the order or larger than the ion thermal speed v_{Ti}, the ion distribution function can be significantly distorted with an appreciable deviation from Maxwellian (Koontaweepunya et al., 2024). Although the major ion fluid terms remain valid in this case, the entire 5-moment model cannot be easily closed, and hence its validity may be questionable. The factor of strong electric field is usually of importance for the high-latitude E region under conditions of severe magnetospheric perturbations (geomagnetic storms or substorms), while at the equatorial E region, the electric fields are typically much weaker so that the closed 5-moment ion-fluid model is usually much more applicable.

The central part of this paper is the derivation of the 5-moment fluid equations for electrons. For the light electrons, unlike the ions, the simple BGK model cannot serve even as a crude approximation. As we explained in Section 4, the reasons for the total BGK model inapplicability are the two major facts: (1) the mean rate of the collisional loss of the electron energy is much less than the corresponding loss of the electron momentum so that the electron behavior cannot be described by a single collisional parameter; (2) the kinetic collisional frequency ν_e has a pronounced electron velocity dependence. The first fact leads to a strong isotropization of the electron velocity distribution, while the speed dependence of the electron velocity distribution is effectively decoupled from the angular dependence in the velocity space. The second fact leads to noticeable modifications of the electron-fluid coefficients and even to the occurrence of additional thermo-diffusion terms. As a result, in the general case, the fluid model coefficients acquire numerical multipliers whose values are determined by some integral relations over the entire electron distribution function, see Equations 52–61. For the Maxwellian function, and especially for the power-law dependencies of the ν_e-speed dependence, these general integral relations reduce to simple algebraic ones, $\nu_e(v_e) \propto v_e^{2\alpha}$; see Equation 62 and Figure 1. From that figure, we see that some numerical multipliers can deviate significantly from unity although remaining in the same order of magnitude. A better knowledge of these fluid coefficients is important for accurate calculations and predictions of the physical characteristics of various wave processes. As our future knowledge of the speed dependence of the kinetic collision rates becomes more precise, using the more general integral relationships obtained here, one can obtain the improved values of the corresponding fluid model coefficients.

The kinetic approach employed in this paper is based on the expansion of the electron velocity distribution in Legendre polynomials (in the velocity space) and keeping the two first terms of such expansion, see Equation 22: the dominant isotropic part, $F_0(\vec{r}, t, v_e)$, and a small directional part, $|\vec{f}_1(\vec{r}, t, v_e)| \cos\vartheta$, where ϑ is the angle between $\vec{f}_1$ and $\vec{v}_e$, and $v_e = |\vec{v}_e|$ is the electron speed. This approach is analogous to that employed by Gurevich (1978) [see also Dimant and Sudan (1995a)], although, as we explained in Section 4.1, Gurevich's fluid equations for electrons, Gurevich (1978), Chapter 5, derived through this kinetic approach, differ from ours. Gurevich's equations are written in a form that does not include explicit adiabatic and frictional heating terms. Purely mathematically, however, these equations might be equivalent to ours, except for the "adiabatic" terms proportional to $(\gamma_{e,i} - 1)$ in Gurevich (1978) Equations (5.3) and (5.4). These terms are extraneous, and their correct equivalent has already been implicitly distributed within the other terms in Gurevich (1978) Equation (5.8)–(5.11) and hence included twice (Gurevich, 1978).

An alternative kinetic approach to electron-fluid description is based on Grad's method (Kissack et al., 1995; Kissack et al., 1997; Kissack et al., 2008a; Kissack et al., 2008b). The latter assumes that only a finite number of parameters characterize the velocity distribution and also implies that the electron velocity distribution is reasonably close to Maxwellian. Our approach is much more general in terms of the ν_e-dependence, but it restricts the angular distribution of the EDF to the simplest linear deviation from the isotropy. This approximation allows calculating vector fluxes like $n_e\vec{V}_e$ or energy fluxes (see below), but higher-order tensor characteristics like an anisotropic pressure, etc., may require an accuracy beyond its field of applicability. Note, however, that high-order tensor characteristics for electrons are not expected to be significant due to the relatively high rate of EDF isotropization associated with a small value of $\delta_{en} \sim (2 - -4) \times 10^{-3}$ within the low-energy electron energy range, $\mathcal{E}_e \equiv m_e v_e^2/2 < 2$ eV (Gurevich, 1978). Note also that under physical conditions when the two methods are applicable, both techniques provide reasonably close quantitative results. At the same time, our kinetic approach provides much simpler, and hence much more practical, algebraic expressions applicable to various small- and medium-scale E-region processes.

6 Conclusion

Based on relevant physical conditions, we have derived improved fluid equations for the E-region ionosphere. In this

derivation, we have used two different approximate kinetic approaches for the E-region ions and electrons.

For the ions, we have employed the simple BGK collision operator (Section 3). This resulted in a full 5-moment set of the continuity, momentum, and energy-balance equations, see Equations 19–21. Although these equations look conventional, our derivation has demonstrated that for the E-region ions with almost equal masses of the ions and neutrals, the BGK collision operator leads to quantitatively accurate frictional and cooling rates.

The central part of this paper is the derivation of the electron-fluid equations. For the electrons, the BGK collisional operator is inapplicable, and we have employed the kinetic approach based on the expansion of the electron distribution function, $f_e(\vec{v}_e)$, in Legendre polynomials over the angles in the velocity space. Physical conditions resulting in efficient isotropization of $f_e(\vec{v}_e)$ allowed us to restrict the treatment to the two highest terms of the Legendre expansion: the dominant isotropic part, $F_0(v_e)$ and a small directional part $\vec{f_1} \cdot \vec{v}_e/v_e$. The former is responsible for calculating the scalar fluid quantities, such as the electron density and temperature, while the directional part allows the calculation of the electron flux (or electric current) density. An important factor in our derivations is the fact that the electron-neutral collisional frequencies are strongly velocity-dependent. Assuming these velocity dependencies to be known, we have derived the full set of the 5-moment equations: the continuity equation, the momentum equation, and the thermal balance equation. Because the E-region electrons in all relevant low-frequency processes are essentially inertialess, the momentum equation reduces to an explicit expression for the electron mean drift velocity given by Equation 48. The most non-trivial result is the thermal balance equation given in the general case by Equation 51, where the parameters are given by Equations 40, 56–55. For the Maxwellian distribution function and the power-law speed dependence of the electron-neutral collision frequency, $\nu_e(v_e) \propto v_e^{2\alpha}$, the integral relationships for the fluid model parameters reduce to simple algebraic expressions given by Equation 62; see also Figure 1.

Comparison of the general energy balance Equation 51with the corresponding equation for the velocity-independent electron collision frequency (see Equation 45) shows that the velocity dependence of the collision parameters results in more complicated heat conductivity, frictional heating, and cooling, as well as in additional terms associated with the plasma motion and gradients in the parallel to $\vec{B}$ direction. These terms look collisionless, but they originate exclusively from the velocity distribution of $\nu_e(v)$. Similar effects in the Hall and Pedersen directions are inconsequential and have been neglected. However, one should not neglect the Hall and Pedersen components in the heat conductivity because the plasma temperature and density gradients in those directions can be much sharper than those in the parallel direction.

In this paper, we discuss only the simple 5-moment sets of fluid equations, although more sophisticated sets of equations, like the 13-moment transport equations, could be used (Schunk and Nagy, 2009). In the highly collisional E-region ionosphere, however, the need for such complicated fluid equations is questionable because the difficulties of implementing them may become comparable to, or even exceed, the difficulties of implementing the more accurate and comprehensive full kinetic theory.

The results of this paper could be used for a routine practical analysis when working with actual data. The improved equations can also serve as a basis for more accurate plasma fluid computer simulations. In the general case, the applicability of the closed 5-moment equations is restricted by reasonably moderate conditions of the equatorial E region. For the high-latitude E-region ionosphere, an accurate description may require using a fully kinetic treatment.

Data availability statement

The original contributions presented in the study are included in the article/Supplementary Material, further inquiries can be directed to the corresponding author.

Author contributions

YD: writing–original draft and writing–review and editing.

Funding

The author(s) declare that financial support was received for the research, authorship, and/or publication of this article. This work was funded by NSF Grants 1755350, 1007789, and 0442075 and NASA Grants 80NSSC21K1322 and 80NSSC19K0080.

Acknowledgments

The author is deeply grateful to Prof. Oppenheim for his long-term support, extensive help, and multiple discussions.

Conflict of interest

The author declares that the research was conducted in the absence of any commercial or financial relationships that could be construed as a potential conflict of interest.

Publisher's note

Supplementary material

The Supplementary Material for this article can be found online at: https://www.frontiersin.org/articles/10.3389/fspas.2024.1466909/full#supplementary-material

References

Aleksandrov, A. F., Bogdankevich, L. S., and Rukhadze, A. A. (1984). *Principles of plasma electrodynamics*, 9. New York: Springer Verlag.

Allis, W. P. (1982). Semidivergence of the Legendre expansion of the Boltzmann equation. *Phys. Rev. A* 26, 1704–1712. doi:10.1103/PhysRevA.26.1704

Bhatnagar, P. L., Gross, E. P., and Krook, M. (1954). A model for collision processes in gases. I. Small amplitude processes in charged and neutral one-component systems. *Phys. Rev.* 94, 511–525. doi:10.1103/PhysRev.94.511

Braginskii, S. I. (1965). Transport processes in a plasma. *Rev. Plasma Phys.* 1, 205.

Dalgarno, A., McDowell, M. R. C., and Williams, A. (1958). The mobilities of ions in unlike gases. *Philosophical Trans. R. Soc. Lond. Ser. A* 250, 411–425. doi:10.1098/rsta.1958.0002

Dimant, Y. S., Khazanov, G. V., and Oppenheim, M. M. (2021). Effects of electron precipitation on E-region instabilities: theoretical analysis. *J. Geophys. Res.* 126, e29884. doi:10.1029/2021JA029884

Dimant, Y. S., and Oppenheim, M. M. (2004). Ion thermal effects on E-region instabilities: linear theory. *J. Atmos. Solar-Terr. Phys.* 66, 1639–1654. doi:10.1016/j.jastp.2004.07.006

Dimant, Y. S., Oppenheim, M. M., Evans, S., and Martinez-Sykora, J. (2023). Unified fluid theory of the collisional thermal Farley-Buneman instability including magnetized multi-species ions. *Phys. Plasmas* 30, 102101. doi:10.1063/5.0155500

Dimant, Y. S., and Sudan, R. N. (1995a). Kinetic theory of low-frequency cross-field instability in a weakly ionized plasma. I. *Phys. Plasmas* 2, 1157–1168. doi:10.1063/1.871394

Dimant, Y. S., and Sudan, R. N. (1995b). Kinetic theory of low-frequency cross-field instability in a weakly ionized plasma. II. *Phys. Plasmas* 2, 1169–1181. doi:10.1063/1.871395

Dimant, Y. S., and Sudan, R. N. (1995c). Kinetic theory of the Farley-Buneman instability in the E region of the ionosphere. *J. Geophys. Res.* 100, 14605–14623. doi:10.1029/95JA00794

Dimant, Y. S., and Sudan, R. N. (1997). Physical nature of a new cross-field current-driven instability in the lower ionosphere. *J. Geophys. Res.* 102, 2551–2564. doi:10.1029/96JA03274

Evans, S., Oppenheim, M., Martínez-Sykora, J., Dimant, Y., and Xiao, R. (2023). Multifluid simulation of solar chromospheric turbulence and heating due to thermal farley-buneman instability. *Astrophys. J.* 949, 59. doi:10.3847/1538-4357/acc5e5

García-Colín, L. S., Velasco, R. M., and Uribe, F. J. (2004). Inconsistency in the Moment's method for solving the Boltzmann equation. *J. Non Equilib. Thermodyn.* 29, 257–277. doi:10.1515/JNETDY.2004.054

Grad, H. (1949). On the kinetic theory of rarefied gases. *Commun. Pure Appl. Math.* 2, 331–407. doi:10.1002/cpa.3160020403

Gurevich, A. V. (1978). *Nonlinear phenomena in the ionosphere*, 10. New York: Springer Verlag. doi:10.1007/978-3-642-87649-3

Itikawa, Y. (2006). Cross sections for electron collisions with nitrogen molecules. *J. Phys. Chem. Reference Data* 35, 31–53. doi:10.1063/1.1937426

Janhunen, P. (1995). On recent developments in E-region irregularity simulations and a summary of related theory. *Ann. Geophys.* 13, 791–806. doi:10.1007/s00585-995-0791-7

Kagan, L. M., and Kelley, M. C. (2000). A thermal mechanism for generation of small-scale irregularities in the ionospheric E region. *J. Geophys. Res.* 105, 5291–5303. doi:10.1029/1999JA900415

Khazanov, G. V. (2011). *Kinetic theory of the inner magnetospheric plasma*. New York: Springer.

Kissack, R. S., Kagan, L. M., and St. -Maurice, J. P. (2008a). Thermal effects on Farley-Buneman waves at nonzero aspect and flow angles. I. Dispersion relation. *Phys. Plasmas* 15, 022901. doi:10.1063/1.2834275

Kissack, R. S., Kagan, L. M., and St. -Maurice, J. P. (2008b). Thermal effects on Farley-Buneman waves at nonzero aspect and flow angles. II. Behavior near threshold. *Phys. Plasmas* 15, 022902. doi:10.1063/1.2834276

Kissack, R. S., St-Maurice, J. P., and Moorcroft, D. R. (1995). Electron thermal effects on the Farley-Buneman fluid dispersion relation. *Phys. Plasmas* 2, 1032–1055. doi:10.1063/1.871383

Kissack, R. S., St. -Maurice, J. P., and Moorcroft, D. R. (1997). The effect of electron-neutral energy exchange on the fluid Farley-Buneman instability threshold. *J. Geophys. Res.* 102, 24091–24116. doi:10.1029/97JA02036

Koontaweepunya, R., Dimant, Y. S., and Oppenheim, M. M. (2024). Non-maxwellian ion distribution in the equatorial and auroral electrojets. *arXiv e-prints , arXiv2408*. doi:10.48550/arXiv.2408.06339

Kovalev, D. V., Smirnov, A. P., and Dimant, Y. S. (2008). Modeling of the Farley-Buneman instability in the E-region ionosphere: a new hybrid approach. *Ann. Geophys.* 26, 2853–2870. doi:10.5194/angeo-26-2853-2008

Lifshitz, E. M., and Pitaevskii, L. P. (1981). *Physical kinetics*. Elsevier.

Makarevich, R. A. (2020). Toward an integrated view of ionospheric plasma instabilities: 5. Ion-thermal instability for arbitrary ion magnetization, density gradient, and wave propagation. *J. Geophys. Res.* 125, e28349. doi:10.1029/2020JA028349

Milikh, G. M., and Dimant, Y. S. (2003). Model of anomalous electron heating in the E region: 2. Detailed numerical modeling. *J. Geophys. Res.* 108, 1351. doi:10.1029/2002JA009527

Oppenheim, M., Dimant, Y., Longley, W., and Fletcher, A. C. (2020). Newly discovered source of turbulence and heating in the solar chromosphere. *Astrophys. J.* 891, L9. doi:10.3847/2041-8213/ab75bc

Oppenheim, M., Otani, N., and Ronchi, C. (1995). Hybrid simulations of the saturated Farley-Buneman instability in the ionosphere. *Geophys. Res. Lett.* 22, 353–356. doi:10.1029/94GL03277

Oppenheim, M., Otani, N., and Ronchi, C. (1996). Saturation of the Farley-Buneman instability via nonlinear electron E×B drifts. *J. Geophys. Res.* 101, 17273–17286. doi:10.1029/96JA01403

Oppenheim, M. M., Dimant, Y., and Dyrud, L. P. (2008). Large-scale simulations of 2-D fully kinetic Farley-Buneman turbulence. *Ann. Geophys.* 26, 543–553. doi:10.5194/angeo-26-543-2008

Oppenheim, M. M., and Dimant, Y. S. (2004). Ion thermal effects on E-region instabilities: 2D kinetic simulations. *J. Atmos. Solar-Terr. Phys.* 66, 1655–1668. doi:10.1016/j.jastp.2004.07.007

Oppenheim, M. M., and Dimant, Y. S. (2013). Kinetic simulations of 3-D Farley-Buneman turbulence and anomalous electron heating. *J. Geophys. Res.* 118, 1306–1318. doi:10.1002/jgra.50196

Robinson, T. R. (1998). The effects of small scale field aligned irregularities on E-region conductivities: implications for electron thermal processes. *Adv. Space Res.* 22, 1357–1360. doi:10.1016/S0273-1177(98)80034-3

Rodbard, M. G., Bezerra, J. A. G., and Kremer, G. M. (1995). A combined Chapman-Enskog and Grad method. II. Ionized gases. *Phys. Plasmas* 2, 642–648. doi:10.1063/1.871416

Rojas, E. L., Burns, K. J., and Hysell, D. L. (2023). Fluid models capturing Farley-Buneman instabilities. *Ann. Geophys.* 41, 281–287. doi:10.5194/angeo-41-281-2023

Schunk, R., and Nagy, A. (2009). *Ionospheres: Physics, plasma Physics, and chemistry*. Cambridge: University Press. doi:10.1017/CBO9780511635342

Schunk, R. W., and Walker, J. C. G. (1971). Transport processes in the E region of the ionosphere. *J. Geophys. Res.* 76, 6159–6171. doi:10.1029/JA076i025p06159

Schunk, R. W., and Walker, J. C. G. (1972). Ion velocity distributions in the auroral ionosphere. *Planet. Space Sci.* 20, 2175–2191. doi:10.1016/0032-0633(72)90071-2

Shkarofsky, J. P., Johnston, T. W., and Bachynski, M. P. (1966). *The particle kinetics of plasmas*. Reading: Addison-Wesley.

Song, M.-Y., Cho, H., Karwasz, G. P., Kokoouline, V., and Tennyson, J. (2023). Cross sections for electron collisions with N2, N2*, and N2+. *J. Phys. Chem. Reference Data* 52, 023104. doi:10.1063/5.0150618

St-Maurice, J. P., and Goodwin, L. (2021). Revisiting the behavior of the E region electron temperature during strong electric field events at high latitudes. *J. Geophys. Res.* 126, e8288. doi:10.1029/2020JA028288

St. -Maurice, J. P., and Kissack, R. S. (2000). The role played by thermal feedback in heated Farley-Buneman waves at high latitudes. *Ann. Geophys.* 18, 532–546. doi:10.1007/s00585-000-0532-x

St-Maurice, J. P., and Schunk, R. W. (1973). Auroral ion velocity distributions using a relaxation model. *Planet. Space Sci.* 21, 1115–1130. doi:10.1016/0032-0633(73)90200-6

St-Maurice, J. P., and Schunk, R. W. (1974). Behaviour of ion velocity distributions for a simple collision model. *Planet. Space Sci.* 22, 1–18. doi:10.1016/0032-0633(74)90119-6

St-Maurice, J. P., and Schunk, R. W. (1977). Auroral ion velocity distributions for a polarization collision model. *Planet. Space Sci.* 25, 243–260. doi:10.1016/0032-0633(77)90135-0

Stubbe, P. (1990). The concept of a kinetic transport theory. *Phys. Fluids B* 2, 22–33. doi:10.1063/1.859535

Velasco, R. M., Uribe, F. J., and García-Colín, L. S. (2002). Inconsistencies in moment methods. *Phys. Rev. E* 66, 032103. doi:10.1103/PhysRevE.66.032103

Zhang, Y., and Varney, R. H. (2024). A statistical survey of e-region anomalous electron heating using poker flat incoherent scatter radar observations. *J. Geophys. Res.* 129, e2023JA032360. doi:10.1029/2023JA032360

frontiers | Frontiers in Astronomy and Space Sciences

TYPE Original Research
PUBLISHED 04 December 2024
DOI 10.3389/fspas.2024.1502618

OPEN ACCESS

EDITED BY
David Hysell,
Cornell University, United States

REVIEWED BY
Eliana Nossa,
The Aerospace Corporation, United States
Sampad Kumar Panda,
K. L. University, India
Ercha Aa,
Massachusetts Institute of Technology, United States
Qian Wu,
National Center for Atmospheric Research (UCAR), United States

*CORRESPONDENCE
Tatsuhiro Yokoyama,
yokoyama@rish.kyoto-u.ac.jp

RECEIVED 27 September 2024
ACCEPTED 23 October 2024
PUBLISHED 04 December 2024

CITATION
Yokoyama T (2024) Simulation study of the impacts of E-region density on the growth of equatorial plasma bubbles.
Front. Astron. Space Sci. 11:1502618.
doi: 10.3389/fspas.2024.1502618

Simulation study of the impacts of E-region density on the growth of equatorial plasma bubbles

Tatsuhiro Yokoyama*

Research Institute for Sustainable Humanosphere, Kyoto University, Uji, Japan

Equatorial plasma bubbles (EPBs) in the ionospheric F region are notorious for causing severe scintillation in radio signals, posing significant challenges for communication and navigation systems. Understanding and forecasting EPB occurrence is crucial from a space weather perspective, given their impact on satellite and terrestrial communication. In this study, we present the impacts of E-region conductivity on the generation of EPBs by using the 3D high-resolution bubble (HIRB) model. By changing the production rate of NO^+ ions in the E region, the flux-tube-integrated linear growth rate of the Rayleigh–Taylor instability can be modified. Multiple simulation runs show that even a moderate variation of the growth rate turns into a significant difference in EPB growth into the top of the ionosphere. This is a major factor that has made forecasting EPB generation quite difficult for several decades.

KEYWORDS

ionosphere, equatorial plasma bubbles, simulation, Rayleigh–Taylor instability, growth rate

1 Introduction

Equatorial plasma bubbles (EPBs) are large-scale plasma density depletions in the equatorial ionospheric F region, typically forming post-sunset due to the development of the Rayleigh–Taylor instability (e.g., Kelley, 2009; Woodman, 2009). This phenomenon was named EPB because the lower density region grows nonlinearly and penetrates through into the top of the *F* region. These bubbles can severely disrupt radio wave propagation by inducing scintillation in amplitude and phase, which affects communication and navigation systems that rely on ionospheric propagation. The concept of EPB was proposed by Woodman and LaHoz (1976) based on radar observations and supported by numerical simulations on a magnetic equatorial plane (Scannapieco and Ossakow, 1976). There have been a number of simulation studies of EPBs since the first outcome reported by Scannapieco and Ossakow (1976). The historical review of the numerical simulation studies of EPBs was presented by Yokoyama (2017).

Despite their critical importance, predicting the day-to-day variability of EPB occurrence remains a significant challenge due to the complex interplay of contributing factors. Several studies have addressed the day-to-day variability of the occurrence of EPBs (e.g., Abdu et al., 2009; Carter et al., 2014; Aa et al., 2023), but it was quite difficult to determine a key factor that controls their occurrence. From the modeling approach, the EPB occurrence characteristics were investigated by using a global

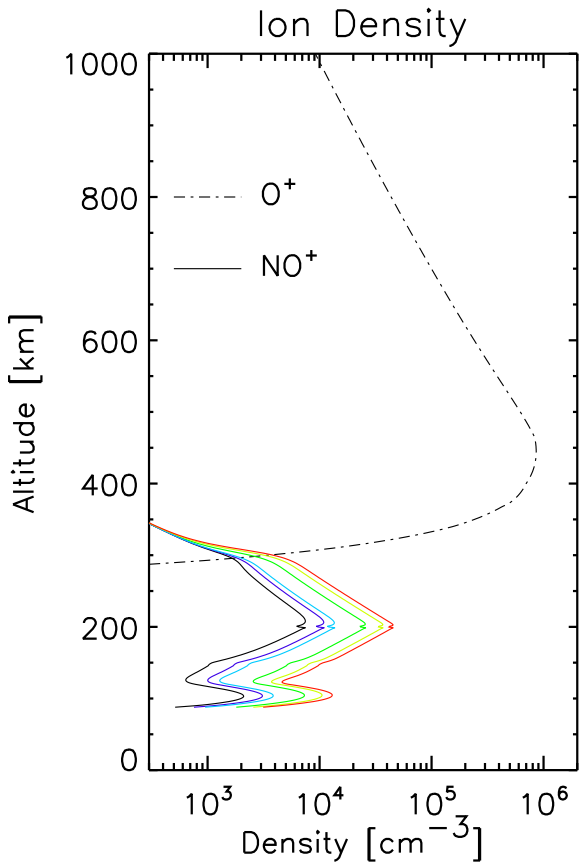

FIGURE 1
Initial density profile.

atmosphere–ionosphere coupled model (Wu, 2015; Shinagawa et al., 2018; Pedatella et al., 2024). The linear growth rate of the Rayleigh–Taylor instability estimated from the simulated parameters shows reasonable seasonal and longitudinal patterns and strong day-to-day variability. Shinagawa et al. (2018) attributed the day-to-day variability to the forcing from the lower atmosphere. The ionospheric altitude variation driven from above (solar and geomagnetic activities) and below (atmospheric activities) makes the occurrence conditions of EPBs more complicated.

This paper aims to address this challenge by utilizing the 3D high-resolution bubble (HIRB) model, which provides a detailed framework for simulating EPB evolution under a range of ionospheric conditions and thereby improves our understanding of their behavior and predictability (Yokoyama et al., 2014; Yokoyama et al., 2015; Yokoyama et al., 2019). The spectral characteristics of the irregularities inside EPBs have been studied using the HIRB model (Rino et al., 2018b; a; Rino et al., 2023), and a comparison with radar observations has been conducted (Tulasi Ram et al., 2017; Tulasi Ram et al., 2020). In this study, we concentrate on the impact of the ionospheric E-region on the generation of EPBs. It has been known that the E-region conductivity contributes to the flux-tube-integrated linear growth rate of the Rayleigh–Taylor instability because the equatorial F region is coupled with the off-equatorial E region by the magnetic flux tube. To the best of our knowledge, however, such contribution of the E-region conductivity has not been carefully studied. Understanding the importance of E-region conductivity will help in understanding the day-to-day variability of EPB occurrence and the prediction of EPB occurrences in the future.

2 Model description

The high-resolution bubble (HIRB) model developed by Yokoyama et al. (2014) is used in this study. It incorporates an advanced 3D numerical simulation framework to accurately replicate the growth and dynamics of EPBs in the equatorial ionosphere. The governing equations in the model are the continuity (Equation 1) and momentum (Equations 2, 3) equations for O^+ (F region) and NO^+ (E region), and electrons, and the divergence-free current condition (Equation 4), which are written as:

$$\frac{\partial N_j}{\partial t} + \nabla \cdot \left(N_j \mathbf{V}_j \right) = S_j. \tag{1}$$

$$e\left(\mathbf{E} + \mathbf{V}_j \times \mathbf{B}\right) + M_j g - \frac{\nabla\left(N_j k_B T\right)}{N_j} + M_j \nu_{jn}\left(\mathbf{U} - \mathbf{V}_j\right) = 0 \tag{2}$$

$$-e\left(\mathbf{E} + \mathbf{V}_e \times \mathbf{B}\right) + M_e g - \frac{\nabla\left(N_e k_B T\right)}{N_e} + M_e \nu_{en}\left(\mathbf{U} - \mathbf{V}_e\right) = 0 \tag{3}$$

$$\nabla \cdot \mathbf{J} = \nabla \cdot \left[e\left(\sum_j N_j \mathbf{V}_j - N_e \mathbf{V}_e \right) \right] = 0. \tag{4}$$

where j stands for each ion species, $N_{j,e}$ is the ion/electron density with quasi-neutrality condition ($\sum_j N_j = N_e$), $\mathbf{V}_{j,e}$ is the ion/electron velocity, S_j represents the chemical terms, e is an electron charge, $\mathbf{E} = \mathbf{E}_0 - \nabla\phi$ is the electric field, $\mathbf{E}_0$ is the background electric field, ϕ is the electrostatic polarization potential, $\mathbf{B}$ is the dipole magnetic field, $M_{j,e}$ is the ion/electron mass, g is the gravitational acceleration, k_B is the Boltzmann constant, $T = T_j = T_e$ is the ion/electron temperature (isothermal condition), $\nu_{jn,en}$ is the ion/electron collision frequency with neutrals, $\mathbf{U}$ is the neutral wind velocity, and $\mathbf{J}$ is the total current density. Background parameters are obtained from NRLMSISE-00 and IRI-2007: F10.7 is 150, local time is 2000, the day of the year is 83, and the longitude is 135°.

The simulation setting in this study is basically the same as those conducted in Yokoyama et al. (2014), except for the plasma density (NO^+) in the E region. Six different initial conditions were set by increasing the production rate of NO^+ ions in Equation 1 by factors of 2, 3, 10, 20, and 30. This modification is applied to all latitudes so that the magnetic field lines with any apex altitudes over the dip equator penetrate the E region at the corresponding latitudes. Increasing NO^+ has negligible impacts on the collision frequency and flux tube electron content gradient. The uniform eastward neutral wind of 120 m s^{-1} is applied in the F region, and the background electric field was set to be zero for simplicity.

3 Results

Figure 1 shows plasma density profiles at the beginning of the simulations. Six solid lines indicate NO^+ densities for six different simulation conditions, and a dotted line indicates the common O^+

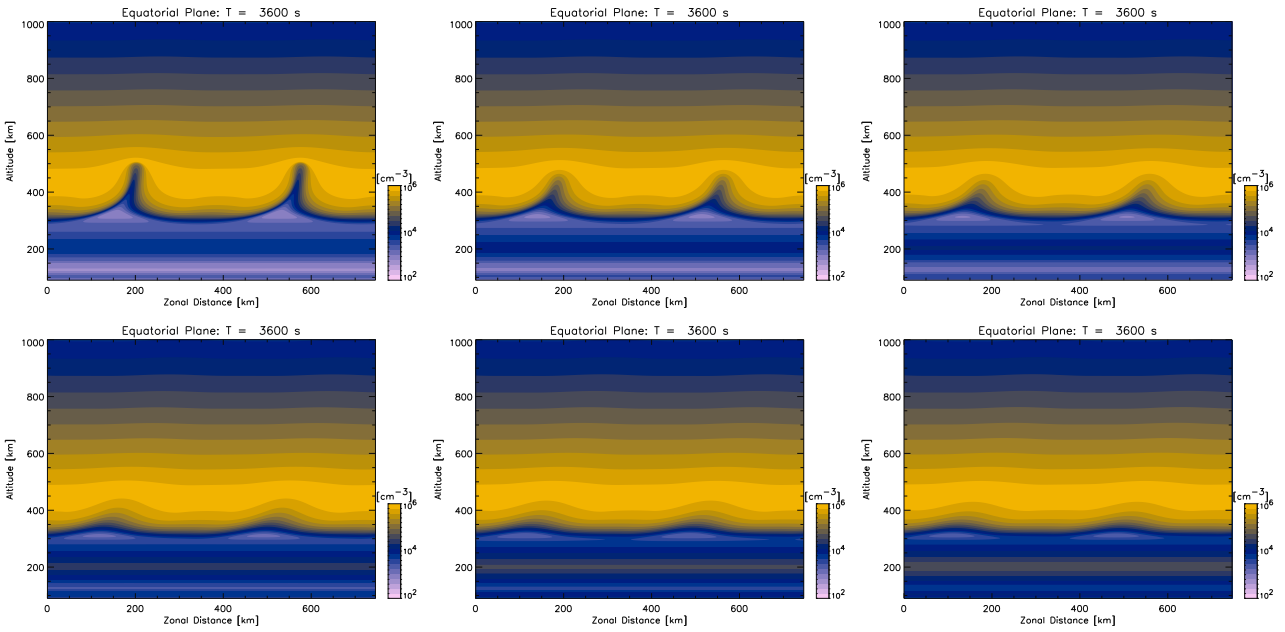

FIGURE 2
Plasma density distribution on a magnetic equatorial plane at $T = 3600$ s for six cases. Larger NO^+ density weakens the growth of EPBs.

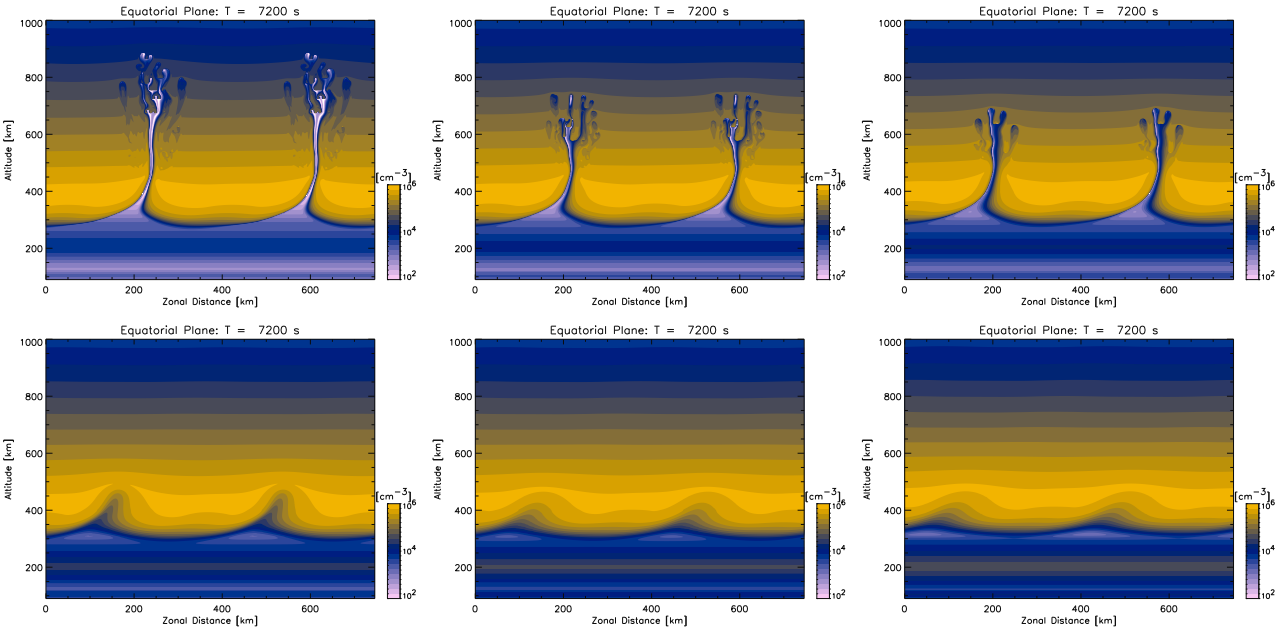

FIGURE 3
Same as Figure 2 at 7,200 s.

density for all cases. The difference of the NO^+ density in the E region between the highest and the lowest cases is less than one order. Then, the initial sinusoidal perturbation resembling a large-scale wave structure (e.g., Tsunoda and White, 1981) is applied by raising the density profile perpendicular to **B** in the same way as Yokoyama et al. (2014). Figure 2 shows plasma density distribution on a magnetic equatorial plane at $T = 3600$ s after the beginning of the simulation for the six cases described above. Results at $T = 7200$ s are shown in Figure 3. It is clearly seen that larger NO^+ density in the E region weakens the growth of EPBs. The initial seedings in the top three cases eventually turned into structured EPBs in the top of the F region, while the seeding stayed at the bottom of the F region in the bottom three cases. Although the difference of the NO^+ density in the E region between the highest and the lowest cases is

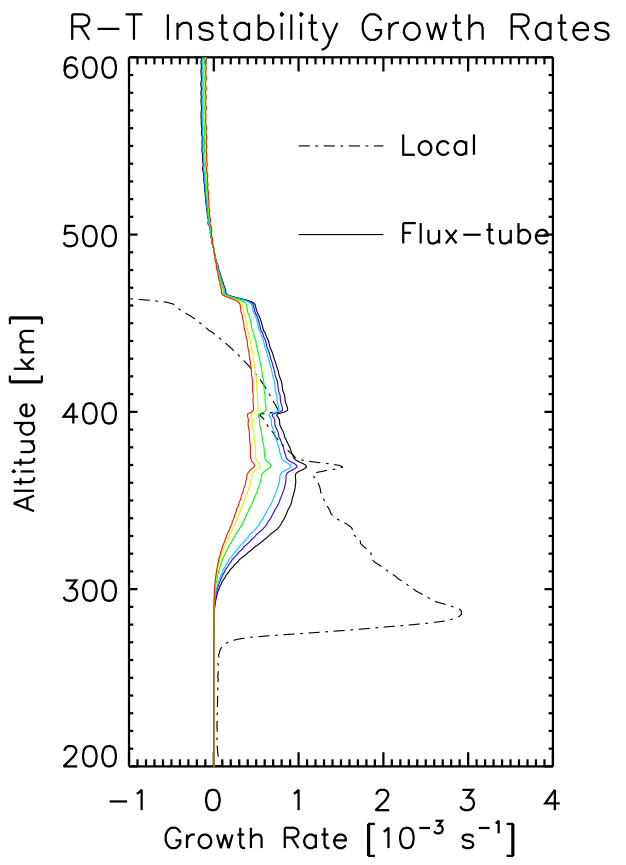

FIGURE 4
Profiles of local and flux-tube-integrated growth rates of Rayleigh–Taylor instability.

less than one order, it has a strong impact on the growth of EPBs. Our simulations reveal critical insights into the dynamics of EPB growth and its sensitivity to E-region plasma density or conductivity.

4 Discussion

The local linear growth rate of Rayleigh–Taylor instability (γ_L) was given as Equation 5 (e.g., Kelley, 2009)

$$\gamma_L = \left(\frac{E_z}{B} - \frac{g}{\nu_{in}}\right)\frac{1}{N}\frac{\partial N}{\partial z}. \quad (5)$$

This formula does not have an E region contribution to the growth rate. In the equatorial and low-latitude ionosphere, the equatorial F region is coupled with the off-equatorial E region along the magnetic flux tubes. The flux-tube-integrated linear growth rate of Rayleigh–Taylor instability (γ_{FT}) was derived by Sultan (1996) and given as Equation 6

$$\gamma_{FT} = \frac{\Sigma_P^F}{\left(\Sigma_P^E + \Sigma_P^F\right)}\left(\frac{E_z}{B}L^3 - \frac{g_e}{\nu_{\text{eff}}^F}\right)K^F, \quad (6)$$

where Σ_P^F and Σ_P^E are the flux-tube-integrated Pedersen conductivities in the F region and the E region, respectively, L is the McIlwain L-parameter, g_e is the downward gravity acceleration, ν_{eff}^F is the flux-tube-integrated effective ion-neutral collision frequency weighted by the electron density, and K^F is the vertical gradient of flux-tube-integrated electron content in the F region. The recombination rate that would appear in this formula is ignored for simplicity.

Figure 4 shows the local and flux-tube-integrated linear growth rate of Rayleigh–Taylor instability at the initial stage for the six simulation cases. The maximum value of the flux-tube-integrated growth rate for the six cases was $1.093\times10^{-3}, 0.980\times10^{-3}, 0.905\times10^{-3}, 0.668\times10^{-3}, 0.539\times10^{-3}, 0.471\times10^{-3}$ in descending order. The difference in the growth rate comes only from the factor $\Sigma_P^F/(\Sigma_P^E+\Sigma_P^F)$ and stays within approximately a factor of 2 among them. Needless to say, the local growth rates are exactly the same in all cases.

Even minor changes in the linear growth rate could lead to significant differences in EPB growth after a few hours. This finding is particularly important in real applications, where variability in E-region conductivity due to factors such as geomagnetic activity or lower atmosphere phenomena can lead to significant changes in EPB behavior. Furthermore, the impact of E-region conductivity on the temporal characteristics of EPBs may suggest that real-time measurements could be valuable for improving EPB forecasting. By integrating E-region conductivity data into predictive models, it may be possible to enhance the accuracy of forecasts and provide more reliable warnings for communication and navigation systems affected by EPBs.

Our simulation results, unfortunately, emphasize the difficulty of forecasting EPBs based on the growth rate estimation, even though we have access to multiple real-time observations. First, we need to obtain the flux-tube-integrated growth rate, which means ionospheric parameters along the magnetic flux tube, such as E-region plasma density at the off-equatorial regions. This information may only be available at limited longitude sectors where sufficient instruments have been installed. Second, even if sufficient observations are available to estimate the flux-tube-integrated growth rate, the threshold of the growth rate by which the evolution of EPBs should be judged is difficult to define. As shown in this study, a moderate variation of the growth rate becomes a significant difference in EPB growth into the top of the ionosphere. This is a major factor that has made forecasting EPB generation quite difficult for several decades.

5 Conclusion

This study advances our understanding of equatorial plasma bubble (EPB) dynamics by employing the 3D high-resolution bubble (HIRB) model to simulate and analyze EPB growth under various ionospheric E-region conditions. A key finding is the significant impact of E-region conductivity on EPB development, even when linear growth rates of the Rayleigh–Taylor instability (RTI) show moderate variation. Increased E-region conductivity leads to weaker EPB growth. This underscores the importance of considering E-region conductivity as a crucial factor in EPB forecasting models. Integrating real-time E-region conductivity measurements into forecasting models could further enhance their accuracy and reliability, offering better predictions and mitigation strategies for communication and navigation systems affected by EPBs. However, our results highlight that traditional linear growth rate analyses alone may not fully capture the complexities of EPB

behavior and suggest the difficulty of predicting EPB generation in advance. Overall, this research contributes valuable insights into the intricate relationship between ionospheric parameters and EPB formation, emphasizing the need for a holistic approach to EPB modeling. Future work should focus on refining these models and incorporating additional factors to improve forecasting capabilities and better understand the nuances of EPB behavior.

Data availability statement

The raw data supporting the conclusions of this article will be made available by the authors, without undue reservation.

Author contributions

TY: conceptualization, data curation, formal analysis, funding acquisition, investigation, methodology, project administration, resources, software, supervision, validation, visualization, writing–original draft, and writing–review and editing.

Funding

The author(s) declare that financial support was received for the research, authorship, and/or publication of this article. This work was supported by JSPS KAKENHI Grant Numbers JP20K04037, JP20H00197, and JP22K21345. The computer simulation was mostly performed on the A-KDK computer system at the Research Institute for Sustainable Humanosphere, Kyoto University. This research is also supported by the Collaborative Research Project on Computer Science with High-Performance Computing at Nagoya University.

Conflict of interest

The author declares that the research was conducted in the absence of any commercial or financial relationships that could be construed as a potential conflict of interest.

The author(s) declared that they were an editorial board member of Frontiers, at the time of submission. This had no impact on the peer review process and the final decision.

Publisher's note

References

Aa, E., Zhang, S.-R., Coster, A. J., Erickson, P. J., and Rideout, W. (2023). Multi-instrumental analysis of the day-to-day variability of equatorial plasma bubbles. *Front. Astron. Space Sci.* 10, 1167245. doi:10.3389/fspas.2023.1167245

Abdu, M. A., Batista, I. S., Reinisch, B. W., de Souza, J. R., Sobral, J. H. A., Pedersen, T. R., et al. (2009). Conjugate point equatorial experiment (COPEX) campaign in Brazil: electrodynamics highlights on spread f development conditions and day-to-day variability. *J. Geophys. Res.* 114, A04308. doi:10.1029/2008JA013749

Carter, B. A., Yizengaw, E., Retterer, J. M., Francis, M., Terkildsen, M., Marshall, R., et al. (2014). An analysis of the quiet time day-to-day variability in the formation of postsunset equatorial plasma bubbles in the southeast asian region. *J. Geophys. Res. Space Phys.* 119, 3206–3223. doi:10.1002/2013JA019570

Kelley, M. C. (2009). "The earth's ionosphere: plasma physics and electrodynamics," in *Boston: int. Geophys. Ser.* 2nd edn, 96. Academic Press.

Pedatella, N. M., Aa, E., and Maute, A. (2024). Quasi 6-day planetary wave oscillations in equatorial plasma irregularities. *J. Geophys. Res. Space Phys.* 129, e2023JA032312. doi:10.1029/2023ja032312

Rino, C., Carrano, C. S., Groves, K. M., and Yokoyama, T. (2018a). A configuration space model for intermediate-scale ionospheric structure. *Radio Sci.* 53, 1472–1480. doi:10.1029/2018RS006678

Rino, C., Yokoyama, T., and Carrano, C. (2018b). Dynamic spectral characteristics of high-resolution simulated equatorial plasma bubbles. *Prog. Earth Planet. Sci.* 5, 83. doi:10.1186/s40645-018-0243-0

Rino, C., Yokoyama, T., and Carrano, C. (2023). A three-dimensional stochastic structure model derived from high-resolution isolated equatorial plasma bubble simulations. *Earth, Planets Space* 75, 64. doi:10.1186/s40623-023-01823-6

Scannapieco, A. J., and Ossakow, S. L. (1976). Nonlinear equatorial spread F. *Geophys. Res. Lett.* 3, 451–454. doi:10.1029/gl003i008p00451

Shinagawa, H., Jin, H., Miyoshi, Y., Fujiwara, H., Yokoyama, T., and Otsuka, Y. (2018). Daily and seasonal variations in the linear growth rate of the Rayleigh–taylor instability in the ionosphere obtained with gaia. *Prog. Earth Planet. Sci.* 5, 16. doi:10.1186/s40645-018-0175-8

Sultan, P. J. (1996). Linear theory and modeling of the Rayleigh–Taylor instability leading to the occurrence of equatorial spread *F. J. Geophys. Res.* 101 (26), 26875–26891. doi:10.1029/96ja00682

Tsunoda, R. T., and White, B. R. (1981). On the generation and growth of equatorial backscatter plumes 1. Wave structure in the bottomside *F* layer. *J. Geophys. Res.* 86, 3610–3616. doi:10.1029/ja086ia05p03610

Tulasi Ram, S., Ajith, K. K., Yokoyama, T., Yamamoto, M., Hozumi, K., Shiokawa, K., et al. (2020). Dilatory and downward development of 3-m scale irregularities in the funnel-like region of a rapidly rising equatorial plasma bubble. *Geophys. Res. Lett.* 47, e2020GL087256. doi:10.1029/2020GL087256

Tulasi Ram, S., Ajith, K. K., Yokoyama, T., Yamamoto, M., and Niranjan, K. (2017). Vertical rise velocity of equatorial plasma bubbles estimated from Equatorial Atmosphere Radar (EAR) observations and HIRB model simulations. *J. Geophys. Res. Space Phys.* 122, 6584–6594. doi:10.1002/2017JA024260

Woodman, R. F. (2009). Spread F – an old equatorial aeronomy problem finally resolved? *Ann. Geophys.* 27, 1915–1934. doi:10.5194/angeo-27-1915-2009

Woodman, R. F., and LaHoz, C. (1976). Radar observations of *F* region equatorial irregularities. *J. Geophys. Res.* 81, 5447–5466. doi:10.1029/ja081i031p05447

Wu, Q. (2015). Longitudinal and seasonal variation of the equatorial flux tube integrated Rayleigh–taylor instability growth rate. *J. Geophys. Res. Space Phys.* 120, 7952–7957. doi:10.1002/2015JA021553

Yokoyama, T. (2017). A review on the numerical simulation of equatorial plasma bubbles toward scintillation evaluation and forecasting. *Prog. Earth Planet. Sci.* 4, 37. doi:10.1186/s40645-017-0153-6

Yokoyama, T., Jin, H., and Shinagawa, H. (2015). West wall structuring of equatorial plasma bubbles simulated by three-dimensional HIRB model. *J. Geophys. Res. Space Phys.* 120, 8810–8816. doi:10.1002/2015JA021799

Yokoyama, T., Jin, H., Shinagawa, H., and Liu, H. (2019). Seeding of equatorial plasma bubbles by vertical neutral wind. *Geophys. Res. Lett.* 46, 7088–7095. doi:10.1029/2019GL083629

Yokoyama, T., Shinagawa, H., and Jin, H. (2014). Nonlinear growth, bifurcation, and pinching of equatorial plasma bubble simulated by three-dimensional high-resolution bubble model. *J. Geophys. Res. Space Phys.* 119 (10). 474–10,482. doi:10.1002/2014JA020708

frontiers | Frontiers in Astronomy and Space Sciences

TYPE Original Research
PUBLISHED 12 December 2024
DOI 10.3389/fspas.2024.1478536

OPEN ACCESS

EDITED BY
Jorge Luis Chau,
Leibniz Institute of Atmospheric Physics (LG), Germany

REVIEWED BY
Marco Milla,
Pontifical Catholic University of Peru, Peru
Magnus Ivarsen,
University of Oslo, Norway

*CORRESPONDENCE
Rattanakorn Koontaweepunya,
rakoon@bu.edu

RECEIVED 09 August 2024
ACCEPTED 11 November 2024
PUBLISHED 12 December 2024

CITATION
Koontaweepunya R, Dimant YS and Oppenheim MM (2024) Non-Maxwellian ion distribution in the equatorial and auroral electrojets.
Front. Astron. Space Sci. 11:1478536.
doi: 10.3389/fspas.2024.1478536

Non-Maxwellian ion distribution in the equatorial and auroral electrojets

Rattanakorn Koontaweepunya*, Yakov S. Dimant and Meers M. Oppenheim

Center for Space Physics, Boston University, Boston, MA, United States

Strong electric fields in the auroral and equatorial electrojets can distort the background ion distribution function away from the Maxwellian. We developed a collisional plasma kinetic model using the Boltzmann equation and a simple BGK collision operator to predict a relatively simple relationship between the intensity of the background electric field and the resulting ion distribution function. To test the model, we perform 3-D plasma particle-in-cell simulations and compared the results to the model. Both the simulation and the analytical model assume a constant ion-neutral collision rate. The simulations show less ion heating in the Pedersen direction than in the analytical model but nearly identical overall heating. The model overestimates heating in the Pedersen direction because the simple BGK operator models collisions as a kinetic friction only in the Pedersen direction. On the other hand, the fully kinetic particle-in-cell code captures the physics of ion scattering in 3-D and therefore heats ions more isotropically. Although the simple BGK analytical theory does not precisely model the non-Maxwellian ion distribution function, it does capture the overall momentum and energy flows and therefore can provide the basis of further kinetic analysis of E-region wave evolution during strongly driven conditions.

KEYWORDS

ion distribution function, BGK collision operator, Maxwell molecule collision model, Pedersen conductivity, PIC simulation, plasma instabilities, ion temperature anisotropy, E-region electrojet

1 Introduction

Strong DC electric fields in the auroral and equatorial electrojets drive plasma instabilities in the E-region ionosphere. When perpendicular to the global magnetic field, these electric fields generate strong cross-field plasma instabilities, such as the Farley–Buneman instability (Farley, 1963; Buneman, 1963), gradient drift instability (Hoh, 1963; Maeda et al., 1963; Simon, 1963), electron thermal instability (Dimant and Sudan, 1995; 1997; Robinson, 1998; St. -Maurice and Kissack, 2000), and ion thermal instability (Kagan and Kelley, 2000; Dimant and Oppenheim, 2004). These plasma instabilities serve to explain the plasma density irregularities that for many years have been observed in the E-region ionosphere by radar and sounding rockets.

Analytical kinetic models of plasma instabilities can accurately describe plasma wave growth and decay, but this often requires numerous approximations, such as eliminating nonlinear terms and simplifying collisional components. Such approximations can limit their applicability. Kinetic simulations of plasma using particle-in-cell (PIC) codes can also solve for wave evolution but can consume a lot of computer power and apply to only a limited

range of parameters. For example, Oppenheim et al. (2008) expended 4 years of CPU time to simulate a 2-D patch of plasma for a quarter of a second, although the simulation required less than 24 h of wall clock time using a supercomputer (see also Oppenheim and Dimant, 2004, Oppenheim and Dimant, 2013, and Oppenheim et al., 2020)]. It is therefore practical to develop a fluid analytical kinetic model which is more computationally efficient than the PIC model while, at the same time, is able to capture the development of kinetic plasma instabilities.

Such a model will need to assume a 0^{th}-order ion distribution function which is not Maxwellian due to the Pedersen drift and collisions with the neutrals. To develop an accurate analytical kinetic model of plasma instabilities in the E-region ionosphere, we need to understand how the electric fields in the electrojets affect the background ion distribution function.

In the ionosphere, strong DC electric fields develop in two places: in high magnetic latitudes and within a few degrees of the magnetic equator. The electric fields in the auroral electrojet come from the current mapping between the magnetosphere and the ionosphere near the poles, while the electric fields in the equatorial electrojet come from the E-region dynamo effect driven by the zonal wind (Kelley, 2009). In the latter case, the zonal wind velocity $\vec{U}$ and the geomagnetic field $\vec{B}$ must satisfy the condition $\nabla \times \left(\vec{U} \times \vec{B}\right) \neq 0$ in order to generate an electrojet and its associated electric fields (Dimant et al., 2016).

The E-region ionosphere is weakly ionized, with neutrals outnumbering ions by more than 10^6 to 1 (Schunk and Nagy, 2009). In the lower E-region, the ions do not gyrate around the geomagnetic field because frequent collisions with neutrals effectively cause them to become unmagnetized (Kelley, 2009). These collisions also prevent ions from accelerating *ad infinitum* along the electric field. As a result, the bulk of the ions in steady state drifts on average with the Pedersen velocity, which is proportional to the electric field divided by the ion-neutral collision rate. On the other hand, the electrons are highly magnetized and mostly drift with the Hall velocity perpendicular to the ions. The relative drift between the ions and electrons causes plasma instabilities such as the Farley–Bunemann instability.

If the external DC electric field in the electrojet is strong enough, it can leads to a large anisotropy in the ion distribution function with clear distortions from the Maxwellian. St-Maurice and Schunk (1979) developed the theory and showed observational evidence for non-Maxwellian ion distribution functions in the high-latitude E- and F-regions. The DC electric field can be especially strong at high latitudes during geomagnetic storms. Compared to the high-latitude E- and F-regions, the equatorial E-region has less intense electric fields, so we expect the typical distortion in the ion distribution to be smaller. Still, even there, extreme geomagnetic storms can intensify the electric fields enough to deviate the ion distribution function significantly from the Maxwellian.

Our study develops a collisional plasma kinetic model which relates the intensity of the external electric field to the ion velocity distribution function. We restrict our treatment to a spatially uniform and quasi-steady ionosphere which represents the background for developing instabilities. To describe the ion-neutral collisions, our kinetic model uses the BGK collision operator (Bhatnagar et al., 1954), which is a mathematically simple way of describing plasma collisions (Nicholson, 1983). Despite its inaccuracy, this simplified operator conserves the particle number and the average momentum and energy of the colliding particles. A hybrid simulation by Kovalev et al. (2008), based on the BGK collision term for ions, gave results comparable to the more accurate hybrid and full PIC simulations (Janhunen, 1995; Oppenheim et al., 1995; Oppenheim et al., 1996; Oppenheim et al., 2008; Oppenheim and Dimant, 2004; Young et al., 2020). Else et al. (2009) found that the constant collision rate BGK model agrees with a more realistic constant mean free path model in regimes where the Pedersen velocity is less than or comparable to the neutral thermal velocity. In this study, we quantify the accuracy of a BGK plasma kinetic model by comparing the analytical results to results from a more accurate fully kinetic PIC simulation.

The paper is organized as follows. Section 2 describes the simulation methods. Section 3 presents the analytical model and compares it to the simulation results. Section 4 discusses the discrepancies between the analytical results and the simulation. Section 5 summarizes our major results and forecasts future research.

2 Simulation methods

We used an EPPIC—electrostatic parallel plasma-in-cell simulator—to simulate the E-region background ions. EPPIC, like other particle-in-cell (PIC) codes, simulates plasma as individual particles. This enables PIC simulations to reproduce the kinetic behaviors of plasma. We are interested in the kinetic behavior of plasma—that is, the distortion of the ion distribution function. For more information about PIC codes, see Birdsall and Langdon (1991). For detailed explanations of EPPIC, see Oppenheim and Dimant (2004), Oppenheim et al. (2008), and Oppenheim and Dimant (2013).

We set the magnetic field to zero in our simulation because the E-region background ions are unmagnetized. We also excluded electrons from our simulation, using instead a uniform background electron plasma that does not respond to any fields. We did this to avoid cross-drift between highly magnetized electrons and highly collisional background ions which would have led to internally generated electric fields and the Farley–Buneman instability (Farley, 1963; Buneman, 1963). This paper only explores the physics of the ion distribution function independent of the electron generated fields. EPPIC simulates background ions as PIC particles and neutrals as a uniform, constant background. Our simulation is in three dimensions (3-D), even though a two-dimensional (2-D) simulation would have sufficed for the behavior we were interested in. Table 1 gives the simulation parameters.

The E-region background ions are highly collisional with the neutrals. In our simulation, we used a constant ion-neutral collision rate which does not depend on the particle's velocity. This is analogous to the Maxwell molecule collision model in Schunk and Nagy (2009) which results in a velocity-independent collision rate. EPPIC employs a statistical method of applying collisional effects to ions. At each time step, it designates a number of ions for collision in accordance with the ion-neutral collision rate specified in the input deck; it then chooses that number of PIC particles at random, independent of ion location and velocity. For each collision, the code creates a neutral molecule assuming a random

10.3389/fspas.2024.1478536

TABLE 1 Simulation parameters.

Simulation parameter	Symbol	Value
Ion parameter		
Ion mass	m_i	5×10^{-26} kg
Ion-neutral collision rate	ν_{in}	1,050s^{-1}
Ion number density	n_0	4×10^{8}m^{-3}
Ion charge	e	1.602×10^{-19} C
Neutral parameter		
Neutral thermal velocity	ν_T	287 m/s
Neutral mass	m_n	5×10^{-26} kg
Simulation parameter		
Grid size	$dx = dy = dz$	0.15 m
Number of grids	(nx, ny, nz)	(1,024, 512, 512)
Time step	dt	5.6×10^{-5} s
Number of time steps	nt	512

thermal distribution with the specified neutral temperature and velocity. The algorithm then collides the PIC ion and the neutral, assuming conservation of energy and momentum, changing the ion's momentum. The algorithm then tabulates the neutral momentum and energy change and discards detailed information about the neutral particle. In the E-region, neutrals are many orders of magnitude more numerous than ions [$n_n/n_i > 10^6$—Schunk and Nagy (2009)]. Therefore, neutrals that collide with ions constitute a very small part of the neutrals and do not affect their overall momentum and temperature.

Section 3.2 details the specific simulation setup as well as the analysis methods used for the simulation results.

3 Results

3.1 Analytical model of the background ion distribution function

3.1.1 Derivation of the distorted ion distribution function

The simplest kinetic equation for the ion distribution function (IDF) with the Bhatnagar–Gross–Krook (BGK) collision term (Bhatnagar et al., 1954) is given by

$$\frac{\partial f}{\partial t}+\frac{e}{m_i}\vec{E}\cdot\frac{\partial f}{\partial \vec{V}}+\vec{v}\cdot\frac{\partial f}{\partial \vec{r}}=-\nu_{in}\left(f-\frac{n_i(\vec{r},t)}{n_0}f_0^{\mathrm{Coll}}\right),\quad(1)$$

where $v=|\vec{v}|$ is the ion speed, ν_{in} is the ion-neutral collision frequency, T_n is the neutral temperature (in energy units), m_i is the ion mass (equal to the neutral mass), $\vec{E}$ is the external electric field, and

$$f_0^{\mathrm{Coll}}(v)\equiv n_0\left(\frac{m_i}{2\pi T_n}\right)^{3/2}\exp\left(-\frac{m_i v^2}{2T_n}\right).$$

The function $f_0^{\mathrm{Coll}}(v)$ is the spatially uniform and stationary ion Maxwellian distribution function, normalized to the mean ion density n_0 with no external electric field. The BGK collision term on the RHS of Equation 1 assumes Maxwell collisions (Schunk and Nagy, 2009) with the given constant a constant ion-neutral collision rate ν_{in} which accurately models Maxwell molecule collisions (Schunk and Nagy, 2009).

Below, we only consider the background conditions with the externally imposed electric field before developing any instabilities, $\vec{E}=\vec{E}_0$. For the corresponding spatially uniform and stationary background ion distribution function $f_0(\vec{v})$, Equation 1 reduces to

$$\vec{a}_0\cdot\frac{\partial f_0}{\partial \vec{V}}=-\nu_{in}\left(f_0-f_0^{\mathrm{Coll}}\right),\quad(2)$$

where $\vec{a}_0\equiv e\vec{E}_0/m_i$ is the free-ion acceleration. By introducing a Cartesian coordinate system with the axis y directed along $\vec{a}_0$ and integrating Equation 2 over the perpendicular velocity components ν_y ν_x and ν_z, we obtain

$$a_0\frac{\partial F_0}{\partial V_y}=-\nu_{in}\left(F_0-F_0^{\mathrm{Coll}}\right).\quad(3)$$

Here,

$$F_0(\nu_y)\equiv\int_{-\infty}^{+\infty}\!\!\int f_0\quad d\nu_x d\nu_z\quad(4)$$

and

$$F_0^{\mathrm{Coll}}(\nu_y)\equiv\frac{n_0}{\sqrt{2\pi}\nu_{Ti}}\exp\left(-\frac{\nu_y^2}{2\nu_{Ti}^2}\right),\quad(5)$$

where $\nu_{Ti}\equiv\sqrt{T_n/m_i}$ is the thermal velocity of the neutral particles ($m_i=m_n$). In the BGK approximation, the ion velocity distribution in the two perpendicular directions remains undisturbed by the field $\vec{E}_0$, so that the full 3-D IDF becomes

$$f_0(\nu_x,\nu_y,\nu_z)=\frac{F_0(\nu_y)}{2\pi\nu_{Ti}^2}\exp\left(-\frac{\nu_x^2+\nu_z^2}{2\nu_{Ti}^2}\right).\quad(6)$$

Plugging Equation 5 into Equation 3 and solving the latter yields

$$F_0(\nu_y)=\frac{n_0\nu_{in}}{2a_0}\exp\left[-\frac{\nu_{in}\nu_y}{a_0}+\frac{1}{2}\left(\frac{\nu_{in}\nu_{Ti}}{a_0}\right)^2\right]\left[1+erf\left(\frac{\nu_y-\nu_{in}\nu_T^2/a_0}{\sqrt{2}\nu_{Ti}}\right)\right],\quad(7)$$

where $erf(y)=(2/\sqrt{\pi})\int_0^y e^{-t^2}dt$ is the error function. Introducing the dimensionless ion velocity $u\equiv\nu_{in}\nu_y/a_0$ and the dimensionless neutral thermal velocity $u_T\equiv\nu_{in}\nu_{Ti}/a_0$, we can recast Equation 7 as

$$G_0(u)=\frac{1}{2}\exp\left(-u+\frac{u_T^2}{2}\right)\left[1+\mathrm{erf}\left(\frac{u-u_T^2}{\sqrt{2}u_T}\right)\right]=\frac{1}{2}\exp\left(-\frac{u^2}{2u_T^2}\right)w\left(-i\,\frac{u-u_T^2}{\sqrt{2}u_T}\right),\quad(8)$$

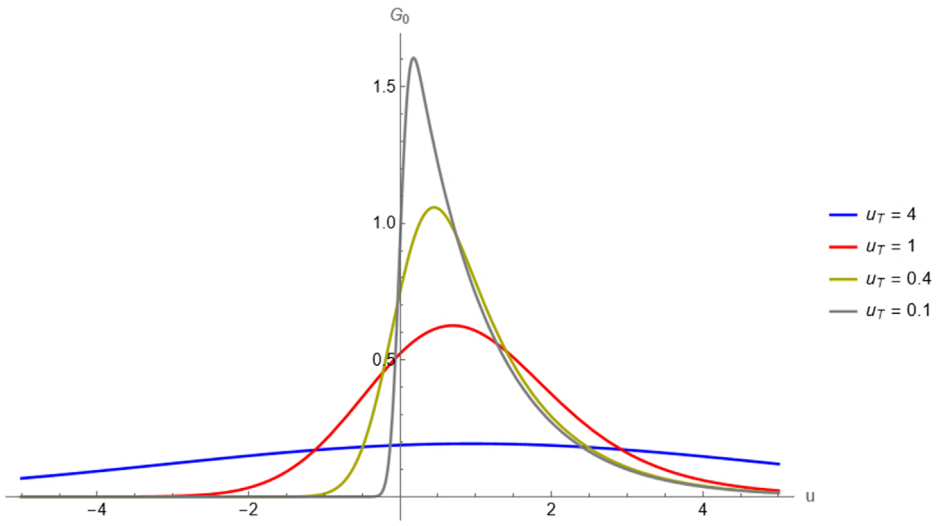

FIGURE 1
Normalized ion distribution function (IDF) for four values of $u_T \equiv v_T/v_{\mathrm{Ped}}$, where $v_{\mathrm{Ped}} = a_0/\nu_{in}$ is the ion Pedersen velocity proportional to E_0. The vertical axis is the function $G_0(u)$, as seen in Equation 8. The horizontal axis is the normalized ion velocity $u \equiv v_y/v_{\mathrm{Ped}}$. Since u is normalized to a_0^{-1}, the IDF is compressed in the horizontal axis by a factor $\propto E_0$; therefore, effective heating does not relate to the full width at half maximum (FWHM) in the usual way. In this plot, curves with smaller FWHM are more strongly heated.

where $G_0(u) = [a_0/(n_0\nu_{in})]F_0(v_y)$ and $w(\zeta) = e^{-\zeta^2}[1 + erf(i\zeta)]$. The function $w(\zeta)$ can be written in terms of the standard plasma dispersion function, $Z(\zeta)$, as $w(\zeta) = -(i/\sqrt{\pi})Z(\zeta)$.

The solution in the form of Equation 8 automatically conserves the number of particles and provides the correct expressions for the Pedersen velocity and effective temperature (see below), as can be deduced from the following integral relationships:

$$\int_{-\infty}^{+\infty} G_0(u)\ du = 1, \quad \int_{-\infty}^{+\infty} uG_0(u)\ du = 1, \quad \int_{-\infty}^{+\infty} u^2 G_0(u)\ du = u_T^2 + 2. \tag{9}$$

Figure 1 shows the normalized ion distribution function in Equation 8 for four values of u_T. Note that $u_T \propto E_0^{-1}$, so the four values of u_T in Figure 1 correspond to four values of E_0. The ion distribution functions with large values of u_T assume Maxwellian shapes, while the ion distribution functions with small values of u_T appear right-skewed when compared to the Maxwellian. The distortion is such that their peaks lie to the left of their bulk velocity, which is equal to one according to Equation 9. Section 3.1.2 explains why the ion distribution function retains the Maxwellian shape at lower higher values of u_T but is distorted at higher lower values of u_T.

3.1.2 Distortion of the ion distribution function in the low and high E_0 limits

The antisymmetrical error function, $erf(\xi)$, at large $|\xi|$ can be approximated as

$$\mathrm{erf}(\xi) \approx \begin{cases} 1 - \dfrac{\exp(-\xi^2)}{\xi\sqrt{\pi}} & \text{if } \xi > 0 \text{ and } \xi \gg 1 \\ -1 + \dfrac{\exp(-\xi^2)}{(-\xi)\sqrt{\pi}} & \text{if } \xi < 0 \text{ and } (-\xi) \gg 1 \end{cases}. \tag{10}$$

Using the bottom approximation from Equation 10, we can show that in the limit where $a_0 \to 0$,

$$G_0(u) \to \frac{1}{\sqrt{2\pi}u_T} \exp\left(-\frac{u^2}{2u_T^2}\right). \tag{11}$$

This corresponds to $f_0 \to f_0^{\mathrm{Coll}}$—the background ion distribution tends toward Maxwellian in the low E_0 limit. Equation 11 does not hold for all values of u. As seen from Equations 8, 11 does not hold if $u \gg u_T^2$. This means that the positive tail of the ion distribution function may deviate significantly from the Maxwellian.

The low E_0 limit can be expressed in terms of the ion Pedersen velocity, $v_{\mathrm{Ped}} = \langle v_y \rangle = a_0/\nu_{in} = eE_0/(m_i\nu_{in})$, and the neutral thermal velocity v_T. If $v_{\mathrm{Ped}} \ll v_T$, then the distortion to the ion distribution function is weak, since the ion distribution function tends toward the Maxwellian. The effective temperature,

$$T_{\mathrm{eff}} = T_n + \frac{mv_{\mathrm{Ped}}^2}{2}, \tag{12}$$

is only slightly higher than T_n, since $mv_{\mathrm{Ped}}^2 \ll T_n$ in this limit.

In the high E_0 limit where $v_{\mathrm{Ped}} \gg v_T$, Equation 8 does not tend toward the Maxwellian, so the ion distribution function will be distorted along the $\vec{E}_0$ direction. The corresponding heating will be very considerable as well, since $mv_{\mathrm{Ped}}^2 \gg T_n$ in Equation 12. Note that the effective thermal velocity, $\sqrt{T_{\mathrm{eff}}/m_i}$, is of the order of the Pedersen velocity: $\sqrt{T_{\mathrm{eff}}/m_i} \approx v_{\mathrm{Ped}}/\sqrt{2}$.

3.2 Background ion distribution functions from the PIC simulation

3.2.1 Kinetic simulation of highly collisional, unmagnetized, $\vec{E_0}$-driven background ions

Our model from Section 3.1 predicts that the background ion distribution function (IDF) will distort away from Maxwellian when E_0 is high enough. Equation 7 gives the one-dimensional IDF we expect to see in the $\vec{E_0}$ direction. To test the validity of our model, we ran four simulation cases using EPPIC. The values of E_0 used in the simulation cases are:

1. $E_0 = 0$ mV/m, which corresponds to $u_T \to \infty$.
2. $E_0 = 24$ mV/m, which corresponds to $u_T = 4$.
3. $E_0 = 94$ mV/m, which corresponds to $u_T = 1$.
4. $E_0 = 235$ mV/m, which corresponds to $u_T = 0.4$.

As before, $u_T \equiv v_T/v_{\text{Ped}}$ is the normalized neutral thermal velocity, $v_T = \sqrt{T_n/m_i}$ is the neutral thermal velocity, and $v_{\text{Ped}} = eE_0/m_i\nu_{in}$ is the ion Pedersen velocity.

Our simulation includes one ion species, one neutral species, and no electrons. The imposed electric field $\vec{E_0}$ points in the y-direction, and there is no imposed magnetic field. As discussed in Section 2, the setup is representative of the plasma condition in the E-region ionosphere where ions are unmagnetized and highly collisional with the neutrals.

Table 1 gives the parameters used across all simulation cases.

3.2.2 Normalization of the discrete ion velocity distribution from the simulation

The simulation outputs a $(v_x \times v_y \times v_z) = (512 \times 512 \times 512)$ array of ion velocity distribution over a 3-D velocity domain. Each dimension of the array covers a 1-D velocity domain of [−20 km/s, 20 km/s]. The grid size is $\Delta v = [20\,km/s - (-20\,km/s)]/512 = 78.125\,m/s$ in each dimension. We reduce the three-dimensional velocity distribution array $f(v_x, v_y, v_z)$ into three one-dimensional velocity distribution arrays—$F_x(v_x)$, $F_y(v_y)$, and $F_z(v_z)$—by summing over two other dimensions. This gives us

$$F_x(v_x) = \sum_{v_y}\sum_{v_z} f(v_x, v_y, v_z)$$

and similarly for $F_y(v_y)$ and $F_z(v_z)$.

To facilitate the comparison with the theory, we normalize $F_x(v_x)$, $F_y(v_y)$, and $F_z(v_z)$ such that the sum of each distribution is equal to $(\Delta v)^{-1}$. This process is analogous to letting the 0^{th} velocity moment of a continuous distribution function equal 1. This in effect normalizes the ion number density to 1. The normalized arrays are given by

$$F'_k(v_k) = \frac{F_k(v_k)}{\sum_{v_k} F_k(v_k)\,\Delta v}, \tag{13}$$

where k is either x, y, or z. The normalization makes it so that $\sum_{v_k} F'_x(v_x) = (\Delta v)^{-1}$ for all k.

3.2.3 Normalization of the continuous ion velocity distribution from the theory

The continuous one-dimensional ion distribution function in the direction parallel to $\vec{E}_0$ direction is given by the theory as $F_0(v_y)$ in Equation 7. For clarity, we reiterate Equation 7 as

$$F^{\text{Theory}_y}(v_y) = \begin{cases} \dfrac{n_0\nu_{in}}{2a_0}\exp\left[-\dfrac{\nu_{in}v_y}{a_0} + \dfrac{1}{2}\left(\dfrac{\nu_{in}v_T}{a_0}\right)^2\right] \\ \quad\left[1 + erf\left(\dfrac{v_y - \frac{v_T^2\nu_{in}}{a_0}}{\sqrt{2}v_T}\right)\right], & \text{if } a_0 \neq 0 \\ \dfrac{n_0}{\sqrt{2\pi}v_T}\exp\left(-\dfrac{v_y^2}{2v_T^2}\right), & \text{if } a_0 = 0 \end{cases},$$

where we incorporate the result in the low E_0 limit from Section 3.1.2.

For the directions perpendicular to $\vec{E_0}$, the theory assumes an undisturbed Maxwellian given by

$$F_j^{\text{Theory}}(v_j) = \frac{n_0}{\sqrt{2\pi}v_T}\exp\left(-\frac{v_j^2}{2v_T^2}\right),$$

where j is either x or z.

To facilitate the comparison with the simulation results, we normalize $F_x^{\text{Theory}}(v_x)$, $F^{\text{Theory}_y(v_y)}$, and $F^{\text{Theory}_z}(v_z)$ such that the area under the curve of each distribution is equal to one. This sets the 0^{th} velocity moment of the distribution to 1 and normalizes the ion number density to 1. The normalized distribution functions are given by

$$F_k'^{\text{Theory}}(v_k) = \frac{F_k^{\text{Theory}}(v_k)}{\int_{-\infty}^{\infty} F_k^{\text{Theory}}(v)\quad dv} = \frac{F_k^{\text{Theory}}(v_k)}{n_0}, \tag{14}$$

where k is either x, y, or z. The normalization makes it so that $\int_{-\infty}^{\infty} F_k'^{\text{Theory}}(v_k)\quad dv_k = 1$ for all k.

3.2.4 Choice of ν_{in} in the theoretical results

Although EPPIC used the ion-neutral collision rate $\nu_{in} = 1050s^{-1}$ as its input, the outputted $F'_y(v_y)$ instead exhibits $\nu_{in} = 1082s^{-1}$ at an effective collision rate of $1082s^{-1}$. The simulation gives the ion bulk velocity $\langle v_y \rangle$, and the relation $\langle v_y \rangle = eE_0/(m_i\nu_{in})$ defines the effective ν_{in}. To ensure compatibility between the simulation results and the theory, we chose the effective ν_{in} in $F_y'^{\text{Theory}}(v_y)$ such that

$$\int_{-\infty}^{\infty} v_y F_y'^{\text{Theory}}(v_y)\quad dv_y = \sum_{v_y} v_y F'_y(v_y)\,\Delta v. \tag{15}$$

The expression on the left-hand side of Equation 15 is the first velocity moment of $F_y'^{\text{Theory}}$, which gives the theoretical bulk velocity of the ions. The expression on the right-hand side of Equation 15 gives the bulk velocity of the simulated ions. By matching these two quantities, we ensure that the theoretical ion distribution function is representative of the condition in the simulated background ions to first order.

We numerically calculated both sides of Equation 15 for $E_0 = 24$ mV/m, $E_0 = 94$ mV/m, and $E_0 = 235$ mV/m. For all of these cases, the effective $\nu_{in} = 1082s^{-1}$ satisfies Equation 15 to within ±2m/s. On the other hand, the PIC $\nu_{in} = 1050s^{-1}$ satisfies Equation 15 only to within $\pm 22 m/s$. Therefore, the simulated background ions exhibit an effective ion-neutral collision rate of $1082s^{-1}$ and not $1050s^{-1}$.

Table 2 shows the matching bulk velocities for the effective $\nu_{in} = 1082s^{-1}$, while Table 3 shows the bulk velocity mismatch for the

TABLE 2 Bulk velocities, directional thermal velocities, and total thermal energies for the effective $\nu_{in} = 1082s^{-1}$.

Case	$\langle v_y \rangle$ (m/s)	$v_{th,y}$ (m/s)	$v_{th,j}$ (m/s)	$\sum v_{th}^2$ (J/kg)	Theory/simulation Energy ratio
E_0 = 0 mV/m					
Simulation	0	287	287	247,107	1
Theory	0	287	287	247,107	
E_0 = 24 mV/m					
Simulation	70	292	289	252,306	0.9978
Theory	70	295	287	251,763	
E_0 = 94 mV/m					
Simulation	279	358	317	329,142	0.9864
Theory	279	400	287	324,738	
E_0 = 235 mV/m					
Simulation	697	606	444	761,508	0.9611
Theory	696	753	287	731,747	

$\langle v_y \rangle$ and $v_{th,y}$ are bulk velocity and thermal velocity in the Pedersen direction, respectively. $v_{th,j} = v_{th,x} = v_{th,y}$ is the thermal velocity in the directions perpendicular to $\vec{E}_0$. $\sum v_{th}^2 = v_{th,y}^2 + 2v_{th,j}^2$ is the total thermal energy per ion mass. The last column shows the total energy ratio between theory and the simulation results.

PIC $\nu_{in} = 1050s^{-1}$. The choice of ν_{in} is irrelevant for $E_0 = 0$mV/m, since the theoretical ion distribution function is an undisturbed Maxwellian.

3.3 Comparison of the theoretical and simulated ion distribution functions

Figure 2A compares the theoretical and simulated ion distribution functions in the Pedersen direction—that is, the direction parallel to $\vec{E_0}$. Equation 14 gives the theoretical ion distribution functions in the Pedersen direction. Equation 13 gives the normalized ion distribution functions for the simulation results. Figure 2A also includes the Maxwellian distribution functions which have the same bulk velocities as the simulation results but assume a neutral thermal velocity of 287 m/s.

In the Pedersen direction, both the theory and the simulation results show ion heating beyond the Maxwellian, although the exact shapes of the distribution differ between the theory and the simulation results. The theoretical ion distribution functions are further right-skewed compared to the simulation, although both are right-skewed compared to the Maxwellian.

Figures 2B, C show the simulated ion distribution functions in directions perpendicular to $\vec{E_0}$. For comparison, the figure includes the undisturbed Maxwellian function which assumes the neutral temperature as the ion temperature. As mentioned in Section 3.1, the theory assumes this undisturbed Maxwellian distribution in the perpendicular directions. The simulation results show ion heating beyond the neutral temperature, especially when E_0 is high. Figures 2B, C are largely identical due to symmetry.

Table 2 reports the bulk and thermal velocities from the theory and simulation. Section 4 discusses the results in more detail.

4 Discussion

In this section, we mostly discuss discrepancies between the analytical results of Section 3.1 and the PIC simulations. On the one hand, the analytical model (hereinafter referred to as "theory") is not perfectly accurate because it is based on the oversimplified BGK collision model. As a result, the theoretical 3-D shape of the ion distribution function turns out to be less accurate than the PIC-derived equivalent (over-distorted in the electric field direction and undisturbed Maxwellian in the two perpendicular directions). On the other hand, the integrated fluid characteristics, such as the ion bulk velocity and the total ion temperature, elevated due to frictional heating by the external electric field, should be accurately represented by this theory, even in the cases of very strong electric fields that result in efficient distortions of the ion distribution function. If there still remain small discrepancies, they may be attributed to imperfectly matching collision rates and to the velocity integration of the PIC determined ion distribution function being performed within an artificially restricted velocity domain. This is especially relevant to the strongly distorted ion distribution function when its high-energy tail can include a noticeable fraction of particles.

TABLE 3 Bulk velocities, directional thermal velocities, and total thermal energies for the PIC $\nu_{in} = 1050 s^{-1}$.

Case	$\langle v_y \rangle$ (m/s)	$v_{th,y}$ (m/s)	$v_{th,j}$ (m/s)	$\sum v_{th}^2$ (J/kg)	Theory/simulation Energy ratio
E_0 = 0 mV/m					
Simulation	0	287	287	247,107	1
Theory	0	287	287	247,107	
E_0 = 24 mV/m					
Simulation	70	292	289	252,306	0.9998
Theory	72	296	287	252,244	
E_0 = 94 mV/m					
Simulation	279	358	317	329,142	1.0010
Theory	287	406	287	329,476	
E_0 = 235 mV/m					
Simulation	697	606	444	761,508	1.0005
Theory	718	773	287	761,914	

$\langle v_y \rangle$ and $v_{th,y}$ are the bulk and thermal velocity in the Pedersen direction, respectively. $v_{th,j} = v_{th,x} = v_{th,y}$ is the thermal velocity in the directions perpendicular to $\vec{E}_0$. $\sum v_{th}^2 = v_{th,y}^2 + 2v_{th,j}^2$ is the total thermal energy per ion mass. The last column shows the total energy ratio between theory and simulation results.

4.1 Thermal velocity mismatch between theory and simulation results

The simulated ion distribution functions show different thermal profiles from those predicted by the theory.

4.1.1 Definition of thermal velocity

For the theory, the thermal velocity in the Pedersen direction is defined in terms of the second velocity moment of the ion distribution function:

$$v_{th,y}^{\text{Theory}} = \sqrt{\int_{-\infty}^{\infty} \left(v_y - \langle v_y \rangle\right)^2 F_y'^{\text{Theory}}(v_y) \quad dv_y},$$

where $F_y'^{\text{Theory}}$ is the normalized ion distribution function from Equation 14, and $\langle v_y \rangle$ is the ion bulk velocity in the Pedersen direction as given in Table 2. In directions perpendicular to $\vec{E_0}$, the thermal velocity is equal to the neutral thermal velocity v_T, since the theory does not account for heating in these directions and assumes an undisturbed Maxwellian.

For the simulation results, the thermal velocity in direction i is given by

$$v_{th,i} = \sqrt{\sum_{v_i} \left(v_i - \langle v_i \rangle\right)^2 F_i'(v_i) \quad dv_i},$$

where i is either x, y, or z, F_i' is the normalized ion distribution function from Equation 13, and $\langle v_i \rangle$ is the ion bulk velocity in direction i as given in Table 2.

Table 2 shows the mismatch in directional heating between the theory and the simulation results. Section 4.1.2 discusses ion heating in directions perpendicular to $\vec{E}_0$, while Section 4.1.3 discusses ion heating in the Pedersen direction.

4.1.2 Underestimation of the thermal velocity in the directions $\perp \vec{E}_0$

The theory underestimates the ion heating in the directions perpendicular to $\vec{E}_0$. In the x and z directions, the theory predicts an ion thermal velocity of 287 m/s which is equal to the neutral thermal velocity v_T.

For larger values of E_0, the simulation shows an increase in the ion thermal velocity, whereas the theoretical thermal velocity remains at 287 m/s. The theory assumes an undisturbed Maxwellian in the directions perpendicular to $\vec{E}_0$, so it does not account for ion heating in these directions. The simulation shows that ion heating is more intense for larger values of E_0. In the most intense $E_0 = 235\, mV/m$, the simulated thermal velocity reaches as much as 444 m/s or about 1.5 times the undisturbed value. The increase in temperature is caused by ion frictional heating (Saint-Maurice and Hanson, 1982) which has been observed in the E-region ionosphere (e.g., Watanabe et al., 1991; Fujii et al., 2002; Zhang and Varney, 2024).

4.1.3 Overestimation of thermal velocity in the direction $\parallel \vec{E}_0$

The theory overestimates the heating in the Pedersen direction. In the y direction, the theory predicts higher ion thermal velocities for higher values of E_0. Table 2 shows the theoretical predictions of the thermal velocities as well as the simulation results.

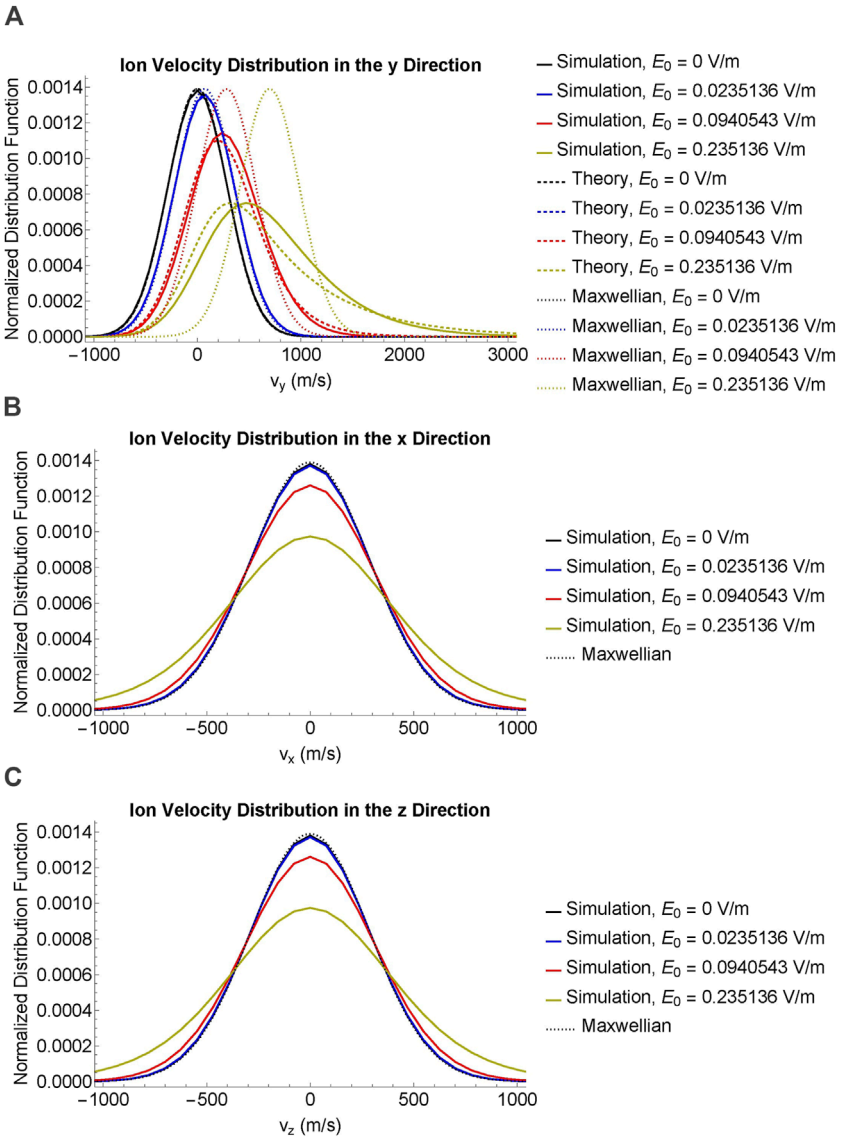

FIGURE 2
Comparison of simulated (solid) and theoretical (dashed) ion velocity distribution functions. Maxwellian functions (dotted) are included for comparison. The imposed electric field strengths are $E_0 = 0\,mV/m$ (black), $E_0 = 24\,mV/m$ (blue), $E_0 = 94\,mV/m$ (red), and $E_0 = 235\,mV/m$ (yellow). **(A)** Comparison of ion velocity functions in the Pedersen direction. **(B, C)** Comparison of ion velocity functions in directions perpendicular to $\vec{E_0}$. The theory assumes an undisturbed Maxwellian in **(B, C)**. Due to symmetry, **(B, C)** are largely identical.

For larger values of E_0, both the theory and the simulation show increased ion thermal velocities beyond the neutral thermal velocity, as expected from ion frictional heating. However, the theory and the simulation results disagree on the exact amount of the heating. The simulation shows that ion heating is less intense in the Pedersen direction than the theory suggests. The discrepancy is larger for larger values of E_0. In the most intense case of $E_0 = 235mV/m$, the simulated thermal velocity only reaches 606 m/s or just 80% of the theoretical value of 753 m/s.

4.1.4 Angular scattering of ions due to elastic collisions with the neutrals

The major difference between the theory and the simulation is the angular scattering of ions in 3-D. The theory models ion heating only in the Pedersen direction; it does not account for ions scattering into directions perpendicular to $\vec{E}_0$. On the other hand, the PIC code is able to capture the physics of ion scattering in 3-D. Angular scattering causes ion heating to be more isotropic in the simulation. The theory underestimates the heating in the directions it does not account for, while at the same time overestimating in the direction it does account for.

We expect the total ion thermal energy to be the same between the theory and the simulation. Section 4.2 compares the total energy between the theory and the simulation.

4.2 Discrepancy in total energy between the theory and the simulation results

The total ion thermal energy differs between the theory and the simulation results. Table 2 gives the total thermal energy per ion mass as well as the total thermal energy ratio between the theory and the simulation results. Although the ratios are close to 1, the total thermal energy from the theory is consistently lower than the total thermal energy from the simulation. Larger values of E_0 exhibit larger energy discrepancies than smaller values of E_0. In the most intense case $E_0 = 235\ mV/m$, the theory captures 96.11% of the total simulated energy, while in the less intense case $E_0 = 24\ mV/m$, the theory captures as much as 98.85% of the total simulated energy.

A possible explanation for the discrepancy in total energy is our choice of ν_{in} as described in Section 3.2.4. The theoretical IDF depends on ν_{in} in the Pedersen direction. We chose ν_{in} retroactively such that the theory matches the simulation results to first order. Table 3 shows a hypothetical situation in which the theory uses the PIC $\nu_{in} = 1050s^{-1}$ as its ion-neutral collision rate instead of the analytical effective value of $1082s^{-1}$. As seen by the mismatch in the bulk velocity, the PIC $\nu_{in} = 1050s^{-1}$ does not satisfy Equation 15. However, the PIC $\nu_{in} = 1050s^{-1}$ shows greater agreement with the simulation results in terms of the total thermal energy.

Comparing Tables 2, 3 shows how sensitive the theoretical IDF is to the value of ν_{in}. We expect the theory to preserve the total thermal energy of the background ions while also giving the correct ion bulk velocity. The theory is able to do both within a margin of error.

4.3 Distortion of the ion distribution function in the equatorial E-region

A typical DC electric field strength in the equatorial E-region is $E_0 = 24$ mV/m. Figure 2 shows only a small distortion in the ion distribution function for $E_0 = 24$ mV/m. Table 2 gives the bulk and thermal velocities for $E_0 = 24$ mV/m.

In the Pedersen direction, the theory predicts a thermal velocity of 295 m/s, while the simulation shows a thermal velocity of 294 m/s. In the directions perpendicular to the Pedersen direction, the simulation shows a thermal velocity of 291 m/s. These numbers are not so different from the Maxwellian thermal velocity of 287 m/s.

The background ion distribution in the equatorial E-region is not likely to distort much from the Maxwellian because the electric field is not strong enough. Both the theory and the simulation show that the distortion is stronger when E_0 is higher. In the Earth's ionosphere, the distortion will be stronger in the auroral E-region where the DC electric field is more intense than the equatorial E-region, especially during periods of geomagnetic storms.

5 Conclusion

We developed a collisional plasma kinetic model for E-region background ions using the simple BGK collision operator (Section 3.1). This simplified analytical model results in the ion distribution function (IDF) distorted in the direction of the external DC electric field $\vec{E}_0$ (the Pedersen direction), while in the two perpendicular directions the velocity distribution remains the undisturbed Maxwellian (Equations 4–7). The reason for this extreme anisotropy lies in the fact that the BGK collisional operator does not include any ion angular scattering in the velocity space. At the same time, even this simplified model provides accurate values for the total Pedersen drift velocity and, given equal masses of the colliding ions and neutrals, for the total effective ion temperature elevated by the frictional heating. Under a sufficiently intense external electric field, the IDF is skewed in the direction of $\vec{E}_0$, so that a strong tail of superthermal-energy ions forms.

We compared this simplified model to the PIC simulation (Section 3.2). The simulation shows less ion heating in the Pedersen direction and more ion heating in the perpendicular directions than the analytical model. The difference in the thermal distribution is due to the ion angular scattering which, unlike the model, is present in the PIC code. There is also a small difference in the total thermal energy between the model and the simulation (Table 2). We have shown that the BGK model is sensitive to the choice of the ion-neutral collision rate, as shown by the alternate results in Table 3 which curiously give a total thermal energy that matches exactly with the simulation despite being unable to reproduce the ion bulk velocity. Still, the difference in Table 2 is not big enough to be consequential. The BGK model shows an overall similar total thermal energy to the PIC simulation.

The shapes of the ion distribution functions differ between the BGK model and the PIC simulation. The more accurate IDF determined by the PIC simulation is somewhere between the analytically determined IDF and the Pedersen-shifted Maxwellian distribution whose temperature equals the total elevated ion temperature. The latter, however, does not show any IDF skewness which is present in both analytical model and PIC simulations.

For the typical electric field strength of the equatorial E-region, the background ion distribution function is well-represented by the shifted and heated Maxwellian function. The situation may be very different at high latitudes where a strong external field may be present during periods of geomagnetic storms. Both the model and the PIC simulation show that, in these cases, the background ion velocity distribution can distort significantly from any Maxwellian. Any accurate model of plasma instabilities in a strongly driven E-region ionosphere must account for the potential non-Maxwellian distribution of the background ions. This modified distribution function can serve as the starting point when evaluating plasma wave growth characteristics using linear kinetic theory.

Data availability statement

The raw data supporting the conclusions of this article will be made available by the authors, without undue reservation.

Author contributions

RK: investigation, writing–original draft, and writing–review and editing. YD: conceptualization, methodology, writing–original

draft, and writing–review and editing. MO: supervision, writing–review and editing, and software.

Funding

The authors declare that financial support was received for the research, authorship, and/or publication of this article. This work was funded by NASA Grants 80NSSC21K1322 and 80NSSC19K0080.

Acknowledgments

Computational resources were provided by the Anvil supercomputer through the NSF/ACCESS program.

Conflict of interest

The authors declare that the research was conducted in the absence of any commercial or financial relationships that could be construed as a potential conflict of interest.

The handling editor JC declared a past co-authorship with the author MO.

Publisher's note

References

Bhatnagar, P. L., Gross, E. P., and Krook, M. (1954). A model for collision processes in gases. I. Small amplitude processes in charged and neutral one-component systems. *Phys. Rev.* 94, 511–525. doi:10.1103/PhysRev.94.511

Birdsall, C. K., and Langdon, A. B. (1991). *Plasma physics via computer simulation*.

Buneman, O. (1963). Excitation of field aligned sound waves by electron streams. *Phys. Rev. Lett.* 10, 285–287. doi:10.1103/PhysRevLett.10.285

Chen, F. F. (2016). *Introduction to plasma physics and controlled fusion*. doi:10.1007/978-3-319-22309-4

Dimant, Y. S., and Oppenheim, M. M. (2004). Ion thermal effects on E-region instabilities: linear theory. *J. Atmos. Solar-Terrestrial Phys.* 66, 1639–1654. doi:10.1016/j.jastp.2004.07.006

Dimant, Y. S., Oppenheim, M. M., and Fletcher, A. C. (2016). Generation of electric fields and currents by neutral flows in weakly ionized plasmas through collisional dynamos. *Phys. Plasmas* 23, 084503. doi:10.1063/1.4961085

Dimant, Y. S., and Sudan, R. N. (1995). Kinetic theory of low-frequency cross-field instability in a weakly ionized plasma. II. *Phys. Plasmas* 2, 1169–1181. doi:10.1063/1.871395

Dimant, Y. S., and Sudan, R. N. (1997). Physical nature of a new cross-field current-driven instability in the lower ionosphere. *J. Geophys. Res.* 102, 2551–2564. doi:10.1029/96JA03274

Else, D., Kompaneets, R., and Vladimirov, S. V. (2009). On the reliability of the Bhatnagar-Gross-Krook collision model in weakly ionized plasmas. *Phys. Plasmas* 16, 062106. doi:10.1063/1.3152329

Farley, J. D. T. (1963). A plasma instability resulting in field-aligned irregularities in the ionosphere. *J. Geophys. Res.* 68, 6083–6097. doi:10.1029/JZ068i022p06083

Fujii, R., Oyama, S., Buchert, S. C., Nozawa, S., and Matuura, N. (2002). Field-aligned ion motions in the E and F regions. *J. Geophys. Res. Space Phys.* 107, 1049. doi:10.1029/2001JA900148

Hoh, F. C. (1963). Instability of penning-type discharges. *Phys. Fluids* 6, 1184–1191. doi:10.1063/1.1706878

Janhunen, P. (1995). On recent developments in E-region irregularity simulations and a summary of related theory. *Ann. Geophys.* 13, 791–806. doi:10.1007/s00585-995-0791-7

Kagan, L. M., and Kelley, M. C. (2000). A thermal mechanism for generation of small-scale irregularities in the ionospheric E region. *J. Geophys. Res.* 105, 5291–5303. doi:10.1029/1999JA900415

Kelley, M. C. (2009). *The Earth's ionosphere: plasma physics and electrodynamics*. Academic Press.

Kovalev, D. V., Smirnov, A. P., and Dimant, Y. S. (2008). Modeling of the Farley-Buneman instability in the E-region ionosphere: a new hybrid approach. *Ann. Geophys.* 26, 2853–2870. doi:10.5194/angeo-26-2853-2008

Maeda, K., Tsuda, T., and Maeda, H. (1963). Theoretical interpretation of the equatorial sporadic E layers. *Phys. Rev. Lett.* 11, 406–407. doi:10.1103/PhysRevLett.11.406

Nicholson, D. R. (1983). *Introduction to plasma theory*, 1. New York: Wiley.

Oppenheim, M., Dimant, Y., Longley, W., and Fletcher, A. C. (2020). Newly discovered source of turbulence and heating in the solar chromosphere. *Astrophysical J.* 891, L9. doi:10.3847/2041-8213/ab75bc

Oppenheim, M., Otani, N., and Ronchi, C. (1995). Hybrid simulations of the saturated Farley-Buneman instability in the ionosphere. *Geophys. Res. Lett.* 22, 353–356. doi:10.1029/94GL03277

Oppenheim, M., Otani, N., and Ronchi, C. (1996). Saturation of the Farley-Buneman instability via nonlinear electron E×B drifts. *J. Geophys. Res.* 101, 17273–17286. doi:10.1029/96JA01403

Oppenheim, M. M., Dimant, Y., and Dyrud, L. P. (2008). Large-scale simulations of 2-D fully kinetic Farley-Buneman turbulence. *Ann. Geophys.* 26, 543–553. doi:10.5194/angeo-26-543-2008

Oppenheim, M. M., and Dimant, Y. S. (2004). Ion thermal effects on E-region instabilities: 2D kinetic simulations. *J. Atmos. Solar-Terrestrial Phys.* 66, 1655–1668. doi:10.1016/j.jastp.2004.07.007

Oppenheim, M. M., and Dimant, Y. S. (2013). Kinetic simulations of 3-D Farley-Buneman turbulence and anomalous electron heating. *J. Geophys. Res. Space Phys.* 118, 1306–1318. doi:10.1002/jgra.50196

Robinson, T. R. (1998). The effects of small scale field aligned irregularities on E-region conductivities: implications for electron thermal processes. *Adv. Space Res.* 22, 1357–1360. doi:10.1016/S0273-1177(98)80034-3

Saint-Maurice, J. P., and Hanson, W. B. (1982). Ion frictional heating at high latitudes and its possible use for an *in situ* determination of neutral thermospheric winds and temperatures. *J. Geophys. Res.* 87, 7580–7602. doi:10.1029/JA087iA09p07580

Schunk, R., and Nagy, A. (2009). Ionospheres: physics, plasma physics, and chemistry. *Cambridge atmospheric and space science series* (Cambridge University Press), 2.

Simon, A. (1963). Instability of a partially ionized plasma in crossed electric and magnetic fields. *Phys. Fluids* 6, 382–388. doi:10.1063/1.1706743

St. -Maurice, J. P., and Kissack, R. S. (2000). The role played by thermal feedback in heated Farley-Buneman waves at high latitudes. *Ann. Geophys.* 18, 532–546. doi:10.1007/s00585-000-0532-x

St-Maurice, J. P., and Schunk, R. W. (1979). Ion velocity distributions in the high-latitude ionosphere. *Rev. Geophys. Space Phys.* 17, 99–134. doi:10.1029/RG017i001p00099

Watanabe, S., Whalen, B. A., Wallis, D. D., and Pfaff, R. F. (1991). Observations of ion-neutral collisional effects in the auroral E region. *J. Geophys. Res.* 96, 9761–9771. doi:10.1029/91JA00561

Young, M. A., Oppenheim, M. M., and Dimant, Y. S. (2020). The farley-buneman spectrum in 2-D and 3-D particle-in-cell simulations. *J. Geophys. Res. Space Phys.* 125, e27326. doi:10.1029/2019JA027326

Zhang, Y., and Varney, R. H. (2024). A statistical survey of E-region anomalous electron heating using poker flat incoherent scatter radar observations. *J. Geophys. Res. Space Phys.* 129, e2023JA032360. doi:10.1029/2023JA032360

frontiers | Frontiers in Physics

TYPE Methods
PUBLISHED 09 January 2025
DOI 10.3389/fphy.2024.1488935

OPEN ACCESS

EDITED BY
James Clemmons,
University of New Hampshire, United States

REVIEWED BY
Catalin Negrea,
Space Science Institute, Romania
Shantanab Debchoudhury,
Embry–Riddle Aeronautical University,
United States

*CORRESPONDENCE
Aaron Kirchman,
ajk335@cornell.edu

RECEIVED 30 August 2024
ACCEPTED 09 December 2024
PUBLISHED 09 January 2025

CITATION
Kirchman A, Hysell D and Fang T-W (2025) Regional simulations of equatorial spread F driven with, and an analysis of, WAM-IPE electric fields.
Front. Phys. 12:1488935.
doi: 10.3389/fphy.2024.1488935

Regional simulations of equatorial spread F driven with, and an analysis of, WAM-IPE electric fields

Aaron Kirchman[1]*, David Hysell[1] and Tzu-Wei Fang[2]

[1]Department of Earth and Atmospheric Sciences, Cornell University, Ithaca, NY, United States, [2]NOAA Space Weather Prediction Center, Boulder, CO, United States

A three-dimensional, regional simulation is used to investigate ionospheric plasma density irregularities associated with Equatorial Spread F. This simulation is first driven with background electric fields derived from ISR observations. Next, the simulation is driven with electric fields taken from the WAM-IPE global model. The discrepancies between the two electric fields, particularly in the evening prereversal enhancement, produce disagreeing simulation results. The WAM-IPE electric fields are then studied through a simple sensitivity analysis of a field-line integrated electrodynamics model similar to the one used in WAM-IPE. This analysis suggests there is no simple tuning of ion composition or neutral winds that accurately reproduce ISR-observed electric fields on a day-to-day basis. Additionally, the persistency of the prereversal enhancement structure over time is studied and compared to measurements from the ICON satellite. These results suggest that WAM-IPE electric fields generally have a shorter and more variable correlation time than those measured by ICON.

KEYWORDS

equatorial spread F, WAM-IPE, plasma drifts, prereversal enhancement, equatorial electrodynamics

1 Introduction

Equatorial Spread F (ESF) is a broad term that refers to a wide range of phenomena observed in the equatorial F-region ionosphere associated with post-sunset instabilities. Its name is derived from its effect of "spreading" ionograms that was first reported by [1]. The associated plasma density irregularities are primarily attributed to collisional interchange instabilities [2–4] or inertial interchange instabilities [3]. Collisional shear instability has been proposed as a preconditioner for ESF activity [5]. The resulting irregularities can cause the scintillation of radio waves traveling through the region. This can compromise critical systems such as communication, navigation, and imaging systems [6, 7]. Avoiding these hazards requires an accurate forecast of ESF events that perform better than climatological estimates. For the purposes of this study, an accurate forecast is one that predicts the presence or absence of robust irregularities on a night-to-night basis and can be validated with radar or satellite observations.

The earliest attempts at forecasting ESF involved analyzing linear growth rates estimated from field-line integrated quantities [8, 9]. These approaches predicted the climatological patterns of ESF occurrences. However, they were unable to produce accurate night-to-night behavior. Additionally, linear growth rate methods failed to explain the observation

of topside irregularities. Other forecast attempts have involved numerical simulations of ESF and its associated irregularities. One of the first simulations that showed topside irregularities was presented by [10]. They showed the nonlinear evolution of interchange instabilities into equatorial plasma bubbles (EPBs) that reached the topside ionosphere. Despite these EPBs penetrating the topside ionosphere, they took significantly longer to develop than bubbles observed in nature. Current work aims at pairing observational data with direct numerical simulations. The observational data can be provided by incoherent radar scatter (ISR) observations taken at Jicamarca Radio Observatory [11] or satellite data such as that from the ICON satellite [12, 13].

One important factor in identifying favorable conditions for ESF and predicting its development is the large-scale zonal electric fields near the day/night terminator. These electric fields produce the vertical $\mathbf{E} \times \mathbf{B}$ plasma drifts that raise and lower the ionosphere. Of particular interest is the evening prereversal enhancement (PRE) that is commonly observed prior to sunset. The strength and timing of the PRE have been closely associated with the occurrence of ESF [14]. Accurately predicting the PRE is crucial for forecasting ESF. Multiple theories of the PRE have been suggested [15–17] and have been shown to produce the PRE in numerical models [18]. A common feature of these theories is a neutral thermospheric wind that generates a dynamo electric field in the equatorial F-region and off-equatorial E-regions. Near the day/night terminator, the steep zonal gradient in conductivity causes this dynamo to produce an enhanced eastward electric field. The lack of a similar but reverse phenomenon in the morning near the dawn terminator is yet to be explained thoroughly. The climatology of the PRE is well captured by the empirical drifts model proposed by [19]. However, the high degree of day-to-day variability remains an open question in equatorial electrodynamics. The regional simulation for ESF that is used in this study has previously been shown to be most sensitive to the strength of the PRE [13] as well as its timing and duration [20].

In this study, observational data are replaced with estimates from a global circulation model (GCM). As in [20], the GCM used is the Whole Atmosphere Model with Ionosphere, Plasmasphere, and Electrodynamics (WAM-IPE) from NOAA. WAM-IPE is run operationally at NOAA Space Weather Prediction Center (SWPC) providing ionospheric and neutral atmosphere state parameter estimates from inputs of solar and geomagnetic activity and lower atmospheric forcing [21]. The model extends the Global Forecast System vertically to approximately 600 km altitude and includes additional upper atmospheric physics. These additional physics involve one-way coupling to an ionosphere-plasmasphere model and a self-consistent electrodynamics solver similar to that used in the NCAR TIE-GCM model [22]. Here, the electric fields produced by this dynamo solver are studied, and their impact on a regional simulation of ESF-related irregularities is analyzed. It is believed that the day-to-day disagreement between WAM-IPE-produced and ISR-observed electric fields prevents accurate reproductions of ESF activity. This conclusion prompts a further analysis of WAM-IPE electric fields and testing whether they can be adjusted in a way that will match ISR observations.

The remainder of this paper is structured as follows. In Section 2, we discuss the regional simulation used to replicate ESF observations. Results from an August/September 2022 campaign are presented and the effects of WAM-IPE electric fields are analyzed. In Section 3, a proxy electrodynamics model is described and used to perform a variety of sensitivity tests on the dynamo electric fields from WAM-IPE. The tests here include adjustments to ionospheric composition and the structure of the thermospheric neutral winds. The effects of these tests are then compared to ISR observations for all nights of the campaign. Next, in Section 4, we compare the temporal evolution of the PRE in WAM-IPE to that observed by the ICON satellite. Correlation times of this structure are discussed and compared to theory. Finally, Section 5 summarizes the results and provides a brief discussion on advancing toward a true forecast of ESF events.

2 Regional simulation

The regional simulation used here is a three-dimensional, multifluid simulation cast in magnetic dipole coordinates [23,24]. It tracks the number densities of four ion species (H^+, NO^+, O_2^+, and O^+) and electrons. Results are validated through comparison with both coherent and incoherent radar observations of irregularities. The simulation was described in detail by [11] and is used here similarly to [20]. For this reason, only a brief description of it is given here.

There are two primary computations performed in the simulation. The first is a linear solver that calculates the electrostatic potential associated with the small-scale electric fields present in irregularities. This means the electric field is broken into two components: a large-scale background electric field $\mathbf{E}_0$, and a gradient of a scalar potential defining the small-scale electric fields, $-\nabla\Phi$. Starting from the inertialess momentum equation and using this split electric field, one can find the following elliptic PDE by enforcing the divergence-free current condition ($\nabla \cdot \mathbf{J} = 0$).

$$\nabla \cdot (\sigma \cdot \nabla\Phi) = \nabla \cdot \left[\sigma \cdot (\mathbf{E}_0 + \mathbf{u} \times \mathbf{B}) - \sum_s q_s \mathbf{D}_s \cdot \nabla n_s + \Xi \cdot \mathbf{g} \right] \quad (1)$$

where σ is the conductivity tensor, Φ is the electrostatic potential, $\mathbf{E}_0$ is the background electric field, $\mathbf{u}$ is the neutral thermospheric wind vector, $\mathbf{B}$ is the geomagnetic field, q_s is the electric charge of species s, $\mathbf{D}_s$ is the diffusivity tensor for a species, n_s is the species number density, Ξ is a tensor containing all the terms describing gravity-driven currents, and $\mathbf{g}$ is the Earth's gravitational field. Equation 1 is solved using a preconditioned stabilized biconjugate gradient method with Robin boundary conditions on all boundaries.

The second computation is a finite-volume code that updates species according to the continuity equation, given by Equation 2.

$$\frac{\partial n_s}{\partial t} + \nabla \cdot (n_s \mathbf{v}_s) = P - L \quad (2)$$

where $\mathbf{v}_s$ is the drift velocity that is calculated using the inertialess momentum equation, and P and L are production and loss terms. The chemical production and loss rates for charge exchange and dissociative recombination are taken from [25]. A flux assignment scheme based on the total variation diminishing (TVD) condition is used with monotone upwind scaling for conservation laws (MUSCLs). Time advancement is performed with a second-order Runge-Kutta scheme with time steps of 7.5 s for 2 h.

Initialization of the simulation is done with empirical and physics-based models paired with ISR observations. Ion

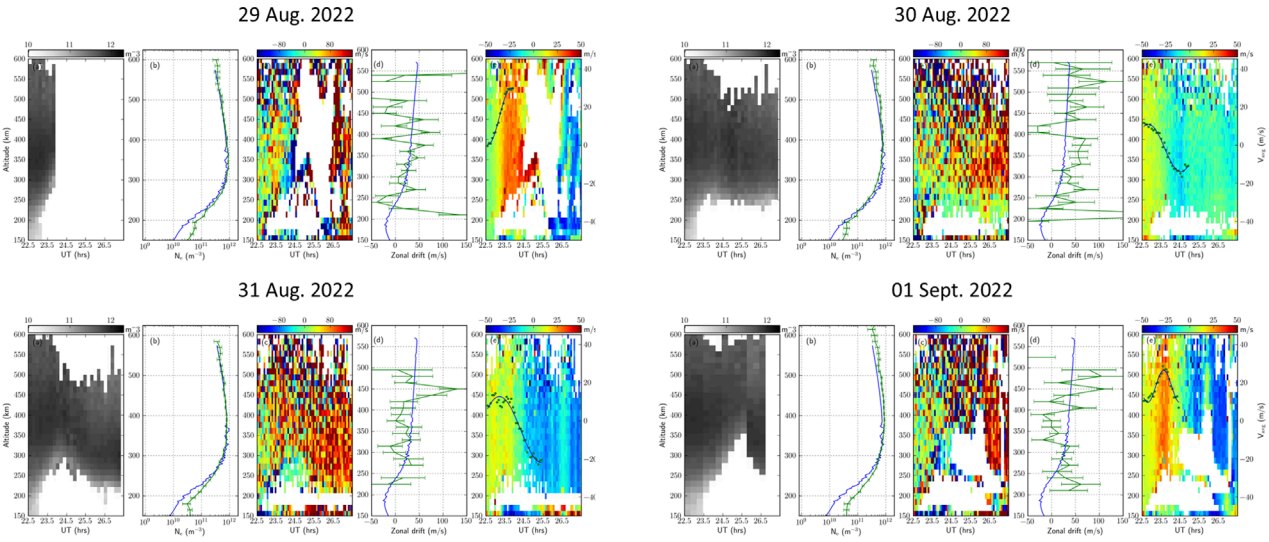

FIGURE 1
ISR data for all four nights of the 2022 campaign. Shown for each night from left to right is **(A)** electron number density, **(B)** an electron number density profile at 2300 UT, **(C)** zonal plasma drift velocities, **(D)** a zonal plasma drift velocity profile at 2300 UT, **(E)** vertical plasma drift velocities. The green curves in panels **(B)** and **(D)** represent ISR-measured values, while the blue curves represent model values (SAMI2 and HWM14, respectively). Plotted against the far right axis in all **(E)** panels are the height-averaged vertical plasma drifts (green scatter points) and the sinusoidal parameterization given by Equation 3 (blue curve).

composition is initialized with IRI-2016, and electron density is initialized by tuning SAMI2 to produce electron density profiles that are in agreement with ISR observations. This tuning is done in two ways: adjusting the F10.7 solar flux parameter and adjusting a second parameter that controls the time history of the background electric fields. Both of these parameters are adjusted until there is optimal congruity between SAMI2-produced profiles and those observed through ISR, as shown in each panel B in Figure 1. This tuning is typically minimal and does not have a large impact on simulation results. Since SAMI2 is a two-dimensional model operating at a single longitude, local time and longitude are considered to be equivalent in order to extrapolate the SAMI2 results to neighboring longitudes. Parameters describing the neutral atmosphere are continuously taken from NRLMSIS 2.0 throughout the simulation.

The driving terms include the background electric fields, $\mathbf{E}_0$, and neutral thermospheric winds, $\mathbf{u}_0$. These are also derived from empirical models and ISR observations. Additionally in this study, the electric fields can be derived from WAM-IPE estimates. HWM14 prescribes the neutral winds throughout the simulation. These winds can be tuned via a multiplicative factor to produce zonal plasma drifts that agree with ISR observations. No such tuning was necessary for the results shown here. In this study, simulation results are compared where the background electric fields are derived from ISR vertical plasma drift measurements, and taken directly from WAM-IPE. Another source for these electric fields that has been explored is those taken from the ion velocity meter (IVM) aboard the ICON satellite [12, 13].

Multiple ISR experiments have been run at Jicmarca Radio Observatory over the last few years. These ISR experiments provide estimates for multiple state parameters of the ionosphere including plasma number density, electron and ion temperatures, and zonal and vertical plasma drift velocities. Figure 1 shows ISR data for all four nights of a 2022 campaign during the hours surrounding sunset. Blank patches in the ISR data correspond to coherent scatter from 3-m irregularities that interfere with the ISR technique and prevent parameter estimation. These irregularities are closely associated with ESF and serve as an indicator of ESF activity here. It can be seen in Figure 1 that 29 Aug. and 01 Sept. experienced particularly strong ESF events with large depletion plumes penetrating the topside ionosphere.

Plotted in green against the right vertical axis in each (e) panel of Figure 1 are height-averaged vertical plasma drift velocities. These averaged drift speeds are parameterized using a sinusoidal function with four parameters: amplitude, V_0, period, τ, UT hour offset, t_0, and vertical offset, c.

$$v(t) = V_0 \sin\left(\frac{2\pi}{\tau}(t - t_0)\right) + c \tag{3}$$

This parameterization describes the zonal background electric fields throughout the 2-hour simulation and adequately captures the strength, timing, and duration of the PRE. It is plotted in blue against the right vertical axis in each (e) panel of Figure 1. The PRE is regularly observed by Jicamarca ISR experiments and it is important to capture for predicting ESF activity.

2.1 Simulation results

Figure 2 shows simulation results for four nights of a 2022 campaign when driven with ISR-derived electric fields. All four nights were during a geomagnetically quiet period. Results are shown 2 hours after initialization, which took place at 2300 UT for the first two nights and 2310 UT for the last two nights. They show ionospheric composition in a zonal-altitudinal slice in the

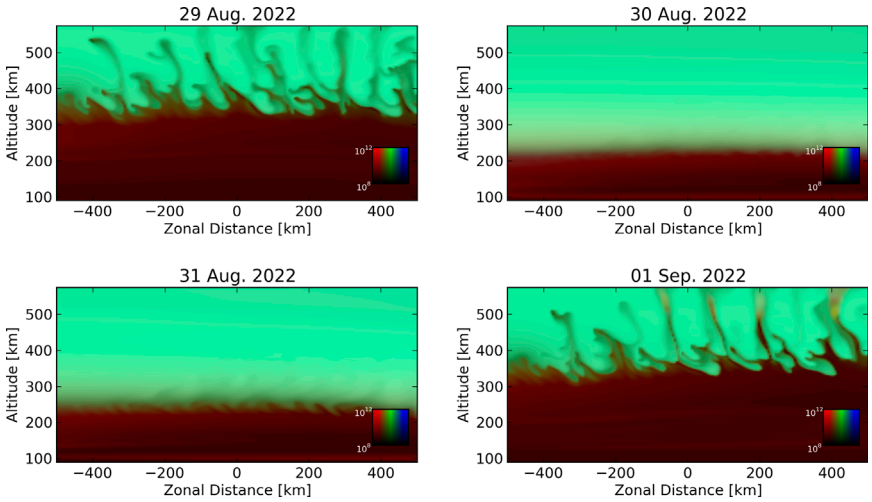

FIGURE 2
Simulation results for four nights of an Aug. 2022 campaign, when driven with ISR-derived electric fields. Ion number densities are represented with brightness according to the scale in the lower-right-hand corner. Red, green, and blue colors represent molecular ions, protons, and atomic oxygen ions. Ion densities are given in units of m^{-3}. Simulation results are shown 2 h after initialization time (see text).

magnetic equatorial plane. Red, green, and blue coloring represents molecular ion, proton, and atomic oxygen ion number density. Strong ESF activity is visible during the first and fourth nights of the campaign in the form of large depletion plumes. These large depletion plumes penetrate well into the topside ionosphere within 2 h of their initialization. This closely resembles the radar observations shown in Figure 1, for all nights of the campaign. These results act as a validation of the regional simulation.

Figure 3 also shows simulation results for the same August/September 2022 campaign with the simulation driven by WAM-IPE background electric fields. Additionally, WAM-IPE provided the initial ion composition and neutral compositions throughout the simulation. The most significant difference between results in Figures 2, 3 is the absence of plumes on the nights of 29 Aug. and 01 Sept. These are examples of missed detections of ESF. ESF activity was observed during both of these nights and replicated in simulations driven with radar data but absent in simulations driven with WAM-IPE estimates. Figure 4 shows the differences between vertical plasma drifts (via zonal background electric fields) in ISR observations (red) and WAM-IPE results (blue) for all four nights of the campaign. It can be seen that the particularly strong PRE observed by ISR on the first and fourth nights is absent in WAM-IPE. This lack of a PRE prevented the rapid growth of irregularities in the simulation. The two nights without ESF activity have significantly weaker PREs and show better agreement between WAM-IPE and ISR.

Another visible difference between the two results is that WAM-IPE exhibits an enhanced molecular ion composition in the valley region compared to that predicted by IRI-2016. This is most noticeable between 100 and 200 km altitudes for all nights in Figure 3. The effects of substituting WAM-IPE compositions into the simulation while being driven with ISR-derived electric fields was studied by [20] along with wind substitutions and electric field substitutions on multiple nights during a Sept. 2021 campaign. Those results indicated that WAM-IPE composition is likely not the source of discrepancy in simulation results. The same conclusion is reached here by noting that the enhanced molecular ion density occurs on all four nights. Missed detections only occur on the nights when WAM-IPE electric fields disagreed with ISR observations. This compositional difference is noted as it is the motivation for studying the effects of enhanced molecular ion densities on the development of electric fields discussed in the following section.

3 Electrodynamics sensitivity analysis

A two-dimensional electrodynamics solver similar to the one used in WAM-IPE was built to serve as a proxy model for WAM-IPE electric fields. The model uses modified apex coordinates [26, 27] and an IGRF magnetic field [28]. In this coordinate system, the two dimensions that are constant along a magnetic field line are the apex longitude, ϕ, and the modified apex latitude, λ. The apex longitude is defined as the centered-dipole longitude of the field line's apex point. The modified apex latitude is defined to be the latitude that a dipole field line with the same apex altitude, h_A, would intersect with a constant reference height h_R. Here, a reference height of 90 km is used as that is considered to be the base of the conducting ionosphere.

Magnetospheric sources are neglected, confining the model to magnetic latitudes below ±60°. These magnetic latitudes are equivalent to apex heights ranging from 90 km to 19,373 km. Assuming equipotential field lines (as done by [29]), the field-line integrated divergence-free current condition results in the following two-dimensional PDE for electrostatic potential, Φ.

$$\frac{\partial}{\partial\phi}\left(\frac{\Sigma_{\phi\phi}}{\cos\lambda}\frac{\partial\Phi}{\partial\phi}+\Sigma_{\phi\lambda}\frac{\partial\Phi}{\partial|\lambda|}\right)+\frac{\partial}{\partial|\lambda|}\left(\Sigma_{\lambda\phi}\frac{\partial\Phi}{\partial\phi}+\Sigma_{\lambda\lambda}\cos\lambda\frac{\partial\Phi}{\partial|\lambda|}\right)$$
$$=(R_E+h_R)\left(\frac{\partial K_\phi^D}{\partial\phi}+\frac{\partial}{\partial|\lambda|}\left[K_\lambda^D\cos\lambda\right]\right) \quad (4)$$

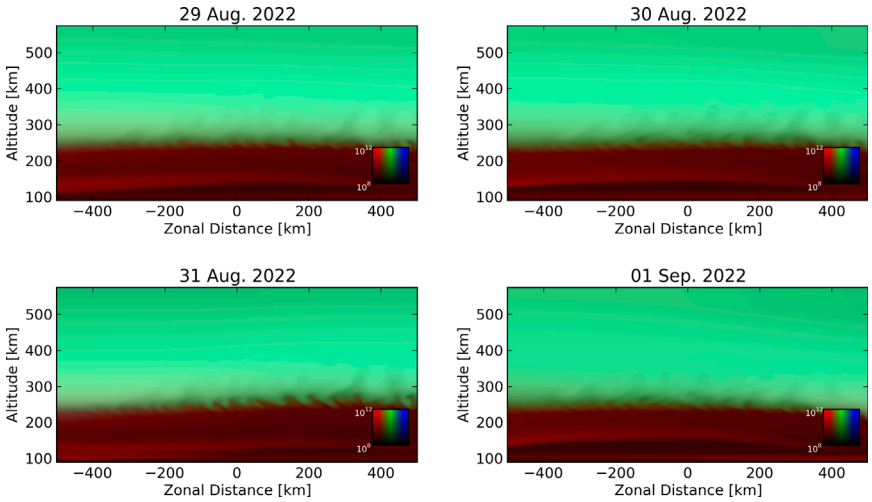

FIGURE 3
Same as Figure 2, but with the simulation being driven with WAM-IPE background electric fields.

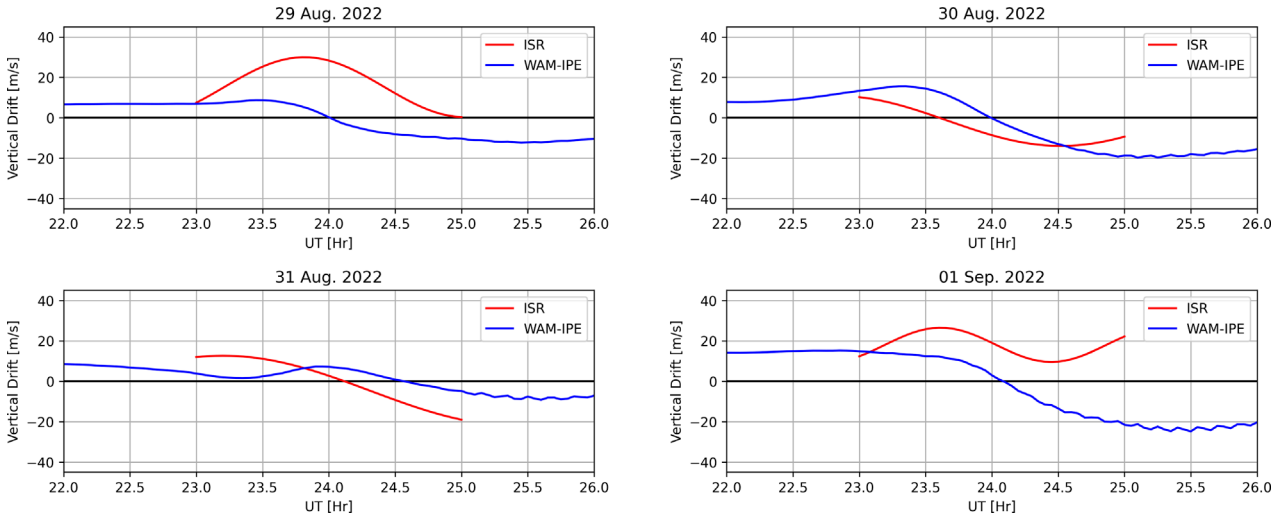

FIGURE 4
Vertical plasma drift velocities taken from ISR observations (red) and WAM-IPE results (blue) for all nights of the 2022 campaign. WAM-IPE values are taken to be at 300 km altitudes directly overhead Jicamarca.

where R_E is the mean radius of the Earth (6,371.2 km), $\Sigma_{\phi\phi}$ and $\Sigma_{\lambda\lambda}$ act in a similar manner as integrated Pedersen conductivities, $\Sigma_{\phi\lambda}$ and $\Sigma_{\lambda\phi}$ act similar to integrated Hall conductivities, and K_ϕ^D and K_λ^D are integrated "wind-driven" current densities that act as source terms for the ionospheric dynamo. All quantities in Equation 4 are constant along a magnetic field line and can be mapped down to a desired height along that field line. A more detailed derivation of Equation 4, along with definitions of integrated quantities, is given in Supplementary Appendix A and [26].

In reality, there is a small potential drop along magnetic field lines suggesting that the electrostatic potential is truly a three-dimensional structure. However, resolving this 3D global structure at a high enough resolution to capture the PRE would be computationally intensive. This is not a concern here as the purpose of this model is to serve as a proxy to the WAM-IPE electrodynamics model which makes the same equipotential field line assumption. Additionally, gravity and pressure-driven currents are also neglected here, although their effects were studied by [30].

The resolution of the model is 4.5° in the ϕ direction and 1.0° in the λ direction. While the grid is uniform in the modified apex latitude dimension, this does not equate to uniform spacing in the apex altitude of field lines. WAM-IPE densities and neutral winds are interpolated to irregularly spaced points along each magnetic field line and then integrated in the manner given in Supplementary Appendix A. The spacing of field line points is determined by the altitudinal distance between neighboring points with 1 km spacing below 150 km, 5 km spacing between 150 and 2000 km, and 100 km spacing above 2000 km. This allows

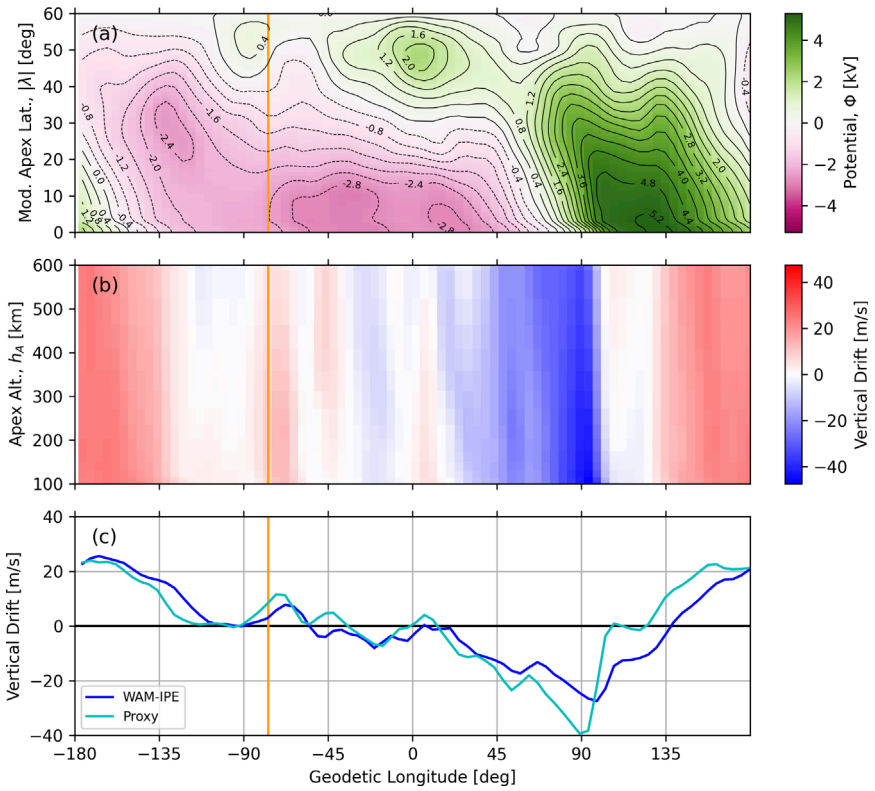

FIGURE 5
Results from the proxy electrodynamics model for all longitudes at 2300 UT of 29 Aug. 2022. **(A)** Electrostatic potential and contours, for all modified apex latitudes. **(B)** Vertical plasma drifts (positive upwards) in the magnetic equatorial plane for apex heights ranging from 100–600 km. The PRE is most prevalent at these altitudes. **(C)** Upward plasma drifts at 300 km altitude from WAM-IPE are shown in the dark blue while proxy model solutions are shown in the light blue curve. The orange line indicates the location of Jicamarca Radio Observatory (76.87°E longitude).

for a better representation of E-region dynamics that occur near the base of the field lines and drive the Sq current system. In solving Equation 4, periodic boundary conditions are used in the ϕ direction. Due to the lack of magnetospheric current sources, the high latitude/altitude boundary condition is $\Phi = 0$. The current in the λ direction is restricted to zero at the low latitude/altitude boundary (i.e., $K_\lambda = 0$).

3.1 Model results

Shown in Figure 5 are the results of the proxy model taken at 2300 UT on 29 Aug. 2022. At this time the day/night terminator is located approximately 7° East of Jicamarca, which is indicated by the vertical orange line in each panel. The values shown in Figure 5 are (a) the electrostatic potential for all modified apex latitudes, (b) upward plasma drift velocities between 100 and 600 km apex altitudes, and (c) upward plasma drift velocities at 300 km altitude compared to WAM-IPE results. The contours of electrostatic potential in Figure 5A act as flowlines for plasma drifts, with clockwise flow around local maxima and counter-clockwise flow around local minima. The enhanced upward velocity that's indicative of the PRE can be seen a few degrees to the East of Jicamarca in each panel. Additionally, Figure 5C validates the proxy model as a reasonable replication of WAM-IPE electric fields.

To compare directly to ISR measurements, the proxy model is solved at 12-minute increments from 2200 UT to 0200 UT. The plasma drift velocities 300 km overhead Jicmarca are recorded and plotted alongside WAM-IPE values. Figure 6 shows time series of zonal and vertical plasma drift velocities from all nights of the 2022 campaign. Note that the proxy model solutions (solid cyan curves) agree with WAM-IPE estimates (solid dark blue curves) within reason. This provides further validation for the model to act as a proxy for WAM-IPE electrodynamics. The first and fourth nights exhibit significant disagreement between the PRE in WAM-IPE and ISR observations (solid red curves), while the second and third nights show similarly small PRE patterns. The dashed lines plotted in Figure 6 show results from the proxy model due to the various sensitivity tests discussed below.

The first sensitivity tested relates to ionospheric composition and is motivated by the observation of enhanced molecular ion densities in WAM-IPE mentioned in Section 2.1. In this test, the proxy model was tested with only 10% of the original molecular ions given by WAM-IPE. Results from this test are plotted in dashed orange lines in Figure 6. Since the decrease of ions in the ionosphere diminishes the conductivity, larger electric fields (therefore larger plasma drift magnitudes) are required to maintain the same current flow. Despite the larger fields, there are minimal effects on the structuring of the PRE, and vertical drifts do not appear to match ISR observations any better than when the full

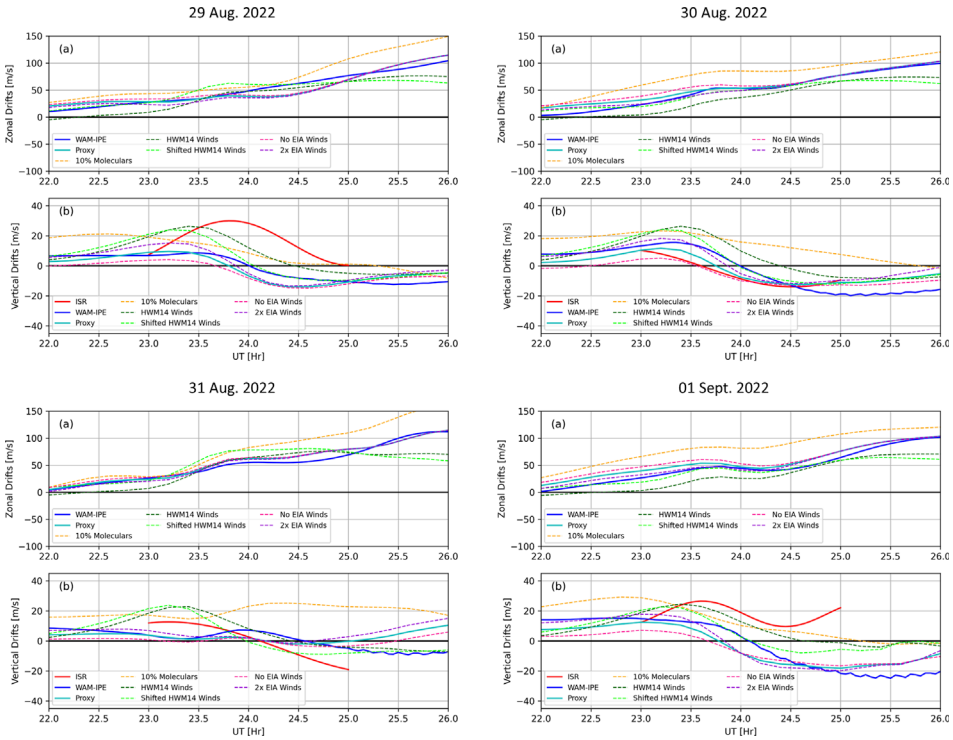

FIGURE 6
Time series of proxy model plasma drifts taken 300 km overhead Jicamarca, compared to WAM-IPE results and ISR observations for each night of the 2022 campaign. Shown for each night are (A) zonal drift velocities and (B) vertical drift velocities. Additionally, results from each sensitivity test are plotted to visualize their impacts on the dynamo electric fields.

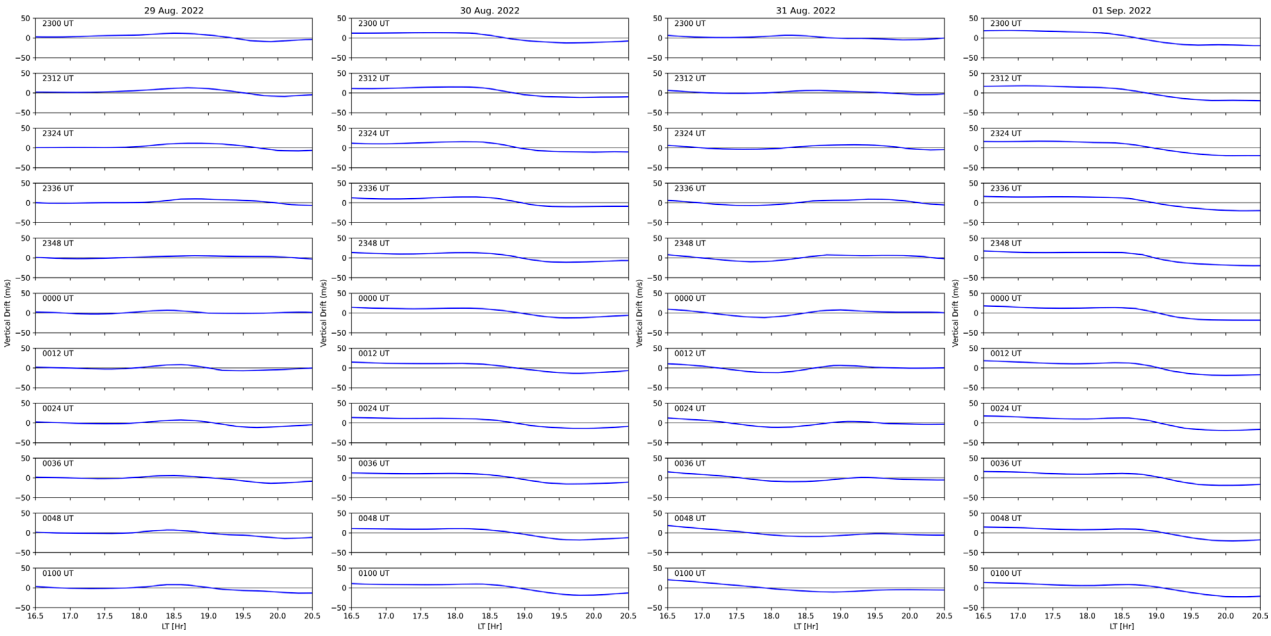

FIGURE 7
WAM-IPE vertical plasma drifts at 300 km altitude as a function of Local Time surrounding the day/night terminator (1830 LT) at 12-minute increments spanning 2 h in UT. All four nights of the 2022 campaign are shown in respective columns. Each subsequent row is 12 min later in UT than the one above it. To follow the terminator properly, each subsequent panel is therefore observing longitudes that are 3° to the west of the previous panel.

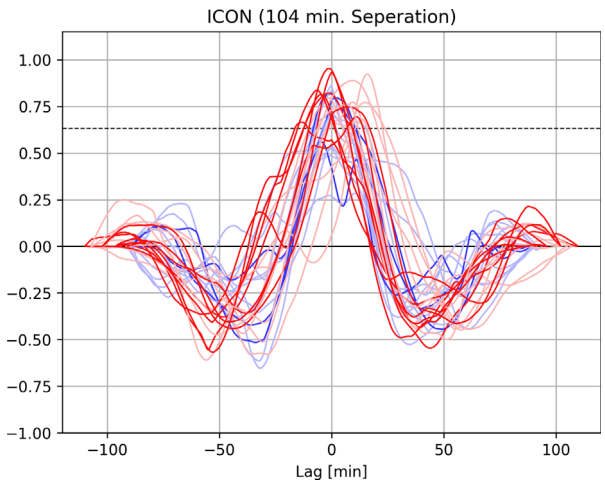

FIGURE 8
Autocorrelation functions of vertical plasma drifts measured by the IVM on the ICON satellite. All orbits are plotted together. Correlations are taken between plasma drifts measured in sequential passes of the ICON satellite through the magnetic equator near sunset. Sequential passes are separated in UT by 104 min. Red colors show August 2022 data and blue colors show October 2022 data. Bright-colored lines indicate nights when ESF irregularities were observed by the satellite, while pastel-colored lines indicate nights when ESF irregularities were not observed. The black dashed line indicates a correlation coefficient of $1 - e^{-1}$.

WAM-IPE composition is used. This acts as further validation of the claim that enhanced molecular ion densities are not the source of inaccurate simulation results.

The next two tests involve using HWM14 winds to drive the dynamo electric fields rather than thermospheric winds provided by WAM-IPE. The first of these tests is a direct substitution of HWM14 winds and is shown in dashed dark green lines, while a second test uses HWM14 winds delayed by 1 hour and is shown in dashed light green lines. The 1-h delay is motivated by results in [13], where this offset produced optimal agreement with ICON satellite wind measurements. Both tests have similar impacts on the time series of horizontal and vertical drifts. It can be seen that these had the most significant impact on the proxy model vertical drifts and improved the agreement with ISR observations on 29 Aug. 2022. However, each of these tests produced a similar PRE on all four nights including the two nights when a weak PRE was observed. This is not surprising as HWM14 is an empirical model that does not capture rapid day-to-day variations.

The final two tests are motivated by results from [31] where it was found that the PRE structure was sensitive to the zonal winds located at magnetic latitudes near the Equatorial Ionization Anamoly (EIA), rather than only those near the day/night terminator. Their results suggested that eliminating the zonal winds near the EIA, diminished the magnitude of the PRE. To test this, the proxy model was first run with no zonal winds for all longitudes where $20 \leq |\lambda| \leq 40$ (shown in dashed pink lines) and then with double the zonal winds in the same region (shown in dashed purple lines). The results here agree with those in [31], with a generally decreased drift magnitude with no EIA winds, and an increased drift magnitude with double EIA winds. However, neither of these tests produced a PRE comparable to that observed by ISR, on either night.

As can be seen in each panel (a) of Figure 6, none of these sensitivity tests significantly impacted the evolution of zonal drift velocities. The regional simulation described above does not appear to be highly sensitive to zonal drifts. However, it is highly sensitive to vertical drifts. Both of these observations highlight the importance of predicting the vertical plasma drifts and the structure of the PRE in forecasting ESF.

4 PRE persistance

The final analysis of WAM-IPE electric fields performed here is on the persistence of the PRE in both magnitude and timing. The empirical model developed by [19] and used in many ionospheric models predicts a global structure of vertical plasma drifts that is predominantly dependent on LT. This means that the PRE can be expected to remain roughly constant in magnitude and position relative to the day/night terminator. Therefore, if the PRE is sampled at the same LT at two different UTs, there should be a strong correlation between the two curves. This is not always observed in WAM-IPE estimates of the vertical plasma drifts.

Figure 7 shows the evolution of WAM-IPE vertical drifts in UT for a span of LT surrounding the day/night terminator. Drifts are shown at 300 km altitude for all nights of the 2022 campaign are shown in 12-minute increments between 2300 UT and 0100 UT. The LT for each panel is constant with the terminator (1830 LT) in the center of the horizontal axis. The UT increases moving down a column, so each subsequent panel moves to the west in longitude. It can be seen that the PRE structure does not remain constant across the 2 hours of samples, and can change rapidly across 36 min, or less. In general, both the PRE peak and the reversal time drift to the west as the night progresses. One significant observation is the disappearance and reappearance of the PRE on 29 Aug. (first column). The PRE is absent at 2348 UT but is weakly present 12 min before and after. It is expected that the PRE would be present, and maintain its magnitude and position, throughout the entire night rather than appear and disappear rapidly.

To study this evolution of the PRE, in-situ data provided by the IVM device aboard the ICON satellite is used for comparison. Ion velocities from ICON are recorded as the satellite passes the magnetic equator near sunset. These measurements were used as a driver of the regional simulation by [12] and [13]. Results presented in those studies highlighted the importance of the PRE in driving the regional simulation. Normalized autocorrelation functions of vertical plasma drift measurements were calculated from consecutive orbits separated by 104 min (the orbital period of ICON). These functions are shown in Figure 8, with red curves representing data from August 2022, and blue curves representing data from October 2022. Bright-colored curves indicate nights when ESF was observed, while pastel-colored curves indicate no ESF activity. The lag time on the horizontal axis represents the lag time relative to when ICON crosses a constant LT sector. Due to the satellite's motion, both temporal and spatial variations are implicitly represented in these datasets. This is not the same as recording the spatial structure of the PRE at a constant LT as is done in Figure 7.

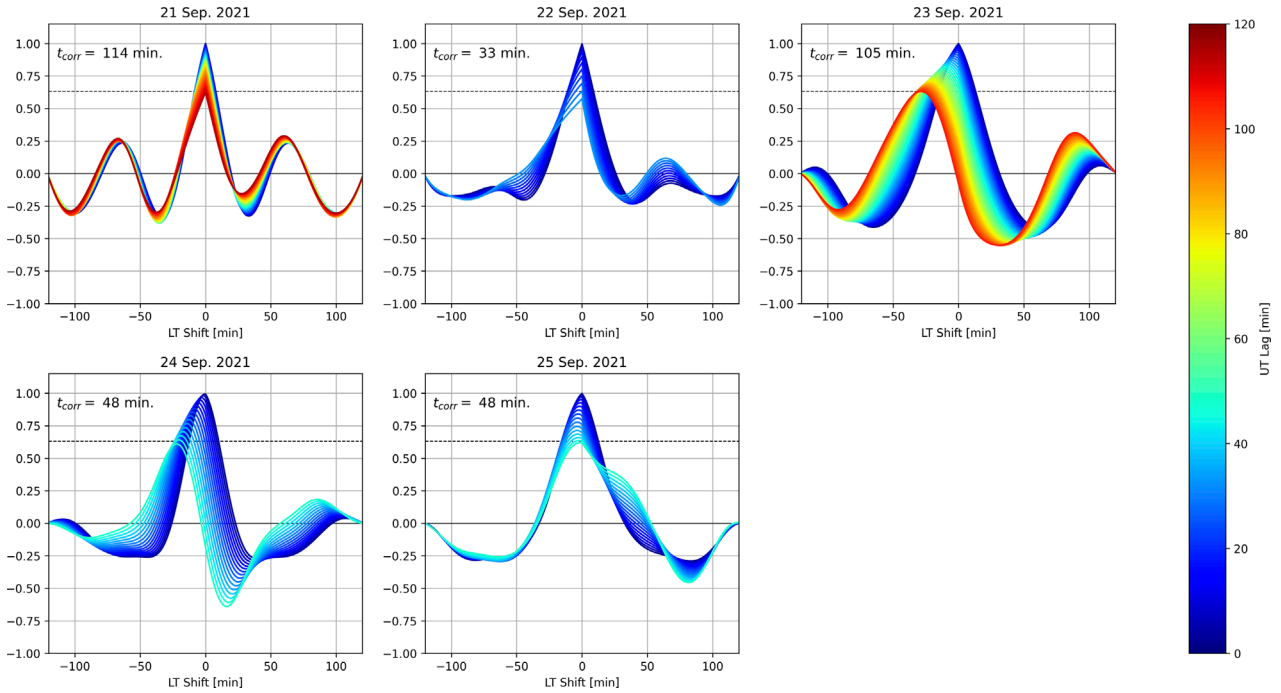

FIGURE 9
Autocorrelation functions of WAM-IPE vertical plasma drifts from 2021 campaign. The horizontal axis is the LT shift (in minutes) of the PRE structure with negative values corresponding to a Westward shift. Multiple autocorrelation functions are plotted on each axis with the color of each line representing the UT lag between the curves being correlated. Details for how these functions are calculated are given in the text. Autocorrelation functions are plotted for increasing lag times until the correlation coefficient decreases by a factor of 1/*e* (dashed black line). Correlation times, t_{corr}, are printed in each panel. Correlation times longer than 120 min are not calculated.

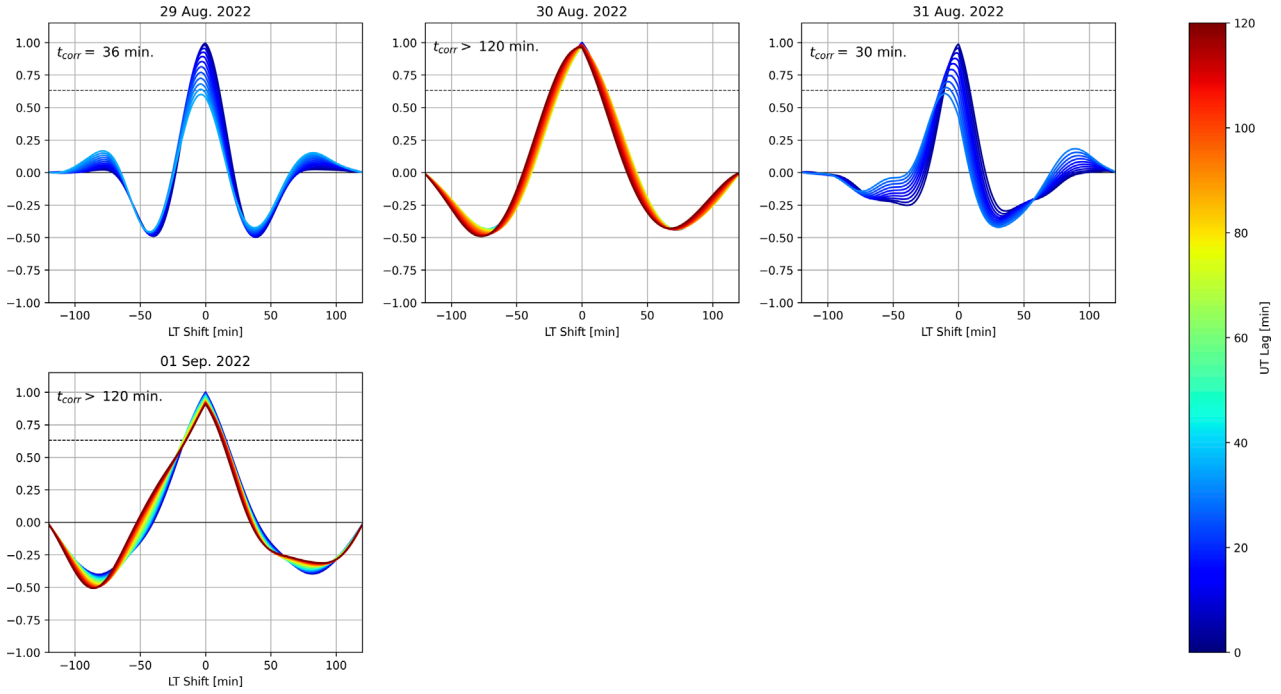

FIGURE 10
Same as Figure 9 but for 2022 campaign.

However, it is an in-situ measurement that can be used as a baseline for the persistence of the PRE.

It can be seen in Figure 8 that the PRE is well correlated across at least 104 min. Here, the correlation time, t_{corr} is defined as the maximum time between measurements with a correlation coefficient that has decreased by a factor less than or equal to $1/e$. Since relatively few autocorrelation functions in Figure 8 have a maximum correlation coefficient less than $1-e^{-1}$ (dashed black line), it is concluded that ICON data suggests a correlation time longer than 104 min. Additionally, the location of the PRE remains relatively constant, as indicated by the small lag times of the peak correlation coefficient. Nights in which ESF was observed exhibit a particularly strong correlation relative to nights without ESF. Based on these results, it can be concluded that the PRE has a correlation time of at least 104 min. This large t_{corr} is in agreement with the empirical model suggested by [19].

Similar, but not equivalent, normalized autocorrelations are taken with WAM-IPE estimates of vertical plasma drifts throughout 2021 and 2022 campaigns and are shown in Figures 9, 10 (WAM-IPE data for the 2021 campaign were analyzed by [20]). The estimates of vertical drifts are recorded at 590 km altitude (the orbital altitude of ICON satellite) and across a 60° wide longitude sector centered around the day/night terminator. Contradictory to the ICON data shown in Figure 8, this solely compares the spatial structure of the PRE. This longitude sector corresponds to ±2 h in LT around the terminator. Autocorrelation functions are calculated by correlating these sectored vertical drifts at two different UTs. Autocorrelation functions with the same UT lag time are then averaged. For example, a 3-minute UT lag time correlation is calculated between 2300 UT and 2303 UT, between 2303 and 2306 UT, between 2306 UT and 2309 UT, and so on before being averaged. The UT lag times are then increased by 3 min until a UT lag time of 120 min is reached or t_{corr} is reached. Correlation times are printed in the upper-left-hand corner of each panel in Figures 9, 10. The horizontal axis is the LT shift (equivalent to a longitudinal shift) of the two longitudinal sectors relative to one another. A positive LT shift corresponds to an Eastward shift. The color of each line plotted is representative of the UT lag time between longitudinal sectors that are being correlated. This essentially separates the spatial and temporal structure of the plasma drifts, which were combined for the ICON data.

It can be seen that t_{corr} is highly variable on a night-to-night basis. Only two of the nine campaign nights show $t_{corr} >$ 120 min, although it should be noted that two other nights (21 Sept. 2021 and 23 Sept. 2021) exhibit strong correlation over at least 104 min. The nights with short correlation times (less than 2 h) have t_{corr} ranging from 114 min to as little as 24 min. In particular, one of the shortest correlation times occurred on 29 Aug. 2022, which is one of the nights when WAM-IPE electric fields prevented the growth of irregularities in the regional simulation. Although the autocorrelation functions shown for each dataset cannot be compared directly, a general understanding of t_{corr} can be gathered from both. The occasional short correlation times in WAM-IPE estimates are contradictory to the regularly observed long correlation times seen in ICON data. There does not appear to be a connection between correlation time and accuracy of the resulting regional simulations. This is evident due to 29 Aug. 2022 having a small t_{corr} value while 01 Sept. 2022 exhibits a large value of t_{corr}, yet both nights were missed detections when the simulation was driven with WAM-IPE electric fields. On the other hand, 30 Aug. 2022 shows a large t_{corr} and 31 Aug. 2022 has a short t_{corr} while both nights had accurate simulations of absent ESF.

5 Conclusion

The regional simulation described in Section 2 is capable of reproducing night-to-night observations of ESF activity when initialized and driven by proper observational data. Most importantly, the simulation is sensitive to the strength, duration, and timing of the PRE. Previous results of the simulation indicate that the most reliable method of determining background electric fields is to derive them from ISR-measured vertical plasma drifts. This, however, is not a true forecast as it relies on real-time radar measurements to reproduce irregularities that are actively present and not about to develop. Additionally, the simulation has a very high computational cost and is unable to run in real time. In an attempt to move towards a true forecast using the simulation, predicted background electric fields taken from WAM-IPE were used to drive the simulation. These attempts were less successful than the ISR-driven results as missed detections were recorded. The lack of night-to-night accuracy in WAM-IPE background electric fields is capable of suppressing instabilities and may also be capable of generating artificial instabilities in the regional simulation.

To analyze the background electric fields from WAM-IPE, a proxy electrodynamics model was developed and used to perform a variety of sensitivity tests. Multiple sensitivities of the dynamo solver were tested related to the ionospheric composition and neutral wind structure. Replacing WAM-IPE winds with HWM14 appeared to improve agreement between the resulting electric fields and ISR observations for some nights, but not others. Other sensitivities tested also did not improve the agreement. These results suggest that there is not a simple substitution or scaling of WAM-IPE parameters that would produce electric fields comparable to ISR observations on a night-to-night basis.

While no sensitivity tests reproduced ISR observations, they did appear to significantly impact the resulting electric fields. In agreement with [31] the PRE appears to rely on the global wind patterns rather than local patterns surrounding the terminator. This highlights the importance of thermospheric wind observations for a potential ESF forecast. [20] suggested disagreement between WAM-IPE and HWM14 thermospheric winds that may also prove detrimental to the resulting electrodynamics. Further exploration and validation of global WAM-IPE neutral wind patterns may improve the day-to-day accuracy of its equatorial electrodynamics estimations.

Additionally, the vertical plasma drifts produced by WAM-IPE electric fields were compared to those measured by the ICON satellite. In particular, we note that ICON data agrees with the theory that the global structure of the vertical drifts and the PRE maintain their shape and vary slowly. As measured by ICON the PRE appears to have a correlation time of at least 104 min In contrast, it was shown that WAM-IPE results may vary the PRE structure rapidly with correlation times dropping to as little as 20 min. Further work is needed to understand the effect of a persistent, or rapidly changing, PRE on ESF development and the growth of irregularities in the regional simulation.

A multitude of factors can affect the growth of irregularities associated with ESF. Contemporary results suggest that the most important of these factors are the background electric fields, the strength and timing of the PRE, and the neutral thermospheric winds that produce the ionospheric dynamo. A true forecast of ESF must capture each of these factors, and others, accurately on a night-to-night basis. Improvement of the night-to-night accuracy in WAM-IPE electric fields is critical to the model acting as the baseline for a regional forecast. Currently, the electric fields predicted by WAM-IPE do no better than climatology and are therefore unable to drive a forecast that is more accurate than climatology. Further sensitivity tests, may indicate additional sources for more accurate variability in the WAM-IPE electric fields.

Data availability statement

The datasets presented in this study can be found in online repositories. The names of the repository/repositories and accession number(s) can be found in the article/Supplementary Material.

Author contributions

AK: Investigation, Methodology, Writing–original draft, Writing–review and editing, Conceptualization, Formal Analysis. DH: Conceptualization, Funding acquisition, Investigation, Methodology, Supervision, Writing–review and editing, Formal Analysis. T-WF: Data curation, Writing–review and editing, Supervision.

Funding

The author(s) declare that financial support was received for the research, authorship, and/or publication of this article. This project is supported by NSF award no. AGS-2028032 to Cornell University and the University of Colorado Boulder. The Jicamarca Radio Observatory is a Instituto Geofisico del Peru facility operated with support from NSF award no. AGS-1732209 through Cornell University.

Acknowledgments

The authors thank Tim Fuller-Rowell for his help in interpreting WAM-IPE data. We also thank the Jicamraca Radio Observatory staff for their help in collecting radar data.

Conflict of interest

The authors declare that the research was conducted in the absence of any commercial or financial relationships that could be construed as a potential conflict of interest.

The author(s) declared that they were an editorial board member of Frontiers, at the time of submission. This had no impact on the peer review process and the final decision.

Publisher's note

Supplementary material

The Supplementary Material for this article can be found online at: https://www.frontiersin.org/articles/10.3389/fphy.2024.1488935/full#supplementary-material

References

1. Booker HG, Wells HW. Scattering of radio waves by the F-region of the ionosphere. *Terrestrial Magnetism Atmos Electricity* (1938) 43:249–56. doi:10.1029/TE043i003p00249

2. Woodman RF, La Hoz C. Radar observations of F region equatorial irregularities. *J Geophys Res (1896-1977)* (1976) 81:5447–66. doi:10.1029/JA081i031p05447

3. Zargham S, Seyler CE. Collisional interchange instability: 1. Numerical simulations of intermediate-scale irregularities. *J Geophys Res Space Phys* (1987) 92:10073–88. doi:10.1029/JA092iA09p10073

4. Kelley MC, Seyler CE, Zargham S. Collisional interchange instability: 2. A comparison of the numerical simulations with the *in situ* experimental data. *J Geophys Res Space Phys* (1987) 92:10089–94. doi:10.1029/JA092iA09p10089

5. Hysell DL, Kudeki E. Collisional shear instability in the equatorial F region ionosphere. *J Geophys Res Space Phys* (2004) 109. doi:10.1029/2004JA010636

6. Woodman RF. Spread F – an old equatorial aeronomy problem finally resolved? *Ann Geophysicae* (2009) 27:1915–34. doi:10.5194/angeo-27-1915-2009

7. Kelley MC, Makela JJ, de La Beaujardière O, Retterer J. Convective ionospheric storms: a review. *Rev Geophys* (2011) 49. doi:10.1029/2010RG000340

8. Haerendel G. *Theory of equatorial spread F*. Max Planck Institute for extraterrestrial Physics (1973).

9. Sultan PJ. Linear theory and modeling of the Rayleigh-Taylor instability leading to the occurrence of equatorial spread F. *J Geophys Res Space Phys* (1996) 101:26875–91. doi:10.1029/96JA00682

10. Scannapieco AJ, Ossakow SL. Nonlinear equatorial spread F. *Geophys Res Lett* (1976) 3:451–4. doi:10.1029/GL003i008p00451

11. Hysell DL, Jafari R, Milla MA, Meriwether JW. Data-driven numerical simulations of equatorial spread *F* in the Peruvian sector. *J Geophys Res Space Phys* (2014) 119:3815–27. doi:10.1002/2014JA019889

12. Hysell DL, Kirchman A, Harding BJ, Heelis RA, England SL. Forecasting equatorial ionospheric convective instability with ICON satellite measurements. *Space Weather* (2023) 21:e2023SW003427. doi:10.1029/2023SW003427

13. Hysell DL, Kirchman A, Harding BJ, Heelis RA, England SL, Frey HU, et al. Using ICON satellite data to forecast equatorial ionospheric instability throughout 2022. *Space Weather* (2024) 22. doi:10.1029/2023SW003817

14. Fejer BG, Scherliess L, de Paula ER. Effects of the vertical plasma drift velocity on the generation and evolution of equatorial spread F. *J Geophys Res Space Phys* (1999) 104:19859–69. doi:10.1029/1999JA900271

15. Rishbeth H. The F-region dynamo. *J Atmos Terrestrial Phys* (1981) 43:387–92. doi:10.1016/0021-9169(81)90102-1

16. Farley DT, Bonelli E, Fejer BG, Larsen MF. The prereversal enhancement of the zonal electric field in the equatorial ionosphere. *J Geophys Res Space Phys* (1986) 91:13723–8. doi:10.1029/JA091iA12p13723

17. Eccles JV. A simple model of low-latitude electric fields. *J Geophys Res Space Phys* (1998) 103:26699–708. doi:10.1029/98JA02657

18. Eccles JV, St. Maurice JP, Schunk RW. Mechanisms underlying the prereversal enhancement of the vertical plasma drift in the low-latitude ionosphere. *J Geophys Res Space Phys* (2015) 120:4950–70. doi:10.1002/2014JA020664

19. Scherliess L, Fejer BG. Radar and satellite global equatorial F region vertical drift model. *J Geophys Res Space Phys* (1999) 104:6829–42. doi:10.1029/1999JA900025

20. Hysell DL, Fang TW, Fuller-Rowell TJ. Modeling equatorial *F* -region ionospheric instability using a regional ionospheric irregularity model and WAM-IPE. *J Geophys Res Space Phys* (2022) 127. doi:10.1029/2022JA030513

21. Fang T-W, Fuller-Rowell T, Kubaryk A, Li Z, Millward G, Montuoro R. Operations and recent development of NOAA's Whole. *Atmosphere Model* (2022) 44:849.

22. Maruyama N, Sun Y-Y, Richards PG, Middlecoff J, Fang T-W, Fuller-Rowell TJ, et al. A new source of the midlatitude ionospheric peak density structure revealed by a new Ionosphere-Plasmasphere model. *Geophys Res Lett* (2016) 43:2429–35. doi:10.1002/2015GL067312

23. Swisdak M. Notes on the dipole coordinate system. (2006).

24. Wohlwend CS. *Modeling the electrodynamics of the low-latitude ionosphere*. Utah State University (2008) Ph.D. thesis.

25. Schunk R, Nagy A. *Ionospheres: physics, plasma physics, and chemistry*. Cambridge, Cambridge University Press (2004).

26. Richmond AD. Ionospheric electrodynamics using magnetic apex coordinates. *J geomagnetism geoelectricity* (1995) 47:191–212. doi:10.5636/jgg.47.191

27. Laundal KM, Richmond AD. Magnetic coordinate systems. *Space Sci Rev* (2017) 206:27–59. doi:10.1007/s11214-016-0275-y

28. Alken P, Thébault E, Beggan CD, Amit H, Aubert J, Baerenzung J, et al. International geomagnetic reference field: the thirteenth generation. *Earth, Planets and Space* (2021) 73:49. doi:10.1186/s40623-020-01288-x

29. Farley DT. A theory of electrostatic fields in the ionosphere at nonpolar geomagnetic latitudes. *J Geophys Res (1896-1977)* (1960) 65:869–77. doi:10.1029/JZ065i003p00869

30. Eccles JV. The effect of gravity and pressure in the electrodynamics of the low-latitude ionosphere. *J Geophys Res Space Phys* (2004) 109. doi:10.1029/2003JA010023

31. Richmond AD, Fang T-W, Maute A. Electrodynamics of the equatorial evening ionosphere: 1. Importance of winds in different regions. *J Geophys Res Space Phys* (2015) 120:2118–32. doi:10.1002/2014JA020934

32. Emmert JT, Richmond AD, Drob DP. A computationally compact representation of Magnetic-Apex and Quasi-Dipole coordinates with smooth base vectors. *J Geophys Res Space Phys* (2010) 115. doi:10.1029/2010JA015326

33. Heelis R. Icon ion velocity meter (ivm) a data. (2023) doi:10.48322/2mv5-xy46

frontiers | Frontiers in Astronomy and Space Sciences

TYPE Original Research
PUBLISHED 20 February 2025
DOI 10.3389/fspas.2025.1517762

OPEN ACCESS

EDITED BY
Marco Milla,
Pontifical Catholic University of Peru, Peru

REVIEWED BY
Cristiano Fidani,
Independent Researcher, Fermo, Italy
Amol Kishore,
University of the South Pacific, Fiji

*CORRESPONDENCE
C. E. Valladares,
valladar@bc.edu

RECEIVED 27 October 2024
ACCEPTED 15 January 2025
PUBLISHED 20 February 2025

CITATION
Valladares CE, Chen Y-J, Bukowski A, Adhya P, Anderson PC, Dey S and Hairston M (2025) Measurements of LSTID and LSTAD using TEC and GOCE data.
Front. Astron. Space Sci. 12:1517762.
doi: 10.3389/fspas.2025.1517762

Measurements of LSTID and LSTAD using TEC and GOCE data

C. E. Valladares [1,2]*, Y.-J. Chen[1], A. Bukowski[3], P. Adhya[4], P. C. Anderson[1], S. Dey[1] and M. Hairston[1]

[1]W. B. Hanson Center for Space Sciences, The University of Texas at Dallas, Richardson, TX, United States, [2]Boston College, Institute for Scientific Research, Chestnut Hill, MA, United States, [3]Climate and Space Sciences and Engineering, University of Michigan, Ann Arbor, MI, United States, [4]Department of Electrical and Computer Engineering, University of South Alabama, Mobile, AL, United States

This paper presents measurements gathered with the Gravity Field and Ocean Circulation Explorer (GOCE) satellite, TEC values collected in the American sector, and Poynting Flux (PF) derived using the electric and magnetic fields from the Defense Meteorological Satellite Program (DMSP) satellites aiming to elucidate the mechanisms controlling the initiation of large-scale traveling atmospheric disturbances (LSTAD) and the transit and asymmetry of concurrent large-scale traveling ionospheric disturbances (LSTID). LSTADs and LSTIDs measured during twelve intense magnetic storms that occurred between 2011 and 2013 are thoroughly analyzed. The LSTAD/LSTID appearance and characteristics are correlated against the PF values and the auroral oval's location, measured by the DMSP satellites. GOCE data and TEC values are used to assess the perturbation of the vertical wind and TEC (∂TEC), inter-hemispheric asymmetry of the appearance of LSTIDs, and the role of the different phases of storms and the structures within interplanetary coronal mass ejections (ICME). Emphasis is devoted to examining LSTADs and LSTIDs during the storms of 5–6 August 2011, 15 July 2012, and 17 March 2013, the supporting material reports on the dynamics of LSTADs and LSTIDs for nine additional storms. During most storms, LSTIDs initiate from both auroral ovals and propagate toward the opposite hemisphere. However, on 5 August 2011 and 15 July 2012, LSTIDs moved only from one hemisphere toward the opposite. Close inspection of the TEC perturbation associated with these events indicates that LSTIDS onsets at opposite hemispheres occur at different times and intensities. This timing delay is produced by the difference in the amount of PF deposited in each hemisphere. It is also indicated that LSTAD's initiation occurs when the PF is above 1 mW/m^2 and when the lower latitude edge of the auroral oval moves equatorward at 65°. In addition, LSTIDs are observed during the passage of ICME sheath (in 6 storms), magnetic clouds (11), and Sunward Loops (1), although they occur when the IMF B_z is predominantly directed southward. The observations suggest that the interhemispheric asymmetries in the LSTIDs initiation, extension, and amplitude occur when the ICME sheath passes, containing rapidly varying IMF B_z sign fluctuations. TEC perturbations associated with the LSTID can be up to 4% of the background TEC value, and the LSTAD neutral density variability measured by GOCE can be up to 8%. LSTIDs are observed during all phases of magnetic storms.

KEYWORDS

large scale traveling atmospheric disturbance, large scale traveling ionospheric disturbance, poynting flux measurements, IMF Bz component, GOCE neutral density

Highlights

- TEC and GOCE measurements are analyzed to understand the initiation of LSTADs and LSTIDs during 12 magnetic storms.
- LSTADs are initiated when the Poynting Flux is >1 mW/m^2 and the auroral oval expands below 65°.
- The equatorward motion of the LSTIDs can be highly asymmetric, coinciding with the interhemispheric asymmetry of the Poynting Flux.

1 Introduction

Atmospheric gravity waves (AGW) propagate through the atmosphere and thermosphere, producing neutral gas disturbances named traveling atmospheric disturbances (TAD). These waves transfer momentum and energy through collisions to the ionized gas, originating from traveling ionospheric disturbances (TID) (Hines, 1960). The ∂U wind associated with AGWs can additionally produce an ion motion along the field lines and an E field through a ∂U × B action that maps to the opposite hemisphere, forming conjugate images of the TID (Jonah et al., 2017). The primary source of short and medium-scale GWs resides in the troposphere due to convective plumes, lightning, and tropical storms (Hocke and Tsuda, 2001; Bishop et al., 2006; Valladares et al., 2017). In addition, tsunamis (Makela et al., 2011), earthquakes (Galvan et al., 2011), winds blowing across a mountain range (Smith et al., 2009), and human-made effects such as explosions and fires (Scott and Major, 2018) create medium and short-scale GWs, respectively. These processes can produce TIDs with different characteristics and spatial and temporal scales at almost any latitude. In contrast, large-scale GWs are primarily initiated in the polar regions due to Joule heating deposited in the auroral E– and F-regions during intense magnetic storms. Large-scale GWs commonly initiate at both auroral ovals and propagate toward the opposite hemisphere (Saito et al., 1998; Shiokawa et al., 2002; Valladares et al., 2009), colliding destructively near the magnetic equator.

This paper presents measurements of large-scale TADs (LSTAD) and LSTIDs made possible by the neutral density values derived from the accelerometer sensor on board the Gravity Field and Ocean Circulation Explorer (GOCE) satellite. These measurements are complemented by concurrent observations of TEC using an extensive network of 2000+ GPS and GNSS receivers that operate in the American sector, providing a comprehensive view of the phenomena. During magnetic storms, considerable particle energy and Poynting Flux (PF) increase the frictional Joule heating at auroral latitudes, launching waves in the ionosphere that propagate equatorward with velocities between 400 and 800 m/s. This article presents the results of an investigation that deals with the role of the PF in initiating LSTADs and LSTIDs. To account for the PF energy input, we use calculations derived from observations performed by the fleet of DMSP satellites. These satellites have an ion drift meter and magnetic field sensors (Knipp et al., 2021) and can measure electromagnetic energy. During steady-state conditions, the PF equals the Joule heating (Thayer and Semeter, 2004) deposited at high latitudes. Consequently, this parameter can be used to investigate their role in the onset times of LSTADs and LSTIDs, their characteristics, and equatorward velocities.

The first studies of LSTIDs were conducted by Ho et al. (1996), Ho et al. (1998) using 150+ globally distributed GPS receivers to demonstrate the simultaneous development of TEC perturbations at both north and south auroral regions. The later expansion of the network of GPS receivers in the American and European sectors brought more complete and spatially extended measurements of LSTIDs (Valladares et al., 2009). Nicolls et al. (2004) employed TEC data from GPS receivers in North America and vertical density profiles from Arecibo to derive a 3-D model of LSTIDs. These authors found that TEC perturbations associated with LSTIDs were about 1 TEC unit and were produced by wind pulses that initiated F-layer vertical motions. Balthazor and Moffett (1997) conducted the first modeling study of LSTIDs using a coupled thermosphere, ionosphere, and plasmasphere model to simulate the transit of LSTADs originating from both auroral ovals. The disturbance propagated toward the geographic equator in the thermosphere and interfered constructively, producing significant density and TEC variations. It is believed that the altitude extension of LSTIDs and their phase at the intersection point may control their propagation into the opposite hemisphere. More recently, Bukowsky et al. (2024) coupled the GITM and SAMI3 models to examine the height and latitudinal propagation of LSTIDs. These authors found that LSTIDs can intrude, propagate into the F-region topside, and reach exospheric altitudes.

Substorms have different dynamics from geomagnetic storms; they occur over a few hours and develop relatively frequently (Akasofu, 1964). During substorms, the incoming energy is released from the magnetotail and injected into the oval region. During these events, Joule heating can increase in the auroral regions. Substorms may also influence the formation and characteristics of LSTADs and LSTIDs. This scientific paper does not address this issue.

This publication introduces LSTADs and LSTIDs for twelve intense magnetic storms that developed during the lifetime of the GOCE satellite to show the variability of the density perturbation amplitude and motions. GOCE was launched into a polar orbit (06:00/18:00 local time) on 17 March 2009 (ESA, 2009). Neutral density and winds were derived from the accelerometer measurements (Bruinsma et al., 2014). The DMSP satellites were also launched into closely polar orbits with DMSP-F15 equatorial passes probing solar local times varying between 16.9 and 15.2 h during the 3 years of this study (2011–2013). DMSP-F16 varied between 18.7 and 17.0 for 3 years, and DMSP-F18 orbit changed between 20.1 and 19.9 local time. This publication also intends to unravel the crucial effects of the different phases of magnetic storms and the characteristics of the Interplanetary Coronal Mass ejections (ICME) in initiating LSTADs and LSTIDs.

The outline of this publication follows. The second section describes the amplitude of the neutral density and wind perturbations due to the LSTADs and the ∂TEC values corresponding to three selected magnetic storms. Section 3 presents the relationship between the LSTIDs' characteristics and evolution and the different characteristics of the ICMEs for three storms presented in Section 2. Section 4 discusses the general characteristics of all twelve magnetic storms and their relationship with solar wind and magnetospheric quantities. Finally, Section 5 presents the conclusions of this study.

2 Analysis of GOCE, DMSP, and TEC data

Research on LSTIDs and TIDs, particularly their association with TEC perturbations, has significantly advanced in the past decade. This is primarily due to the ability to accurately extract the TEC perturbation linked to density changes over large areas, often caused by tropospheric, thermospheric, or magnetospheric influences. In many cases, the origin of these TEC perturbations can be inferred (Vadas and Crowley, 2010; Valladares et al., 2017). It is understood that a downward electromagnetic PF vector in an E region can intensify the Joule heating (J·E), leading to increased ion and neutral temperatures and the generation of upward and downward neutral motions. This substantial energy deposition, mainly in the auroral oval, is anticipated to create a large-scale wave (LSTAD) system that moves poleward and equatorward.

When the PF vector reaches the high latitude E region, large-scale waves with a scale size ranging between 10° and 20° are formed. As shown below, these waves propagate toward lower latitudes and can last a few hours. Zonal displacement is, in a way, inhibited due to the large longitudinal extension of precipitation PF. Based on the GOCE measurements of the neutral wind, the amplitude of the vertical wind associated with these waves is observed to reach amplitudes as large as ±20 m/s. During the lifetime of the GOCE satellite, thirteen intense geomagnetic storms with SYM-H < −100 nT occurred. However, the storm of 13 October 2012 had no GOCE data recorded. Therefore, all other twelve magnetic storms were thoroughly analyzed, ensuring the validity and reliability of our findings. The results of nine storms can be revised in the Supplementary Material.

The rest of this section reports three storms selected based on the variability of their ∂TEC, the downward PF, and the IMF B_z. These events are 5–6 August 2011, 15 July 2012, and 17 March 2013, corresponding to observations during solstice and equinox seasons. All 12 events were analyzed, spanning the solstice (5) and equinox (7). The significance of the satellite data, particularly the combined observations of ∂(Neutral Density), PF, and particle precipitation by the GOCE and DMSP, both flying in the sun-synchronous orbit, ascending during sunset and descending during sunrise, provides an easy way to identify and distinguish thermosphere conditions and the magnetospheric inputs acting on the dawn and dusk sectors. The ∂TEC data from the American continent covers all local times and will be correctly compared to the satellite data, ensuring a comprehensive and sound data analysis.

In addition, the DMSP satellites provide particle precipitation measurements that allow us to infer the locations of the edges of the auroral oval. Our processing and conclusions are also further favored by including additional ancillary data, such as the three components of the IMF and the solar wind's density, velocity, temperature, and plasma β (Section 3).

2.1 General description of the storms of 2011–2013

Figure 1 shows the SYM-H values (four top panels) and the height of GOCE (four lower panels) corresponding to the last 4 years of the satellite lifetime (i.e., 2010–2013). Using red, this Figure displays thirteen intense magnetic storms (SYM-H < −100 nT) that developed during these years. The lower panels exhibit the daily variability of the satellite's height, which changed between 260 and 290 km. It remained at this level until August 2012, when it decreased to an average of 260 km. The altitude was further reduced in May 2013, originating the spacecraft's final decay and reentry in November 2013.

Figure 2 displays the neutral density measured by GOCE on 24 May 2011 and between 09:29:50 and 10:00:00. The pass corresponds to the ascending (sunset) phase of the GOCE satellite. At this time, no LSTIDS were present, and no other neutral density fluctuations, such as the equatorial thermal anomaly, were seen at low latitudes (Hocke and Tsuda, 2001; Bishop et al., 2006; Valladares et al., 2017; Makela et al., 2011; Galvan et al., 2011). However, the neutral density presents large variability at polar magnetic latitudes above 80°. To avoid these unwanted high latitude effects, our processing and algorithm extraction of the neutral density perturbation associated with TIDs were restricted to the latitudinal range of −63° and 63°. It is indicated that our analysis aims to identify neutral density changes due to the passage of LSTIDs that start near the auroral oval. We tried different fitting algorithms and found that a 7th-order polynomial curve can reproduce all the essential latitudinal and altitudinal features of the background neutral density variability during non-storm conditions. The upper panel of Figure 2 displays the neutral density in black and the fit in red. The excellent fit produces noise-type differences of less than 3% of the background density. The lower panel of Figure 2 displays in red the difference between the measured neutral density and the 7th-order polynomial fitting. The amplitudes are lower than 0.10×10^{11} Kg or a relative variation of ~2.5%. As shown below, these differential density profiles develop significant perturbations during intense magnetic storms with amplitudes 4 or 5 times those values.

Figure 3 illustrates how we assemble the low-resolution and extended GOCE plots (left panels) that help us identify LSTADs. These observations correspond to three consecutive days, including the magnetic storm's onset, main, and recovery phases on 5-6 August 2011. This Figure shows consecutive ascending passes, built by removing the background density and vertical wind (see center and right frames) for each pass individually. Both neutral density and the vertical wind values were processed independently using a 7th-order polynomial fit. The center and right frames of Figure 3 show, from top to bottom, the neutral density, the difference between the measured and fitted values, the difference between the processed and fitted vertical wind in green, and the correlation function and the peak of the cross-correlation between the neutral density and vertical wind differences (∂density and ∂wind). The fact that the correlation and cross-correlation are equal implies that the density and wind variability are in phase. The orange arrows point out the relative location of the individual passes and the "low-res" graph on the left. Each pass of GOCE becomes a single vertical line on the left side of Figure 3, with the positive and negative excursions of the differences displayed in red and blue, respectively. The top frame displays the neutral density variability (∂density), and the bottom frame for the vertical wind (∂wind). The usefulness of the "low-res" figure dwells on its ability to provide a rapid and accurate view of the presence of significant ∂density perturbations (e.g., LSTADs). The left frames show high ∂density (top) and ∂wind (bottom) values between 20 UT on 5 August 2011 and 02 UT on 6 August 2011.

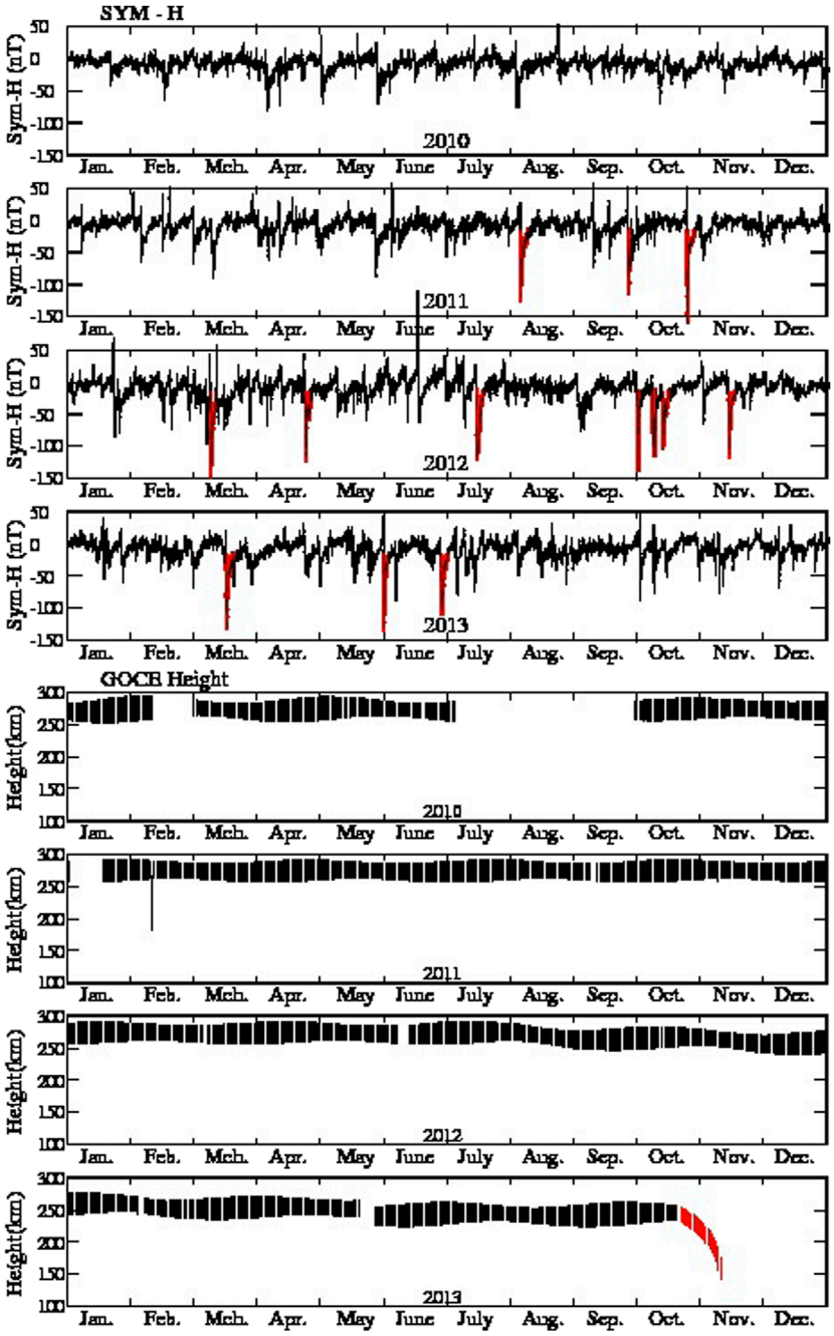

FIGURE 1
The top four panels display the SYM-H values measured between 2010 and 2013 during the operations of the GOCE satellite. The times of the intense magnetic storms are shaded in red. The lower four panels show the variation in the altitude of the GOCE satellite and the time of reentry in red in November 2013.

2.2 The storm of 5–6 August 2011

Figure 4 shows the SYM-H, the three components of the IMF, and the auroral electrojet (AE) index corresponding to the first intense magnetic storm in 2011. We display 3 days' worth of data covering the time of the sudden commencement, the main, and part of the recovery phase. The Auroral Electrojet (AE) index is derived from geomagnetic variations in the H component using 10 to 13 magnetic stations located in the northern hemisphere's auroral zone (Davis and Sugiura, 1966). The AE index represents the overall activity of the electrojets, and the AO index measures the equivalent zonal current averaged over all longitudes. The IMF B_z component is negative (yellow shading) between 18 UT on 5 August 2011 and 04 UT the following day. However, a positive excursion of B_z with sharp boundaries occurred between 22 and 24 UT on 05 August 2011. The commencement and

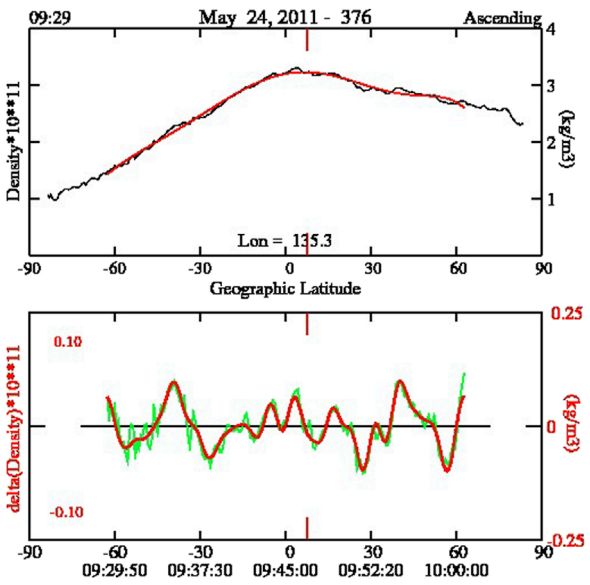

FIGURE 2
Neutral density data was measured by the GOCE satellite on 24 May 2011. This is a generic plot corresponding to quiet magnetic conditions. The top panel shows this curve's neutral density and a polynomial fit (red). The lower panel shows the difference between the measured and the fitted curves (green trace) and the filtered trace (in green).

main phases of the storm coincided with this extended period of predominant B_z negative.

Figure 5A illustrates the ground projection of the field lines in the American sector between ±62° magnetic latitude. The ∂TEC values detected within the red region are used to construct the keogram presented in Figure 5B. These field lines cross the magnetic equator between 84° and 76° West longitude. At this longitude, the magnetic field lines are aligned almost parallel to the geographic north-south direction. The ∂TEC values that make the keogram presented here are derived by fitting a running 5th-order polynomial to all the GPS passes and each station individually. The difference between the measured TEC and the fitted curve constitutes the ∂TEC perturbation values associated with the passage of TIDs. Nevertheless, other ionospheric events, such as equatorial plasma bubbles (EPB), can alter the LSTID identification by creating quasi-random features that sometimes obliterate the TID signatures. The resolution of the keogram is 3 min and 0.5° in latitude. The standard deviation of the ∂TEC perturbation is <0.1 TEC units. The transit of the LSTIDs across the continent is seen in the keogram as prominent red and blue slanted lines between 19 UT on 5 August 2011 and 06 UT having amplitudes above 1 TEC unit, indicated by a black arrow near 22 UT. The unique feature of this plot is the consistent southward motion of the LSTIDs that reach −40° geographic latitude and the absence of LSTIDs moving northward. Contrary to these observations, previous measurements and simulations have concluded that LSTIDs initiate almost simultaneously near both auroral ovals and encounter close to the magnetic equator (Valladares et al., 2009; Bukowski et al., 2023). In addition to the LSTIDs, Figure 5B shows several other features, such as small, slanted segments produced by medium and small-scale TIDs and nearly vertical lines seen near 11 UT produced by the morning solar terminator.

Figure 6 shows 3 days of "low-res" measurements to demonstrate the intrinsic relationship between the PF, the oval expansion, the development of LSTAD, and the vertical neutral wind perturbation, encompassing the sudden commencement, the main phase and part of the recovery phase of the first storm of 2011. These plots also support our contention that different longitude or MLT sectors have different energy inputs (e.g., PF or particle) and originate LSTADs with distinct characteristics. The eight frames of Figure 6 are labeled descending for sunrise passes (left side panels) and ascending for sunset orbits (right side). From top to bottom, Figures 6A–D show the PF for the northern (between 90° and 50°) and southern hemispheres (between −50° and −90°), the ∂(neutral density), and the ∂(vertical wind). Blue and light blue circles indicate the poleward and equatorward boundaries of the auroral oval, respectively. The dark blue and green dots near the lower horizontal axis indicate times when GOCE crosses the African and South American continents. Panels 6g and h are reproduced from Figure 3 to place the LSTAD differences in the dawn and dusk sectors in context. A significantly enhanced PF is observed right after the beginning of the sudden commencement of the storm (19 UT). The PF energy reaches a value above 0.03 W/m^2 near 23 UT on 05 August 2011. At the same time, the auroral oval moves equatorward, extending between 55° and 70° in the Northern Hemisphere (NH) and Southern Hemisphere (SH) and for both sunrise and sunset sectors. Concurrently, with the enhanced PF and the expansion of the auroral oval, a significant increase in the ∂(neutral density) variability above the noise level is observed (Figure 6C). An amplitude larger than 20% variations and 20 m/s (Figure 6D) are seen between 22 UT and 06 UT. We believe that the large density and vertical wind perturbations indicate the initiation and transit of LSTADs. The right panels show a different behavior (Figures 6E–H). The ascending passes (near sunset) show an early penetration of the auroral oval to lower latitudes and a higher asymmetry of the northern and southern hemispheres PF. Although the NH reports values above 0.03 W/m^2, the SH PF contains numbers less than 0.01 and occurs sporadically, delaying the initiation and intensity of LSTADs/LSTIDs in the SH. We believe this lack of PF measurements is due to values smaller than the detectability level of the drift and magnetic field sensors. The earlier oval expansion of the sunset sector, for at least 90 min, is also accompanied by a similar early occurrence of ∂(neutral) perturbations (LSTAD): Figures 6G, H display perturbation extending between 20 UT and 02 UT. Figures 6C, G contain a black line near the bottom of the frame representing the sum of the absolute values of the ∂(neutral density) in percentage. Peak values above 2000 and 1,000 units are observed in the sunrise and sunset sectors, respectively. This line is a good indicator of the presence of LSTADs.

Figure 7 presents ∂TEC values measured over North, Central, and South America on 5 August 2011. The six frames are separated by 30 min to give a glimpse of the southward motion of the NH ∂TEC and the weak and late initiation of the SH ∂TEC. The encircled numbers designate positive ∂TEC perturbations moving southward in red and northward motions in blue. The ∂TEC increase (red and yellow shadings) seen at 16° geographic latitude (labeled 2) in the image corresponding to 21:00 UT and another detected at −10° (labeled 1) are used to follow the motion of the LSTID. These

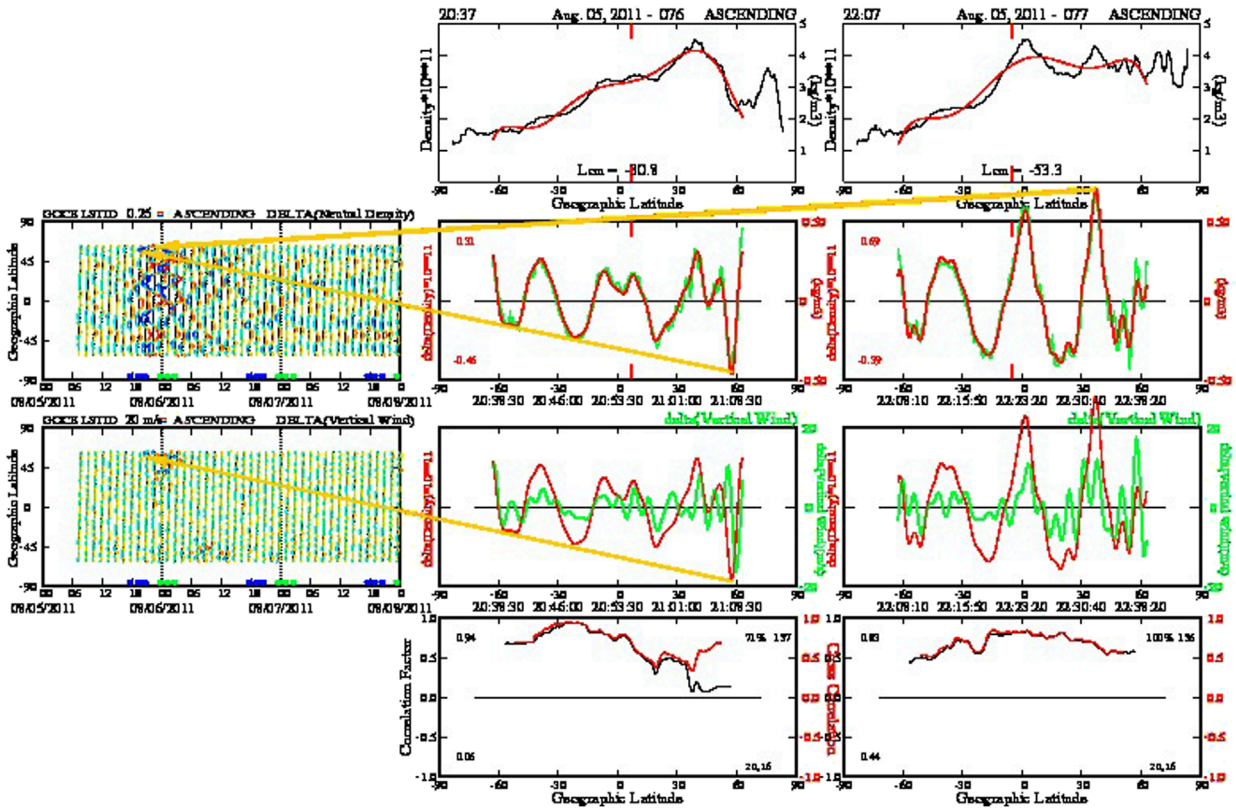

FIGURE 3
A series of neutral density and vertical wind plots demonstrate how the 3-day low-resolution plots on the left side were constructed. Each vertical line in the left panels corresponds to a density profile taken during the ascending pass, as shown on this figure's central and right sides. The left panels show the ∂density at the top and ∂(the vertical wind) at the bottom.

∂TEC features are detected 30 min later at 5° and −20°, then at 22 UT move to −5° and −30° latitude, and finally, the frame for 22:30 UT shows the ∂TEC features displaced at −16° and −40° geographic latitude. A series of new LSTIDs is observed to appear later and move southward. Figure 7 indicates that several ∂TEC originating in the NH cross the equatorial line, follow into the opposite hemisphere, and seem to continue up to the southern auroral oval. The image corresponding to 21:30 UT shows the appearance of a weak ∂TEC perturbation at −60° latitude labeled 1 in blue that originates in the SH oval and propagates northward. New ∂TEC moving northward are seen later at 22:30 and 23:00 UT. The nature of this low amplitude LSTID agrees with the weak PF energy deposited in the SH, corroborating a link between PF, Joule heating, and the amplitude of LSTIDs.

In summary, we observe strong LSTAD and LSTID activity during substantial PF deposition, oval expansion, prominent IMF B_z southward (−20 nT), and concurrent AE index over 2000 nT. The storm LSTADs observed in the sunset sector are detected during the sudden commencement and main phases. The following subsections present other cases when LSTAD activity is reported during different seasons, local times, and magnetospheric inputs.

The supporting material contains Supplementary Movie S1, which shows the ∂TEC variability between 17 UT on 5 August 2011 and 02 UT on 6 August 2011. This movie corroborates the steady and spatially uniform motion of the LSTID and provides additional information on the initiation and expansion of ∂TEC perturbations. In the NH, ∂TEC perturbations initiate at 18:03; however, LSTIDs start at 19:18 UT at the SH. The different LSTIDs start times in opposite hemispheres and their unequal velocity and amplitude (LSTAD) make the TIDs encounter at −35° geographic latitude. Although this interaction destroys the SH LSTID, the NH perturbations probably reach the southern auroral oval.

2.3 The storm of 15 July 2012

This storm occurred during the summer solstice (NH), in which the LSTADs presented characteristics similar to those of the 5–6 August 2011 storm. Figure 8 summarizes the ionospheric and magnetospheric parameters that characterize intense storms (e.g., ∂TEC, SYM-H, and IMF). The storm had a lengthy recovery period, with steady IMF B_z near −15 nT lasting 32 h, with a sharp decline and reversal at 14 UT on 16 July 2012. The keogram shows a continuous transit of LSTIDs during the period of B_z southward conditions. However, the LSTIDs show asymmetric motion with a predominant southward direction during the storm's sudden commencement, a time of B_z rapid sign fluctuations (see arrow near 0 UT on 15 July 2012). This behavior is reminiscent of the LSTIDs observed on the 5 August 2011 storm. However, later that day and during the storm's recovery phase (after 18 UT and between the

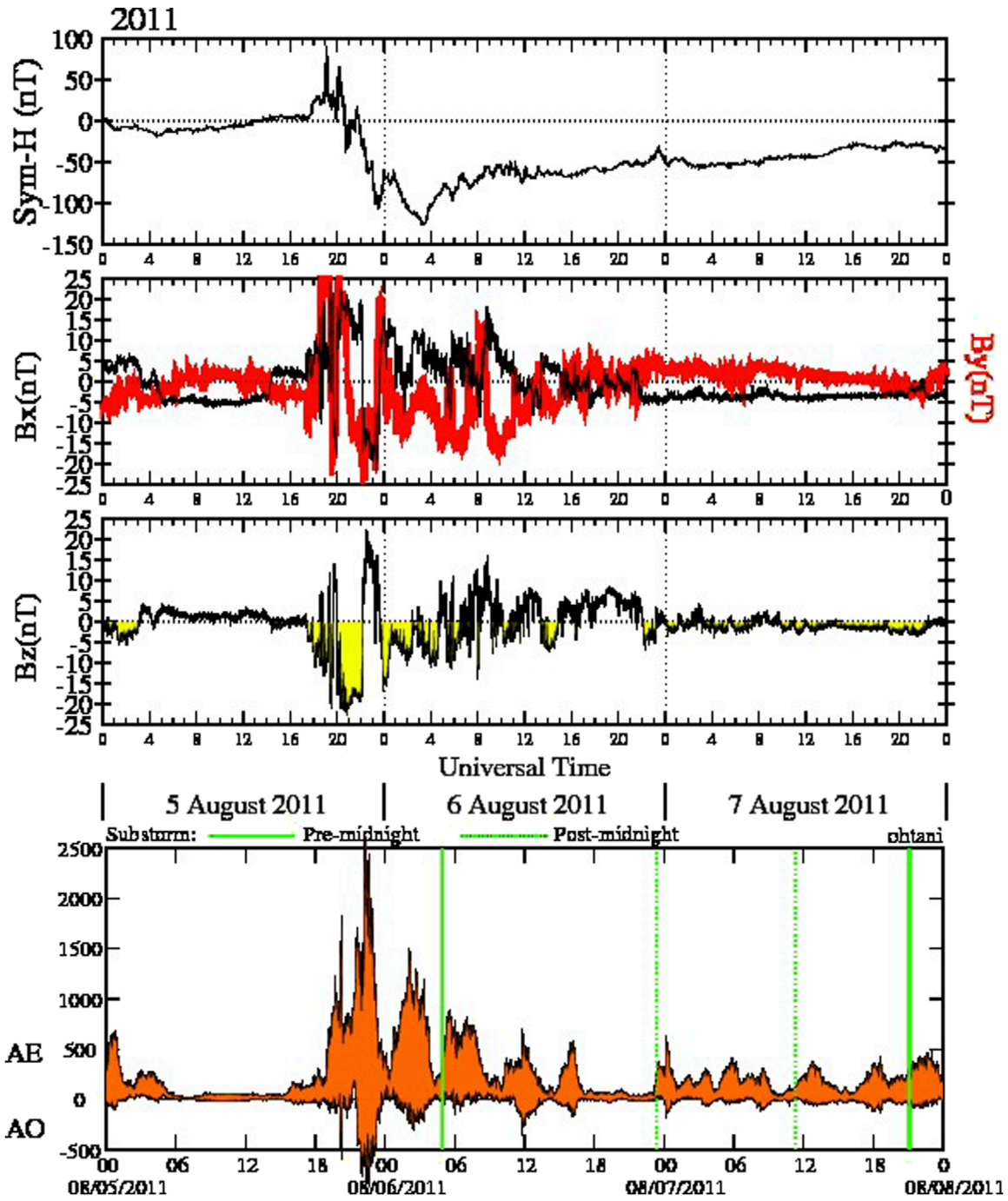

FIGURE 4
This figure shows solar wind and ionospheric parameters starting 05 August 2011 for three consecutive days. It displays, from top to bottom, the SYM-H values, the IMF B_x and B_y, the B_z parameters, and the AE and AO indices.

second and third arrows), the LSTID motion becomes symmetric, and LSTIDs move simultaneously from both auroral ovals toward the magnetic equator.

Figure 9 shows prominent intensifications of the PF and expansions of the auroral oval into latitudes equatorward of 65°. In the NH, the PF penetrates latitudes below 65° at 18 UT on 14 July 2012 during descending (sunrise) and ascending (sunset) passes. This effect is delayed in the SH until 21 UT; here, the PF is also smaller by a factor of 2. The enhanced PF and the oval expansion last 40 h, covering the storm's commencement, main, and recovery phases. The neutral density and vertical wind perturbations display values more significant than 10% and 20 m/s, respectively. The neutral density perturbations corresponding to sunset (Figures 9G, H) present significant amplitudes exceeding 10% and 20 m/s in the southern hemisphere and not much in the NH. During sunrise (Figures 9C, D), perturbations develop on both NH and SH auroral ovals. Despite the much larger PF in the NH, the LSTADs seem to start simultaneously. The summation traces

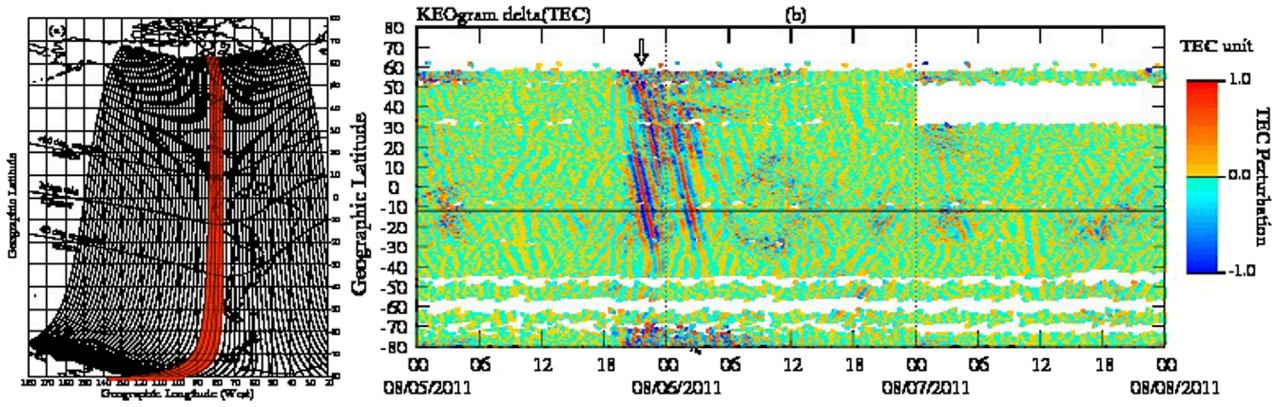

FIGURE 5
(A) The red band on the left side displays the area used to select ∂TEC values to construct the Keogram displayed on the right side. **(B)** The dark red and blue diagonal bands represent the LSTIDs measured with the GPS receivers. See the description of this figure for more information on the temporal and latitudinal variability of the keogram.

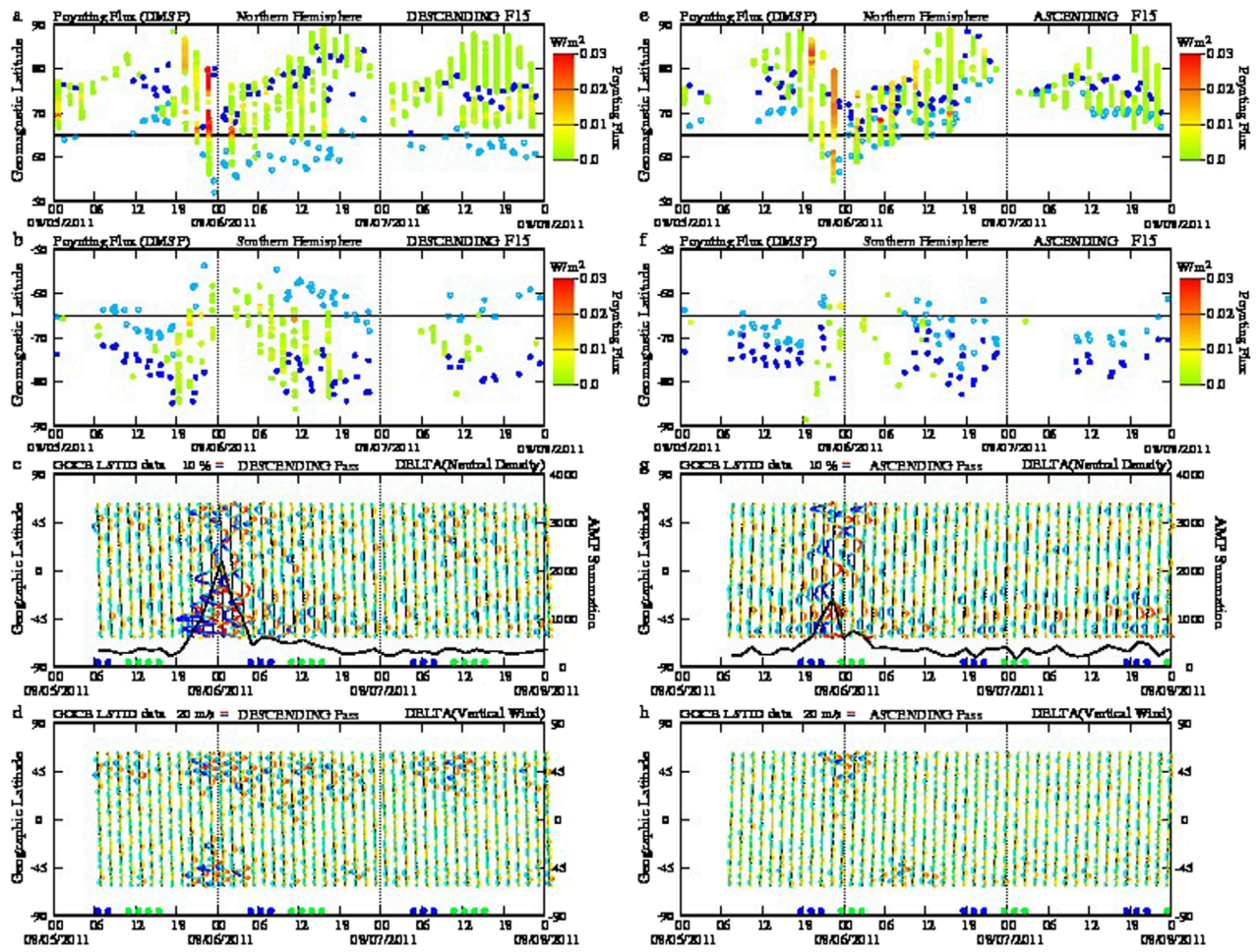

FIGURE 6
A collage of eight frames showing the PF for the ascending and descending DMSP passes for the northern and southern hemispheres for the same 3 days of Figures 5, 6. **(C,D,G,H)** Display low-res plots of the neutral density and vertical wind perturbations after analyzing each GOCE pass. The PF intensity is colored from green to red to display values between 0.001 and 0.03 W/m^2. The blue and light blue dots in panels **(A,B,E,F)** indicate the boundaries of the auroral oval. The thick line in panels **(C,G)** points out integrated values of the absolute values of the ∂density.

10.3389/fspas.2025.1517762

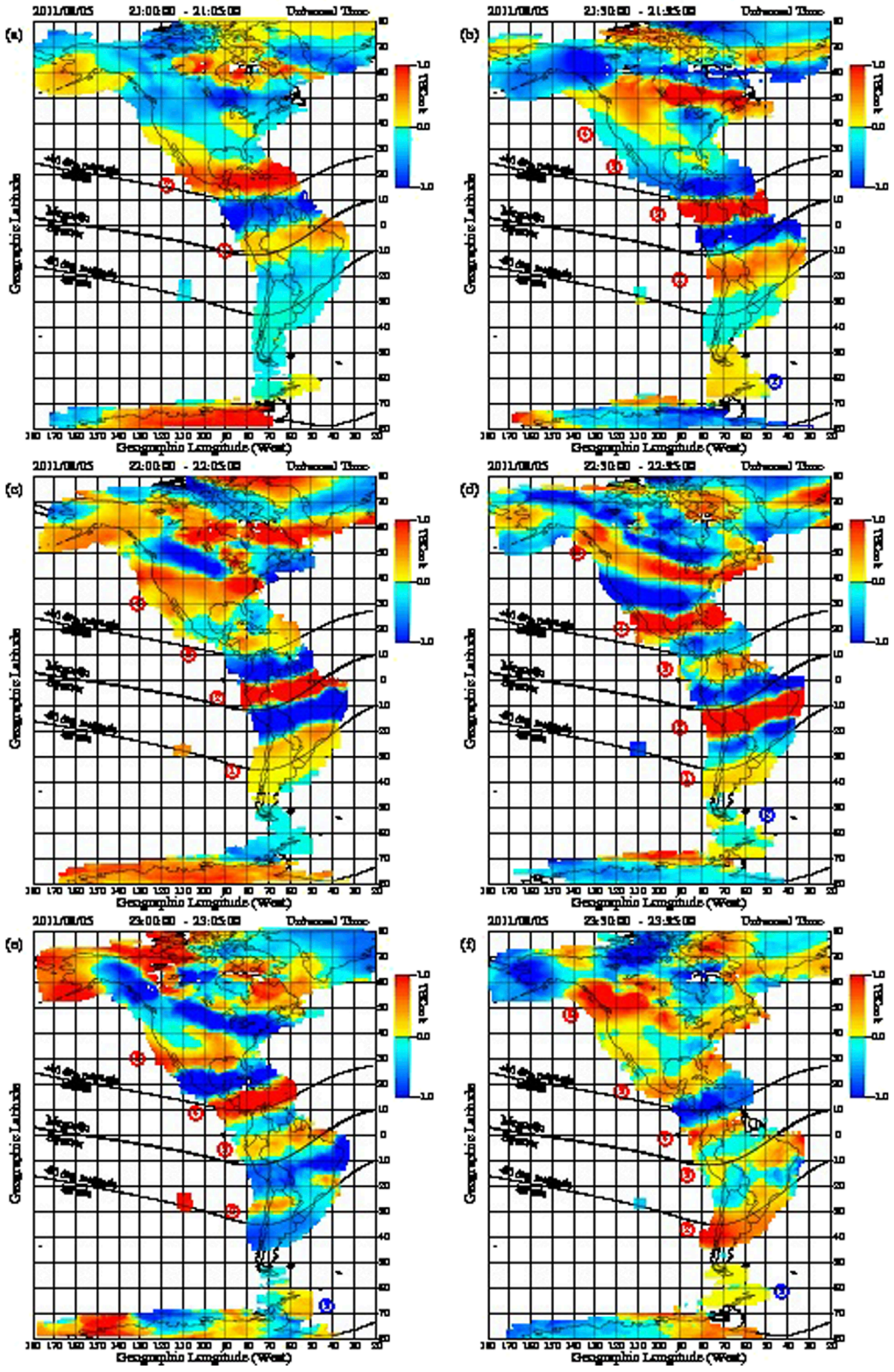

FIGURE 7
A sequence of 6 ∂TEC maps in the American sector for times extending between 21:00 UT and 23:30 UT. These plots were built by subtracting the TEC daily variability. Positive (negative) ∂TEC perturbations are displayed in red (blue). Note the values peaking at ± 1 TEC units. Red (blue) numbers inside circles indicate the motion of the different ∂TEC layers in the NH (SH). Note very small values of the ∂TEC perturbations near the southern auroral oval. Panel **(A)** corresponds to 21:00 UT. **(B)** 21:30 UT. **(C)** 22:00 UT. **(D)** 22:30 UT. **(E)** 23:00 UT. **(F)** 23:30 UT.

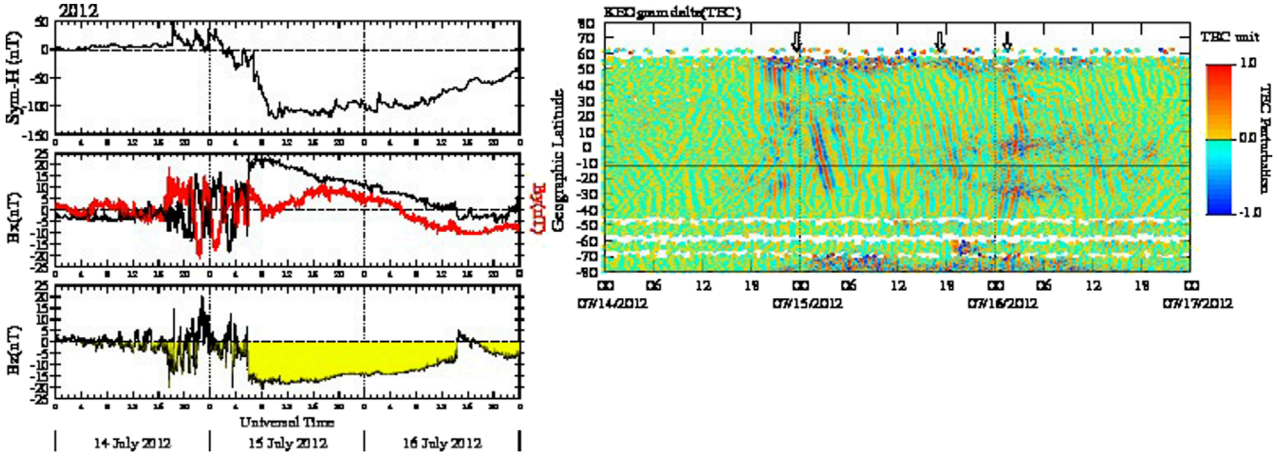

FIGURE 8
The left side shows the SYM-H and the three components of the IMF for 3 days encompassing the magnetic storm of 15 July 2012. Note the long period of B_x and B_z nearly constant values. The right frame shows the keogram for these 3 days using a format similar to the one in Figure 5.

at the bottom of Figures 9C, H display several periods above the "noise" level.

Figure 10 displays six images of ∂TEC measured between 00:30 and 05:00 UT. This sequence of LSTIDs shows variable and asymmetric behavior in some respects similar to the LSTIDs that developed during the storm of 5 August 2011. Although LSTIDs were triggered from both hemispheres here, the SH LSTIDs compassed much smaller amplitudes and were annihilated near or south of the magnetic equator. The NH ∂TEC continued drifting toward the southern auroral oval, where they faded. The first frame, corresponding to 00:30 UT, shows two positive perturbations labeled with red numbers moving southward and three positive ∂TEC (using blue numbers) drifting northward between South America and Antarctica. The ∂TEC image for 01:00 UT displays the three crests (∂TEC perturbations) using blue numbers displaced further north and crests 1 and 2 (using red numbers) closer to the magnetic equator. The SH LSTID encounters the NH LSTIDs traveling south, destroying the former near the magnetic equator. NH crest 1 (labeled with red numbers) continues moving southward and encounters two more SH crests (labeled 2 and 3 in blue) between 02 and 03 UT, but they are not seen later. The ∂TEC image for 04 UT exhibits the first crest reaching the southern tip of South America across an area devoid of northward-moving LSTIDs. Supplementary Movie S2 shows the LSTIDs' initiation and departure from both auroral ovals. The organized motion of the LSTIDs starts near 00:30 UT when they initiate a journey to the opposite hemisphere. As indicated above, the movie reaffirms that the motion of the NH LSTIDs to the opposite hemisphere can be asymmetric and destroy the southern LSTIDs at latitudes south of the magnetic equator.

2.4 The storm of 17 March 2013

This event has been called the St. Patrick's Day Storm of 2013 by Amaechi et al. (2018) and Zhu et al. (2022). Results relevant to our study were conducted by Liu et al. (2018), who reported on the spatial response of the neutral temperature during this storm using SABER and SOFIE measurements. Smith et al. (2009) investigated joule heating asymmetries using the GITM model. Their simulations showed maximum heating in the SH (07:35 UT) and later in the NH (16:40 UT). Other research efforts have compared the St. Patrick Storm of 2013 and 2015 (Xu et al., 2017; Alberti et al., 2017; Dmitriev et al., 2017; Shreedevi et al., 2020). Verkhoglyadova et al. (2016) discussed the storm's IMF and other solar wind conditions. This section presents LSTADs measured by GOCE and LSTIDs derived from TEC values recorded in the American sector during the St. Patrick's Day Storm to establish the connection between the magnetospheric PF inputs and the response on the thermosphere and ionosphere. The keogram of Figure 11 displays slanted lines starting from both high-latitude regions and ending near the magnetic equator. This is the signature of LSTIDs propagating toward the opposite hemisphere with nearly equal amplitude and velocity. This Figure demonstrates that during the St. Patrick's Day Storm of 2013, LSTIDs were observed between 12 and 24 UT (times indicated using 2 arrows). This period is also consistent with both cases presented above in which LSTIDs develop when B_z is directed south, the oval expands, and PF increases to levels higher than 10 mW/m^2. It is worth noting that this storm generates peak ∂TEC perturbations near 0.5 TEC units. This may be associated with the low value of IMF B_z south and smaller PF than in the other two storms.

Figure 12 displays the DMSP's measured PF and the neutral perturbations derived from GOCE's measurements. Although the NH PF is almost the same in the sunrise and sunset local periods, the afternoon sector SH PF presents an earlier initiation and oval expansion than the NH counterpart (see Figures 12E, F). Higher neutral density and vertical wind perturbations are observed in the morning than in the afternoon local times (Figures 12C, D, G, H). The ∂neutral density is higher than 10%, and vertical wind fluctuations are larger than 20 m/s. Based on this LT asymmetry in the production of LSTADs, it is expected that LSTIDs should be observed mainly around the 12 UT periods when the American continent is in the morning sector. It is indicated that unlike the storm corresponding to 15 July 2012, the St. Patrick's Day Storm of

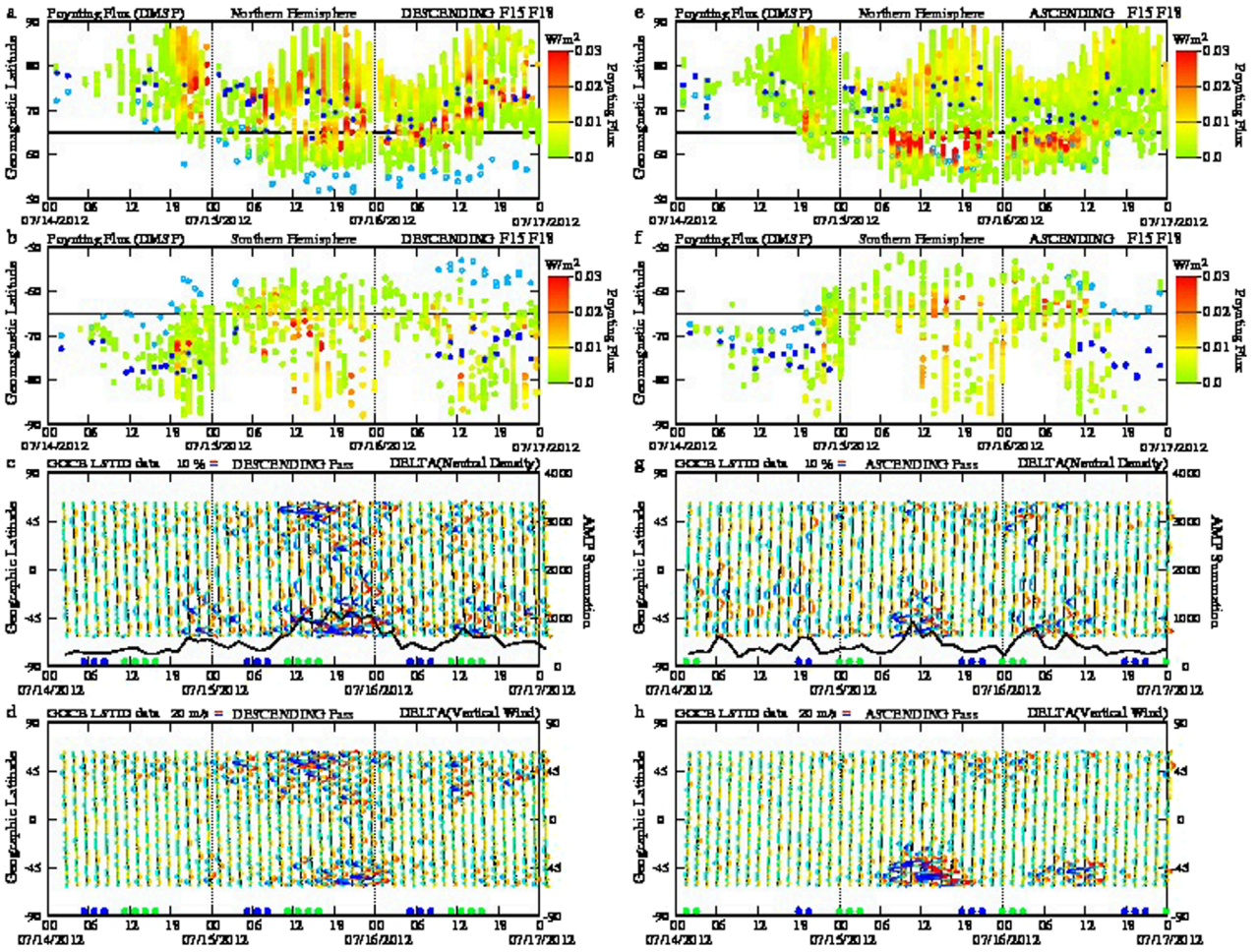

FIGURE 9
It has the same format as Figure 6 but corresponds to 15 July 2012. Note the long period of intense PF inflow and oval extension up to magnetic latitudes less than 65°. This event coincides with a period of B_z south condition. Large ∂density and ∂(vertical wind) are observed between 06 UT on 15 July 2012 and 06 UT on 16 July 2012. **(A,B,E,F)** show the Poynting Flux and the boundary of the auroral oval. **(C,D,G,H)** display low-res plots of the density and vertical wind perturbations.

2013 shows a B_z southward condition only for 12 h (12 – 24 UT) and values higher than −10 nT.

Figure 13 shows a sequence of 6 frames with LSTIDs moving from both high-latitude regions toward the opposite hemisphere and meeting near the magnetic equator. These figures demonstrate that LSTIDs can be generated almost simultaneously, merged, and later annihilated. Frame b corresponding to 17:30 UT exhibits a merging of both positive crests labeled 1 for LSTIDs arising from both hemispheres. This new region labeled 1 in blue keeps moving north, and it is observed at 18 UT (frame c) at 0° geographic latitude, where it vanishes. The SH crest labeled 2 merges with the NH crest labeled 3 after 19 UT, producing a single structure labeled 3 in red in frame f corresponding to 19:30 UT.

Supplementary Movie S3 presents a series of LSTIDs propagating equatorward between 15 and 24 UT. It displays with more detail both sequences of LSTIDs, one from the NH and another from the SH, which encounter near but north of the magnetic equator, where they both annihilate. This behavior of the ∂TEC/LSTIDs is compatible with the keogram of Figure 11, in which the slanted lines (the signature of LSTIDs) between 12 and 24 UT on 17 March 2013 originate from both north and south auroral ovals and meet near the magnetic equator. The motion of the LSTIDs is disorganized near the northern polar cap, likely due to large-scale density structures like storm-enhanced densities. However, at latitudes south of 60°, their variability at constant magnetic longitude and equatorward motion becomes evident.

3 Solar wind dependencies

Intense magnetic storms are attributed to the passage of Interplanetary Coronal Mass Ejections (ICME) that impinge the Earth's magnetosphere. ICMEs are formed when ejecta material from the Sun interacts with the background non-disturbed solar wind, and a shock is formed in the forefront (Tsurutani and Gonzalez, 1997; Gonzalez et al., 2007). The ICME's shock is followed by the sheath region that contains elevated solar wind

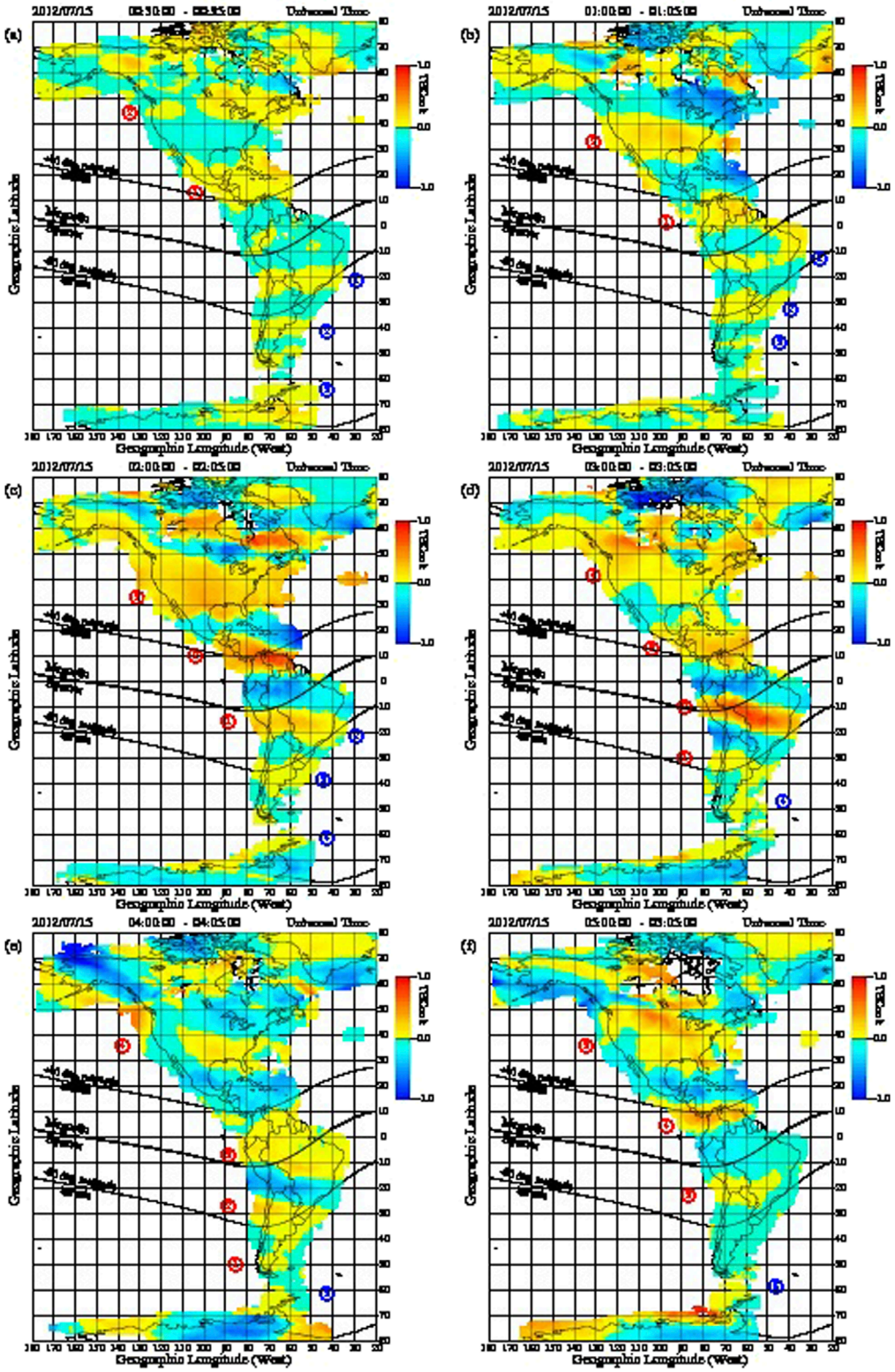

FIGURE 10
This figure is similar to Figure 7 but corresponds to 15 July 2012. LSTIDs originated in the NH and are seen south of the magnetic equator and transiting at latitudes near the southern auroral oval. See the text for a description of this event. **(A)** corresponds to 00:30 UT. **(B)** 01:00 UT. **(C)** 02:00 UT. **(D)** 03:00 UT. **(E)** 04:00 UT. **(F)** 05:00 UT.

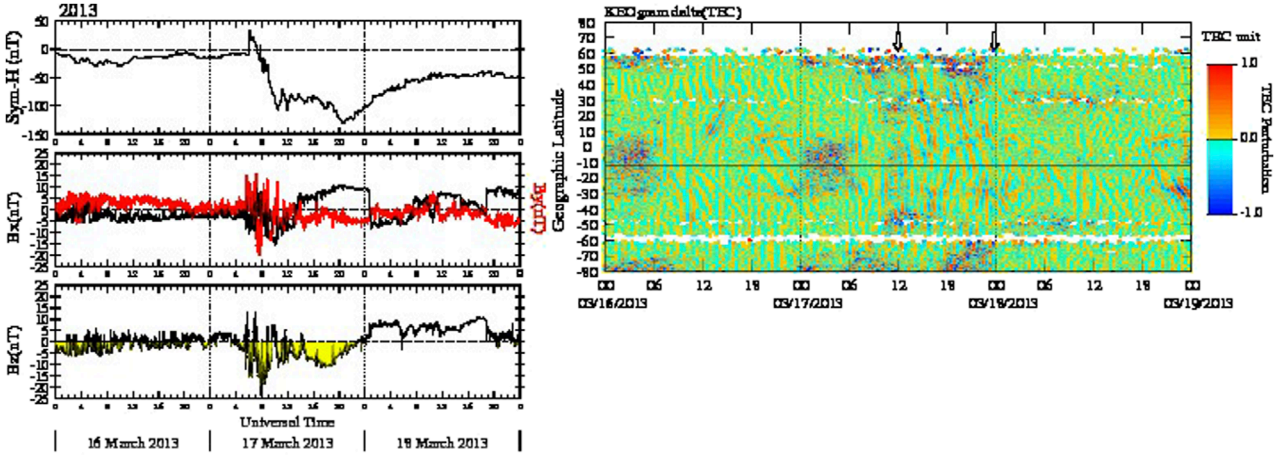

FIGURE 11
It is the same as Figure 8 but corresponds to the storm on 17 March 2013. This event shows slated lines between 12 and 24 UT on 17 March 2013.

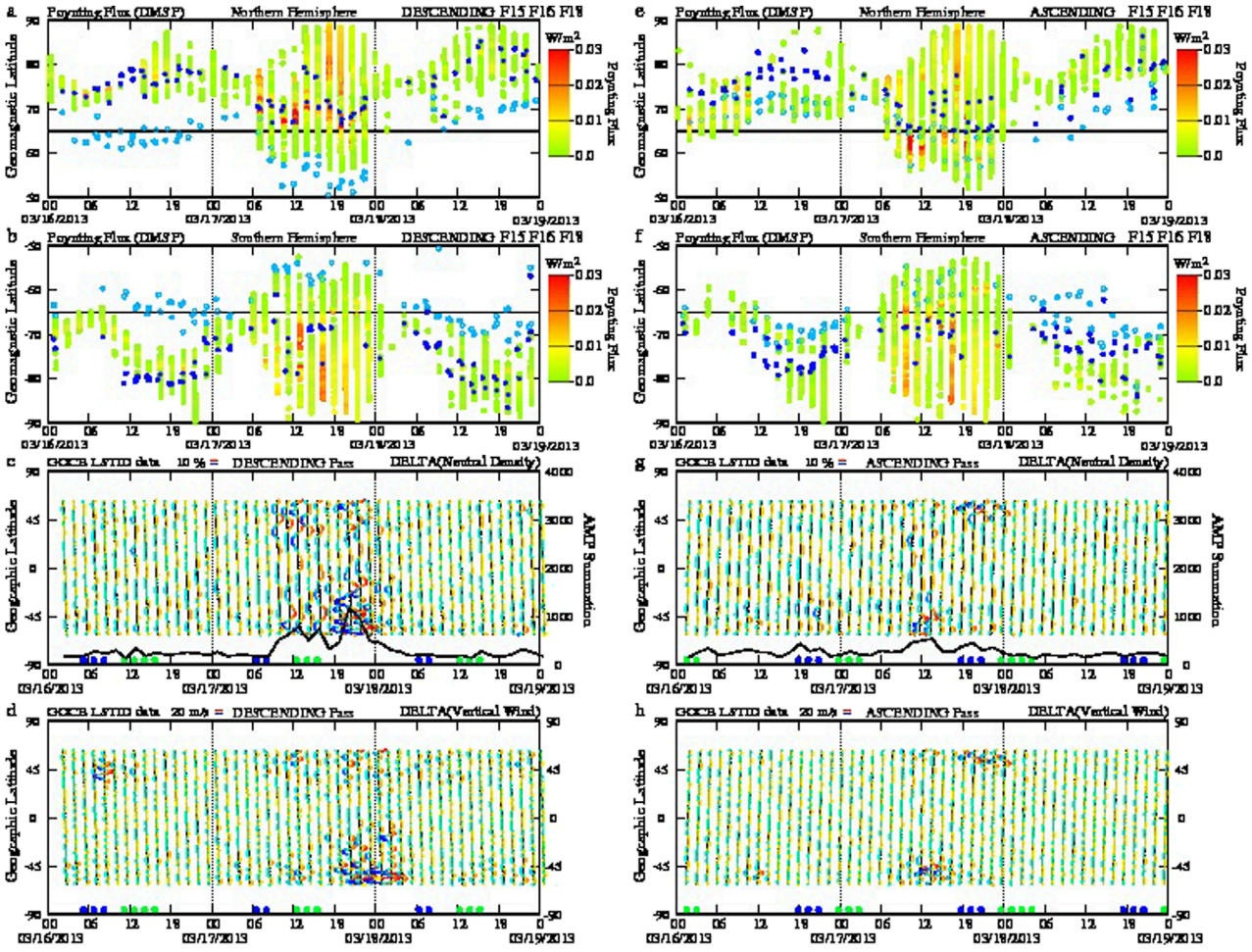

FIGURE 12
It has the same format as Figures 6, 9 but corresponds to 17 March 2013. A considerably high PF is observed in the northern and southern hemispheres. See the text for a description of LSTIDs getting annihilated near the magnetic equator. **(A,B,E,F)** show the Poynting Flux and the boundary of the auroral oval. **(C,D,G,H)** display low-res plots of the density and vertical wind perturbations.

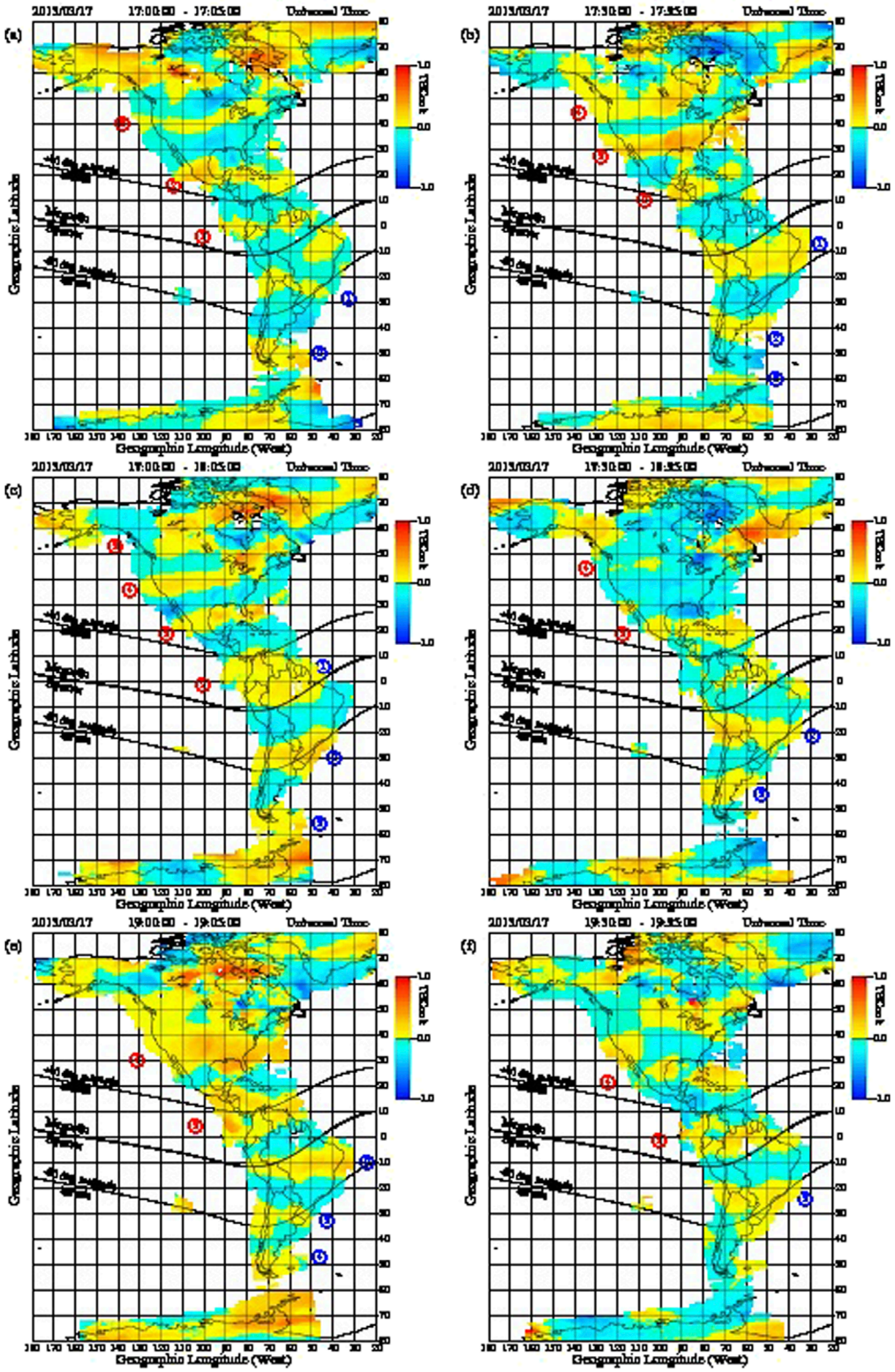

FIGURE 13
Same format as Figures 7, 10 but for 17 March 2013. Here, the sequence of ∂TEC maps starts at 17:00 UT and extends until 19:30 UT. The amplitude of the LSTIDs is smaller than in both previous storms. **(A)** corresponds to 17:00 UT. **(B)** 17:30 UT. **(C)** 18:00 UT. **(D)** 18:30 UT. **(E)** 19:00 UT. **(F)** 19:30 UT.

velocity and a highly variable IMF, densities, temperatures, and plasma β. Immediately upstream from the sheath are magnetic clouds (MC), sometimes consisting of sunward or antisunward coronal loops presenting steady IMF, low plasma β, and temperature (Rouillard, 2011; Verkhoglyadova et al., 2016). These different ICME regions can affect the ionosphere and thermosphere differently, inducing distinct responses in the thermosphere-ionosphere system. As stated earlier, this publication deals with forming LSTADs and their indirect visualization in the ionosphere using ∂TEC values measured by GPS receivers. This section aims to find a relationship between the characteristics of the downward PF, the appearance and asymmetry of the LSTADs/LSTIDs, and the passage of ICMEs with different regions. A clear relationship between ICME, PF, and LSTADs will allow us to forecast the initiation of LSTIDs, severity, temporal characteristics, and symmetry/asymmetry.

Figures 14–16 display the three components of the solar wind velocity, the IMF inputs, the density, temperature, and plasma β values (frames from a through j). It also shows the integrated PF along the DMSP trajectory (frame k), a summation of the ∂neutral density detected by GOCE (from the thick line in panels 6c and 6g), and a measure of the LSTIDs amplitude and velocity detected in the American sector using a cross-correlation analysis (frames m, n, o, and p). It is noted that while GOCE and DMSP passes are fixed in a local time frame to near sunset and sunrise hours, ∂TEC measurements occur at all local times. For this reason, a one-to-one comparison between ∂TEC measured in the American sector and satellite observations is made cautiously. These figures also display the different regions of the ICME that have been colored using orange to indicate the sheath region, green to point out the magnetic cloud itself, blue to display a sunward loop connected to the Sun, and yellow to illustrate a high-speed stream (HSS). The arrival time of the ICME shock (https://lweb.cfa.harvard.edu/shocks/wi_data/wi_2012.html), as well as the starting and ending times of the storm magnetic cloud (MC), have been presented (https://wind.nasa.gov/ICME_catalog/ICME_catalog_viewer.php) for solar cycles 23 and 24, and listed by Miteva et al. (2018) and Samwel and Miteva, (2023). These times are used to mark the limits of the different ICME regions. In other cases, we used the solar wind and IMF values described by Verkhoglyadova et al. (2016). These authors indicate that the HSS consists of the solar wind with speeds close to or more than the ICME speed and plasma with variable temperature and β values.

3.1 The ICME of 5–6 August 2011

The ICME shock arrived at 17:32 UT on 5 August 2011, followed by an ICME sheath extending until 09:10 UT on 6 August 2011 (Figure 14). The shock was identified as a V_x increase of more than 200 km/s. Simultaneously, the IMF B field grew by 30 nT, the solar wind density, temperature, and plasma β augmented by 15 cm^{-3}, an order of magnitude, and 15 units, respectively. An MC followed, lasting until 22:40 UT on 06 August 2011, when a sudden increase in the solar wind V_x was seen and decayed on 09 August 2011. This time is beyond the limits of Figure 14.

Figures 14K–P present several parameters derived from direct measurements of the DMSP and GOCE satellites, providing the downward PF and the thermosphere response in the form of LSTADs. In 2011, the ascending orbit of the DMSP-F15 satellite was locked in local time near 16.5 h. Thus, the PF is compared with the ∂TEC measured in the American sector between 20 and 23 UT. The northern hemisphere's trajectory-integrated PF (full black dots in Figure 14K) reaches quantities above 60 kW/m. This downward PF in the NH is initiated when the IMF B_z becomes less than −5 nT, but later, higher PF values are seen when the IMF B_z is less than −20 nT. In contrast, the PF on the SH (empty circles in Figure 14K) is sporadic and less than 15 kW. The integrated ∂N (Figure 14L), measured by GOCE, increases linearly between the shock and 01 UT on 6 August 2011, when the integrated PF is larger than 60 kW. LSTADs are observed in both the sheath and MC regions; however, no LSTADs are detected during the passage of the high-speed stream (HSS) region. Figures 14M, N show the ∂TEC variations at fixed geographic latitudes. They present a quasi-sinusoidal signature of LSTIDs and are used to calculate the southward velocity of the LSTIDs using a cross-correlation algorithm applied to the ∂TEC fluctuations measured at two pairs of geographic latitudes. One pair at latitudes north of the magnetic equator (24° and 18°) and the other at latitudes south of the magnetic equator (−30° and −35°). The ∂TEC values along these constant latitude lines, called here KEO lines, show an increase in the amplitude of the ∂TEC fluctuations for 24° and 18° (dotted line) geographic latitudes (Figures 14M, N). The peak amplitude and the time delay expressed in m/s provided by the cross-correlation functions are shown in Figures 14O, P. The appearance of LSTIDs in the NH KEO line coincides with the times of large integrated ∂N (Figure 14L) and significant PF in the NH. As stated in section 2.2, the weakened PF < 15 kW/m detected in the SH leads to LSTIDs containing small amplitudes rapidly overrun and annihilated by LSTIDs that move southward from the NH. The cross-correlation algorithm gives downward velocities in both longitude sectors in agreement with the keograms of Figure 5 and the Supplementary Movie S1. In addition, it is significant that the LSTIDs show a decrease in their southward motion (Figure 14P), as seen at later UT times.

3.2 The ICME of 15 July 2012

Figure 15 shows the solar wind, magnetosphere, thermosphere, and ionospheric parameters corresponding to the storm of 15 July 2012 using the same format as Figure 14. This storm also presents well-defined sheath-type ICME characteristics similar to the 5-6 August 2011 storm. The shock arrival is at 17:39 UT on 14 July 2012. The MC starts near 07 UT on 15 July 2012 and ends at 15:30 on 16 July 2012. A part of the MC consists of a sunward loop, where the IMF B_x points toward the Sun. Within the sheath region, the IMF B field contains a B_z south condition during the storm's first 6 h (18- 24UT). At this time, the downward trajectory-integrated PF rises to 45 kW/m in the NH but only 15 kW in the SH. There is a slight increase in the integrated ∂(neutral density) values, but it is high enough to create significant LSTIDs shown in the KEO line for the NH (Figure 15M). It is indicated that during this period, the keogram of Figure 8 shows barely slanted lines in the NH that reach up to −20° in geographic latitude. No apparent signature of LSTIDs is seen in the SH. Nevertheless, Supplementary Movie S2 displays small ∂TEC perturbations created at 00:30 UT and later at 01:30 UT in the Southern auroral oval.

10.3389/fspas.2025.1517762

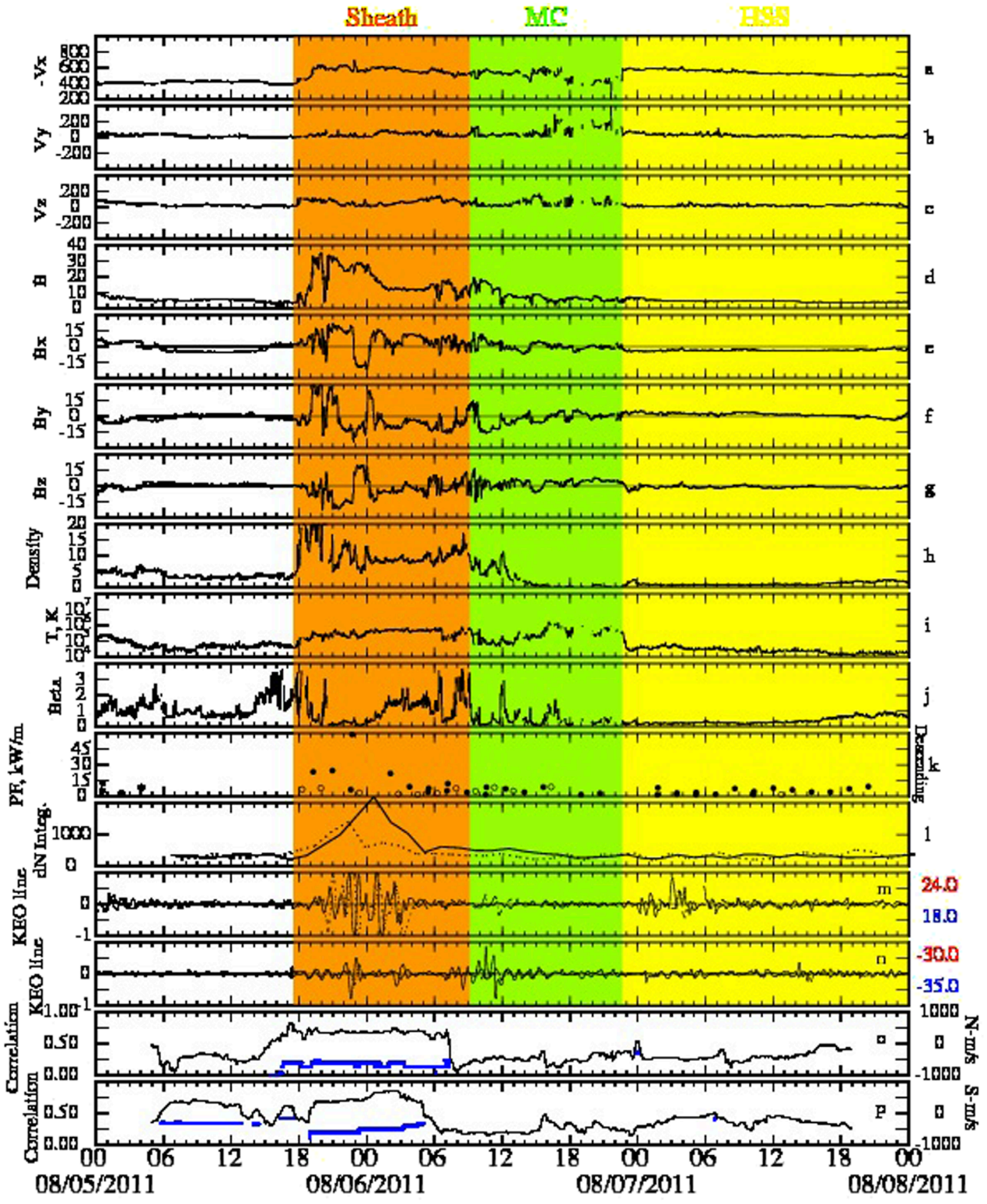

FIGURE 14
Interplanetary, thermospheric, and ionospheric parameters for days between 05 and 07 August 2011. **(A–J)** show the three components of the solar wind, the amplitude of the IMF, the three components of IMF B field, the solar wind density, temperature, and the plasma β. **(K)** displays the PF for the descending passes. The northern hemisphere (SH) flow is shown using full (empty) dots. **(L)** evinces the integrated absolute value of the ∂density for descending (ascending) passes using a continuous (broken) line. **(M,N)** show two KEO lines each that have been extracted from the keogram of Figure 5 at two constant geographic latitudes. **(O,P)** show the peak of the cross-correlation functions and the velocities derived from the offset of the peaks.

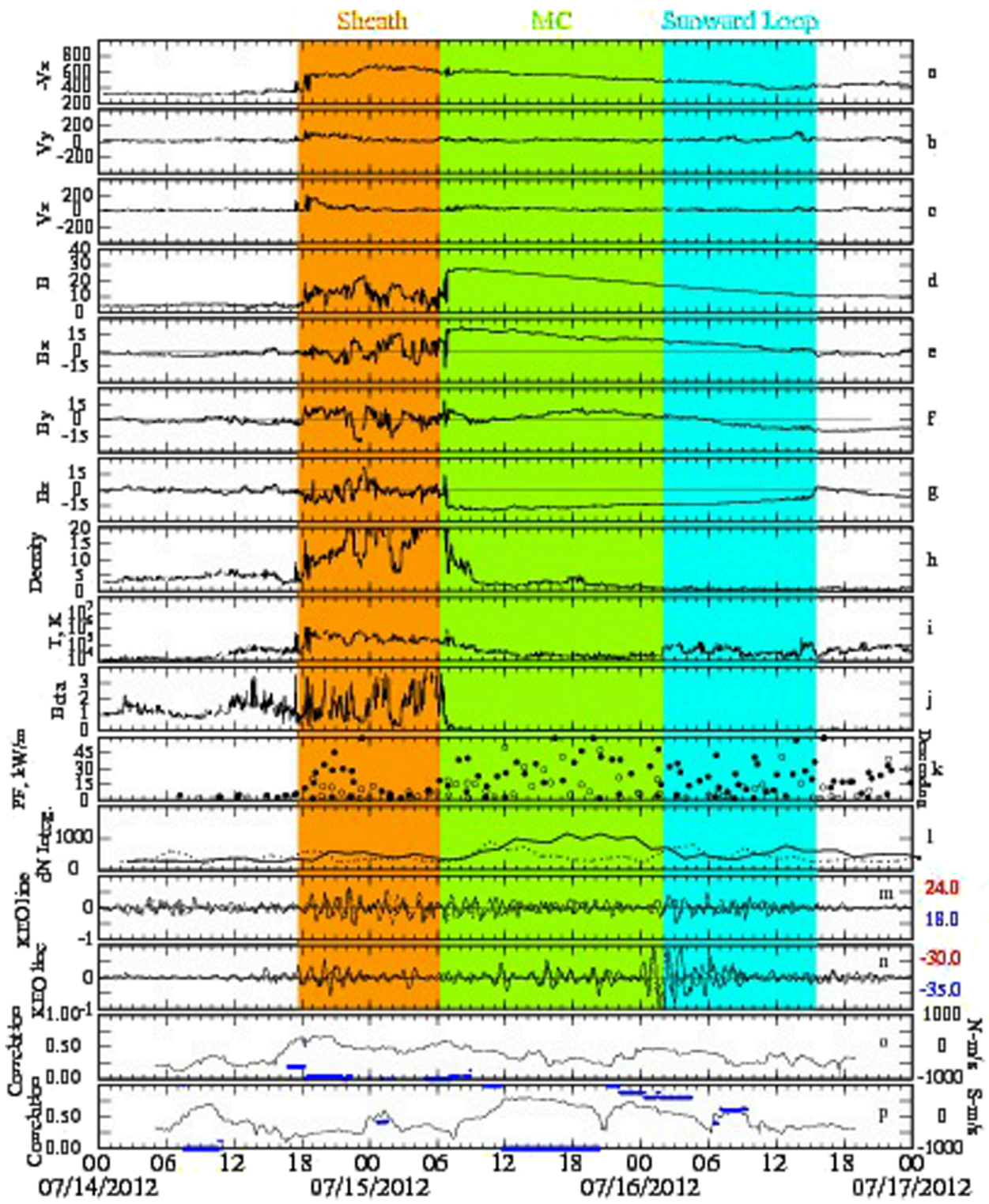

FIGURE 15
Same as Figure 15 but corresponds to 15 July 2012. **(A–L)** show the three components of the solar wind, the amplitude of the IMF, the three components of IMF B field, the solar wind density, temperature, the plasma β, the PF, and the integrated absolute value of the ∂density. **(M,N)** were derived using the keogram of Figure 8. **(O,P)** show the peak of the cross-correlation functions.

Between 07 UT on 15 July 2012 and the end of the MC, the integrated PF becomes equal in both hemispheres (see full and empty circles in Figure 15K), increasing to 60 kW/m. In addition, the solar wind density, temperature, and plasma β are low and constant. However, B_x and B_z are large and slowly decrease between 20 and 0 nT. This period coincides with

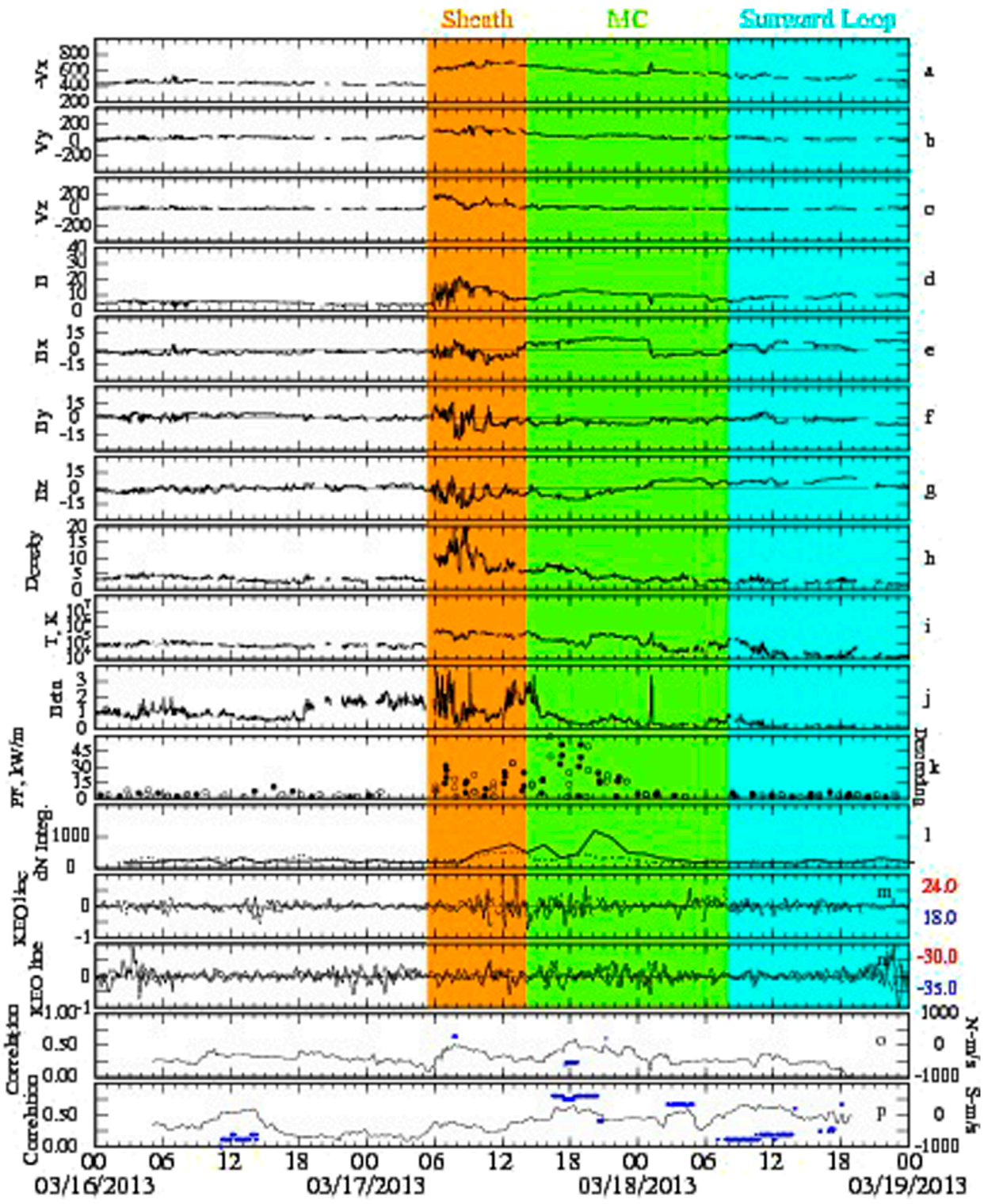

FIGURE 16
It is the same as Figures 14, 15 but corresponds to 17 March 2013. **(A–L)** show the three components of the solar wind, the amplitude of the IMF, the three components of IMF B field, the solar wind density, temperature, the plasma β, the PF, and the integrated absolute value of the ∂density. **(M,N)** were derived using the keogram of Figure 11. **(O,P)** show the peak of the cross-correlation functions.

the formation of large (>10%) LSTADs and ∂(neutral wind) (20 m/s) in both descending and ascending orbits and at both the northern and southern hemispheres (Figures 9C, D, G, H). This period also contains several LSTIDs seen, especially near the sunrise (descending passes). The KEOgram of Figure 8 displays equatorial convergent slanted lines that originate at both hemispheres in

both north and south auroral ovals. In summary, LSTADs and LSTIDs occur during the early part of the ICME sheath region and later on, all during periods when the IMF B_z is directed southward.

3.3 The ICME of 17 March 2013

Figure 16 displays solar, magnetospheric, and ionospheric parameters similar to the frames shown in Figures 14, 15. The ICME shock occurred at 05:10 UT on St. Patrick's Day in 2013. At this time, elevated V_x, IMF magnitude, solar wind density, and temperature are identified, defining the start of the sheath region. The MC is observed lasting between 14:10 UT on St. Patrick's Day and ending on 19 March 2013 (beyond the plot extension). B_z is directed southward between the arrival of the shock and 22 UT on 17 March 2013. During this time, encompassing the sheath and part of the MC, an increase in the integrated ∂N is seen in Figure 16L, together with enhanced PF that maximized at 18 UT on 17 March 2013 (Figure 16K). The amplitude of the KEO lines also rises in Figures 16M, N, together with the cross-correlation factor and the velocity of Figures 16O, P, implying the existence of LSTIDs.

It is indicated that at 08:00 UT on 18 March 2013, a region containing a sunward-directed B_x component, likely connected to the Sun (blue shading), displays no PF above the noise level (Figure 16K), no LSTADs (Figure 16L) and absence of LSTIDs in the KEO lines of Figures 16M, N. This period contains an IMF Bz directed northward that seems to produce unfavorable conditions for the inflow of PF. Contrary to the sunward loop observed on 16 July 2012 (Figure 15), the sunward loop of 18 March 2013 does not reveal any association with LSTADs or LSTIDs.

4 Discussion

We have used several derived physical values measured by the ACE, DMSP, and GOCE satellites to elucidate the solar wind, magnetospheric, and thermospheric conditions that support the formation of LSTIDs. Ground-based observations of ∂TEC data in the American sector have also been analyzed to fully define the asymmetry, amplitude, and timing differences in the appearance of LSTIDs at different hemispheres. Our main conclusion is the dominance of the IMF B_z parameter in dictating the appearance or not of LSTADs and LSTIDs. Our first finding, based on SYM-H values, suggests that these large-scale ∂TEC structures can occur during the sudden commencement, the main phase, or even during the recovery phase of a storm. LSTIDs can happen immediately after the ICME shock, within the sheath region, and during the plasma cloud. Our data also confirms that LSTIDs were observed when the sunward loop passed on 16 July 2012. Figures 14–16 have allowed us to understand the role of PF on the amplitude, asymmetry, and timing of initiating LSTADs. Future constellations of multiple satellites are expected to provide a more robust and precise relationship between solar wind drivers and the ionosphere responses in the form of LSTIDs.

The joint analysis of satellite and TEC data during three intense magnetic storms between 2011 and 2013 has significant implications for the formation, transit, and fate of LSTADs and LSTIDs. Our findings shed new light on the PF measurements during these storms, revealing significant interhemispheric asymmetries and temporal delays that seem to influence the triggering, transit, and sometimes late termination of some LSTADs. The resulting interhemispheric and local time (sunset vs. sunrise) asymmetries are detected in their velocity, amplitude, and the region where the LSTIDs meet. Past experimental and modeling studies have suggested that LSTAD/LSTID should meet near the geographic or magnetic equator, but our results demonstrate that this is not always the case. It is necessary to look carefully at the amplitude and timing of the PF deposited in each hemisphere to determine the meeting location, which can be at the magnetic equator or latitudes as far from the equator as the opposite auroral oval. We observe that when the PF in the NH is three times the value in the SH (Figure 15K), LSTIDs emanating from the southern oval do not pass magnetic latitudes north of −40°.

The PF, thermospheric, and ICME observations for the storms of 05 August 2011 and 15 July 2012 indicated a deep asymmetry in the origin of LSTIDs. However, Supplementary Movies S1, S2 point out the formation of delayed and weak LSTIDs in the SH that are easily overrun by the much stronger NH LSTIDs. LSTIDs in the SH are likely triggered an hour or more later than in the NH. This different behavior between the NH and SH LSTIDs, as well as LSTADs, is based on the asymmetry of the trajectory-integrated PF deposited in both auroral ovals. A common factor during asymmetric behavior is that both cases develop near the start of the storm and during the sheath phase of the ICME. The sheath is commonly characterized by variable solar wind parameters such as the IMF, density, temperature, and plasma β. It is essential to mention that rapid IMF B_z transitions were observed during both storms. These quick changes in the reconnection area may disturb the conjugacy of the PF deposited along the flux tubes. During the passage of magnetic clouds and long periods of constant southward-directed B_z, we observe equal PF in both hemispheres and symmetric LSTIDs that start simultaneously from both north and south auroral ovals that meet near the magnetic equator, where they get annihilated. Systematic analysis of the other 9 intense storms between 2011 and 2013 implies an absence of trajectory-integrated PF and, consequently, no LSTIDs when the IMF B_z is directed north or when the polarity of IMF B_z changes slowly.

It has been demonstrated that the appearance and transit of LSTADs and LSTIDs mainly occur during southward B_z conditions, and strong events develop under steady values less than −15 nT. The PF is larger than 1 $mW/m^{2,}$ and the auroral oval moves equatorward at 65° (−65° magnetic latitude in the southern hemisphere). The trajectory-integrated PF is at least 5 kW/m. In summary, the key factors leading to LSTAD activity are IMF B_z directed southward and, concurrently, a significant PF. LSTAD generation lasts only as long as the electromagnetic energy is active. It can be as short as a few hours or longer than 24 h (ICME of 15 July 2012).

Several authors have suggested that the PF energy deposited at high latitudes can dissipate as Joule heating in the ionosphere and the thermosphere at altitudes below 200 km (Thayer and Semeter,

TABLE 1 LSTID and solar wind characteristics during the storms of 2011–2013.

Magnetic storms	ICME layers	Max PF (mW/m^2)	Min Bz	SYM/ASYM	∂TEC Amplitude
6 August 2011	**Sheath**, MC, HSS	45.00	−18 nT	ASYM	1.10
26 September 2011	**Sheath, MC**, HSS	35.00	−30 nT	SYM	0.90
24 October 2011	**Sheath, MC**, HSS	20.00	−12 nT	SYM	1.00
9 March 2012	Sheath, **MC**	41.00	−15 nT	SYM	0.70
24 April 2012	Sheath, **MC**, HSS	32.00	−14 nT	SYM	0.95
15 July 2012	Sheath, **MC**, SL	55.00	−12 nT	ASYM, SYM	0.90
1 October 2012	**Sheath, MC**, SL	30.00	−20 nT	SYM	0.70
8 October 2012	**Sheath, MC**, HSS	35.00	−13 nT	SYM	0.75
13 November 2012	Sheath, **MC, HSS**	39.00	−14 nT	SYM	0.70
17 March 2013	**Sheath, MC**, SL	27.00	−15 nT	SYM	1.00
1 June 2013	**Sheath, MC**, Sheath	41.00	−20 nT	SYM	0.80
28 June 2013	**Sheath, MC**, HSS	45.00	−10 nT	SYM	0.85

ICME layers using bold letters indicate the presence of LSTADs and LSTIDs during their passage.

2004; Valladares and Carlson, 1991). Lu et al. (1995) used an ionosphere-thermosphere general circulation model to demonstrate that 94% of the PF energy is converted into Joule heating. This heat source then increases the temperature, leading to density and wind flow increases (Mayr and Harris, 1978). An essential product of this change in energy transfer is the production of waves that propagate equatorward with a vertical wind component and propagate equatorward. It is also expected that auroral energy, in the form of electron precipitation, may influence the final amount of heating deposited to form LSTADs.

The low data satellite sampling (100 min between passes) of the LSTADs by GOCE and PF by DMSP satellites prevents us from making a more definite relationship about their temporal chain of events. During the 5-6 August 2011 magnetic storm, we detected a significant asymmetry in the amplitude and the launch time of the LSTADs. We believe the diminishing PF and the limited expansion of the auroral oval in the South produce the late onset time in the southern hemisphere.

Table 1 illustrates and quantifies the patterns of LSTIDs observed during 12 intense magnetic storms (SYM-H < −100 nT). It is indicated that higher PF values produce higher ∂TEC values and asymmetric transit of LSTIDs.

Our results suggest that most LSTIDs analyzed here move from opposite hemispheres, meet near the magnetic equator, and are typically destroyed. They will likely create a series of smaller-scale structures during their final fate. We have observed that in most cases, LSTADs/LSTIDs encounters occur near the magnetic equator but can develop at other latitudes, as seen on the storms of 5–6 August 2011 and 15 July 2012. This process will undoubtedly increase the ionosphere and thermosphere density "noise" level, which could act as a seed and help initiate EPBs. According to this hypothesis, LSTIDs may have a more significant role. Furthermore, GOCE and TEC data support the role of weak storms in generating LSTADs and LSTIDs (not shown here). These findings underscore the importance of our research and its potential to advance our understanding of LSTADs and LSTIDs significantly.

5 Conclusion

This investigation has led to the following significant findings:

1. A careful analysis of 12 storms (SYM-H < −100 nT) between 2011 and 2013 concluded that LSTID/∂TEC perturbations developed on all 12 storms. Most of the observed LSTID events were seen during the ICME sheath and magnetic cloud. Although a few LSTID events occurred during sunward loops and HSS events. Concurrent LSTADs were detected by the GOCE satellite for each event. Asymmetric or delayed initiation and propagation were observed in two events that happened during the passage of the ICME sheath region. During these cases, asymmetric PF was seen in the northern and southern hemispheres. These two cases (5–6 August 2011 and 15 July 2012) presented rapid polarity reversals of the IMF B_z component. LSTIDs events that developed during the MC or other ICME regions are mainly symmetric with deposited PF equal on both hemispheres.
2. In agreement with previous LSTID observations and simulations, we observed ∂TEC perturbations moving toward the opposite hemisphere. In most events, the LSTIDs encountered were near the geographic or magnetic equator, where they were destroyed and annihilated. However, during the two events mentioned above, the LSTID meeting region

was close to the auroral oval in the opposite hemisphere. In these cases, the travel time of the LSTIDs was close to 3 h. The asymmetric LSTIDs behavior was associated with an asymmetric and delayed PF inflow. The amplitude of the LSTIDs observed with a large network of GPS and GNSS receivers was a function of the background TEC that maximizes during the summer solstice months and the equinoxes. Values above 1 TEC unit were found during 7 of the 12 storms.

3. While analyzing these 12 events, we defined two new parameters to help us determine the presence and sources of magnetospheric and thermospheric inputs. One quantity consists of the amount of neutral density perturbation, which is given by the absolute value of ∂(neutral density) integrated between ±63°. The second value is the trajectory-integrated PF measured by the different DMSP satellites. The latter parameter was organized for each hemisphere independently.
4. The GOCE, DMSP, and ∂TEC data presented here show that neutral density and wind perturbations could be as large as 10% and 20 m/s, respectively. The trajectory-integrated PF needs to be as large as a few kW/m to trigger LSTADs. It is suggested that larger PFs generate larger ∂TEC amplitudes. The amplitude of ∂TEC varied between 0.2 and over 1 TEC unit. The minimum threshold of TID detectability is 0,1 TEC unit.

These new results are expected to encourage the development of forecasting capability for the initiation, asymmetry, and intensity of LSTIDs. Solar wind measurements at 1 AU and real-time processing of satellite-measured PF in both hemispheres are suggested as crucial to achieving a forecast capability for LSTADs and LSTIDs. It is also indicated that these new observations would potentially foster a predicting algorithm of LSTID/∂TEC perturbations, inspiring further research and development in this field.

Data availability statement

The datasets presented in this study can be found in online repositories. The names of the repository/repositories and accession number(s) can be found below: https://cdaweb.gsfc.nasa.gov/index.html.

Author contributions

CV: Writing - original draft. Y-JC: Data curation, Investigation, Methodology, Resources, Software, Validation, Writing–review and editing, Writing–original draft. AB: Conceptualization, Data curation, Investigation, Resources, Software, Validation, Writing–original draft, Writing–review and editing. PA: Conceptualization, Data curation, Investigation, Resources, Writing–review and editing, Writing–original draft. PCA: Funding acquisition, Project administration, Resources, Supervision, Validation, Writing–review and editing. SD: Data curation, Investigation, Resources, Writing–review and editing. MH: Data curation, Methodology, Resources, Writing–review and editing.

Funding

The author(s) declare that financial support was received for the research, authorship, and/or publication of this article. The work presented here started when CV was a Research Scientist at the University of Texas at Dallas (UTD) and continued at Boston College (BC). During his tenure at UTD, he was partially supported by NSF Grant AGS-1933056 and NASA Grants 80NSSC20K0195 and 80NSSC20K177. CV was the principal investigator of AFOSR Grant FA9550-21-1-0277, which aimed to expand the low-latitude Ionospheric Sensor Network. At BC, the research was based upon work supported by NASA under award No. 80NSSC23M0193. YC was partially supported by NASA Living with a Star Grant 80NSSC20K1775. PC and SD were supported by NASA grants 80NSSC22K0173 and 80NSSC20K0195. MH partially worked under NASA contracts.

Acknowledgments

The authors also thank NASA/GSFC's Space Physics Data Facility for making the data available. GOCE data were downloaded from the ESA archive at https://earth.esa.int/eogateway/missions/goce/data, @ ESA (European Space Agency, 2009).

Conflict of interest

The authors declare that the research was conducted in the absence of any commercial or financial relationships that could be construed as a potential conflict of interest.

Generative AI statement

The author(s) declare that no Generative AI was used in the creation of this manuscript.

Publisher's note

Supplementary material

The Supplementary Material for this article can be found online at: https://www.frontiersin.org/articles/10.3389/fspas.2025.1517762/full#supplementary-material

References

Akasofu, S.-I. (1964). The development of the auroral substorm. *Planet. Space Sci.* 12, 273–282. doi:10.1016/0032-0633(64)90151-5

Alberti, T., Consolini, G., Lepreti, F., Laurenza, M., Vecchio, A., and Carbone, V. (2017). Timescale separation in the solar wind-magnetosphere coupling during St. Patrick's Day storms in 2013 and 2015. *J. Geophys. Res. Space Phys.* 122, 4266–4283. doi:10.1002/2016JA023175

Amaechi, P. O., Oyeyemi, E. O., and Akala, A. O. (2018). The response of African equatorial/low-latitude ionosphere to 2015 St. Patrick's Day geomagnetic storm. *Space weather.* 16, 601–618. doi:10.1029/2017SW001751

Balthazor, R. L., and Moffett, R. J. (1997). A study of atmospheric gravity waves and travelling ionospheric disturbances at equatorial latitudes. *Ann. Geophys.* 15, 1048–1056. doi:10.1007/s00585-997-1048-4

Bishop, R. L., Aponte, N., Earle, G. D., Sulzer, M., Larsen, M. F., and Peng, G. S. (2006). Arecibo observations of ionospheric perturbations associated with the passage of Tropical Storm Odette. *J. Geophys. Res.* 111, A11320. doi:10.1029/2006JA011668

Bruinsma, S. L., Doornbos, E., and Bowman, B. R. (2014). Validation of GOCE densities and evaluation of thermosphere models. *Adv. Space Res* 54 (4), 576–585. doi:10.1016/j.asr.2014.04.008

Bukowski, A., Ridley, A., Huba, J. D., Valladares, C., and Anderson, P. C. (2024). Investigation of large scale traveling atmospheric/ionospheric disturbances using the coupled Sami3 and GITM models. *Geophys. Res. Lett.* 51, e2023GL106015. doi:10.1029/2023GL106015

Davis, T. N., and Sugiura, M. (1966). Auroral electrojet activity index *AE* and its universal time variations. *J. Geophys. Res.* 71 (3), 785–801. doi:10.1029/JZ071i003p00785

Dmitriev, A. V., Suvorova, A. V., Klimenko, M. V., Klimenko, V. V., Ratovsky, K. G., Rakhmatulin, R. A., et al. (2017). Predictable and unpredictable ionospheric disturbances during St. Patrick's Day magnetic storms of 2013 and 2015 and on 8–9 March 2008. *J. Geophys. Res. Space Phys.* 122, 2398–2423. doi:10.1002/2016JA023260

European Space Agency, (2009). GOCE thermosphere data collection. Version 1.0. doi:10.5270/esa-l8g67jw

Galvan, D. A., Komjathy, A., Hickey, M. P., and Mannucci, A. J. (2011). The 2009 Samoa and 2010 Chile tsunamis as observed in the ionosphere using GPS total electron content. *J. Geophys. Res.* 116, A06318. doi:10.1029/2010JA016204

Gonzalez, W. D., Echer, E., Clua-Gonzalez, A. L., and Tsurutani, B. T. (2007). Interplanetary origin of intense geomagnetic storms (*Dst* < −100 nT) during solar cycle 23. *Geophys. Res. Lett.* 34, L06101. doi:10.1029/2006GL028879

Hines, C. O. (1960). *Can. J. Phys.* 38 (11), 1441–1481. doi:10.1139/p60-150

Ho, C. M., Mannucci, A. J., Lindqwister, U. J., Pi, X., and Tsurutani, B. T. (1996). Global ionosphere perturbations monitored by the Worldwide GPS Network. *Geophys. Res. Lett.* 23, 3219–3222. doi:10.1029/96GL02763

Ho, C. M., Mannucci, A. J., Sparks, L., Pi, X., Lindqwister, U. J., Wilson, B. D., et al. (1998). Ionospheric total electron content perturbations monitored by the GPS global network during two northern hemisphere winter storms. *J. Geophys. Res.* 103 (A11), 26409–26420. doi:10.1029/98JA01237

Hocke, K., and Tsuda, T. (2001). Gravity waves and ionospheric irregularities over tropical convection zones observed by GPS/MET Radio Occultation. *Geophys. Res. Lett.* 28, 2815–2818. doi:10.1029/2001GL013076

Jonah, O. F., Kherani, E. A., and De Paula, E. R. (2017). Investigations of conjugate MSTIDS over the Brazilian sector during daytime. *J. Geophys. Res. Space Phys.* 122, 9576–9587. doi:10.1002/2017JA024365

Knipp, D., Kilcommons, L., Hairston, M., and Coley, W. R. (2021). Hemispheric asymmetries in Poynting flux derived from DMSP spacecraft. *Geophys. Res. Lett.* 48, e2021GL094781. doi:10.1029/2021GL094781

Liu, X., Yue, J., Wang, W., Xu, J., Zhang, Y., Li, J., et al. (2018). Responses of lower thermospheric temperature to the 2013 St. Patrick's Day geomagnetic storm. *Geophys. Res. Lett.* 45, 4656–4664. doi:10.1029/2018GL078039

Lu, G., Richmond, A. D., Emery, B. A., and Roble, R. G. (1995). Magnetosphere-ionosphere-thermosphere coupling: effect of neutral winds on energy transfer and field-aligned current. *J. Geophys. Res.* 100 (A10), 19643–19659. doi:10.1029/95JA00766

Makela, J. J., Lognonné, P., Hébert, H., Gehrels, T., Rolland, L., Allgeyer, S., et al. (2011). Imaging and modeling the ionospheric airglow response over Hawaii to the tsunami generated by the Tohoku earthquake of 11 March 2011. *Geophys. Res. Lett.* 38, L00G02. doi:10.1029/2011GL047860

Mayr, H. G., and Harris, I. (1978). Some characteristics of electric field momentum coupling with the neutral atmosphere. *J. Geophys. Res.* 83 (A7), 3327–3336. doi:10.1029/JA083iA07p03327

Miteva, R., Samwel, S. W., and Costa-Duarte, M. V. (2018). The Wind/EPACT proton event catalog (1996–2016). *Sol. Phys.* 293 (2), 27. arXiv:1801.00469. doi:10.1007/s11207-018-1241-5

Nicolls, M. J., Kelley, M. C., Coster, A. J., González, S. A., and Makela, J. J. (2004). Imaging the structure of a large-scale TID using ISR and TEC data. *Geophys. Res. Lett.* 31, L09812. doi:10.1029/2004GL019797

Rouillard, A. P. (2011). Relating white light and *in situ* observations of coronal mass ejections: a review. *A Rev. JASTP* 73, 1201–1213. doi:10.1016/j.jastp.2010.08.015

Saito, A., Fukao, S., and Miyazaki, S. (1998). High resolution mapping of TEC perturbations with the GSI GPS Network over Japan. *Geophys. Res. Lett.* 25, 3079–3082. doi:10.1029/98GL52361

Samwel, S., and Miteva, R. (2023). Correlations between space weather parameters during intense geomagnetic storms: analytical study. *Adv. Space Res.* 72, 3440–3453. doi:10.1016/j.asr.2023.07.053

Scott, C. J., and Major, P. (2018). The ionospheric response over the UK to major bombing raids during World War II. *Ann. Geophys.* 36, 1243–1254. doi:10.5194/angeo-36-1243-2018

Shiokawa, K., Otsuka, Y., Ogawa, T., Balan, N., Igarashi, K., Ridley, A. J., et al. (2002). A large-scale traveling ionospheric disturbance during the magnetic storm of 15 September 1999. *J. Geophys. Res.* 107 (A6). doi:10.1029/2001JA000245

Shreedevi, P. R., Choudhary, R. K., Thampi, S. V., Yadav, S., Pant, T. K., Yu, Y., et al. (2020). Geomagnetic storm-induced plasma density enhancements in the southern polar ionospheric region: a comparative study using St. Patrick's Day storms of 2013 and 2015. *Space weather.* 18, e2019SW002383. doi:10.1029/2019SW002383

Smith, S., Baumgardner, J., and Mendillo, M. (2009). Evidence of mesospheric gravity-waves generated by orographic forcing in the troposphere. *Geophys. Res. Lett.* 36, L08807. doi:10.1029/2008GL036936

Thayer, J. P., and Semeter, J. (2004). The convergence of magnetospheric energy flux in the polar atmosphere. *J. Atmos. Solar-Terrestrial Phys.* 66 (10), 807–824. doi:10.1016/j.jastp.2004.01.035

Tsurutani, B. T., and Gonzalez, W. D. (1997). "The interplanetary causes of magnetic storms: a review," in *Magnetic storms*. Editors B. T. Tsurutani, W. D. Gonzalez, Y. Kamide, and J. K. Arballo (Washington, D. C: American Geophysical Union). doi:10.1029/GM098p0077

Vadas, S. L., and Crowley, G. (2010). Sources of the traveling ionospheric disturbances observed by the ionospheric TIDDBIT sounder near Wallops Island on 30 October 2007. *J. Geophys. Res.* 115, A07324. doi:10.1029/2009JA015053

Valladares, C. E., and Carlson, H. C., Jr (1991). The electrodynamic, thermal, and energetic character of intense Sun-aligned arcs in the polar cap. *J. Geophys. Res.* 96 (A2), 1379–1400. doi:10.1029/90JA01765

Valladares, C. E., Sheehan, R., and Pacheco, E. E. (2017). "Observations of MSTIDs over south and Central America," *Ionospheric Space weather longitude and hemisphere dependences and lower atmosphere forcing, geophysical monograph*. Editors F.-R. Yizengaw, P. H. Doherty, and S. Basu 1st Edn (John Wiley and Sons, Inc), 220.

Valladares, C. E., Villalobos, J., Hei, M. A., Sheehan, R., Basu, Su., MacKenzie, E., et al. (2009). Simultaneous Observation of traveling ionospheric disturbances in the northern and southern hemispheres. *Ann. Geophys* 27, 1501–1508. doi:10.5194/angeo-27-1501-2009

Verkhoglyadova, O. P., Tsurutani, B. T., Mannucci, A. J., Mlynczak, M. G., Hunt, L. A., Paxton, L. J., et al. (2016). Solar wind driving of ionosphere-thermosphere responses in three storms near St. Patrick's Day in 2012, 2013, and 2015. *J. Geophys. Res. Space Phys.* 121, 8900–8923. doi:10.1002/2016JA022883

Xu, Z., Hartinger, M. D., Clauer, C. R., Peek, T., and Behlke, R. (2017). A comparison of the ground magnetic responses during the 2013 and 2015 St. Patrick's Day geomagnetic storms. *J. Geophys. Res. Space Phys.* 122, 4023–4036. doi:10.1002/2016JA023338

Zhu, Q., Lu, G., Maute, A., Deng, Y., and Anderson, B. (2022). Assessment of using field-aligned currents to drive the Global Ionosphere Thermosphere Model: a case study for the 2013 St Patrick's Day geomagnetic storm. *Space weather.* 20, e2022SW003170. doi:10.1029/2022SW003170

frontiers | Frontiers in Astronomy and Space Sciences

TYPE Original Research
PUBLISHED 29 August 2025
DOI 10.3389/fspas.2025.1503134

OPEN ACCESS

EDITED BY
Nicholas Pedatella,
National Center for Atmospheric Research,
United States

REVIEWED BY
Artem Smirnov,
GFZ German Research Centre for Geosciences, Germany
Magnus Ivarsen,
University of Oslo, Norway

*CORRESPONDENCE
Enrique L. Rojas,
erojasv@mit.edu

RECEIVED 28 September 2024
ACCEPTED 14 February 2025
PUBLISHED 29 August 2025

CITATION
Rojas EL, Aricoche JA and Milla MA (2025) Modeling ionograms and critical plasma frequencies with neural networks.
Front. Astron. Space Sci. 12:1503134.
doi: 10.3389/fspas.2025.1503134

Modeling ionograms and critical plasma frequencies with neural networks

Enrique L. Rojas[1]*, Jhassmin A. Aricoche[2] and Marco A. Milla[3]

[1]MIT Haystack Observatory, Massachusetts Institute of Technology, Westford, MA, United States,
[2]Department of Electrical and Computer Engineering, Cornell University, Ithaca, NY, United States,
[3]Department of Electronic Engineering, Pontificia Universidad Catolica del Peru, Lima, Peru

Ionosondes offer broad spatial coverage of the lower ionosphere, supported by a global network of affordable instruments. This motivates the exploration of new methods that exploit this geographical coverage to capture spatially dependent characteristics of electron density distributions using data-driven models. These models must have the versatility to learn from ionogram data. In this work, we used neural networks (NN) to forecast ionograms across two solar activity cycles. The ionosonde data was obtained from the digisonde at the Jicamarca Radio Observatory (JRO). Each NN comprises one NN that estimates the ionogram trace and another one that estimates the critical frequency. Two forecasting models were implemented. The first one was trained with all available data and was optimized for accurate predictions along that time range. The second one was trained using a rolling-window strategy with just 3 months of data to make short-term ionogram predictions. Our results show that both models are comparable and can often outperform predictions by empirical and numerical models. The hyperparameters of both models were optimized using a specialized library. Our results suggest that a few months of data was enough to produce predictions of comparable accuracy to the reference models. We argue that this high accuracy is obtained with short time series because the NN captures the dominant periodic drivers. Finally, we provide suggestions for improving this model.

KEYWORDS

neural networks, forecasting, ionosonde, ionograms, ionosphere

1 Introduction

Space weather is highly nonlinear, where several neutral and plasma regimes are interconnected (McGranaghan, 2024). Steady-state conditions are usually in reasonable agreement with empirical models built by fitting historical data to some basis expansion. Nevertheless, the events that drive space weather require state-of-the-art, interconnected numerical models of considerable sophistication to be modeled. Even these sophisticated numerical models are limited in accuracy, are often not open to the public, or require computational resources unavailable to most of the community. Unlike the numerical models, data-driven frameworks based on machine–learning have a simple mathematical structure but rely on a comprehensive sampling of the potential scenarios to be reproduced (Camporeale et al., 2018; Camporeale, 2019).

Electron density distribution is probably one of the most important dynamical variables for modeling the Earth's plasma environment because it directly influences ionospheric conductivity, wave propagation, and energy transfer processes

(Kelley, 2009). Even though there are currently many numerical and empirical models, they often suffer from the abovementioned limitations. Furthermore, direct measurements of electron density profiles are very sparse over time and in different geographical locations. For example, the altitude profiles obtained with incoherent scatter radars have the appropriate resolution but have very low geographical coverage. Moreover, indirect measurements of electron density profiles for the bottom side ionosphere are relatively abundant in the form of total electron content (TEC) and ionogram measurements. Several NN have been trained to predict TEC (Uwamahoro et al., 2018) and ionosonde-derived parameters (Gowtam and Ram, 2017).

An NN trained to predict electron density profiles from geophysical parameters and previous densities could be used as a local forecasting model. This forecasting NN should be capable of estimating virtual heights before attempting to estimate electron densities. Furthermore, forecasting ionograms may be useful for estimating the impact of radio-propagating signals. This work describes how two NNs were trained and tested to reproduce ionograms obtained with Jicamarca's ionosonde. Section 2 first details the considerations for choosing the models' architectures and parameters. Then, we show how the outputs from IRI (International Reference Ionosphere) and SAMI2 (SAMI2 is Another Model of the Ionosphere) were processed to compare them with the estimated outputs. Then, in Section 3, we assess both the NNs' capacity for f_0F_2 and ionogram predictions compared to test ionsonde measurements and IRI predictions. In Section 4, we propose an explanation for the accuracy of the second model despite using small data sets. Finally, Section 5 outlines the conclusions and briefly comments on our future work.

2 Input data, architecture design, and reference models

In this section, we describe the mathematical relation between the forecasted variable (the ionogram) and the physical parameters of the ionospheric plasmas. Furthermore, we describe the time series used as model inputs, the NNs' structure, and the reference ionograms obtained from other models. All the NNs described in this work were built using `TensorFlow`.

2.1 Building the input and output data sets

Given a electron density profile $n_e(z)$ that only depends on height (z), the virtual height of a wave of frequency f propagating vertically can be represented by (Reyes, 2017):

$$h(f) = \int_0^{z_r} \frac{dz}{\sqrt{1 - 80.62\frac{n_e(z)}{f^2}}} \tag{1}$$

Here, $n_e^2(z_r) = f^2/80.62$. Furthermore, this expression only captures the O-mode of the wave. The $h(f)$ profiles (Equation 1) describe most ionogram O-mode traces, measured using fast frequency sweeps. We can assume that during the experimental construction of the $h(f)$, the electron density does not change. On the other hand, the time evolution of n_e obeys the continuity equation (Kelley, 2009):

$$\partial_t n_e + \nabla \cdot (n_e \boldsymbol{v}_e) = P_e(n_e) - L_e(n_e) \tag{2}$$

The terms P_e and L_e of Equation 2 are the production and loss functions, respectively. These two functions will depend on the electron density and other local variables like the neutral density and electron temperature. As a first approximation, we can say that electron velocity $\boldsymbol{v}_e$ will be dominated by the electric and magnetic fields and, to a lesser extent, pressure gradients and momentum exchange with other species. If we integrate the continuity equation over the time needed to build an ionogram, we will get that.

$$\begin{aligned} &\int_0^T \partial_t n_e \approx 0 \Rightarrow \int_0^T P_e(n_e) - L_e(n_e) - \nabla \cdot (n_e \boldsymbol{v}_e) dt \approx 0 \\ &\Rightarrow \langle P_e(n_e) \rangle \approx \langle L_e(n_e) \rangle + \langle \nabla \cdot (n_e \boldsymbol{v}_e) \rangle \end{aligned} \tag{3}$$

We use the notation $\int_0^T g dt = \langle g \rangle$. During an ionosonde measurement, the electron density should be such that, in a defined volume, the number of produced electrons is approximately the same as the number of electrons lost by recombination plus the number of electrons moving stated by Equation 3.

Even though all the variables involved in P_e, L_e, and $\boldsymbol{v}_e$ can be measured, these values are rarely obtained simultaneously and are too few to use for training a statistical model like a NN. Instead, we use measurements correlated to these functions, hoping the correlation is strong enough for our model to have good predictive power. We will use standard geophysical parameters, F10.7, Kp, MgII, and time, as model inputs. We expect the solar activity proxies F10.7 and MgII to be directly correlated to P_e because of photoionization and indirectly correlated to $\boldsymbol{v}_e$ because solar flux affects the electrodynamic of the ionosphere (Laštovička and Burešová, 2023). Another factor affecting the electrodynamics is the geomagnetic fluctuations captured by Kp, so we estimate that its effect will be through $\boldsymbol{v}_e$. Then, the causal relations will be:

$$\left.\begin{array}{ll} \text{F10.7, MgII} & \rightarrow P_e \\ \text{Kp} & \rightarrow \boldsymbol{v}_e \end{array}\right\} \Rightarrow n_e \Rightarrow h(f) \tag{4}$$

Time was chosen to be represented as a superposition of a cosine and a sine with annual periodicity. This is standard practice in linear models when a dominant periodicity is known. Building a time series of the trigonometric functions makes the fitting linear. Figure 1 shows 10 months of the input time series. DNS and DNC indicate the sine and cosine time series. Notice that the time series are not continuous; these gaps correspond to times when there is no ionosonde data or the data did not pass our quality filters.

The ionogram data was obtained from JRO's digisonde and filtered using the ARTIST's quality flags. Times corresponding to geomagnetic events (Kp > 3) and ionograms with fewer than 10 points were removed from the study. Figure 2 shows the monthly median and median absolute deviation (MAD) of all the ionograms used for training. Notice that the MAD is more prominent near the critical frequencies of both the F and E regions, indicating that the ionograms are more variable and more challenging to model. The usual solar annual and semiannual periodicities can be seen as well.

FIGURE 1
Time series of various geophysical parameters. From top to bottom: Kp, $sin(\omega_y t)$, $cos(\omega_y t)$, f10.7, and MgII time series. ω_y is an annual frequency and t indicates the time index.

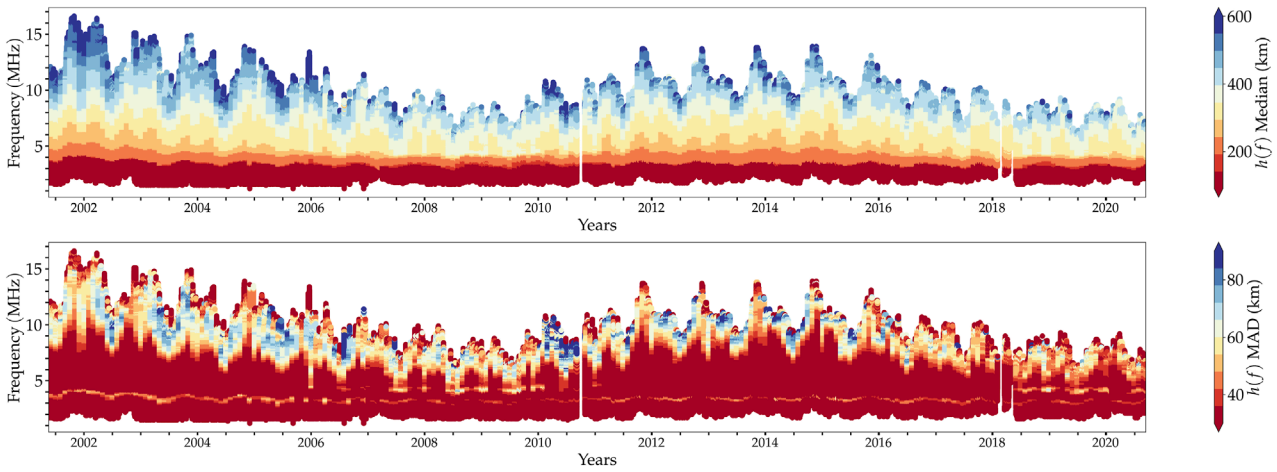

FIGURE 2
Top: Monthly median of ionograms measured with JRO's digisonde. The color indicates virtual heights and the vertical axis frequency. Bottom: Median absolute deviation (MAD(x) = median(|x – median(x)|)) of the monthly ionograms.

2.2 Ionograms from empirical models: IRI and SAMI2

To evaluate the accuracy of our model, we compared it against two established ionospheric models: IRI and SAMI2. IRI is an empirical model based on extensive observational data, designed to capture the average behavior of the ionosphere (Bilitza et al., 2022). In contrast, SAMI2 is a physics-based model that solves the ionospheric plasma fluid equations, though it simplifies the system to a 2D geometry and is sensitive to initial conditions. Both models are easy to use and are open to the space physics community. We obtained electron densities as discretized profiles of N elements from these models, and using (Equation 1), we estimated the virtual heights via trapezoidal integration with a correction for the reflection height (Reyes, 2017):

$$h(f) = \int_0^{z_r} dz n_g(z) \approx \sum_k^{N-2} \Delta z \frac{n_g(z_k) + n_g(z_{k+1})}{2} + \frac{2 n_g(z_{N-1}) \Delta z}{n_g(z_{N-1})^2 - n_g(z_N)^2} \tag{5}$$

We define the group refractive index of the O-mode in (Equation 5) as $n_g(z) = (1 - 80.62 \frac{n_e(z)}{f^2})^{-1/2}$. This method was validated against Gaussian quadrature, showing no significant differences in accuracy.

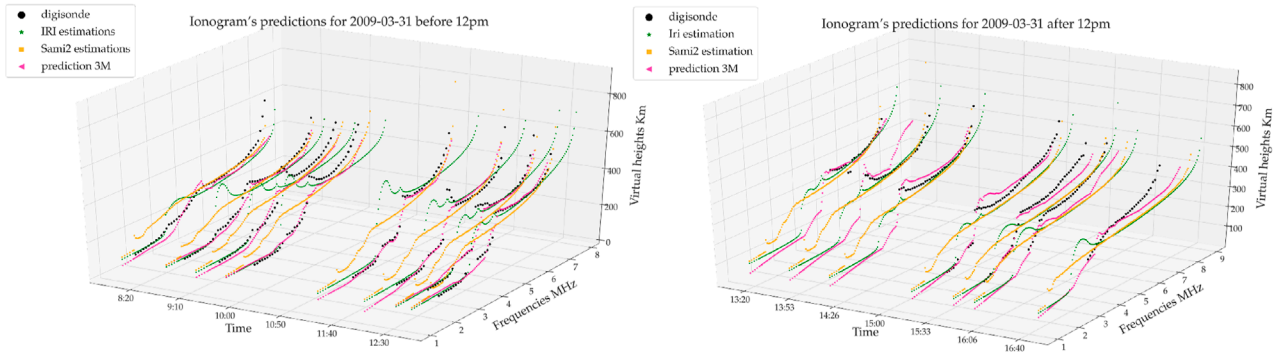

FIGURE 3
Some sample ionograms for morning (left) and afternoon (right). The ionograms for SAMI2 and IRI were calculated using (Equation 5). The "prediction 3M" ionograms correspond to the estimated obtained with our first model using 3 months of data.

2.3 Proposed forecasting models and training strategies

We used two NNs to simulate ionograms: one used a regression model to predict virtual heights, and the other predicted the critical frequency. Regression NNs predict continuous values by learning patterns from input data, making them suitable for forecasting virtual heights, as they can model the smooth variations typically observed in ionograms. By comparing a regression and a classification NN for calculating the critical frequency, we found that the latter more often produced lower discrepancies with the data. The training data for the classification NN consisted of virtual height labels 0 when they did not correspond to the critical frequency and 1 when they did. This NN was trained to predict the occurrence of critical frequencies in ionogram curves as a predictor of label 1 based on the structure of each ionogram. We found that a classification NN and a regression NN were often more effective in determining the critical frequency and the virtual heights, respectively.

To optimize the architecture of our neural networks, we employed Optuna (Akiba et al., 2019), an optimization framework based on Python. Optuna automates the search for optimal hyperparameters using a trial-based approach through efficient sampling techniques and pruning algorithms to explore a large search space. For our model, we used Optuna to fine-tune the learning rates, test different activation functions (ReLU and Swish), and determine the optimal number of nodes per layer. The exact architecture of the NNs can vary because the architecture parameters are part of the hyperparameter optimization process. However, most NNs generated through this process have five layers, use the `Swish` activation function, and an initial learning rate of approximately 10^{-4}.

We conducted a series of tests to inform the design of our model. For these tests, we used datasets spanning both 1-month and 3-month periods, specifically selecting months corresponding to solstices and equinoxes. Figure 3 shows some predicted ionograms by our model, SAMI2, and IRI, together with real ionograms measured with JRO's digisonde. The ionograms obtained with IRI have a visible oscillation near the E-to-F region transition, and the ones obtained with SAMI2 seem to underestimate the variation in this same region. The model's performance was evaluated by forecasting ionograms and f_oF_2 values and calculating the root mean square errors (RMSE) compared to the real values obtained with the ionosonde. We also compared the RMSE for predictions made using IRI and SAMI2. The results of these comparisons are summarized in Tables 1, 2.

Across all datasets, our model demonstrated higher accuracy in forecasting ionograms than IRI and SAMI2. The 3-month training dataset did not consistently outperform the 1-month dataset. In most cases, the model trained on 1 month of data yielded better accuracy than the 3-month training. This unexpected result raises questions about the influence of training data size on model performance, which we aim to explore further in future work. Regarding the f_oF_2 forecasts, our model generally achieved superior accuracy relative to IRI and SAMI2, except for the solar maximum equinox case. Additionally, the 3-month dataset test during the solar maximum solstice produced a forecast that, while less accurate than IRI, still outperformed SAMI2.

These initial results led us to further investigate the influence of the training data time span on the accuracy of our forecasts. To do so, we developed two specialized NNs: `IoNNo-C` and `IoNNo-R`.

`IoNNo-C` was designed to capture long-term behavior and was trained using the complete dataset spanning 18 years. Our goal with `IoNNo-C` is to model the climatological behavior of the ionosphere and capture finer variabilities that may have been overlooked by empirical models like IRI, which are designed to capture global average behavior. To optimize `IoNNo-C`, we employed a sliding window technique for hyperparameter tuning. Initially, a set of hyperparameters is selected, and the model is trained on 3 months of data before being evaluated on the following month. This process is repeated over the next 4-month interval, with the average loss function calculated across all windows. After multiple iterations, the set of hyperparameters that results in the lowest average loss function is chosen, ensuring that the model's parameters do not favor any specific subset of the data.

On the other hand, `IoNNo-R` was developed for short-term predictions. It is trained using only 3 months of data, with

TABLE 1 RMSE of predicted virtual heights (km).

	1 month of data	3 months of data	IRI	Sami2
Solar Min. Solstice[a]	43.47	51.69	87.23	81.15
Solar Min. Equinox[b]	25.64	30.37	82.86	70.07
Solar Max. Solstice[c]	53.04	40.20	54.45	91.68
Solar Max. Equinox[d]	32.46	31.15	67.00	49.23

[a]December 2009.
[b]March 2009.
[c]June 2014.
[d]March 2013.

TABLE 2 RMSE of predicted critical frequencies (MHz).

	1 month of data	3 months of data	IRI	Sami2
Solar Min. Solstice[a]	0.44	0.47	1.12	0.59
Solar Min. Equinox[b]	0.58	0.51	1.00	0.75
Solar Max. Solstice[c]	0.62	0.82	0.67	1.47
Solar Max. Equinox[d]	1.81	1.53	1.25	0.70

[a]December 2009.
[b]March 2009.
[c]June 2014.
[d]March 2013.

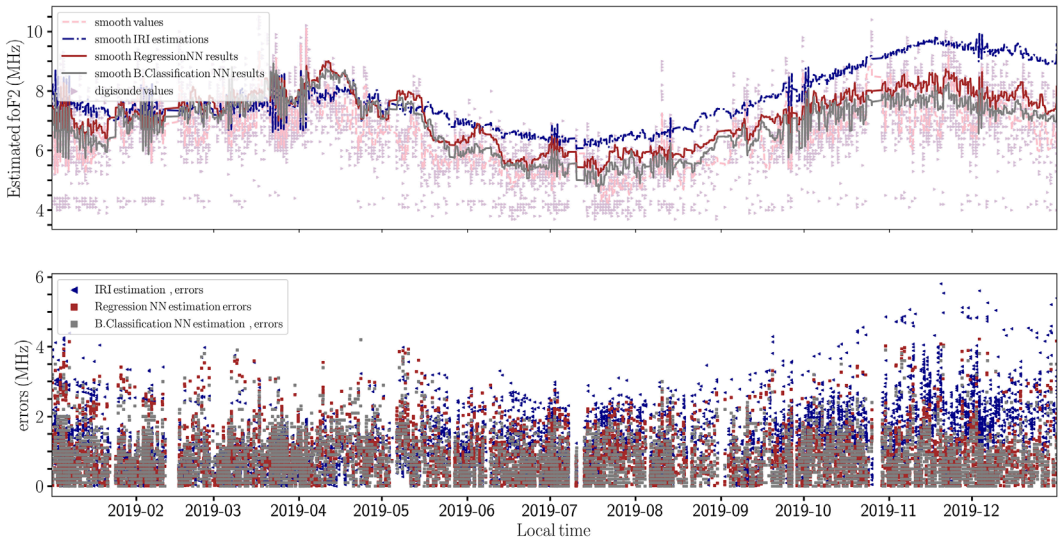

FIGURE 4
Top: The points in the background correspond to the digisonde data and the models' estimates. The lines were obtained by smoothing the direct outputs for better visualization. Bottom: The absolute errors for critical frequency estimates of both IRI and IoNNo-C.

hyperparameters selected to minimize the error for the last week of training data. It is this hyperparameter tuning with recent data that makes this forecasting "shorter-termed." Furthermore, all the ionograms used in this model were averaged hourly to avoid geophysical noise's impact in the prediction. This approach aims to maximize the accuracy of immediate, short-term forecasts, providing a complementary perspective to the long-term trends captured by IoNNo-C.

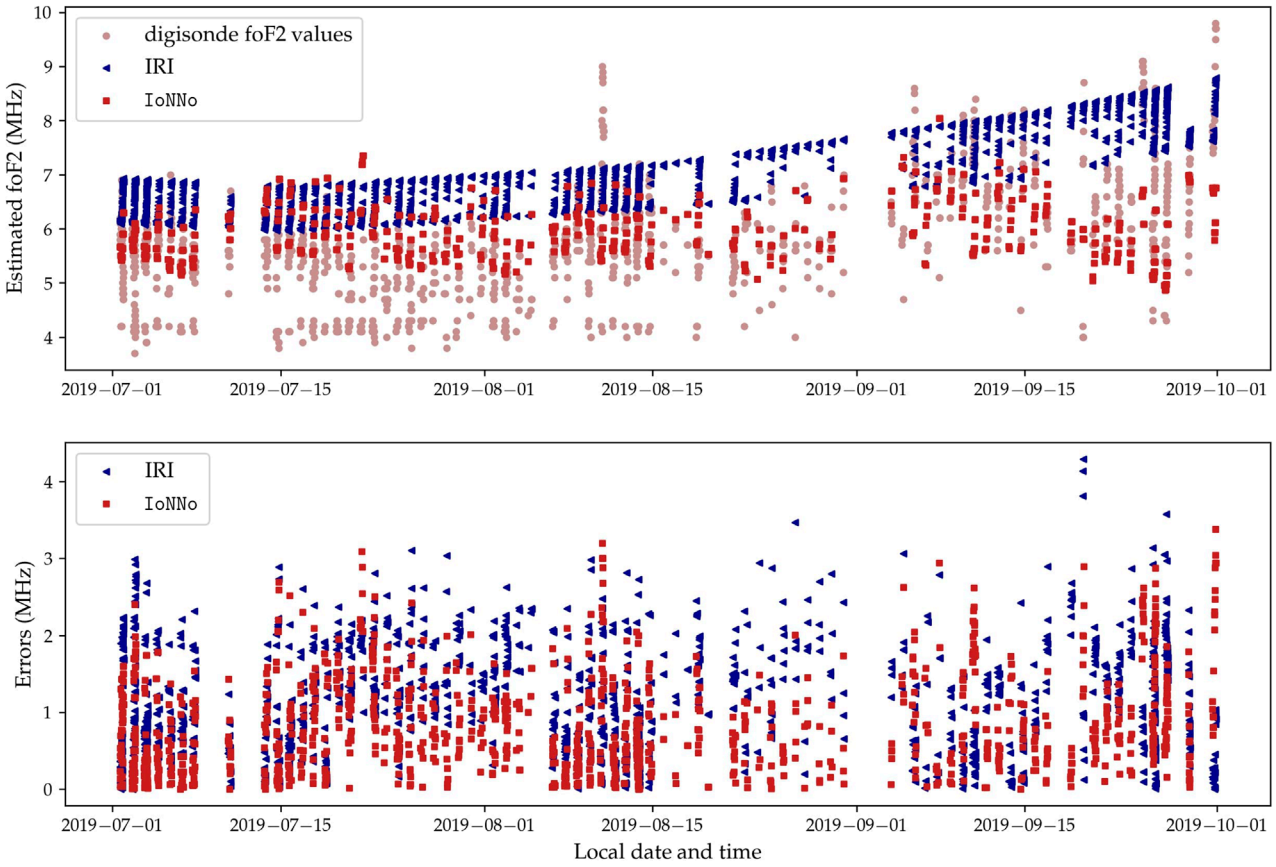

FIGURE 5
Top: The purple and red triangles and light-blue squares correspond to the digisonde measurements, IoNNo-R predictions, and IRI estimates, respectively. Bottom: The absolute errors for critical frequency estimates of both IRI and IoNNo-R.

3 Assessing predictions

Each model serves a distinct forecasting needs. IoNNo-R is designed to explore the predictive power of smaller datasets, focusing on short-term, higher-accuracy forecasting. The key feature of IoNNo-R is that its hyperparameters are tuned using data immediately preceding the forecasted period. In contrast, IoNNo-C is built to capture the climatological behavior of the ionosphere over a longer timescale. Because IoNNo-C is trained for the geographic region where the forecasts will be applied, we expect it to provide more accurate predictions than global models that generalize across different locations.

We applied IoNNo-C to predict f_oF_2 values for the last year of data, which had been extracted from the training set. Furthermore, we trained IoNNo-C with a regression and a classification NN for the critical frequency prediction for comparison. On the top of Figure 4 we can see the smoothed digisonde values (dashed pink line), IRI predictions (dashed blue line), and IoNNo-C predictions (continuous red and gray lines for the regression and classification NN, respectively). From this figure, we observe that IRI systematically overestimates f_oF_2 values from May to December. In the plot below, we compare the absolute errors of IoNNo-C (red and gray squares for the regression and classification NN, respectively) and IRI (blue triangles). The binary classification version of IoNNo-C achieves slightly better accuracy than its regression counterpart. Moreover, the average improvement of IoNNo-C over IRI is approximately 1 MHz, with IRI exhibiting more extreme outliers.

For shorter-term predictions, we utilized IoNNo-R. Based on the results with IoNNo-C, we decided to use a classification NN for the virtual height forecasting in IoNNo-C. Figure 5 demonstrates IoNNo-R's performance in predicting f_oF_2 compared to IRI from July to September 2019. In the top plot, the digisonde values are marked with light red circles, while the IRI and IoNNo-R predictions are indicated with blue triangles and red squares, respectively. IRI's systematic overestimation of f_oF_2 compared to the digisonde measurements is still visible in this shorter time range. Although IoNNo-R predictions are closer to the actual values, a systematic shift relative to the digisonde's values is still noticeable, particularly in the first half of the time range. Nevertheless, IoNNo-R shows an average f_oF_2 error improvement of around 1 MHz compared to IRI, matching the improvement seen in IoNNo-C.

Figure 6 analyzes the absolute error statistics for ionogram predictions made by IoNNo-R over the same time interval shown in Figure 5. The figure depicts the distribution of errors, where each box spans the first to third quartiles, with an orange line indicating the median. The whiskers extend up to 1.5

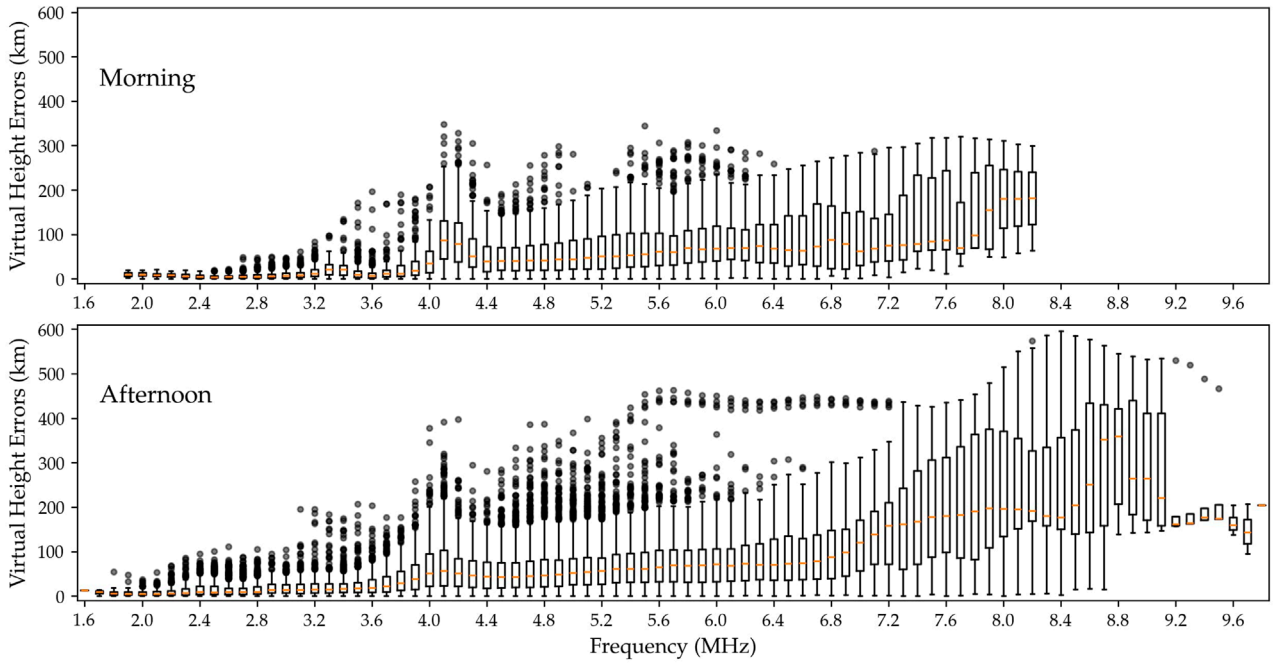

FIGURE 6
Statistics of virtual height absolute errors of IoNNo-R compared to the digisonde's ionograms for the same times shown in Figure 5. Each box extends from the first quartile to the third quartile of the virtual heights for each frequency, with a line at the median. The whiskers extend from the box sides to the farthest virtual height lying within 1.5× the inter-quartile range. Points outside the whiskers are indicated independently with gray dots. The top and bottom plots indicate the morning and afternoon ionograms, respectively.

times the interquartile range, and any outliers beyond this range are plotted individually. The top and bottom plots represent morning and afternoon ionograms, respectively. In both cases, the model's accuracy noticeably decreases as it approaches critical frequencies. However, the afternoon ionograms show significantly less precision, with a greater number of outliers across all frequencies, and higher variability at the upper frequency range.

Our analysis has several limitations and shortcomings that need to be acknowledged. First, the accuracy of our comparisons between our models and IRI and SAMI2 relies on the assumption that the ionograms we used are close to the correct values. Although we filtered out ionograms with low-quality flags, our results still depend on the precision of this labeling process. Additionally, our approximation for the virtual height, as expressed in Equation 1, is valid only when the ionosphere is perfectly stratified. This limits its applicability in cases where horizontal gradients are significant, meaning that our model may not fully capture the complexities of certain ionospheric conditions. Finally, the number of samples used to calculate the ionograms using Equation 5) will affect the final form of the virtual height profile. Nevertheless, our numerical tests suggest that the number of points is well within the limit for which the ionogram's numerical error is smaller than the absolute error of our model predictions.

Moreover, while our models demonstrate promising results, further experiments are necessary to optimize hyperparameters not yet considered in our current framework and optimize the ones we consider in larger parameter spaces. Another limitation is that our models, in their current form, do not incorporate previous information on the ionospheric state. This means that they can not capture temporal dependencies or short-term fluctuations. To address this, we are currently exploring the use of recurrent neural networks that can learn from the time evolution of f_0F_2 and virtual heights, potentially enhancing the models' ability to forecast rapidly changing conditions (Hu and Zhang, 2018).

Finally, smoothing the ionograms before training could help remove transient variability. By reducing this variability, we anticipate that our models' accuracy could improve, providing more reliable forecasts in a broader range of scenarios.

4 Parameter periodicity and predictive power

Our results suggest that even relatively small data sets can be used to train NNs that can match and even outperform IRI and SAMI2 in predicting ionograms and f_of_2. Even though this might sound surprising at first, after inspection, we think this should be expected because of the periodic nature of the dominant drivers of the system. For instance, (Wang et al., 2011), analyzed N_mF_2 time series from ionosondes at different geographical locations and found that the dominant periodicities were consistent with known geophysical and heliophysical periodic forcing.

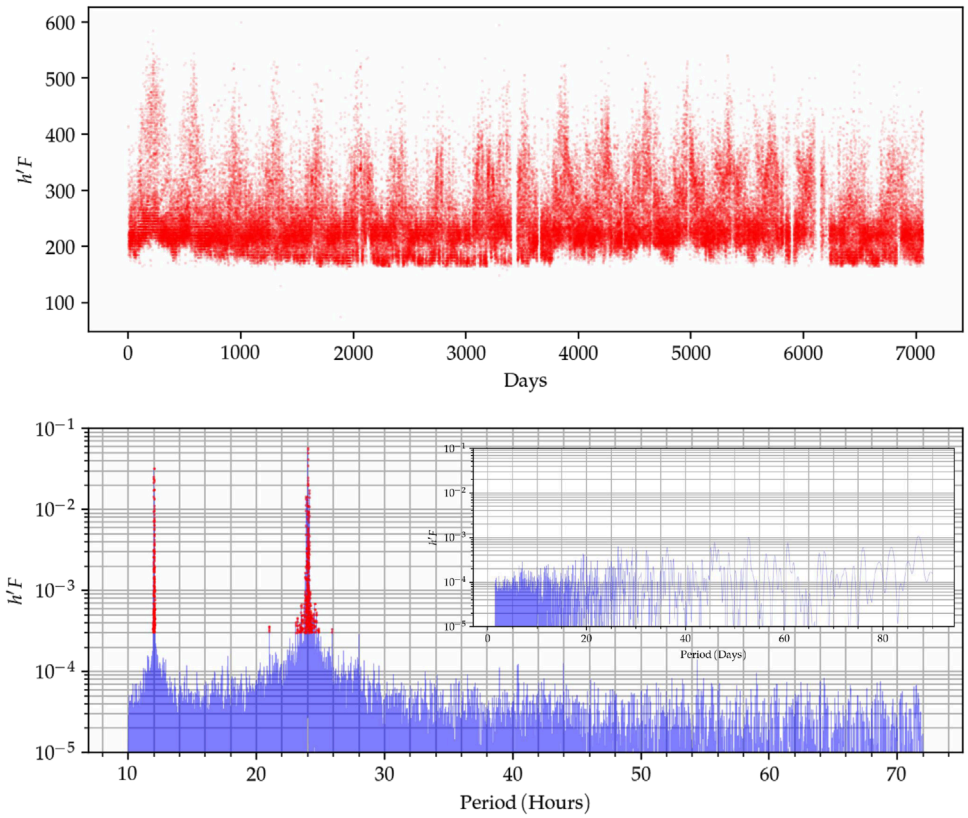

FIGURE 7
Top: Time series of the $h'F$ parameter. Bottom: Periodograms of $h'F$ up to periods of 70 hours, where the red dots indicate amplitudes significantly larger than expected by white noise. Within the hour-scale periodogram there is a smaller one showing a day-scale periodogram.

We can illustrate this by analyzing the periodicity in representative ionosonde parameters. Figure 7 shows a time series of the parameter h'F and its corresponding periodogram. The analysis was done using the Lomb-Scargle method, which is usually recommended over Fourier transforms when gaps are present in the data (VanderPlas, 2018). The h'F parameter captures the virtual height of the bottom of the F region, which is a good proxy for ionogram variability. The red dots in the periodogram indicate the frequency components well above the amplitude that can be assigned to random fluctuations. Notice how the red dots cluster around several well-defined peaks at the diurnal and semidiurnal periods with amplitudes much larger than the smaller components.

The spectral analysis of h'F shows that most of the energy is encapsulated to a few modes. Therefore, we might improve our forecasting efficiency by focusing on predicting the evolution of only the dominant modes using standard time series methods. Nevertheless, it should be considered that given their simplicity of usage current implementation of NNs are still a great forecasting alternative even when its possible to use a sparse representation. Moreover, the NNs have the advantage of possibly capturing nonlinear interactions, which are difficult to include in standard time series models. However, there are currently modeling approaches that are able to exploit the sparse representation of periodic time series and the versatility of NN (Triebe et al., 2021).

5 Conclusion

This study leveraged nearly 2 decades of digisonde data to train NNs for ionogram prediction. Initial small-scale tests on months of equinoxes and solstices indicated that a simple NN could outperform ionogram predictions generated by established models like IRI and SAMI2 in certain situations. We developed two models with distinct datasets and training strategies based on these results. `IoNNo-C` was trained on the complete dataset, with its hyperparameters tuned to avoid favoring any subset of the data. In contrast, `IoNNo-R` was trained on only 3 months of data, with hyperparameters specifically optimized to fit the last segment of the training period to improve short-term forecasts.

Our findings show that IoNNo-C consistently produced more accurate f_oF_2 estimates over a full year of predictions, outperforming IRI. Similarly, `IoNNo-R` also surpassed IRI's f_oF_2 predictions for the studied time intervals, though we observed that the accuracy of ionogram predictions declined at higher frequencies.

Improving short-term ionogram forecasts is crucial before attempting to train a NN to derive electron densities directly

from ionograms. However, our results suggest that even short-term datasets may be sufficient for producing accurate ionogram forecasts. We argued that this could be because the dominant periodic forces in the ionosphere are well-resolved within 3 months of data, providing enough temporal information to capture key patterns in ionospheric behavior.

Data availability statement

The datasets generated for this study can be found in the repository "Training data for IoNNo model" located at https://doi.org/10.5281/zenodo.13840721.

Author contributions

ER: Conceptualization, Data curation, Formal Analysis, Investigation, Methodology, Project administration, Resources, Software, Supervision, Validation, Visualization, Writing – original draft, Writing – review and editing. JA: Conceptualization, Data curation, Formal Analysis, Investigation, Methodology, Software, Visualization, Writing – review and editing. MM: Conceptualization, Formal Analysis, Supervision, Writing – review and editing.

Funding

The author(s) declare that financial support was received for the research, authorship, and/or publication of this article. MIT staff was partially supported by NSF grant AGS-1952737. The ionosonde data was obtained from Jicamarca's Radio Observatory database. The Jicamarca Radio Observatory is a facility of the Instituto Geofisíco del Perú operated with support from NSF award AGS-1732209.

Acknowledgments

The authors would like to thank Reynaldo Rojas for his suggestions for the training of the neural networks.

Conflict of interest

The authors declare that the research was conducted in the absence of any commercial or financial relationships that could be construed as a potential conflict of interest.

Generative AI statement

The author(s) declare that no Gen AI was used in the creation of this manuscript.

Publisher's note

All claims expressed in this article are solely those of the authors and do not necessarily represent those of their affiliated organizations, or those of the publisher, the editors and the reviewers. Any product that may be evaluated in this article, or claim that may be made by its manufacturer, is not guaranteed or endorsed by the publisher.

References

Akiba, T., Sano, S., Yanase, T., Ohta, T., and Koyama, M. (2019). "Optuna," in *Proceedings of the 25th ACM SIGKDD international Conference on knowledge discovery data mining (ACM)*, 2623–2631. doi:10.1145/3292500.3330701

Bilitza, D., Pezzopane, M., Truhlik, V., Altadill, D., Reinisch, B. W., and Pignalberi, A. (2022). The International Reference Ionosphere Model: A Review and Description of an Ionospheric Benchmark. *Reviews Geophy.* 60, e2022RG000792. doi:10.1029/2022RG0007921

Camporeale, E. (2019). The challenge of machine learning in space weather: nowcasting and forecasting. *Space weather.* 17, 1166–1207. doi:10.1029/2018SW002061

Camporeale, E., Wing, S., Johnson, J., Jackman, C. M., and McGranaghan, R. (2018). Space weather in the machine learning era: a multidisciplinary approach. *Space weather.* 16, 2–4. doi:10.1002/2017SW001775

Gowtam, V. S., and Ram, S. T. (2017). An artificial neural network-based ionospheric model to predict nmf2 and hmf2 using long-term data set of formosat-3/cosmic radio occultation observations: preliminary results. *J. Geophys. Res. Space Phys.* 122 (11), 743–755. doi:10.1002/2017JA024795

Hu, A., and Zhang, K. (2018). Using bidirectional long short-term memory method for the height of f2 peak forecasting from ionosonde measurements in the australian region. *Remote Sens.* 10, 1658. doi:10.3390/rs10101658

Kelley, M. C. (2009). *The Earth's Ionosphere: Plasma Physics and Electrodynamics*. 2nd Edn. San Diego, CA: Academic Press. Available online at: https://www.elsevier.com/books/the-earths-ionosphere/kelley/978-0-12-088425-4.

Laštovička, J., and Burešová, D. (2023). Relationships between fof2 and various solar activity proxies. *Space weather.* 21. doi:10.1029/2022SW003359

McGranaghan, R. M. (2024). Complexity heliophysics: a lived and living history of systems and complexity science in heliophysics. *Space Sci. Rev.* 220, 52. doi:10.1007/s11214-024-01081-2

Reyes, P. (2017). *Study of waves observed in the equatorial ionospheric valley region using Jicamarca ISR and VIPIR ionosonde* (Ph.D. Dissertation). Urbana, Illinois: University of Illinois at Urbana-Champaign. Available online at: http://hdl.handle.net/2142/98349.

Triebe, O., Hewamalage, H., Pilyugina, P., Laptev, N., Bergmeir, C., and Rajagopal, R. (2021). Neuralprophet: explainable forecasting at scale

Uwamahoro, J. C., Giday, N. M., Habarulema, J. B., Katamzi-Joseph, Z. T., and Seemala, G. K. (2018). Reconstruction of storm-time total electron content using ionospheric tomography and artificial neural networks: a comparative study over the african region. *Radio Sci.* 53, 1328–1345. doi:10.1029/2017RS006499

VanderPlas, J. T. (2018). Understanding the lomb–scargle periodogram. *Astrophysical J. Suppl. Ser.* 236, 16. doi:10.3847/1538-4365/aab766

Wang, W., Lei, J., Burns, A. G., Qian, L., Solomon, S. C., Wiltberger, M., et al. (2011). Ionospheric day-to-day variability around the whole heliosphere interval in 2008. *Sol. Phys.* 274, 457–472. doi:10.1007/s11207-011-9747-0

Frontiers in
Astronomy and Space Sciences

Explores planetary science and extragalactic astronomy in all wavelengths

Advances the understanding of our universe - from planetary science to extragalactic astronomy, to high-energy and astroparticle physics.

Discover the latest Research Topics

See more →

Frontiers

Avenue du Tribunal-Fédéral 34
1005 Lausanne, Switzerland
frontiersin.org

Contact us

+41 (0)21 510 17 00
frontiersin.org/about/contact